OCRWM	MODEL COVER SHEET	1. QA: QA Page 1 of 290

2. Type of Mathematical Model

X Process Model ☐ Abstraction Model ☐ System Model

Describe Intended Use of Model

3. Title

Dike/Drift Interactions

4. DI (including Rev. No. and Change No., if applicable):

MDL-MGR-GS-000005 REV 00

5. Total Attachments	6. Attachment Numbers - No. of Pages in Each
	I-22, II-36, III-20

	Printed Name	Signature	Date
7. Originator	E.S. Gaffney	SIGNATURE ON FILE	17 Sep 03
8. CSO	J.L. Younker	SIGNATURE ON FILE	9-18-03
9. Checker	G.N. Keating	SIGNATURE ON FILE	9-17-03
10. QER	K.O. Gilkerson	SIGNATURE ON FILE	9-22-03
11. Responsible Manager/Lead	K.M. Cline	SIGNATURE ON FILE	10/8/03
12. Responsible Manager	J.L. King	SIGNATURE ON FILE	10/8/03

13. Remarks

Supporting authors: B. Damjanac, E. Sonnenthal, N.R. Warpinski, K.H. Wohletz, and C. Detournay.

TER-02-0100 has been addressed by including a summary of this AMR's outputs and output DTNs in Section 8 of this report.

OFFICE OF CIVILIAN RADIOACTIVE WASTE MANAGEMENT
MODEL REVISION RECORD

2. Model Title:

Dike/Drift Interactions

3. DI (including Rev. No. and Change No., if applicable):

MDL-MGR-GS-000005 REV 00

4. Revision/Change No.	5. Description of Revision/Change
Rev 00	Initial Issue

CONTENTS

Page

CONTENTS (Continued)

Page

CONTENTS (Continued)

Page

CONTENTS (Continued)

Page

CONTENTS (Continued)

Page

INTENTIONALLY LEFT BLANK

FIGURES

Page

FIGURES (Continued)

Page

FIGURES (Continued)

Page

FIGURES (Continued)

Page

FIGURES (Continued)

Page

FIGURES (Continued)

Page

FIGURES (Continued)

Page

FIGURES (Continued)

Page

TABLES

Page

INTENTIONALLY LEFT BLANK

ACRONYMS, ABBREVIATIONS, AND SYMBOLS

1D	one dimensional
2D	two dimensional
3D	three dimensional
BSC	Bechtel SAIC Company
CM	configuration management
CRWMS M&O	Civilian Radioactive Waste Management System Management and Operating Contractor
DIRS	Document Input Reference System
DTN	Data Tracking Number
EBS	engineered barrier system
FCI	fuel-coolant interaction
FEPs	features, events, and processes
GPa	gigapascal (10^9 pascals, SI unit of pressure)
K	kelvin (SI unit of temperature)
kg	kilogram (SI unit of mass)
kJ	kilojoule (10^3 joules, SI unit of energy)
LEFM	linear-elastic fracture mechanics
m	meter (SI unit of distance)
MPa	megapascal (10^6 pascals, SI unit of pressure)
NRC	U.S. Nuclear Regulatory Commission
OCRWM	Office of Civilian Radioactive Waste Management
Pa-s	pascal-second (SI unit of dynamic viscosity)
PKN	Perkins-Kem-Nerdgren
QA	quality assurance
Re	Reynolds number
s	second (SI unit of time)
SI	System International (The International System of Units)
TSPA	Total System Performance Assessment
TSPA-LA	Total System Performance Assessment-License Application
TWP	technical work plan

ACRONYMS, ABBREVIATIONS, AND SYMBOLS (Continued)

V	version
W	watt (SI unit of power)
WP	waste package
YMP	Yucca Mountain Project
YMRP	Yucca Mountain Review Plan

1. PURPOSE

1.1 SCOPE OF WORK

This report documents the model of events associated with a potential intrusion of magma from a volcanic dike into a drift or drifts in the Yucca Mountain Nuclear Waste Repository. The following topics are included in this report:

- A discussion of dike propagation, which provides the basis for describing the path that a representative dike, or swarm of dikes, would follow during an event.

- A discussion of magma flow, which evaluates the interaction at the junction of the propagating dike with the drift and the movement of magmatic products into and down drifts and, potentially, through a drift to the surface by way of access drift or a secondary dike opened up along the drift.

- A discussion of gas flow and conductive cooling of a magma-filled drift, describing how an adjacent drift that has not been intersected by a dike could be affected by post-intrusion phenomena. Note that a gas flow analysis is also addressed in *Igneous Intrusion Impacts on Waste Form and Waste Packages* (BSC 2003 [DIRS 161810]) , and those results are consistent with the results presented in this report.

This breakdown of topics is roughly in the order in which events related to a volcanic event would occur. Figure 1 is an artist's portrayal of four stages of dike/drift interaction. The first two stages, "initial encounter" and "magma intrusion," are discussed in this report under the overall heading of dike propagation. The "eruption" stage indicates the potential for magma to move beyond the repository to the surface and is discussed under the heading of magma flow. In this depiction, the main flow of the magma continues along the original trajectory of the dike after magma has filled a drift. A failed attempt by the magma to breakout along a pre-existing fracture system at the end of the drift is also shown. Surface events of an eruption are described in BSC 2001 [DIRS 160130] and the recent update BSC 2003 [DIRS 161838]. [Note: A unique six-digit numerical identifier (the Document Input Reference System [DIRS] number) is placed in the text following each reference callout whose purpose is to assist the reader in locating a specific reference in the DIRS database.] The fourth, "cooling and diffusion" stage occurs over the course of a few decades following an intrusion in the repository. This last stage includes transport of corrosive volcanic gases and heat through the rock and through backfilled access drifts separating individual drifts.

The logical flow of the discussion of models in the report roughly follows the chronology depicted in Figure 1. However, there is some interaction between various parts of the model. Figure 2 shows the arrangement of the model discussion in Section 6 and which elements interact by feeding to or being fed by other elements. The models presented in this report support the conceptual basis for the TSPA igneous groundwater transport model and volcanic eruption model, which purposely are implemented as two separate models: one for intrusion and one for eruption. The TSPA-LA model report discusses the technical basis for implementing the models in this manner.

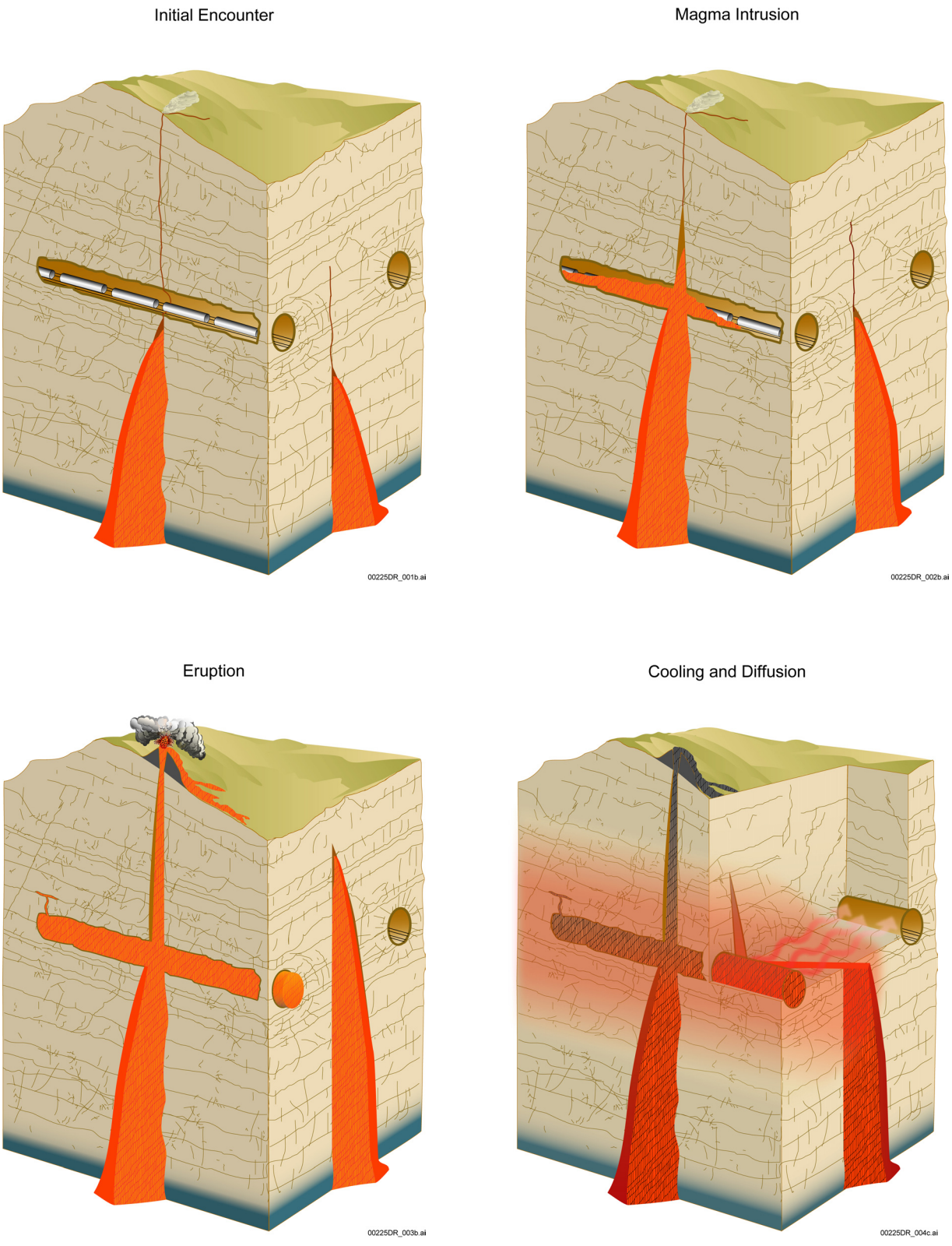

Figure 1. Artist's Representation of the Stages of Interaction Between a Volcanic Dike and Drifts

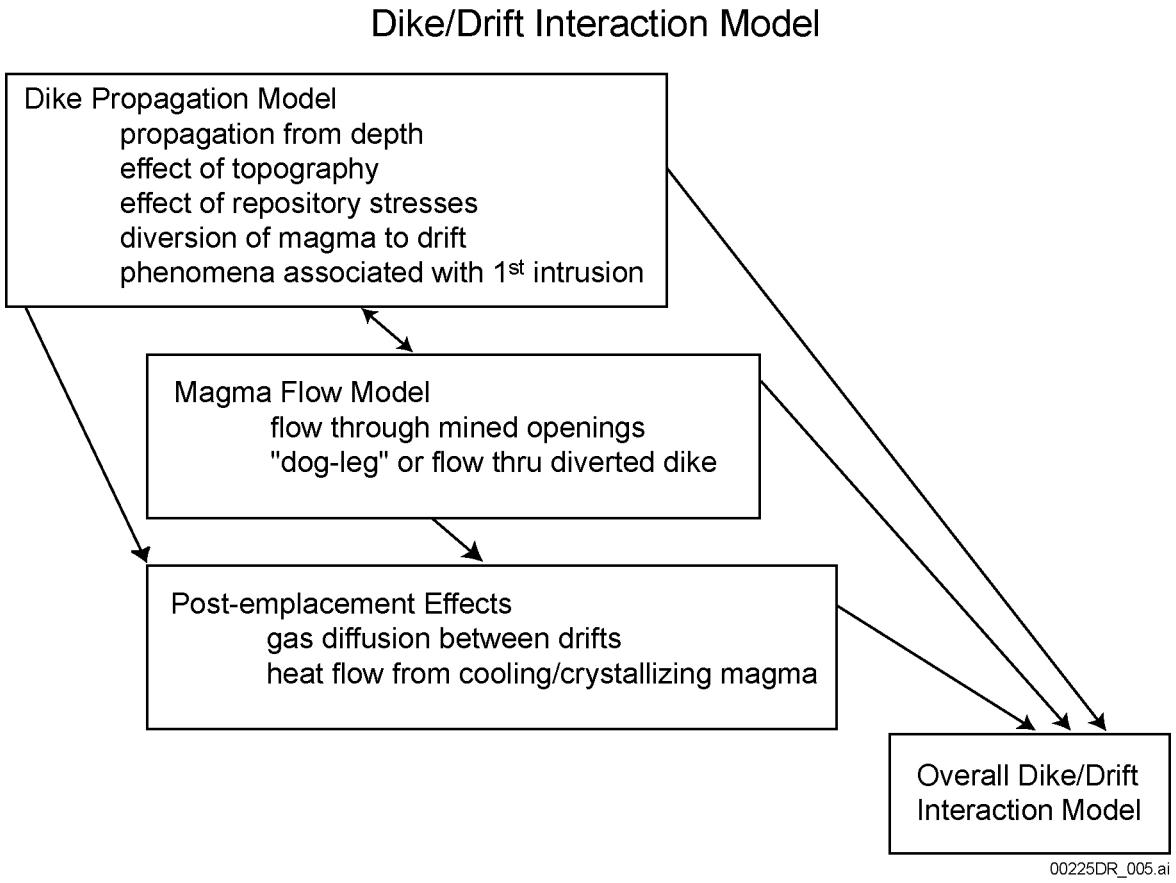

Figure 2. Logical Flow of Discussion of the Elements of the Dike/Drift Interaction Model

1.1.1 Dike Propagation Near Drifts

The objective of the dike propagation modeling is to provide realistic input conditions to the magma and gas flow studies to assess the interaction of the magmatic products with the drift, waste packages, and debris in the drifts. Of particular importance are the manner in which the dike intersects the repository, the pressure (and pressure history) of the magma and volatiles, the width of the dike (and thus the amount of magma available to flow into the drifts) as a function of time, and the effect of magma loss into the repository on the aforementioned items.

The dike propagation mathematical model calculates: (1) the pressure conditions and dike parameters that would exist at the point of intersection with the repository for use as initial conditions for the magma flow analysis; (2) the effect that magma loss into the repository would have on subsequent dike growth; (3) the change in stresses adjacent to the repository due to the presence of the dike; and (4) the properties of a possible “dog-leg” dike initiating along a drift at some distance from the original dike/drift intersection. The model investigates the effects of in-situ and thermally induced stress fields on the dike path, i.e., potential deflection of the dike away from the repository. Stress analysis (presented in Section 6.3.9.2.2) shows that a shielding effect of increased horizontal stresses at the repository level, which could cause the dike deflection, would be limited in both time and space after waste emplacement.

The model provides support for determining boundary conditions (related to dike propagation) for "leak-off" of magma into a drift. The model accommodates changing conditions to which the dike might react along a pathway including, the undisturbed area below the repository, the altered area around the repository, and finally, conditions that would occur as the dike continues upward and after it has passed through the zone of influence of the repository. The results of this model support the report *Features, Events, and Processes: Disruptive Events* (BSC 2003 [DIRS 163573]) by providing a quantitative description of the features that such a dike would exhibit.

1.1.2 Magma Flow

The magma flow model and supporting analyses address the interaction of magma with drifts. The model describes the conceptual structure that is the basis for the analyses presented in this report. The model calculates conditions that could occur if pressurized magma were to encounter a representative emplacement drift; temperature and phase changes are not included directly in the backfill interaction portion of the magma flow model. This approach provides the basis for a description of the potential state of emplacement drifts after a dike intrusion. The model also provides support for determining the potential for initiation of new fractures or reopening of existing joints inside the drift as a result of dike/drift interaction, and the possibility of the dike continuing on its path at the initial point of dike/drift intersection or its being diverted. It describes the magmatic products that could be found in drifts that are fully or partially engulfed in magma or that have products developed from magmatic gases, and it describes the cooling of magma in secondary dikes that might begin to grow out of a drift after intrusion. It does not describe the engineered barrier system (EBS) component damage conditions but describes the magmatic products and environmental conditions to which these components might be exposed. It supports the analysis report *Features, Events, and Processes: Disruptive Events* (BSC 2003 [DIRS 163573]) by providing a quantitative description of the events and processes that would result from such an interaction and the analysis report *Number of Waste Packages Hit by Igneous Intrusion* (BSC 2003 [DIRS 161851]) by providing the basis for describing the post-intrusion state of intersected drifts. The results of the model are compared with a U.S. Nuclear Regulatory Commission (NRC) alternative conceptual model, which postulates that the intrusive event initiates with a wall of hot high-pressure magma across the entire 5.5-m diameter cross-section of an emplacement drift and results in rapid compression of the air and shock waves reverberating in the drifts (Woods et al. 2002 [DIRS 163662]).

1.1.3 Post-Emplacement Phenomena

Development of the gas flow analysis addresses the potential migration of volcanic gases from a drift that has been filled with magma (either effusive or pyroclastic) through the surrounding tuff to an adjacent drift that has not been intruded. This approach provides the basis for evaluating the potential for corrosion of waste packages by magmatic gases containing corrosive gases such as sulfur, chlorine, and fluorine. Evaluation of heat flow to adjacent drifts by thermal conduction is also addressed in analysis of post-emplacement phenomena. This analysis includes flow of both sensible heat and latent heat by thermal conduction and provides the basis for evaluating the potential for degradation of waste packages by heating. This analysis supports the analysis

report *Number of Waste Packages Hit by Igneous Intrusion* (BSC 2003 [DIRS 161851]) by quantifying the effect of a dike on nearby drifts that have not been intruded.

1.1.4 Igneous Intrusion Impacts on Waste Packages and Waste Forms

This report does not describe the effects on waste packages and waste form resulting from a volcanic event. An engineered barrier system report, *Igneous Intrusion Impacts on Waste Packages and Waste Form* (BSC 2003 [DIRS 161810]), analyses magma flow and gas flow with emphasis on in-drift geochemical and disruptive effects on waste packages and waste form, explicitly for an intrusive scenario. Both reports mutually corroborate conclusions regarding the impact of magma flow, gas flow, thermal conduction and geochemical impacts, either implicitly or explicitly for effusive or pyroclastic conditions. The studies may use different assumptions appropriate for the emphasis of the two documents, but are generally consistent as both derive the basis for the separate models from the report *Characterize Eruptive Processes at Yucca Mountain* (ANL-MGR-GS-000002, BSC 2003 [DIRS 161838]). Together, both provide the technical basis for the TSPA-LA disruptive event model and consequence models.

1.2 BACKGROUND

The following sections discuss the conceptual model of dike/drift interaction used for past Yucca Mountain TSPA analyses and present the objectives of this report as defined by the *Technical Work Plan for Igneous Activity Analysis for Disruptive Events* (BSC 2003 [DIRS 164143]) for this activity.

1.2.1 Previous Reports

This report represents a major revision to information included in *Dike Propagation Near Drifts* (CRWMS M&O 2000 [DIRS 151552]). The present document expands the numerical analytical support for the conceptual model of dike/drift interaction.

Earlier versions of the technical work plan (TWP) indicated that the magma and gas flow analysis would examine the interaction of magmatic products with "waste packages and debris" in drifts. The scope of this model report has changed. Output from this model report could be used by the Waste Package and Waste Form Departments for determining effects on EBS components.

1.3 LIMITATIONS OF MODEL AND ANALYSES

Outputs from this report are used to address the stress field and to determine the viability of potential dike propagation conceptual models or in other intermediate geotechnical models. The magma flow analysis and post-emplacement studies examine a range of potential conditions for each magma parameter that controls the characteristics of the flow conditions. No parameters are passed directly to the *Total System Performance Assessment-License Application* (TSPA-LA); rather, parameter time histories could be used by the waste form and waste package groups to determine possible damage states, which then are passed to the TSPA-LA.

1.3.1 Models

This report addresses the models and analyses that support the Dike/Drift Interactions Model—the limitations of which are addressed in the following section.

1.3.1.1 Limitations of Dike Propagation Model

The principal limitation of the dike propagation model is that it addresses the growth of a dike due to upward movement of an incompressible magma, whereas real magma would be compressible (BSC 2001 [DIRS 160130], pp. 33–38). The effect of compressibility was addressed in the *Final Report of the Igneous Consequences Peer Review Panel* (Detournay et al. 2003 [DIRS 162914], pp. 44–45), which concluded that the two significant differences resulting from compressibility are "the substantial increase in the flow velocity at the magma front and the amount by which this exceeds the velocity of the magma front. Both effects increase the gas flux into the cavity relative to the flux out." But, they conclude that at "cavity pressures below the dike normal stress (lower by an amount that exceeds the dike excess pressure, so perhaps a few MPa), the tip becomes unstable." Hence, the effect of compressibility would be to increase the tendency for the dike tip to accelerate as it approaches the ground surface.

1.3.1.2 Limitations of Magma Flow

The main limitation of the magma flow model is that it treats the magma as a single compressible or incompressible phase. This limitation occurs as a result of the analytical formulations used to describe the flow of magma out of the dike and into the drifts. Thus, the processes and effects associated with expansion of a pyroclastic flow into a drift were not modeled.

1.3.1.3 Limitations of Post-Emplacement Analysis

The general limitations of the post-emplacement gas flow analysis are documented in the model report *Drift-Scale Coupled Processes (DST and THC Seepage) Models* (BSC 2003 [DIRS 163506]). The main limitations of the post-emplacement heat flow analysis are that the thermal diffusivity of the magma and the surrounding rock are taken to be equal and that the variation of the thermal diffusivity with temperature is not considered. Latent heat of crystallization of the magma is addressed in an approximate manner.

2. QUALITY ASSURANCE

Development of this model report and the supporting activities have been determined to be subject to the Yucca Mountain Project's Quality Assurance (QA) program (BSC 2003 [DIRS 164143], Section 8.1, Work Packages P4A1224DF1/ADEM03, P4D1224DFU/ADET03, 8191225DUA). Approved QA procedures identified in the TWP (BSC 2003 [DIRS 164143], Section 4) have been used to conduct and document the activities described in this model report. The TWP also identifies the methods used to control the electronic management of data (BSC 2003 [DIRS 164143], Section 8.4).

The model report discusses phenomena associated with a potential volcanic intrusion into the drift complex of the repository, which is an important threat to compliance with the post-closure performance objectives proscribed in 10 CFR 63.113 [DIRS 156605]. Therefore it is classified as a "Quality Level – 1" with regard to importance to waste isolation, as defined in AP-2.22Q, *Classification Criteria and Maintenance of the Monitored Geologic Repository Q-List*. The report contributes to the analysis and modeling data used to support performance assessment. The conclusions do not directly impact engineered features important to safety, as defined in AP-2.22Q, except for the possible change to backfill design contained in Section 6.4.10.1.4.

INTENTIONALLY LEFT BLANK

3. USE OF SOFTWARE

3.1 SOFTWARE TRACKED BY CONFIGURATION MANAGEMENT

The computer codes used directly in this modeling activity are summarized in Table 1. The qualification status of the software is indicated in the electronic DIRS database. All software was obtained from configuration management (CM) and is appropriate for the application. Qualified codes were used only within the range of validation.

Table 1. Computer Software

Software Title and Version (V)	Software Tracking Number	Code Usage	Computer, Type, Platform, and Location
NPHF2D, V 1.0 [DIRS 163665]	10904-1.0-00	Dike Propagation Model; performs numerical modeling supporting analysis of magmatic dike propagation and analysis of the dike/drift interaction where magma enters a drift, modified and requalified for this task.	PC; Windows; LAN
TOUGHREACT, V 3.0 [DIRS 161256]	10396-3.0-00	Drift-Scale Gas Flow Model simulations; couples multiphase fluid flow, heat flow, aqueous and gaseous species transport, and kinetic and equilibrium mineral-water-gas reactions	DEC-Alpha with Unix OSF1 V5.1 and OSF1 V5.0, Sun Solaris 5.5.1, Linux Redhat 7.2
FLAC3D, V 2.1 [DIRS 161947]	10502-2.1-00	Analyzes regional stresses, accounting for topography; analyzes backfill deformation by magma; analyzes opening of pre-existing fractures by magma	PC Windows 2000/NT 4.0
UDEC, V 3.1 [DIRS 161949]	10173-3.1-00	Analyzes opening of pre-existing fractures by magma	PC Windows 2000/NT 4.0

3.2 EXEMPT SOFTWARE

Standard, built-in functions of Microsoft Excel 2000 (9.0.3821 SR-1) for the Dell Inspiron 8000 computer or Microsoft Excel 97 for the Compaq V900 computer were used to calculate some parameters. This software is exempt from the QA requirements.

INTENTIONALLY LEFT BLANK

4. INPUTS

4.1 DATA, PARAMETERS, AND OTHER MODEL INPUTS

This subsection identifies all input parameters and other forms of model inputs that are used in the analyses detailed in this report.

Input information used in this model report comes from several sources, which are summarized in Table 2. The data are fully appropriate for the discussion of dike/drift interactions in this model report. The qualification status of the input sources is provided in the Technical Data Management System (TDMS).

This report may be affected by technical product input information that requires confirmation. Any changes to the document that may occur as a result of completing the confirmation activities will be reflected in subsequent revisions. The status of the input information quality may be confirmed by review of the DIRS database.

4.1.1 Data and Parameters

The input parameters for this model report are listed in Table 2. Input parameters [DIRS 164744] for the gas flow analysis are found in the model report *Drift-Scale Coupled Processes (DST and THC Seepage) Models* (BSC 2003 [DIRS 163506]). Inputs for the thermomechanical model in Sections 6.3.9.1.1 and 6.3.9.2.2 can be found in *Drift Degradation Analysis* (BSC 2003 [DIRS 162711]).

In many cases where a single value is given for a parameter, the value has been selected as a single value that is within the range of values in the cited document. Where the results of the input are not sensitive to the exact value of the input parameter, values may have been rounded while staying in the appropriate range. Uncertainties of the parameters are addressed in Section 6, as indicated in Table 2.

Table 2. Input Parameters Used in Dike/Drift Interaction Model

Model or Analysis Parameter	Source	Section where Discussed
Dike Propagation and Flow into Drifts Model		
Regional topography	BSC 2003 [DIRS 162711]	6.3.4.1
Repository layout	BSC 2003 [DIRS 162711]	6.3.4.1
Ratio of horizontal principal stresses to vertical stress	BSC 2003 [DIRS 162711]	6.3.4.1
Orientations of horizontal principal stresses	BSC 2003 [DIRS 162711]	6.3.4.1
Stratigraphy near repository	BSC 2003 [DIRS 162711]	6.3.4.1
Young's modulus of host rock	DTN: MO0304DQRIRPPR.002 [DIRS 164462]	6.3.4.1
Poisson's ratio of host rock	DTN: MO0304DQRIRPPR.002 [DIRS 164462]	6.3.4.1
Bulk specific heat of host rock	BSC 2003 [DIRS 162711]	6.3.4.1

Table 2. Input Parameters Used in Dike/Drift Interaction Model (Continued)

Model or Analysis Parameter	Source	Section where Discussed
Bulk thermal conductivity of host rock	BSC 2003 [DIRS 162711]	6.3.4.1
Fault properties	BSC 2003 [DIRS 162711]	6.3.4.1
Heat release and removal	BSC 2003 [DIRS 162711]	6.3.4.1
Bulk density of host rock	DTN: SNL02030193001.027 [DIRS 108410]	6.3.4.2
Young's modulus of host rock	DTN: MO0304DQRIRPPR.002 [DIRS 164462]	6.3.4.2, 6.4.3.4
Poisson's ratio of host rock	DTN: MO0304DQRIRPPR.002 [DIRS 164462]	6.3.4.2, 6.4.3.4
Bulk density of magma	DTN: LA0107GV831811.001 [DIRS 160708]	6.3.4.2
Bulk viscosity of magma	DTN: LA0107GV831811.001 [DIRS 160708]	6.3.4.2
Magma far-field velocity	DTN: LA0107GV831811.001 [DIRS 160708]	6.3.4.2
Dike far-field width	DTN: LA0107GV831811.001 [DIRS 160708]	6.3.4.2
Horizontal stress vs. depth	Stock et al. 1985 [DIRS 101027] and SNF37100195002.001 [DIRS 131356]	6.3.4.2
Drift diameter	BSC 2003 [DIRS 162289]	6.3.4.3, 6.3.4.4
Drift spacing	BSC 2003 [DIRS 162289]	6.3.4.3, 6.3.4.4
Magma vesicle-free density	DTN: LA0107GV831811.001 [DIRS 160708]	6.3.4.3
Magma Flow to the Surface Model		
Turnout dimension	BSC 2003 [DIRS 164493]	6.4.5.1
Friction angle of backfill	Fruchtbaum 1988 [DIRS 161774]	6.4.5.1
Dilation of backfill	Marachi et al. 1972 [DIRS 157883]	6.4.5.1
Cohesion of backfill	Duncan et al. 1980 [DIRS 161776]	6.4.5.1
Pressure of magma	BSC 2003 [DIRS 162711]	6.4.5.2
Drift diameter	BSC 2003 [DIRS 162289]	6.4.5.2
Young's modulus of host rock	DTN: MO0304DQRIRPPR.002 [DIRS 164462]	6.4.5.2
Poisson's ratio of host rock	DTN: MO0304DQRIRPPR.002 [DIRS 164462]	6.4.5.2
Bulk density of magma	DTN: LA0107GV831811.001 [DIRS 160708]	6.4.5.2
Bulk viscosity of magma	DTN: LA0107GV831811.001 [DIRS 160708]	6.4.5.2, 6.4.5.3
Magma thermal diffusivity	Detournay et al. 2003 [DIRS 162914]	6.4.5.3

Table 2. Input Parameters Used in Dike/Drift Interaction Model (Continued)

Model or Analysis Parameter	Source	Section where Discussed
Drift diameter	BSC 2003 [DIRS 162289]	6.4.5.3
Drift spacing	BSC 2003 [DIRS 162289]	6.4.5.3
Magma far-field velocity	DTN: LA0107GV831811.001 [DIRS 160708]	6.4.5.3
Specific heat of magma	Spera 2000 [DIRS 164109]	6.4.5.3
Latent heat of magma	Spera 2000 [DIRS 164109]	6.4.5.3
Intrusion temperature	DTN: LA0107GV831811.001 [DIRS 160708]	6.4.5.3
Solid fraction vs. temperature	Detournay et al. 2003 [DIRS 162914], ApTbl 2E	6.4.5.3
Post-Emplacement Effects		
Temperature	BSC 2003 [DIRS 163506], Table 6.2-1 DTN: LB0302DSCPTHCS.001	6.5.1.4
pH	BSC 2003 [DIRS 163506], Table 6.2-1 DTN: LB0302DSCPTHCS.001	6.5.1.4
Pore-water composition	BSC 2003 [DIRS 163506], Table 6.2-1 and DTN: MO0005PORWATER.000 [150930]	6.5.1.4
Gas composition	BSC 2003 [DIRS 163506], Table 6.2-1 and DTN: MO0005PORWATER.000 [DIRS 150930]	6.5.1.4
Specific heat of magma	Spera 2000 [DIRS 164109]	6.5.2.1.1
Latent heat of magma	Spera 2000 [DIRS 164109]	6.5.2.1.1
Intrusion temperature	DTN: LA0107GV831811.001 [DIRS 160708]	6.5.2.1.1
Average thermal diffusivity of host rock and magma	Detournay et al. 2003 [DIRS 162914]	6.5.2.1.1

4.2 CRITERIA

The general requirements to be satisfied by Total System Performance Assessment (TSPA) are stated in 10 Code of Federal Regulations (CFR) 63.114 [DIRS 156605]. Technical requirements to be satisfied by TSPA are identified in the Yucca Mountain *Projects Requirements Document* (Canori and Leitner 2003 [DIRS 161770]). The acceptance criteria that will be used by the NRC to determine whether the technical requirements have been met are identified in the *Yucca Mountain Review Plan* (YMRP) (NRC 2003 [DIRS 163274]). The pertinent requirements and criteria for this model report are summarized in Table 3.

Table 3. Project Requirements for This Model Report

Requirement Number*	Requirement Title*	10 CFR 63 Link	YMRP Acceptance Criteria†
PDR-002/T-015	Requirements for Performance Assessment	10 CFR 63.114 (a)–(c) and (e)–(g); 10 CFR 63.21(c)(1)-(3), (9), (10), (15), (19)	Criteria 1 to 4 for *Volcanic Disruption of Waste Packages*; Criteria 1 of *Airborne Transport of Radionuclides*; Criteria 1 to 5 for *Mechanical Disruption of Engineered Barriers*

NOTE: * from Canori and Leitner 2003 [DIRS 161770]
† from NRC 2003 [DIRS 163274], Sections 2.2.1.3.10.3, 2.2.1.3.11.3

Links between the acceptance criteria identified in Sections 2.2.1.3.2.3, 2.2.1.3.10.3, and 2.2.1.3.11.3 are described in Appendix III of this model report.

4.3 CODES AND STANDARDS

No other standards or code requirements other than those referenced in Section 4.2 apply to this model report.

5. ASSUMPTIONS

This section summarizes the assumptions used by the Dike/Drift Interactions Model. Assumptions specific to each component of this report are described in the main text of Section 6, and only the subsection numbers for those discussions are identified here. Assumptions are grouped within this section according to the individual supporting analyses they affect.

5.1 DIKE PROPAGATION ASSUMPTIONS

1. *Assumption:* The analysis of dike propagation in Sections 6.3.8 and 6.3.9.2.3.2 assumes that the magma is incompressible, whereas real magma is a mixture of liquid and gas (with or without solids) that can be highly compressible (BSC 2001 [DIRS 160130]).

   Sources of assumed behavior: This is the standard assumption for hydrofracture analysis.

   Rationale: The numerical model used has been developed for oil-field hydrofracture applications, which use liquid water as the driving fluid. For those applications, incompressibility liquid is a good assumption. The dike propagation model is insensitive to the compressibility of the magma, as discussed in Detournay et al. (2003 [DIRS 162914]). In addition, magma incompressibility in the magma flow model is found not to have a major effect on crack opening rates (see Section 6.4.10.2.1).

   Need for confirmation: At this time, there is no need to confirm this assumption, because the model is insensitive to the compressibility of magma.

2. *Assumption*: The analysis of dike propagation in Section 6.3.8 and 6.3.9.2.3.2 assumes that a dike can be represented by a 2D hydraulic fracture, whereas the problem of a dike propagating away from a deep magma source is a 3D problem.

   Sources of assumed behavior: This is a standard assumption for hydraulic fracturing analyses in order to make the problem tractable. Dike/drift interaction is simulated using a 3D model described in Section 6.3.9.2.3.3.]. Section 6.3.5 argues that a dike propagating upward near the surface takes on a reasonable 2D character and, although the early time modeling of the dike may not be accurate using a 2D model, the late time behavior (which is the behavior of interest) can be appropriately modeled using a 2D approach that specifically takes account of the presence of the free surface.

   Rationale: The problem of a dike propagating away from a deep magma source clearly is a 3D problem. Remote from the source, the dike can be approximated by so called PKN (Perkins and Kern 1961 [DIRS 163644]; Nordgren 1972 [DIRS 163641]) and KGD (Khristianovic and Zheltov 1955 [DIRS 164511]) models. The KGD model assumes that dike deformation and propagation result from plane strain. This model is appropriate if the dike strike length is limited by faults or pre-existing fractures and if there is small shear resistance in fault planes to dike opening. The PKN model assumes an elliptical-shaped horizontal cross-section of the dike. In this case plane strain (2D) is present within a vertical cross-section, particularly if strike length is large in comparison to length in

vertical plane and far from the free surface. Otherwise, conditions of deformation and propagation are 3D.

Need for confirmation: Confirmation of validity of 2D assumption is justified for the case where the dike tip is near the free surface.

3. *Assumption*: The analysis of dike propagation in Sections 6.3.8, 6.3.9.2.3.2, and 6.3.9.2.3.3 assumes that the rock behaves elastically, whereas the actual rock behavior for a dike-scale event may be inelastic.

   Sources of assumed behavior: This is a standard assumption for hydraulic fracturing analyses in order to make the problem tractable and is the only possible approach given the absence of in situ data indicating non-linear behavior.

   Rationale: Elastic behavior is a reasonable assumption for small-scale pressurized fractures in the Earth, but a dike will cross many joints, faults, bedding planes, and other discontinuities in the rock and will generate significant earthquakes as slippage occurs in response to the large changes in stress generated by the inflated, propagating dike. No information is available from any source on the rock behavior of large, heterogeneous masses. Regardless, inelastic effects will serve to increase the width of the dike and decrease the pressure. These are competing effects at the repository level, with the pressure being the primary boundary condition for subsequent calculations of magma and gas flow, but the width of the dike provides a constraint on how much magma may be lost into the drift. Since the pressure is the main factor for the subsequent calculation, it is believed that using elastic behavior is a conservative assumption because it serves to generate the highest pressures.

   Need for confirmation: Confirmation is not required because additional information would have a negligible effect on the analysis.

4. *Assumption*: The analysis of dike propagation in Sections 6.3.8, 6.3.9.2.3.2, and 6.3.9.2.3.3 assumes that the rock properties are linear, although rocks typically exhibit considerable nonlinearity.

   Sources of assumed behavior: This is a standard assumption for hydraulic fracturing analyses in order to make the problem tractable.

   Rationale: Most rocks have nonlinear behavior, with lower moduli (a) at low stress and (b) in the ground in the presence of joints and bedding planes. Non-linear behavior would be very difficult to incorporate into a hydraulic fracture model and little data are available on in situ rock behavior. However, linear-elastic behavior will produce the greatest possible pressure and is, thus, a conservative assumption.

   Need for confirmation: Confirmation is not required because linear-elastic behavior is conservative.

5. *Assumption*: The analysis of dike propagation in Sections 6.3.8, 6.3.9.2.3.2, and 6.3.9.2.3.3 assumes that the rock mass is a homogeneous, isotropic material, although actual rock

masses (a) are typically transversely isotropic due to bedding, (b) are jointed and faulted, and (c) have many stratigraphic units, each having different values of Young's modulus and Poisson's ratio.

Sources of assumed behavior: This is a standard assumption for most hydraulic fracturing analyses.

Rationale: In general, the rock properties of the strata below the repository and joints and faults deep in the Earth are not well known. However, although it is true that the deformation at any one point is a cumulative effect of the deformation everywhere in the dike, the influence of any point on another point decreases with distance. Thus, in lieu of a capability to incorporate multiple layers (which the model does not have) and in the absence of detailed information on other rock properties, the dike behavior near the repository is best modeled by using the rock properties at the repository. This approach is not necessarily a conservative assumption but, rather, is the only assumption that can be made to obtain tractable models and sufficiently complete input parameters.

Need for confirmation: Confirmation is not required because this is the only possible assumption for analyzing the behavior of a deep-source dike.

6. *Assumption*: The analysis of dike propagation in Sections 6.3.8, 6.3.9.2.3.2, and 6.3.9.2.3.3 assumes that the dike is propagating as a single vertical fracture, although many hydraulic fractures and dikes are known to exhibit multiple fracture strands and *en echelon* behavior.

   Sources of assumed behavior: This is a standard assumption for hydraulic fracturing analyses in order to make the problem tractable.

   Rationale: Although many hydraulic fractures and dikes are known to exhibit multiple fracture strands and *en echelon* behavior, the overall dike behavior is still reasonably modeled with a single fracture, based on over 50 years of oilfield experience. Obviously, the more complex behavior observed in the field is due to complexities of the formation that are not known or otherwise available for modeling endeavors. Furthermore, dikes probably exhibit the least complexity of pressurized fractures in the Earth because the high viscosity of the magma does not allow easy penetration of the fluid into joints or faults, and thus, secondary fracture strands are not easily initiated.

   Need for confirmation: Confirmation is not required because additional information would have a negligible affect on the analysis.

7. *Assumption*: The analysis of dike propagation in Sections 6.3.8, 6.3.9.2.3.2, and 6.3.9.2.3.3 assumes that the magma flow is laminar whereas Reynold's numbers may exceed the threshold for transition to turbulence.

   Sources of assumed behavior: This is a standard assumption for hydraulic fracturing analyses in order to make the problem tractable.

   Rationale: Laminar flow of the magma in the dike is essential for pressure drop calculations under the Poiseuille formulation (see Section 6.3.1.1). Laminar flow is

expected to occur for Reynold's numbers less than 2,000. The Reynold's number for flow in a fracture could approach and even exceed 2,000 for some combinations of conditions. However, for an incompressible fluid of fixed viscosity, Reynold's numbers greater than or equal to 2,000 would require flow conditions exceeding the physical limitations of dike and/or magma flow conditions. Nothing is known about possible transition behavior of magma, and fully turbulent flow is unlikely for any possible set of conditions. Thus, it is reasonable to assume laminar flow behavior under all circumstances.

Need for confirmation: Confirmation is not required because the assumption is conservative and additional information would have a negligible affect on the analysis.

8. *Assumption*: The analysis of dike propagation in Sections 6.3.8, 6.3.9.2.3.2, and 6.3.9.2.3.3 assumes that the lubrication approximation is appropriate for modeling dike propagation even though the Reynold's numbers exceed those under which this assumption is valid.

   Sources of assumed behavior: This is a standard assumption for hydraulic fracturing analyses in order to make the problem tractable and is theoretically appropriate for a dike.

   Rationale: The lubrication approximation is appropriate (and exact) for slow motion of viscous fluids so that the viscous forces are considerably greater than the inertial forces, thus allowing the inertial forces to be neglected. These flows are also called creeping motion. However, creeping motion can be considered as solutions of the full Navier-Stokes equations for cases where $Re \rightarrow 0$ (ratio of inertial to viscous forces goes to zero). As noted in the previous assumption, Reynolds numbers can be fairly large, which would appear to negate the use of this approximation. However, the actual reason the lubrication approximation is appropriate is that flow in a long 2D fracture is a "parallel flow," which is identical to the one-dimensional (1D) lubrication equation with the exception of an additional time derivative of the velocity and the dropping of one spatial derivative. Since hydraulic fractures, and more certainly dikes, are slowly varying with time and position, the time derivative is negligible and the spatial derivative drops out as well. Consequently the steady "parallel flow" approximation is the same as the 1D lubrication equation. In support of this reduction, the "lubrication approximation" has been used for 40 years in hydraulic fracturing (with larger Reynold's numbers) with good success and no apparent discrepancies. Thus, this approximation appears reasonable and appropriate here.

   Need for confirmation: Confirmation is not required because this assumption has proven adequate for hydraulic fracturing analyses with larger Reynold's number and is theoretically appropriate for a dike.

9. *Assumption*: The analysis of dike propagation in Sections 6.3.8, 6.3.9.2.3.2, and 6.3.9.2.3.3 assumes that the fluid has Newtonian behavior whereas a magma is a complex melt mixture that may have non-Newtonian characteristics.

   Sources of assumed behavior: This is a simple and widely used assumption about magma behavior.

Rationale: A Newtonian fluid is one that obeys Stokes' law of friction, for which the relationship between stress and rate of strain is linear. This formulation considerably simplifies calculations of fluid resistance and is known to apply to many common fluid systems. Although a more complex fluid behavior could be used (e.g., with yield stress and power-law behavior), little is known about magmas, and the additional parameters in those models would incorporate uncertain parameters. It seems more appropriate to retain the Newtonian framework and vary the viscosity to account for possible differences.

Need for confirmation: Confirmation is not required because additional information would have a negligible affect on the analysis.

10. *Assumption*: The analysis of dike propagation in Sections 6.3.8 and 6.3.9.2.3.2 assumes that linear-elastic fracture mechanics governs the fracture propagation criterion whereas the dike propagation problem may be considerably more complex.

    Sources of assumed behavior: This is a standard assumption for hydraulic fracturing analyses in order to make the problem tractable.

    Rationale: Linear-elastic fracture mechanics (LEFM) is a discipline that has been well studied and is widely applicable to small-scale fractures in the laboratory, mines, concrete, and other typical engineering applications. In hydraulic fracturing, however, the fracture toughness of the rock generally has a negligible effect, and the applicability of fracture toughness has been questioned for large-scale fractures propagating under internal pressure. The dike propagation problem is concerned with an even larger-scale feature and undoubtedly involves anelastic behavior in the surrounding rock. Thus, LEFM may not be strictly appropriate for this application. However, the LEFM formulation allows the fracture toughness to be used as a parameter that is indicative of the resistance of the rock to fracture, whatever the actual mechanism may be. Treated as a parameter, fracture toughness can be used to investigate the effect of any mechanism that resists fracture growth and thus increases the pressure.

    Need for confirmation: Confirmation is not required because additional information would have a negligible affect on the analysis.

11. *Assumption*: The analysis of dike propagation in Sections 6.3.8, 6.3.9.2.3.2, and 6.3.9.2.3.3 assumes that the surface is horizontal, whereas the repository is in a mountain.

    Sources of assumed behavior: This is a standard assumption for hydraulic fracturing analyses in order to make the problem tractable.

    Rationale: The surface topography at Yucca Mountain is relatively severe, but the dike propagation model treats it as a horizontal surface. This approach is a conservative assumption because the additional load of the mountain could serve to deflect any dike away from the mountain (e.g., into the basins). However, analysis of in-situ stresses in Section 6.3.9.1.1 demonstrates that topography has negligible effect on the dike path.

    Need for confirmation: Confirmation is not required because additional information would have a negligible affect on the analysis.

12. *Assumption:* The analysis of dike propagation in Sections 6.3.8 and 6.3.9.2.3.2 assumes that the dike rises from a depth equal to or larger than 2l^*, where l^* is the characteristic length defined in Eq. 19, Section 6.3.8.1.

    Sources of assumed values: As explained in Attachment I, at depths greater than 2l^* the dike propagation solution produces a self-similar solution. Therefore, if the actual source depth is greater than 2l^*, it is sufficient to start the simulation at the depth equal to 2l^*.

    Rationale: A likely source depth will be greater than the 8160 m, the largest depth used in the dike propagation simulations.

    Need for confirmation: Confirmation is not required because this assumption is equivalent to using the postulated value. Additional information would negligibly affect the analysis.

13. *Assumption:* The analysis of dike propagation in Section 6.3.9.2.3.2 assumes that the pressure of the vapor in the cavity above the magma in the growing dike is between 0 and 2.1 MPa.

    Sources of assumed values: The values assumed are between atmospheric pressure, which is the ambient pore pressure in the unsaturated zone, and the horizontal far-field stress (perpendicular to the dike) at the repository level. The specific values are taken to be consistent with the scaling relations for fluid-driven crack propagation as described in Attachment I.

    Rationale: The pressure will be substantially lower than either the horizontal far-field stress or the vapor pressure of the magma because the rock into which the dike is intruding has a very high gas permeability.

    Need for confirmation: Confirmation is not required, because the largest gas pressure considered of 2.1 MPa is relatively close to the expected value of the horizontal far-field stress. Gas pressures in the tip cavity that are equal to or are approaching the horizontal far-field stress will cause dike tip instability.

14. *Assumption:* The analysis of dike propagation using a 2D model in Section 6.3.9.2.3.2 assumes that between 0 and 40 percent of the flow of the growing dike is diverted into the drifts when the magma front reaches the drift.

    Sources of assumed values: The bleed-off will, by definition, be between 0 and 100 percent.

    Rationale: These values were chosen to illustrate the effect of magma bleed-off on the continued upward propagation of the dike tip after intersection of drifts, subject to stability of the numerical scheme used in the calculation.

    Need for confirmation: The analysis of magma flow in drifts indicates that 100 percent may be realistic until the drift is filled. However, a 2D model, in which the localized leak-off is smeared, becomes numerically unstable when more than 40 percent of magma from the dike is diverted into the drifts. Therefore, the dike/drift interaction for condition

of 100 percent magma diversion into the drifts is simulated using a 3D model described in Section 6.3.9.2.3.3.

5.2 MAGMA FLOW ASSUMPTIONS

15. *Assumption:* The analysis of magma flow into a drift in Section 6.3.9.2.3.1 assumes that the flow is incompressible. The assumption of magma incompressibility in the magma flow model is found not to have a major effect (Section 6.4.10.2.1).

    Sources of assumed behavior: Standard hydraulic engineering models.

    Rationale: The assumption of incompressibility is required to allow solution of the flow equations using a simple spreadsheet tool.

    Need for confirmation: At this time, there is no need to confirm this assumption, as stated above.

16. *Assumption:* The analysis of magma flow in Section 6.3.9.2.3.1 assumes that the magma flow into the drift is effusive rather than pyroclastic.

    Sources of assumed behavior: Effusive flow can arise from a wet magma source if the magma nearest the front has degassed due to prolonged exposure to low tip-cavity pressure and highly permeable country rock (see Assumption 13).

    Rationale: Analysis of pyroclastic flow is not possible with the approach used. Effusive behavior is also consistent with Assumption 15.

    Need for confirmation: The assumed effusive behavior represents one end member of a continuum of possible behaviors for magma erupting at a free surface. In TSPA-LA, volcanic eruption is modeled separately from an intrusive event. For intrusive conditions, pyroclastic flow will not result in the very large 3D expansions that would be expected for an extrusive pyroclastic event. Therefore, the effusive assumption will be better than it might be for an extrusive model, but confirmation of the behavior of a restricted pyroclastic intrusion may be appropriate. For the eruption model, the pyroclastic nature of the event does not need to be investigated so long as both models account for source terms separately and results of the dog-leg analyses continue to support the TSPA eruptive model. (See Section 6.4.11.3.)

17. *Assumption:* The analysis of magma flow in Section 6.3.9.2.3.1 assumes that the internal pressure of the magma at the magma/drift interface is between 3 MPa and 15 MPa.

    Sources of assumed values: The analysis report *Characterize Eruptive Processes at Yucca Mountain, Nevada* (BSC 2001 [DIRS 160130]).

    Rationale: These values were chosen to represent the range from slightly above atmospheric to well above the overburden pressure.

Need for confirmation: Confirmation is not required because additional information would have negligible affect on the analysis.

18. *Assumption:* The analysis of magma flow in Section 6.3.9.2.3.1 assumes that the length of drift available to be filled by magma is 500 m.

    Sources of assumed values: This is just below the upper limit of drift length in *Repository Design, Repository/PA IED Subsurface Facilities* (BSC 2003 [DIRS 162289]).

    Rationale: The response of shorter drift sections can readily be inferred from analysis of a 500-m drift, and extrapolation to the maximum of 800 m is uncomplicated.

    Need for confirmation: Confirmation is not required because additional information would negligibly affect the analysis.

19. *Assumption:* The analysis of magma flow in Section 6.3.9.2.3.1 assumes that the diameter of a waste package is 1 m.

    Sources of assumed values: A simple value was selected arbitrarily.

    Rationale: The analysis is used to show the general nature of the effect of waste packages on the flow, not to generate predictions of magma behavior.

    Need for confirmation: Confirmation is not required because the results can be extrapolated to realistic values.

20. *Assumption:* The analysis of backfill deformation in Section 6.4.10.1 assumes that the density of the backfill is 1000 kg/m^3.

    Sources of assumed values: Approximated.

    Rationale: The analysis is very insensitive to the value of density used.

    Need for confirmation: Confirmation is not required because additional information would negligibly affect the analysis.

5.3 DRIFT SCALE GAS FLOW ASSUMPTIONS

The general assumptions of the Drift-Scale Gas Flow are documented in the model report *Drift Scale Coupled Processes (DST and THC Seepage) Models* (BSC 2003 [DIRS 163506]). Specific assumptions for this analysis are presented below.

21. *Assumption:* Temperature of the volcanic gas is fixed at 573 K in Section 6.5.1.

    Sources of assumed values: Approximated, based on maximum temperature verified for thermodynamic data used.

    Rationale: For the "higher-temperature" results, the volcanic gas temperature is assumed fixed at 573 K and the pressure in the drift at ~88 MPa, which is done because the

thermodynamic data for aqueous and gaseous species used in the calculations are not verified above that temperature. Despite being well below the temperature of the volcanic gases as they are first exsolved from the magma, the temperature is high enough to show the effects of boiling of pore water in the rock surrounding the drifts. Thermal analyses discussed in Section 8.5 also indicate that temperatures at a distance of about 2.5 m from the drift wall will be above 573 K only for the first 3 years after intrusion. At greater ranges or longer times, there will be little effect at all. For the "lower-temperature" results, the temperature is fixed at 296 K, which eliminates the boiling zone and allows for more rapid transport of the soluble volatiles CO_2 and SO_2. As such, it provides an upper limit on their mobility.

Need for confirmation: Confirmation is not required because higher temperatures would result in a larger boiling zone, which would further retard the gas migration, as indicated by the comparison of the high and low temperature results.

5.4 MAGMA COOLING AND SOLIDIFICATION ASSUMPTIONS

The magma cooling and solidification analysis in section 6.5.2 is intended to illustrate the scale of temperature changes around a drift, and especially at the range of adjacent drifts, that would result from cooling and solidification of magma that has filled a drift. Specific assumptions for this analysis are presented below.

22. *Assumption:* Density of host rock is 1980 kg/m^3 and density of magma in filled drift is 2800 kg/m^3.

    Sources of assumed values: Approximated, based on density of rocks of similar composition.

    Rationale: The density appears only indirectly in the calculations by way of the thermal diffusivity (defined as the thermal conductivity divided by the product of the density and the heat capacity). As such, the density *per se* does not affect the calculation as long as it is chosen so that the correct thermal diffusivity is obtained. As discussed in Section 6.5.2.3.1, the values of diffusivity are consistent with those used by the Igneous Consequences Peer Review Panel in their Final Report (Detournay et al. 2003 [DIRS 162914]).

    Need for confirmation: Confirmation is not required because the results are insensitive to the specific value used.

INTENTIONALLY LEFT BLANK

6. MODEL DISCUSSION

The dike/drift interaction model describes processes that would occur if an igneous intrusion were to intercept the repository. The model consists of two separate models, a dike propagation model and a model of magma flow to the surface, and of supporting analyses and applications. These products describe processes ranging from initial propagation of the dike from depth, how the repository structure itself modifies that propagation, magma breakout to the surface, and late-time effects such as cooling and gas transport.

Figure 3 provides a summary outline indicating where important parts of the models and analyses are to be found in this section and, in parentheses ( ), the software used in the models and analyses.

Highlights of the Organization of this Section

6.3 DIKE PROPAGATION MODEL
- 6.3.1.1 Propagation From Depth (NPHF2D [DIRS 163665])
- 6.3.8 Base-Case Model Results (NPHF2D [DIRS 163665])
  - 6.3.8.2 Dike Properties at Intersections with Drifts (NPHF2D [DIRS 163665])
- 6.3.9 Supporting Analyses and Model Applications
  - 6.3.9.1 Effect of Natural Stresses on Dike Propagation (FLAC3D [DIRS 161947])
  - 6.3.9.2 Effect of Repository Structure on Dike Propagation (FLAC3D [DIRS 161947], spreadsheet)
  - 6.3.9.2.3 Diversion of Magma Into a Drift (NPHF2D [DIRS 163665], FLAC3D [DIRS 161947], spreadsheet)

6.4 MODEL FOR MAGMA FLOW
- 6.4.10 Model Results
  - 6.4.10.1 Flow Through Mined Openings (FLAC3D [DIRS 161947])
  - 6.4.10.2.1 Crack Opening Rates (UDEC [DIRS 161969], FLAC3D [DIRS 161947])
- 6.4.11 Supporting Analyses and Model Applications
  - 6.4.11.1 Stress-Related Effects (spreadsheet)
  - 6.4.11.2 Fracture Criteria
  - 6.4.11.3 Results of “Dog-Legs” Stress Calculations
  - 6.4.11.4 Magma Cooling Rates (spreadsheet)
  - 6.4.11.5 Synthesis for Dog-Leg

6.5 POST-EMPLACEMENT EFFECTS

NOTE: Number to the left of the model analysis description indicates section of this report where the model or analysis is discussed. Entry in parentheses () is name(s) of software employed in model or analysis.

Figure 3. Highlights of the Organization of this Section

6.1 MODELING OBJECTIVES

The objective of the modeling discussed in this report is to provide a description of the mechanical, thermal and chemical environment encountered by waste packages should a volcanic event disrupt the repository.

6.2 FEATURES, EVENTS, AND PROCESSES INCLUDED IN THE MODEL

The development of a comprehensive list of features, events, and processes (FEPs) potentially relevant to postclosure performance of the potential Yucca Mountain repository is an ongoing, iterative process based on site-specific information, design, and regulations. The approach for developing an initial list of FEPs in support of the *Total System Performance Assessment for the Site Recommendation* (CRWMS M&O 2000 [DIRS 153246]) was documented in Freeze et al. (2001 [DIRS 154365]). The initial FEPs list contained 328 FEPs, of which 176 were included in *Total System Performance Assessment for the Site Recommendation* models (CRWMS M&O 2000 [DIRS 153246], Tables B-9 through B-17). To support the TSPA-LA, the FEPs list was re-evaluated in accordance with the Enhanced FEP Plan (BSC 2002 [DIRS 158966], Section 3.2).

In the TWP for igneous activity analysis (BSC 2003 [DIRS 164143]), Tables 3 and 4 provide a listing of both included and excluded FEPs for each of the disruptive events (DE) analysis and model reports. One FEP, 1.2.04.01.00 Igneous Activity, that was listed as included in the TWP, was deleted during the FEPs review for TSPA-LA and conducted as part of the Enhanced FEPs Plan. The description of the FEP was found to be entirely redundant with more specific igneous related FEPs. The TSPA-SR FEPs 1.2.04.02.0A, Igneous Activity Causes Changes to Rock Properties; 1.2.04.05.00, Magmatic Transport of Waste; and 1.2.10.02.00, Hydrologic Response to Igneous Activity, were previously, and continue to be, excluded. The technical basis for exclusion of these FEPs was previously provided in CRWMS M&O (2000 [DIRS 151553]).

Table 4 provides a list of FEPs that are included in the TSPA-LA through the use of the results of the analysis described in this document. Details of the implementation of these FEPs are summarized in Section 6.3 through Section 6.5.

For each of the included FEPs listed in Table 4, the implementation in TSPA-LA is described in this analysis report. Details of the implementation are summarized here in the table, including specific reference to sections within this document. The parameters that address the included FEPs are also listed. The sources of input for these parameters are described in Section 4 for input parameters, and elsewhere in Section 6 if they were specifically developed within this document.

Table 4. Included Features, Events, and Processes for This Model Report and Their Disposition in TSPA-LA

TSPA-SR FEP Number, Name, and Description	TSPA-LA FEP Number, Name and Description	Section Where Disposition is Described	Summary of TSPA-LA Disposition
1.2.04.03.00 Igneous Intrusion into Repository *Magma from an igneous intrusion flows into the drifts and extends over a large portion of the repository site, forming a sill. The sill could be limited to the drifts or a continuous sill could form along the plane of the repository, bridging between adjacent drifts.*	1.2.04.03.0A Igneous Intrusion into Repository *Magma from an igneous intrusion flows into the drifts and extends over a large portion of the repository site, forming a sill, dike, or dike swarm depending on the stress conditions. This could involve multiple drifts. The sill could be limited to the drifts or a continuous sill could form along the plane of the repository, bridging between adjacent drifts.*	Section 6.3 contains the overall model description, assumptions and simplifications. Section 6.3.8 contains the mathematical description of the base-case model. Sections 6.3.9.2 and 6.3.9.3 contain an analysis of the effect on dike propagation of magma and gas losses from a dike when it intersects a drift. Section 6.4.10 contains analyses of the formation of dikes and sills at repository level after a dike has intercepted a drift.	This FEP is partially addressed, and the consequences constrained, by consideration of potential dike paths and dimensions, which takes the form of a dike-propagation analysis. The dike-propagation analyses presented in this model report include use of a numerical code based on a displacement-discontinuity boundary-element formulation. The code includes all essential elements necessary for the simulation of hydraulic fracturing: fracture propagation, viscous fluid flow inside the fracture, and fluid leak-off in the surrounding formation. Fracture propagation is based on linearly elastic fracture mechanics. The approach is elastic and assumes plane-strain conditions of deformation. The dike propagation model described in this model report applies a fracture-propagation approach using representative igneous dike properties to calculate key parameters such as dike width, dike pressure, and dike propagation velocity as the repository is approached and intersected. The sensitivity of the crack path to other model parameters (e.g., magma viscosity) and initial conditions (e.g., dike velocity at depth or driving pressure) is also considered. The model also uses an existing quantitative stress analysis to aid in evaluating how the stress field around the repository could influence propagation of a basaltic igneous dike and accommodates changing conditions along the pathway to which the dike may react including the undisturbed area below the repository, the altered area around the repository, and finally, conditions that apply as the dike continues upward after it has passed through the zone of influence of the repository. Input parameters and values or ranges of values are provided in Section 4. These parameters include the following: • Rock Properties (Young's modulus, Poisson's ratio, density, specific heat, thermal conductivity) • Magma Properties (density, viscosity, latent heat, ascent rate, intrusion temperature, solidus temperature, specific heat, thermal conductivity, pressure) • Magma Flow Rate at Source • Horizontal In-Situ Stress versus Depth • Depth of the Repository • Drift Properties (diameter, depth, spacing, invert thickness)

Table 4. Included Features, Events, and Processes for This Model Report and Their Disposition in TSPA-LA (Continued)

TSPA-SR FEP Number, Name, and Description	TSPA-LA FEP Number, Name and Description	Section Where Disposition is Described	Summary of TSPA-LA Disposition
1.2.04.03.00 Igneous Intrusion into Repository (Continued)	1.2.04.03.00A Igneous Intrusion into Repository (Continued)		The dike propagation model provides various output that are used as input parameters for the magma and gas flow model and for assessing the formation of sills and secondary dikes. The dike propagation numerical model calculates and provides output to determine: • The location of the tip of and fluid-front in the propagating fracture over time and with respect to the repository level • The pressure conditions and dike parameters over time at the point of intersection with the repository, for use as initial conditions for the magma-drift analysis (magma and gas flow model) • The effect of the magma loss into the repository on subsequent dike growth • The change in horizontal and vertical stresses on the repository due to the presence of the dike The output of the dike propagation model is not used directly in the TSPA-LA model but is used to refine the conceptual model of dike propagation. The model output provides support for: • Determining the potential for initiation of new fractures or reopening of existing joints inside the drift as a result of dike/drift interaction • The likelihood of the dike continuing on its path at the initial point of dike/drift intersection or its being diverted • The selected boundary conditions (related to dike propagation) for “leak-off” of magma into a drift The output of this model provides the support for a conceptual dike propagation model that precludes development of a conduit extending from the original point of drift intersection to encompass the entire length of the drift (forming a “dog-leg”), and addresses the conditions pertaining to flow into drifts at the point of intersection. In this way, the model implicitly defines the manner in which igneous intrusion into the repository is included in the TSPA-LA model—that is, by defining the maximum length of an intersected drift that is involved in the direct flow path and providing input for the magma and gas flow model. As noted in the TWP for igneous activity analysis (BSC 2003 [DIRS 164143], this FEP is also addressed in *Characterize Framework for Igneous Activity* (ANL-MGR-GS-000001).

Table 4. Included Features, Events, and Processes for This Model Report and Their Disposition in TSPA-LA (Continued)

TSPA-SR FEP Number, Name, and Description	TSPA-LA FEP Number, Name and Description	Section Where Disposition is Described	Summary of TSPA-LA Disposition
1.2.04.04.00 Magma Interacts with Waste *An igneous intrusion in the form of a dike occurs through the repository, intersecting waste. This leads to accelerated waste container failure (e.g., attack by magmatic volatiles, damage by fragmented magma, thermal effects) and dissolution of waste (Commercial Spent Nuclear Fuel (CSNF), Defense Spent Nuclear Fuel (DSNF), and DOE High Level Waste (DHLW).*	1.2.04.04.0A Igneous Intrusion Interacts with EBS Components *An igneous intrusion in the form of a dike occurs through the repository, intersecting the repository drifts. Magma, pyroclastics, and volcanic gases enter the drift and interact with the EBS components including the drip shields, the waste packages, and the invert. This leads to accelerated drip shield and waste package failure (e.g. attack by magmatic volatiles, damage by flowing or fragmented magma, thermal effects) and dissolution or volatilization of waste.*	Section 6.3.9.2.2 contains an analysis of the diversion of magma into a drift.Section 6.3.9.4 provides an analysis of the phenomena associated with the beginnings of an intrusion, including both peak and "final" environmental values. Section 6.4.10 contains an analysis of the backfill's ability to block magma flow through access drifts. Section 6.5 provides analyses of post-emplacement behavior, including cooling of magma in a drift and migration of volcanic gases out of a filled drift, which can be used to determine effects on adjacent drifts.	This FEP is partially addressed, and the consequences constrained, by consideration of potential interaction of the drift and other EBS Components with magma flowing into an intersected drift. The magma and gas flow model addresses conditions that could occur when pressurized magma encounters a representative emplacement drift and its influence on the rock properties near the drift. The model uses standard design equations from hydraulic engineering to describe the flow of magma into a drift after magma has risen to repository level. In addition, one derived equation is used to account for viscous drag in the dike as magma flows into a drift. The parameters used as input in this model related to this FEP include the following: • Magma: Density, Latent Heat, Ascent Rate, Intrusion Temperature, Solidus Temperature, Specific Heat, Thermal Conductivity, Viscosity, and Pressure • Emplacement Drift: Diameter, Spacing, Invert Thickness • Backfill: Density, Constitutive Properties • Access Drift: Height, Width. The magma and gas flow model output defines: • The environmental conditions created by magmatic interaction with a model emplacement drift, both empty and with an element simulating a single, long, waste package the length of the drift. • The environmental conditions (temperature, pressure, velocity of material, etc.) as a function of the distance from the point of dike intersection. • Distribution of magmatic products as a function of distance from the point of dike intersection. The outputs of the Magma and Gas flow Model (i.e., environmental conditions along the drift) could be used as inputs to determine and constrain the direct (Zone 1) and indirect (Zone 2) igneous-related waste-package damage status, as documented in *Igneous Intrusion Impacts on Waste Package and Waste Form* (BSC 2003 [DIRS 161810]). The outputs of the model indicated that the entire length of an intersected drift has the potential to be filled, at least partially, with either magma or pyroclastic materials. The temperature history outputs from the magma and gas flow model suggest that any waste package in contact with either magma or pyroclastic materials will be exposed to conditions at or near thermal limitations of the waste-package materials. Therefore, the TSPA-LA model assumes that all waste packages present in an intersected drift provide no further protection. The output of the backfill analysis indicates that the backfill in access drifts, as currently designed, will not be an effective barrier to magma flow. An approach to make the backfill more effective is included as a part of this analysis. The outputs of the model are also used as inputs to the indirect (Zone 2) igneous-related waste-package damage status to define the potential for volcanic gas migration in adjacent areas of the repository. The outputs also support the conceptual approach of *Number of Waste Packages Hit by Igneous Intrusion* (BSC 2003 [DIRS 161851]), which is used to determine the source term for calculating igneous-related dose. Consequently, the results of this model report and the related FEP are considered to be implicitly included in the TSPA-LA.

6.3 DIKE PROPAGATION MODEL

The conceptual model for dike propagation is one that broadens a hydraulic fracture model (1) for applications near a free surface and (2) with a sink point to model magma loss into a repository. The basic components of a hydraulic fracture or dike model include (1) the elastic deformation of a crack due to the internal pressure of the fluid, (2) the viscous losses of the moving magma within the fracture, (3) fluid losses into the surrounding medium, and (4) a crack propagation criterion that accounts for the resistance of the rock to fracture. These components must be calculated interactively to assure proper coupling of the various mechanisms. Because of the many unknowns associated with modeling a dike over distances of thousands of meters, the model was necessarily simplified by considering only a 2D geometry.

A dike is a pressurized fracture, much like a hydraulic fracture created in an oil or gas well, which is fed by a high-pressure source of magma deep in the earth. The high pressure of the magma in the dike pushes aside the surrounding rock, often creating widths of several meters or more. Nevertheless, the restricted width of the dike induces frictional losses in the high-viscosity magma that result in a pressure drop along the length of the dike. Thus, the overall problem is an interaction that results in a balance between the high pressure that opens the dike (width) and the appropriate restriction (width) that keeps the pressure at the required level through viscous losses.

Another important mechanism in hydraulic fracturing is seepage of fluid into the surrounding medium, but the magma viscosity is too high for the magma to leak into the pores of the host rock. One important additional feature that is included in the present dike propagation model is a "sink" parameter, that is, the ability to extract magma from the fracture at a specified location. This feature is included to model the loss of magma into the repository.

Inelastic processes associated with the crack tip are typically incorporated in hydraulic fracture models by way of a fracture toughness, a measure of the energy required to open new crack surfaces. However, large-scale fractures are not thought to have any dependency on fracture toughness. A second unique feature is the inclusion of the free surface in the model. Most, if not all, hydraulic fracture and dike models consider the propagation in an infinite medium, and effects near a free surface are not accounted for. Such effects, like unstable growth and an altered width distribution, can be evaluated in the dike propagation model.

In general, a dike propagating from a source at depth would be expected to start out with a radial front that expands outward from the source. Nevertheless, most dikes have relatively short surface expressions (relative to their depth) that suggest some mechanism, such as bounding faults, have restricted their lateral propagation. Thus, at least near the surface (in the vicinity of the repository), a 2D approximation of dike propagation is a reasonable assumption for calculating dike parameters.

6.3.1 Model Description

A detailed description of the mathematical formulation of the dike propagation model can be found in Attachment I.

6.3.1.1 Propagation From Depth

The elastic deformation can be modeled using either analytic or numerical approaches, but numerical approaches have much more flexibility and therefore are used in this application. In particular, the boundary-element approach—specifically the displacement discontinuity method—is used here because of its simplicity and flexibility for crack problems (Crouch and Starfield 1983 [DIRS 139600]).

This method is based on the analytic solution to the problem of a finite line crack whose opposing sides have been displaced relative to one another in an infinite elastic solid. A crack is divided into N sections, each of which has a constant displacement over its segment, but every segment may have a different displacement from other segments. Because the analytic solution for a single element is known, the numerical solution is found by summing the effects of all N elements; however, in this application the elemental discontinuities are not known and must be calculated. If the pressure is known everywhere in the crack, then values of the elemental displacement discontinuities that are necessary to produce the pressure can be calculated by solving a system of equations. In this way, the general deformation of the crack can be determined as accurately as desired by increasing the number of elements.

The rock material that is deforming is considered to be a linear-elastic material characterized by Young's modulus, E, and Poisson's ratio, ν. This approach is clearly an appropriate assumption for small, fluid-filled fractures but may be questioned for large-scale dikes where many faults, joints, and bedding discontinuities may be intersected and respond anelastically. Linear elastic behavior would be a conservative assumption because anelastic behavior would serve to increase dike widths and reduce pressures at the repository.

The viscous pressure drop along the length of the dike is calculated assuming laminar flow of a Newtonian fluid through parallel plates (Poiseuille flow) in the lubrication approximation of the Navier-Stokes equation ($dp/dx = 12q\mu/w^3$). The lubrication approximation is generally considered appropriate for slow-moving viscous laminar fluids in narrow apertures, such as magma flow through a dike. The Poiseuille flow approximation is valid because the dike width is a very slowly varying function of depth, particularly as the dike gets longer and approaches the repository.

The primary assumptions are Newtonian viscosity and laminar flow. Little is known about the rheological characteristics of magma in dikes, so the Newtonian assumption was deemed appropriate because it involves the fewest unknown parameters (e.g., pseudoplastic or Bingham plastic behavior would require two parameters). The laminar approximation is valid for the flow rates, dike widths, and magma viscosities that are anticipated, but Reynold's numbers may exceed thresholds for laminar/turbulent transition in some cases, primarily because of the wide fracture and high density of the material. For a magma density = 2280 kg/m^3, dike width of 1 m,

dike velocity of 1.5 m/sec, and viscosity of 10 Pa-s, the Reynolds number is 684 (laminar). No attempt is made to consider any transition effects because this would be largely speculative.

Standard hydraulic fracture models consider the leak-off of fracture fluid into the surrounding rock formations. However, in the dike propagation case, the rock formations encountered by the dike will be impermeable to the liquid magma. Thus, no generalized leak-off is included in this model. However, leak-off of volatiles is still anticipated (this will affect the tip-cavity zone) and a localized leak-off is available, as will be discussed in adaptations below.

A crack propagation criterion is used in some hydraulic fracture models to include the effect of rock resistance to fracture, but it is also ignored in many models because the effects are negligible for large-scale fractures. In the dike propagation model, fracture toughness effects are included and can be evaluated. However, the scale of a dike is so large that it is not likely that the details of stress intensity calculations are strictly applicable. For example, the stresses are extremely large (on the order of several MPa) around the fracture tip and extend for many tens of meters. Damage likely occurs throughout this region, negating any rigorous use of LEFM. In this model, the fracture toughness is used as a convenient parameter for assessing possible scale-dependent, anelastic behavior that may provide additional resistance to fracture growth.

In addition to the fracture toughness, the tip region is also affected by a fluid lag zone. As the propagating dike approaches the level of the drifts, the crack tip separates from the magma front because of the inability of the high-viscosity fluid to reach the very narrow tip. This separation results in a vapor-filled cavity, which is the first part of the propagating dike that encounters the drift. Cavity formation is followed some time later by magma. A significant difference between the present model and the analysis of the previous version of this report, *Dike Propagation Near Drifts* (CRWMS M&O 2000 [DIRS 151552]), is that the cavity pressure is taken to be negligible in the present model because of the very high gas permeability of the tuff. To evaluate tip-cavity effects, a range of values is used to assess reasonable values of a tip pressure that might develop. In conjunction with other aspects of the model, the tip pressure controls the length of the tip-cavity region.

In addition to these standard components of a hydraulic fracture model, the dike propagation model also includes the effect of a free surface in the deformation calculations. In this case, the solution for a displacement dislocation in a half space (Hills et al. 1996 [DIRS 163626]) is used. This formulation allows for the correct deformation in the proximity of a free surface.

The other nonstandard addition to the model is a localized leak-off capability that simulates the loss into the repository when the dike intersects it. This localized leak-off can use any functional form of the fluid loss because it is controlled by an input parameter table that specifies the rate as a function of time after intersection.

The dike propagation model calculates the growth history of a dike propagating toward the surface in the vicinity of the repository. No attempt is made to model the topography of the site, as a complex surface topography formulation is beyond the capabilities of any current model. However, aspects of topographical features can be accounted for through the incorporation of a horizontal in-situ stress distribution that reflects the stresses around the repository. In addition,

the heated repository can also be considered by using appropriate prescribed horizontal stresses taken from the thermomechanical modeling of the repository.

Although the dike may be deflected because of topographic and/or thermomechanical stress effects, the modeling performed here makes the conservative assumption that the dike will propagate through the repository.

As the magma rises in the dike, the flow is concentrated toward the center of the dike, with the magma at the very edge of the dike not moving upward at all. The shearing between the center of the dike and the walls will result in elongation of any vapor bubbles in that part of the magma and thus, lowering the effective viscosity, so there may be a tendency for slug flow in the center of the dike.

There are two possibilities for the state of the magma in the center as it moves upward into the cavity. One is that, as magma rises in the dike and approaches the cavity, it releases gas in a steady way. Stasiuk et al. (1996 [DIRS 164459]) describe a silicic volcanic conduit exposed in southwestern New Mexico that shows clear evidence of this process. The other is that the liquid and vapor phases of the magma are so closely coupled that the release of gas is more catastrophic. (The conceptual model adopted for the present report assumes the former style.) A simple Stokes law analysis indicates that bubbles will rise even faster than the liquid magma, breaking as they approach the surface, just as is seen when water in a pot is heated from below and boils. The net result of this behavior is that the liquid at the magma front has lost much of its volatile content and is therefore not likely to produce violent explosive behavior when it first encounters the drift. Both gas and liquid interact with the drift, but their flow is largely decoupled on the scale of the hydrodynamics of the two fluids. This makes it feasible to treat the liquid magma as an incompressible fluid.

6.3.2 Model Uncertainties

Given that the dike propagation problem is relatively complex, any attempt at numerical modeling will have numerous embedded uncertainties. The approach taken in the base-case modeling is a 2D model of a 3D process. Although the large scale of a dike is very favorable for creating 2D processes in the center of the dike, the effect of 3D features is beyond the scope of this report.

Similar uncertainties exist with regard to fluid and rock properties. The modeling requires that the fluid be incompressible and the properties constant so that minimal differentiation (particularly vertically) within the magma is allowed except in the separate tip cavity. Clearly, there is also a large range of possible magma properties (viscosity and density) that could be employed, but evaluation of a range of conditions results in a bounding of the problem.

The boundary-element approach also requires a constant material-property set for the host rock, and any variation, either between layers or laterally, is not accounted for. Rather, a uniform, average condition is used in the calculation. This approach results in a model that does not account for stratigraphy, but it is not evident that the average result would be much different if layers could be included. The effect of topography can be accounted for with respect to its effect on stress—which should be the dominating feature of topography—but other plausible effects

(e.g., a modified free surface, rotation of the stress field, etc.) are not considered with the current model.

The dike propagation model is very flexible with respect to the far-field stress and either a density-defined stress field or an applied side load can be used. However, in the present model, the applied far-field stress affects only the condition of dike propagation. The stress gradient, which controls the magma pressure gradient, is defined by rock mass density and coefficient of lateral stress only. Consequently, magma buoyancy is independent of the applied far-field stress (e.g., repository-induced thermal stresses). Also, exact values for the stresses are based on only three stress measurements in the vicinity of Yucca Mountain (Stock et al. 1985 [DIRS 101027]) and also by calculations of the stress field that might develop with heating of the repository (see Section 6.3.9.2.2).

For a large-scale dike, analysis of the important mechanisms suggests that the fracture criterion is immaterial for dike propagation. However, the application of LEFM principles to a problem of this scale has been questioned, and some other criterion could potentially be more appropriate. The LEFM approach was employed here, but elevated values of fracture toughness were considered to assess possible effects. Coupled with the fracture criterion is the pressure in the fluid-tip cavity. This pressure is controlled by the dike-fracture criterion, the permeability of the host rock, the pore pressure of the host rock, the exsolution of vapor from the magma, and the overall dike parameters. At this time, there is no method to calculate the tip-cavity pressure, so a range of values from atmospheric to considerably higher levels is employed.

Self-similar (far field) conditions of dike ascent are defined by the dike aperture and magma velocity. The model boundary conditions were calculated to match the expected range of dike velocities and apertures. The magma source is taken to be at a depth that is effectively equivalent to an infinite depth. The model allows only an injection-rate boundary condition at the source. It requires positive buoyancy of the magma to keep it moving vertically upward; otherwise, the magma will stagnate or form a sill. Conditions at Yucca Mountain (a gradient of the smaller horizontal stress and magma density) are expected to result in negative buoyancy (i.e., the magma unit weight is larger than the gradient of horizontal far-field stress). Ranges of magma density and the gradient of far-field stress were considered in the analysis.

Once the dike reaches the free surface, the calculations terminate. As a result, it is not possible to calculate any evolution of the conditions after intersection. Some assumptions are made about the continued development of the dike, but these are extrapolations of prior conditions.

6.3.2.1 Future Uncertainties

Future uncertainties in state, parameters, and processes are primarily those associated with the range of possible dike source conditions and magma properties. In-situ stresses are not likely to change significantly except due to heating, which has already been accounted for using the thermomechanical response of the repository. Rock properties far from the repository drift will not change over this time frame, which is minute compared to usual geologic changes. The potential for changes in the rock properties adjacent to drifts has been addressed in BSC 2003 [DIRS 162711]. Thus, changes in magma outflow and viscosity are the most-likely variable

properties. Because a range of these parameters is considered, it is expected that most future uncertainties have already been accounted for.

6.3.3 Alternative Models for Dike Propagation

An igneous dike is a fracture that propagates upward from some deep source toward the surface. This process is essentially the hydraulic fracturing problem (with some complications and some simplifications) and can only be modeled in any realistic sense by using a hydraulic-fracture type model. In actual practice, there are a number of analytic and commercial oil and gas hydraulic-fracture models available (including those used in geothermal hot-dry-rock and waste-injection applications), and there are hydraulic-fracture models adapted to the igneous dike problem. Each of these applications is discussed and considered.

6.3.3.1 Analytic Solutions of the Hydraulic-Fracture Problem

Although analytic solutions may not be sufficiently versatile to solve complex problems with free surfaces and loss into repositories, they are quite adequate for solving fracture propagation problems in general homogeneous media and are thus useful for comparisons and parameter estimation. The first hydraulic-fracture models were developed using a combination of two landmark papers on the topic. These included a paper on "Widths of Hydraulic Fractures" by Perkins and Kern (1961 [DIRS 163644]) and another on "Optimum Fluid Characteristics for Fracture Extension" by Howard and Fast with an appendix by Carter (Howard and Fast 1957 [DIRS 163628], Appendix) that was the basis for constructing a joint model.

Perkins and Kern considered 2D fractures in both Cartesian and radial geometries with laminar and turbulent flow for both Newtonian and pseudo-plastic rheologies. In the Cartesian geometry, the dimensions of the dike are a width (w) in the direction of crack opening, a length (L) in the direction of crack propagation, and a height (H) orthogonal to the other two. This situation can be analyzed as a 2D problem as long as L is very large compared to w. Perkins and Kern took the two previously developed width equation for fractures inflated by constant pressure (Sneddon 1946 [DIRS 163648]):

$$w = \frac{2\left(1-\nu^2\right)\left(p-\sigma\right)L}{E}\text{, for Cartesian geometry} \qquad \text{(Eq. 1)}$$

and:

$$w = \frac{8\left(1-\nu^2\right)\left(p-\sigma\right)R}{\pi E}\text{, for radial geometry} \qquad \text{(Eq. 2)}$$

where:

p = pressure of fluid in dike
σ = stress component normal to the dike
R = radius of the dike
E = Young's modulus of the confining rock
ν = Poisson's ratio of the confining rock

and added two pressure-drop equations of the form:

$$\frac{dp}{dx} = \frac{32Q\mu}{\pi H w^3} \quad \text{(Eq. 3)}$$

where:

x = the spatial coordinate in the L-direction
Q = the volume flux of the driving fluid
μ = the dynamic viscosity of the driving fluid

for linear flow through an elliptic cross-section, and

$$p = p_w - \frac{6Q\mu \ln[r/r_w]}{2\pi w^3} \quad \text{(Eq. 4)}$$

where:

p = the pressure at radius r
p_w = the driving pressure
r_w = the radius of the source flux, Q, where the dike width is w

for radial flow through a constant-aperture fracture. In addition, Perkins and Kern added a mass-conservation formulation and solved for widths and pressures, obtaining equations of the form:

$$w_{\max} = 3\left[\frac{2(1-\nu^2)Q\mu L}{E}\right]^{\frac{1}{4}} \text{ for the Cartesian case} \quad \text{(Eq. 5)}$$

and:

$$w_{\max} = 3\left[\frac{(1-\nu^2)Q\mu R}{\pi^2 E}\right]^{\frac{1}{4}} \text{ for radial conditions} \quad \text{(Eq. 6)}$$

where $w_{\max}$ is the maximum fracture width.

Using volumetric considerations (e.g., volume = rate x time), the length of the fracture could be found as:

$$L = 0.6\left[\frac{EQ^3}{2(1-\nu^2)\mu H^4}\right]^{\frac{1}{5}} t^{\frac{4}{5}} \text{ for the Cartesian case} \quad \text{(Eq. 7)}$$

and

$$R = \left[\frac{EQ^3}{16\pi^2 \left(1-\nu^2\right)\mu} \right]^{\frac{1}{9}} t^{\frac{4}{9}} \text{ for radial conditions.} \quad \text{(Eq. 8)}$$

where t is time.

The contribution by Howard and Fast (1957 [DIRS 163628]) to the hydraulic-fracturing problem was the incorporation of leak-off into the reservoir in the form of a square-root-of-time approximation. Although leak-off into the surrounding rocks is not necessary for dike propagation, an appendix in their paper written by R.D. Carter (Howard and Fast 1957 [DIRS 163628], Appendix) provided a more accurate coupling of width, pressure, and leak-off equations. Carter's equation, as it is known, expresses the area (height × length) of a fracture as a function of the width, leak-off, flow rate and time. Coupled with Perkins and Kern's equations (Equations 7 and 8), this solution allowed for analytic calculations of fracture growth in a much more exact form than the Perkins and Kern solution. Nevertheless, the Perkins and Kern solution is very useful in estimating fracture parameters for most situations and can be used as a check on any model that predicts the length, width, and pressure of a fracture that has a constrained height (height in this case is the major dimension *not* aligned with fluid flow; length is the major dimension aligned with fluid flow). This type of fracture has an elliptic crack profile (e.g., in the minor dimension).

Nordgren (1972 [DIRS 163641]) applied the Carter-type solution for fractures in the Cartesian case and obtained:

$$w_{\max} \approx 2.5 \left[\frac{2\left(1-\nu^2\right)Q^2\mu}{EH} \right]^{\frac{1}{5}} t^{\frac{1}{5}} \quad \text{(Eq. 9)}$$

and:

$$L = 0.68 \left[\frac{EQ^3}{2\left(1-\nu^2\right)\mu H^4} \right]^{\frac{1}{5}} t^{\frac{4}{5}} \quad \text{(Eq. 10)}$$

which is a relatively small change over the Perkins and Kern solution.

Geertsma and de Klerk (1969 [DIRS 163624]) provided analytic solutions for 2D fractures that had a constant-width profile (e.g., the fracture extends to infinity or exhibits full slip at some boundary). For such a case, the width is given by:

$$w_{\max} \approx 2.27 \left[\frac{2\left(1-\nu^2\right)Q\mu L^2}{E} \right]^{\frac{1}{4}} \text{ for the Cartesian case} \quad \text{(Eq. 11)}$$

and:

$$w_{\max} \approx 2\left[\frac{2(1-\nu^2)Q\mu R}{E}\right]^{\frac{1}{4}} \text{ for radial conditions.} \qquad \text{(Eq. 12)}$$

Because the dike propagation modeling being performed here is applying the 2D approximation used by Geertsma and de Klerk (1969 [DIRS 163624]), these equations are most appropriate for direct comparison with the model results.

Although such analytic conceptual models are useful for parameter estimation, they are not appropriate for the dike propagation problem (1) in the vicinity of the free surface and (2) with a sink point at some single location. Thus, these models cannot be used to provide the detail needed for understanding magma flow into a shallow repository due to an intersecting dike.

6.3.3.2 Industrial Hydraulic-Fracture Models (Oil and Gas Applications)

Industrial hydraulic-fracture models are based on the same concepts as the analytic solutions given above, but numerical solutions allow considerable flexibility, particularly with respect to height evolution and length factors. Some of the major available industrial packages are FracPro, Stimtech, MFrac, and TerraFrac, each available from a software provider.

Because these are proprietary industrial models, no exact accounting for their equations, algorithms, and applications can be made, but general principles associated with these models are documented in the literature and elsewhere. The most significant differences between the analytic solutions and the industrial models are the ability to handle variable height growth (into other layers having different stresses and other properties), compressible fluids (e.g., for foam-fracturing fluids), and proppant transport (e.g., for carrying sand to keep the fracture open after the treatment ends and the pressure drops). Many other factors can also be accounted for, such as different types of leak-off behavior, different fracture-tip propagation conditions, 3D coupling effects, and others.

An overview of these types of models, a comparison of their results, and references on the equations/algorithms can be found in Warpinski et al. (1993 [DIRS 163649]; 1994 [DIRS 163657]). In general, these review papers show that these models can result in widely different fracture geometries (and pressures) for the same input parameters, largely because of many unknown factors in the algorithms. In addition, these models are primarily appropriate for fracturing far away from the free surface in layered media (where fractures are relatively confined between horizontal strata). These limitations clearly make the industrial models unsuitable for the present application, and no further use is made of these models.

6.3.3.3 Hydraulic-Fracture Dike Propagation Models

There are a number of models of dike propagation using hydraulic-fracture models, but with the addition of the effects of buoyancy (buoyancy is normally ignored in most hydraulic-fracture models). Buoyancy has been found to be important for its effect on upward growth of the dike and for the effect of magma density on the width profile of the dike. Examples of these models

are those due to Spence and Turcotte (1985 [DIRS 127068]; 1990 [DIRS 127086]), Lister (1990 [DIRS 126865]; 1995 [DIRS 163635]), Lister and Kerr (1991 [DIRS 126889]), and Turcotte et al. (1987 [DIRS 134364]) among others. These models have quite adequately shown how the buoyancy effects are a critical element of dike propagation.

However, none of these models has a free surface that can model the changing behavior of the dike as the surface is approached. In addition, a singular leak-off point (e.g., into the repository) is not available for any of these models and, thus, these models cannot be used for calculations of the dike interaction with the repository in the vicinity of the free surface. No other use is made of these models except as validation comparisons.

6.3.3.4 Alternative to the Present Model for Magma Flow Into Drifts

Woods et al. (2002 [DIRS 163662]) present a model for flow of magma from a dike to a drift. As mentioned in Section 6.3.3.5, there is another possible state for the magma in the center of the dike as moves upward into the cavity.

An alternative to the model adopted in this section is that the liquid and vapor phases of the magma are so closely coupled that the gas is trapped in the liquid. As the magma rises into the advancing cavity, the decompression is rapid enough that the bubbles formed are not able to coalesce into larger bubbles. In this case, the two phases will be very closely coupled, and the magma will expand almost as a single phase, even though its bulk expansion will be controlled primarily by the vapor constituent. Because of the very low cavity pressures, the vapor will expand rapidly as the magma rises, and the flow of magma will accelerate upward (the only direction in which it is unconstrained) until it reaches the drifts. When magma reaches the drifts, the expansion will then occur both into the drift and upward into the crack tip, which precedes the magma front.

Woods et al. (2002 [DIRS 163662]) assume that the magma consists of liquid and vapor fractions that are fully coupled, meaning that they are constrained to move at exactly the same velocities and that they are at the same pressures and temperature. They also assume that the vapor is always at equilibrium with the liquid—that is, that vapor exsolves (or dissolves) from the liquid instantaneously in response to pressure changes. They then solve the hydrodynamic equations in a quasi-one-dimensional form in which the flow in both the dike and the drift is treated as being in the same direction, but the cross-section of the flow varies along the flow direction, as does the amplitude of the gravity vector.

The cross-sectional area in the vicinity of the dike-drift intersection is modified to provide some constriction to represent the change in direction of the flow and the restricted area where the two separate volumes intersect. The equations used do not solve for any motions transverse to the direction of flow, and as such, the model is *not* 2D. The boundaries of the drift and dike are treated as impermeable and rigid. The initial condition is that magma at high pressure fills the dike portion of the model and air at atmospheric pressure fills the remainder of the computational volume. This condition results in a model that is mathematically quite tractable.

The Woods et al. (2002 [DIRS 163662], pp. 19-2 to 19-3) model results in a wall of magma accelerating into the drift at speeds reaching

> …tens to hundreds of meters per second, with the density decreasing as the pressure falls. Air is displaced and compressed ahead of the magma-volatile mixture and, as a result, a shock forms in the air and moves down the drift at speeds of several hundred meters per second. …on reaching the end of the drift, the shock is reflected and its amplitude increases by an order of magnitude. The shock then propagates back upstream, moving into the magma-volatile mixture and back towards the dike at speeds of 20–30 m/s. As the shock moves through the magma-volatile mixture, the mixture is recompressed. A region of higher pressure, of order several MPa, and hence higher density, develops between the end of the drift and the shock… The calculations suggest that, if the dike intersects the drift 200–300 m from the end of a closed drift, then the pressure within this drift will build up to about the initial level in the dike in a time of order 10 s.

6.3.3.4.1 Analysis of the Woods et al. Model

The model of Woods et al. (2002 [DIRS 163662]) represents a valuable first step toward developing a valid model of the flow of magma from a dike into a drift. By reducing the dimensionality from the fully 3D nature of the real case, that model reduced the problem to one that is mathematically tractable enough that numerous specific scenarios can be addressed. However, the initial and boundary conditions in the Woods et al. (2002 [DIRS 163662]) model are unrealistic. In particular, the initial condition is not physically realizable and leads to results that are not achievable in nature. As described in Section 6.3.8.2, magma does not fill the propagating crack completely, nor does the crack reach its full width immediately after opening. Rather, there will be a vapor-filled tip, which is expected to be on the order of tens to hundreds of meters long. Near the tip, this crack will be only millimeters wide. Even if the magma were to fill the crack nearly to the tip, the cross-sectional area of the intersection would be only a fraction of a square meter in this early phase, rather than the ~5.5 m^2 assumed by the Woods et al. (2002 [DIRS 163662]) model. This cross-section would gradually increase as the crack propagated beyond the repository, a process that could take seconds to minutes.

Although the evolution of the cross-section is difficult to predict in detail, its rate of growth can be estimated from results of Section 6.3.9.2.3.1. If the velocity of the tip is twice that of the magma front near the surface and the tip cavity is 100 m long, then the area growth rate will be on the order of: (drift diameter)•(dike width at drift – dike width at tip)/[(cavity length)/(velocity of tip)] = (5.5 m)•(1 m – 0 m)/[(100 m)/(2 m/s)] = 0.11 m^2/s.

With such an opening rate, almost 50 s would elapse before the full drift cross-section of 5.5 m^2 is exposed. However, this estimate is also inappropriate because the magma will not extend into the narrow parts of the tip cavity. This result is better understood as the rate at which the connection opens between the atmosphere in the drifts and the volcanic vapors in the tip cavity. Nevertheless, the area of magma exposed to the drift cannot increase more rapidly than the magma's upward velocity multiplied by the diameter of the drift. For effusive magma, this rate would be about 5 m^2/s; for a pyroclastic flow rising at 100 m/s, this rate might be as high as

500 m^2/s. The former rate is unlikely to produce any shock waves in the drift; loading at the latter rate may require further investigation.

The assumption of rigid, impermeable boundaries in the Woods et al. (2002 [DIRS 163662]) model adds to the severity of the consequences of magma interaction with drifts. Air pressurized by the shock they describe would seep into the walls of the drift, reducing the pressure behind the shock and decreasing its amplitude as it propagated. An even larger effect is to be expected at the blocked end of the drift, where the shock will encounter backfill. The backfill is quite compressible and will not reflect an incident shock wave nearly as efficiently as the rigid wall assumed in the calculation. In addition, the edge of the backfill will not be a vertical wall, as required by the 1D numerical model of Woods et al. (2002 [DIRS 163662]), but will lie at the angle of repose. The net result of these real-world situations will be to greatly reduce the amplitude of reflection of any shock that might develop.

Woods et al. (2002 [DIRS 163662]) have developed a model that ignores phase separation between the silicate liquid and the volatiles. Although this assumption may provide an adequate estimate of steady flow in such a mixture, it is precisely the response to dynamic events such as shocks and rapid decompression that is not well treated with this assumption. In situations with such high accelerations, the differences in density between the vapor and the silicate magma become important, and they will move at different speeds. Only later, as viscous forces have had a chance to act, will the velocities approach each other. If these effects were included in the model, the result would be to reduce the sharpness of both compression and decompression waves and to increase dissipation of kinetic energy. Shock waves would be considerably dampened when propagating through such mixtures.

Woods et al. (2002 [DIRS 163662], p. 19-2) state that "the drift is assumed to be empty, and since the drift cross-sectional area is much larger than that of a 1.8-m-diameter canister, *A(x)* is taken to be the total drift cross-sectional area." Although it is true that the ratio of area of the drift (~23.8 m^2) to that of a canister (~2.5 m^2) is large, a more important comparison would be that of hydraulic radii, $R_h = A/P$, where A is the cross-sectional area and P is the perimeter (both exterior and interior) of the flow. The ratio of hydraulic radii is about 0.67, whereas the ratio of open areas is about 0.89. The smaller value will result in more drag and loss of energy in the flows than in the Woods et al. (2002 [DIRS 163662]) model.

By not considering waste canisters, the Woods et al. (2002 [DIRS 163662]) model eliminates another mechanism for energy dissipation in the shock wave that their model produces. In a "cold repository" design, the canisters are to be separated by several meters along the axis of the drift. The alternate radial expansion and contraction of flow as a shock passes over such separated canisters will act in the same manner as a silencer does on a gun, dissipating the shock produced by the accelerating bullet as it exits the barrel. The small canister spacing in a "hot repository" design (Williams 2003 [DIRS 162731]) would considerably diminish this effect.

In summary, the Woods et al. (2002 [DIRS 163662]) model of magma expansion into a drift overestimates the violence of the encounter. Realistic boundary conditions including compressible walls and backfill, permeable country rock and backfill, phase separation in the magma-volatile mixture, partial blockage of the drift by waste canisters and other engineering features, and the axial spacing of the canisters would combine to greatly reduce the amplitude of

any shock wave that might form in the initial encounter. More importantly, use of realistic initial conditions would preclude the formation of a shock wave for all but the most rapid magma ascent rates.

A complete analysis of this model for magma expansion into drifts is beyond the scope of the present report. Such an analysis would require solving equations for compressible flow in a manner similar to the calculations reported by Woods et al. (2002 [DIRS 163662]), although in three dimensions with very different initial conditions and more realistic boundary conditions than were used in that work.

6.3.3.5 Partially Coupled Liquid and Vapor Phases

A third model for magma and gas flow in drifts is a partially coupled model in which the vapor phase and the condensed-liquid phase are free to move at different velocities subject to viscous drag of the continuous phase on the discontinuous one. This model is probably the most realistic of all the models, including alternate models, considered for magma and gas flow in drifts. It is also the most complicated and difficult to simulate numerically.

The previous version of this report (CRWMS M&O 2000 [DIRS 151552]) describes several scenarios related to this mode of partially coupled flow into drifts. These should be modified to account for cavity pressures less than the magma vapor pressure. A partial list of features that would be required for a thorough analysis of the partially coupled model includes:

- Momentum exchange between vapor and condensed phases is needed to simulate viscous drag accurately.
- Energy exchange between vapor and condensed phases is necessary to reproduce the nearly isothermal nature of the expansion of dusty or droplet-laden clouds.
- Mass exchange between vapor and condensed phases is required to simulate the exsolution/resolution of vapor from silicate-dominated liquid in response to pressure changes.
- 3D simulations are required for the most accurate analysis, although much could be learned from 2D simulations.
- Material models for solids should include compressible and incompressible properties to allow a range of boundary conditions for country rock and backfill to be investigated.
- Surface tension will be important in addressing the partial degassing of magma exposed to lower vapor pressures, whether in a drift or in the dike-tip cavity.
- An effective equation of state of variable mixtures of gases is needed to follow the behavior of volcanic gases including H_2O, CO_2, and SO_2.
- The viscosity of the liquid phase must be allowed to vary with temperature and with composition (due to the pressure-driven solubility of water and other vapors) of the liquid.

- The viscosity of the liquid phase also must be allowed to mimic the increase or decrease in effective viscosity of magma due to bubbles or small crystals.

- The ability to change from a state in which the liquid phase is continuous to one in which the vapor phase is continuous, is necessary to simulate fragmentation that occurs as a mixed-phase magma decompresses.

A complete analysis of this model for partially coupled liquid and vapor magma and gas expansion into drifts is beyond the scope of the present report. A code with all of the listed features has not been identified, although a code with the first seven features does exist but is not qualified. It may be possible to address this alternative model in detail in a revision of this report.

6.3.4 Description of Input

Inputs for each analysis supporting the dike propagation model are discussed individually in the following sections.

6.3.4.1 Inputs for Topographic and Thermal Effects

A large-scale, 3D analysis was used for calculation of in-situ (topography induced) and thermally induced stresses. Regional topography, layout of the repository, ratios of horizontal principal stresses to the vertical stress, orientations of the horizontal principal stresses, stratigraphy in the vicinity of the repository, elastic properties of each geological unit (Young's modulus and Poisson's ratio), thermal properties for each geological unit (conductivity, specific heat, and coefficient of thermal expansion), position and mechanical properties (friction angle) of two faults in vicinity of the repository, heat released by the waste as a function of time and amount of heat removed by ventilation were the inputs for this model. All of the inputs and their sources are described in *Drift Degradation Analysis* (BSC 2003 [DIRS 162711]).

6.3.4.2 Inputs for Two-Dimensional Dike Propagation

The input data for the Dike Propagation Model consists of formation (rock) properties, magma properties, boundary stresses, and dike parameters. There are uncertainties in these parameters because of the scale of the calculations (dike length of several kilometers) and the possible changes in properties over such distances. Sources for these inputs are tabulated in Section 4.1.

The problem of dike propagation is formulated in this model in dimensionless form (Attachment I). Rock mass density and magma density are combined into a dimensionless group called relative density, **D**. Confining stress, pressure in the crack tip, magma viscosity, and density, Young's modulus and Poisson's ratio of the rock , rock mass density, gravitational acceleration and the magma supply rate, are combined to form a dimensionless group called reference stress, **S**. A third dimensionless group, called toughness, is formed from the fracture toughness of the host rock, the elastic properties of the host rock, the magma viscosity and the magma supply rate. Conditions of dike assent are calculated from the values of these dimensionless groups, not directly from the dimensional parameters listed here as input. A range of relative density between 2.67 and 20.28 is reported. Relative stresses were between –0.25 and +2.15. A single value of toughness equal to 3.7×10^{-3} was used for all calculations discussed in

detail, although one calculation with toughness of 0.37 was done to check that the results are insensitive to small values of this parameter.

The model boundary condition is the magma injection rate at the source depth which may be cast in terms of the far-field magma velocity and the far-field dike width. From the range of magma velocity and dike widths described in BSC (2001 [DIRS 160130], Table 7), a single value of $10 m^2/s$ is used for the magma injection rate, and the far-field width and velocity are restricted to match that value.

The formation properties (those of the repository country rock) include Young's modulus, Poisson's ratio, and density, which have been measured and are available as qualified (Q) data. A fourth parameter, fracture toughness, has not been specifically measured for the repository, although one paper in the literature exists concerning its measurement for the volcanic rocks. This lack is not a problem because fracture toughness probably is almost irrelevant at this scale. In the analysis reported here fracture toughness is treated as a parameter that is always small but may span a few orders of magnitude to account for nonideal processes that may be associated with dike propagation. A limitation of the model is that the rock mass, which in reality is a heterogeneous, layered medium, is represented as homogeneous and isotropic. Considering the scale (kilometers) of the analyzed problem, and that the main objective of the analysis is to describe phenomena associated with dike propagation in the vicinity of the repository, elastic properties (Young's modulus of 15 GPa and Poisson's ratio of 0.21) were selected to be representative of TSw1 and TSw2 thermal-mechanical units (BSC 2003 [DIRS 162711], Attachment V, Table V-5). The input value for density of rock mass (2400 kg/m^3) was selected as representative of saturated density of Tptpln unit (DTN: SNL02030193001.027). This density is not a direct input to the calculation. Rather, it is used to establish a value for magma buoyancy.

The magma properties include density and viscosity, which are derived from the study *Characterize Eruptive Processes at Yucca Mountain, Nevada* (BSC 2001 [DIRS 160130]). In addition, this study provides the dike velocity and width distributions that are used to obtain the source flow rate for the dike propagation. A range of magma densities between 1500 and 2280 kg/m^3 was considered in the analysis. Magma density varies depending on composition of magma but is also a function of depth (i.e., pressure). Magma viscosity is a complicated function of composition, (both silicate and volatile), temperature and pressure; viscosities between 10 and 40 Pa s were used in the analysis. Results in this report are for a viscosity of 10 Pa s, the more conservative condition from the perspective of dike/drift interaction. Some supplementary results for 40 Pa s can be found in Attachment II.

The boundary stresses include the overburden stress, which is obtained by integrating the density of the overlying rock, and the distribution of the minimum principal horizontal in-situ stress (against which the dike must open). The distribution of the minimum principal horizontal in-situ stress is taken from either (1) stress measurements at Yucca Mountain for in-situ conditions or (2) thermomechanical modeling of the repository due to heating. Both cases are considered in these calculations and serve as the two logical end points of possible stress distributions.

A model limitation is that the actual ground surface topography cannot be represented. Instead the ground surface is assumed in the model to be planar. Average elevation of the repository is

1073m, as calculated from (BSC 2003 [DIRS 164493]). Height of the overburden varies between 250 and 400 m (BSC 2002 [DIRS 159124]). Depth of the repository of 300m was used as an input for the analysis.

In-situ stress measurements (DTN: SNF37100195002.001 [DIRS 131356]) show that (1) the ratio of the minor horizontal principal stress to the vertical stress is 0.361 and (2) the ratio of the major horizontal principal stress to the vertical stress is 0.617. A ratio (the coefficient of horizontal stress) of the horizontal stress normal to the dike to the vertical stress of 0.5 was used as an input for most of calculations. However, some results were obtained for the ratio equal to 1.

6.3.4.3 Inputs for Magma Flow Into Drifts

The inputs for the magma flow into drifts analysis are the diameter and spacing of drifts, the density and viscosity of the magma, the velocity of the magma front approaching the drift level, and the width of a dike at drift level. Values for these variables were taken from approved sources described in Table 2, the drift properties from repository design documents, and the magma properties and the dike width from previous reports. The values used are listed in Table 5.

Table 5. Input Parameters and Their Values for the Magma Flow Into Drifts Analysis

Input variable	Units	Value
drift diameter	m	5.5
drift spacing	m	80
density of magma	kg/m3	2000
viscosity of magma	Pa-s	1 or 10
magma supply velocity	m/s	1 or 10
dike width	m	1.

The waste package (WP) diameter was varied to illustrate how the presence of WPs will affect the flow of magma. As such, two values were used, 0 m and 1 m. The former represents a drift with no WPs, which is not of any concern for release of waste; the latter is merely a nominal value so that the effect of WPs on reducing magma flow can be illustrated. It is less than half the diameter of WPs intended to be emplaced. The effect of reduced flow due to WPs in a drift is greater than just that of a reduced open cross-section of a drift. The presence of the waste packages also adds "wetted perimeter," which will result in increased viscous drag. This combined effect is included in the equations to be solved as the "hydraulic radius" (R_h) defined as the open cross-sectional area divided by the wetted perimeter of the flow. It should be noted that the hydraulic radius of an open circular tube is only one-half of the physical radius.

The rounded value of 80 m (instead of the design value of 81 m) is used for the spacing between drifts. This affects the results by reducing the total amount of magma available to flow into the drifts by 1.2 percent.

The magma density is a nominal value that is more than the fully expanded density that would be found in a pyroclastic flow but less than the fully condensed value provided in the *Characterize*

Eruptive Processes at Yucca Mountain, Nevada report (BSC 2001 [DIRS 160130]). It is intended to represent a magma which is partially degassed enough to flow into the drift effusively. The results of the analysis are affected only for the case of flow from a dike into a pipe, which is the controlling mode of flow when the magma supply rate and magma viscosity are high, and then only late in the short history of filling a drift.

The magma viscosity and magma supply velocity are chosen to represent the lower and upper ends of the ranges described in *Characterize Eruptive Processes* at Yucca Mountain, Nevada (BSC 2001 [DIRS 160130]). Use of these high and low values allows illustration of the effects of these variables on the solution. The dike width is a representative value consistent with the same report.

6.3.4.4 Inputs for Three-Dimensional Dike Propagation

This model uses all of the input parameters used in the 2D dike propagation model. Additional inputs are magma bulk modulus and details of geometry abstracted in the 2D model: drift diameter of 5.5 m and drift spacing of 81 m. (Sources of the inputs are given in Table 2.) However, 3D analysis was done for narrower range of parameters indicated in Table 6 (derived from inputs listed in Table 2). The analysis used a magma bulk modulus of 50 MPa because larger bulk modulus does not affect results but significantly increases calculation time.

Table 6. Simulated Combinations of Dike-Rise Model Parameters

Case	Young's Modulus (Gpa)	Poisson's Ratio	Rock Density (kg/m^3)	Magma Density (kg/m^3)	Magma Viscosity (Pa-s)	Magma Bulk Modulus (Mpa)	Magma Injection Rate (m^2/s)
1	15	0.21	2400	1141	10	50	0.45
2	15	0.21	2400	1001	10	50	0.25

6.3.5 Assumptions and Simplifications

Although most assumptions and simplifications have been noted in the model component section, they are repeated here for completeness. Assumptions and simplifications include:

- Magma compressibility (Assumption 1 in Section 5.1): The analysis of dike propagation assume that the magma is incompressible, whereas real magma is a mixture of liquid and gas (with or without solids) that can be highly compressible (BSC 2001 [DIRS 160130]). This is the standard assumption for hydrofracture analysis. This numerical model used has been developed for oil-field hydrofracture applications, which use water as the driving fluid. For these applications, incompressibility is a good assumption. Using the assumption of magma incompressibility in the magma flow model is not expected to have a major effect.

- 2D calculation (Assumption 2 in Section 5.1): Although the problem of a dike propagating away from a deep magma source clearly is a 3D problem, the behavior as the dike approaches the surface is considerably more constrained. First, the breadth of the fracture—the extent of the dike along strike (e.g., surface length)—is generally much

less than the length of the dike from source to tip. This characteristic is probably due to cumulative inelastic effects as the dike intersects more joints, faults, and other discontinuities and inhomogeneities. Second, the effect of the free surface will attract the dike as it approaches, thus limiting further breadth. As a result, the dike propagating upward near the surface takes on a reasonable 2D character that is much more amenable to modeling. Thus, although the early time modeling of the dike may not be accurate using a 2D model, the late time behavior (which is the behavior of interest) should be appropriately modeled using a 2D approach that specifically takes account of the presence of the free surface.

- Elastic behavior (Assumption 3 in Section 5.1): Elastic behavior is a reasonable assumption for small-scale pressurized fractures in the Earth but may be questionable for a dike-scale event. A dike would cross many joints, faults, bedding planes, and other discontinuities in the rock and would generate earthquakes as slippage occurs in response to the changes in stress generated by the inflated, propagating dike. However, inelastic effects will serve to increase the width of the dike and decrease the pressure. These are competing effects at the repository level, with the pressure being the primary boundary condition for subsequent calculations of Magma and Gas Flow, but the width of the dike provides a constraint on how much magma may be lost into the drift. Since the pressure is the main factor for the subsequent calculation, it is believed that using elastic behavior is a conservative assumption because it serves to generate the highest pressures.

- Linear-elastic properties (Assumption 4 in Section 5.1): Most rocks have nonlinear behavior, with lower moduli (a) at low stress and (b) in the ground in the presence of joints and bedding planes. However, linear-elastic behavior would produce the greatest possible pressure and is, thus, a conservative assumption.

- Homogeneous, isotropic material (Assumption 5 in Section 5.1): Rocks are typically transversely isotropic due to bedding and are jointed and faulted. In addition, there are many stratigraphic units with different values of Young's modulus and Poisson's ratio. In general, the rock properties of the strata below the repository are not known, and characteristics of joints and faults deep in the Earth are not known. However, although it is true that the deformation at any one point is a cumulative effect of the deformation everywhere in the dike, the influence of any point on another point decreases with distance. Thus, in lieu of a capability to incorporate multiple layers (which the Dike Propagation Model does not possess) and in the absence of detailed information on other rock properties, the dike behavior near the repository is best modeled by using the rock properties at the repository. This approach is not necessarily a conservative assumption but, rather, is the only assumption that can be made to obtain tractable models and sufficiently complete input parameters.

- Single fracture (Assumption 6 in Section 5.1): Although many hydraulic fractures and dikes are known to exhibit multiple fracture strands and *en échelon* behavior, the overall dike behavior is still reasonably modeled with a single fracture. Obviously, the more complex behavior observed in the field is due to complexities of the formation that are not known or otherwise available for modeling endeavors. Furthermore, dikes probably

exhibit the least complexity of pressurized fractures in the Earth because the high viscosity of the magma does not allow easy penetration of the fluid into joints or faults, and thus, secondary fracture strands are not easily initiated.

- Laminar flow (Assumption 7 in Section 5.1): Laminar flow of the magma in the dike is essential for pressure drop calculations under the Poiseuille formulation (e.g., $dp/dx = 12q\mu/w^3$). Laminar flow is expected to occur for Reynold's numbers less than 2,000. Because the Reynold's number for flow in a fracture is given by $Re = 2\rho V_f w/\mu$, Reynolds numbers do approach and even exceed 2,000 for some combinations of conditions. However, nothing is known about possible transition behavior of magma, and fully turbulent flow is unlikely for any possible set of conditions. Thus, it seems reasonable to assume laminar flow behavior under all circumstances.

- Lubrication approximation (Assumption 8 in Section 5.1): The lubrication approximation is appropriate (and exact) for slow motion of viscous fluids so that the viscous forces are considerably greater than the inertial forces, thus allowing the inertial forces to be neglected. These flows are also called *creeping motion*. However, creeping motion can be considered as solutions of the full Navier-Stokes equations for cases where $Re \rightarrow 0$ (ratio of inertial to viscous forces goes to zero). As noted in the previous assumption, Reynolds numbers can be fairly large, which would appear to negate the use of this approximation. However, the lubrication approximation is appropriate because flow in a long 2D fracture is a "parallel flow," which is identical to the 1D lubrication equation with the exception of an additional time derivative of the velocity and the dropping of one spatial derivative. Because hydraulic fractures—and more certainly dikes—are slowly varying with time and position, the time derivative is negligible, and the spatial derivative drops out as well. Consequently the steady "parallel flow" approximation is the same as the 1D lubrication equation. In support of this reduction, the "lubrication approximation" has been used for 40 years in hydraulic fracturing (even larger Reynold's numbers) with good success and no apparent discrepancies. Thus, this approximation appears reasonable and appropriate here.

- Newtonian fluid (Assumption 9 in Section 5.1): A Newtonian fluid is one that obeys Stokes' law of friction, for which the relationship between stress and rate of strain is linear. This formulation considerably simplifies calculations of fluid resistance and is known to apply to many common fluid systems. Although a more complex fluid rheology could be used (e.g., with yield stress and power-law behavior), little is known about magmas, and the additional parameters in such models would be populated with guessed quantities. It seems more appropriate to remain within the Newtonian framework and vary the viscosity to account for possible differences.

- Stress intensity factor governs tip behavior (Assumption 10 in Section 5.1): LEFM is a discipline that has been well studied and is widely applicable to small-scale fractures in the laboratory, mines, concrete, and other typical engineering applications. However, in hydraulic fracturing, the fracture toughness of the rock is generally irrelevant (small effect), and the applicability of LEFM has been questioned for large-scale fractures propagating under internal pressure. The dike propagation problem is concerned with an even larger-scale feature and undoubtedly involves anelastic behavior in the surrounding

rock. Thus, LEFM may not be strictly appropriate for this application. However, the LEFM formulation allows the fracture toughness to be used as a parameter that is indicative of the resistance of the rock to fracture, whatever the actual mechanism may be. Treated as a parameter, fracture toughness can be used to investigate the effect of any mechanism that resists fracture growth and thus increases the pressure.

- Horizontal free surface (Assumption 11 in Section 5.1): The surface topography at Yucca Mountain is relatively severe, but the dike propagation model treats it as a horizontal surface. This approach is a conservative assumption because the additional load of the mountain could serve to deflect any dike away from the mountain (e.g., into the basins). However, analysis of in-situ stresses in Section 6.3.9.1.1 demonstrates that topography has negligible effect on the dike path.

6.3.6 Boundary and Initial Conditions

The boundary conditions associated with the medium include the horizontal principal minimum in-situ stress and overburden stress acting within the formation. The free surface is already accounted for in the model and requires no additional considerations. The boundary conditions associated with the dike are the source depth and source flow rate, as well as a crack-tip condition and a fluid-front condition. The crack tip has an asymptotic form imposed on it based on the propagation criterion, whereas the pressure at the fluid front must be the tip-cavity pressure, and the velocity at the fluid front is derived from a formulation of the average velocity at that point. The initial condition is a uniform half-space with no dike present.

6.3.7 Model Formulation for the Base-Case Model

In the basic formulation of this 2D solution (see Attachment I), there are two independent variables in the Dike Propagation Model—the time t (or depth of the tip) and the distance from the tip. When the tip is deep, the solution is self-similar, so all variables scaled by $L(t)$ are independent of time.

All dike parameters are functions of the position within the dike at a particular time. In addition, the stresses calculated around the dike are functions of the position variables (both x and z), and these stresses depend also on the location of the dike relative to the free surface (e.g., the free surface restricts the self-similar nature that would apply in an infinite space).

Thus, when the full suite of information extracted from the model is applied, it is appropriate to consider t, x, and z to all be independent parameters.

6.3.7.1 Variables and Parameters

The dependent variables are:

- Dike-tip position
- Magma-front position
- Pressure distribution along the length of the dike
- Dike-width distribution (actually, the full deformation field around the dike)

- Magma-velocity distribution
- Stress perturbations around the dike (in both directions)
- Stress-intensity factor at the tip of the crack.

Parameters include:

- Rock properties:
  - Young's modulus
  - Poisson's ratio
  - Density
  - Fracture toughness
- Magma properties:
  - Viscosity
  - Density
  - Source depth
- Crack tip pressure
- Sink parameters:
  - Sink time (zero time is when the dike intersects the repository)
  - Sink rate (flow rate into drift)
- Distribution of the horizontal principal stress
- Overburden stress.

6.3.8 Model Results

The model results consist of 24 separate model runs of NPHF2D V1.0 [DIRS 163665] for a variety of parameters. (These runs are documented in Table 7 as Cases 8–10 and 13–33; Cases 1 through 7, 11, and 12 are model runs not used in this analysis.) These results can be used to assess the effects of magma viscosity and density, dike flow rate (or far-field width and velocity), in-situ stress, leak-off, and cavity-tip pressure on the conditions in the dike as it intersects the repository.

A summary of the cases run and the input parameters are given in Table 7. This summary records the relevant parameters for each of the actual code calculations. Details of the simulations and results obtained can be found in Attachment II.

Table 7. Input Parameters for 3 Base Cases and 21 Derived Cases Discussed in Text

Base Cases

Case	Initial Depth (m)	Element Size (m)	Magma Density (kg/m^3)	D	w_∞ Dike Width (m)	v_∞ Magma Velocity (m/s)	l^* Scaling Length (m)
8	2000	5	1500	2.67	0.511	19.6	945
9	3400	8.5	2000	6.02	0.670	14.9	1625
10	7500	18.75	2280	20.28	1.005	9.95	3652

Derivative Cases

Case	D	p_o (MPa)	σ (MPa)	S	Sink Strength (%)	Sink Depth (m)	Comments
13	2.67	0.424	0	-0.05	0	N/A	Increased cavity pressure
14	20.28	0.864	0	-0.20	0	N/A	Increased cavity pressure
15	20.28	0	0	0	10	533	Sink at 300 m for v* = 1 m/s
16	20.28	0	0	0	10	1066	Sink at 600 m for v* = 1 m/s
17	6.02	0	0	0	10	590	Sink at 300 m for v* = 1 m/s
18	6.02	0	0	0	10	1179	Sink at 600 m for v* = 1 m/s
19	20.28	0	0	0	20	533	Sink at 300 m for v* = 1 m/s
20	20.28	0	0	0	20	1066	Sink at 600 m for v* = 1 m/s
21	2.67	0	0	0	40	375	Sink at 300 m for v* = 1 m/s
22	6.02	0	0	0	40	351	Sink at 300 m for v* = 1 m/s
23	20.28	0	0	0	5	533	Sink at 300 m for v* = 1 m/s
24	20.28	0	0	0	15	1066	Sink at 600 m for v* = 1 m/s
25	6.02	0	11.0	1.30	0	N/A	Increased confining stress
26	6.02	0	10.3	1.59	0	N/A	Increased confining stress
27	20.28	0	9.26	2.15	0	N/A	Increased confining stress
28	2.67	2.12	0	-0.25	0	N/A	Increased cavity pressure
29	2.67	0	11.0	1.30	15	375	Sink at 300 m for v* = 1 m/s, Increased confining stress
30	6.02	0	10.3	1.59	20	351	Sink at 300 m for v* = 1 m/s, Increased confining stress
31	6.02	0	10.3	1.59	10	351	Sink at 300 m for v* = 1 m/s, Increased confining stress
32	6.02	0	10.3	1.59	25	351	Sink at 300 m for v* = 1 m/s, Increased confining stress
33	2.67	0	11.0	1.30	10	375	Sink at 300 m for v* = 1 m/s, Increased confining stress

Output DTN: SN0304T0504203.001

NOTES: Derivative cases have the same geometric and magma properties as base cases with the same **D**, except for cases 22, 30, 31, and 32, which have a magma density of 1000 kg/m^3 instead of 2000 kg/m^3.

Distances in Comment column are meters below ground level.

All cases have the following rock properties:

ρ_r=2398 kg/m^3, E=15 GPa, v=0.21, K_{Ic}=3 MPa-$m^{½}$.

All cases have the following magma properties:

μ=10 Pa-s, q_∞=10 m^2/s.

Cases 8, 9, and 10 were base cases that used different source depths, element sizes, and magma densities. The three dimensionless groups in the calculations are given by:

$$\mathbf{D} = \frac{\rho_r g}{\delta'} \qquad \text{(Eq. 13)}$$

and:

$$\mathbf{S} = \frac{\sigma - p_o}{\left(\mu' E'^3 \delta'^2 q_\infty\right)^{\frac{1}{6}}} \qquad \text{(Eq. 14)}$$

where: $\delta' = (p_r - p_f)g$

$\mu' = 12\mu$

$E' = E/(1-\nu^2)$

ρ_r = the rock density

μ = the magma viscosity

E = Young's modulus

ν = Poisson's ratio

g = the gravitational constant

σ = the stress acting against the dike

p_o = the pressure in the tip-cavity region of the dike

q_∞ = far-field magma flux

The controlling parameters are all listed, as appropriate, in the Table 7. Since the results (assuming neglegible fracture toughness) are only sensitive to two dimensionless groups, **D** and **S**, the values of these two groups are included in Table 7. All cases in Table 7 use fracture toughness of K_{Ic} = 0.3 MPa $m^{1/2}$. Corresponding dimensionless fracture toughness, is 3.7×10^{-3}, which implies that the dike propagates under conditions of practically no resistance to fracture.

One case, not listed in Table 7, was simulated using extremely large (for rocks) fracture toughness of 30 MPa $m^{1/2}$ (dimensionless toughness 0.37). The motivation was to account for all nonlinear processes in the vicinity of the dike tip neglected in LEFM. The results for this case were similar to results for cases with 100 times smaller toughness, i.e., no resistance to fracture. Fracture toughness was not considered any further in the analyses.

The parameters l^*, w_∞, and v_∞ are also scaling parameters for length, crack width, and velocity. The length scaling is given by:

$$l^* = \left[\frac{\mu' E'^3 q_\infty}{\delta'^4}\right]^{\frac{1}{6}} \qquad \text{(Eq. 15)}$$

whereas the width and velocity scaling parameters are simply the far-field dike width and velocity, as given by:

$$w_\infty = \left[\frac{\mu' q_\infty}{\delta'} \right]^{\frac{1}{3}} \quad \text{(Eq. 16)}$$

and:

$$v_\infty = q_\infty / w_\infty \quad \text{(Eq. 17)}$$

where ρ_f is the magma density.

The sink depth and sink strength are parameters used to define a local loss of fluid at some level (e.g., the repository) and have specific physical values.

Notice in Table 7 that the various cases considered are for dikes starting at varying depths (all much greater than depths of interest), as well as having varying stress, cavity pressure, sink locations and strengths, and an infinite number of combinations of other parameters depending on the dimensionless groups. The comments in the final column of the lower part of Table 7 give a brief summary of the intent of the particular derivative run.

For cases in which **S** is zero, the only group controlling behavior is **D**. For these situations, any number of combinations of rock density, magma viscosity, far-field width, and far-field velocity can be used to assess possible conditions. For example, Case 8 is run with a rock density of approximately 2400 kg/m^3, but this case is also used to assess the situation where the in-situ stress is made much lower by rescaling the rock density (e.g., to 1200 kg/m^3 to approximate the lower stresses thought to exist in Yucca Mountain). This rescaling allows for the evaluation of topographic changes on the stress state (see Section 6.3.9.1). **D** values for the various cases are 2.67, 6.02, and 20.28, so a wide variety of conditions are possible.

A higher tip-cavity pressure is not likely but is possible under some conditions. Hence, a number of cases (13, 14, and 28) have been run with a higher cavity pressure. These are discussed in detail in Section 6.3.9.2.3.3.1.

The possibility of leak-off into the repository is handled in Cases 15 to 24 and 29 to 33, but care must be taken in how these results are used. Since the location of the sink scales along with the dike tip and magma front, the correct position of the repository will only be attained for one set of parameters. The comments in Table 7 reflect that position for the case of interest. See Section 6.3.9.2.3.2.2 for analyses of such conditions. The likelihood of higher confining stresses during the heated stage is considered in Cases 25–27 and 29-33, for which an additional horizontal stress is applied to the rock. To evaluate a number of possible situations, these stresses are coupled with various leak-off conditions.

6.3.8.1 Rescaling Nondimensional Results to Dimensional Values

To convert the nondimensional code results to dimensional values, the results must be manipulated. There is more than one way to accomplish this, but one case is illustrated here to indicate to the reader how it is done.

The first step is to determine the appropriate scaling parameters (the characteristic quantities). They are formulated as follows:

$$l^* = \left[\frac{\mu' E'^3 q_\infty}{\delta'^4} \right]^{\frac{1}{6}} \quad \text{(Eq. 18)}$$

$$p^* = \left[\mu' E'^3 q_\infty \delta'^2 \right]^{\frac{1}{6}} \quad \text{(Eq. 19)}$$

$$t^* = \left[\frac{\mu' E'}{\delta'^2 q_\infty} \right]^{\frac{1}{2}} \quad \text{(Eq. 20)}$$

where:

$\delta' = 10(\rho_r - \rho_f)$,
$\mu' = 12\mu$
$E' = E/(1-\nu^2)$.

In these equations, ρ_r is the rock density, ρ_f is the magma density, μ is the magma viscosity, E is Young's modulus, ν is Poisson's ratio, and q_∞ is the flow rate at infinity.

For Case 8, one of the base-case examples from the calculations:

E = 1.5 x 10^{10} Pa
ν = 0.21
ρ_r = 2400 kg/m^3
ρ_f = 1500 kg/m^3
μ = 10 Pa-s
q_∞ = 10 m^2/s

the resulting scaling parameters are:

l^* = 945.01 m
p^* = 8488595.88 Pa
t^* = 48.309 s

In addition, the far-field width and velocity can be found as:

$$w_\infty = \left[\frac{\mu' q_\infty}{\delta'} \right]^{\frac{1}{3}} \text{ and } v_\infty = q_\infty / w_\infty \text{ respectively} \quad \text{(Eq. 21)}$$

giving w_∞ = 0.5112 m and v_∞ = 19.56 m/s. These values are representative of the width and tip velocity that would develop as a steady-state condition were achieved (i.e., when the dike gets very long). Given these five scaling parameters, the results can be directly nondimensionalized.

The nondimensional results are calculated as a function of two dimensionless groups given by:

$$\mathsf{D} = \frac{\rho_r g w_\infty^2}{\mu' v_\infty} \qquad \text{(Eq. 22)}$$

$$\mathsf{S} = \frac{\sigma - p_o}{\sqrt{\frac{\mu' E' v_\infty}{w_\infty}}} \qquad \text{(Eq. 23)}$$

where:

σ = the stress acting against the dike
p_o = the pressure in the tip-cavity region of the dike
other parameters as defined earlier

However, for each of the base cases the additional constant stress, σ, acting against the dike (e.g., this would be added for the case of a heated repository), and the value of p_o is also zero. Thus, the second parameter (Equation 23) is zero, and only the first one (Equation 22) needs to be satisfied in any rescaling.

The dimensionless solution (obtained for certain values of dimensionless groups **D** and **S**) is the solution for any combination of dimensionless parameters that maintain dimensionless groups invariant. For example, if the solution is obtained for **D** = 2.67, it is a solution for all combinations of input parameters $\rho_r, g, w_\infty, \mu'$ and v_∞ which satisfy the relation:

$$\frac{\rho_r g w_\infty^2}{\mu' v_\infty} = 2.67 \qquad \text{(Eq. 24)}$$

If it is assumed that ρ_r and g are fixed, an infinite number of dimensional solutions can be generated for combinations of μ', w_∞ and v_∞ which satisfy condition:

$$\frac{w_\infty^2}{\mu' v_\infty} = \frac{2.67}{\rho_r g} \qquad \text{(Eq. 25)}$$

New dimensional solution ($\tilde{\mu}', \tilde{w}_\infty$ and $\tilde{v}_\infty$) can be derived from an existing one (μ', w_∞ and v_∞) according to relation:

$$\frac{\tilde{w}_\infty^2}{\tilde{\mu}' \tilde{v}_\infty} = \frac{w_\infty^2}{\mu' v_\infty} \qquad \text{(Eq. 26)}$$

Assuming 1000 times increase in viscosity and $\tilde{v}_\infty = 0.01$ m/s, then $\tilde{w}_\infty = 0.3655$ according to

$$\tilde{w}_\infty = \sqrt{1000 \frac{w_\infty^2}{v_\infty} \tilde{v}_\infty} \quad \text{(Eq. 27)}$$

However, by changing w_∞ and v_∞, the scaling parameters are also changed. The scaling parameters expressed as functions of w_∞ and v_∞ are as follows (See Section II.4 of Attachment II.):

$$l^* = \sqrt{\frac{E' \tilde{w}_\infty^3}{\tilde{\mu}' \tilde{v}_\infty}} \quad \text{(Eq. 28)}$$

$$p^* = \sqrt{\frac{E' \tilde{\mu}' \tilde{v}_\infty}{\tilde{w}_\infty}} \quad \text{(Eq. 29)}$$

$$t^* = \sqrt{\frac{E' \tilde{w}_\infty^3}{\tilde{\mu}' \tilde{v}_\infty^3}} \quad \text{(Eq. 30)}$$

Using these scaling parameters, the dimensionless data can be converted to new dimensional data having the higher viscosity and the different far-field velocity and far-field width. However, note that all of these parameters are interrelated and only certain combinations of values can be recovered. For this case, the new scaled parameters are 799 m, 7177 kPa, and 79908 s.

6.3.8.2 Dike Properties at Intersection With Drifts

The model results presented in Section 6.3.8 are in nondimensional form and must be scaled, as discussed in Section 6.3.8.1, to derive results in dimensional form that are more readily applied. Some examples are given below. These results are presented as histories of (1) the opening of the dike at the same depth and (2) the net pressure applied to the dike walls at a specified vertical position. For all the data extracted in this section, the specified depth is 300 m, the nominal repository depth.

The opening is 0.0 m as the crack tip passes the specified depth. In general, the crack will open before the magma front reaches the depth. Because the calculations stop when the crack tip reaches the surface, the final crack opening is generally less than the far-field value or the expected post-emplacement value.

The net pressure is the difference between the fluid pressure applied to the walls of the crack and the component of in-situ stress normal to the crack (p_0-σ). A low, constant value of net pressure indicates that magma has not yet penetrated into the dike tip cavity to repository level. The position of the magma front is indicated by a sudden increase in the net pressure. After the magma front has passed the specified position, the net pressure rises to a small positive value that is what drives further crack growth.

The environmental conditions for these examples are summarized in Table 8, which is extracted from Table 7 (which are derived from input values in Table 2) . All scaled results use a 10 Pa·s viscosity.

Table 8. Environmental Conditions for Scaled Cases

Case Number	Figure Number	Buoyancy (Pa/m)	p_0 (MPa)	σ (MPa)	v_∞ (m/s)	Sink Strength (% of q_∞)
8	4b, 6a, 7a	3000	0	0	1	-
8	7b	3000	0	0	5	-
9	4c, 5c	8000	0	0	1	-
10	4a, 5b, 8a	1200	0	0	1	-
10	8b	1200	0	0	5	-
14	5a	1200	0.486	0	1	-
21	6b	3000	0	0	1	40
25	5d, 9a	8000	0	4.40	1	-
25	9b	8000	0	6.58	5	-
25	9c	8000	0	7.82	10	-
25	9d	8000	0	8.66	15	-

These rescaled results illustrate the effect of environmental changes on dike propagation. Figure 4 shows the results for base Cases 10, 8, and 9 in order of increasing buoyancy of the rising magma relative to the host rock. The buoyancy parameter is:

$$\delta' = (\rho_r - \rho_f)g, \qquad \text{(Eq. 31)}$$

which is actually the negative buoyancy. For these three cases, the buoyancy is 1.2 kPa/m, 3 kPa/m and 8 kPa/m, respectively.

The red curves begin at the first time step with a finite crack width at repository depth, and they end when the crack becomes unstable and rushes to the ground surface at nearly acoustic velocity (kilometers per second). Comparing the three plots, it is seen that the least buoyant case (Figure 4a) requires 113 s for the crack to reach the surface, the next most buoyant (Figure 4b) takes 105 s to reach the surface, and the most buoyant case (Figure 4c) reaches the surface after only 84 s. This demonstrates that increasing buoyancy results in faster crack propagation.

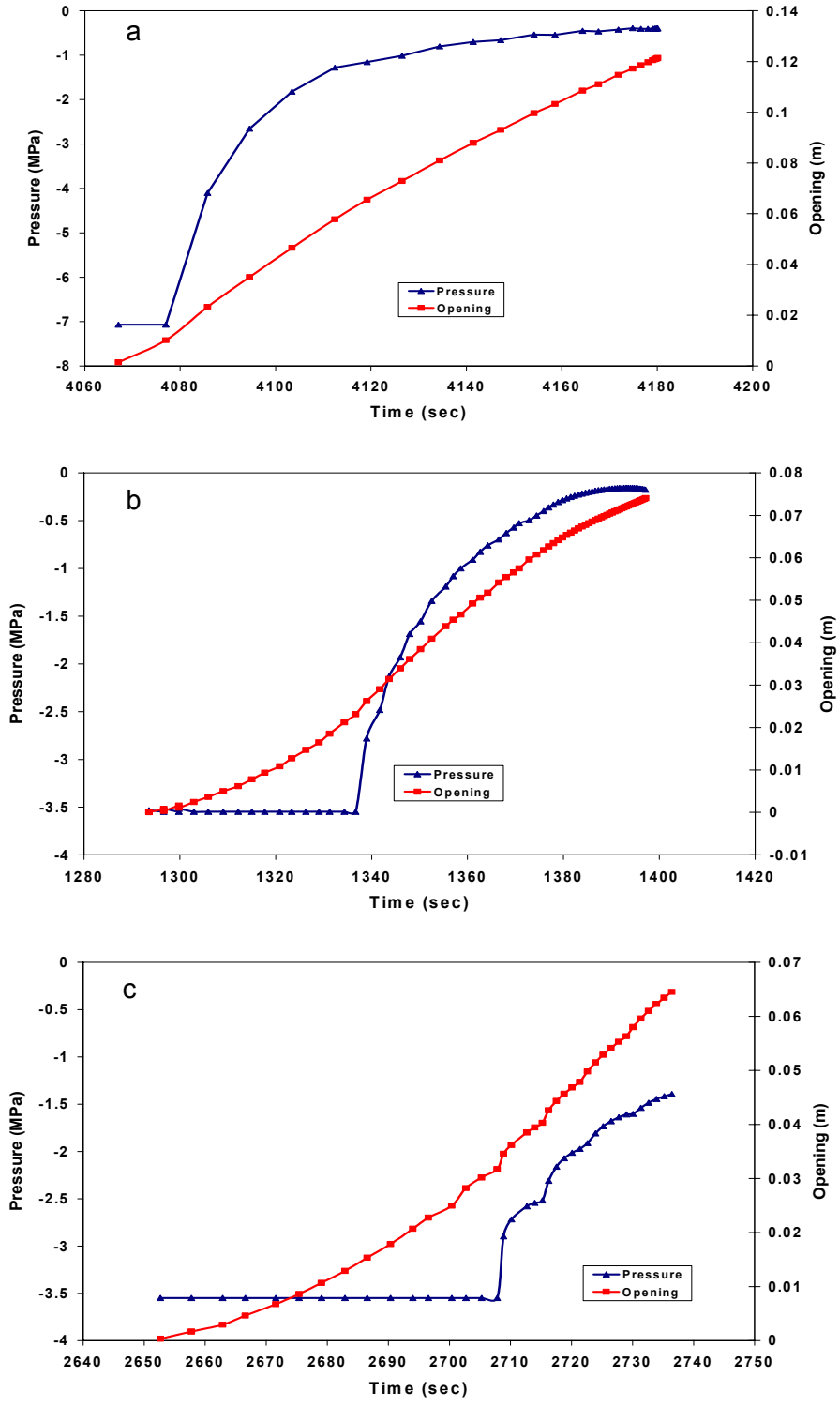

NOTE: a) Case 10, v_∞ = 1 m/s, buoyancy = 1.2 kPa/m
b) Case 8 with v_∞ = 1 m/s, buoyancy = 3. kPa/m
c) Case 9 with v_∞ = 1 m/s, buoyancy = 8. kPa/m

Figure 4. Crack Width (red) and Net Pressure on Dike Walls for the Three Base Cases

The initial flat portions of the blue curves indicate that at the beginning of the crack opening there is no pressure acting on the walls of the crack as it grows past the repository. Comparing the three curves, it is evident that even as increasing buoyancy shortens the time for the crack to reach the surface, it lengthens the time lag between the crack tip and the magma front.

The effect of net pressure on dike propagation is illustrated by the differences seen in Figure 5, again using cases given in Table 7. The top pair of plots, 5a and 5b, show the growth in the crack width (red) and net pressure for two cases differing only in the gas pressure in the tip cavity. The plot in Figure 5b is the same as Figure 4a, with no pressure in the cavity, whereas the plot in Figure 5a has a gas pressure in the cavity of 0.486 MPa. The effect of this change is not large, but it can be seen. With added pressure, the time needed for the crack to extend from repository depth to the surface is 95 s, 18 s less than without the added gas pressure in the cavity. The lag between the crack tip and the magma front is also probably larger for the pressurized case (Figure 5a), but the time step is too long in both examples to substantiate that conclusion unequivocally.

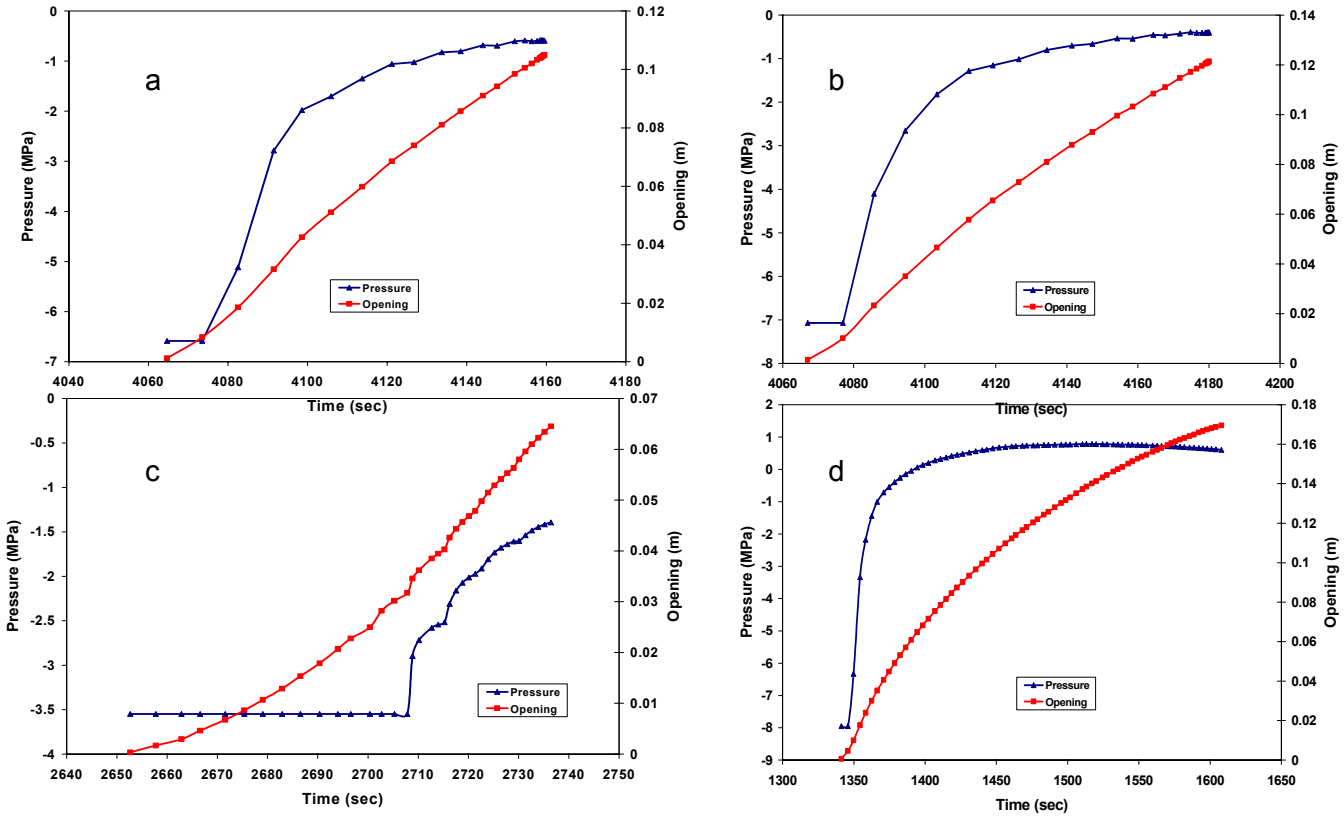

NOTE: a) Case 14 with v_∞ = 1 m/s, buoyancy = 1.2 kPa/m, cavity pressure = 0.86 MPa
b) Case 10 with v_∞ = 1 m/s, buoyancy = 1.2 kPa/m, pressure = 0. MPa
c) Case 9 with v_∞ = 1 m/s, buoyancy = 8 kPa/m, applied stress = 0. MPa
c) Case 25 with v_∞ = 1 m/s, buoyancy = 8 kPa/m, applied stress = 11. MPa

Figure 5. Crack Width (red) and Net Pressure (blue) on Dike Walls Based on Cases 14, 10, 9, and 25

The lower pair, Figures 5c and 5d, illustrate the effect of changes in the dike-normal confining stress. The case shown in 5c is the same as shown in Figure 4c, with only the overburden-induced horizontal stress, whereas 5d has an additional horizontal stress of 11 MPa. This added stress increases the time for the crack to reach the free surface by a factor of more than 3, from 84 s to 267 s. Even more dramatic is the decrease in the lag of the magma front behind the tip from 56 s to only 7 s.

These two effects are consistent because the variable related to net pressure that controls the crack speed is proportional to $(p_0-\sigma)$, where p_0 is the gas pressure in the tip cavity and σ is the excess confining stress, so the two variables will have opposite effects.

The effect of leak-off of magma into the drift is illustrated in Figure 6. These cases are identical except for the diversion in Figure 6b of 40 percent of the far-field magma flux into the tunnel when the magma reaches that level. As expected, there is no difference in the simulations before the magma front arrives 44 seconds after the crack tip.

The oscillations in Figure 6b are not due to a real oscillation of the magma but to numerical instability. That instability results because, as the magma first rises above the floor of the drift, the full 40 percent is not really available to be diverted until the magma has risen above ~40 percent of the diameter of the drift. (Calculations with greater than 40 percent leak-off resulted in uncontrolled numerical instability.) After about 15 s, the instability damps out, and the rise of the magma above the drift commences. However, with much of the magma supply unavailable to move farther up the crack, the crack takes 83 s (after the 15 s transition time) to reach the surface instead of 60 s without the diversion as seen in Figure 6a.

A greater far-field velocity for the magma causes faster crack growth, and in some cases, results in the crack breaching the surface before the magma front has risen to repository level. This is seen in Figure 7, where the velocity for the medium buoyancy case 8 is 1 m/s in 7a and 5 m/s in 7b. In 7b, the crack reaches the surface after only 12 s, before any magma reaches the repository level. Figure 8 presents a similar pair of plots for the lower buoyancy case 10. In this case, the higher velocity magma does reach drift level before the crack tip reaches the surface, but only ~1.5 s before.

When there is a strong confining stress on the propagating dike, the effect of far-field velocity still persists as can be seen in Figure 9. Note that these graphs are not shown at the same scale. Although the flat portion of the blue curves lengthens from 9a) through 9d) the time represented actually decreases from 7 s (9a) to 2 s (9d).

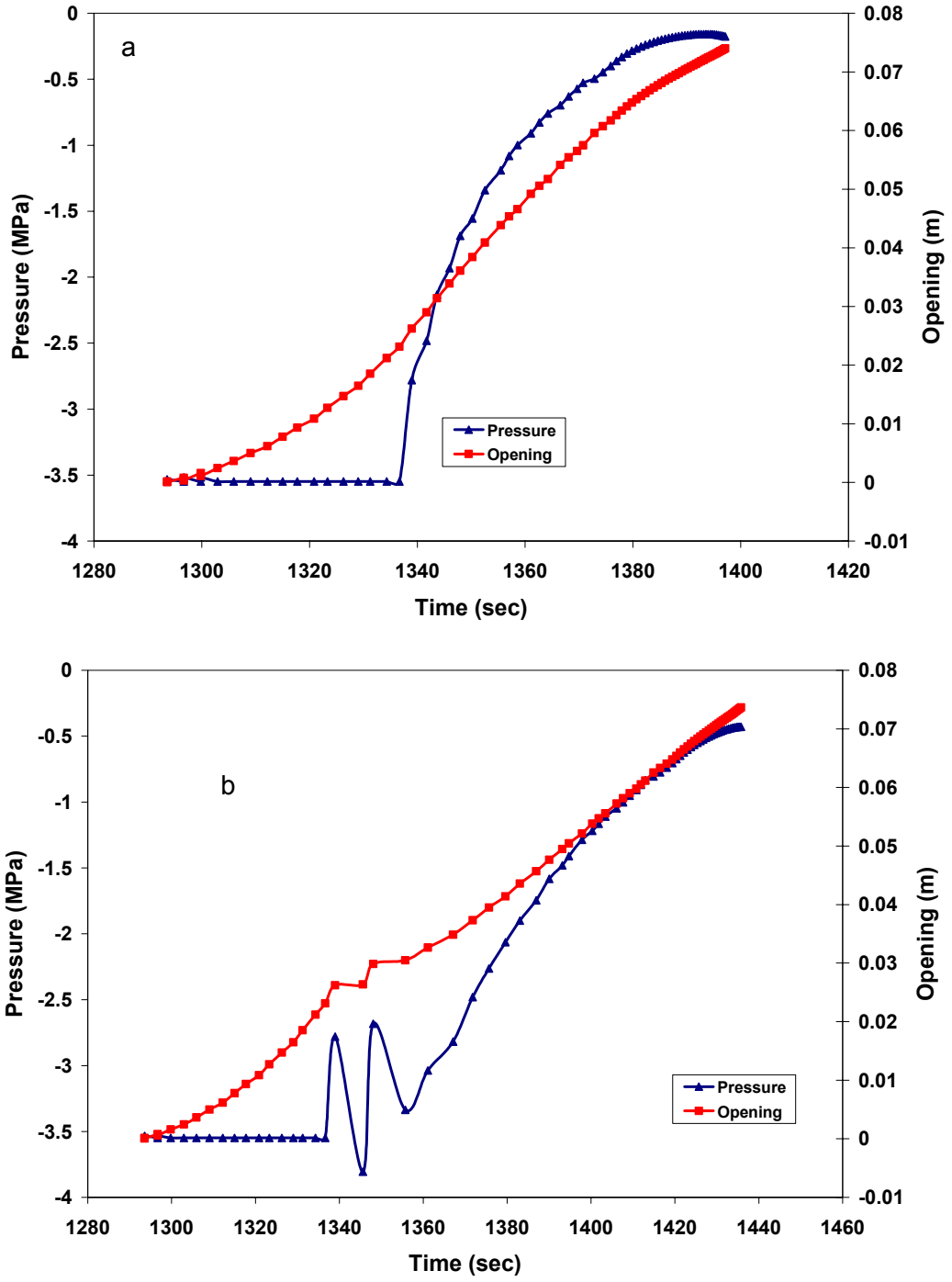

NOTE: a) Case 8 with v_∞ = 1 m/s, buoyancy = 3 kPa/m, no leak-off
b)Case 21 with v_∞ = 1 m/s, buoyancy = 3 kPa/m, 40 percent of magma flux diverted into drift

Figure 6. Crack Width (red) and Net Pressure (blue) on Dike Walls Based on Cases 8 and 21

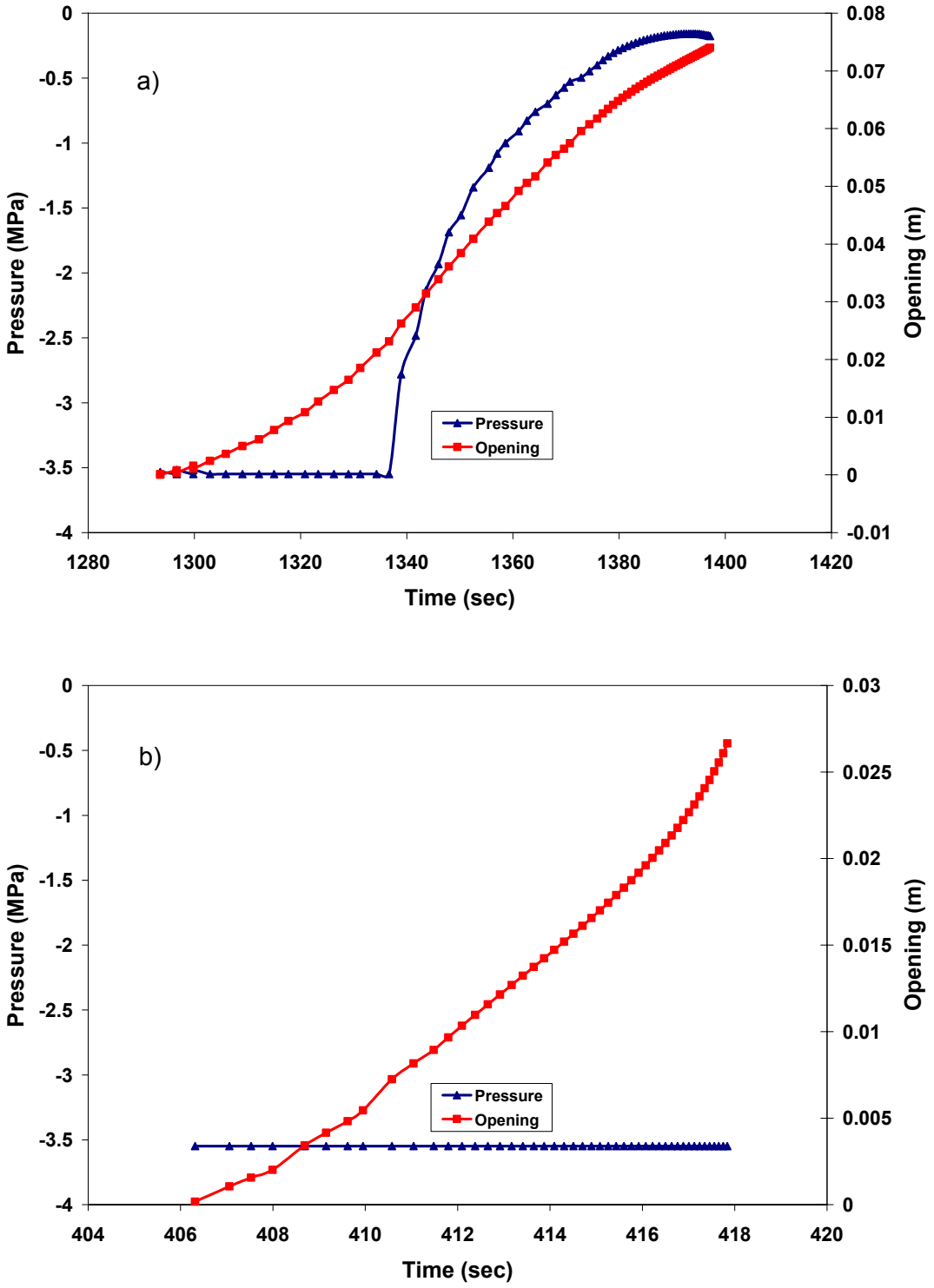

NOTE: a) Case 8 with v_∞ = 1 m/s, buoyancy = 3 kPa/m
b) Case 8 with v_∞ = 5 m/s, buoyancy = 3 kPa/m

Figure 7. Crack Width (red) and Net Pressure (blue) on Dike Walls Based on Case 8

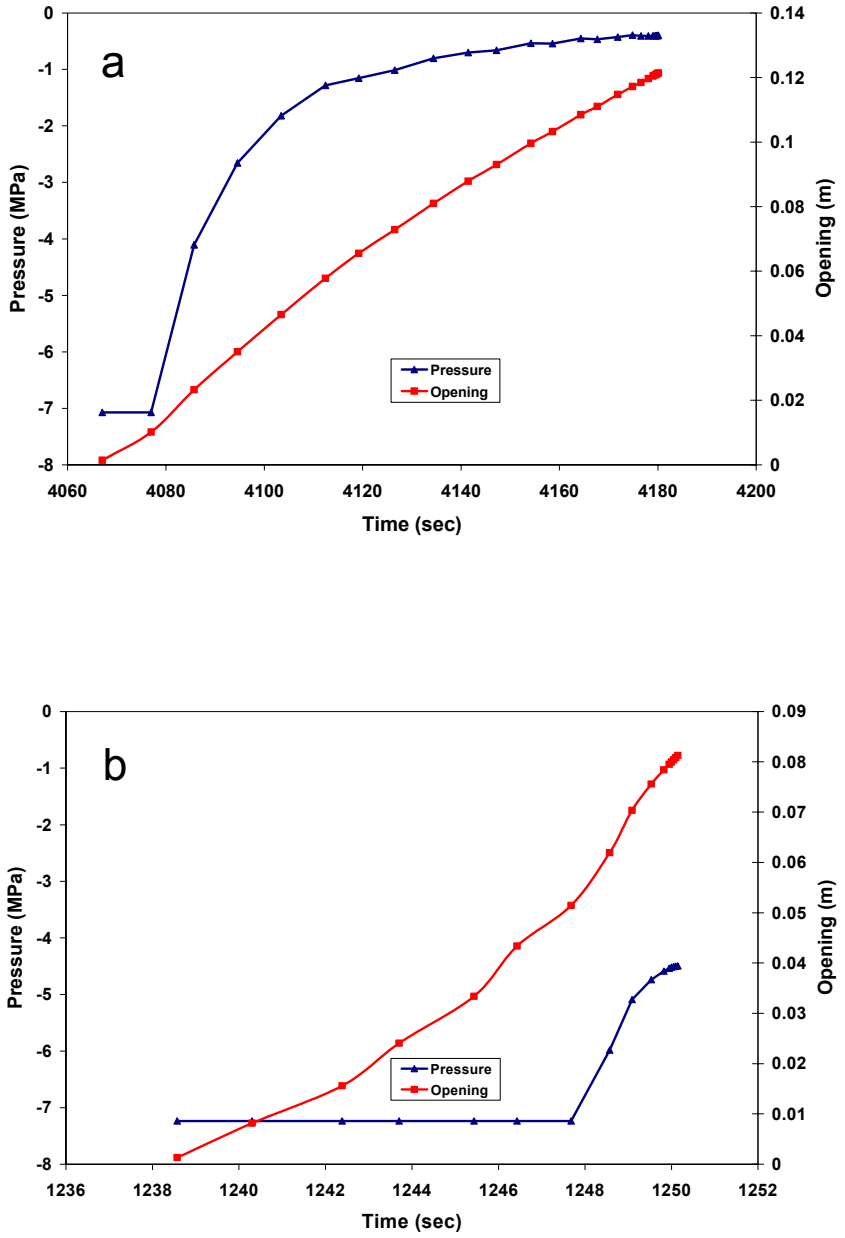

NOTE: a) Case 10 with v_{∞} = 1 m/s, buoyancy = 1.2 kPa/m
b) Case 10 with v_{∞} = 5 m/s, buoyancy = 1.2 kPa/m

Figure 8. Crack Width (red) and Net Pressure (blue) on Dike Walls Based on Case 10

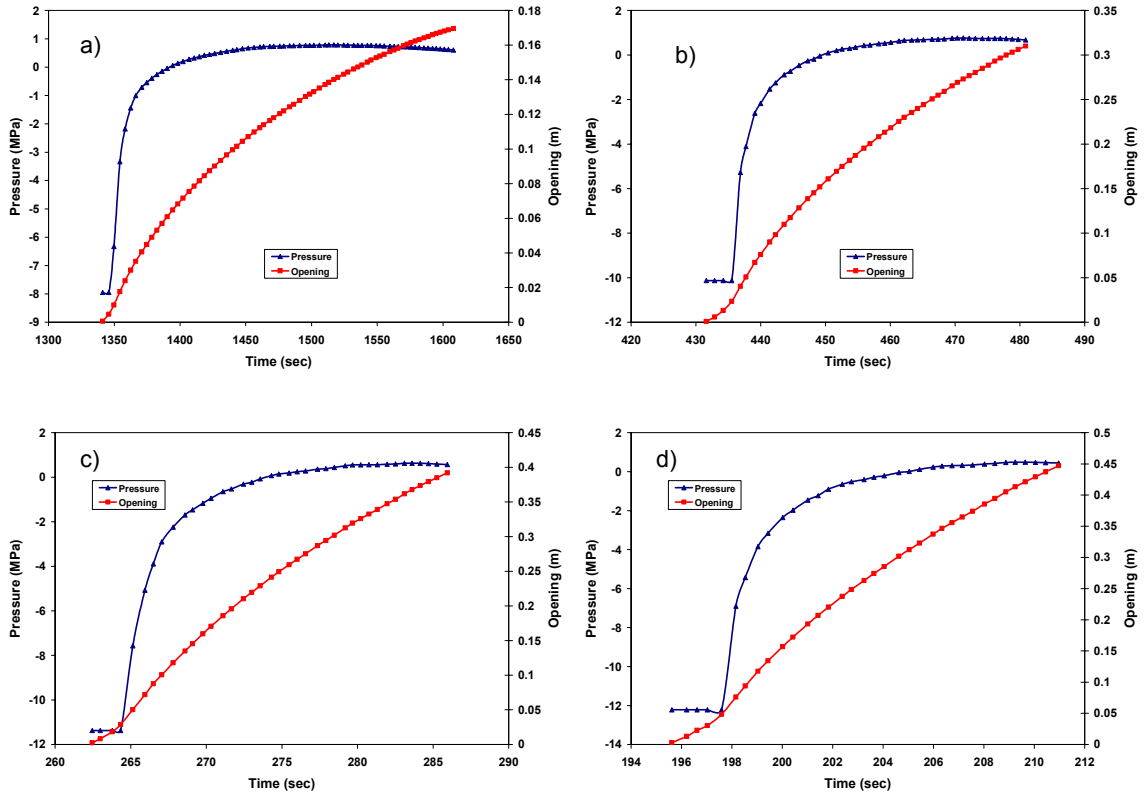

NOTE: a) v_∞ = 1 m/s; b) v_∞ = 5 m/s; c) v_∞ = 10 m/s; d) v_∞ = 15 m/s.

Figure 9. Crack Width (red) and Net Pressure (blue) on Dike Walls for Case 25

6.3.9 Supporting Analyses and Model Applications

6.3.9.1 Effect of Natural Stresses on Dike Propagation

6.3.9.1.1 Topography

Large-scale, 3D, thermomechanical analysis of regional stresses accounting for topography at the Yucca Mountain site was conducted using the FLAC3D code (V2.1, STN: 10502-2.1-00). Detailed description of this analysis is found in BSC (2003 [DIRS 162711]). The topography of the site and its representation in the model are shown in Figure 10. Contours of the vertical stress and orientations of the principal stresses are shown in Figures 11a (larger scale in the vertical plane at N232000) and 11b (smaller scale in the vertical plane at N235000).

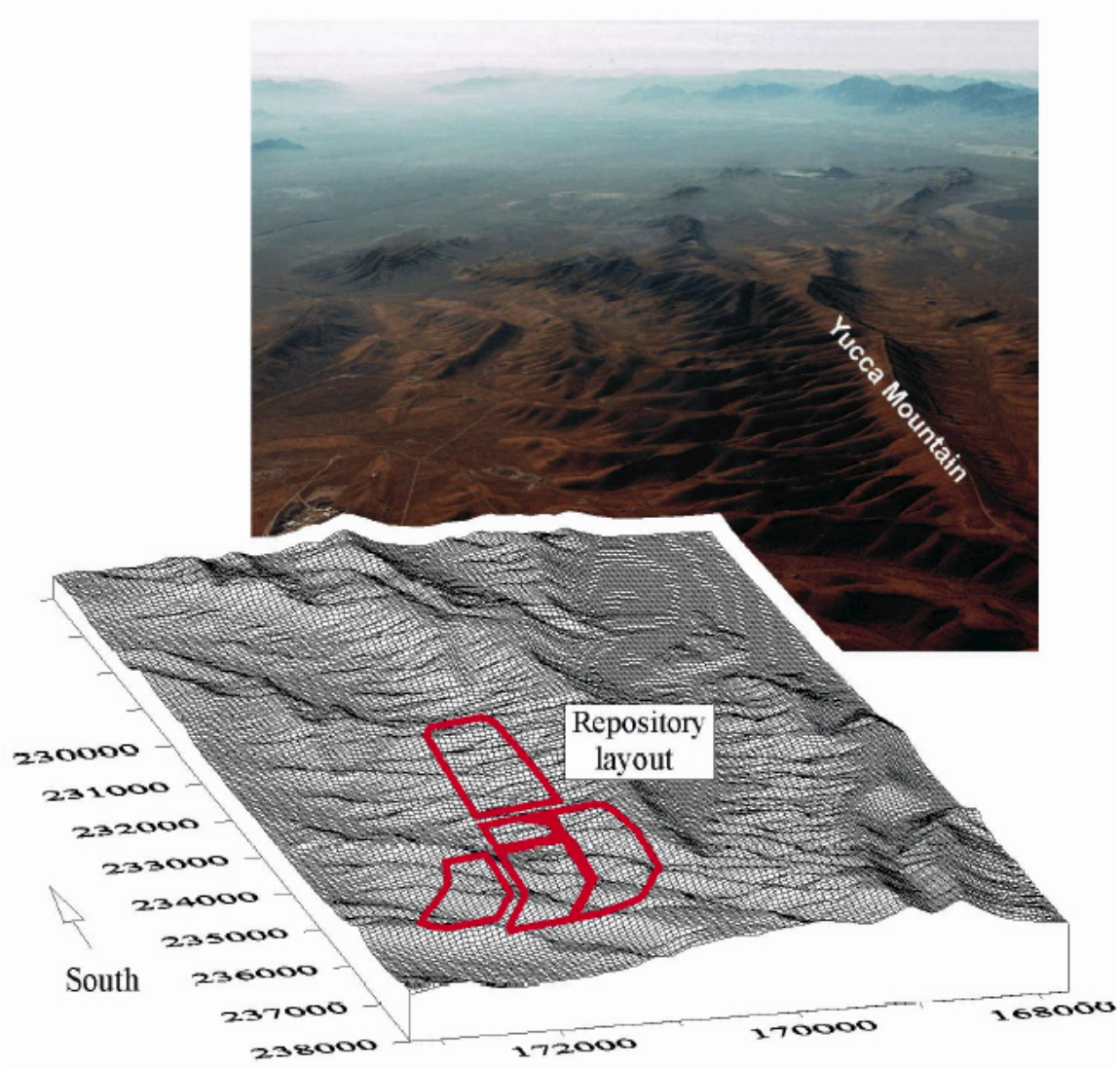

Source: BSC 2003 [DIRS 162711]

Figure 10. Topography at Yucca Mountain Nuclear Waste Repository Site

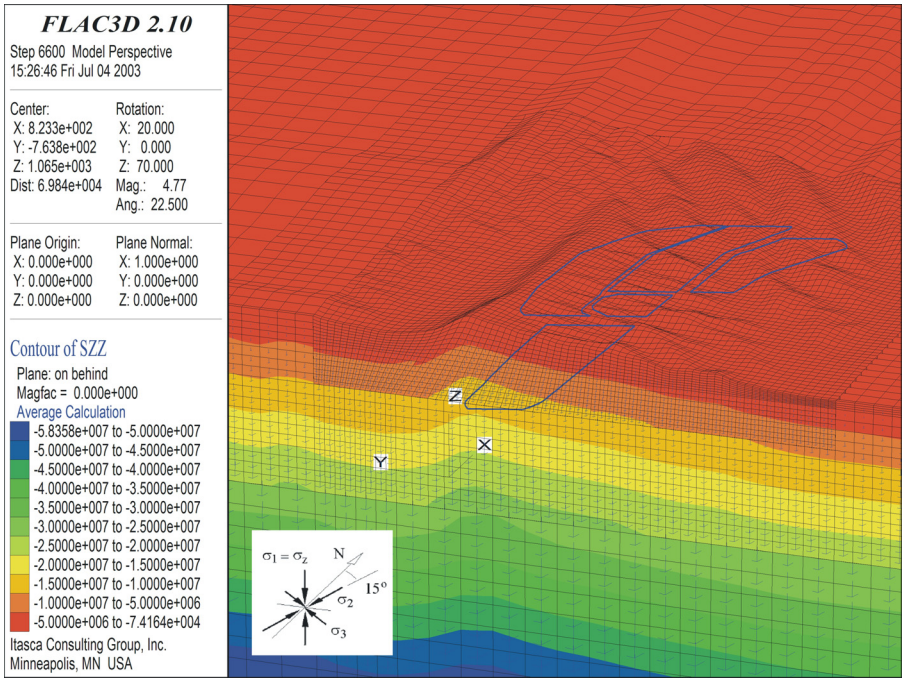

Source: BSC 2003 [DIRS 162711]

NOTE: Negative stresses are compressive. Stress scale in Pa.

Figure 11a. Contours of Vertical Normal Stress and Stress Tensors Due to Topography at Yucca Mountain Nuclear Waste Repository Site: Section Through N232000

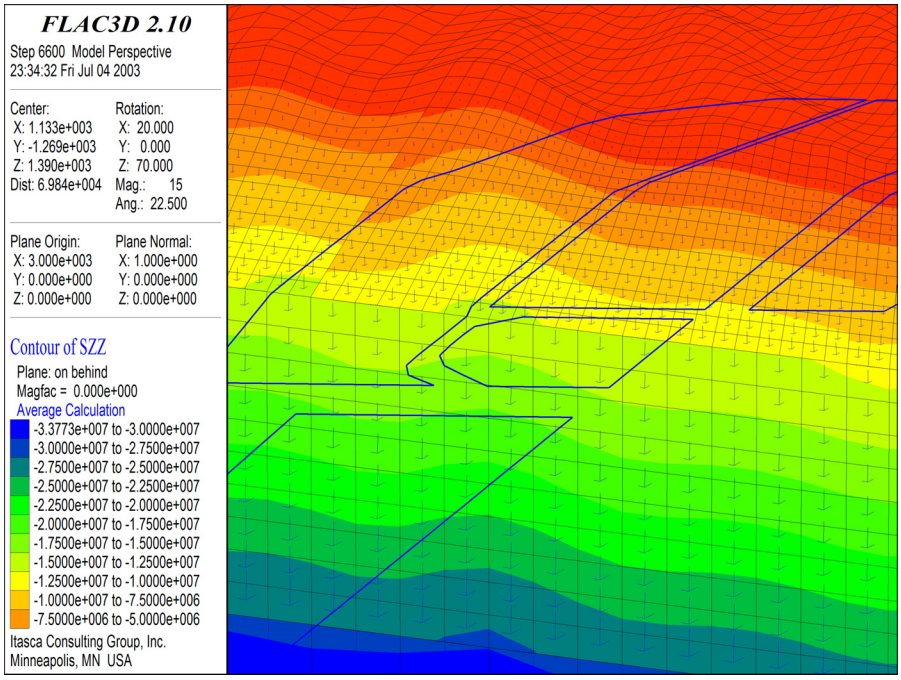

Source: BSC 2003 [DIRS 162711]

NOTE: Negative stresses are compressive. Stress scale in Pa.

Figure 11b. Contours of Vertical Normal Stress and Stress Tensors Due to Topography at Yucca Mountain Nuclear Waste Repository Site: Section Through N235000

The in-situ stress state at Yucca Mountain (before heating) is such that the vertical stress is the maximum principal compressive stress, whereas two other principal stresses of smaller magnitude are in the horizontal plane. The vertical in-situ stress is gravitational (a function of topography). The horizontal stresses are adjusted in the model (being statically undetermined) to match measurements of horizontal stresses (DTN: SNF37100195002.001[DIRS 131356]). The in-situ stress profiles (normal stress components in the directions of the global coordinate axes) from the analysis, along the vertical scanline at (N171000, E235000), are shown in Figure 12. (The horizontal normal stresses in the directions of the global coordinate axes are almost coincident with the horizontal principal stresses.)

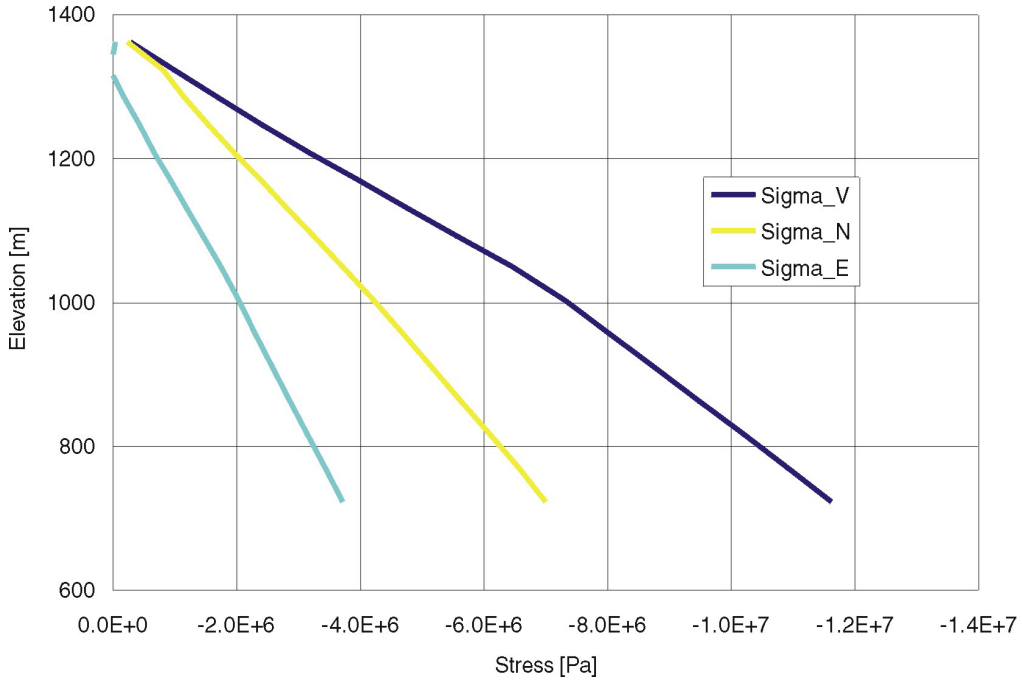

Source: BSC 2003 [DIRS 162711]

NOTES: Sigma_V is the vertical stress; Sigma_N and Sigma_E are the two normal horizontal stresses in directions of the global coordinate axes. These normal stresses are almost coincident with principal stresses.

Figure 12. Variation of Initial In-Situ Stresses With Depth at Yucca Mountain Nuclear Waste Repository Along the Vertical Scanline at E171000, N235000

There is a conjecture that heterogeneity of in-situ stresses and rotation of the major principal stress from the vertical direction due to topography can have an effect on the dike path and potentially divert it from the repository. (The repository is designed to be under the mountain—that is, the region of expected increased stresses.) To address this conjecture, it is clear, from Figures 11a and 11b, that the topography above the repository will have negligible effect on the dike path. There is a variation of the magnitude of the vertical stress, which increases at the repository (compared to vertical stresses in the neighboring valleys) due to larger overburden of the mountain. However, the vertical stress always remains the major principal stress, and, what is more important from the perspective of the direction of dike propagation, direction of the major principal stress always remains vertical (see Figures 11a and 11b). Based on current

understanding of stress state, the topography at the Yucca Mountain will not cause deflection of the dike.

6.3.9.2 Effect of Repository Structure on Dike Propagation

6.3.9.2.1 Stresses Due to Excavation of the Drift

The stress concentrations around a circular drift extending in the *z*-direction that are induced by the far-field stresses are well known and, at the tunnel wall, are given by:

$$\sigma_\theta = (\sigma_x + \sigma_y) - 2(\sigma_x - \sigma_y)\cos(2\theta) - 4\tau_{xy}\sin(2\theta) \quad \text{(Eq. 32)}$$

$$\sigma_{zz} = \sigma_z - 2\nu(\sigma_x - \sigma_y)\cos(2\theta) - 4\nu\tau_{xy}\sin(2\theta) \quad \text{(Eq. 33)}$$

$$\tau_{\theta z} = 2(-\tau_{xz}\sin\theta + \tau_{yz}\cos\theta) \quad \text{(Eq. 34)}$$

$$\tau_{r\theta} = \tau_{rz} = 0 \quad \text{(Eq. 35)}$$

where:

θ = the angle around the drift as measured from the *x* axis towards the *y* axis
σ_x, σ_y, σ_z = the far-field normal components of stress
τ_{xy} τ_{yz}, and τ_{zx} = the far-field shear stresses
σ_{zz} = the axial component of stress
σ_θ = the hoop stress
$\tau_{r\theta}$ and τ_{rz} = radial shear stress factors, which are zero at the tunnel wall (until pressurized by magma, which is considered later).

All of these stresses are at the drift wall, where the stress concentration is highest. Stress changes from the drift excavation are of limited spatial extent and decay quickly as a function of distance from the drift wall and become almost equal to unperturbed, far-field stress state at a distance of 3× radii from the drift wall. They will have insignificant effect on dike propagation.

6.3.9.2.2 Thermal Stresses

On average, the vertical stresses (statically determined) would not change as a result of heating. If heating increases the magnitude of the horizontal principal stresses such that both become larger than the vertical principal stress, the repository could be shielded from potential volcanic intrusion for a period of time (while the conditions of such stress "inversion" exist).

The temperature and stress changes due to heat generated by the emplaced waste were simulated through the entire regulatory period of 10,000 years. Detailed description of this analysis is found in BSC 2003 [DIRS 162711]. The maximum increase in horizontal stress due to heating occurs between 500 and 1000 years after waste emplacement.

Figures 13a, 13b, and 13c show the stress profiles after 500, 1000, and 2000 years, respectively, along the vertical scanline at N171000, E235000.

Between 500 and 1000 years of heating the vertical stress becomes the least-compressive stress over a height of approximately 200 m and, at most, 3 MPa smaller than the smaller horizontal principal stress (Figures 13a and 13b). For duration of heating longer than 1,000 years the stress difference and the spatial extent of the region with stress inversion decrease. After 2000 years (Figure 13c) of heating, normal stress in EW direction is only 1 MPa larger than the vertical stress.

Figures 13a, 13b, and 13c show that the stress change due to heating extends to a depth of about 100 m below the repository (that is, repository elevation of 1083 m). Considering the repository width of more than 1 km, it is almost impossible for the dike propagating towards the central portion of the repository to turn and pass by the repository without intersecting any part of it.

Realistic potential for dike deflection will exist only near the edges of the repository and for the limited time during the regulatory period (between 500 and 2000 years after waste emplacement). It was conservatively assumed in the further considerations that the repository would not have an effect on the dike path.

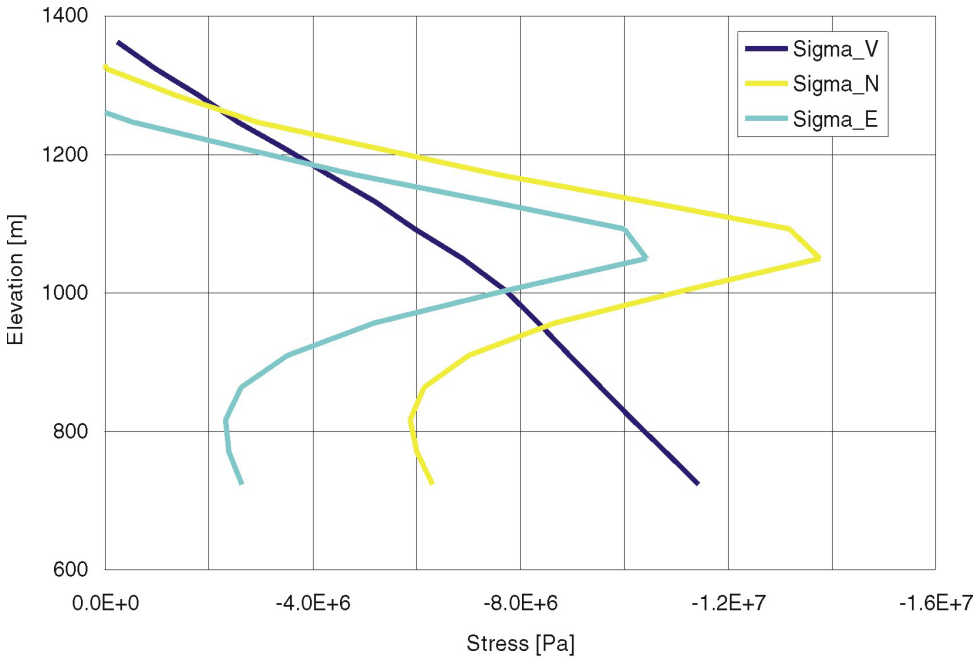

Source: BSC 2003 [DIRS 162711]

NOTES: Sigma_V is the vertical stress; Sigma_N and Sigma_E are the two normal horizontal stresses in directions of the global coordinate axes. These normal stresses are almost coincident with principal stresses.

Figure 13a. Predicted Variation of Stresses With Depth at Yucca Mountain Nuclear Waste Repository Along the Vertical Scanline at E171000,N235000 After 500 Years of Heating

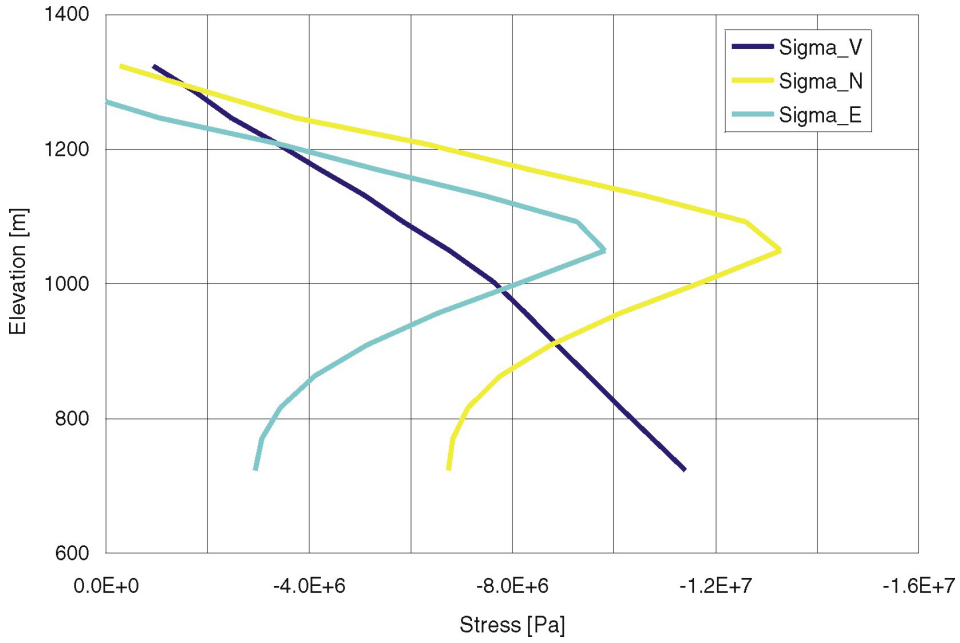

Source: BSC 2003 [DIRS 162711]

NOTES: Sigma_V is the vertical stress; Sigma_N and Sigma_E are the two normal horizontal stresses in directions of the global coordinate axes. These normal stresses are almost coincident with principal stresses.

Figure 13b. Predicted Variation of Stresses With Depth at Yucca Mountain Nuclear Waste Repository Along the Vertical Scanline at E171000, N235000 After 1000 Years of Heating

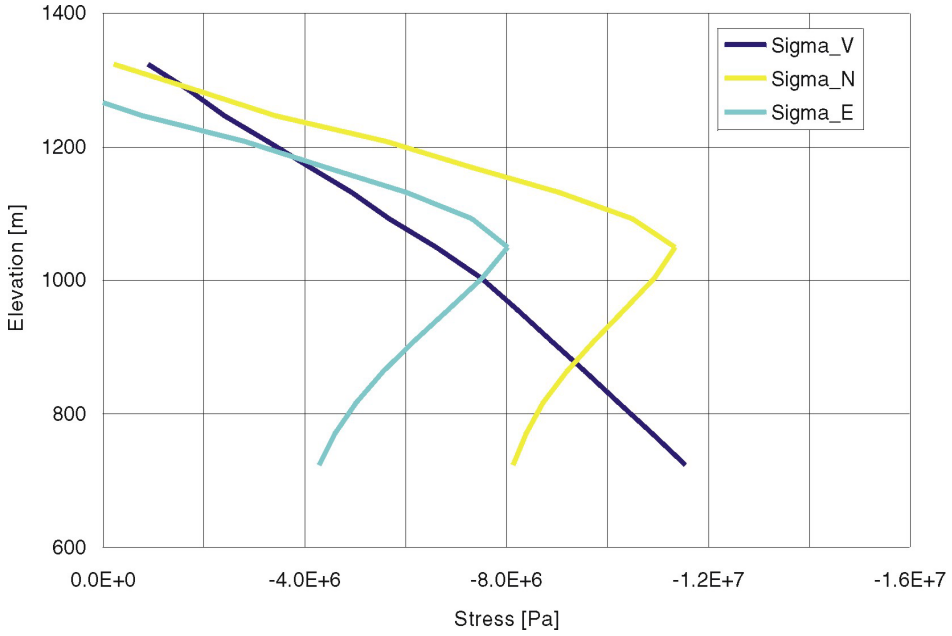

Source: BSC 2003 [DIRS 162711]

NOTES: Sigma_V is the vertical stress; Sigma_N and Sigma_E are the two normal horizontal stresses in directions of the global coordinate axes. These normal stresses are almost coincident with principal stresses.

Figure 13c. Predicted Variation of Stresses With Depth at Yucca Mountain Nuclear Waste Repository Along the Vertical Scanline at E171000, N235000 After 2000 Years of Heating

6.3.9.2.3 Diversion of Magma Into a Drift

In the absence of a fully coupled model to simulate the flow of magma from a dike into a drift, the problem has been approximated by considering separately the supply of magma at the drift level and the flow that would occur given that supply. Supply has been addressed in Section 6.3.8.2. This section considers the flow.

6.3.9.2.3.1 Flow Into Drifts

The assumption of effusive flow (Assumption 16 in Section 5.2) permits solution of the flow equations using a simple spreadsheet tool. Standard hydraulic engineering equations for flow over a weir, through an orifice from a half-space, and through a pipe can be used to model the flow of such a fluid. Details of the equations are included below in Section 6.3.9.2.3.1.4.

In the model used, magma rises in the dike (starting at height 0.0 m at the bottom of the drift at time 0.0 s) driven by its velocity at great depth. For each time step, the volume of magma rising above the 0.0 level can either flow into the drift or continue up the dike. The amount going into the drift is taken to be the minimum of that calculated by the various equations. Any magma that does not flow into the drift is held in the dike above the 0.0 level; that magma, plus any new magma rising in the next time step, is available to flow into the drift.

Initially, the magma flows into the drift as it would flow through a weir of circular cross section until the height of the magma reaches the top of the drift. After the magma height exceeds that of the drift, the problem is analogous to a fluid draining out of a tank through an orifice. Because the dike is fairly thin (on the order of 1 m with about 80 m between drifts) and has a viscosity substantially larger than water (on the order of 10–100 Pa-s), the orifice equation is modified to include the effect of viscous drag in the drift following the method of Detournay et al. (2003 [DIRS 162914], Appendix 3.5).

When the drift becomes sufficiently filled that viscous drag in the drift controls loss from the dike, the magma flow into the drift is subject to the pipe-flow equation balanced by viscous drag in the dike. For this equation, the length L is taken to be the cumulative discharge from prior flow divided by the cross-sectional area of the drift.

6.3.9.2.3.1.1 Description of Input

Input for the model is found in Table 2 and consists of:

- Engineered system properties:
  - Drift diameter (taken to be 5.5 m)
  - Waste package diameter (either 0 m or 1 m)
  - Drift spacing (taken to be 80 m)

- Natural system properties:
  - Magma density (taken to be 2000 kg/m^3)
  - Magma viscosity (either 10 Pa-s or 100 Pa-s)
  - Magma rise velocity at depth (either 1 m/s or 10 m/s)
  - Dike width (taken to be 1 m).

6.3.9.2.3.1.2 Assumptions, Idealizations, and Simplifications

In order to demonstrate the effects of deviations of magma viscosity and supply rate, calculations of magma flow have been done with two values of viscosity and two supply rates, using values that span the qualified input parameters listed in Table 2.

It is assumed (Assumption 16 in Section 5.2) that the magma entering the drift from the dike is partially degassed so that it does not explosively decompress. This assumption is required in order to apply the hydraulic equations used to analyze magma flow in drifts. It is consistent with the limited observations that are available (at Hawaii and at Parícutin in Mexico) of magma behavior before magma in a new dike reaches the surface.

The weir equation will give an overestimate of the flow into the drift because it assumes that material flowing into the drift does not build up just inside the drift to decrease the head driving flow over the weir. Any frictional losses at the weir interface are also ignored. Similar comments apply to the orifice equation.

The definition chosen for L (the length of the drift filled with magma) leads to inaccuracy in the discharge Q that is difficult to predict simply. This approximation is equivalent to taking the magma front in the drift to be vertical, which it certainly will not be. Early in the flow history, the fact that viscous drag on the walls only occurs along the bottom of the flow will probably result in greater discharge. Later, as the length L becomes long compared to the slope times the drift diameter, this approximation will become closer to reality.

The idealization of the drift cross-section as being perfectly circular ignores the drift invert, which is on the order of 4 percent of the cross-sectional area of the entire drift. The result will be a slight decrease in the hydraulic radius of the drift and in the volume of the drift and a change of the real weir cross-section that will be considerable at the earliest times of the flow. The decrease in the hydraulic radius will result in slightly lower discharge rate from the dike into the drift. The decrease in the volume of the drift will lead to a shorter time to fill the drift at a fixed discharge rate. These two effects have an opposite sign but do not exactly cancel each other. The effect on the weir discharge is limited to the very earliest times of flow into the drift.

The model idealizes the blockage of the drift to be only obstruction by waste packages, packed end-to-end. This approach ignores the effects of rails, pallets and drip shields, and the effects of gaps between waste packages on the flow. The presence of rails, pallets, and drip shields will reduce the total volume to be filled by the magma and will increase the viscous drag forces. The gaps between waste packages will result in a larger volume to be filled and a longer time to fill the drift with magma. The net result of these compensating errors will be little change in the time required for magma to fill the drift.

6.3.9.2.3.1.3 Initial and Boundary Conditions

The initial condition consists of magma beneath the end of the drift at the height of the invert. The magma is moving upward at the chosen magma rise velocity. The drift is a horizontal tube, the diameter of which is 4× the hydraulic radius; the drift is initially empty (except for the decreased hydraulic radius in obstructed cases).

All surfaces except the magma-free surface, if any, are rigid, and the equations are based on a no-slip boundary.

6.3.9.2.3.1.4 Mathematical Formulation

The governing equations are those for flow of a liquid over a weir (weir equation), out of a tank through a circular orifice well below the top of the liquid in the tank (orifice equation), radially toward a point of discharge between two parallel plates (plate-drain equation), and through a pipe (pipe equation). The first two equations (Henderson 1966 [DIRS 164124]) are used separately. A simultaneous solution to the pipe equation and the plate-drain equations is used. Geometric configuration and nomenclature are illustrated in Figure 14.

The weir equation for weir of arbitrary shape:

$$Q = \sqrt{2}g\int_0^H w(h)\sqrt{h}dh \qquad \text{(Eq. 36)}$$

where:

Q = the discharge rate through the weir
H = the height of water in the weir
$w(h)$ = the width of the weir at height h

For a circular cross-section of radius a, this equation reduces to:

$$Q(H) = 2^{1.5} g\sqrt{aH^2 - \frac{H^3}{3}} \qquad \text{(Eq. 37)}$$

and the wetted cross-section of the flow is:

$$2a^2 \cos^{-1}\left(\frac{a-h}{a}\right) - (a-h)\sqrt{2ah - h^2} \qquad \text{(Eq. 38)}$$

The orifice equation for flow from a half-space through a circular hole of radius a is:

$$Q = \pi a^2 \sqrt{2gh} \qquad \text{(Eq. 39)}$$

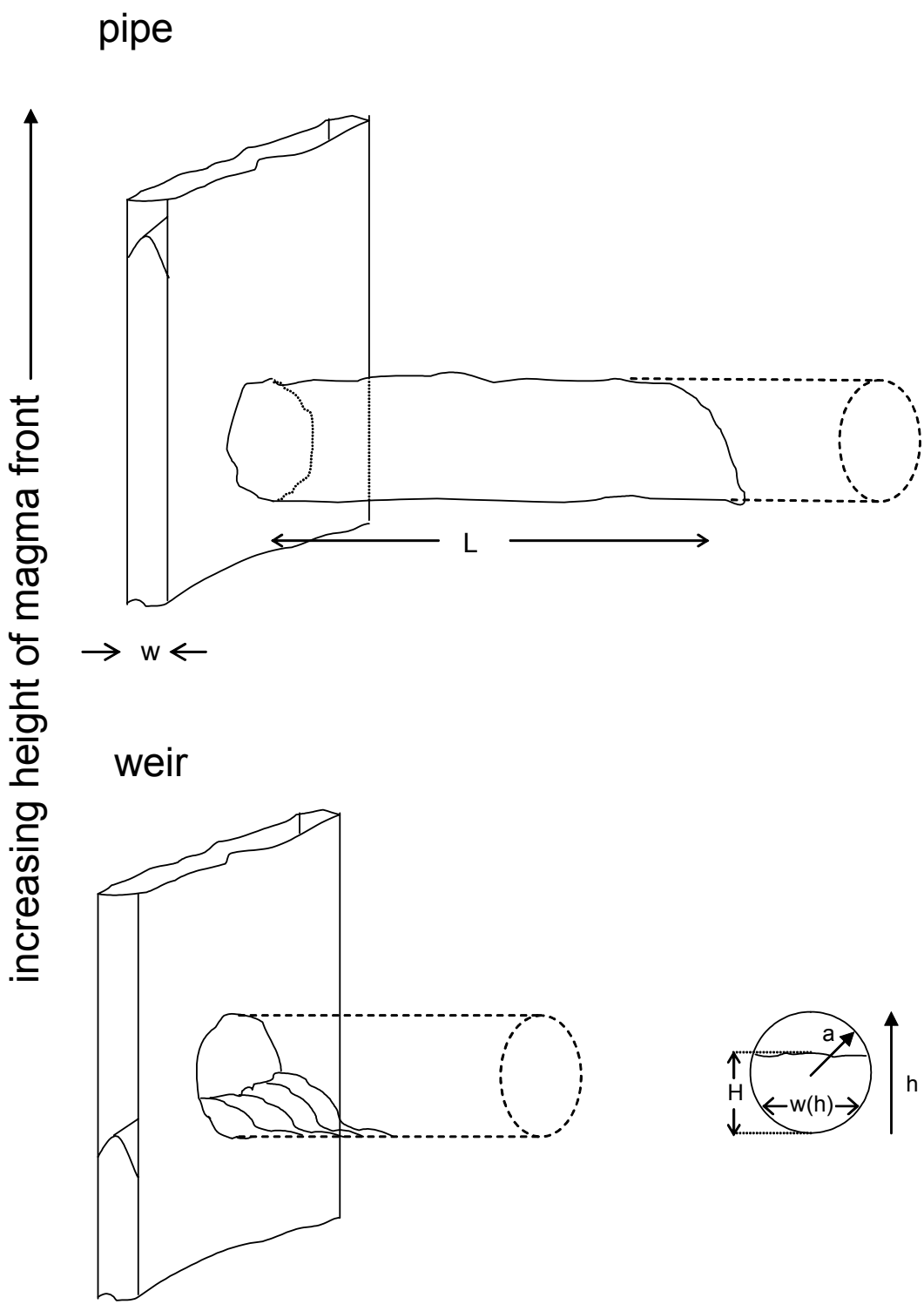

NOTE: The figure represents flow of magma for two distinct situations. In the lower drawing, the magma has not risen to the top of the drift, and a weir equation (Equation 37) is used. In the upper drawing, viscous drag in either the dike or the drift limits flow and Equation 42 is appropriate.

Figure 14. Schematic Representing Flow of Magma From Dike Into Drift

The equation for flow out of a dike into a pipe is derived following the method of Detournay et al. (2003 [DIRS 162914], Appendix 3.5, p. 62), who gives the flux from a dike through a circular hole q_2 as:

$$q_2 = 5.3\frac{2\pi a w^3}{3\eta(d/2)}(\rho g H - P) \quad \text{(Eq. 40)}$$

and the flux down a pipe as:

$$q_3 = \frac{\pi a^4}{8\eta L}P \quad \text{(Eq. 41)}$$

where:

a = the radius of the hole or drift
w = the width of the dike (different from *w(h)* in the weir equation)
η = the magma viscosity
d = the spacing between drifts
ρ = the magma density
H = now the height of magma above the drift
P = the pressure at the dike/drift interface
L = the length of drift filled with magma.

Equating q_2 and q_3 yields the flux under the dual constraint of flow in the dike and flow in the drift (pipe-flow equation). After rearranging, this equation becomes:

$$q_{pipe} = \frac{4}{3}(5.3)\frac{a w^3 \rho g H}{d\eta}\left[1 + \frac{32}{3}(5.3)\frac{a w^3 L}{d a^4}\right]^{-1} \quad \text{(Eq. 42)}$$

Defining a "scaling volume", V^*, as:

$$V^* = \frac{4}{3}(5.3)\frac{a w^3}{d} \cong 7.07\frac{a w^3}{d} \quad \text{(Eq. 43)}$$

this equation simplifies to:

$$q_{pipe} = V^*\frac{\rho g H}{\eta}\left(1 + 8V^*\frac{L}{a^4}\right)^{-1} \quad \text{(Eq. 44)}$$

6.3.9.2.3.1.4.1 Variables and Parameters

The variables are the magma rise velocity (1 m/s or 10 m/s), the magma viscosity (10 Pa-s or 100 Pa-s), and the open cross-sectional area in the drift (waste packages present or absent).

Parameters include the magma properties (density and dike width) and the engineered properties (drift diameter and drift spacing).

6.3.9.2.3.1.5 Model Testing, Sensitivities, and Calibration Activities

The weir, orifice, and pipe-flow equations have been tested exhaustively over the past century on innumerable water-control features. Their application to magma has not been verified but is based on the underlying physics of fluid flow. The equations were implemented in an Excel spreadsheet and are documented in Scientific Notebook Number SN-LANL-SCI-279-V1, pages 12–22, dated March 25, 2003 (Gaffney 2002 [DIRS 163631]).

6.3.9.2.3.1.6 Results

Eight cases have been evaluated for the expected flow of magma into drifts. The eight cases cover variations in magma-rise velocity, magma viscosity, and whether the drifts are empty or filled with waste packages. These cases are listed in Table 9.

Table 9. Cases Evaluated for Magma Flow Into Drift

Model	Magma Viscosity (Pa-s)	With or Without Waste Packages	Magma Rise Speed (m/s)
1	100	without	1
2	10	without	1
3	100	with	1
4	10	with	1
1 (10)	100	without	10
2 (10)	10	without	10
3 (10)	100	with	10
4 (10)	10	with	10

DTN: N/A

The results are presented in Figures 15 through 19, showing, respectively, the discharge rate out of the dike as a function of time, the length of drift filled as a function of time, the discharge rate as a function of the length of drift filled, the average velocity of magma at the dike-drift interface, and the height that magma rises above the drift invert.

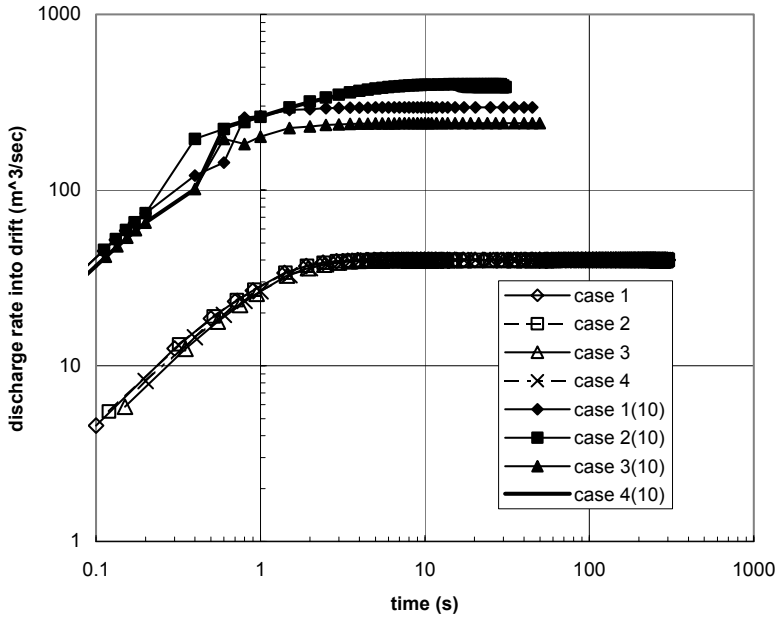

DTN: LA0303EG831811.001

Figure 15. Discharge Rate for Effusive Magma Flowing Into Drifts as a Function of Time

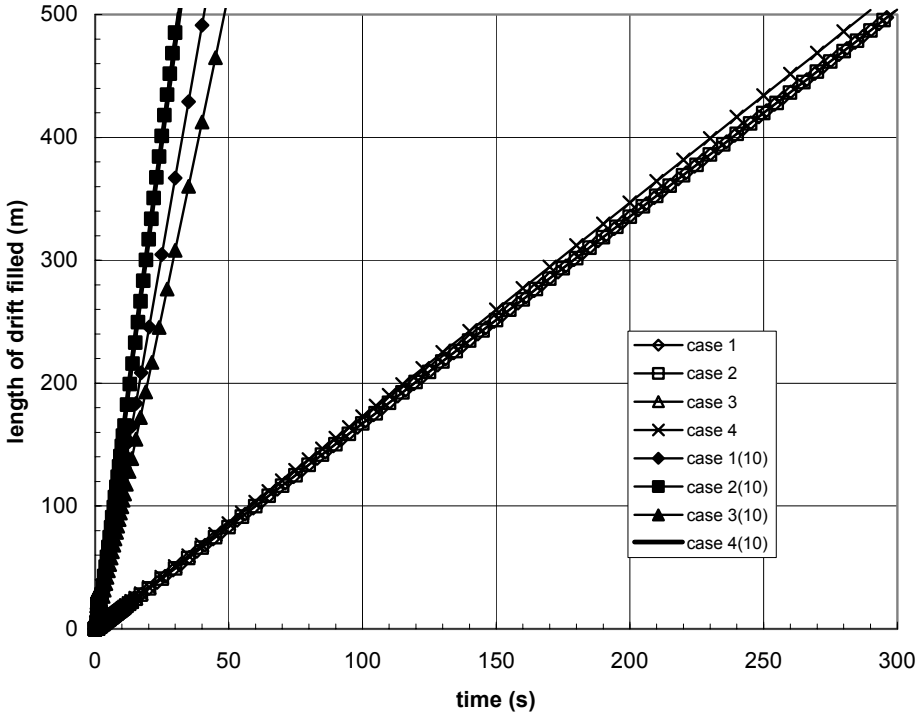

DTN: LA0303EG831811.001

Figure 16. Length of Drift Filled by Effusive Magma Flowing Into Drifts as a Function of Time

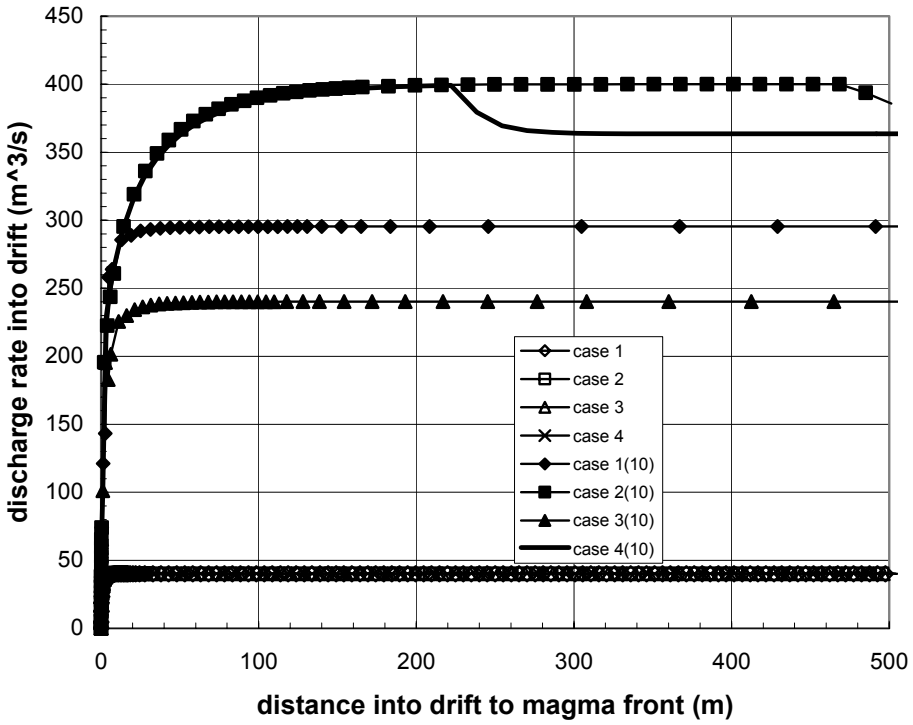

DTN: LA0303EG831811.001

Figure 17. Discharge Rate for Effusive Magma Flowing Into Drifts as a Function of Length of Drift Filled

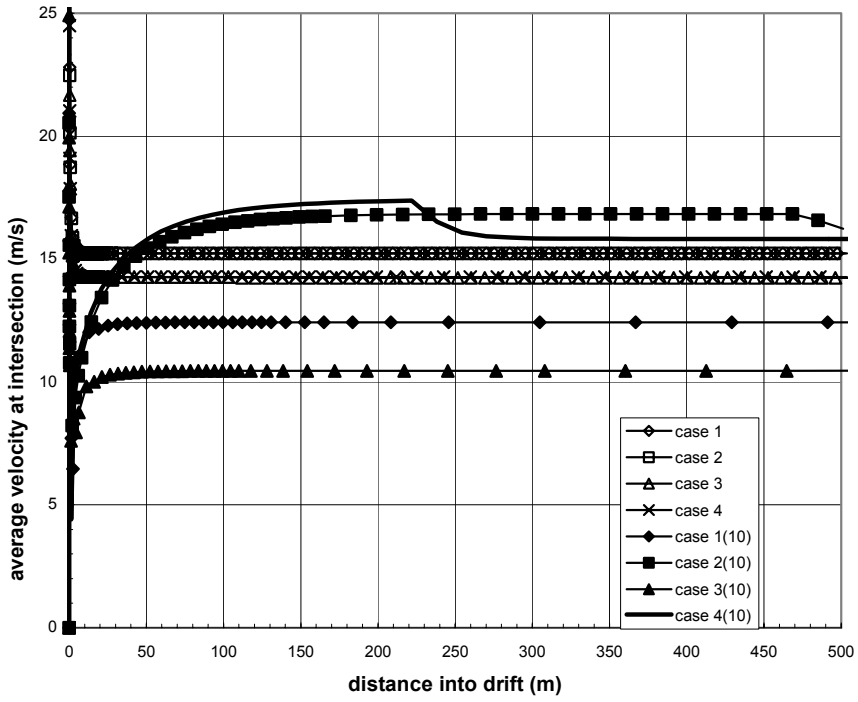

DTN: LA0303EG831811.001

Figure 18. Average Horizontal Velocity for Effusive Magma Flowing Into Drifts as a Function of Time at Dike-Drift Intersection

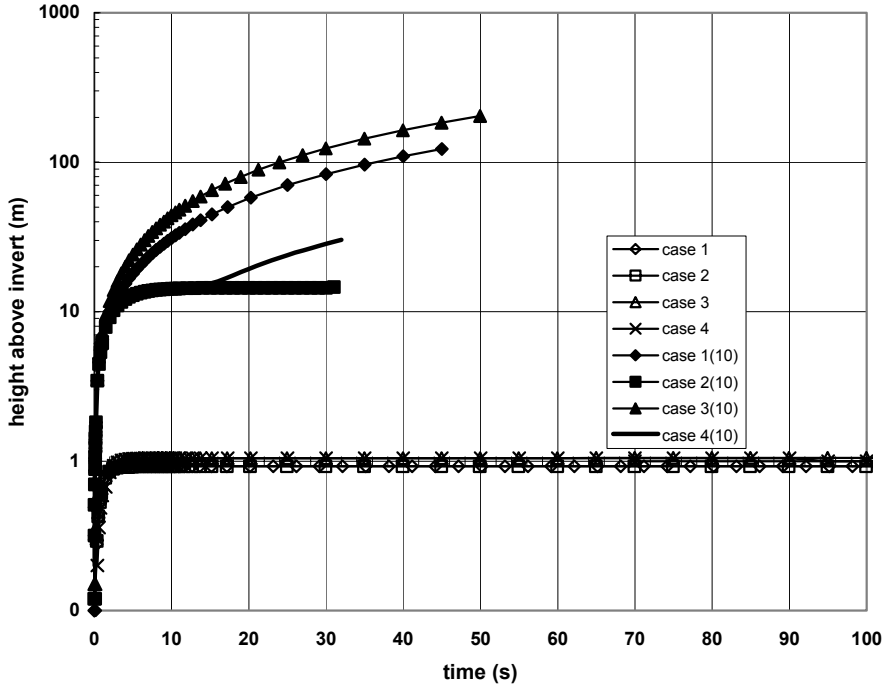

DTN: LA0303EG831811.001

Figure 19. Height of Magma in Dike Above Invert for Effusive Magma Flowing Into Drifts as a Function of Time

6.3.9.2.3.1.7 Discussion

This model ignores any exsolution of gas from the magma or growth in size of bubbles of gas already exsolved. It addresses simple effusive flow.

The weir equation will give an overestimate of the flow into the drift because it assumes that material flowing into the drift does not build up just inside the drift to decrease the head driving flow over the weir. Any frictional losses at the weir interface are also ignored. Similar comments apply to the orifice equation for small heights of the magma rise in the dike above the drift. This approach only affects the results for small discharges and small velocities occurring early in the encounter.

The definition chosen for L leads to inaccuracy in the discharge Q that is difficult to predict simply. In effect, the definition assumes that the magma front in the drift is vertical, which it certainly will not be. Early in the flow history, the fact that viscous drag on the walls only occurs along the bottom of the flow (open-channel flow) will probably result in greater discharge. Later, as the length L becomes long compared to the slope of the front of the magma times the drift diameter, this equation should become a good approximation to the actual behavior.

For the purposes of this calculation, the dimensions of an empty drift have been used. The effect of waste packages filling the drift have been accounted for by considering a smaller "hydraulic radius" (R_h) for the filled case. The hydraulic radius is the cross-sectional area divided by the

perimeter of the flow. For a circular pipe, R_h is equal to half of the geometric radius. For a 5.5-m-diameter drift, R_h = 1.375 m. With a 1-m-diameter cylinder blocking part of the flow, R_h is reduced to 1.01 m.

The ultimate limit to discharge from dike to drift is that, when integrated, it can not exceed the total amount of magma that has risen above the base of the drift. If the dike is 1 m thick with magma rising at 1 m/s, 80 m^3/s are available to discharge into drifts that are at 80-m intervals. Because the discharge will go into drift segments on both sides of the dike, this condition puts a limit of 40 m^3/s on the discharge into one segment. If the magma were rising at 10 m/s, then this limit would be 400 m^3/s. The only cases for which the drift rather than the magma supply provides the ultimate limit to discharge into the drift are for the more rapidly propagating dikes (10 m/s). Then the more viscous magma (100 Pa-s) is limited by wall friction in the drift to discharges below about 300 m^3/s for an open drift and below 250 m^3/s for a drift with waste packages.

6.3.9.2.3.1.8 Summary

The analysis of this section shows that the rate of magma flow into drifts will be limited by the rate of magma supply, except when the supply is very large (v_∞ on the order to 10 m/s) and the magma viscosity is high (on the order of 100 Pa-s). Only for high supply rates will magma rise much above the drift level before the drifts are filled. The time needed to fill 500 m of drift will be on the order of 30 to 300 seconds, depending on the supply rate. The results can be linearly scaled to other drift lengths.

6.3.9.2.3.2 One-Dimensional Dike Propagation Models

The effect on dike propagation of leak-off of driving fluid into drifts was investigated using NPHF2D V 1.0 [DIRS 163665] by incorporating a localized leak-off into the models of dike propagation. These were Cases 15 to 24 and 29 to 33 referenced in Section 6.3.8. The intent was to couple the 2D model of dike propagation with a model of magma flow inside the drifts. The results of Section 6.3.9.2.3.1 indicate that, under very general conditions, all of magma from the dike will flow into the drifts. Although under such circumstances a 2D model is not a proper approximation of flow conditions inside the dike, the effects of leak-off of up to 40 percent of flow rate inside the dike are investigated using a 2D model. (Leak-off of 100 percent was analyzed using a 3D model discussed in Section 6.3.9.2.3.3) Effects of increased gas pressure in the tip cavity and of increased confining stress were also addressed. The reader is referred to Attachment II for details. This section summarizes the most relevant results.

6.3.9.2.3.2.1 Effect of Pressure Inside the Tip Cavity

Magmas have a certain amount of volatiles (gases and steam). At high pressures, the gases are completely dissolved in the magma. As the magma pressure falls below a certain threshold pressure (i.e., as the magma approaches the ground surface), exsolution takes place, and gases form bubbles inside the melt. The volumetric percentage of the bubbles increases as the magma pressure decreases. In the magma near the tip cavity, the gases move (due to the pressure gradient) and are released into the cavity. At the same time, as pressure builds inside the cavity, the gases will leak-off from the cavity into the surrounding rock formations. The model

discussed in this report does not simulate any of these processes. However, a simplified analysis (Detournay et al. 2003 [DIRS 162914]), based on consideration of the gas diffusivity in tuff at Yucca Mountain, shows that the cavity gas pressure may be insignificantly larger than the gas pressure in the surrounding formation (i.e., atmospheric pressure). Because this simplified analysis is still preliminary, the effect of gas pressure inside the tip cavity on the conditions of dike propagation was investigated.

The results of the numerical model are shown in Figures 20 and 21. Two cases were considered: a) 1 MPa cavity gas pressure for **D**=2.67 (Case 28) and b) 0.49 MPa cavity gas pressure for **D**=20.28 (Case 14), both for the case of ρ_r = 2400 kg/m^3, η = 10 Pa-s, and v_∞ = 1 m/s.

Note that the cavity gas pressure does not significantly affect the velocity of the magma front. The velocity of the dike tip is affected, particularly when the tip gets close to the ground surface (i.e., when the cavity pressure becomes a significant proportion of the horizontal far-field stress). Thus, the cavity pressure increases the cavity length. Also, the cavity pressure reduces the maximum magma pressure at a given depth.

Neglecting the cavity gas pressure is a conservative assumption with respect to the analysis of the magma flow inside the repository drifts because it will overpredict both the rate of change of magma pressure and the maximum magma pressure.

6.3.9.2.3.2.2 Effect of Magma Leak-Off to Drifts

Simulations were done with leak-off of 40 percent of the far-field magma flux at 300 m depth. Results, in the form of plots of velocity of the crack tip and of the magma front as functions of time, are presented in Figure 22.

By comparing the three cases, it is seen that the main effect of leak-off is to slow the motion of both the crack tip and the magma front, the greater effect being on the magma front. Leak-off has very little effect on the crack tip in the case for which the tip is already close to the surface and accelerating rapidly (Figure 22, middle panel). When the dike is thinner (Figure 22, top panel) or when there is higher confining pressure (Figure 22, bottom panel), there is more retardation. But the leak-off considered in these cases (20 and 40 percent) does not prevent the dike tip from reaching the surface, nor does it completely arrest the progress of the magma front in any of the cases studied.

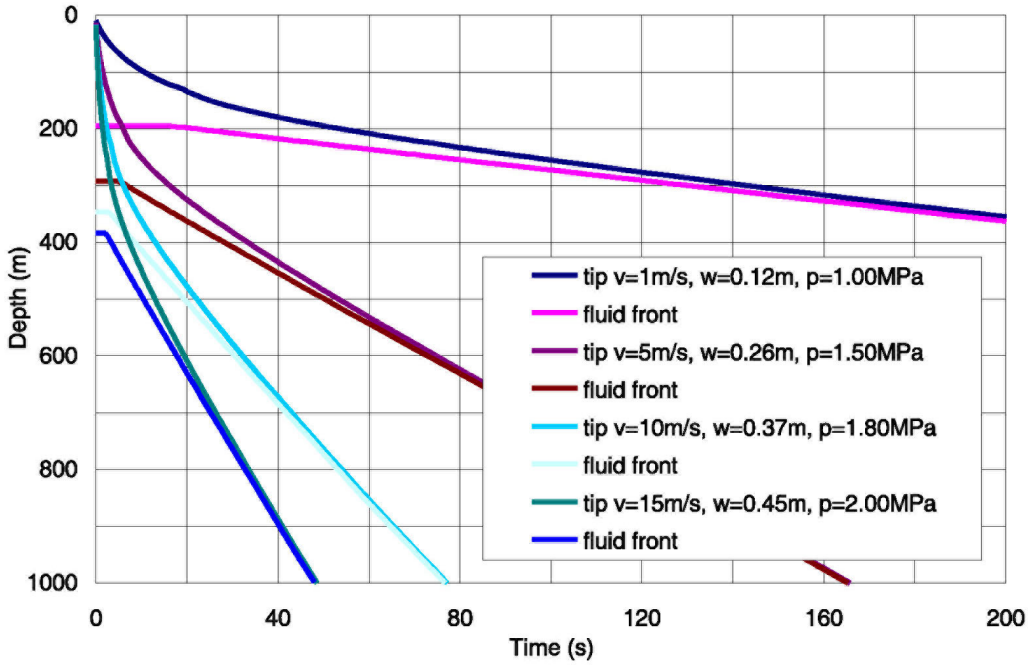

DTN: SN0304T0504203.001

Figure 20. Dike Tip and Fluid Front Depths as Functions of Time Before Surface Breakout for ρ_r = 2400 kg/m^3, η = 10 Pa-s, and 1.0 MPa Cavity Gas Pressure

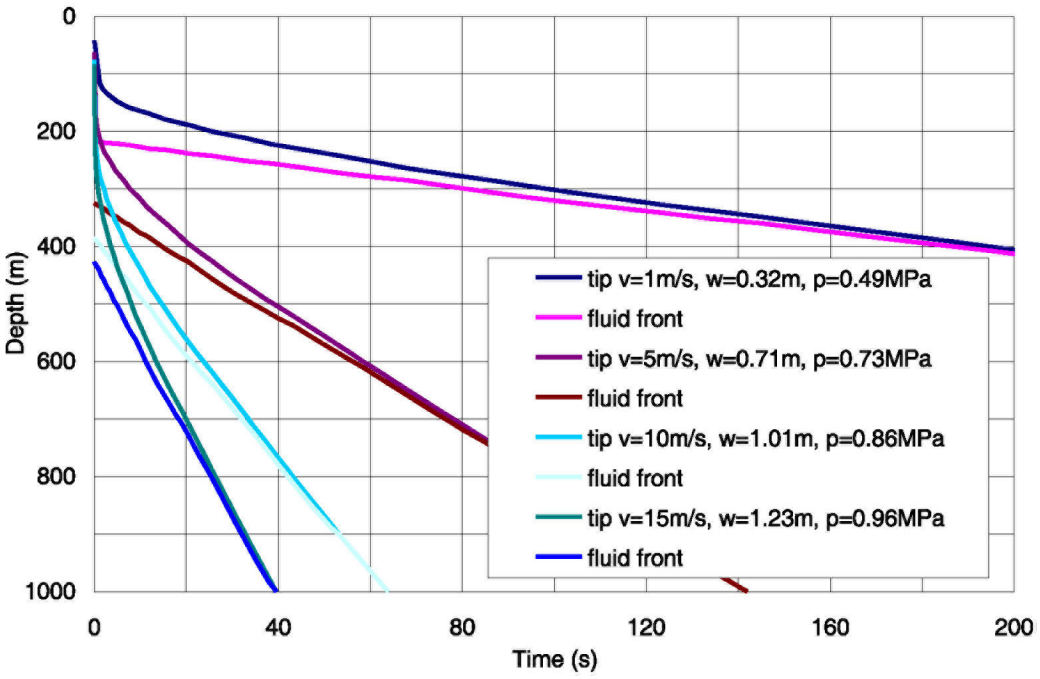

DTN: SN0304T0504203.001

Figure 21. Dike Tip and Fluid Front Depths as Functions of Time Before Surface Breakout for ρ_r = 2400 kg/m^3, η = 10 Pa-s, and 0.49 MPa Cavity Gas Pressure

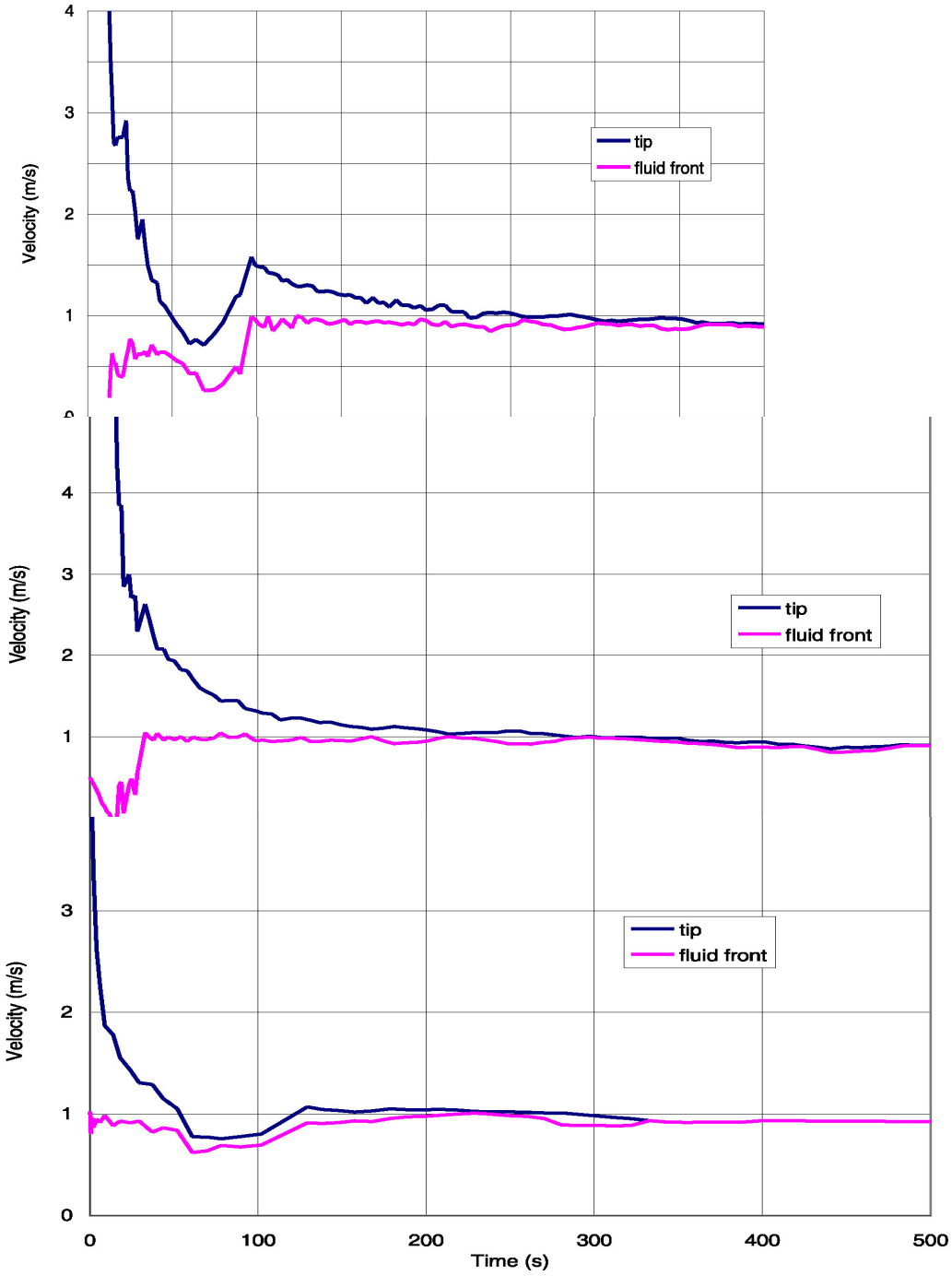

DTN: SN0304T0504203.001

NOTES: Top panel: ρ_r = 1200 kg/m^3, η = 10 Pa-s, v_∞ = 1 m/s, w_∞ = 0.16 m, and 40% leak-off at 300 m
Middle panel: ρ_r = 1200 kg/m^3, η = 10 Pa-s, v_∞ = 1 m/s, w_∞ = 0.25 m, and 40% leak-off at 300 m
Bottom panel: ρ_r = 2400 kg/m^3, η = 10 Pa-s, v_∞ = 1 m/s, w_∞ = 0.32 m, and 20% leak-off at 300 m

Figure 22. Dike-Tip and Fluid-Front Depths as Functions of Time Before Surface Breakout for Various Leak-Off Rates

6.3.9.2.3.3 Three-Dimensional Dike Propagation Models

The analyses in Section 6.3.9.2.3.1 showed that, assuming approximate boundary conditions at the intersection between the dike and the drift, the total magma flow inside the dike will be diverted into the drifts if the supply velocity is 1 m/s. In this analysis, the flow of the magma inside the dike toward the drift as a sink was considered in an approximate way.

The analysis presented in the present section investigated, using a 3D, coupled hydromechanical model, the dike-drift interaction representing the drift as an area sink of correct dimensions (i.e., 5.5 m diameter). The objectives of the analysis were to investigate (1) the flow rates of the magma from the dike to the drifts, considering conditions of 2D flow inside the dike, and (2) what the level is that the magma front inside the dike will reach by the time the drifts are filled with the magma.

All analyses discussed in this section were done using FLAC3D V 2.1 (STN: 10502-2.1-00).

6.3.9.2.3.3.1 Analysis of Dike Propagation

The geometry of the model of dike propagation is shown Figure 23. The model represents the portion of the dike between the vertical plane along the drift and the vertical symmetry plane halfway between the drifts. Symmetry conditions are assumed on those two planes in both the mechanical and the flow models.

The model extends 900 m below the repository level and 600 m on each side perpendicular to the dike. A stress boundary condition is applied on the model vertical boundaries parallel with the dike. The bottom model boundary is restrained in the vertical direction. The top model boundary, corresponding to the ground surface, is free.

The magma is injected into the dike at the bottom of the model. A boundary condition of zero pressure in the magma is applied at the intersection between the dike and the drift. The vertical in-situ stress in the rock mass is gravitational. The stress state in the horizontal plane is assumed to be isotropic, with magnitude of the horizontal principal stress equal to half of the vertical stress magnitude.

One vertical layer of zones represents the dike. Magma flow is confined to that layer of zones only; there is no flow in the rest of the model. The fluid flow model implemented in the model uses Darcy's law as a transport law:

$$q_i = k_{ij}(p - \rho_f z g)_j \qquad \text{(Eq. 45)}$$

where k_{ij} is the permeability tensor, p is magma pressure, ρ_f is magma density, z is elevation relative to a reference plane, and g is the gravitational constant. However, the magma flow rate per dike width is considered to follow the Poiseuille law:

$$q_i = -\frac{a^3}{12\mu}(p - \rho_f z g)_i \qquad \text{(Eq. 46)}$$

where a is the dike aperture and μ is magma viscosity. To correctly simulate magma flow inside the dike using, the permeability tensor of the zones that represent the dike is calculated during the simulation according to the following relation:

$$k_{ij} = \delta_{ij} \frac{a^3}{12 \mu d} \quad \text{(Eq. 47)}$$

where d is the thickness of the layer of zones that represents the dike.

The dike thickness is not explicitly represented in the model because it is zero initially, and even later, when the dike opens due to magma injection, it is much smaller than any characteristic length of the model. Instead an arbitrary small value, d, is selected to be the thickness of zones that represents the dike. With the correction of permeability shown in Equation 47, the arbitrary number has no effect on the model solution. The dike aperture, a, is calculated during the simulation as a function of model deformation.

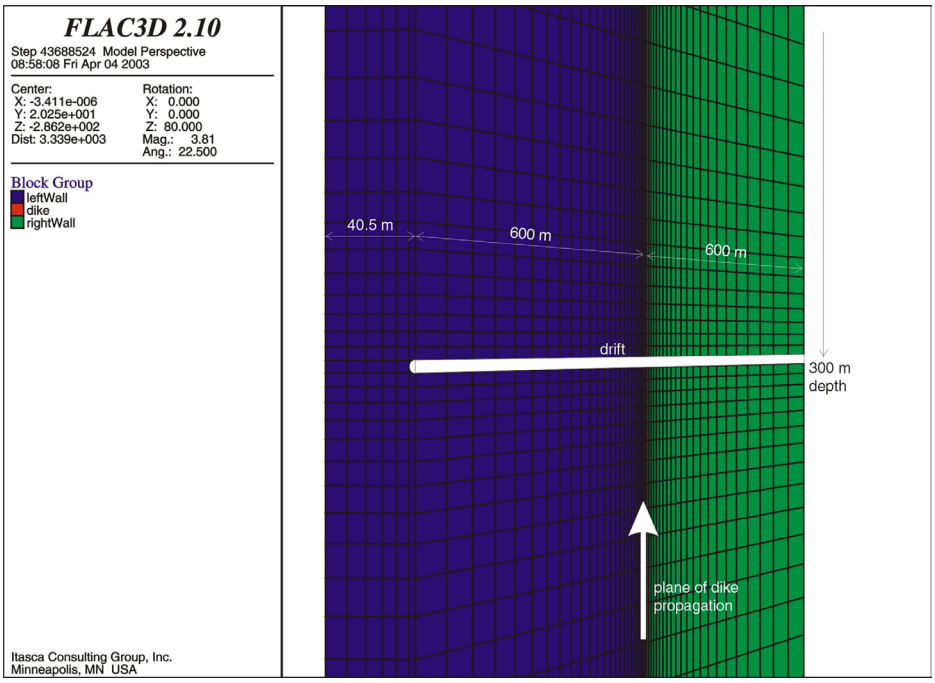

Output DTN: MO0307MWDDDINT.000

Figure 23. Geometry of the Dike Model

Two combinations of model parameters listed in Table 10 were simulated. Both cases correspond to a magma front velocity far from the ground surface of 1 m/s. Consequently, the wide-aperture case corresponds to the dike aperture (far from the ground surface) of 0.45 m; Case 2 corresponds to the dike aperture (far from the ground surface) of 0.25 m.

Table 10. Simulated Combinations of Dike-Rise Model Parameters

Case	Young's Modulus (Gpa)	Rock Density (kg/m^3)	Magma Density (kg/m^3)	Magma Viscosity (Pa-s)	Magma Compressibility (Mpa)	Magma Injection Rate (m^2/s)
1	15	2400	1141	10	50	0.45
2	15	2400	1001	10	50	0.25

Output DTN: MO0307MWDDDINT.000

6.3.9.2.3.3.2 Results for Dike Propagation

6.3.9.2.3.3.2.1 Wide-Aperture Case

The results for the wide-aperture case are illustrated in Figures 24 through 29.

Figure 24 shows the contours of the horizontal stress perpendicular to the dike and the displacement vectors at the end of the simulation. The plot illustrates that, far from the dike tip and the magma front (i.e., at the bottom of the model), the magma pressure and pressure gradient are determined by the in-situ conditions in the rock mass. The maximum displacement results in the dike aperture of 0.47 m that is close to the far-field dike aperture of 0.45 m. This result indicates that the artificial bottom boundary is sufficiently far from the repository level.

The magma flow rate out of the dike as a function of time (Figure 25) shows that approximately 1040 s after the magma front reaches the repository level, the model approaches steady state in which complete magma flow rate inside the dike (Q = 0.45 m^2/s x 40.5 m = 18.23 m^3/s) is diverted into the drift. (In reality, steady state will be achieved only if the drifts are not filled with the magma after 1040 s.)

Positions of the magma front at three different states during the simulation (all states are after the magma front has reached the repository level) can be determined from contour plots of saturation shown in Figures 26 through 28. (The magma front coincides with the contour line of 50 percent saturation.) It seems that, in this case, the magma front moves to a maximum of approximately 80 m (see Figure 28) above the repository level before the drifts are filled with the magma.

Contours of the magma pressure and the flow vectors at steady state are shown in Figure 29. It is clear that the entire flow is diverted into the drift.

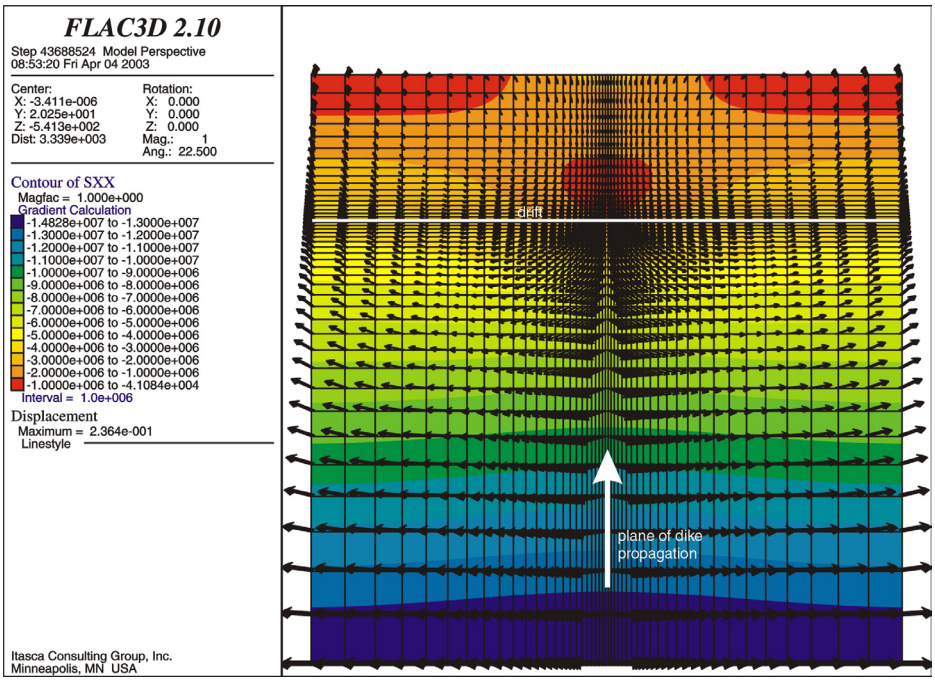

Output DTN: MO0307MWDDDINT.000

Figure 24. Contours of Horizontal Stress (Pa) Perpendicular to the Drift and Displacement Vectors (m) After 1642 Seconds of Simulation: Wide-Aperture Case

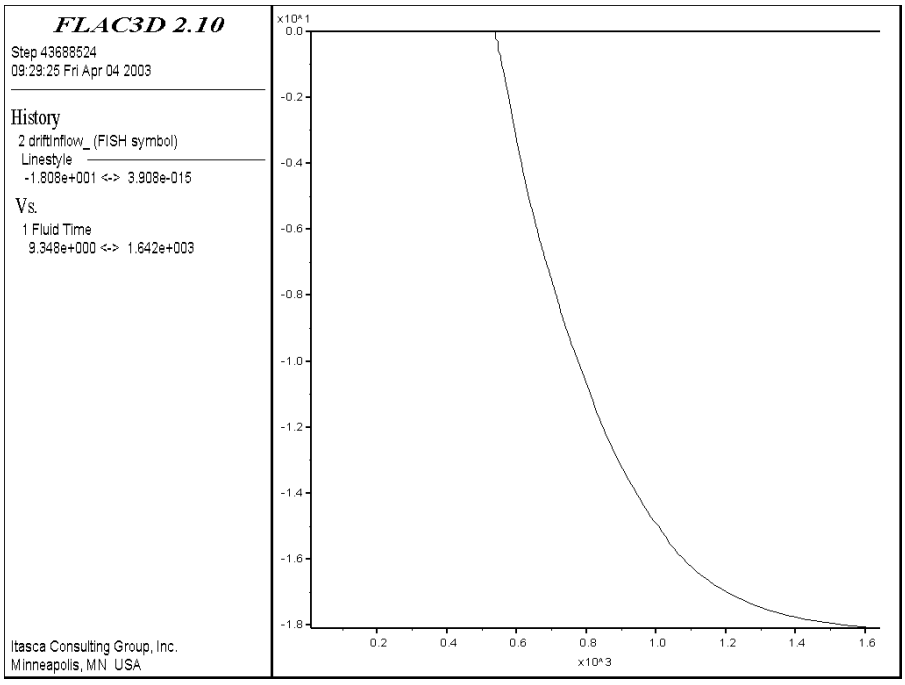

Output DTN: MO0307MWDDDINT.000

Figure 25. History of the Rate of Magma Outflow (m^3/s) From the Dike as a Function of Time (s): Wide-Aperture Case

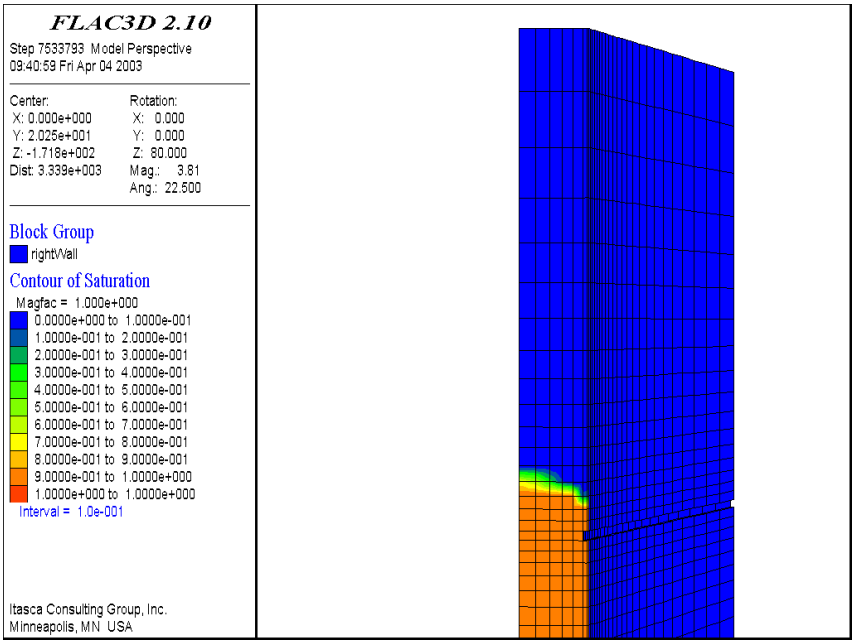

Output DTN: MO0307MWDDDINT.000

NOTE: The left wall of the dike is hidden.

Figure 26. Contours of Saturation of Dike With Magma 602 Seconds After Start of Simulation: Wide-Aperture Case

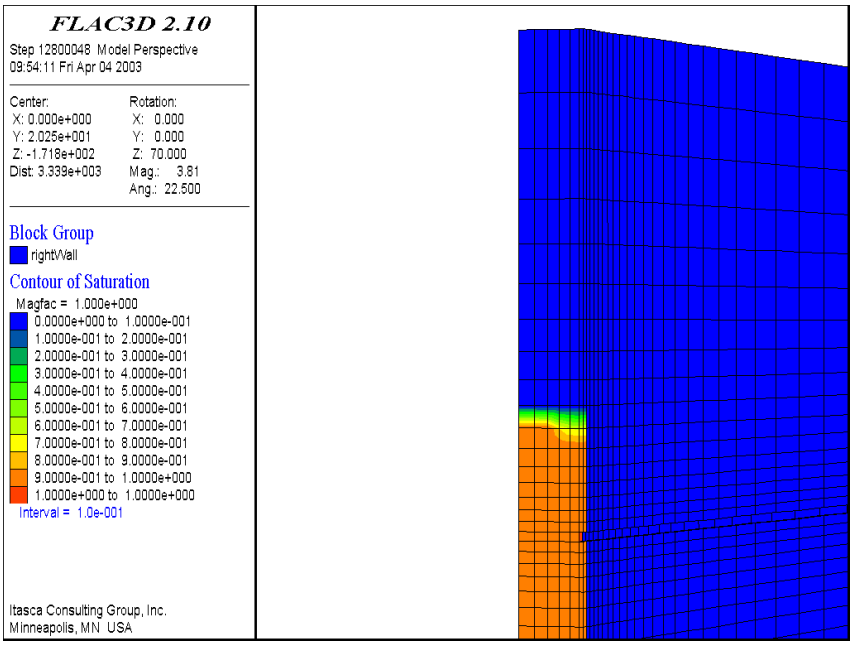

Output DTN: MO0307MWDDDINT.000

NOTE: The left wall of the dike is hidden.

Figure 27. Contours of Saturation of Dike With Magma 798 Seconds After Start of Simulation: Wide-Aperture Case

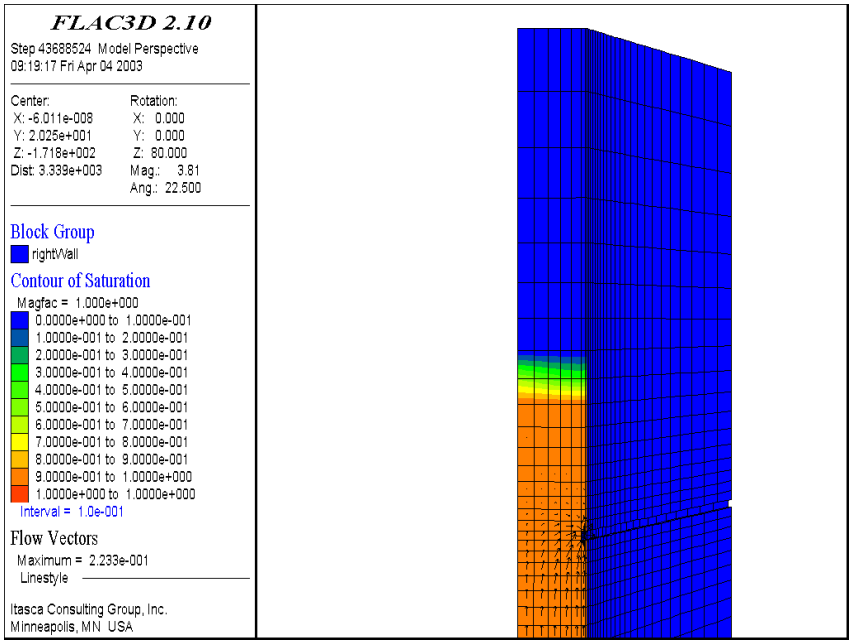

Output DTN: MO0307MWDDDINT.000

NOTE: The left wall of the dike is hidden.

Figure 28. Contours of Saturation of Dike With Magma 1642 Seconds After Start of Simulation: Wide-Aperture Case

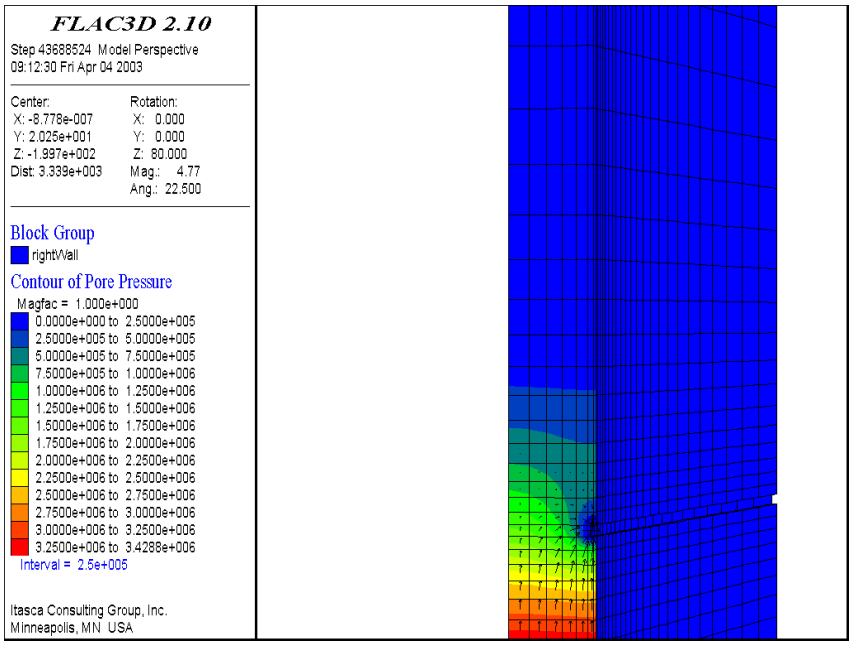

Output DTN: MO0307MWDDDINT.000

NOTE: The left wall of the dike is hidden.

Figure 29. Contours of Magma Pressure (Pa) Inside the Dike 1642 Seconds After Start of Simulation: Wide-Aperture Case

6.3.9.2.3.3.2.2 Narrow-Aperture Case

It appears from the evolution of the magma flow rate out of the dike (Figure 30), that it takes about 1150 s after magma starts to flow into the drifts for the narrow-aperture case to approach steady state (10.13 m^3/s). The maximum elevation the magma front can reach before the drifts are filled with magma is approximately 120 m above the repository level (saturation contours shown in Figure 31), which is more than in the wide-aperture case. Contours of the magma pressure and the flow vectors for the narrow-aperture case are shown in Figure 32.

In both cases analyzed, the magma does not reach the ground surface before the drifts are filled with the magma. Therefore, it is necessary to investigate conditions of magma injection into pre-existing joints inside the drifts to assess potential for a "dog-leg" scenario.

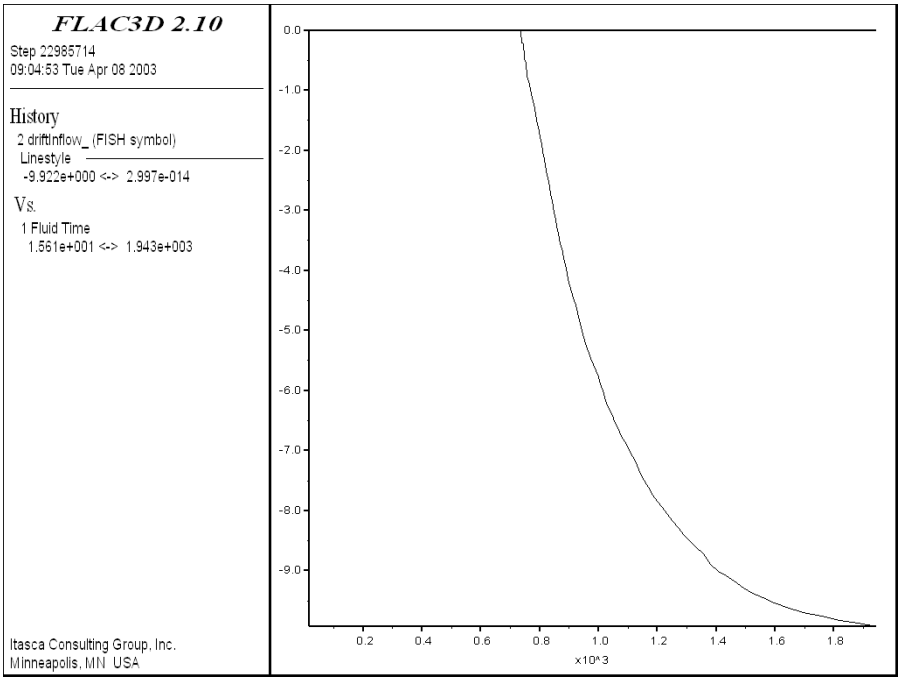

Output DTN: MO0307MWDDDINT.000

Figure 30. History of the Rate of Magma Outflow (m^3/s) From the Dike as a Function of Time (s): Narrow-Aperture Case

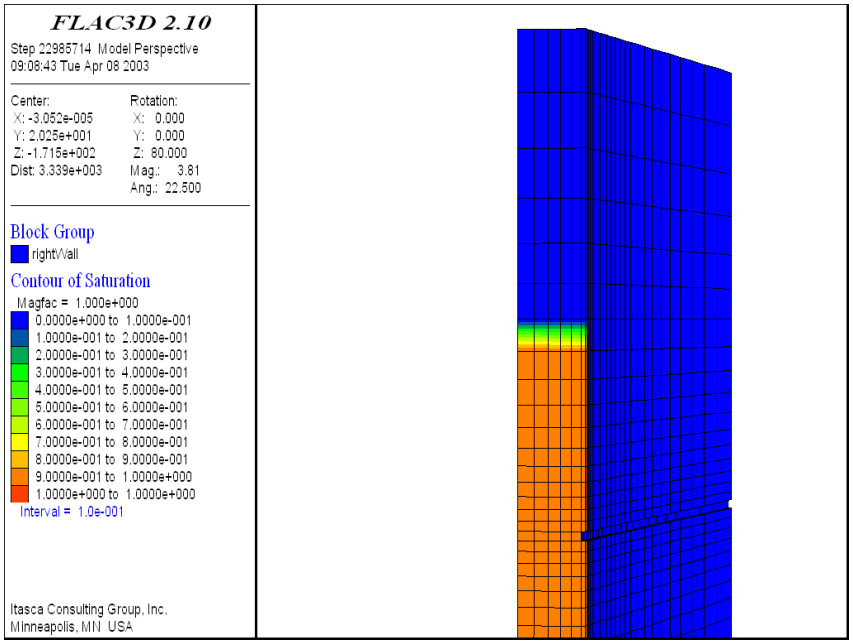

Output DTN: MO0307MWDDDINT.000

NOTE: The left wall of the dike is hidden.

Figure 31. Contours of Saturation of Dike With Magma 1943 Seconds After Start of Simulation: Narrow-Aperture Case

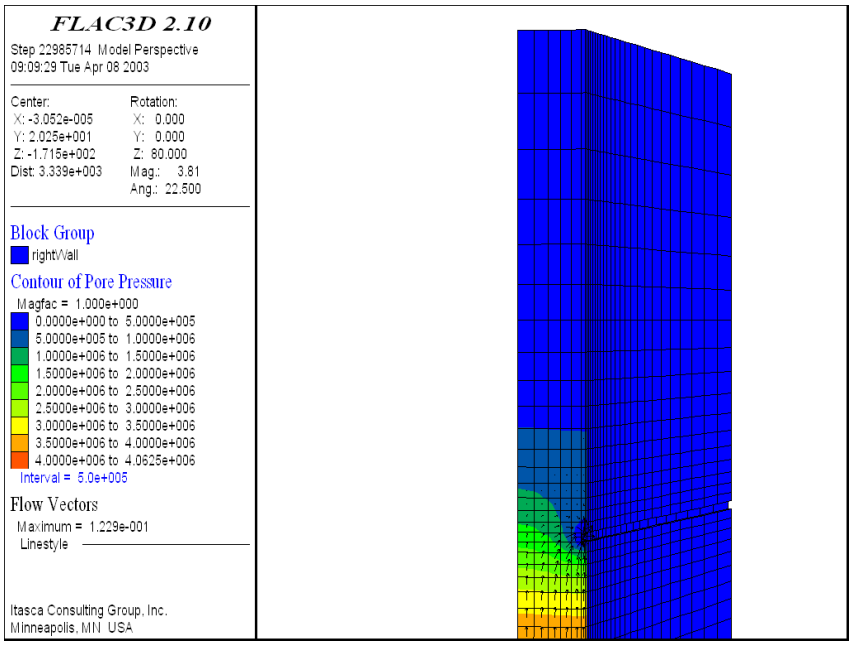

Output DTN: MO0307MWDDDINT.000

NOTE: The left wall of the dike is hidden.

Figure 32. Contours of Magma Pressure (Pa) Inside the Dike 1943 Seconds After Start of Simulation: Narrow-Aperture Case

6.3.9.2.3.4 Discussion

The 3D calculations in Section 6.3.9.2.3.3 are in general agreement with those of the two previous sections, and the three sets of results can be used to draw a coherent picture of the interaction between magma in a dike and drifts.

Section 6.3.8.2 described the earliest times in the interaction between a dike and a drift. It was found that the magma can be expected to follow, by many seconds to a few minutes, the tip cavity of the propagating dike. This cavity is filled with vapor, which will be at nearly atmospheric pressure because of the high gas permeability of the surrounding tuff. As the crack tip approaches the free surface, it accelerates; for most cases studied, it is moving at a speed that is at least twice that of the magma front in the dike. By the time the magma reaches the drift level, the crack tip is expected to be located between about 50 m above the drifts and the surface.

Section 6.3.9.2.3.1. described the flow of effusive magma from a rising dike into a drift. It was found that the drift will take virtually all of the flow that emerges between centerlines of drifts (40.5 m on either side of the drift axis) when the magma is rising at 1 m/s. A 500-m-long drift will fill in about 5 minutes, filling from invert to back. For magma rising at 10 m/s, the drift cross-section will not accommodate all of the upward-emerging flow, so the magma will rise above the drift level before the drift is full. With the added pressure of magma above the drift, the time needed to fill the drift in this case is less than a minute. Most of these results are insensitive to changes in the viscosity by an order of magnitude. An exception is the height that magma would be expected to rise above the drift before filling; the less-viscous magma rises only about 12 to 25 m, whereas the more viscous magma rises 100 to 200 m. The velocity of magma emerging from the dike into the drift for all cases studied is between 10 and 17 m/s.

The 3D analysis of Section 6.3.9.2.3.3 also showed the magma rising between drifts while also flowing into the drifts. The magma pressure directly above the drift is greatly reduced by the leak-off into the drift, and the magma front over the drift is also retarded relative to its height at the centerline between drifts.

Initial and boundary conditions for the three sets of analyses do not permit exact comparison. Still, when taken together, these three sections provide an estimate of the environment in drifts subject to effusive flow.

6.3.9.3 Effect on Dike Propagation of Material Losses From Dike

6.3.9.3.1 Gas Seepage

Because of the very high permeability of the surrounding tuff to gas flow (Detournay et al. 2003 [DIRS 162914]), the pressure in the tip cavity preceding the magma in the dike will be nearly atmospheric. This characteristic will reduce the rate of crack growth relative to that which would occur in an impermeable rock with similar elastic properties. For example, compare Cases 14 and 25 with, respectively, Cases 10 and 9 in Figure 5.

6.3.9.3.2 Loss of Hydrofracture Driving Fluid Due to Flow Into Drift

The analysis of the dike-drift interaction was carried out using a 2D model in which the effect of magma flow into the emplacement drifts was represented as a leak-off at the repository level. The leak-off was assumed to be continuous at the repository level and was calculated by dividing the actual flow into the drifts by their spacing. This was because the magma flow in the dike was represented as 1D. This approach is an acceptable approximation if the magma flow rate from the dike into the drifts is a relatively small portion of the total flow rate inside the dike.

These calculations were discussed above in Section 6.3.9.2.3.2.2. As can be seen from Figure 22, leak-off has little effect on the propagation of the crack tip for the nominal case, although the magma front does stall temporarily at drift level. For thinner dikes or greater confining stress, the crack tip progress to the surface is delayed somewhat, but not stopped.

6.3.9.4 Phenomena Associated With First Intrusion Into Drift

6.3.9.4.1 Shock Formation and Propagation

The shock wave calculated by Woods et al. (2002 [DIRS 163662]) is an artifact of their initial conditions. The presence of a tip cavity preceding magma in the dike will result in a gradual exposure of magma to the drift.

Intrusion of magma into a drift could result in shock-wave formation if there is standing water in the invert. In such a situation, magma could entrap the standing water, causing a hydrovolcanic explosion. Such explosions, which are not uncommon in nature, are analogous to fuel-coolant interaction (FCI) explosions encountered in industry.

A hydrovolcanic outburst in a drift could produce strong shock in the air filling the drift. Because of the lateral confinement of the drift walls, such a shock would not dissipate due to geometric spreading. However, there are many features of the drift environment that would act to attenuate a shock. Among them are:

- Permeable drift walls and invert fill
- Irregularities in drift walls
- Obstructions of variable diameter in the drift
- Deformable drip shielding
- Spacing between waste canisters (“cold repository” design only)
- Support cradles for waste canisters.

Detailed analysis of the effects of these and other features on shock propagation in drifts is beyond the scope of this report, but many of them acting in concert could do much to attenuate hydrovolcanic shocks.

6.3.9.4.2 Vesiculation and Fragmentation of Magma in Drift

This report addresses primarily the behavior of partially degassed magma, which flows as a slightly compressible or incompressible fluid. It is clear that there must be a region between the fully compressed, gas-laden magma and the atmosphere where the magma loses its gas, either

slowly with bubbles rising to the top and releasing gas into the tip cavity, drift, or atmosphere or, more violently, with rapid fragmentation and formation of a pyroclastic multiphase fluid. Proper consideration of the latter process is beyond the scope of this report. The earlier version of this report *Dike Propagation Near Drifts* (CRWMS M&O 2000 [DIRS 151552]) contains a qualitative discussion of the phenomena that would accompany such processes.

6.3.9.4.3 Peak and "Final" Values

Table 11 presents estimated peak and "final" values for environmental variables caused by the intrusion of effusive magma into drifts at Yucca Mountain. "Final" refers to conditions after condensed phases in the magma have stopped moving.

Table 11. Values for Environmental Variables Resulting From the Intrusion of Effusive Magma Into Drifts

Environmental Variable (units)	Peak Value	"Final" Value	Uncertainty	Remarks
Temperature (K)	1379	1379	+63/–60	Depends on water content of magma, see *Characterize Eruptive Processes at Yucca Mountain, Nevada* (BSC 2001 [DIRS 160130], Table 4, Fig. 2).
Pressure (MPa) if dike repressurizes	65	65	+100/–65	Depends on water content of magma. See BSC (2001 [DIRS 160130]).
Magma Density (kg/m^3) if dike repressurizes	2556	2556	+107/–82	Depends on water content of magma. See BSC (2001 [DIRS 160130]).
Pressure (MPa) without repressurization	0.2	0.2	+0/–0.1	Atmospheric at top of drift. overburden pressure at base of drift.
Magma Density (kg/m^3) without repressurization	1970	1970	+83/–67	Assumes 30% vesicles. Depends on water content of magma See BSC (2001 [DIRS 160130]).
Magma Velocity in drift (m/s)	15	0	±7	Uncertainty is only for peak value. See Section 6.3.9.2.3.1.6
Dynamic Pressure due to magma (MPa)	0.6	0	+0.7/–0.4	= (magma velocity)^2 • magma density
Time to fill drift (s)	—	290	+10/–10	See Section 6.3.9.2.3.1.6 Depends on magma rise velocity

Output DTN: SN0304T0504203.001

6.3.10 Use of Output

It was planned initially to couple the Dike Propagation Model with the Magma and Gas Flow Model. The coupling would work as follows: the dike magma pressure and opening at the intersection between the dike and the drift would be calculated in the Dike Propagation Model and used as the boundary conditions in the Magma and Gas Flow Model; magma flow rate into the drifts (leak-off) would be calculated in the Magma and Gas Flow Model and used as boundary condition in the Dike Propagation Model. However, the analysis of the magma flow rate inside the drifts (Section 6.3.9.2.3.1) shows that entire magma flow inside the dike will be diverted into the drifts. Consequently, the coupling was not necessary. Further, a 2D model is not a good representation of magma flow in the vicinity of the repository level (e.g., radial magma flow towards the drifts, magma rise between the drift) for large leak-off rates. Instead, a 3D

model (described in Section 6.3.9.2.3.3) was used to simulate magma flow inside the dike when the dike intersects the drifts.

The output of this Magma Flow Model component can be used to define the time required for waste canisters to be engulfed in magma, after magma rising in a dike reaches the base of the drift.

6.4 MODEL FOR MAGMA FLOW

This section discusses two manifestations of a magma flow model in which magma may reach the surface after having encountered the drifts of the repository. The intent of this approach is to determine if either of those manifestations, or an alternative, is likely to occur at Yucca Mountain.

6.4.1 Model Description

It was shown in Section 6.3 that magma from a dike that intersects a repository drift will fill the drift in only a few minutes. Since the total anticipated eruptive volume is much larger than the volume of the emplacement drifts, the magma will continue upward until it reaches the surface unless it loses so much of its volatile content that it becomes neutrally buoyant. The two manifestations of this model treated in this section are (1) magma flows through mined opening, overtopping backfill and reaches the surface through access drifts and (2) the pressure in the drift rises enough to open pre-existing cracks far down the drift from the point of initial encounter, which cracks then grow to the surface where eruption occurs. Similar manifestations were part of the scenario proposed by Woods et al. (2002) [DIRS 163662]).

These two manifestations are both addressed by 3D hydro-mechanical simulation using the FLAC3D code [DIRS 161947]. For manifestation (1) the extent to which pressure, applied to the open end of the back fill by the rising magma will deform the backfill is evaluated. There are two competing effects:

- The magma may merely press down the backfill and then flow over the top
- If the backfill exhibits sufficient shear strength, pressure on the open face may result in an upward heave farther back from the face and seal the drift. A potential design change to prevent this type of behavior is also investigated.

For the second manifestation, FLAC3D [DIRS 161947] and UDEC [DIRS 161949] are used to predict the rate at which such cracks would grow, so that the time required for a new dike to open could be compared with the time needed for a narrow dike in cold rock to effectively freeze. Supporting analyses are used to determine the stress environment surrounding a drift filled with magma.

6.4.2 Model Documentation

The interaction between magma flowing through mined openings and backfill has not been documented previously. The documentation in this report constitutes all of the extant documentation.

The analysis of the dog-leg scenario is derived from suggestions of Woods et al. (2002 [DIRS 163662]). A conceptual model is described in which, after a dike intersected a drift at Yucca Mountain, the drift was filled with magma, and the pressure in the magmatic system again increased sufficiently to generate a new opening some length down the drift. In their model, this new opening propagated to the surface and became the main surface opening of the system.

6.4.3 Uncertainties

Uncertainties associated with this model include:

- Configuration of the repository structure
- Material and interfacial properties of the backfill
- Properties of the magma

Extent of repressurization of the magma in a drift after the drift has filled with magma Properties of the rock surrounding the drift, especially of the rock between the drift and the surface.

6.4.4 Alternative Models

6.4.4.1 Woods et al. Model of Magma Flow to the Surface

Woods et al. (2002 [DIRS 163662]) described a conceptual model in which, after a dike intersected a drift at Yucca Mountain, the drift was filled with magma and the magmatic system, including the drift, was repressurized; this repressurization generated a new opening some length down the drift or caused a magma flow to the surface through access drifts. In their model, this new opening propagated to the surface and became the main opening of the system. Specifically, they state (p. 19-3):

> "The precise location of the preferred magma pathways from the drift to the surface will depend on many factors … we compare three different cases which might bound the range of possibilities … (Case 1) that the deep dike path continues to the surface without any major perturbation by the repository system, (Case 2) that the pathway to the surface is shifted to a new position, 500 m along a drift with an area of 20 m^2, and (Case 3) that the magma uses the main access drift to the repository for flow to the surface… Breakout from the access drift, which is likely to be closed at each end, may occur at a variety of locations (e.g., structural weaknesses, ventilation shafts)… in the case in which the flow is diverted along a drift, the flow pressure is elevated relative to lithostatic in the upper kilometer or so as the flow advances along the drift (case 2) and main drift (case 3) towards the surface. … If a conduit formed initially in response to flow down a 4-km-long access drift, these large flow pressures would be likely to cause significant widening of the conduit or the formation of additional conduits."

The calculations of Woods et al. (2002 [DIRS 163662]), especially when viewed in conjunction with the high pressure accompanying the shock waves calculated in their model of magma flow into drifts (see Section 6.3.4.4), might lead one to conclude that a high probability for magma to

flow through a drift to the surface exists. However, it must be emphasized that this alternative model does not make any evaluations of the relative likelihood of the three cases.

Woods et al. (2002 [DIRS 163662]) calculate steady state magma velocities where the flow is constrained to equal the sound speed in highly compressible magma at the point where it emerges from the surface. This assumption of "choked" flow results in high driving pressures at depth, and modest (10s of m/s) flow velocities through the drift. Their calculation does not address the approach to the final steady state from an initial transient solution. Although this is one possible model, it is also possible that the flow could separate into vapor and liquid fractions moving at different velocities (see Section 6.3.4.5).

The access drifts connecting individual emplacement drifts within the repository are planned to be backfilled, specifically to reduce the chance that magma could follow them to the surface. However, there will be a small (order 0.3 m) space open at the top of the backfill. This would restrict the flow very substantially from the 50 m^2 cross-section used for the case 3 calculations of Woods et al. (2002 [DIRS 163662]). But the backfill is a loose granular material and may be subject to erosion, which could, in turn, result in cross-sections approaching the value used in case 3. Section 6.4.10 contains an analysis of the fate of backfill subjected to magmatic loads.

The analysis of Woods et al. (2002 [DIRS 163662]) is purely dynamical and does not address the thermal aspects of magma flow to the surface. Thermal aspects were addressed by the Igneous Consequences Peer Review Panel (Detournay et al. 2003 [DIRS 162914]) for case 2, in which a new dike is initiated 500 m along a drift from the original point of intersection. The Panel concluded that it was unlikely that a new dike beginning from the repository could grow to any appreciable dimension before it cooled, so much as to become effectively solid. Section 6.4.11 contains an elaboration of that thermal analysis.

6.4.4.2 Conduit Formation Along Original Dike Trajectory

It was shown in Section 6.3 that during an encounter with a drift, the crack will intersect the drift before the magma. Thus, it is concluded that the most likely scenario for magma to erupt to the surface after intruding the drift complex is for it to continue along the trajectory of the original dike.

The analysis report *Characterize Eruptive Processes at Yucca Mountain, Nevada* (BSC 2001 [DIRS 160130]) describes the basic processes by which the sheet flow of a dike is transformed into the more concentrated flow of a conduit. Results of Section 6.3.9.2.3.3 indicate that, as magma continues up the original dike path while also being diverted into the drifts, the vertical velocity will be lower directly above a drift than at the midpoint between two drifts.

In a dike, there is a delicate balance between heat supplied from magma flowing upward and heat lost to the cold walls. Many dikes fail to reach the surface at all because they freeze in place when they propagate into colder rocks (Lister 1995 [DIRS 163635]). A change of an order of magnitude in the pressure driving the dike can cause flow to slow drastically above drift intersections. As a result, it may be expected that a conduit is more likely to form between drifts than directly over a drift. No credit is taken for the possibility that the conduit might not intersect drifts in BSC (2003 [DIRS 161851]).

The *Final Report of the Igneous Consequences Peer Review Panel* (Detournay et al. 2003 [DIRS 162914], Section 3.4.5) concludes that the conditions necessary for a new dike to grow "cannot easily be met by dikes initiating from a drift."

6.4.4.3 Sill Formation

Another alternative model is that the magma in the dike loses so much gas as it stalls in its upward motion upon encountering the drift complex, that the magma in the upper portion of the dike loses its positive buoyancy. If this were to occur, the magma would cease its upward movement. It then could either form a sill near the repository level or, if it became negatively buoyant, it could sink back from whence it came.

Supporting analyses in Section 6.4.11.4 do provide some insight into the question of sill formation; it is found to be unlikely. Evaluation of the extent of buoyancy loss due to leaking of vapors into the repository is beyond the scope of this report.

6.4.5 Description of Input

6.4.5.1 Inputs for Magma/Backfill Interaction

The inputs for this model are the mechanical properties of the backfill, the magma pressure, and the geometric configuration of the model elements; the values used are summarized in Table 12. The sources are listed in Table 2. The backfill properties were selected to be representative of relatively compressible backfill.

Details of the model are presented below in Section 6.4.10.1.1.2. Magma pressures of 4 and 8 MPa were considered as representative of pressures needed to open a dike under in-situ and heated conditions, respectively. The geometric configuration was taken to be representative of the turnouts between the ends of emplacement drifts; this is described in detail in Section 6.10.4.1.1.1.

Table 12. Input Parameters for Flow Through Mined Openings Analysis

Magma Pressure in Drift (MPa)	Backfill Friction Angle (deg)	Backfill Density (kg/m^3)	Backfill Cohesion (MPa)	Backfill Dilation (deg)	Turnout Width (m)	Turnout Total Height (m)	Turnout Base Height (m)	Turnout Crown Radius (m)
4 or 8	40	1000	0	5	8	7	3	4

Source: BSC 2003 [DIRS 164493]

6.4.5.2 Inputs for Crack Opening Rates Analysis

The inputs for the crack opening analysis are in-situ stress state, drift geometry (diameter of 5.5 m), elastic properties of rock mass, joint properties and magma properties. The sources are listed in Table 2. Input values are listed in Tables 13a–c.

Table 13a. Input Parameters for Crack Opening Rates Analysis: Initial Stress

Overburden (m)	Coefficient Along Drift	Coefficient Perpendicular to Drift
250,300	0.35,0.50	0.5

Table 13b. Input Parameters for Crack Opening Rates Analysis: Rock Mass

Initial Crack Aperture (mm)	Young's Modulus of Rock (GPa)	Poisson's Ratio	Joint Normal Stiffness (GPa/m)	Joint Shear Stiffness (GPa/m)
1,3	5,15	0.21	20	20

NOTE: Values are representative of the Topapah Springs lower lithophysal unit (BSC 2003 [DIRS 162711], Attachment V, Table V-8.

Table 13c. Input Parameters for Crack Opening Rates Analysis: Magma

Magma Pressure in Drift (MPa)	Bulk Modulus of Magma (MPa)	Magma Density (kg/m^3)	Magma Viscosity (Pa-s)
4,8,10	50,500	1000	10,100

The sources of the inputs for overburden and ratios of horizontal stresses to vertical stress (referred to in Table 13a as coefficients along and perpendicular to the drift) are the same as the sources for the inputs discussed in Section 6.3.4.2. Also, the sources for the elastic properties of the rock mass and the magma properties are the same as the sources for the inputs discussed in Section 6.3.4.2.

Somewhat wider ranges for Young's modulus and magma viscosity were considered in the crack opening analysis. Young's modulus of 5 GPa is representative of poor quality rock mass at the repository level. The increased viscosity of 100 Pa s addresses the effect of magma cooling on the viscosity.

One value for the magma density was used throughout the analysis because it has a negligible effect on the result of this analysis. To account for conditions of potential plugging of the dike and maximum increase in the thermally induced stress, a magma pressure of 10 MPa was used as an input in the analysis in addition to 4 MPa and 8 MPa. The results of this analysis are not sensitive to the joint normal and shear stiffnesses. Those input parameters were selected to correspond to the lower bound of measured values (BSC 2003 [DIRS 162711] Table V-4). (Smaller joint stiffness results in larger calculation time step.) The same argument was used in selection of the input for magma bulk modulus. The analysis showed that there is insignificant effect on the results when the magma bulk modulus was increased from 50 MPa to 500 MPa. Based on measurement (Olsson and Brown 1997 [DIRS 106453]) the initial joint opening is less than 1 mm. The joint openings of 1mm and 3mm were used as inputs for the analysis.

6.4.5.3 Inputs for Magma Cooling Rates Analysis

The inputs for the magma cooling rates analysis are the thermal diffusivity and specific heat of the magma (heat capacity), the latent heat of crystallization of the magma (heat of fusion), the intrusion temperature, and the viscosity of crystal-free magma. The solution presented here makes the assumption that thermal properties (specific heat and thermal diffusivity) of the magma and the host rock are the same. The magma effective solidification temperature (T_s) is also required and is derived in the analysis (Section 6.4.11.4.1.1). Table 2 gives input sources.

The thermal diffusivity and specific heat of the magma, and its latent heat are selected to be consistent with the values used by the final Igneous Consequences Peer Review Report (Detournay et al. 2003 [DIRS 162914]), which are consistent with Spera (2000 [DIRS 164109]). The intrusion temperature is taken as the liquidus temperature from the report *Characterize Eruptive Processes* (BSC 2001 [DIRS 160130]). The crystal-free viscosity is from the same source. The values used are included in Table 14.

Table 14. Input Parameters for Thermal Calculations

Water (%)	Approx. Latent Heat ($J\ kg^{-1}$)[1]	Approx Specific Heat ($J\ kg^{-1}K^{-1}$)[1]	Approx Diffusivity (m^2s^{-1})[2]	Intrusion Temperature (°C)[3]	Crystal-free Viscosity (Pa-s)[3]	T_s (°C)[3]
0	3.50×10^5	1100	3.00×10^{-7}	1169	48	1135
0.5	3.50×10^5	1100	3.00×10^{-7}	1153	37	1108
1.0	3.50×10^5	1100	3.00×10^{-7}	1137	30	1083
2.0	3.50×10^5	1100	3.00×10^{-7}	1106	19	1034
3.0	3.50×10^5	1100	3.00×10^{-7}	1076	13	998
4.0	3.50×10^5	1100	3.00×10^{-7}	1046	9.1	964

Sources:
[1]Spera 2000 [DIRS 164109]
[2]Detournay et al. 2003 [DIRS 162914]
[3]DTN: LA0107GV831811.001 [DIRS 160708]

6.4.6 Assumptions and Simplifications

As stated in Section 5, the model assumes that the backfill density is 1000 kg/m^3. The results are very insensitive to this value.

The Double-Yield constitutive model used for the backfill treats the backfill as a continuum, whereas it is in fact a granular medium. However, under normal contact conditions the high viscosity of magma relative to the small grain size of the backfill, will prevent the magma from penetrating the backfill. Hence use of a continuum model is appropriate.

6.4.7 Boundary and Initial Conditions

This is discussed separately below for magma flow through mined openings and for opening and growth of new dikes.

6.4.8 Model Formulation

This is discussed separately below for magma flow through mined openings and for opening and growth of new dikes.

6.4.9 Testing, Sensitivity and Calibration Activities

This is discussed in Section 7.

6.4.10 Model Results

6.4.10.1 Flow Through Mined Openings

The plan for the underground storage of radioactive waste at Yucca Mountain includes a series of parallel emplacement drifts, 5.5 m in diameter, connected via turnouts to East and West mains, 7.62 m in diameter (BSC 2003 [DIRS 164493]). After disposal of the waste and closure of the repository, the mains and sections of the turnouts would be backfilled. In the scenario of volcanic intrusion into the repository, a number of the emplacement drifts will be intersected by the volcanic dike and, subsequently, filled with magma. The analysis presented in this section investigates the effectiveness of the backfill to contain the magma in only those emplacement drifts that are intersected by the dike and to prevent it from spreading into the mains and other emplacement drifts.

This model report presents the results of a series of numerical simulations, carried out as part of this study, using the computer code FLAC3D V2.1 (STN: 10502-2.1-00). The analysis is preliminary, and the focus is on mechanical considerations. Magma flow is not modeled; instead, an applied mechanical pressure accounts for the effect of the magma. The conservative assumption that the magma imposes hydrostatic pressure on the exposed surfaces was made. The evolution of the pressure was not considered. Various assumed levels of the magma pressure were applied on the model, and the problem was solved statically.

Section 6.4.10.1.2.1 presents the conceptual model used to study the effect of magma pressure on the backfill, assuming the original design (i.e., with a gap between the top of the backfill and the turnout crown). The sealing effect offered by adding a portion of tight backfill in the design is studied in Section 6.4.10.1.2.2. An approach to backfill design intended to contain a possible spread of magma into the mains is suggested in Section 6.4.10.1.4.

6.4.10.1.1 Model Description

6.4.10.1.1.1 Geometry

A section of a horseshoe-shaped turnout backfilled as shown in Figure 33 was considered. A system of reference axes is selected, with the positive y-axis vertically upward, as indicated in the figure. The radius of the crown is 4 m, the height of the base is 3 m, and the width of the turnout is 8 m. The turnout is backfilled to a height, H. The backfill extends along the turnout to the main on one side and terminates in a slope at the angle of repose of the fill on the other side.

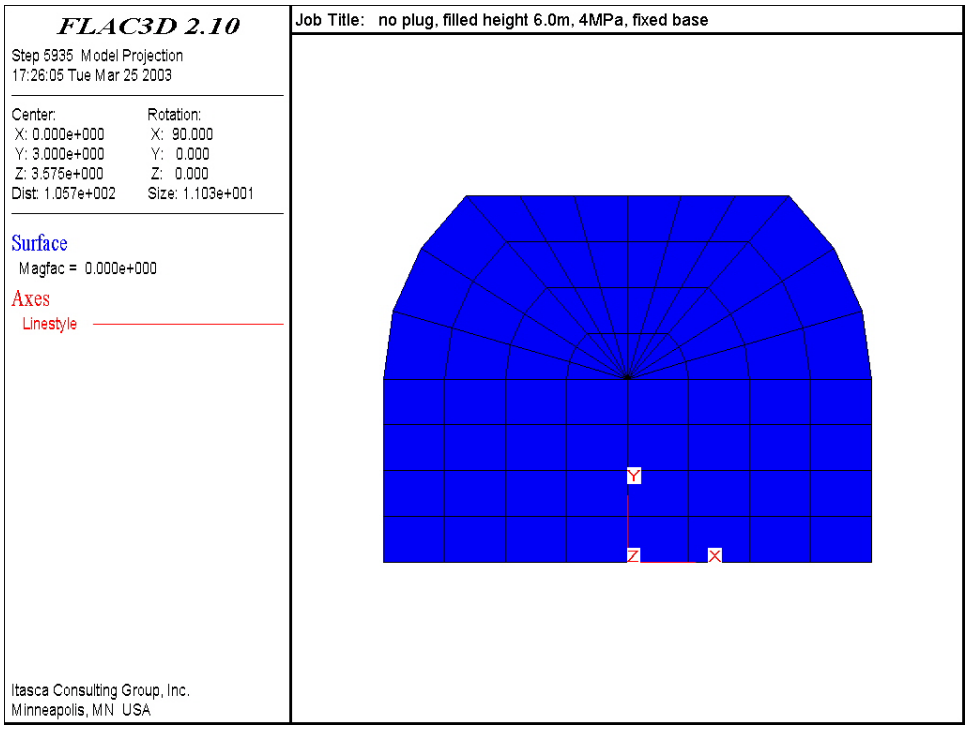

Output DTN: MO0307MWDDDINT.000

Figure 33. Turnout: Backfill in Horseshoe Section

The turnout walls are assumed to be rigid in the model. The effect of the magma on the fill in the turnout is represented simply by applying mechanical pressure to the slope. The response of the backfill, contained within the rigid walls, is modeled.

The backfilling usually leaves a gap of the order of 1 m or less between the roof and the fill. It is anticipated that the magma pressure will cause the fill material to "heave" some distance ahead of the slope surface, so that the gap may close. This mechanism has been investigated, and results are presented in Section 6.4.10.1.2.2. A maximum magma pressure of 8 MPa has been assumed, with intermediate results at 4 MPa. (See Figure 12.)

The model of a backfilled turnout segment is shown in Figure 34. The boundary at the main is a vertical plane kinematically constrained; the slope is modeled as a flat surface inclined at the angle of repose. The drift is assumed to be filled over a length of 30 m, measured from the top of the inclined section. The model contains 1,280 zones.

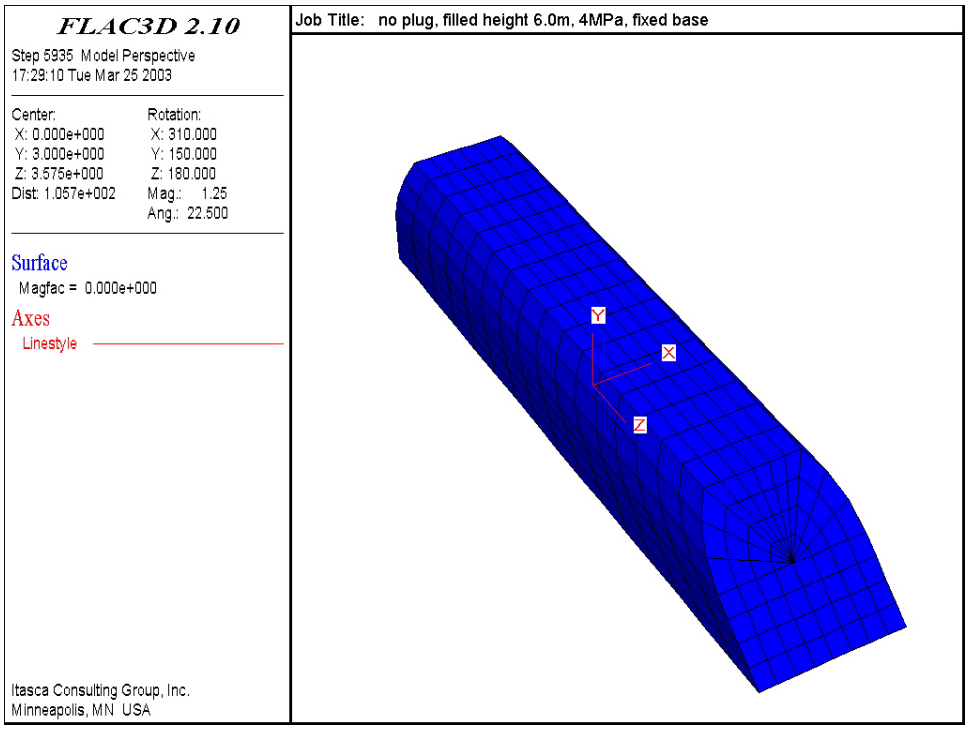

Output DTN: MO0307MWDDDINT.000

Figure 34. FLAC3D Model of a Backfilled Turnout Segment

6.4.10.1.1.2 Backfill Material Model

The numerical simulations have been carried out using the finite-difference code in FLAC3D V2.1 (STN: 10502-2.1-00). The constitutive behavior of the backfill material is represented using the Double-Yield model. This elastoplastic model accounts for Mohr-Coulomb shear failure as well as plastic volumetric compaction.

The emphasis of the analysis is placed more on qualitative than on quantitative data. The constitutive model properties used for the simulations are generic. The relationship between the cap pressure and the plastic volumetric strain was included in tabular form and generates the stress-strain curve of Clark (1991 [DIRS 164336]). The ratio of the elastic bulk to shear modulus is 0.75. Numerical test of the constitutive model using a uniaxial strain path results in a vertical strain of about 10 percent for an applied stress of 8 MPa. For an elastic material, this value would correspond to a Young's modulus of 80 MPa. For comparison, the Young's modulus of crushed basalt at 7 MPa would be about 200 MPa, according to Marachi et al. (1972 [DIRS 157883]).

The following properties (see Table 2) were used in the simulations:

friction angle: 40^{o}
dilation: 5^{o}
cohesion: 0
density: 1000 kg/m^3.

6.4.10.1.1.3 Simulation Procedure

The simulations start with the model at a normally consolidated state: in static equilibrium under gravity. The boundary conditions used to reach this stage are fixed displacements at the base (i.e., floor) and roller boundaries on the other surfaces that are in contact with the turnout wall and with the main. After the model has been cycled to equilibrium in small strain, the displacements are reset to zero in preparation for the rest of the calculation.

The simulation proceeds in large strain. The mechanical pressure, representing the effect of the magma, is applied gradually (unrelated to the time evolution of magma pressure) on the slope up to the target values of 4 MPa and 8 MPa. The model is cycled to equilibrium before the results are analyzed.

Initial simulations were carried out assuming that the load was applied on the backfill slope only. (Magma flow inside the gap and magma pressure on the backfill inside the gap were neglected.) This assumption is the most favorable condition (from the perspective of magma containment). If such loading conditions resulted in a gap on the top of the backfill, the simulated backfill design would certainly not contain the magma within the emplacement drift. However, if the gap was found to close (or remain closed) due to the pressure on the backfill slope only, the loaded area was extended in the next calculation step by adding full pressure inside the gap (i.e., on the exposed surface of the backfill that originally was not on the backfill slope or that was in contact with the turnout crown).

6.4.10.1.1.4 Interaction between Backfill and Drift Roof

As deformation of the backfill takes place, the fill must remain contained within the turnout perimeter, and a numerical algorithm must be used to enforce this condition. Interface logic was used in the early stages of the analysis. This approach was abandoned due to difficulties encountered in the logic for contact detection between two nonplanar surfaces.

To accomplish this, a technique was developed that does not require explicit modeling of the drift. It consists of adding, at each computational step, a force normal to the backfill surface and proportional to the overlap of the mesh representing the backfill and the contour of the drift crown. (Only positive overlaps are considered.) The technique makes use of the FISH module embedded in FLAC3D V2.1 (STN: 10502-2.1-00), which allows internal variables to be modified to extend the domain of application of the code. The maximum relative overlap between fill and crown is less than 0.6 percent.

This technique has proven to be very efficient for this application. The implementation assumes a frictionless contact between the fill and the drift crown. However, in principle, the restriction could be modified to account for frictional contact.

6.4.10.1.2 Model Results

6.4.10.1.2.1 Original Design

Two sizes for the gap on top of the backfill were considered: 1.0 m and 0.5 m. In the first case, the height of the fill is 6 m. (The height of the turnout is 7 m.) The behavior of the fill under magma pressure depends on the frictional character of the contact between the backfill material and the drift walls. As mentioned above, the numerical technique for roof detection assumes a frictionless contact at the crown. The extreme cases of rough and smooth frictional contacts at the base of the drift are contrasted below.

In the smooth-contact case, roller-type boundary conditions are imposed at the base of the drift. The grid deformation at the end of the simulation for 8 MPa pressure is presented in Figure 35. The fill material, pushed like a piston, heaves in a rather uniform manner, thereby filling and closing the gap. The maximum vertical displacement at the end of the simulation is about 98 cm, which falls short of completely closing the gap by 2 cm.

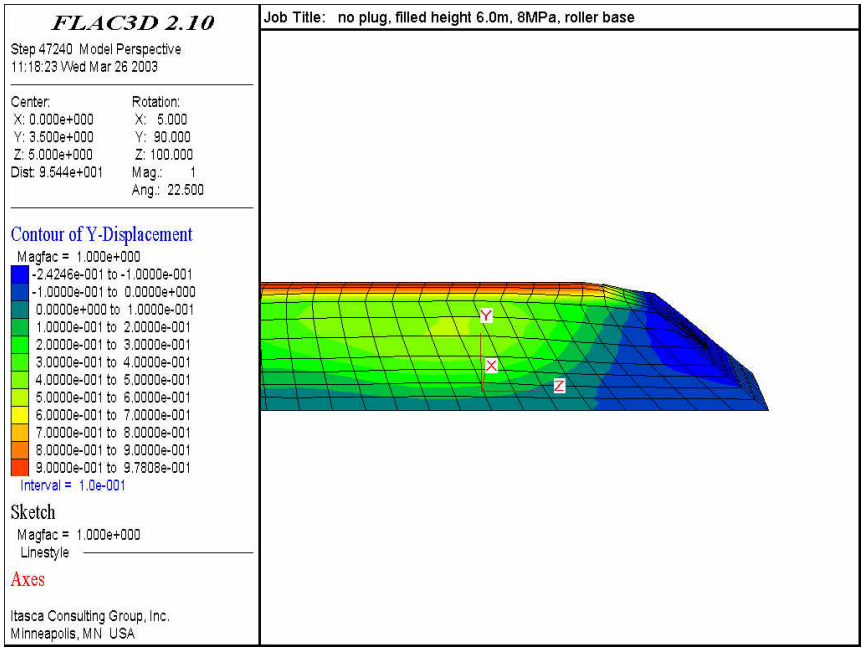

Output DTN: MO0307MWDDDINT.000

Figure 35. Vertical Displacement Contours and Deformed Mesh at 8 MPa Pressure for 6-m Backfill Height—Smooth Case

In the rough-contact case, the base of the drift is fixed. This condition is considered to be a very conservative assumption for analysis of gap closure. Constrained by these boundary conditions, the fill deforms in a nonuniform manner and is seen to heave and form a hump at some distance away from the slope (see Figure 36). The maximum vertical displacement on the hump, about 84 cm (compared with the "uniform" 98 cm heave in the smooth case), falls short of closing the gap by 16 cm.

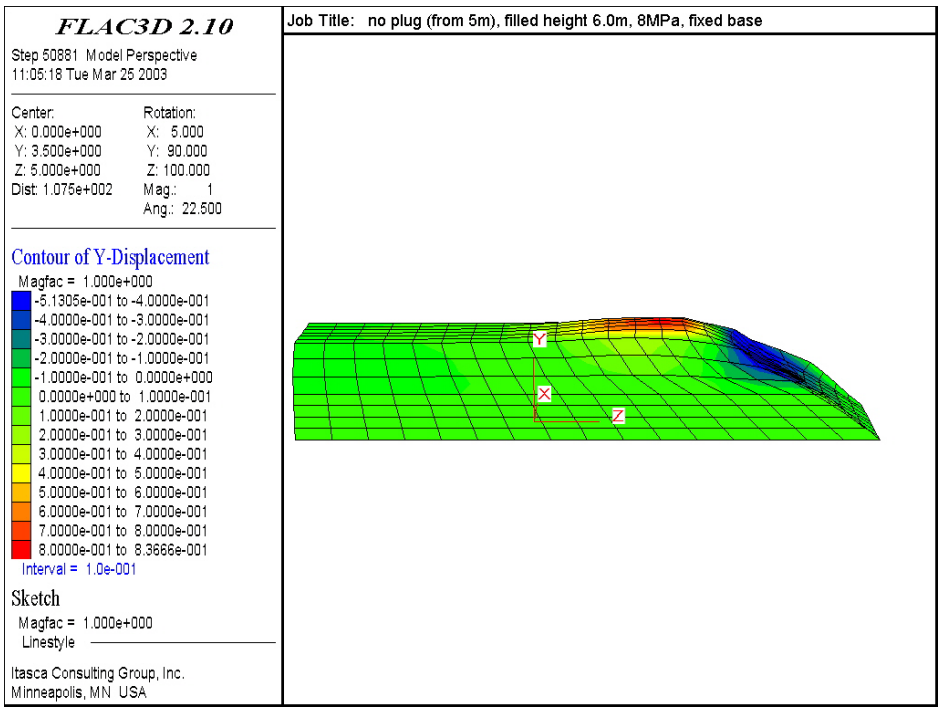

Output DTN: MO0307MWDDDINT.000

Figure 36. Vertical Displacement Contours and Deformed Mesh at 8 MPa Pressure for 6-m Backfill Height—Rough Case

In the second case, the simulations are repeated—this time for a fill height of 6.5 m (i.e., 0.5 m larger than the height in the first example). The deformed mesh for the smooth-contact case with a pressure of 8 MPa is shown in Figure 37. In this case, the maximum vertical displacement is 49.6 cm, only a few millimeters short of closing the gap. The results for the rough-contact case for 8 MPa pressure are presented in Figure 38. The fill heaves at the back of the slope by a maximum amount of 47.5 cm (50 cm is required to fill the gap).

The simulations for the smooth-contact cases are presented to illustrate one possible closing mechanism. They are not conservative and, therefore, cannot be used to demonstrate safety against magma intrusion. On the other hand, although the initial gap sizes (between 0.5 m and 1 m) considered in the analyses are believed to be realistic if the turnout is not tightly filled, the closures observed for the rough-contact simulations are not large enough to prevent propagation of magma through the gap toward the main (since the gap will not close completely). As mentioned earlier, advance of the magma front has not been considered in the analysis. (No magma pressure has been applied on the free upper surface of the fill.) If advance of the magma had been taken into account, the calculated gap closure would have been less.

Taking these factors into consideration, it appears that the risk of magma spreading into the mains cannot be eliminated based on these simulations. The conclusion assumes, of course, that the magma-backfill interaction is properly addressed in the model and that the constitutive model properties adopted in the simulation are reasonable for the fill.

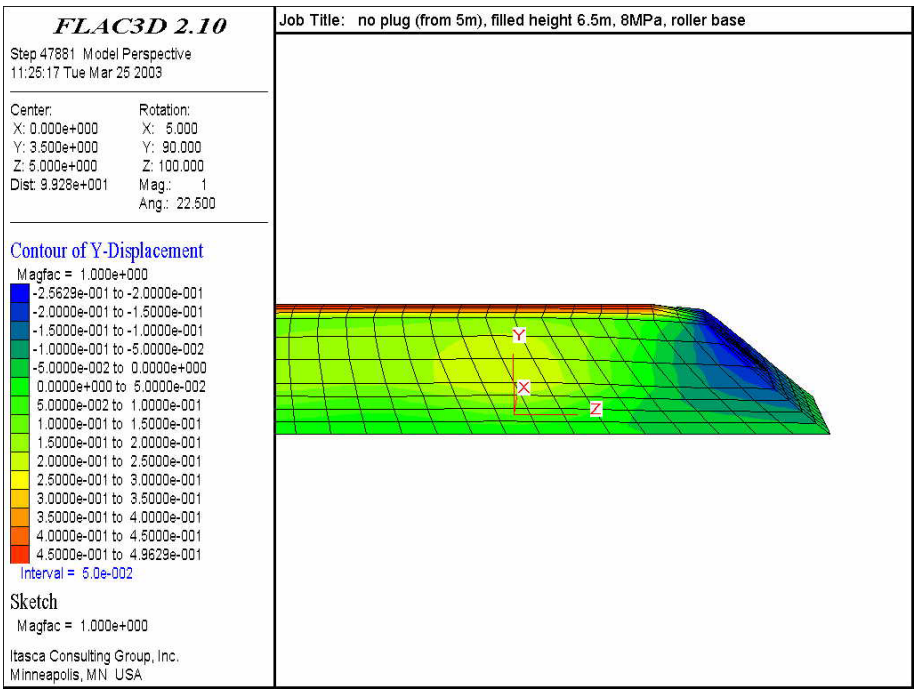

Output DTN: MO0307MWDDDINT.000

Figure 37. Vertical Displacement Contours and Deformed Mesh at 8 MPa Pressure for 6.5-m Backfill Height—Smooth Case

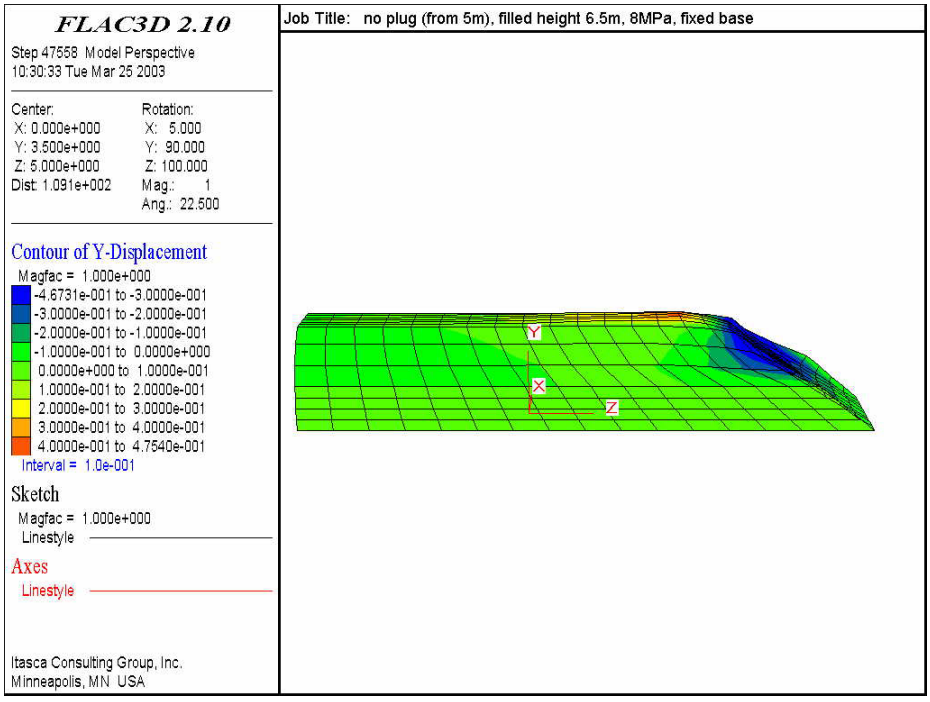

Output DTN: MO0307MWDDDINT.000

Figure 38. Vertical Displacement Contours and Deformed Mesh at 8 MPa Pressure for 6.5-m Backfill Height—Rough Case

6.4.10.1.2.2 Tight Backfill

It appears, from the numerical simulation results obtained so far, that an engineering barrier would be beneficial in preventing possible magma spreading into the main. One possibility is to tight backfill (or plug) a portion of the turnout. There are certain issues that compromise the idea of tight backfill plug; it is difficult to backfill tightly a drift that is not inclined. Furthermore, no matter how tightly backfill is placed against the back of the drift, it cannot be guaranteed that a gap of the order of a few centimeters will not open over a period of 10,000 years due to settlements of the fill (e.g., ground shaking causes compaction of cohesionless materials). Nevertheless, the sealing capabilities of such a plug are investigated numerically. The rough case for frictional contact at the base of the drift and a fill height of 6 m for the analysis is used. The grid adopted for the simulation is shown in Figure 39. Two cases are considered corresponding to initial plug lengths of 2 m and 5 m (measured at the crown).

The deformed grids, after application of 4 MPa and 8 MPa pressures for the 2-m plug, are shown in Figures 40 and 41, respectively. Displacement vectors fields in the longitudinal profiles for the 4 MPa and 8 MPa pressures are presented in Figures 42 and 43.

The fill material behind the plug heaves as a result of the applied pressures. At the same time, as the backfill slope is pushed down, the backfill loses contact with part of the roof. However, it appears, from the results of these simulations, that the plug still maintains a seal over part of its length, even at 8 MPa pressure.

This impression is misleading. One important factor has not been taken into account in the simulations: the area over which the magma pressure is applied is not updated as the plug detaches from the roof. In reality, as it flows, the magma will exert pressure on the slope, all the way up to the contact with the roof. Because of the geometry of the slope, there will be a component of the magma pressure acting in the direction normal to the backfill surface and away from the roof. As a result, a fracture-propagation-type mechanism develops that causes progressive detachment of the backfill from the roof as the magma flows into the gap that is created. The mechanism is illustrated in Figure 44.

This effect is illustrated in Figures 45 to 47. To produce these figures, the simulation for a 2-m-long plug subjected to 4 MPa pressure on the slope is continued by further applying the full 4 MPa pressure on the deformed slope, up to the contact with the roof, and cycling the model to equilibrium. As the plug becomes more detached, pressure is applied to the newly created interfacial surfaces. After a first application of 4 MPa pressure, the backfill deforms and some new interfacial surface is formed. The resulting deformations are shown in Figure 45. In the second step, the 4 MPa magma pressure is applied to the newly formed surfaces of Figure 45, and the new state of deformation in the fill is determined. Additional surfaces are opened up. The results are shown in Figure 46. In the third stage, the 4 MPa pressure is applied to the fill slope and to the newly extended surfaces. The results are shown in Figure 47. The results of simulations for a 5-m plug, which are not included, show the same trend.

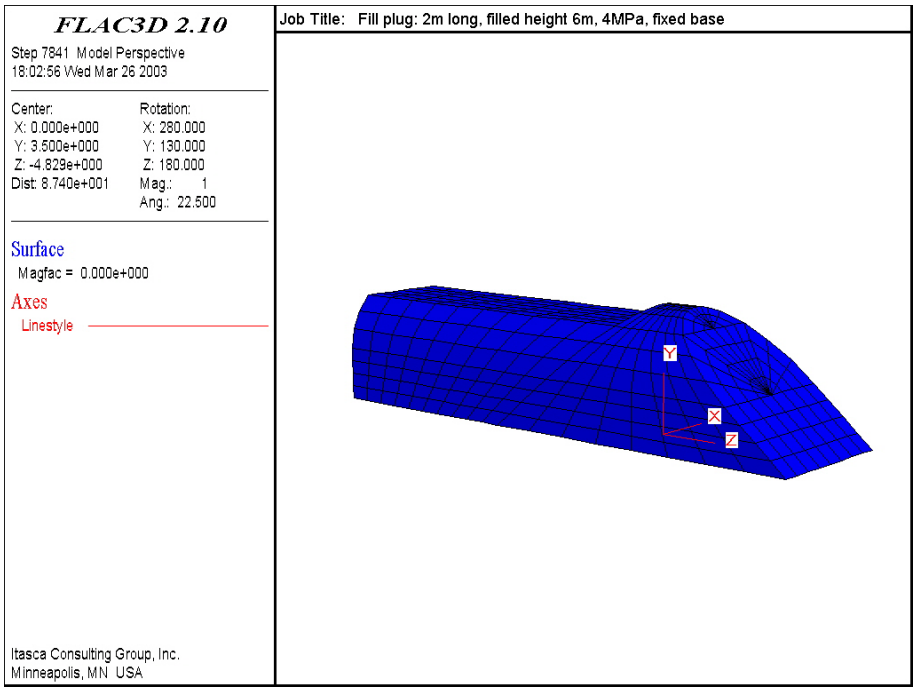

Output DTN: MO0307MWDDDINT.000

Figure 39. FLAC3D Grid for Turnout Segment With Plug

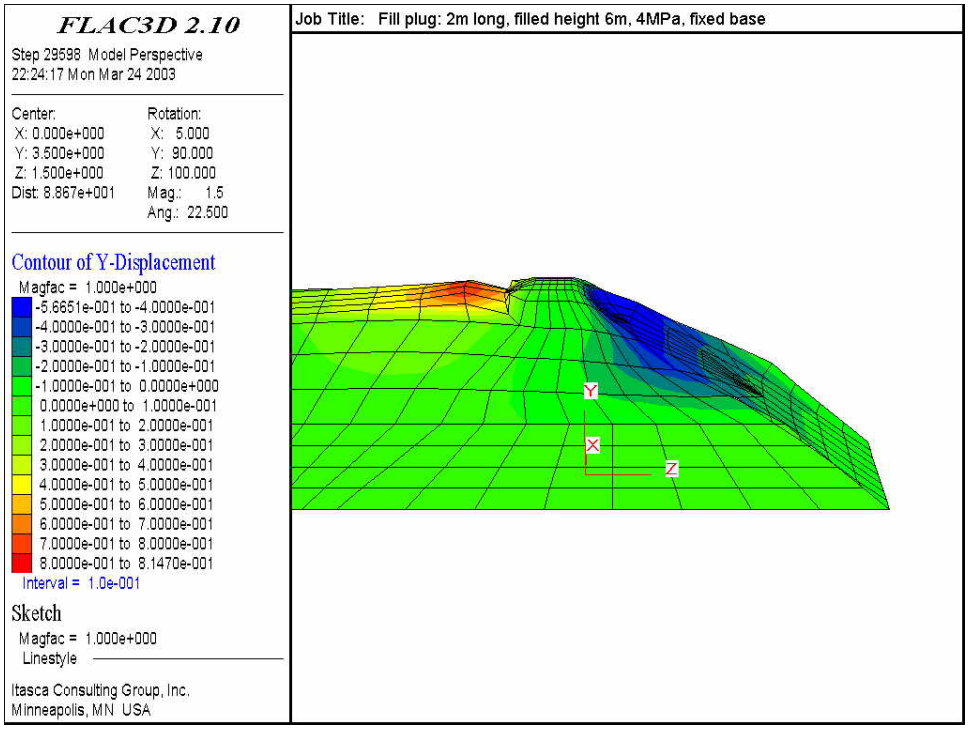

Output DTN: MO0307MWDDDINT.000

Figure 40. Vertical Displacement Contours and Deformed Mesh at 4 MPa Pressure—2-m Plug Case

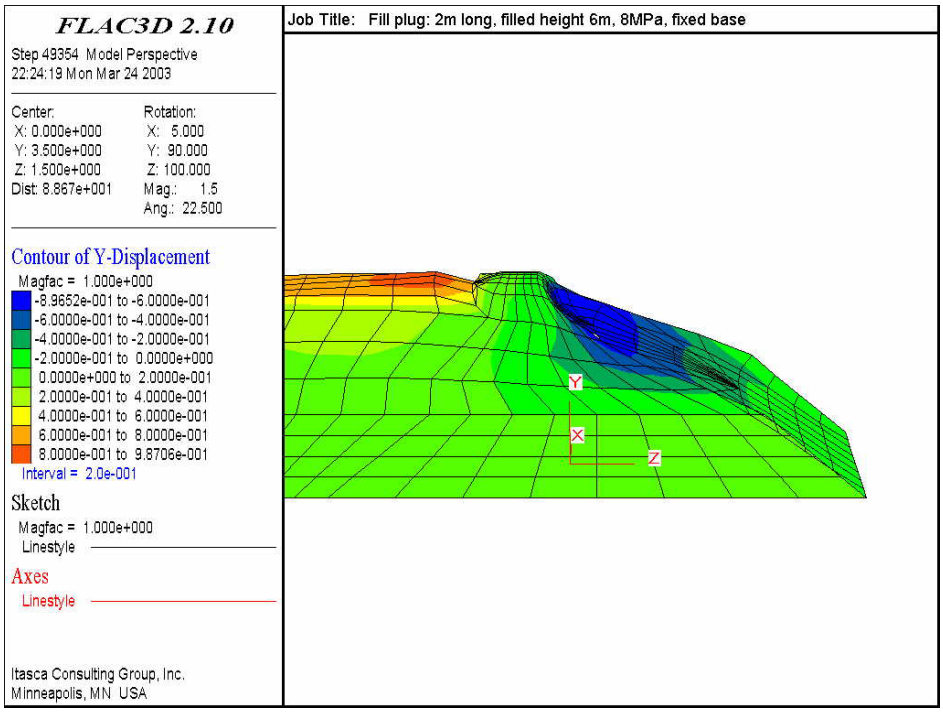

Output DTN: MO0307MWDDDINT.000

Figure 41. Vertical Displacement Contours and Deformed Mesh at 8 MPa Pressure—2-m Plug Case

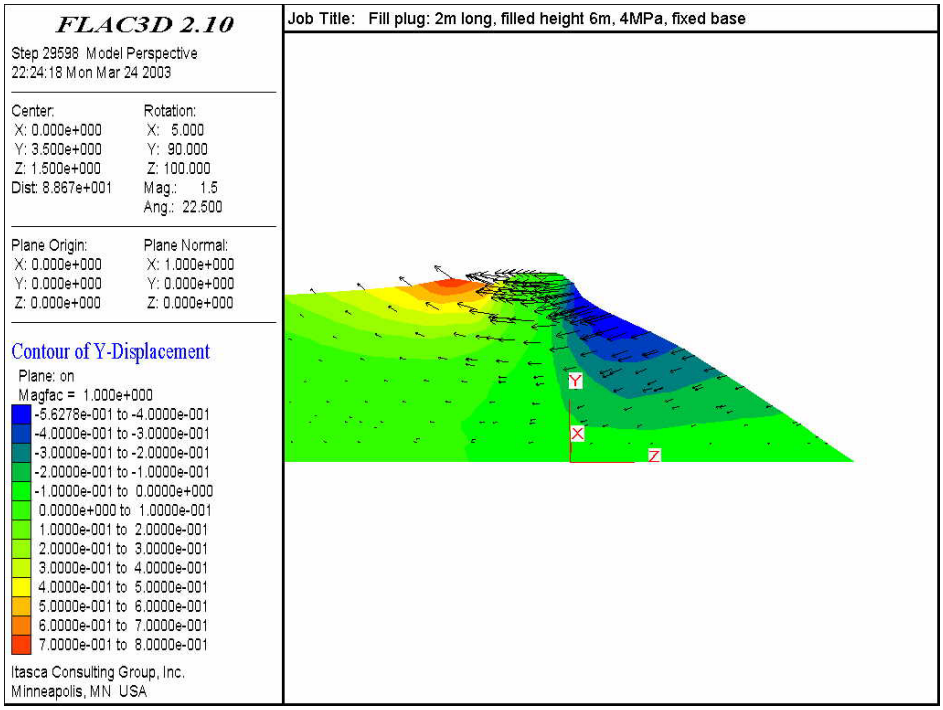

Output DTN: MO0307MWDDDINT.000

Figure 42. Profile of Vertical Displacement Contours and Displacement Vectors on the Plane x = 0 at 4 MPa Pressure—2-m Plug Case

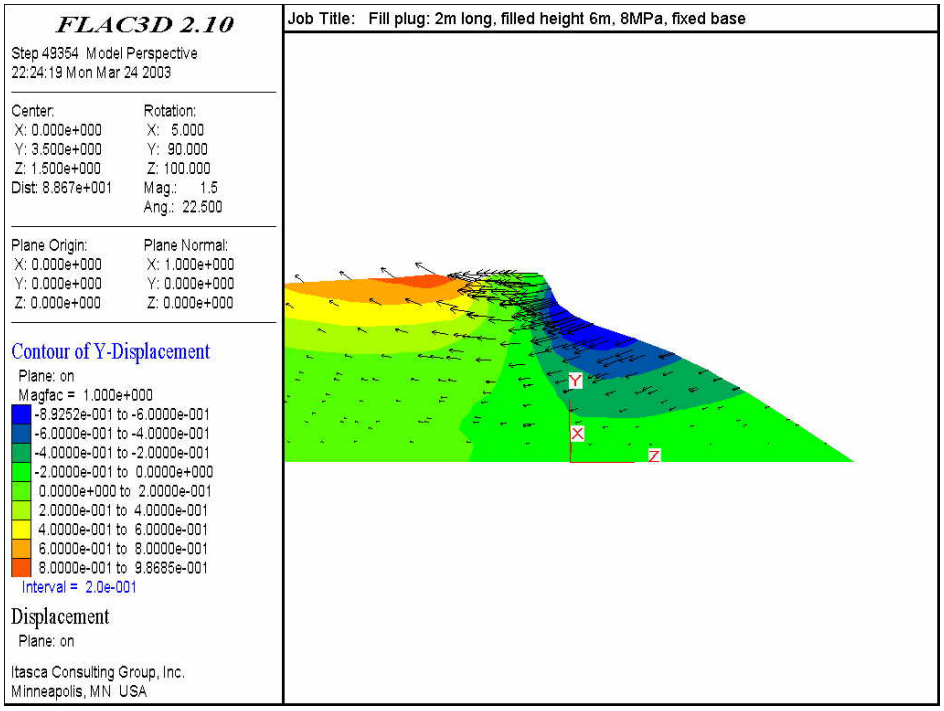

Output DTN: MO0307MWDDDINT.000

Figure 43. Profile of Vertical Displacement Contours and Displacement Vectors on the Plane x = 0 at 8 MPa Pressure—2-m Plug Case

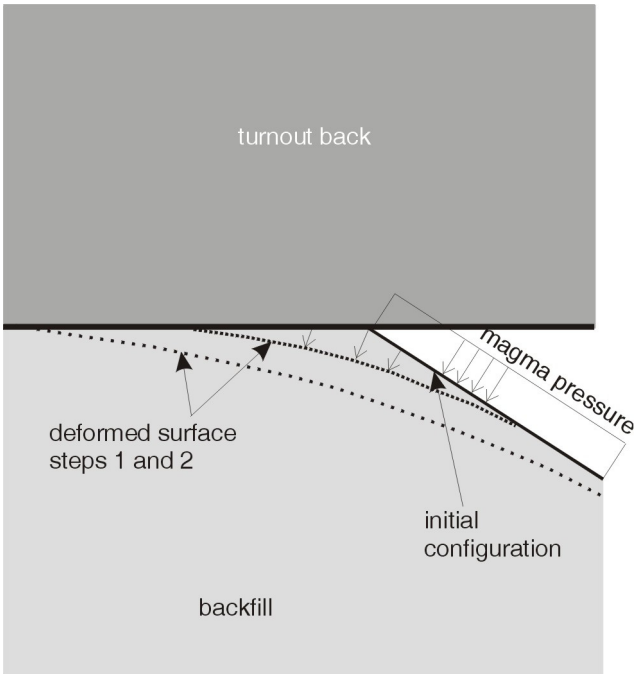

Output DTN: MO0307MWDDDINT.000

Figure 44. Mechanism of Gap Creation

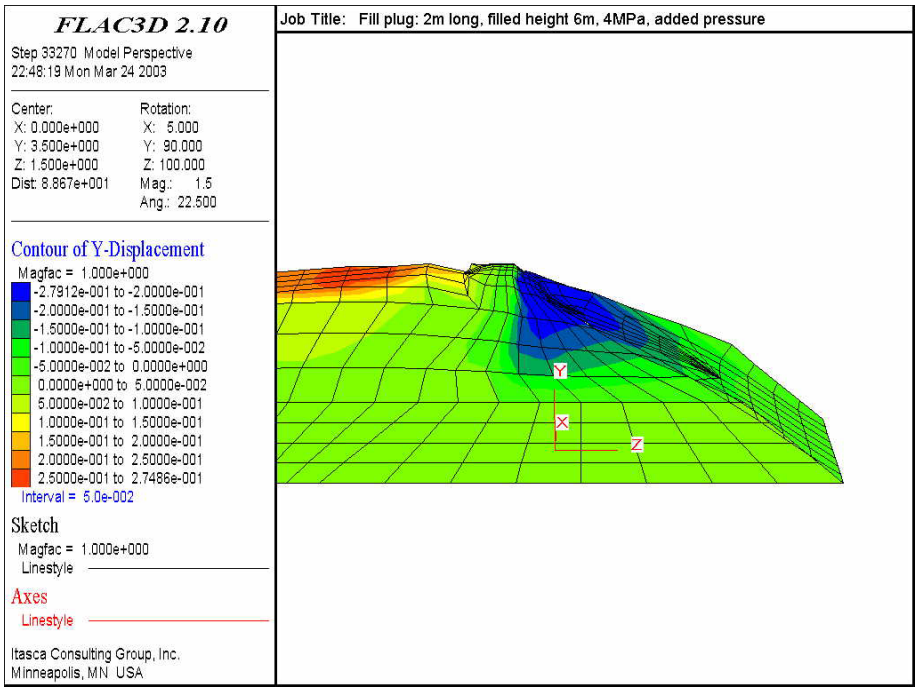

Output DTN: MO0307MWDDDINT.000

Figure 45. Vertical Displacement Contours and Deformed Mesh After First Application of 4 MPa Pressure to the Roof—2-m Plug Case

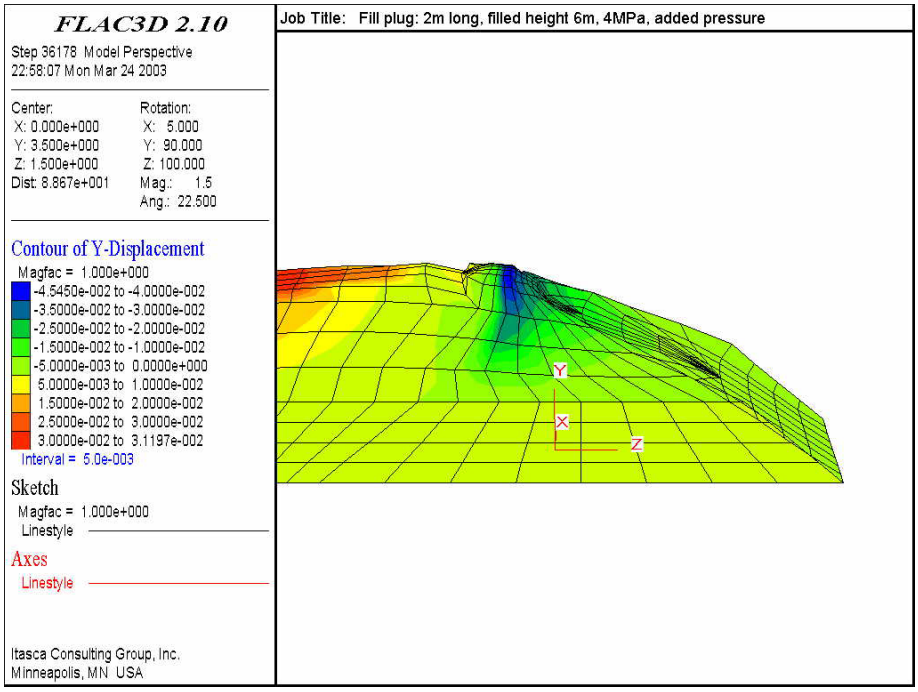

Output DTN: MO0307MWDDDINT.000

Figure 46. Vertical Displacement Contours and Deformed Mesh After Second Application of 4 MPa Pressure to the Roof—2-m Plug Case

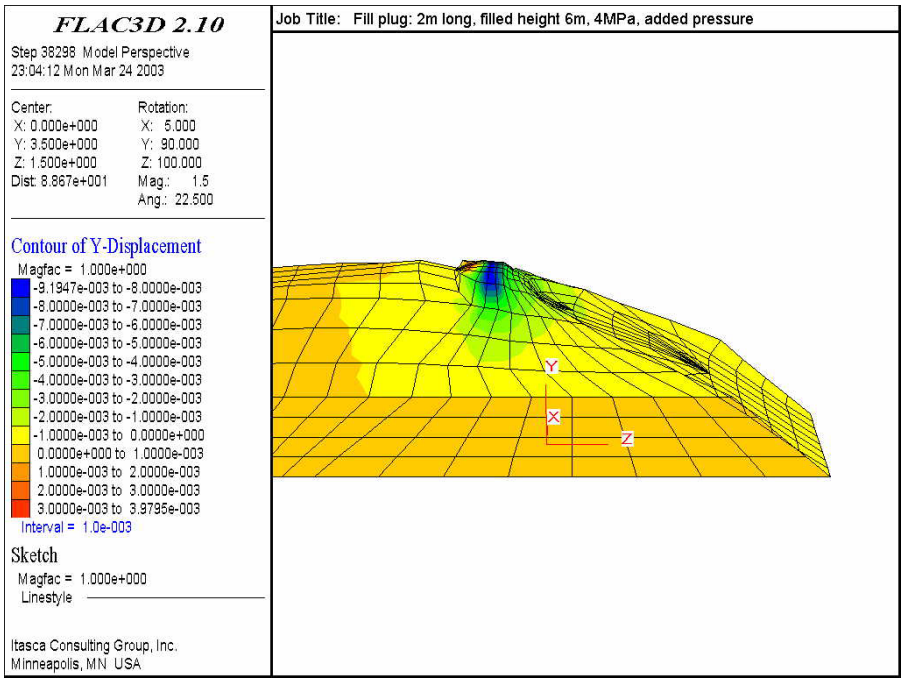

Output DTN: MO0307MWDDDINT.000

Figure 47. Vertical Displacement Contours and Deformed Mesh After Third Application of 4 MPa Pressure to the Roof—2-m Plug Case

The results of numerical simulations with tight backfill segments show the progression of a gap forming at the roof as the magma advances. This effect is caused by the existence of a component of pressure acting on the fill in the direction normal to the roof. It occurs because of the geometry of the fill slope near the contact with the roof. A similar mechanism would be expected to develop for the case of a pressure gradient along the new surface, instead of a constant full pressure over the entire length of the gap to the tip of the magma, as assumed in this analysis.

6.4.10.1.3 Magma Freezing

Magma freezing is one mechanism that could retard magma propagation by restricting passage at the tip of the flow. Freezing is explained by a large increase in magma viscosity resulting from conductive heat loss in a thin boundary layer that is in contact with the rock. The thickness of this boundary layer controls the magnitude of the resulting constriction. It is a function of the original size of the opening through which the magma flows, the magma velocity, the temperature differential between the magma and the rock, and the thermal properties of the magma and the rock.

A typical value for the thickness of a boundary layer that would grow in the time it takes to fill the drift has been cited in the literature as being of the order of a few centimeters (Detournay et al. 2003 [DIRS 162914], Section 5, p. 58). It seems, therefore, that one cannot rely on freezing as an argument to prevent propagation of the magma because the gap that the magma creates on the top of the tight backfill is at least of the order of centimeters and possibly tens of centimeters in aperture. (For example, a magma pressure of 8 MPa can cause up to 10 percent strain in the

backfill. For the turnout height considered here, this results in a gap opening of more than 0.5 m.) The magma freezing argument is not tenable for openings of such dimensions.

6.4.10.1.4 Potential Backfill Modification

The problem with the plug design discussed above is that it allows for the progression of a gap as the magma advances, with no negative feedback. In addition, it has been seen that opening of a gap at the backfill/wall interface is made possible because the direction of applied pressure on the fill is not parallel to the wall. There are numerous engineering solutions such as backfill "keyways" developed into the roof or plugs made from cementitious materials that could be used to prevent magma flow into adjoining emplacement drifts. These will be investigated during the detailed design phase of the repository.

6.4.10.1.5 Conclusions

A set of numerical simulations was performed with the computer code FLAC3D V2.1 (STN:10502-2.1-00) to help identify a possible backfill emplacement designs and to test its efficiency in the prevention of magma spreading from an emplacement drift into the main. The analysis was restricted to mechanical considerations, and magma flow was not modeled. However, the main conclusions are expected to be the same if magma flow were included. The effect of the magma on the backfill material was taken into account by means of an applied mechanical pressure. The drift walls were assumed to be rigid. The backfill constitutive behavior was simulated using the Double-Yield continuum model, and a set of generic backfill properties was used.

The behavior of the fill, under influence of the pressure applied by the magma, is seen to depend on the frictional properties of the contact with the drift wall. For the unrealistic assumption of smooth-contact conditions, a piston-like behavior is observed. For realistic rough-contact conditions, the fill is seen to heave in a hump, away from the fill slope.

The sealing efficiency of a segment of tight backfill was evaluated using numerical experiments. The experiments show progression of a gap forming at the roof as the magma advances. The effect is caused by the existence of a pressure component acting on the fill in the direction normal to the back and occurs because of the sloping geometry of the fill near the contact with the back.

Magma freezing is one mechanism that could control advancement of the magma. However, the effect alone is probably inadequate to stop magma in even the tight-backfill situation. There are numerous engineering solutions such as backfill "keyways" developed into the roof or plugs made from cementitious materials that could be used to prevent magma advancement into adjoining emplacement drifts. These will be investigated during the detailed design phase of the repository.

The propagation of a dike, and its potential interaction with a repository drift will occur under violent dynamic conditions. The dike tip will most likely consist of a fractured zone, not the clean fracture as idealized in these models. As it propagates, the stress rotations and concentrations ahead of the dike tip will induce great damage to the rock mass, through new fracturing, as well as inducing dynamic slip episodes on existing fractures. Given the highly fractured nature of the repository host rock, it is not considered possible that the dike would intersect the drift without causing significant damage to the opening. Yet, this has not been considered in this report. It has been shown in a separate report for Yucca Mountain on "drift degradation" that massive roof fall can occur from seismic loading. Hence, it could be expected that massive caving of the drift roof and walls would occur and constitute a substantial obstacle to any magma flow. Mixing of magma and rock debris would significantly increase the magma viscosity, both by cooling and by changing the magma composition. Quantification of these effects to the point where they could be included into a probabilistic analysis may be beyond present modeling capabilities.

6.4.10.2 The "Dog-Leg" Scenario

Woods et al. (2002 [DIRS 163662]) described a drift filling and a new dike opening to the surface at some distance from the original dike, with the magma flow being diverted through the drift and carrying the entire drift contents to the surface. This section presents a model of the opening of pre-existing cracks in a drift filled with magma. This is combined with supporting analyses and applications below (Section 6.4.11) to provide an overall discussion of that "dog-leg" scenario.

6.4.10.2.1 Crack Opening Rates

It appears, from the analysis of dike-drift interaction, that in some cases (discussed in Sections 6.3.9.2.3.1 and 6.3.9.2.3.3) once the dike intersects the emplacement drifts the magma front inside the dike will not propagate very far above the repository level while magma flows into the drifts.

To assess the possibility of a "dog-leg" scenario (i.e., magma finding a new path to the ground surface by re-opening some of the existing joints inside the drifts), the conditions of magma injection into the joints intersecting the drift were investigated. It is of interest to determine the rates of the magma front movement inside the secondary dike and the rate of the secondary dike opening.

This section discusses results of simulations of magma injection into pre-existing joints inside the emplacement drifts. Simulations discussed here investigate sensitivity of the model predictions to variation of its parameters, such as magma compressibility, magma viscosity, magma pressure, initial joint aperture, rock mass stiffness (Young's modulus), and initial stress state. The conservatism of this analysis derives from the fact that magma freezing inside the joints was not considered, and the effect of the dike on the stresses around the drift is neglected.

All analyses discussed in this section were done using two numerical codes: UDEC V3.1 [DIRS 161969] and FLAC3D V2.1 [DIRS 161947].

All simulated cases of magma injection into pre-existing joints inside the emplacement drifts are summarized in Table 15. (The order in which the cases are listed in Table 15 does not indicate a relation between different cases, only the sequence in which they were simulated.)

Table 15. Summary of Analyzed Cases of Magma Injection Into Joints

Case	Crack Orientation with Respect to Drift*	Initial Crack Aperture (mm)	Magma Pressure in Drift (MPa)	Initial Stress			Bulk Modulus of Magma (MPa)	Young's Modulus of Rock (GPa)	Magma Viscosity (Pa-s)
				Over-burden (m)	Coeff. Along Drift	Coeff. Perp. to Drift			
101	vertical along	1	4	300		0.5	50	15	10
102	vertical along	1	8	300		0.5	50	15	10
103	vertical along	1	10	250		0.5	50	15	10
104	horizontal	1	8	300		0.5	50	15	10
105	vertical perp.	1	10	300	0.35	0.5	50	15	10
106	vertical along	1	4	300		0.5	50	5	10
107	vertical along	1	4	300		0.5	500	15	10
108	vertical perp.	1	8	300	0.35	0.5	50	15	10
109	vertical perp.	1	8	300	0.5	0.35	50	15	10
110	vertical along	1	8	250		0.5	50	15	10
111	vertical along	3	8	250		0.5	50	15	10
112	vertical along	3	8	250		0.5	50	5	10
113	vertical along	3	8	250		0.5	500	5	10
114	vertical along	3	8	250		0.5	500	15	10
115	vertical along	1	8	250		0.5	50	5	10
116	vertical along	1	8	250		0.5	50	15	100
117	vertical along	1	10	250		0.5	50	15	100
118	vertical along	3	8	250		0.5	50	15	100
119	vertical along	3	8	250		0.5	50	5	100
120	vertical along	1	8	250		0.5	50	5	100

Output DTN: MO0307MWDDDINT.000

NOTES: *Crack Orientation: vertical along = a vertical crack along the drift; vertical perp. = a vertical crack perpendicular to the rift

The results for Cases 101 through 105 (base cases) are shown in Figures 48 through 73. The following plots are shown for each case:

- Displacement vector field and hydraulic aperture along the joint at the end of the simulation
- Stress tensor field (colored by the magnitude of the minor principal stress) and pore pressure along the joint at the end of simulation
- Evolution of joint aperture at seven locations indicated in Table 16 (for Cases 101 through 104) and Table 17 (for Case 105)
- Evolution of magma pressure inside the joint at seven locations indicated in Table 16 (for Cases 101 through 104) and Table 17 (for Case 105)
- Position (distance from the drift periphery) of the magma front inside the joint as a function of time.

Table 16. Drift Periphery to Recording Point Distances for Cases 101 Through 104 and 106, 107, and 110 Through 120

Point	Distance (m)
1	0.46
2	0.92
3	1.83
4	3.67
5	7.79
6	16.04
7	32.14

DTN: N/A

NOTES: Distances are measured from the drift periphery to the points at which histories of aperture and pressures are recorded for the various cases.

Table 17. Drift Periphery to Recording Point Distances for Cases 105, 108, and 109

Point	Distance (m)
1	0.00
2	1.40
3	3.08
4	5.08
5	10.34
6	22.71
7	43.79

DTN: N/A

NOTES: Distances are measured from the drift periphery to the points at which histories of aperture and pressures are recorded for the various cases.

The results indicate that, with the exception of Case 103, the distance of the magma front from the drift periphery after 300 s will be between 5 m and 60 m. However, for the same time, 300 s after the drifts are completely filled with magma, the main dike would reach ground surface (assuming a magma front velocity of 1m/s). The additional conservatism of this analysis is due to the fact that magma freezing inside the joints was not considered.

Case 103 represents extremely conservative conditions. Magma pressure inside the drift of 10 MPa is assumed whereas stresses in the rock mass are due to in-situ far-field conditions (no thermal effects). Plugging the main dike conduit at an elevation above the repository level could result in an increase in magma pressure without an increase in rock-mass stresses. However, it is not likely that magma pressure could reach 10 MPa because the main conduit would most likely re-open at lower pressures. Even for such extreme conditions, the velocity of a magma front inside a joint is approximately 0.5 m/s (with a trend to decrease as the pressure gradient decreases in response to the increasing length of the magma-filled portion of the joint), which is less than the expected velocity of the magma front inside the main dike.

The results from the Cases 106 through 120 are presented in Figures 74 through 129. These cases investigate sensitivity of the model predictions to variation of its parameters, such as magma compressibility, magma viscosity, magma pressure, initial joint aperture, rock mass stiffness (Young's modulus), and initial stress state.

The aperture and the magma pressure histories for Cases 106, 107, and 110 through 120 are presented at the locations specified in Table 16; the aperture and the magma pressure histories for Cases 108 and 109 are presented at the locations specified in Table 17.

Sensitivity of Case 101 to variation of Young's modulus of the rock mass is investigated in Case 106. Young's modulus of the rock mass in Case 106 is 5 GPa (poor quality lithophysal rock, between categories 1 and 2), which compares to 15 GPa in Case 101 (good quality lithophysal rock, between categories 4 and 5, and also representative of nonlithophysal rock

mass). The results (shown in Figures 74 through 77) indicate that, in the case of more compliant rock mass, the increase in the joint aperture is larger (5.5 mm aperture 800 s after injection compared to 2.2 mm aperture 800 s after injection in Case 101) but still relatively small, indicating that, in this case, the magma would freeze due to conductive heat loss into the surrounding rock mass.

To investigate the effect of magma compressibility, Case 107 (Figures 78 through 81) was simulated assuming magma bulk modulus to be 500 MPa (compared to 50 MPa in Case 101). Increased bulk modulus of the magma resulted in a reduced simulation time step, but the results for Cases 101 and 107 after 3000 s are almost identical. Magma compressibility does not affect the results in this case.

Cases 108 and 112 (Figures 82, 83, and 94 through 97), for a 3D model of a joint, perpendicular to the drift, compare with Case 105. Both new cases are for 8 MPa magma pressure (Case 105 is for 10 MPa). Case 109 represents the condition of a larger normal stress along the drift (perpendicular to the joint): 50 percent of the vertical stress compared to 35 percent of the vertical stress for Cases 105 and 108. All three cases indicate instability (due to the magma pressure being larger than the horizontal far-field stress perpendicular to the joint), but there is a clear trend of the reduction in the rate of joint opening from Case 105 to 108 and from Case 108 to 109. After 500 s of magma injection, the joint aperture in Case 105 is approximately 8 cm, in Case 108 (Figure 82) it is 8 mm, and in Case 109 (Figure 84) it is 4 mm.

The maximum vertical stress at the repository level is about 8 MPa. Under such conditions, the 10 MPa magma pressure considered in Case 103 is unrealistic. Case 110 (Figures 86 through 89) investigates the effect of reduction in magma pressure from 10 MPa (considered in Case 103) to 8 MPa. The rate of fracture opening significantly reduces from Case 103 to Case 110. The maximum joint opening of 1.2 cm is reached in 9 s in Case 103, whereas it took almost 60 s in Case 110.

All the analyses discussed so far assume the initial joint aperture to be 1 mm. This assumption is reasonable and even conservative considering measurements of joint apertures (Olsson and Brown 1997 [DIRS 106453]). However, to investigate the effect of the initial joint aperture on model response, Case 111 (Figures 90 through 93) is simulated using the very conservative assumption for the initial joint aperture to be 3 mm.

All model parameters between Cases 110 and 111 are the same, except that the initial joint aperture in Case 110 is 1 mm and in Case 111 is 3 mm. The maximum joint aperture of 1.2 cm is reached after 18 s (Figure 92) in Case 111 compared to almost 60 s in Case 110. Cases 112 (Figures 94 through 97) and 115 (Figures 106 through 109) investigate the effect of stiffness of the rock mass:

- Case 110 is for a Young's modulus of the rock mass of 15 GPa compared to Case 115 for a Young's modulus of 5 GPa (both cases are for a 1-mm joint aperture).

- Case 111 is for a Young's modulus of the rock mass of 15 GPa compared to Case 112 for a Young's modulus of 5 GPa (both cases are for a 3-mm joint aperture).

The effect of the stiffness of the rock mass is much more pronounced between Cases 111 and 112 and Cases 110 and 115 than between Cases 101 and 106. The joint aperture of the order of 1 cm is achieved in Cases 112 and 115 for less than a second (Figures 96 and 108, respectively).

The effect of rock mass deformability is more significant in cases in which magma pressure causes complete joint opening (i.e., Cases 110, 111, 112, and 115) compared to cases (e.g., Cases 101 and 106) that consider injection of magma into a closed joint. It also appears that rock mass deformability has a more profound effect on the potential for the opening of a secondary dike inside the drift than the initial joint aperture.

It should be noted that joints with long trace lengths exist in good quality rock (i.e., nonlithophysal rock mass and better quality lithophysal rock mass). Such rock is characterized with a Young's modulus equal to or larger than 15 GPa. Poor quality rock mass at the repository level in Yucca Mountain (e.g., highly fractured lower lithophysal—Tptpll) is characterized by a large number of joints that are at small spacing with short trace lengths and not continuous. This kind of medium will not be susceptible to a mechanism of localized fracture propagation. Instead, it is more likely that magma will be injected into exposed lithophysae and into a number of noncontinuous, mutually intersecting joints. Such a process will lead to quick magma freezing due to heat loss.

Cases 113 and 114 (Figures 98 through 105) investigate the effect of an increase in magma bulk modulus from 50 MPa to 500 MPa relative to Cases 111 and 112. It appears from the results that such an increase in magma bulk modulus has a minor effect on the model results.

All of the results presented to this point assumed magma viscosity to be 10 Pa s. As magma enters the drift and is being injected into the joints, it will cool off and, before freezing, magma viscosity will increase. Because a dimensional and scaling analysis was not carried out, simulations of Cases 116 through 120 (Figures 110 through 129) were conducted to investigate the effect of an increase in magma viscosity from 10 Pa s to 100 Pa s. As expected, an increase in magma viscosity results in a proportional increase in time scale. For example, in Case 103 (viscosity 10 Pa s), it takes 9.5 s for the maximum joint aperture to reach 1.2 cm, whereas in Case 117 (viscosity 100 Pa s), the same maximum joint aperture of 1.2 cm is reached in 95 s.

Even if the argument of magma freezing is not used, among all of the 20 analyzed cases, only in Cases 112 and 115 does a magma front inside the joint move faster than 0.5 m/s. That result implies that the magma front inside the original dike (which could also be 80 m or more above the repository level) will reach the ground surface much sooner than the magma injected into joints inside the drift.

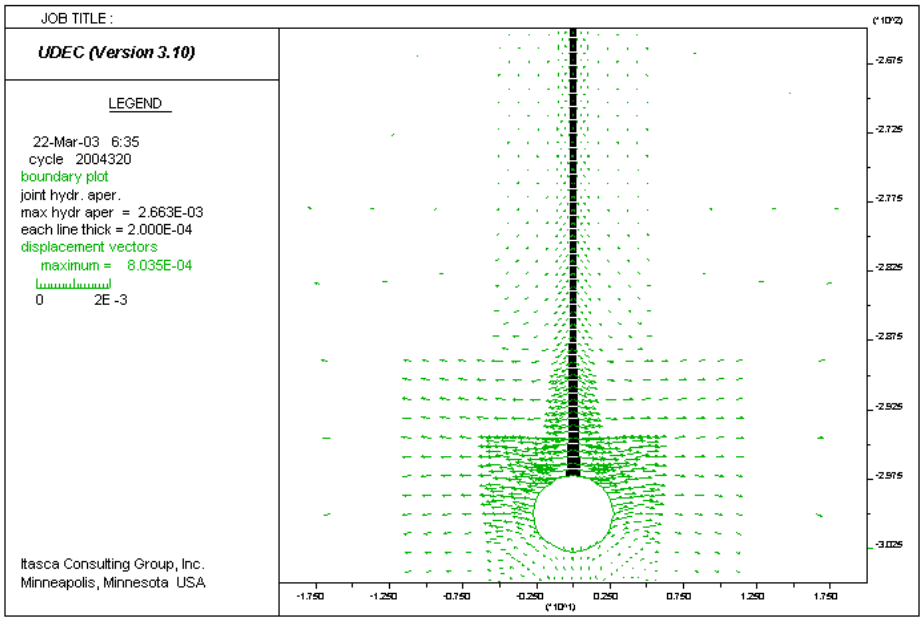

Output DTN: MO0307MWDDDINT.000

NOTES: Thickness of the black line is proportional to the hydraulic aperture of the joint; deformation is due to pressure change inside the joint only.

Figure 48. Displacement Vector Field (m) and Hydraulic Aperture (m) Along the Vertical Fracture: Case 101

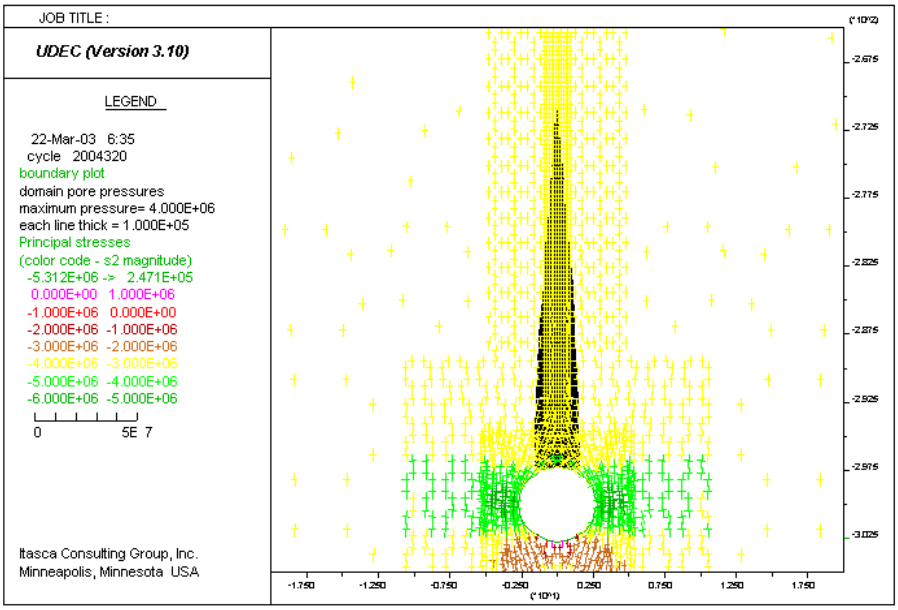

Output DTN: MO0307MWDDDINT.000

NOTES: Thickness of the black line is proportional to magma pressure in the joint; color of stress tensors indicates the magnitude of the minor principal stress.

Figure 49. Stress Tensor Field (Pa) and Pore Pressure (Pa) Along the Joint: Case 101

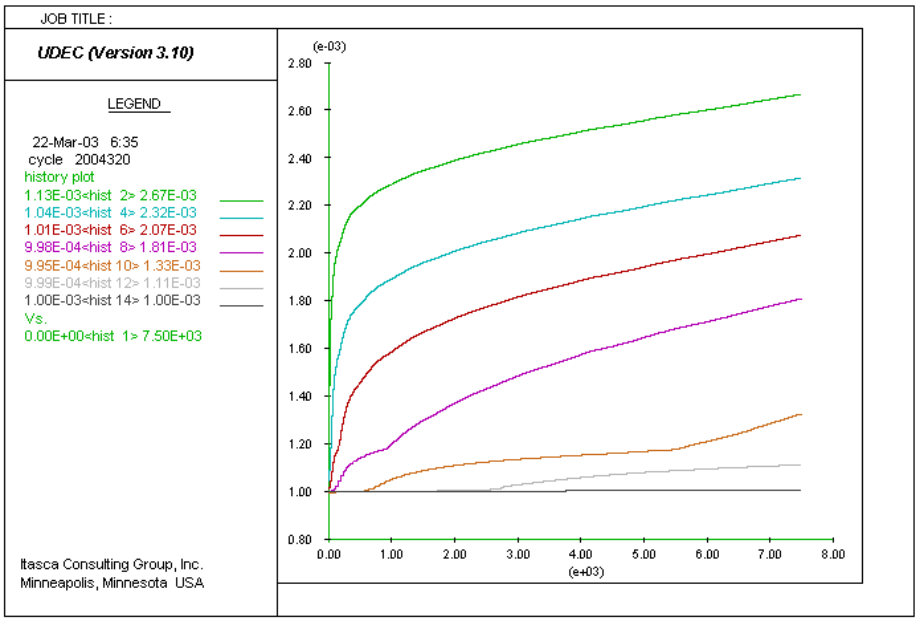

Output DTN: MO0307MWDDDINT.000

NOTES: Increasing history numbers correspond to points from Table 15, maintaining the same sequence. Time is in seconds.

Figure 50. Histories of Joint Hydraulic Aperture (m) at Seven Locations Along the Joint: Case 101

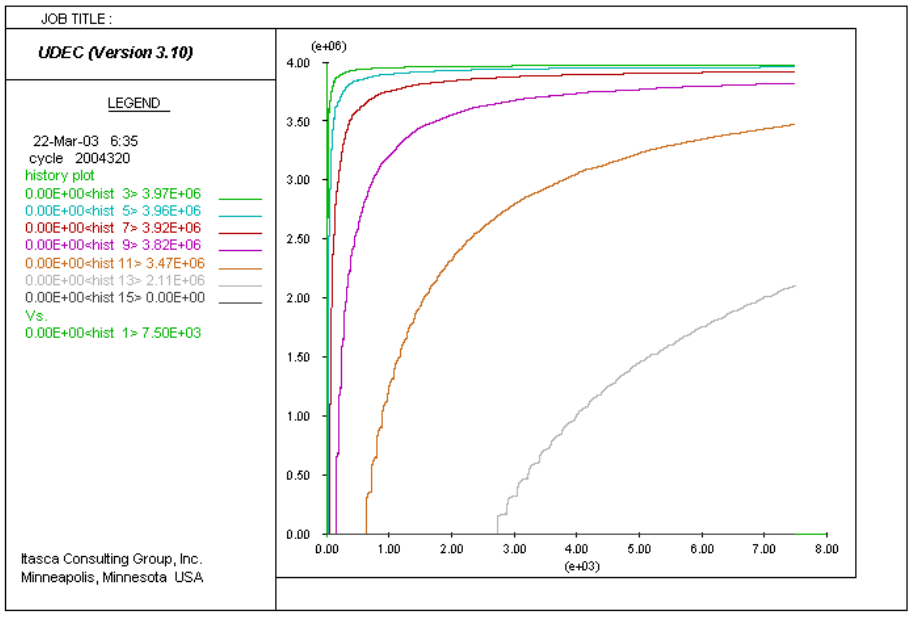

Output DTN: MO0307MWDDDINT.000

NOTES: Increasing history numbers correspond to points from Table 15, maintaining the same sequence. Time is in seconds.

Figure 51. Histories of Pore Pressure (Pa) at Seven Locations Along the Joint: Case 101

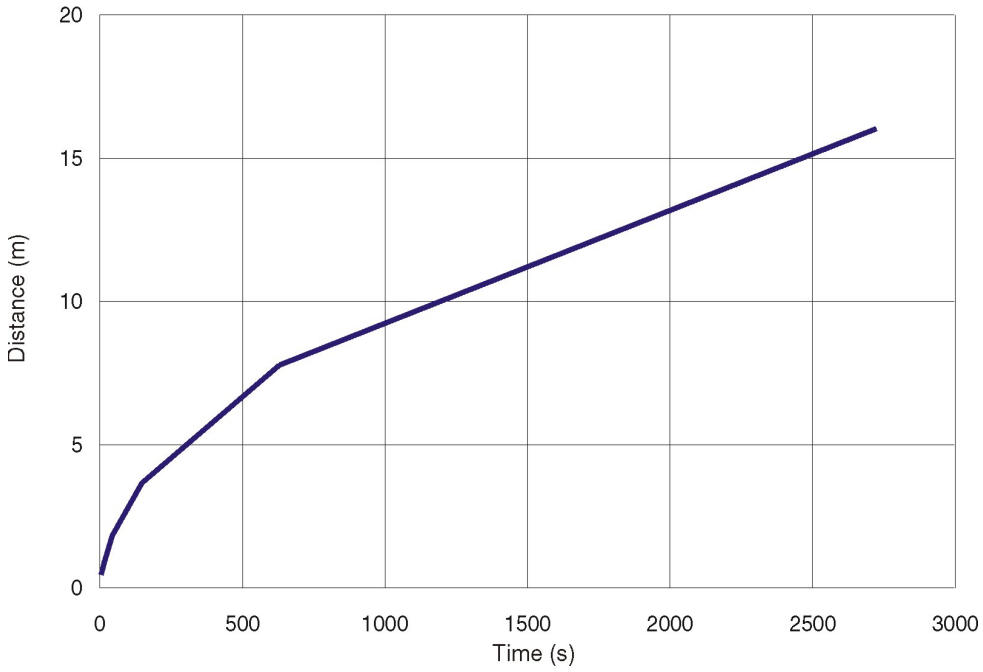

Output DTN: MO0307MWDDDINT.000

Figure 52. Location (Relative to the Drift Periphery) of the Magma Front Inside a Joint as a Function of Time: Case 101

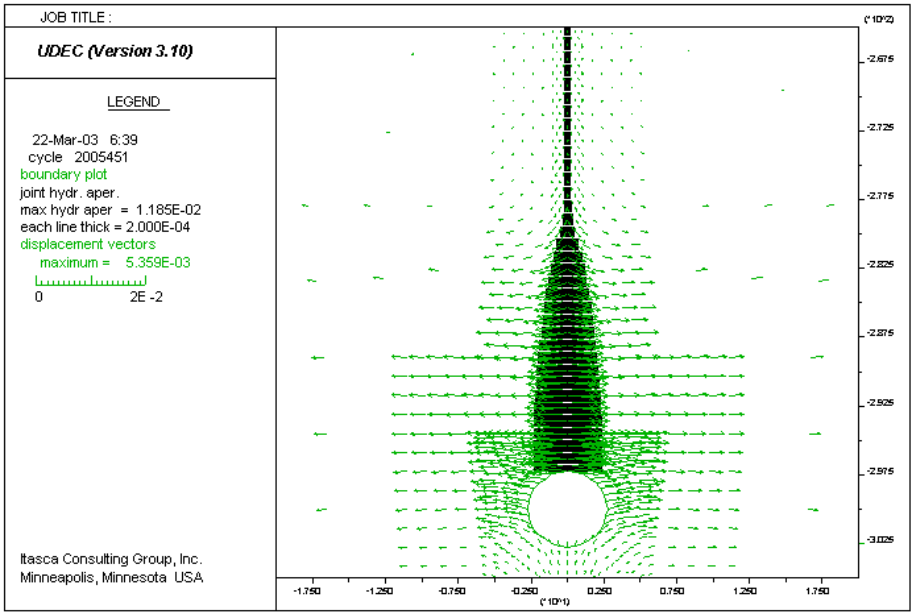

Output DTN: MO0307MWDDDINT.000

NOTES: Thickness of the black line is proportional to hydraulic aperture of the joint; deformation is due to pressure change inside the joint only.

Figure 53. Displacement Vector Field (m) and Hydraulic Aperture (m) Along the Vertical Fracture: Case 102

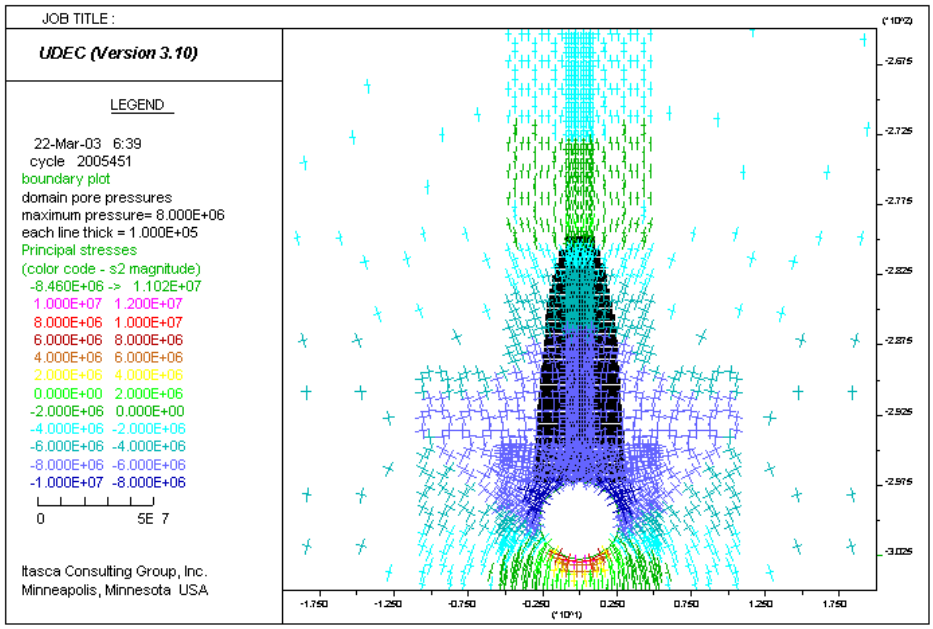

Output DTN: MO0307MWDDDINT.000

NOTES: Thickness of the black line is proportional to magma pressure in the joint; color of stress tensors indicates the magnitude of the minor principal stress.

Figure 54. Stress Tensor Field (Pa) and Pore Pressure (Pa) Along the Joint: Case 102

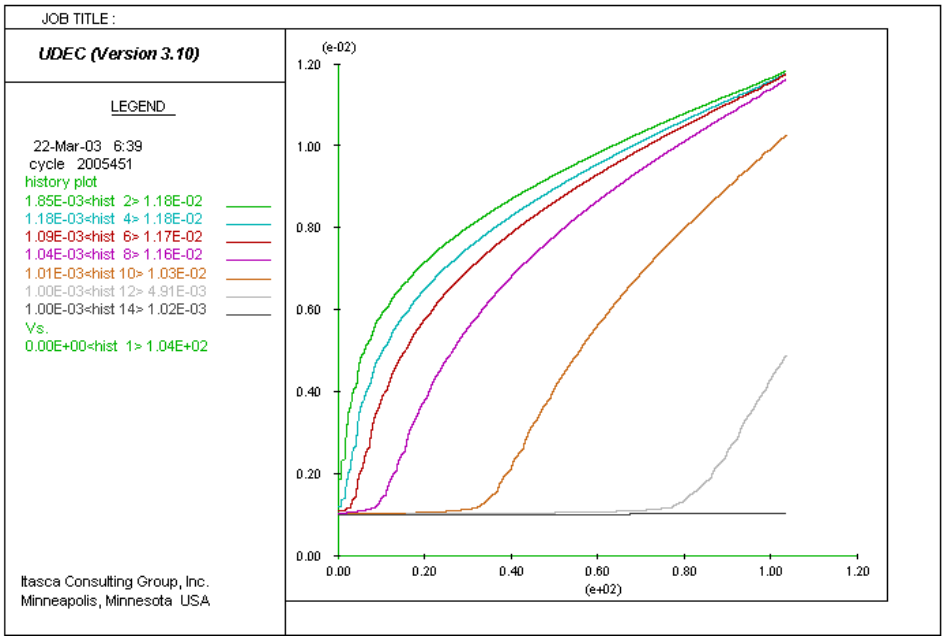

Output DTN: MO0307MWDDDINT.000

NOTES: Increasing history numbers correspond to points from Table 15, maintaining the same sequence. Time is in seconds.

Figure 55. Histories of Joint Hydraulic Aperture (m) at Seven Locations Along the Joint: Case 102

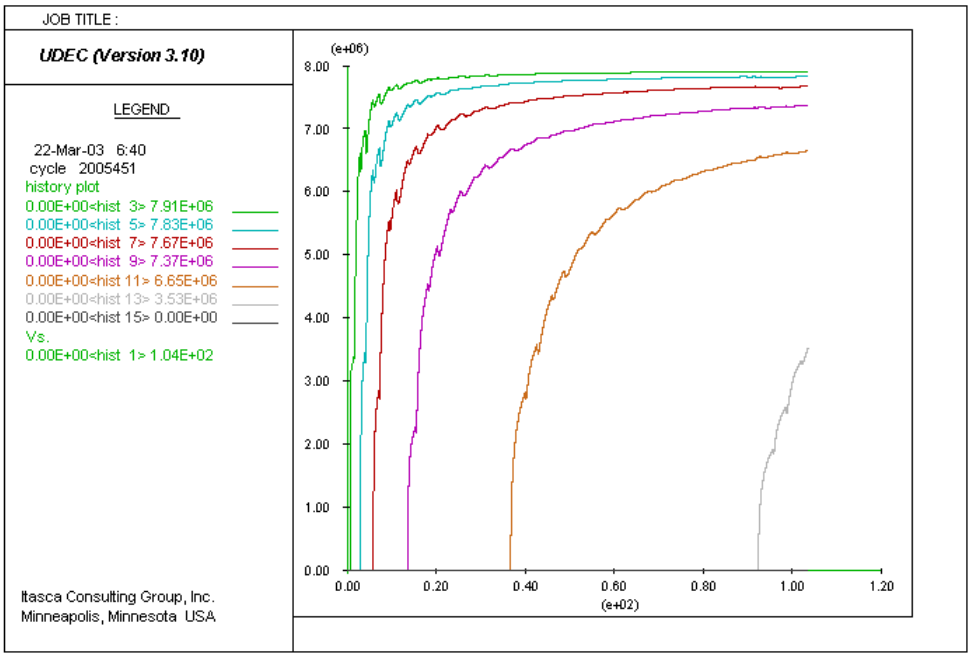

Output DTN: MO0307MWDDDINT.000

NOTES: Increasing history numbers correspond to points from Table 15, maintaining the same sequence. Time is in seconds.

Figure 56. Histories of Pore Pressure (Pa) at Seven Locations Along the Joint: Case 102

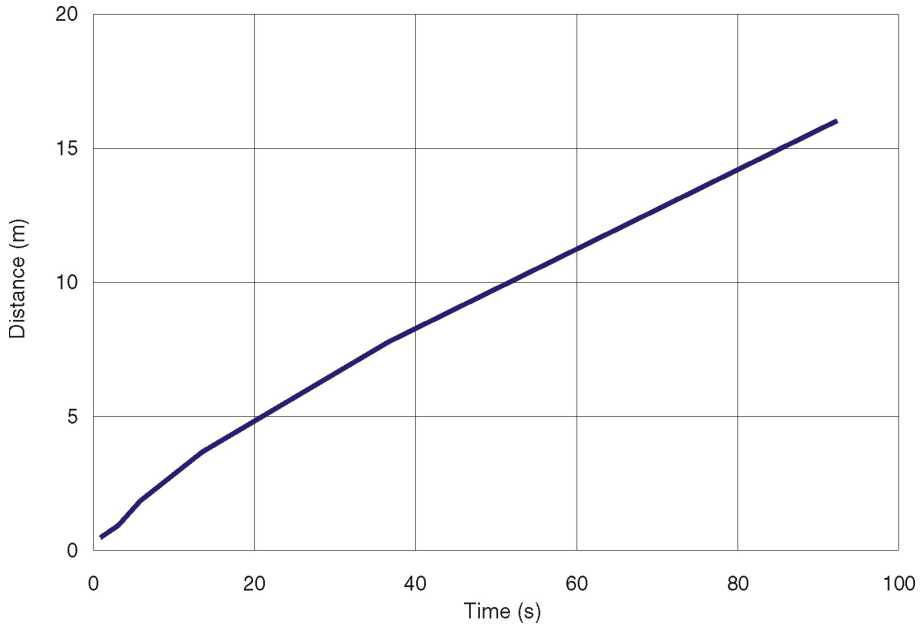

Output DTN: MO0307MWDDDINT.000

Figure 57. Location (Relative to the Drift Periphery) of the Magma Front Inside a Joint as a Function of Time: Case 102

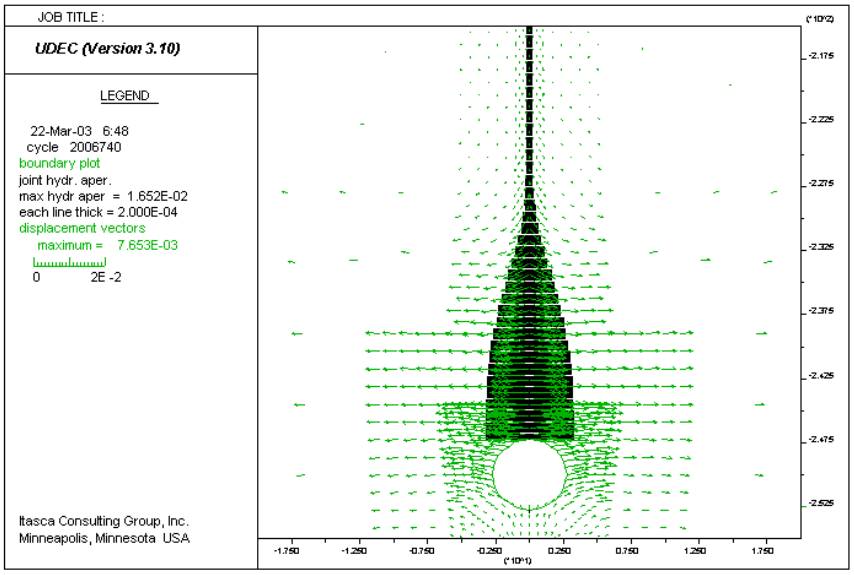

Output DTN: MO0307MWDDDINT.000

NOTES: Thickness of the black line is proportional to hydraulic aperture of the joint; deformation is due to pressure change inside the joint only.

Figure 58. Displacement Vector Field (m) and Hydraulic Aperture (m) Along the Vertical Fracture: Case 103

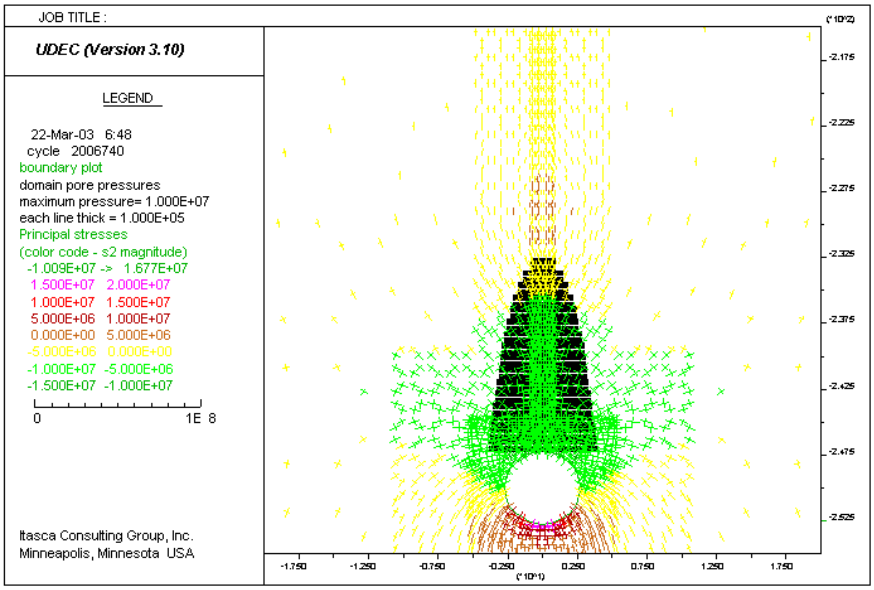

Output DTN: MO0307MWDDDINT.000

NOTES: Thickness of the black line is proportional to magma pressure in the joint; color of stress tensors indicates the magnitude of the minor principal stress.

Figure 59. Stress Tensor Field (Pa) and Pore Pressure (Pa) Along the Joint: Case 103

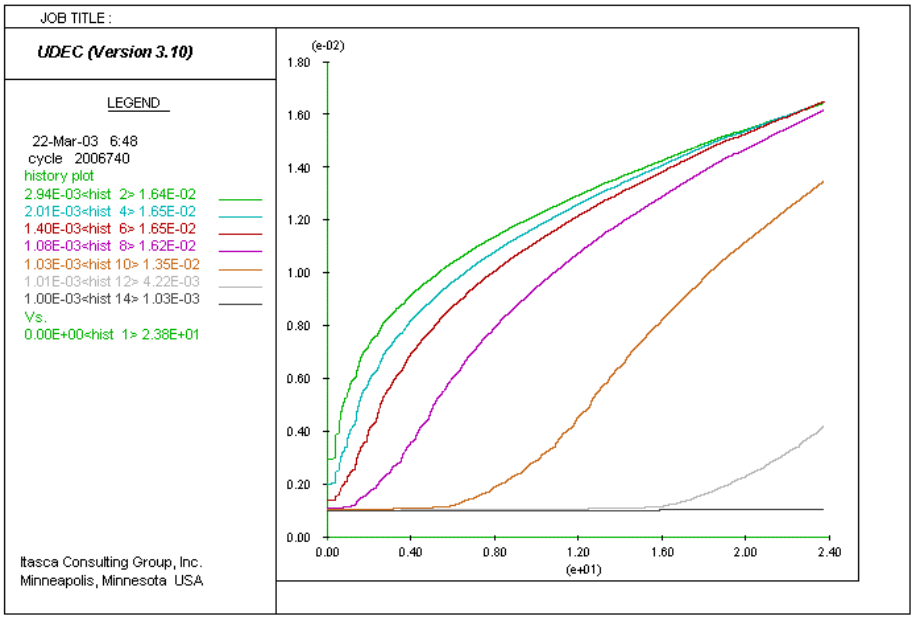

Output DTN: MO0307MWDDDINT.000

NOTES: Increasing history numbers correspond to points from Table 15, maintaining the same sequence. Time is in seconds.

Figure 60. Histories of Joint Hydraulic Aperture (m) at Seven Locations Along the Joint: Case 103

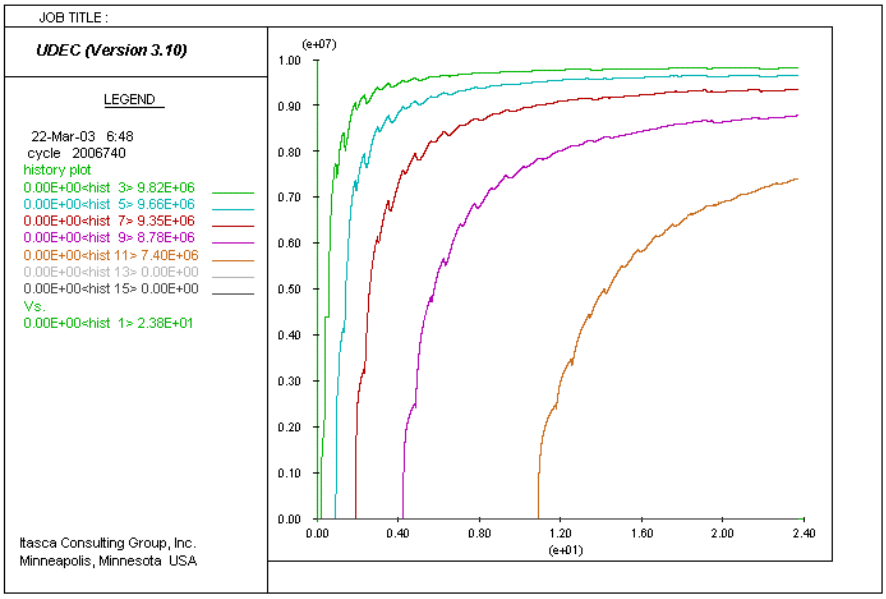

Output DTN: MO0307MWDDDINT.000

NOTES: Increasing history numbers correspond to points from Table 15, maintaining the same sequence. Time is in seconds.

Figure 61. Histories of Pore Pressure (Pa) at Seven Locations Along the Joint: Case 103

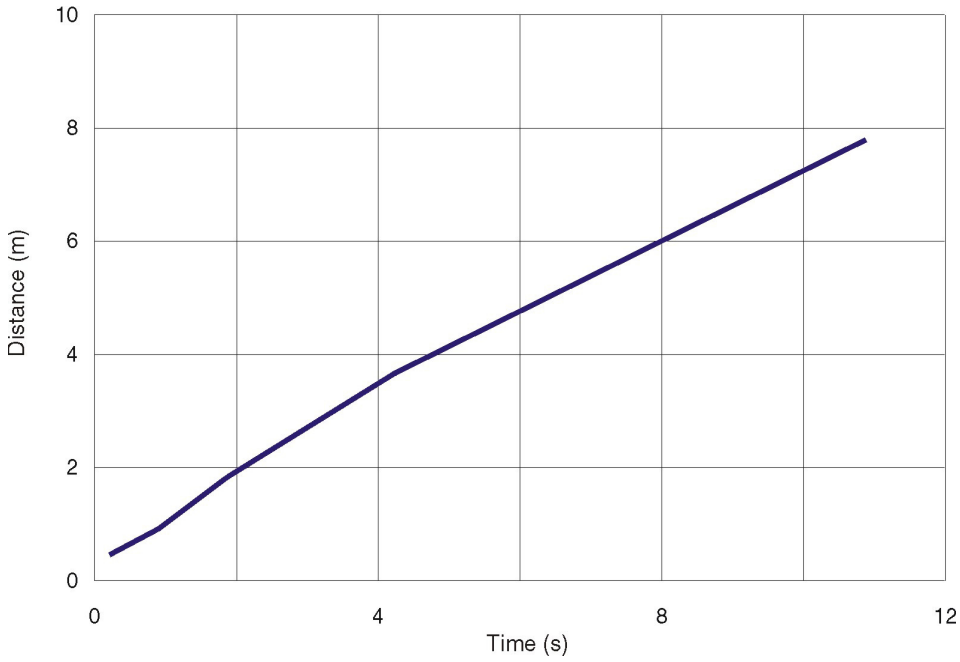

Output DTN: MO0307MWDDDINT.000

Figure 62. Location (Relative to the Drift Periphery) of the Magma Front Inside a Joint as a Function of Time: Case 103

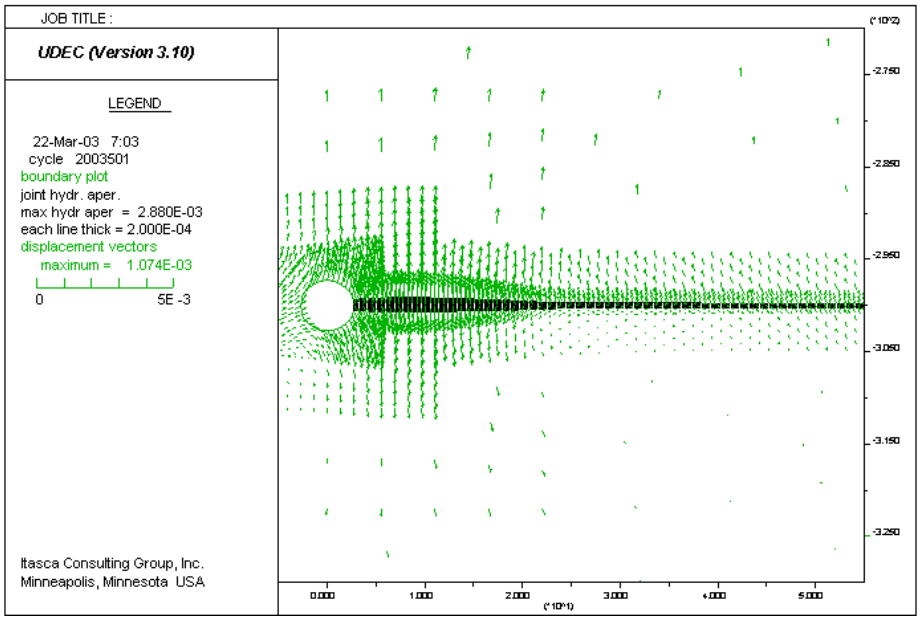

Output DTN: MO0307MWDDDINT.000

NOTES: Thickness of the black line is proportional to hydraulic aperture of the joint; deformation is due to pressure change inside the joint only.

Figure 63. Displacement Vector Field (m) and Hydraulic Aperture (m) Along the Vertical Fracture: Case 104

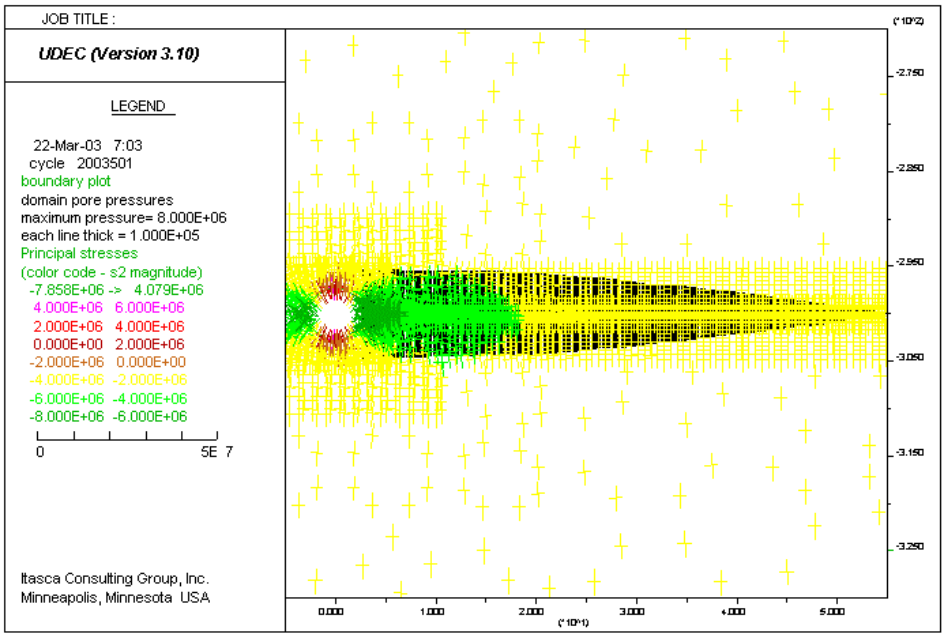

Output DTN: MO0307MWDDDINT.000

NOTES: Thickness of the black line is proportional to magma pressure in the joint; color of stress tensors indicates the magnitude of the minor principal stress.

Figure 64. Stress Tensor Field (Pa) and Pore Pressure (Pa) Along the Joint: Case 104

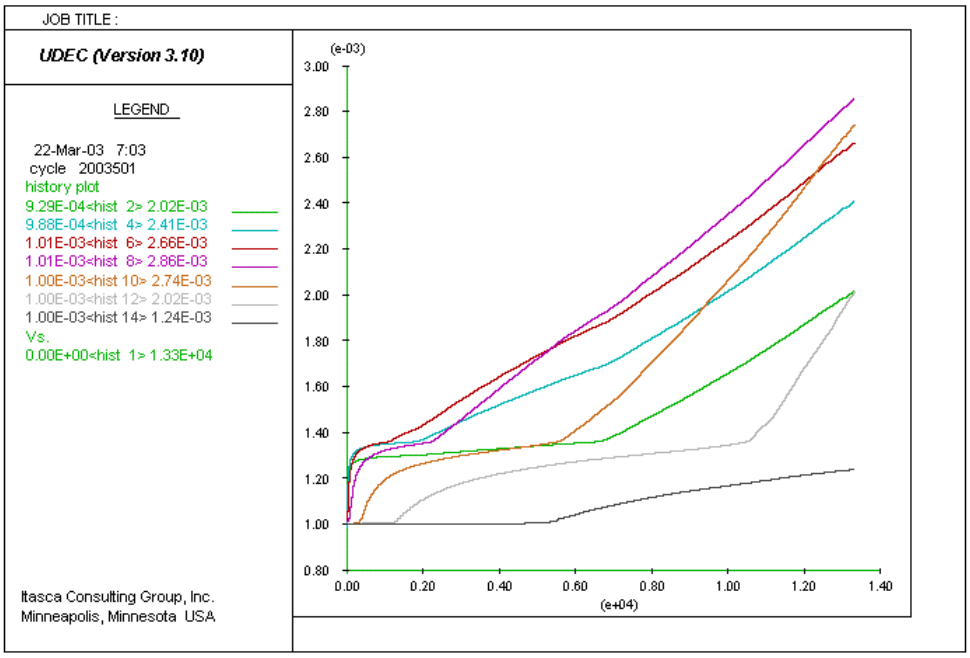

Output DTN: MO0307MWDDDINT.000

NOTES: Increasing history numbers correspond to points from Table 15, maintaining the same sequence. Time is in seconds.

Figure 65. Histories of Joint Hydraulic Aperture (m) at Seven Locations Along the Joint: Case 104

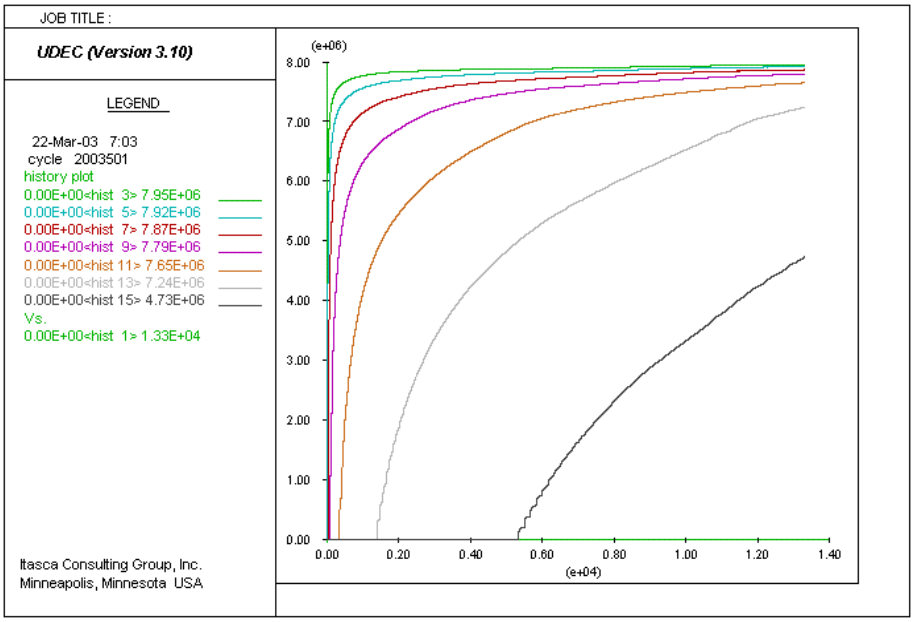

Output DTN: MO0307MWDDDINT.000

NOTES: Increasing history numbers correspond to points from Table 15, maintaining the same sequence. Time is in seconds.

Figure 66. Histories of Pore Pressure (Pa) at Seven Locations Along the Joint: Case 104

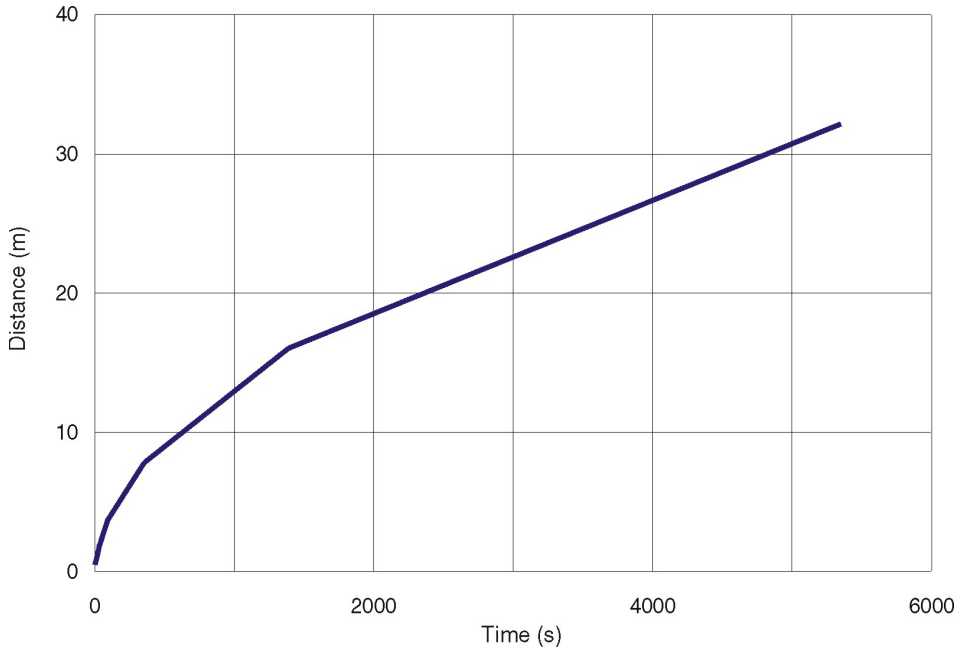

Output DTN: MO0307MWDDDINT.000

Figure 67. Location (Relative to the Drift Periphery) of the Magma Front Inside a Joint as a Function of Time: Case 104

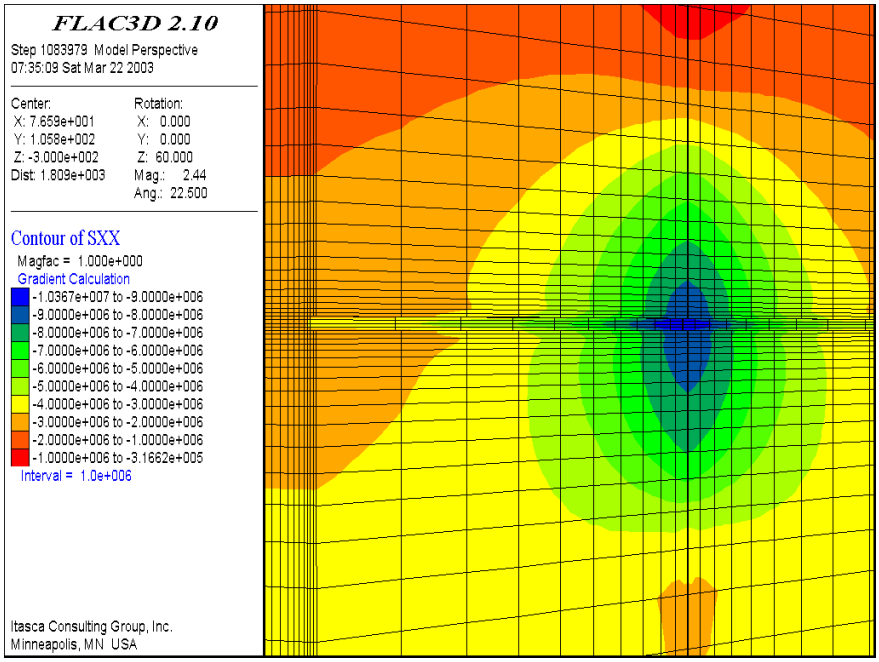

Output DTN: MO0307MWDDDINT.000

Figure 68. Contours of the Stress (Pa) in the Direction of the Drift: Case 105

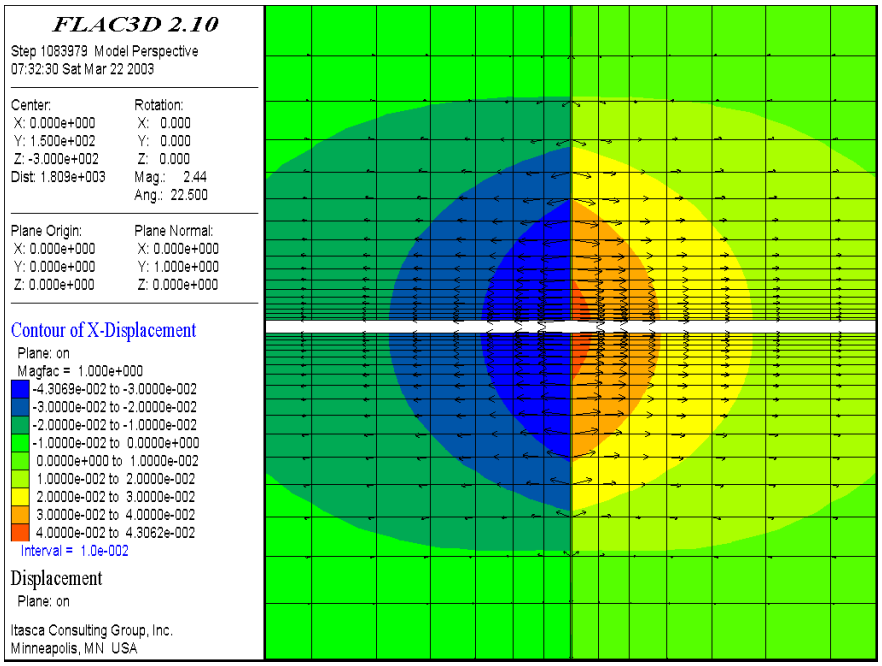

Output DTN: MO0307MWDDDINT.000

NOTE: Deformation is due to pressure change inside the joint only.

Figure 69. Contours of the Displacement (m) in the Direction of the Drift and Displacement Vector Field (in the Section Along the Drift): Case 105

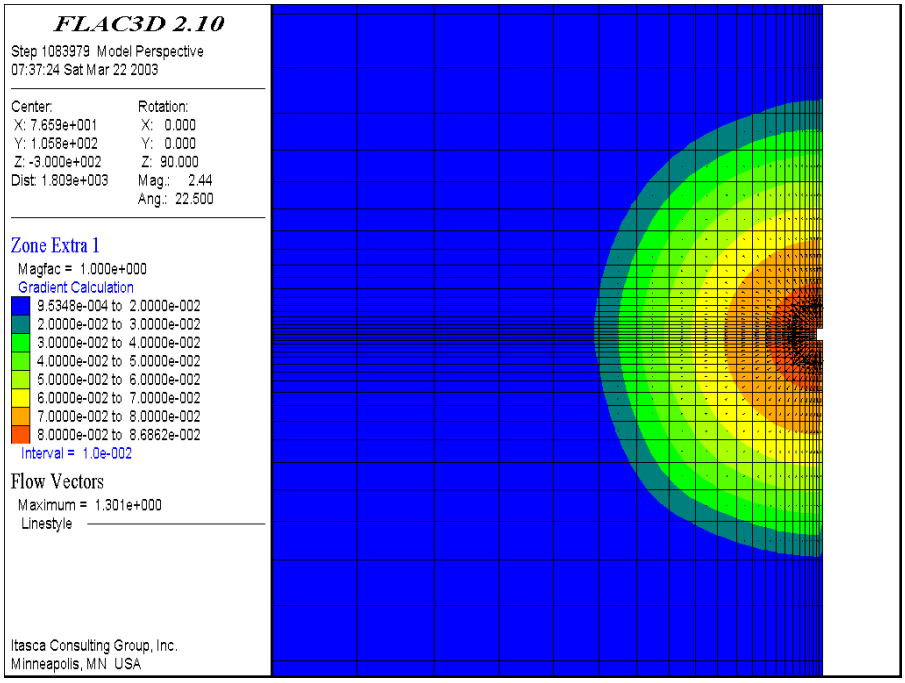

Output DTN: MO0307MWDDDINT.000

Figure 70. Contours of the Hydraulic Aperture (m) and Flow Vectors (m/s) in the Plane of the Joint: Case 105

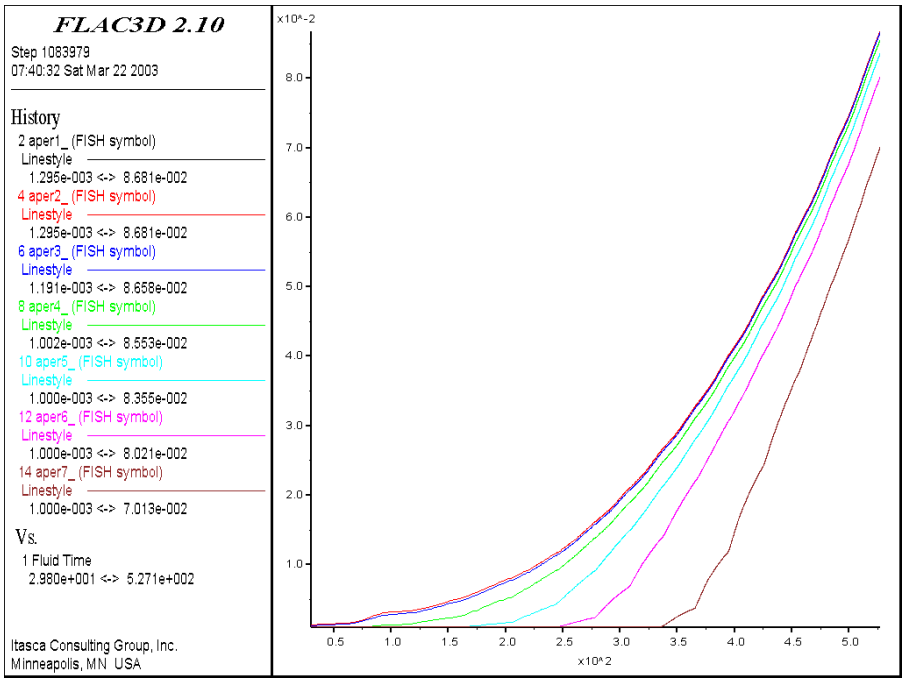

Output DTN: MO0307MWDDDINT.000

NOTES: Increasing history numbers correspond to points from Table 15, maintaining the same sequence. Time is in seconds.

Figure 71. Histories of Joint Hydraulic Aperture (m) at Seven Locations Along the Joint: Case 105

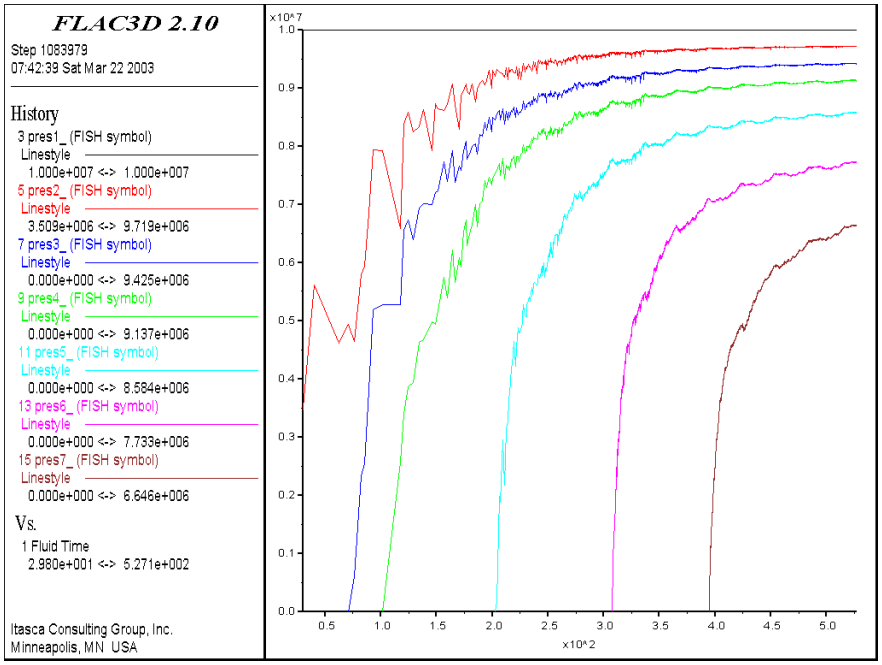

Output DTN: MO0307MWDDDINT.000

NOTES: Increasing history numbers correspond to points from Table 16, maintaining the same sequence. Time is in seconds.

Figure 72. Histories of Pore Pressure (Pa) at Seven Locations Along the Joint: Case 105

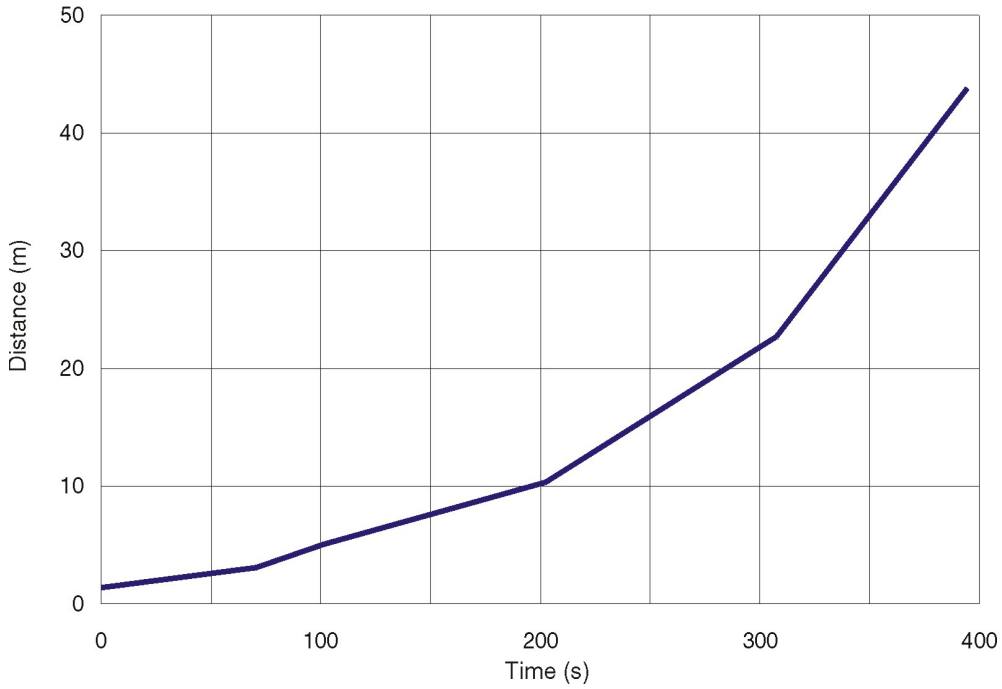

Output DTN: MO0307MWDDDINT.000

Figure 73. Location (Relative to the Drift Periphery) of the Magma Front Inside a Joint as a Function of Time: Case 105

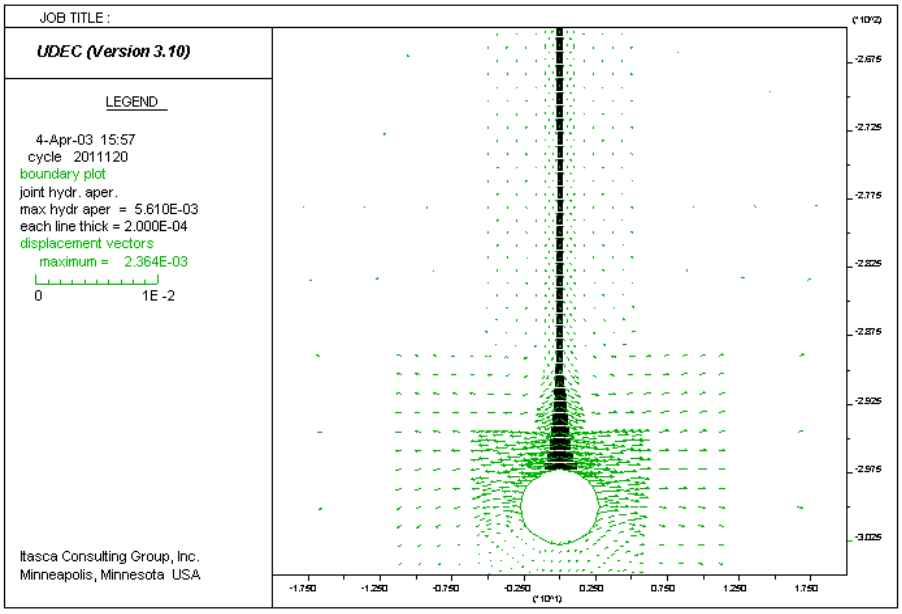

Output DTN: MO0307MWDDDINT.000

NOTES: Thickness of the black line is proportional to hydraulic aperture of the joint; deformation is due to pressure change inside the joint only.

Figure 74. Displacement Vector Field (m) and Hydraulic Aperture (m) Along the Vertical fracture: Case 106

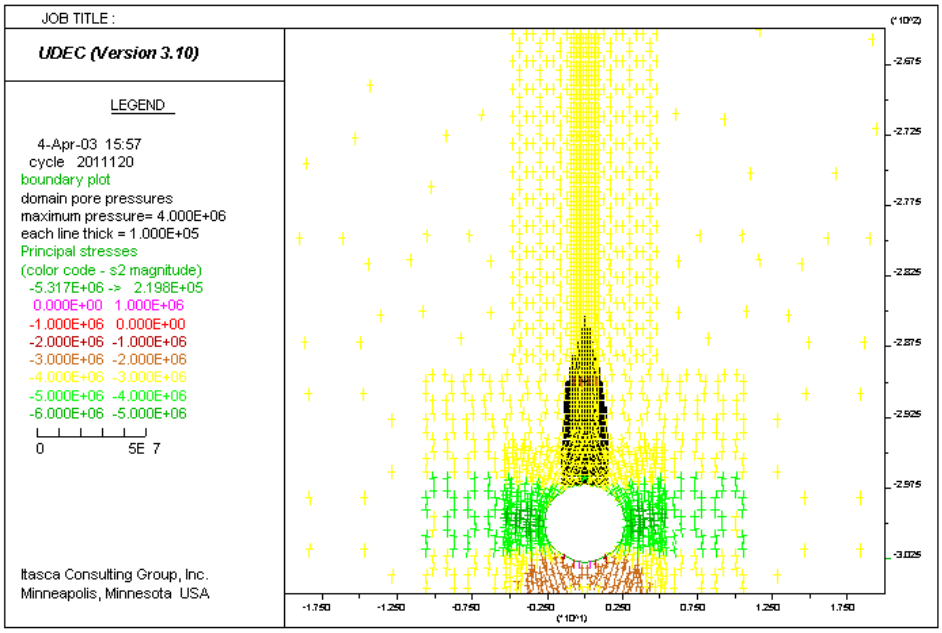

Output DTN: MO0307MWDDDINT.000

NOTES: Thickness of the black line is proportional to magma pressure in the joint; color of stress tensors indicates according to the magnitude of the minor principal stress.

Figure 75. Stress Tensor Field (MPa) and Pore Pressure (MPa) Along the Joint: Case 106

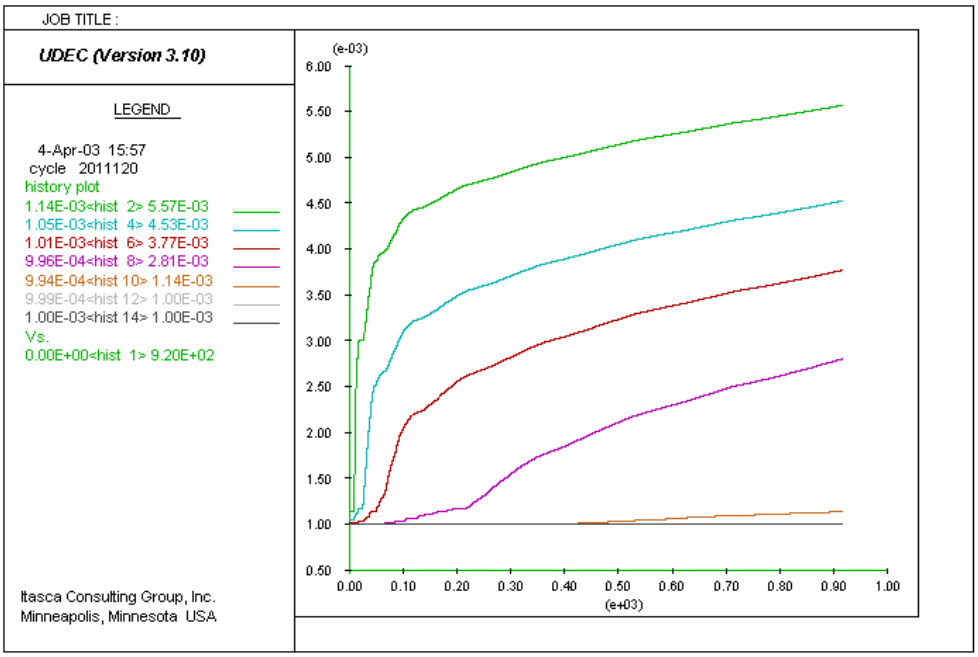

Output DTN: MO0307MWDDDINT.000

NOTES: Increasing history numbers correspond to points from Table 16, maintaining the same sequence. Time is in seconds.

Figure 76. Histories of Joint Hydraulic Aperture at Seven Locations Along the Joint: Case 106

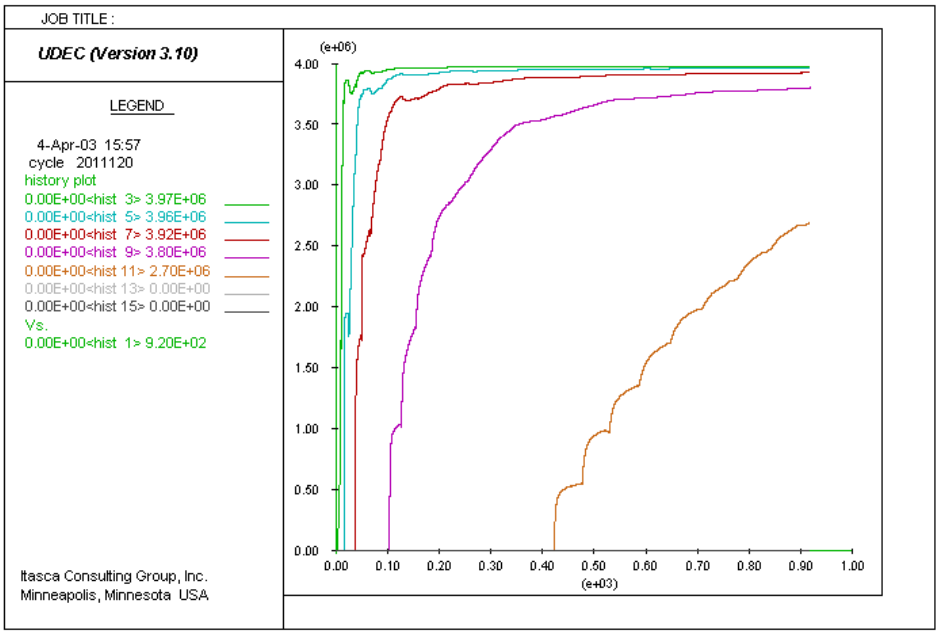

Output DTN: MO0307MWDDDINT.000

NOTES: Increasing history numbers correspond to points from Table 15, maintaining the same sequence. Time is in seconds.

Figure 77. Histories of Pore Pressure at Seven Locations Along the Joint: Case 106

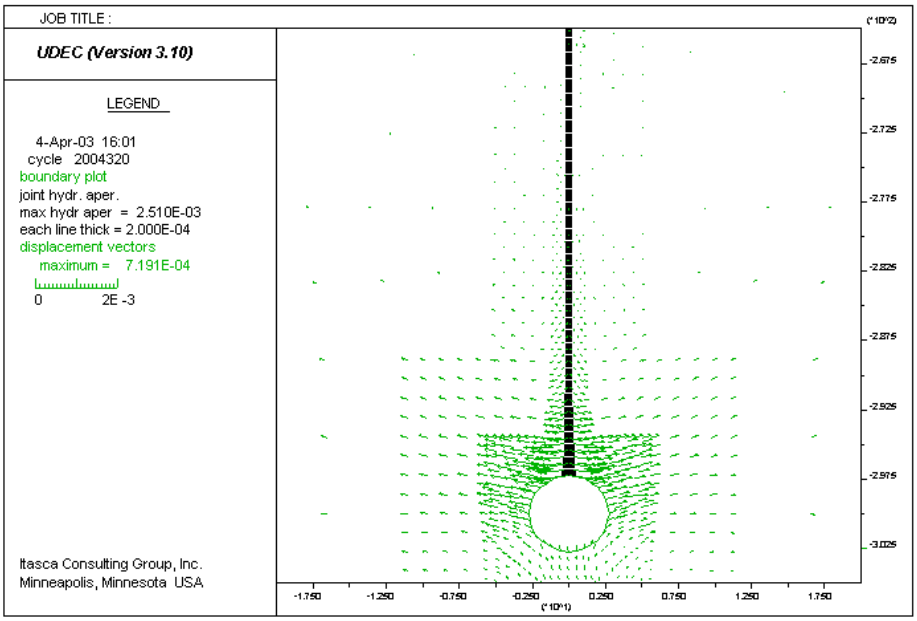

Output DTN: MO0307MWDDDINT.000

NOTES: Thickness of the black line is proportional to hydraulic aperture of the joint; deformation is due to pressure change inside the joint only.

Figure 78. Displacement Vector Field (m) and Hydraulic Aperture (m) Along the Vertical Fracture: Case 107

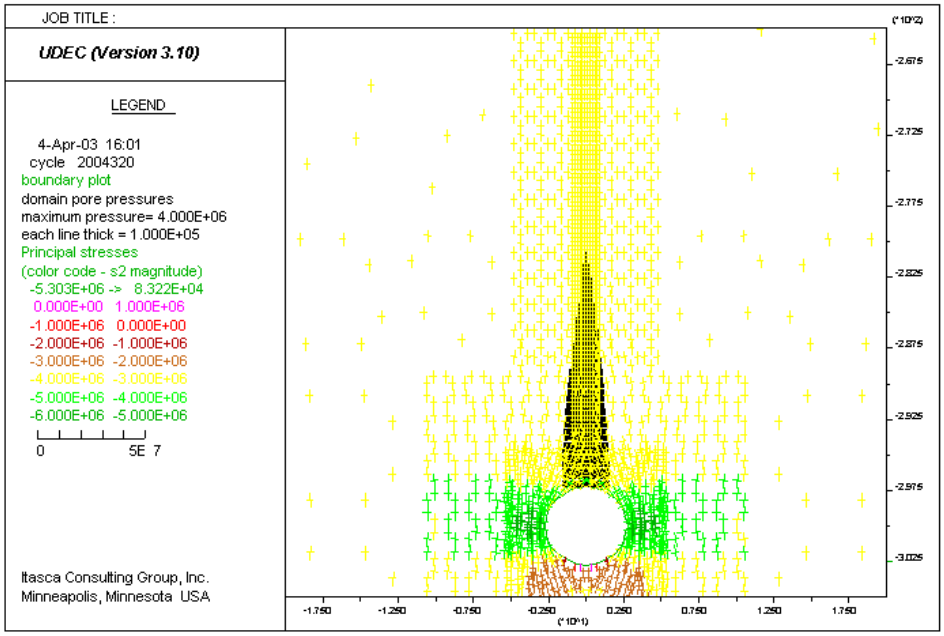

Output DTN: MO0307MWDDDINT.000

NOTES: Thickness of the black line is proportional to magma pressure in the joint; color of stress tensors indicates the magnitude of the minor principal stress.

Figure 79. Stress Tensor Field (MPa) and Pore Pressure (MPa) Along the Joint: Case 107

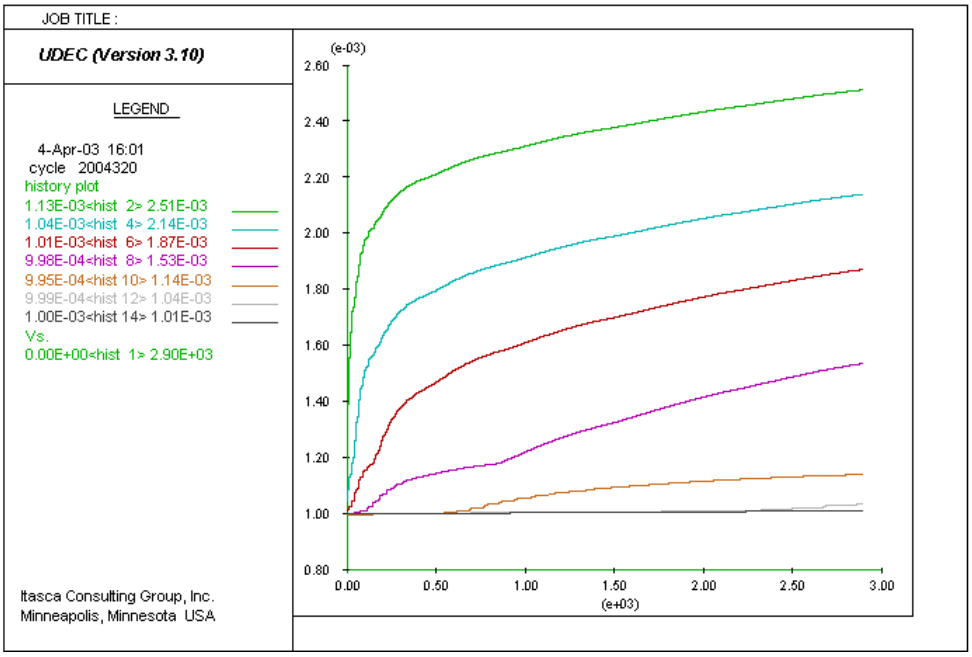

Output DTN: MO0307MWDDDINT.000

NOTES: Increasing history numbers correspond to points from Table 15, maintaining the same sequence. Time is in seconds.

Figure 80. Histories of Joint Hydraulic Aperture at Seven Locations Along the Joint: Case 107

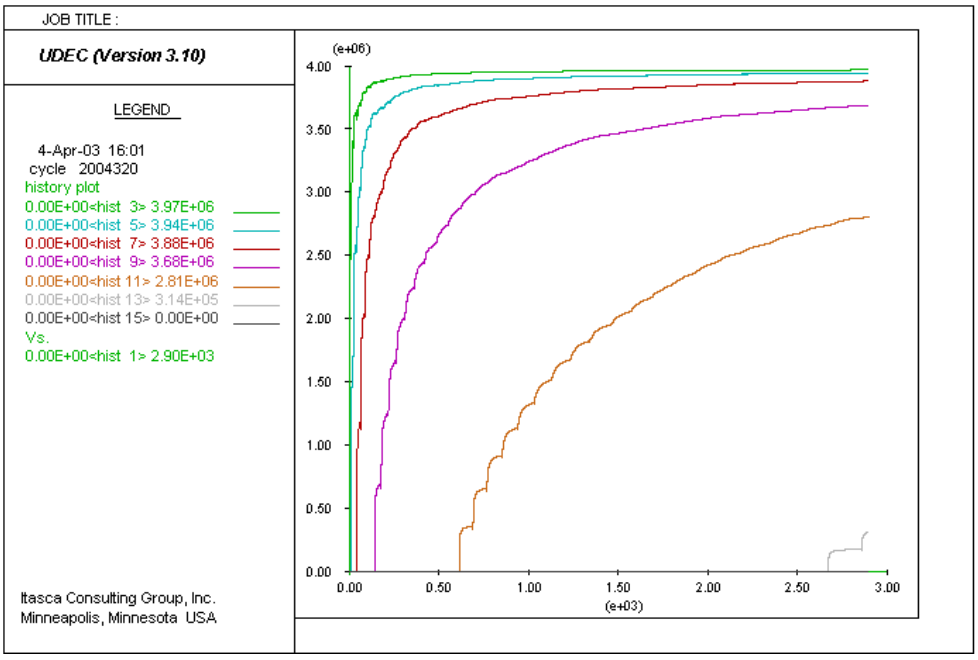

Output DTN: MO0307MWDDDINT.000

NOTES: Increasing history numbers correspond to points from Table 15, maintaining the same sequence. Time is in seconds.

Figure 81. Histories of Pore Pressure at Seven Locations Along the Joint: Case 107

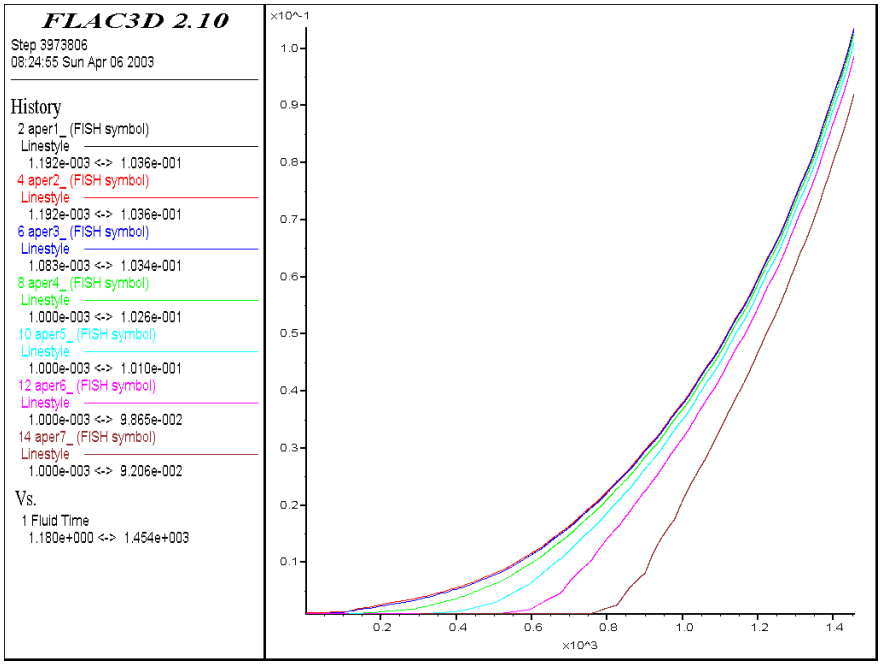

Output DTN: MO0307MWDDDINT.000

NOTES: Increasing history numbers correspond to points from Table 16, maintaining the same sequence. Time is in seconds.

Figure 82. Histories of Joint Hydraulic Aperture at Seven Locations Along the Joint: Case 108

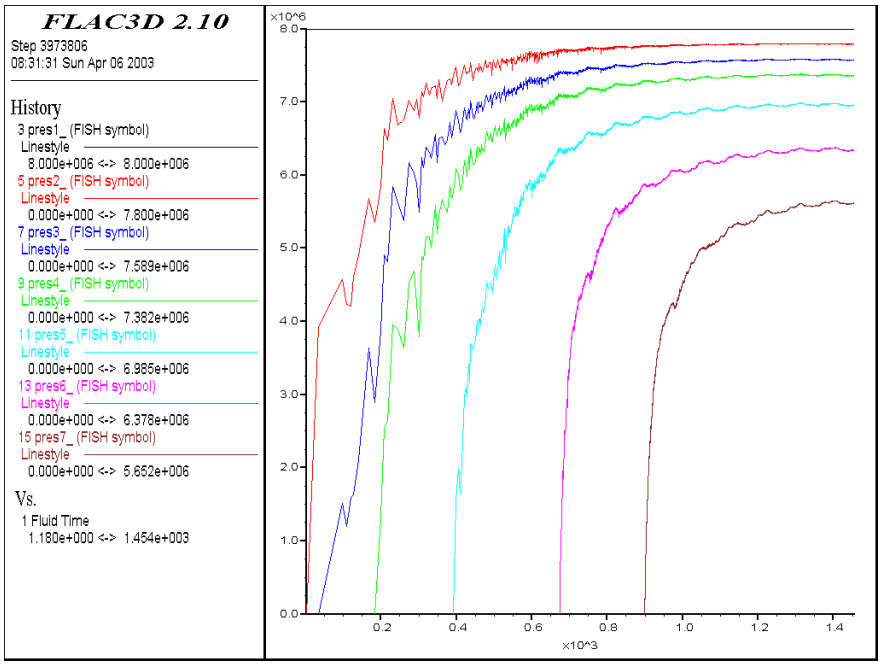

Output DTN: MO0307MWDDDINT.000

NOTES: Increasing history numbers correspond to points from Table 16, maintaining the same sequence. Time is in seconds.

Figure 83. Histories of Pore Pressure at Seven Locations Along the Joint: Case 108

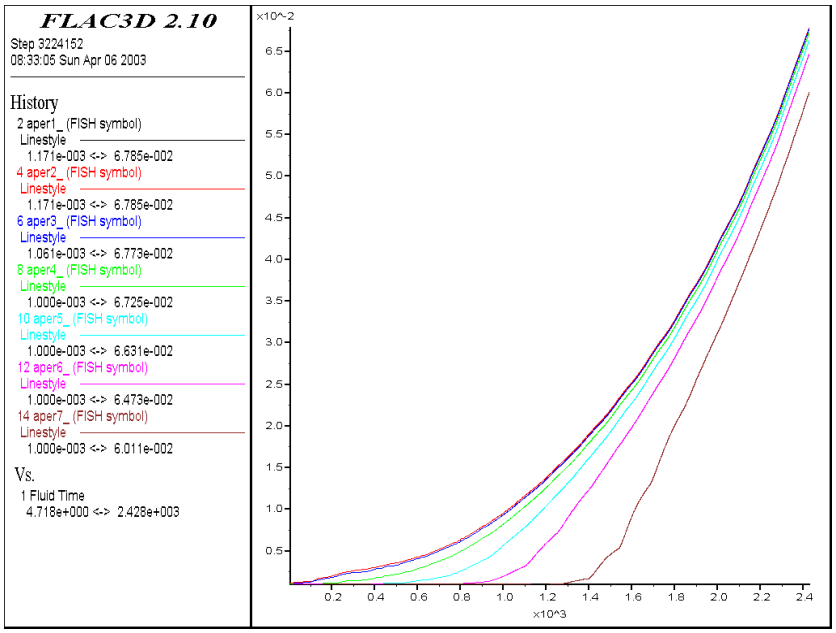

Output DTN: MO0307MWDDDINT.000

NOTES: Increasing history numbers correspond to points from Table 16, maintaining the same sequence. Time is in seconds.

Figure 84. Histories of Joint Hydraulic Aperture at Seven Locations Along the Joint: Case 109

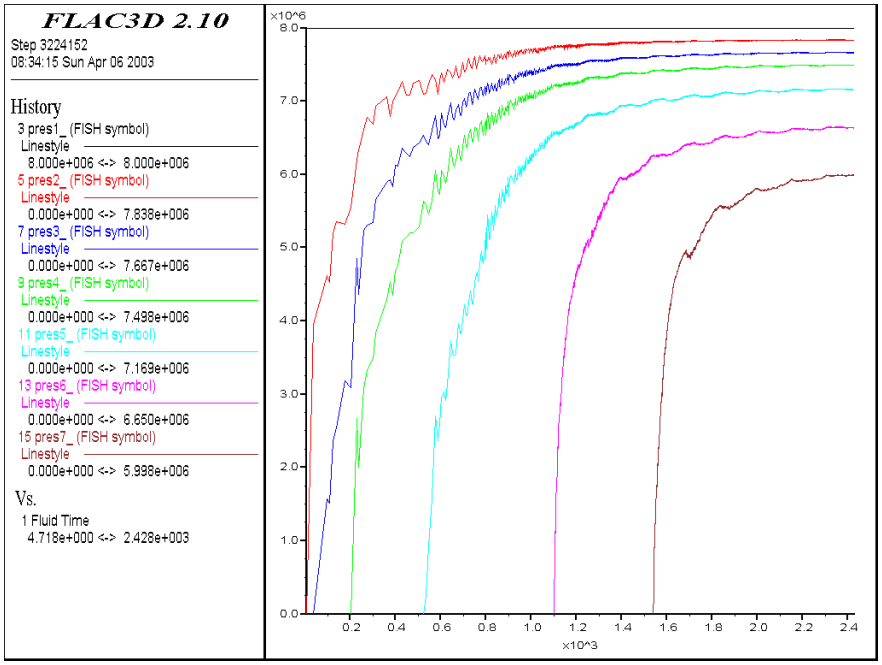

Output DTN: MO0307MWDDDINT.000

NOTES: Increasing history numbers correspond to points from Table 16, maintaining the same sequence. Time is in seconds.

Figure 85. Histories of Pore Pressure at Seven Locations Along the Joint: Case 109

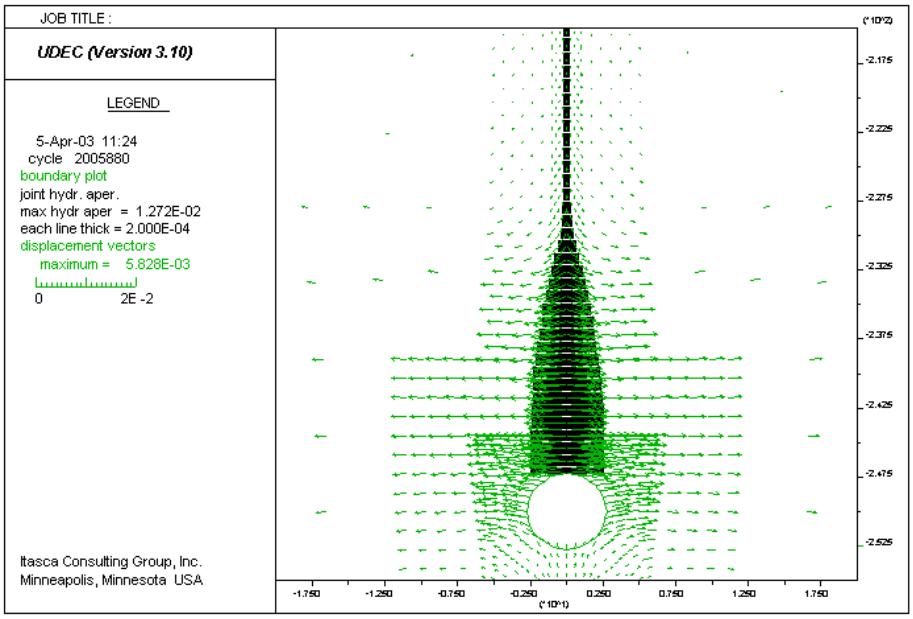

Output DTN: MO0307MWDDDINT.000

NOTES: Thickness of the black line is proportional to hydraulic aperture of the joint; deformation is due to pressure change inside the joint only.

Figure 86. Displacement Vector Field (m) and Hydraulic Aperture (m) Along the Vertical Fracture: Case 110

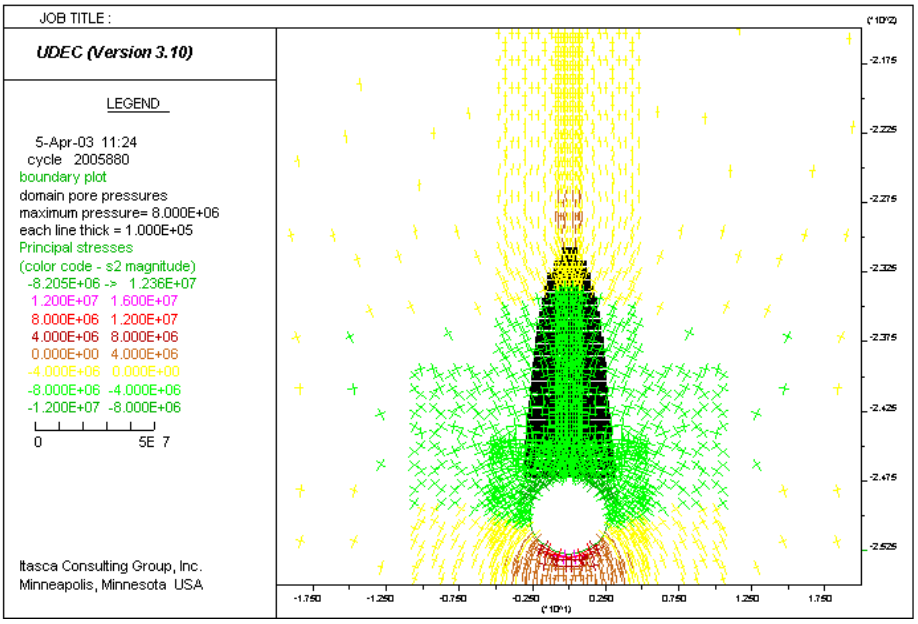

Output DTN: MO0307MWDDDINT.000

NOTES: Thickness of the black line is proportional to magma pressure in the joint; color of stress tensors indicates the magnitude of the minor principal stress.

Figure 87. Stress Tensor Field (MPa) and Pore Pressure (MPa) Along the Joint: Case 110

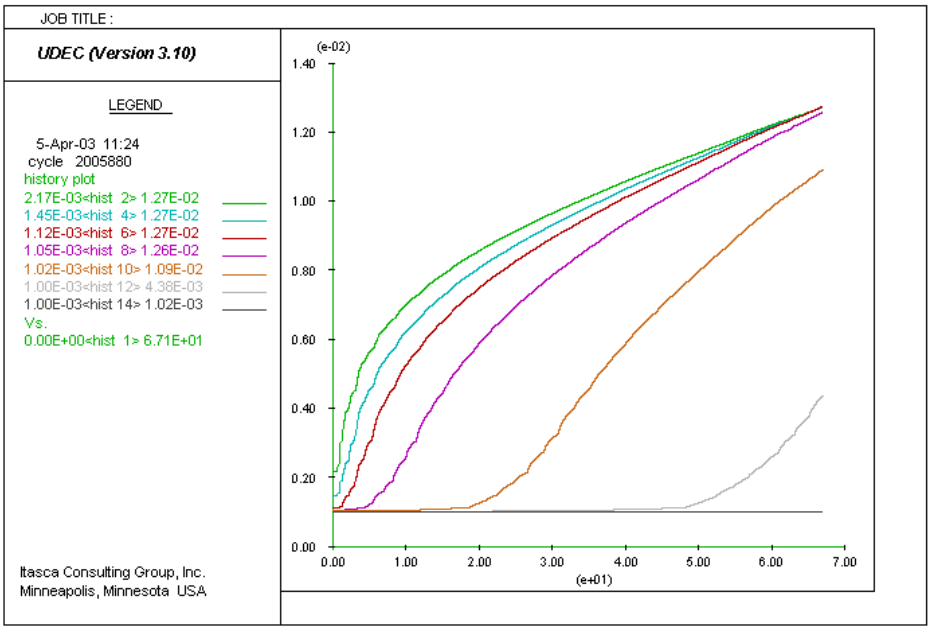

Output DTN: MO0307MWDDDINT.000

NOTES: Increasing history numbers correspond to points from Table 15, maintaining the same sequence. Time is in seconds.

Figure 88. Histories of Joint Hydraulic Aperture at Seven Locations Along the Joint: Case 110

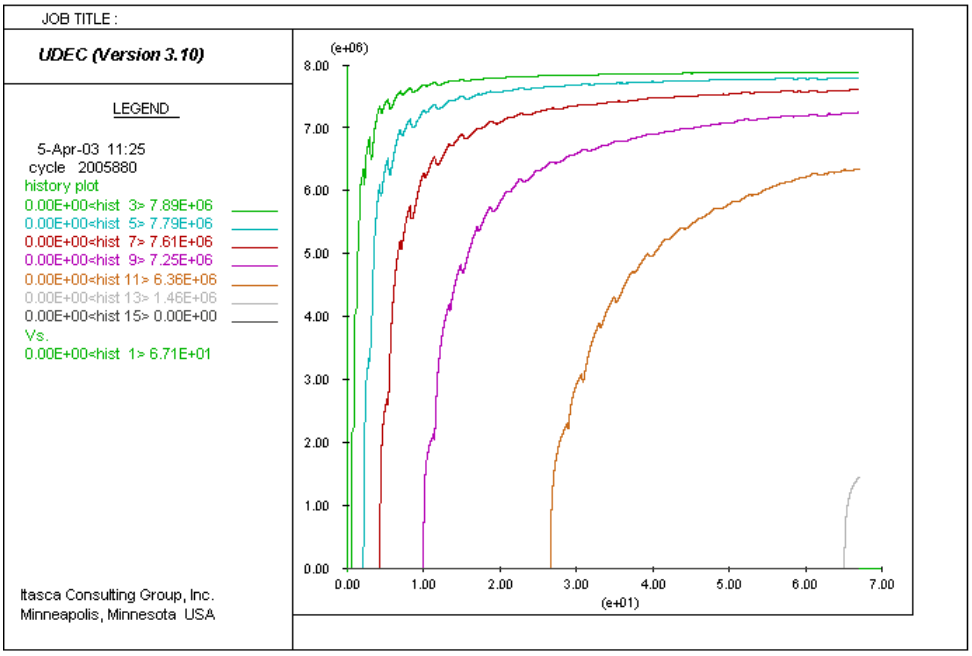

Output DTN: MO0307MWDDDINT.000

NOTES: Increasing history numbers correspond to points from Table 15, maintaining the same sequence. Time is in seconds.

Figure 89. Histories of Pore Pressure at Seven Locations Along the Joint: Case 110

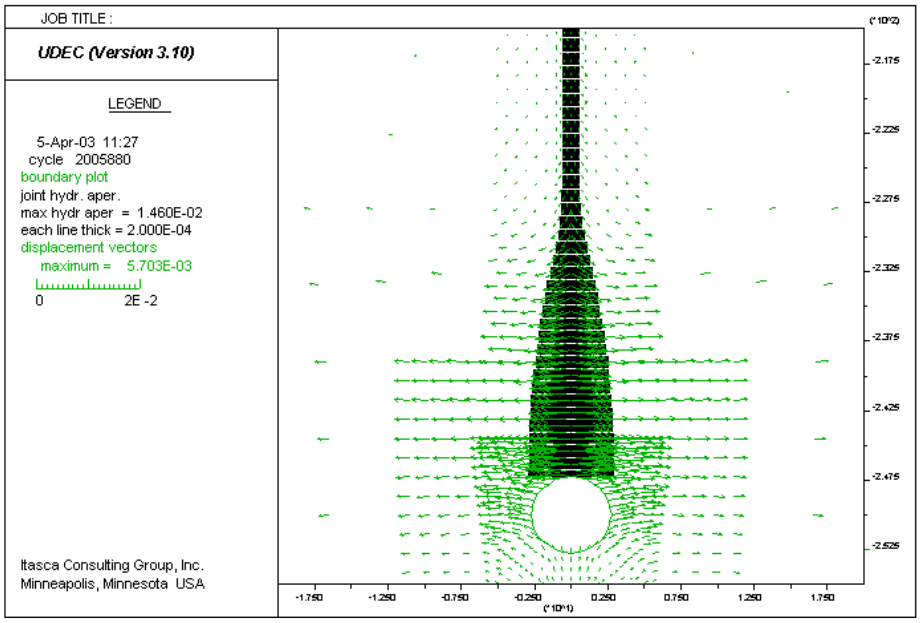

Output DTN: MO0307MWDDDINT.000

NOTES: Thickness of the black line is proportional to hydraulic aperture of the joint; deformation is due to pressure change inside the joint only.

Figure 90. Displacement Vector Field (m) and Hydraulic Aperture (m) Along the Vertical Fracture: Case 111

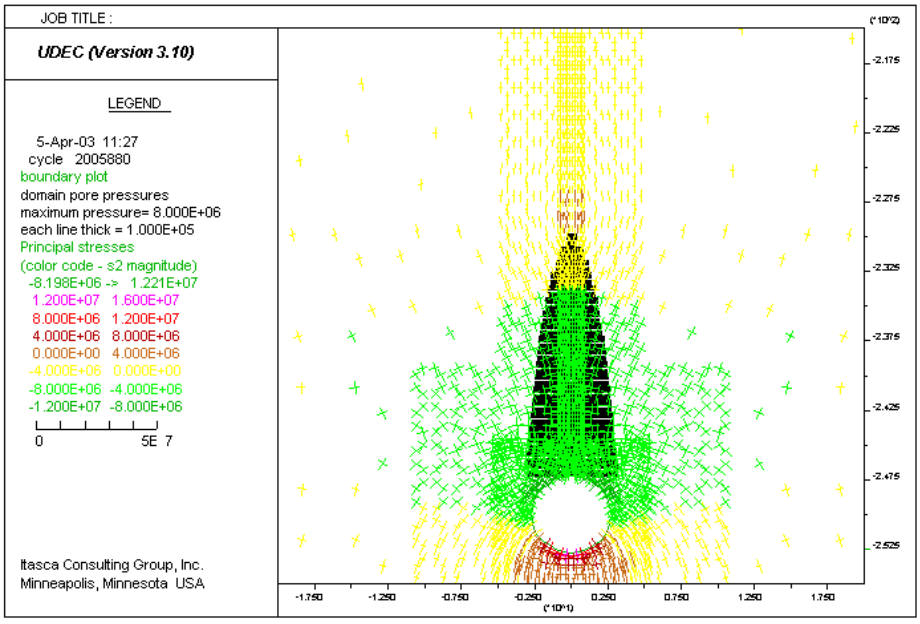

Output DTN: MO0307MWDDDINT.000

NOTES: Thickness of the black line is proportional to magma pressure in the joint; color of stress tensors indicates the magnitude of the minor principal stress.

Figure 91. Stress Tensor Field (MPa) and Pore Pressure (MPa) Along the Joint: Case 111

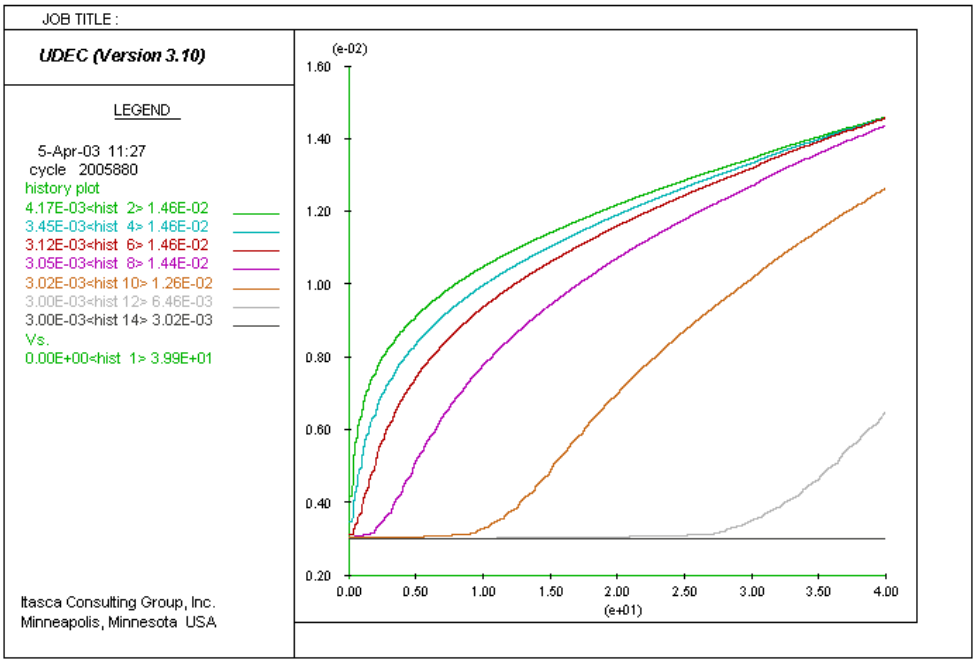

Output DTN: MO0307MWDDDINT.000

NOTES: Increasing history numbers correspond to points from Table 15, maintaining the same sequence. Time is in seconds.

Figure 92. Histories of Joint Hydraulic Aperture at Seven Locations Along the Joint: Case 111

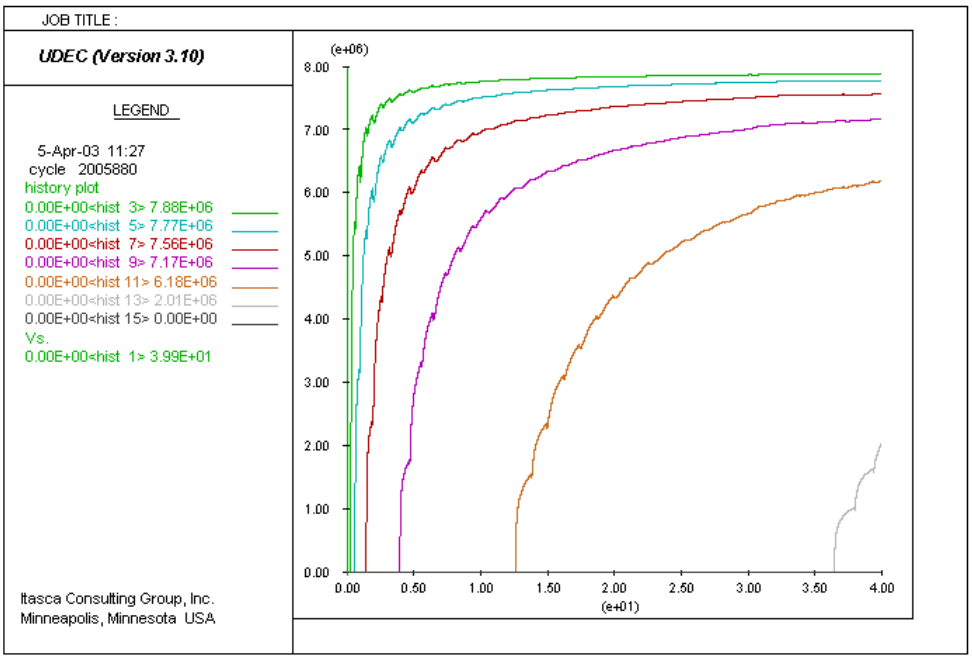

Output DTN: MO0307MWDDDINT.000

NOTES: Increasing history numbers correspond to points from Table 15, maintaining the same sequence. Time is in seconds.

Figure 93. Histories of Pore Pressure at Seven Locations Along the Joint: Case 111

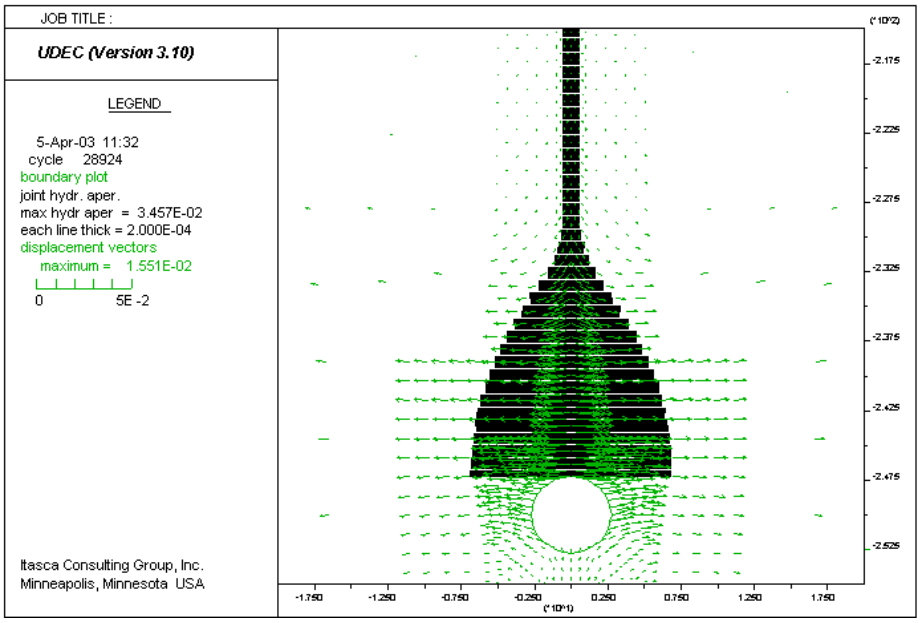

Output DTN: MO0307MWDDDINT.000

NOTES: Thickness of the black line is proportional to hydraulic aperture of the joint; deformation is due to pressure change inside the joint only.

Figure 94. Displacement Vector Field (m) and Hydraulic Aperture (m) Along the Vertical Fracture: Case 112

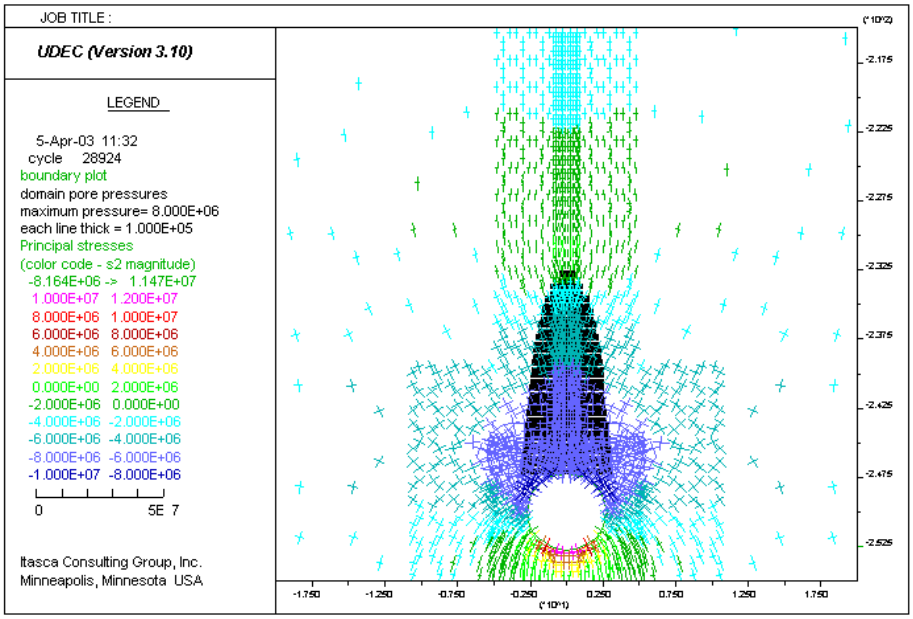

Output DTN: MO0307MWDDDINT.000

NOTES: Thickness of the black line is proportional to magma pressure in the joint; color of stress tensors indicates the magnitude of the minor principal stress.

Figure 95. Stress Tensor Field (MPa) and Pore Pressure (MPa) Along the Joint: Case 112

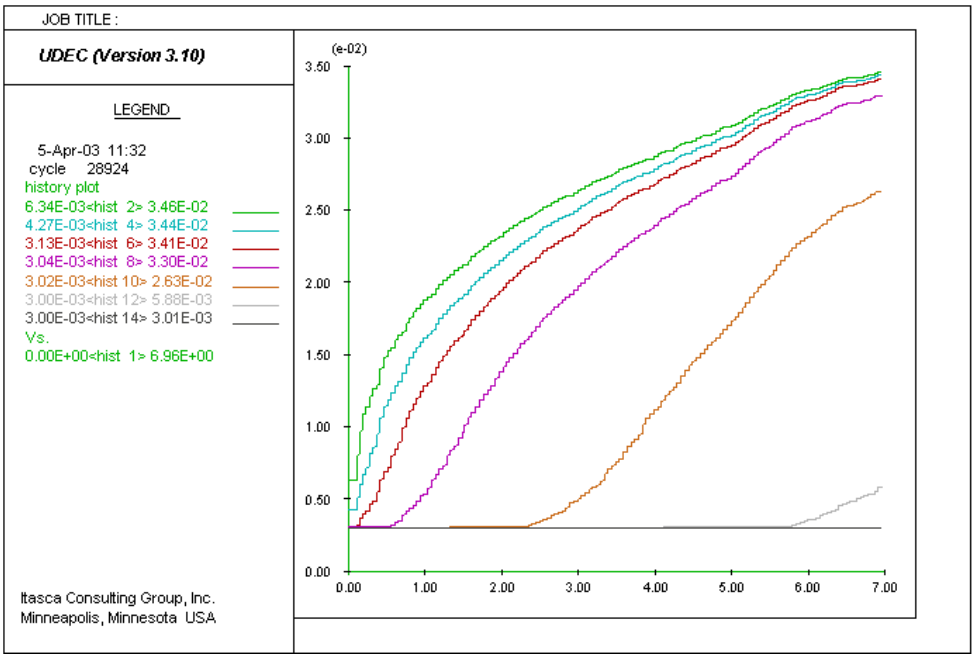

Output DTN: MO0307MWDDDINT.000

NOTES: Increasing history numbers correspond to points from Table 15, maintaining the same sequence. Time is in seconds.

Figure 96. Histories of Joint Hydraulic Aperture at Seven Locations Along the Joint: Case 112

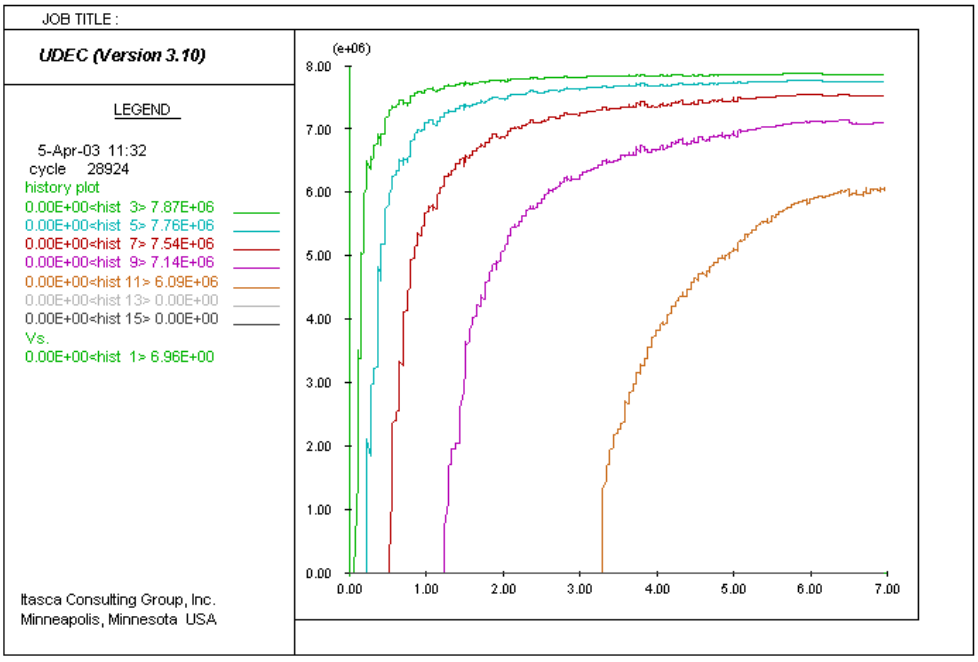

Output DTN: MO0307MWDDDINT.000

NOTES: Increasing history numbers correspond to points from Table 15, maintaining the same sequence. Time is in seconds.

Figure 97. Histories of Pore Pressure at Seven Locations Along the Joint: Case 112

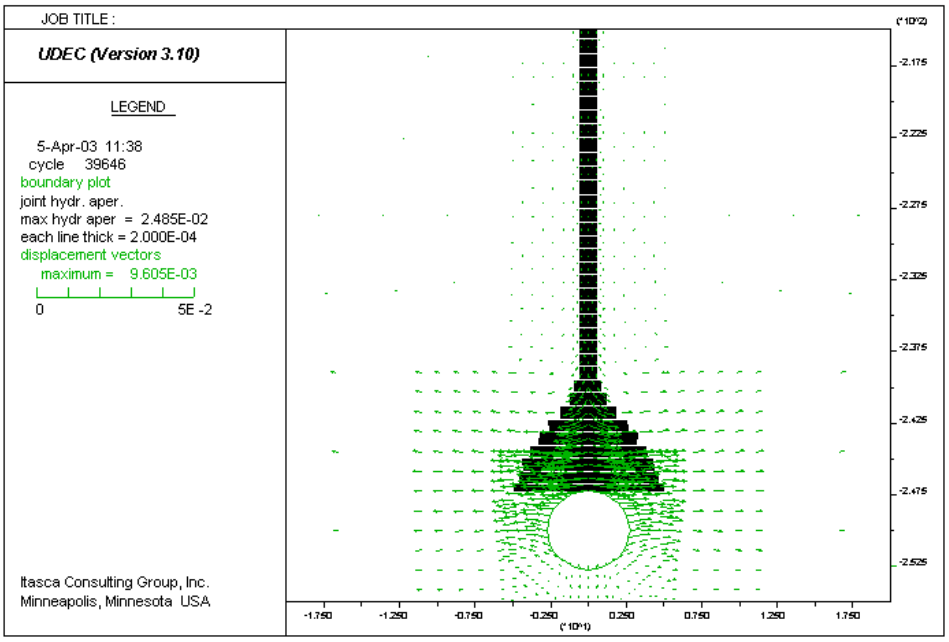

Output DTN: MO0307MWDDDINT.000

NOTES: Thickness of the black line is proportional to hydraulic aperture of the joint; deformation is due to pressure change inside the joint only.

Figure 98. Displacement Vector Field (m) and Hydraulic Aperture (m) Along the Vertical Fracture: Case 113

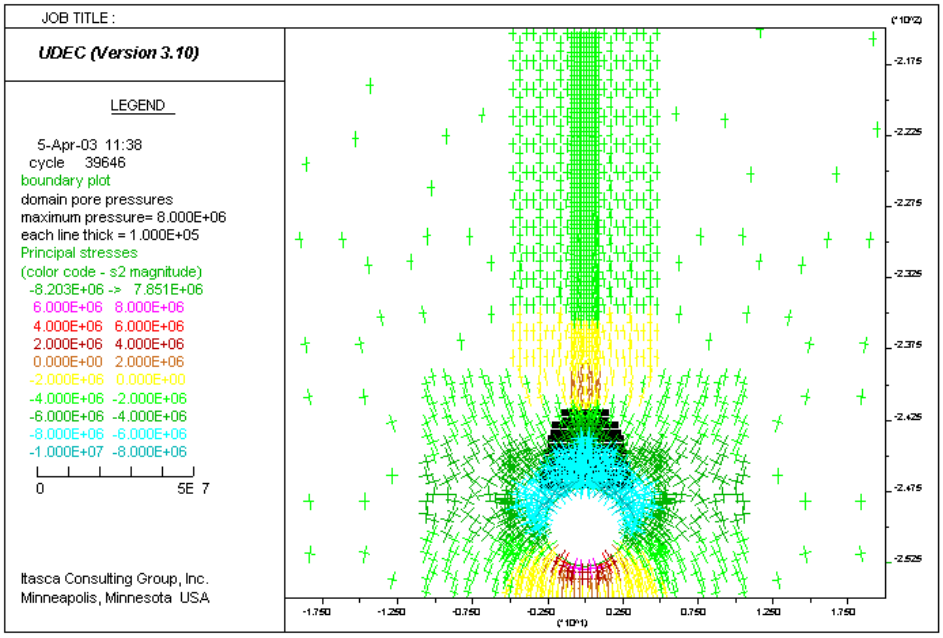

Output DTN: MO0307MWDDDINT.000

NOTES: Thickness of the black line is proportional to magma pressure in the joint; color of stress tensors indicates the magnitude of the minor principal stress.

Figure 99. Stress Tensor Field (MPa) and Pore Pressure (MPa) Along the Joint: Case 113

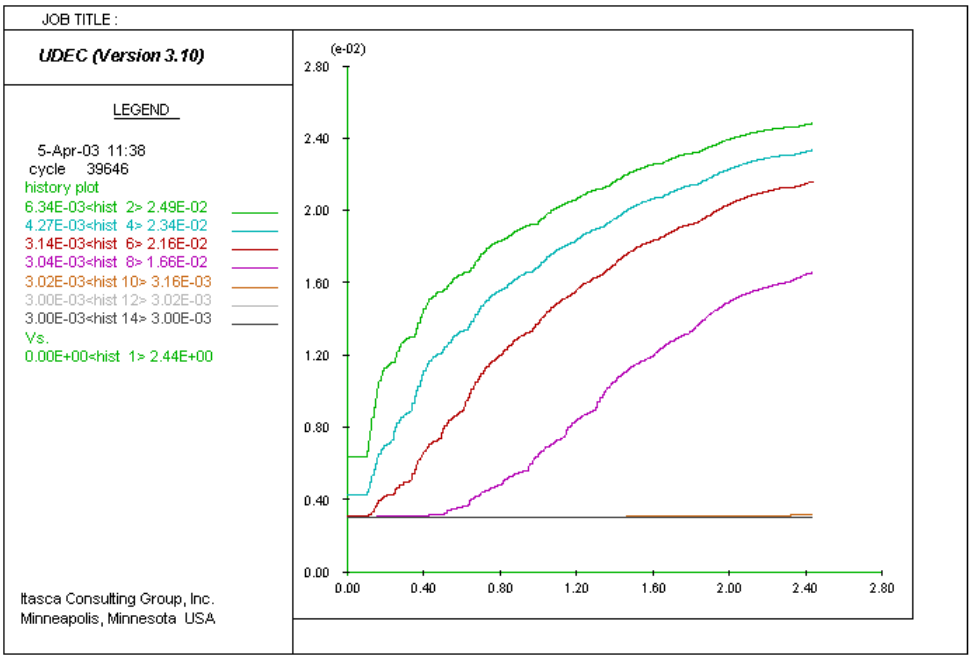

Output DTN: MO0307MWDDDINT.000

NOTES: Increasing history numbers correspond to points from Table 15, maintaining the same sequence. Time is in seconds.

Figure 100. Histories of Joint Hydraulic Aperture at Seven Locations Along the Joint: Case 113

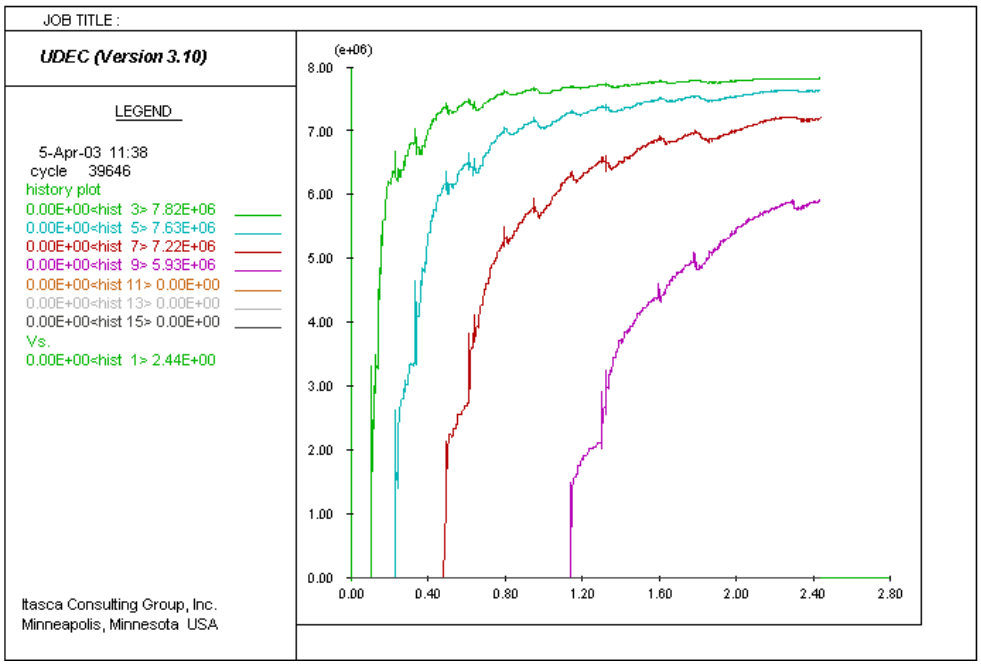

Output DTN: MO0307MWDDDINT.000

NOTES: Increasing history numbers correspond to points from Table 15, maintaining the same sequence. Time is in seconds.

Figure 101. Histories of Pore Pressure at Seven Locations Along the Joint: Case 113

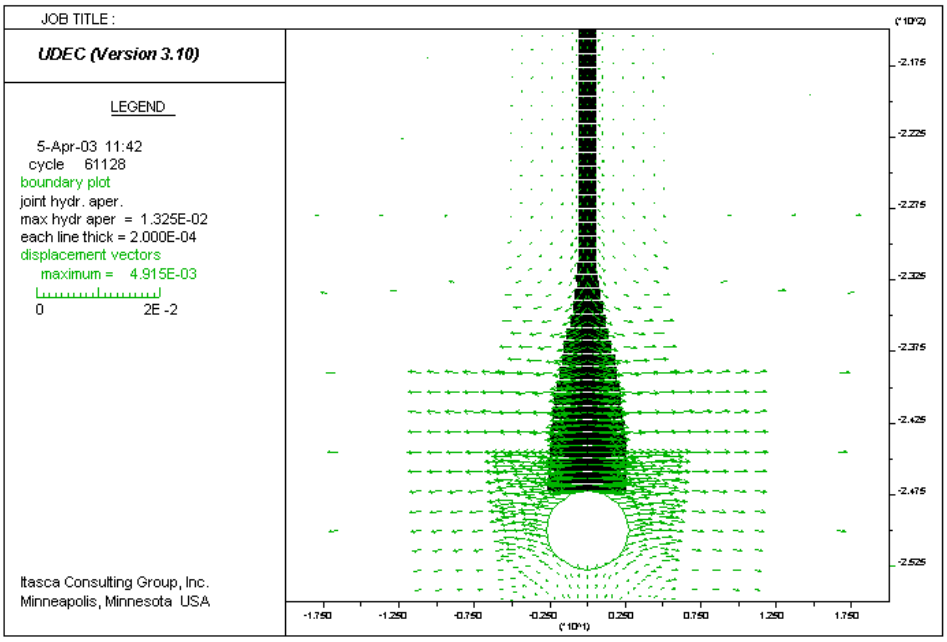

Output DTN: MO0307MWDDDINT.000

NOTES: Thickness of the black line is proportional to hydraulic aperture of the joint; deformation is due to pressure change inside the joint only.

Figure 102. Displacement Vector Field (m) and Hydraulic Aperture (m) Along the Vertical Fracture: Case 114

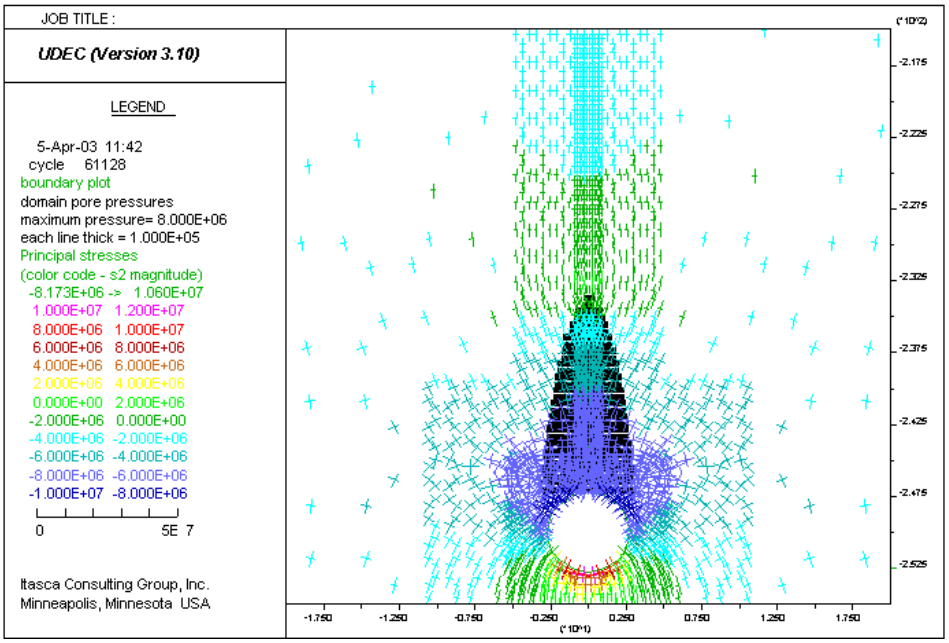

Output DTN: MO0307MWDDDINT.000

NOTES: Thickness of the black line is proportional to magma pressure in the joint; color of stress tensors indicates the magnitude of the minor principal stress.

Figure 103. Stress Tensor Field (MPa) and Pore Pressure (MPa) Along the Joint: Case 114

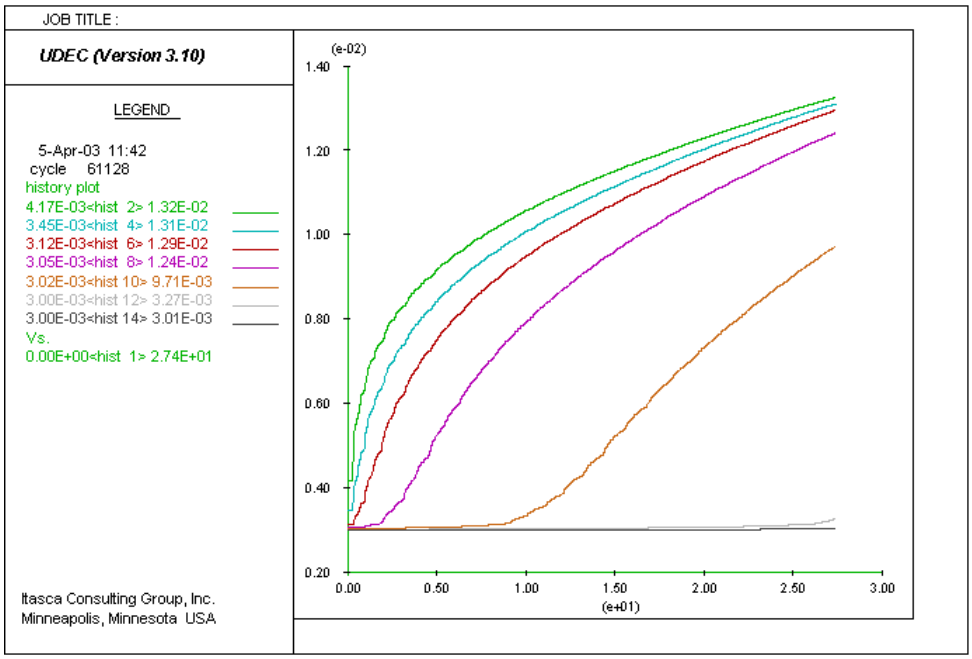

Output DTN: MO0307MWDDDINT.000

NOTES: Increasing history numbers correspond to points from Table 15, maintaining the same sequence. Time is in seconds.

Figure 104. Histories of Joint Hydraulic Aperture at Seven Locations Along the Joint: Case 114

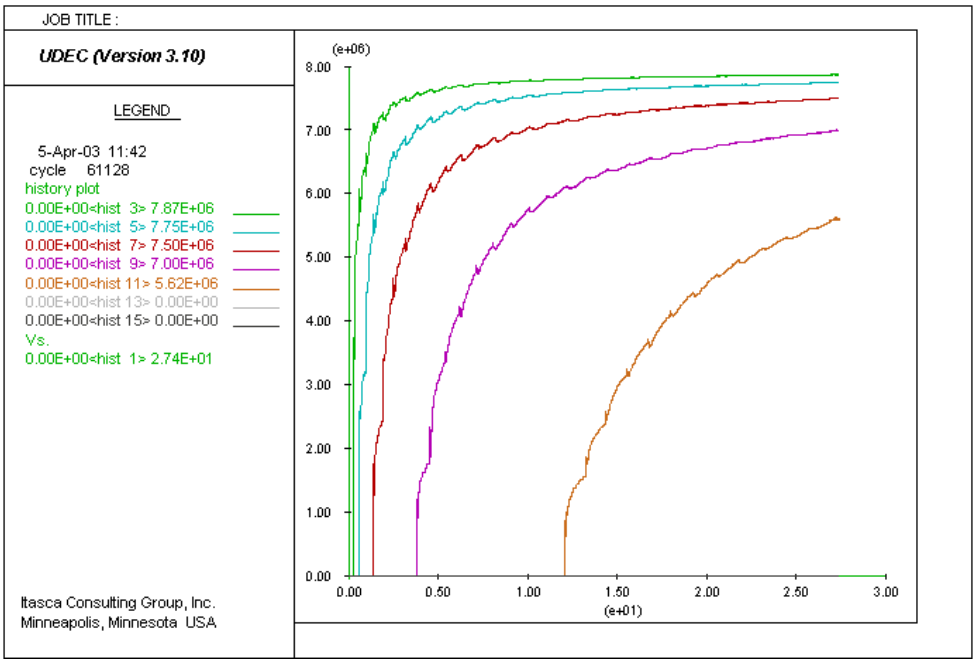

Output DTN: MO0307MWDDDINT.000

NOTES: Increasing history numbers correspond to points from Table 15, maintaining the same sequence. Time is in seconds.

Figure 105. Histories of Pore Pressure at Seven Locations Along the Joint: Case 114

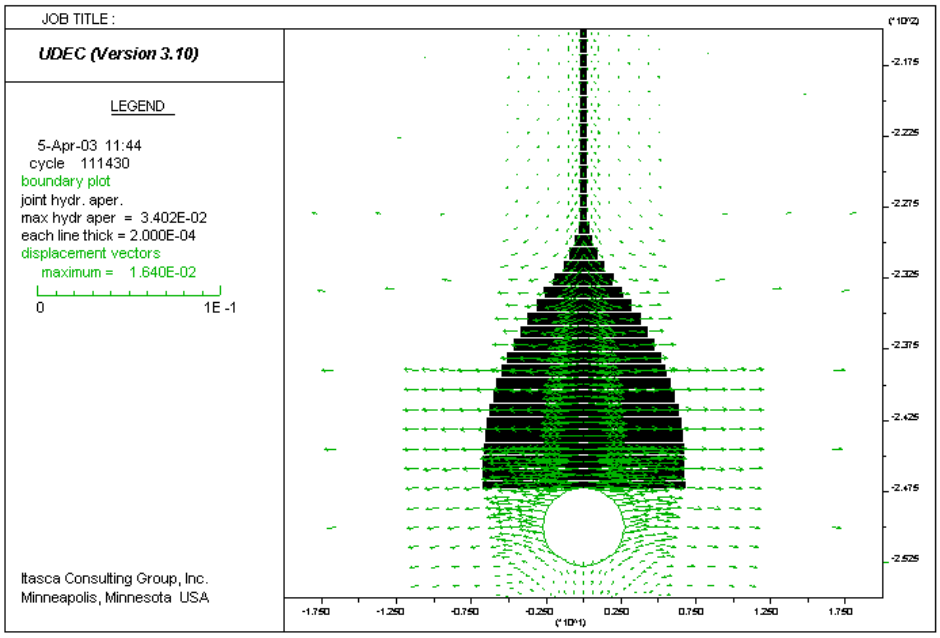

Output DTN: MO0307MWDDDINT.000

NOTES: Thickness of the black line is proportional to hydraulic aperture of the joint; deformation is due to pressure change inside the joint only.

Figure 106. Displacement Vector Field (m) and Hydraulic Aperture (m) Along the Vertical Fracture: Case 115

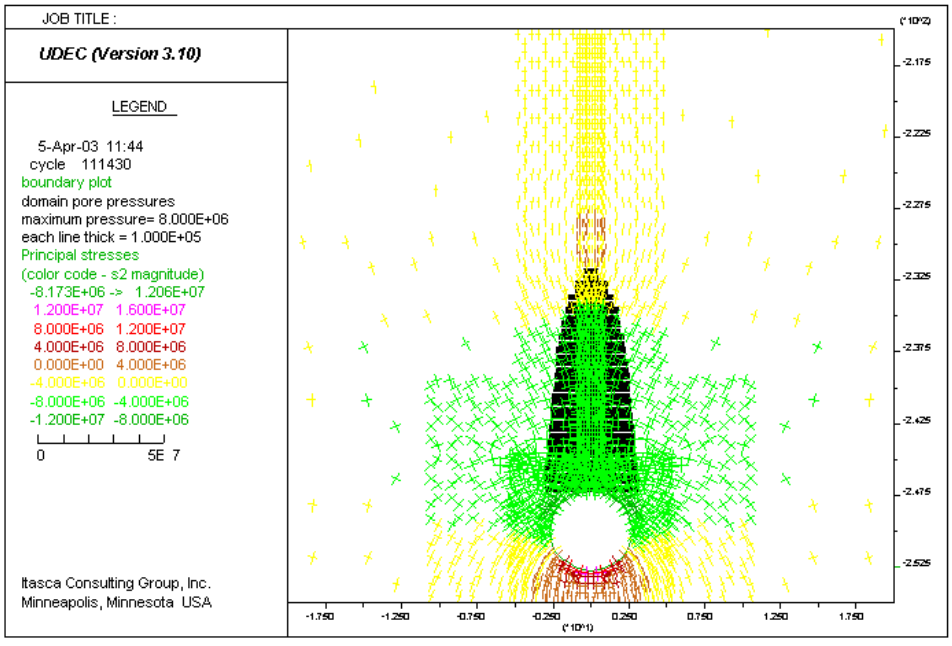

Output DTN: MO0307MWDDDINT.000

NOTES: Thickness of the black line is proportional to magma pressure in the joint; color of stress tensors indicates the magnitude of the minor principal stress.

Figure 107. Stress Tensor Field (MPa) and Pore Pressure (MPa) Along the Joint: Case 115

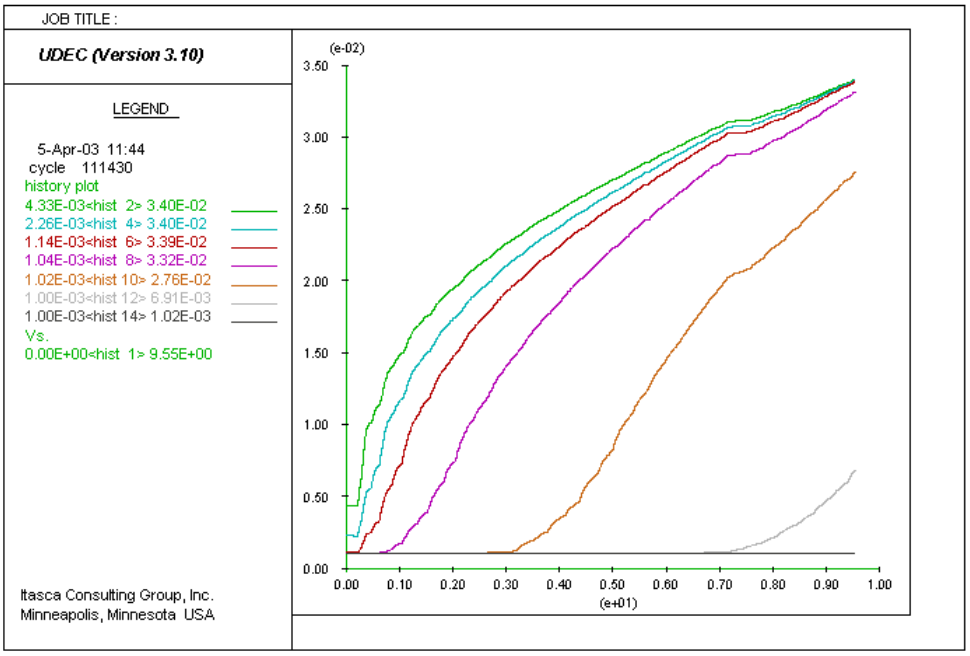

Output DTN: MO0307MWDDDINT.000

NOTES: Increasing history numbers correspond to points from Table 15, maintaining the same sequence. Time is in seconds.

Figure 108. Histories of Joint Hydraulic Aperture at Seven Locations Along the Joint: Case 115

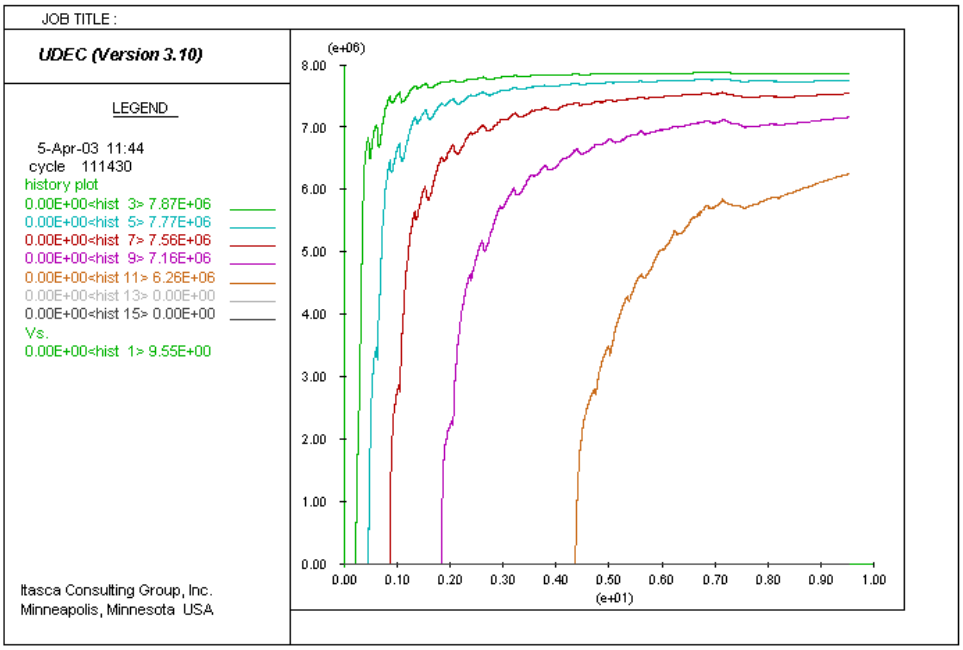

Output DTN: MO0307MWDDDINT.000

NOTES: Increasing history numbers correspond to points from Table 15, maintaining the same sequence. Time is in seconds.

Figure 109. Histories of Pore Pressure at Seven Locations Along the Joint: Case 115

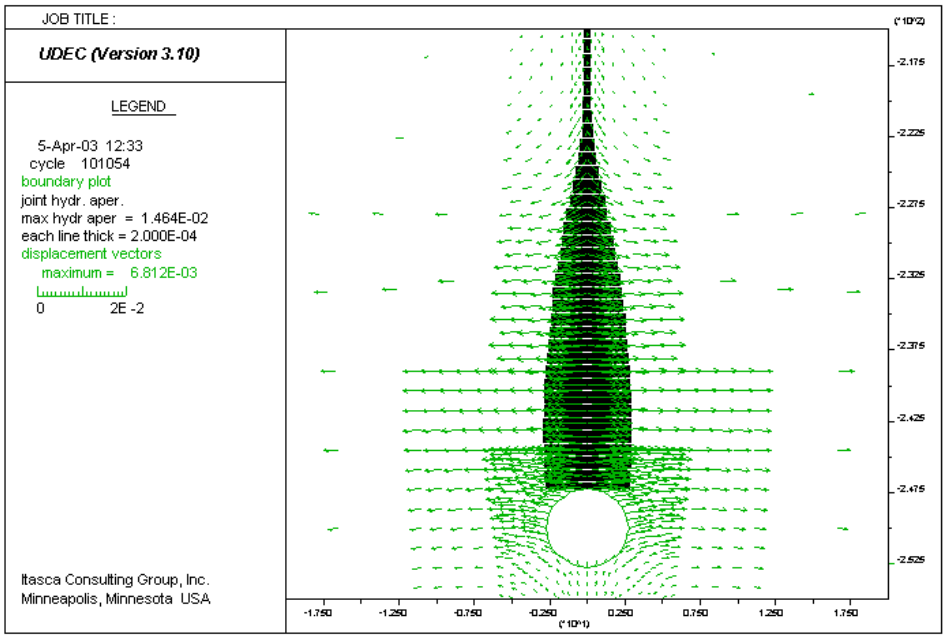

Output DTN: MO0307MWDDDINT.000

NOTES: Thickness of the black line is proportional to hydraulic aperture of the joint; deformation is due to pressure change inside the joint only.

Figure 110. Displacement Vector Field (m) and Hydraulic Aperture (m) Along the Vertical Fracture: Case 116

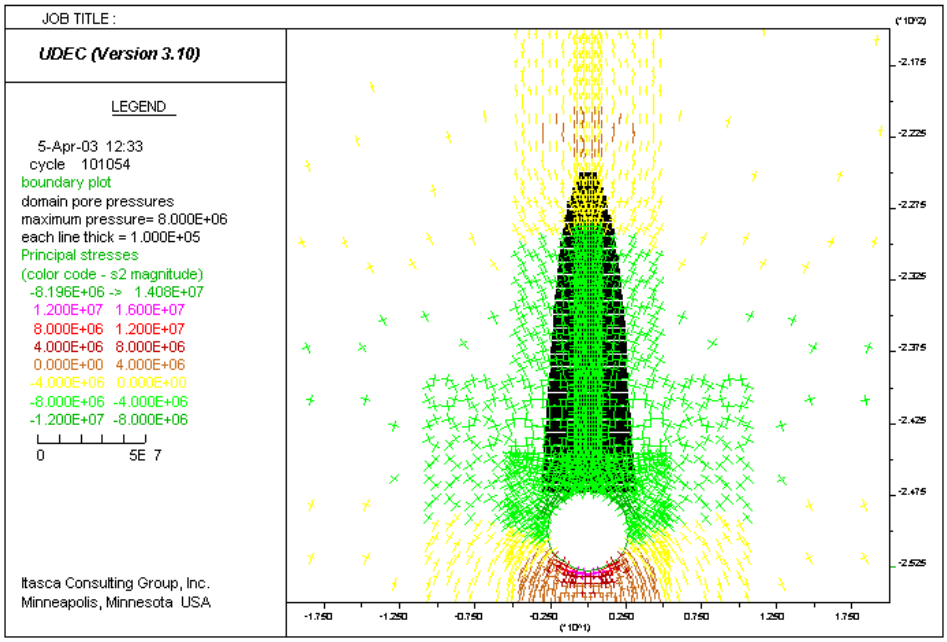

Output DTN: MO0307MWDDDINT.000

NOTES: Thickness of the black line is proportional to magma pressure in the joint; color of stress tensors indicates the magnitude of the minor principal stress.

Figure 111. Stress Tensor Field (MPa) and Pore Pressure (MPa) Along the Joint: Case 116

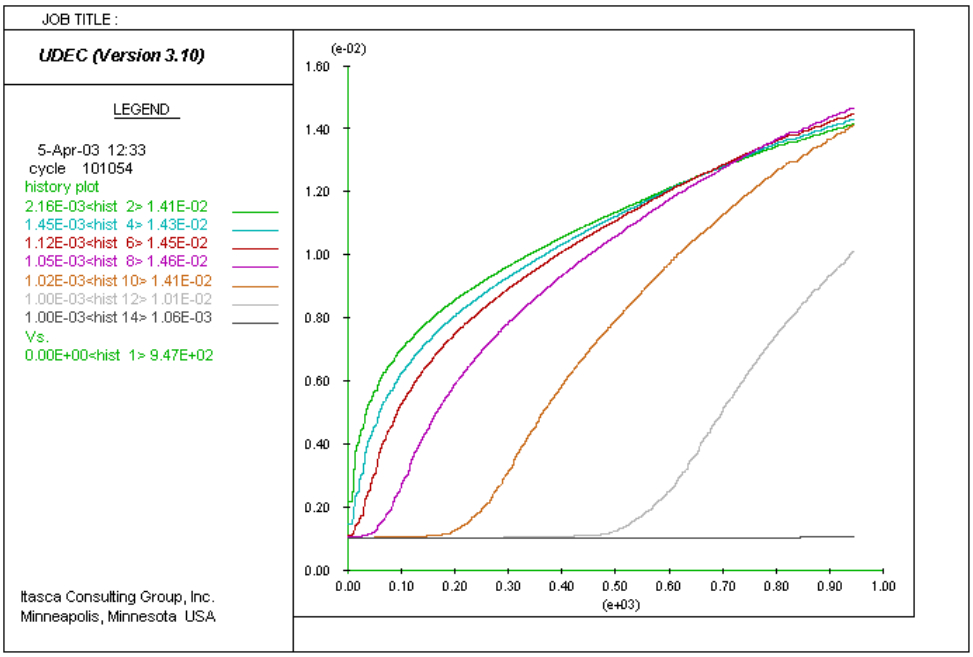

Output DTN: MO0307MWDDDINT.000

NOTES: Increasing history numbers correspond to points from Table 15, maintaining the same sequence. Time is in seconds.

Figure 112. Histories of Joint Hydraulic Aperture at Seven Locations Along the Joint: Case 116

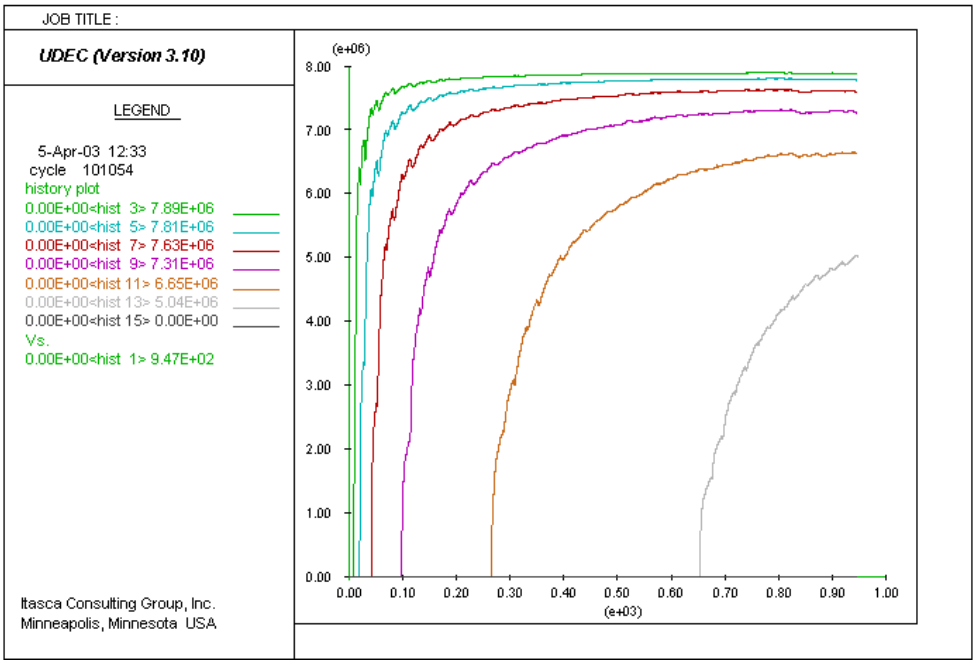

Output DTN: MO0307MWDDDINT.000

NOTES: Increasing history numbers correspond to points from Table 15, maintaining the same sequence. Time is in seconds.

Figure 113. Histories of Pore Pressure at Seven Locations Along the Joint: Case 116

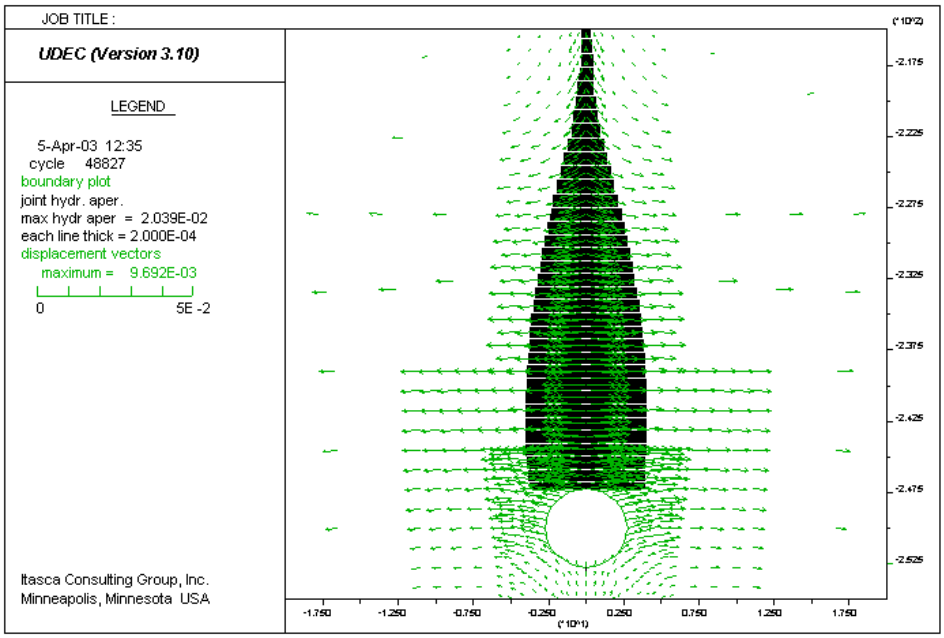

Output DTN: MO0307MWDDDINT.000

NOTES: Thickness of the black line is proportional to hydraulic aperture of the joint; deformation is due to pressure change inside the joint only.

Figure 114. Displacement Vector Field (m) and Hydraulic Aperture (m) Along the Vertical Fracture: Case 117

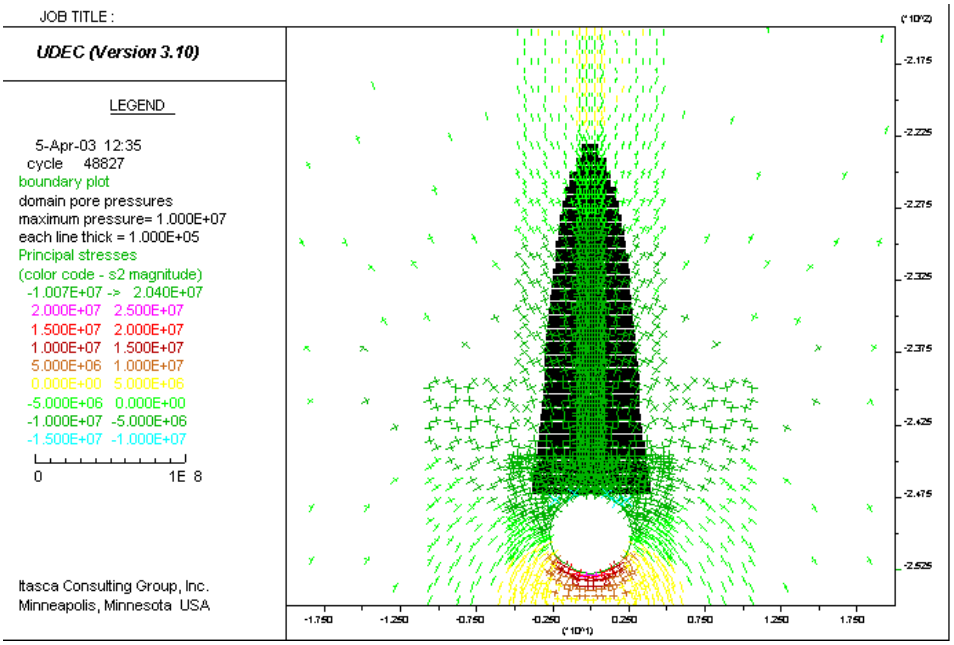

Output DTN: MO0307MWDDDINT.000

NOTES: Thickness of the black line is proportional to magma pressure in the joint; color of stress tensors indicates the magnitude of the minor principal stress.

Figure 115. Stress Tensor Field (MPa) and Pore Pressure (MPa) Along the Joint: Case 117

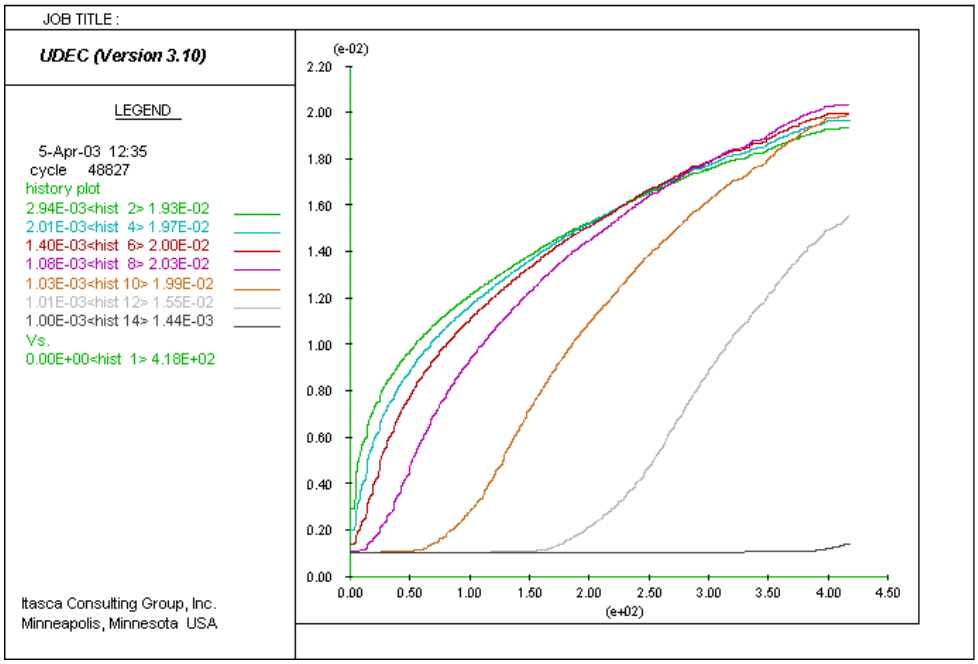

Output DTN: MO0307MWDDDINT.000

NOTES: Increasing history numbers correspond to points from Table 15, maintaining the same sequence. Time is in seconds.

Figure 116. Histories of Joint Hydraulic Aperture at Seven Locations Along the Joint: Case 117

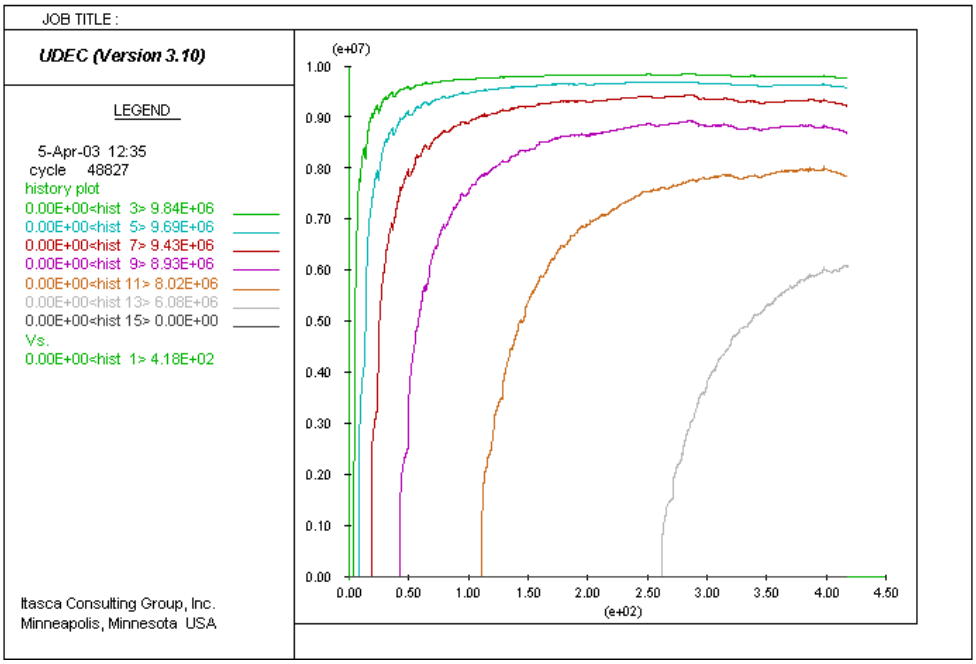

Output DTN: MO0307MWDDDINT.000

NOTES: Increasing history numbers correspond to points from Table 15, maintaining the same sequence. Time is in seconds.

Figure 117. Histories of Pore Pressure at Seven Locations Along the Joint: Case 117

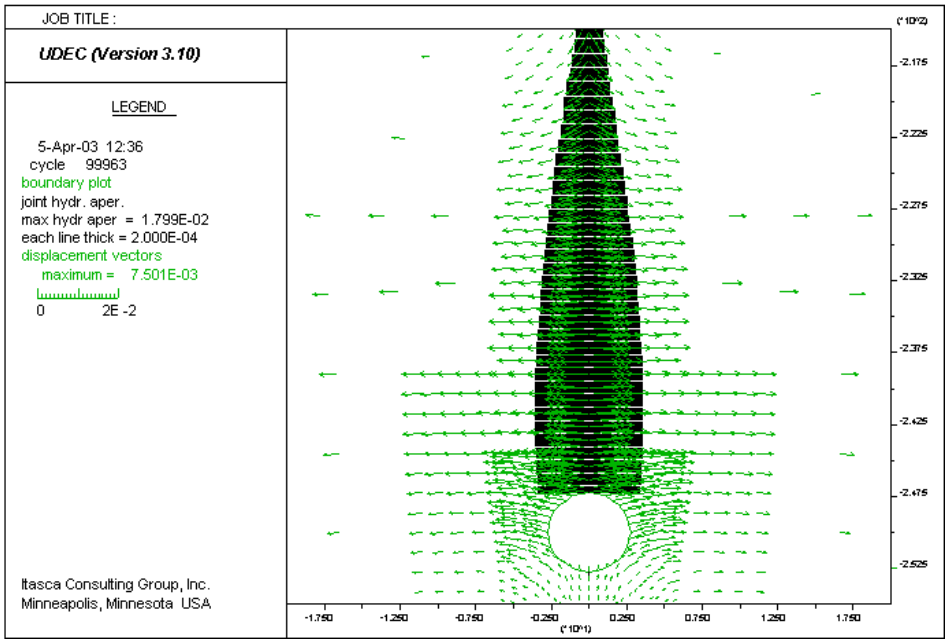

Output DTN: MO0307MWDDDINT.000

NOTES: Thickness of the black line is proportional to hydraulic aperture of the joint; deformation is due to pressure change inside the joint only.

Figure 118. Displacement Vector Field (m) and Hydraulic Aperture (m) Along the Vertical Fracture: Case 118

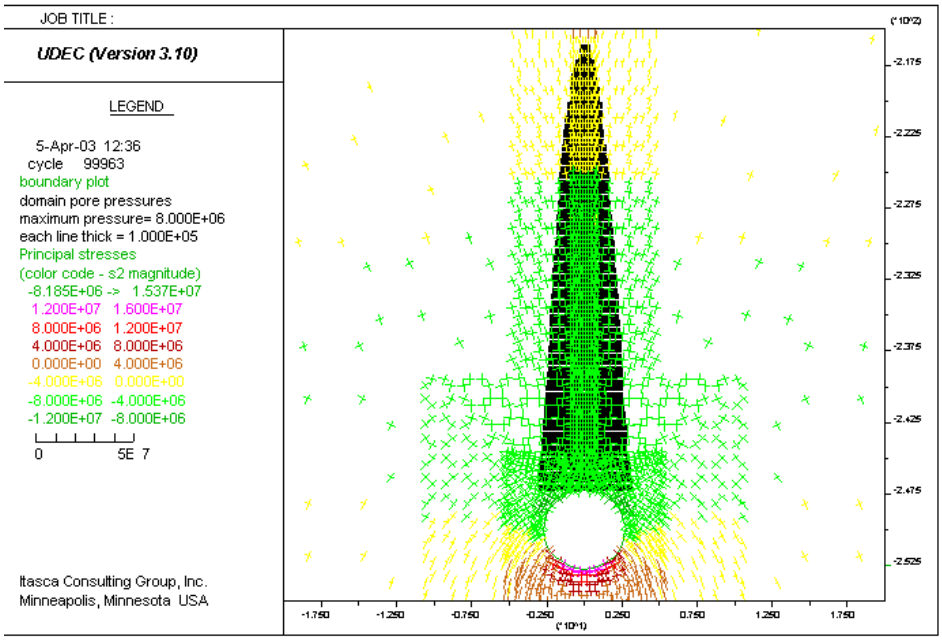

Output DTN: MO0307MWDDDINT.000

NOTES: Thickness of the black line is proportional to magma pressure in the joint; color of stress tensors indicates the magnitude of the minor principal stress.

Figure 119. Stress Tensor Field (MPa) and Pore Pressure (MPa) Along the Joint: Case 118

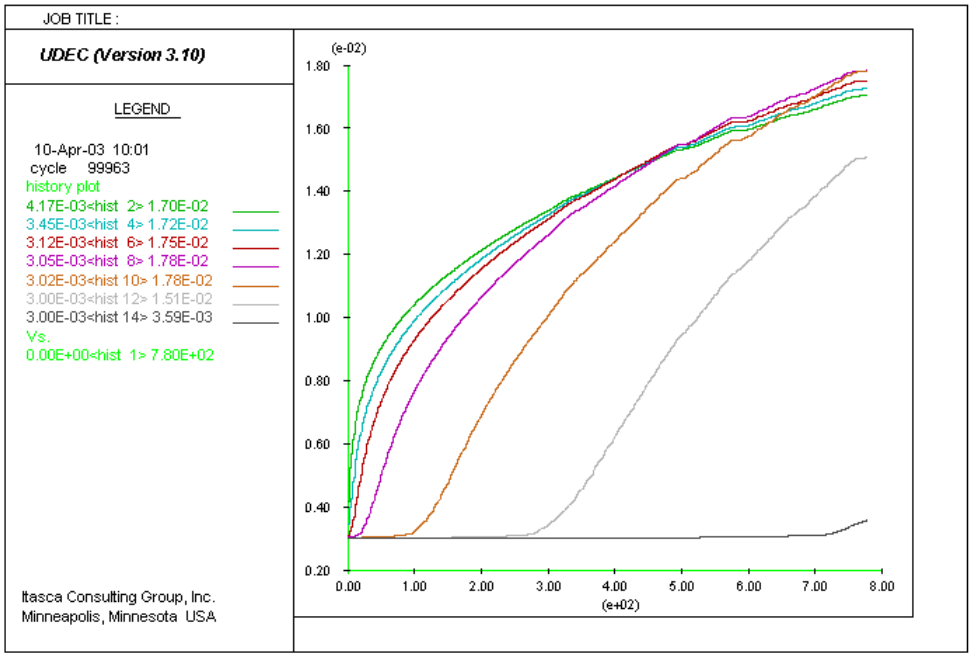

Output DTN: MO0307MWDDDINT.000

NOTES: Increasing history numbers correspond to points from Table 15, maintaining the same sequence. Time is in seconds.

Figure 120. Histories of Joint Hydraulic Aperture at Seven Locations Along the Joint: Case 118

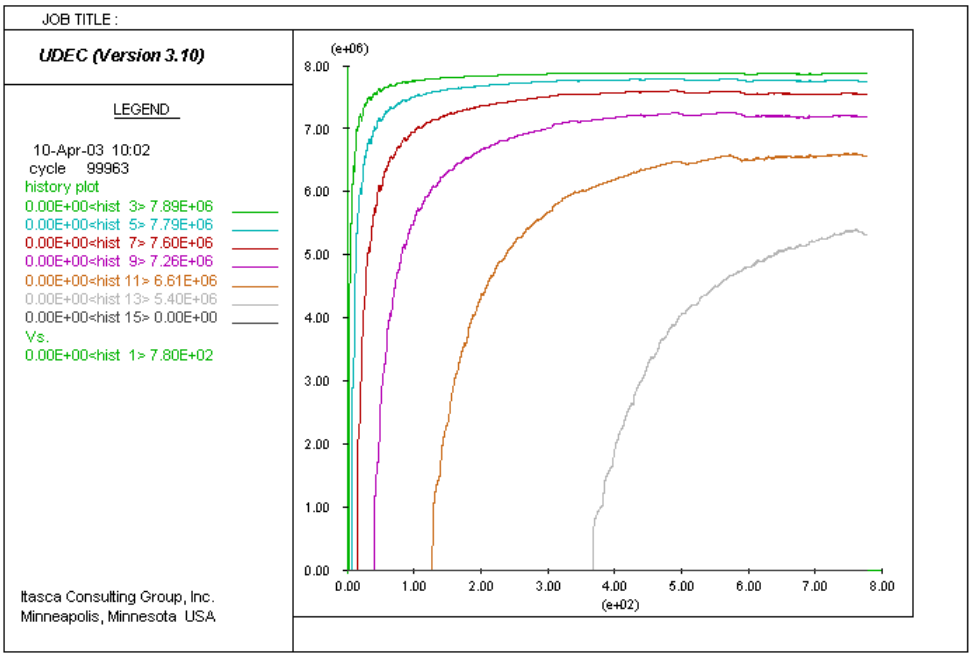

Output DTN: MO0307MWDDDINT.000

NOTES: Increasing history numbers correspond to points from Table 15, maintaining the same sequence. Time is in seconds.

Figure 121. Histories of Pore Pressure at Seven Locations Along the Joint: Case 118

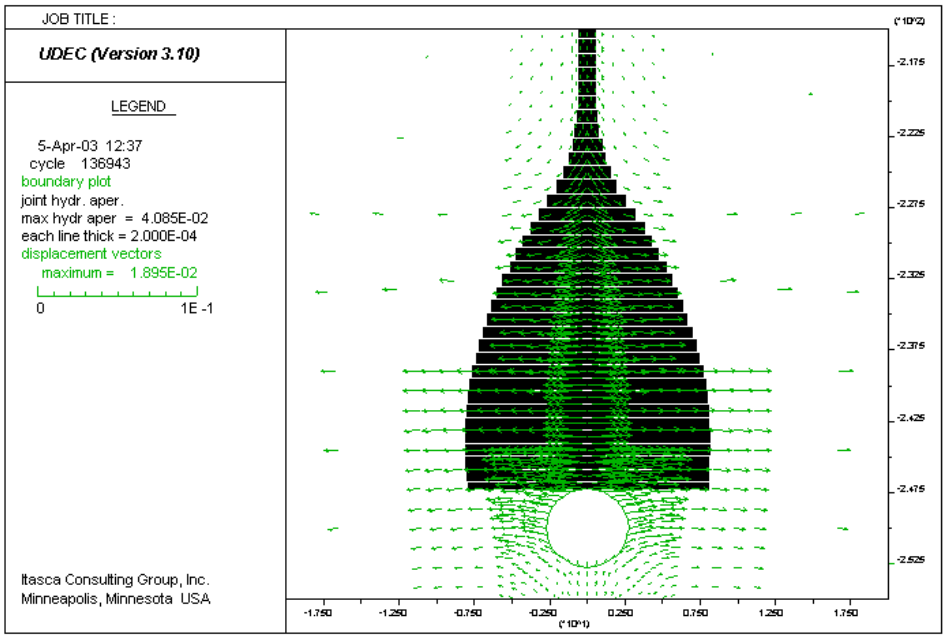

Output DTN: MO0307MWDDDINT.000

NOTES: Thickness of the black line is proportional to hydraulic aperture of the joint; deformation is due to pressure change inside the joint only.

Figure 122. Displacement Vector Field (m) and Hydraulic Aperture (m) Along the Vertical Fracture: Case 119

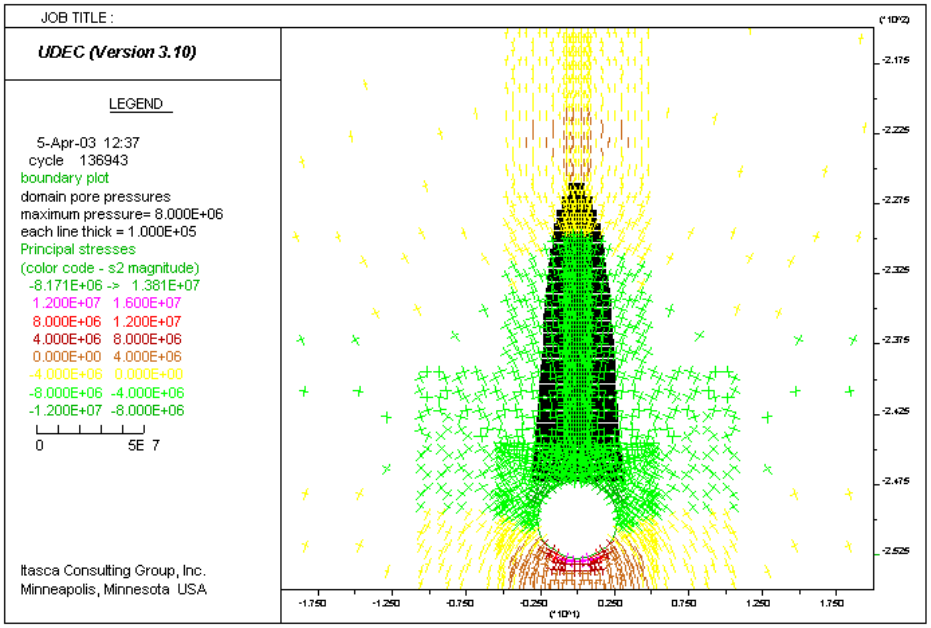

Output DTN: MO0307MWDDDINT.000

NOTES: Thickness of the black line is proportional to magma pressure in the joint; color of stress tensors indicates the magnitude of the minor principal stress.

Figure 123. Stress Tensor Field (MPa) and Pore Pressure (MPa) Along the Joint: Case 119

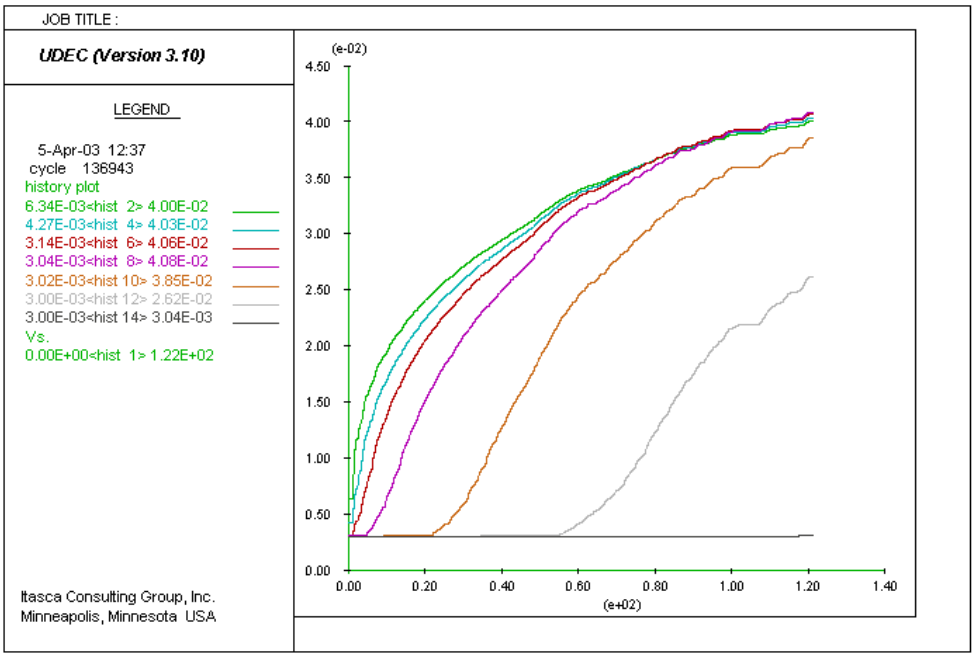

Output DTN: MO0307MWDDDINT.000

NOTES: Increasing history numbers correspond to points from Table 15, maintaining the same sequence. Time is in seconds.

Figure 124. Histories of Joint Hydraulic Aperture at Seven Locations Along the Joint: Case 119

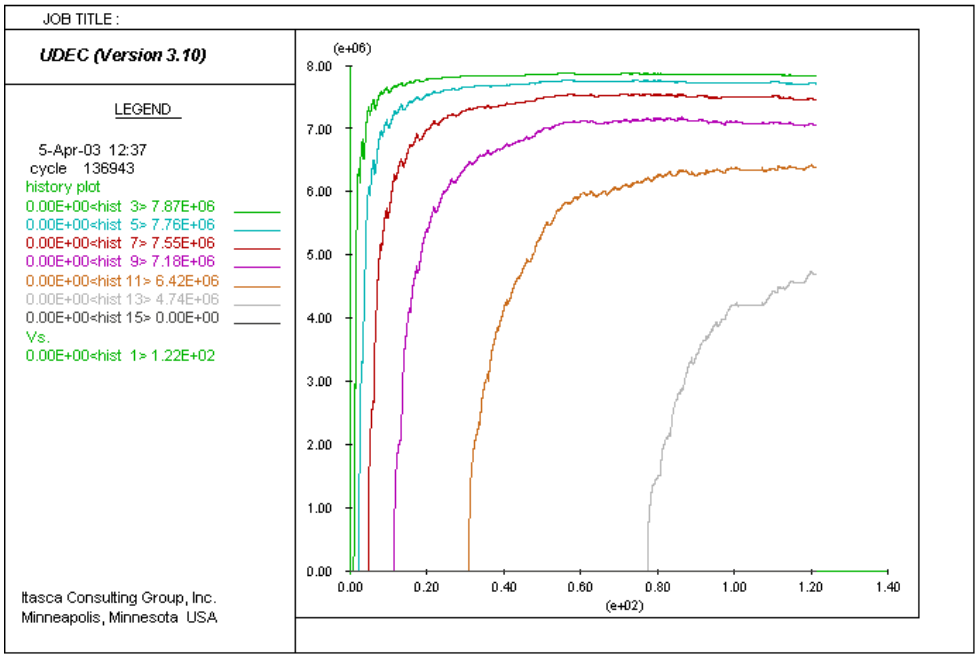

Output DTN: MO0307MWDDDINT.000

NOTES: Increasing history numbers correspond to points from Table 15, maintaining the same sequence. Time is in seconds.

Figure 125. Histories of Pore Pressure at Seven Locations Along the Joint: Case 119

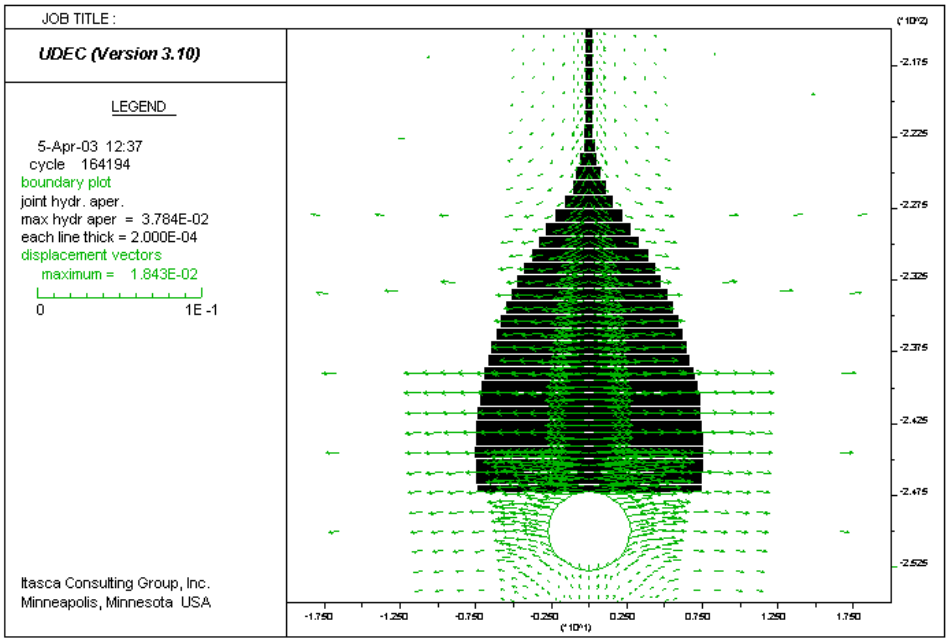

Output DTN: MO0307MWDDDINT.000

NOTES: Thickness of the black line is proportional to hydraulic aperture of the joint; deformation is due to pressure change inside the joint only.

Figure 126. Displacement Vector Field (m) and Hydraulic Aperture (m) Along the Vertical Fracture: Case 120

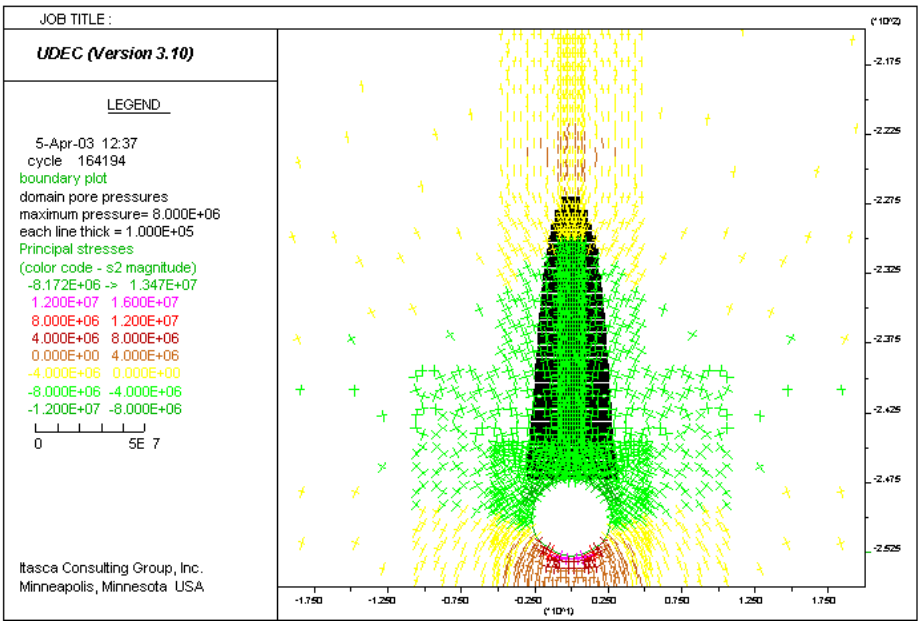

Output DTN: MO0307MWDDDINT.000

NOTES: Thickness of the black line is proportional to magma pressure in the joint; color of stress tensors indicates the magnitude of the minor principal stress.

Figure 127. Stress Tensor Field (MPa) and Pore Pressure (MPa) Along the Joint: Case 120

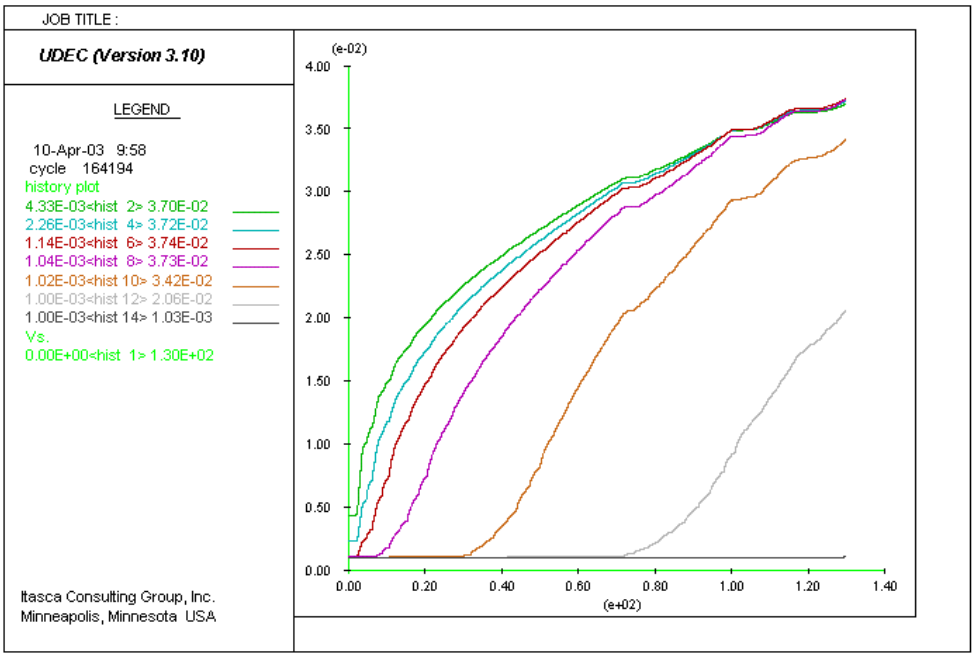

Output DTN: MO0307MWDDDINT.000

NOTES: Increasing history numbers correspond to points from Table 15, maintaining the same sequence. Time is in seconds.

Figure 128. Histories of Joint Hydraulic Aperture at Seven Locations Along the Joint: Case 120

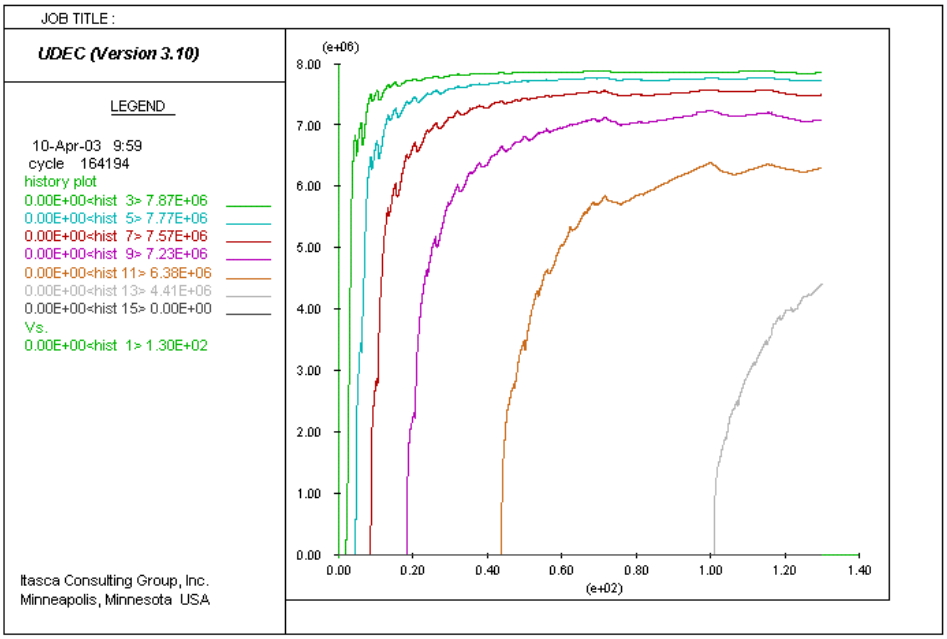

Output DTN: MO0307MWDDDINT.000

NOTES: Increasing history numbers correspond to points from Table 15, maintaining the same sequence. Time is in seconds.

Figure 129. Histories of Pore Pressure at Seven Locations Along the Joint: Case 120

6.4.11 Supporting Analyses and Model Applications

6.4.11.1 Stress-Related Effects

Initial evaluation of the possibility of the development of a dog-leg dike system should concentrate on the analysis of the altered stress field around the dike and the resultant stress concentrations around the drift(s). The stress concentrations around the drift can be compared with the magma pressure in the drift to determine if a new fracture could be initiated from the drift, and the altered minimum stress can be calculated to determine whether the magma pressure is sufficient to overcome the least-principal in-situ stress at the repository level.

Prior to the formation of the dike, the repository is characterized by some far-field principal stresses with known orientations and values. These stresses may change with time due to heating, but calculations of those changes are available using a thermomechanical model of the repository. The repository is also characterized by various material properties, but only Poisson's ratio is actually required for this analysis.

6.4.11.1.1 Effective In-Situ Stresses

The effective in-situ stresses are given by:

$$\sigma_1 = S_1 - \alpha P$$
$$\sigma_2 = S_2 - \alpha P \qquad \text{(Eq. 48)}$$
$$\sigma_v = S_v - \alpha P$$

where

S_1, S_2, and S_v are the principal in-situ stresses
P = is the pore pressure
α = Biot's modulus.

All subsequent equations involving the principal far-field stresses will use the effective stress form. However, because the pore pressure at the repository level is zero, the effective stresses are equal to the total stresses, and Biot's modulus is not required.

6.4.11.1.2 Addition of Dike-Stress Perturbation

The presence of a pressurized dike results in additional stresses that must be superposed on the virgin/thermal in-situ stresses. However, because the dike is aligned normal to the minimum principal in-situ stress and the dike calculation is 2D, there are only perturbations to four of the stress components. The values of these stress perturbations come from the NPHF2D code [DIRS 163665] calculations and are represented by:

σ_{dv} : the stress perturbation of the dike in the vertical direction
σ_{dh} : the stress perturbation of the dike in the horizontal plane

τ_{dhv}: the shear stress in the horizontal-vertical plane

$\sigma_{dp} = \nu(\sigma_{dv} + \sigma_{dh})$: the stress parallel to the dike (out of plane)

With the presence of the dike, the new stress field is characterized by:

$$\begin{aligned} \sigma_1' &= S_1 + \nu(\sigma_{dv} + \sigma_{dh}) \\ \sigma_2' &= S_2 + \sigma_{dh} \\ \sigma_v' &= S_v + \sigma_{dv} \\ \tau_{2v}' &= \tau_{dhv} \end{aligned} \qquad \text{(Eq. 49)}$$

Note that because of the existence of some shear in the minimum/vertical plane, the principal stresses would be rotated slightly by the presence of the dike.

6.4.11.1.3 Transformation of Principal and Dike Stresses into the Drift Plane

Due to geometric simplifications, the transformation of superposed principal and dike stresses is straightforward. The drifts are assumed to be horizontal so that the vertical stress is always normal to the tunnel. It is only necessary to rotate the horizontal stresses into a new plane aligned with the drift, which adds a shear stress, and then also appropriately distribute the shear from the dike. The rotation is taken through the angle φ from the maximum principal horizontal in-situ stress to the axis of the drift.

These rotations yield stresses σ_x, σ_y, and σ_z and shear stresses τ_{xy}, τ_{yz}, and τ_{xz}, given by:

$$\begin{aligned} \sigma_x &= \sigma_1' \cos^2\varphi + \sigma_2' \sin^2\varphi \\ \sigma_y &= \sigma_1' \sin^2\varphi + \sigma_2' \cos^2\varphi \\ \sigma_z &= \sigma_v' \\ \tau_{xy} &= \frac{1}{2}(\sigma_1' - \sigma_2')\sin(2\varphi) \\ \tau_{yz} &= \tau_{2v}' \cos(\varphi) \\ \tau_{xz} &= \tau_{2v}' \sin(\varphi) \end{aligned} \qquad \text{(Eq. 50)}$$

In this rotated space, z is vertical, x is along the axis of the drift, and y is normal to the drift.

6.4.11.1.4 Drift Stress Concentration

The stress concentrations around the drift that are induced by the far-field stresses are well known and, at the tunnel wall, are given by:

$$\begin{aligned} \sigma_\theta &= (\sigma_x + \sigma_y) - 2(\sigma_x - \sigma_y)\cos(2\theta) - 4\tau_{xy}\sin(2\theta) \\ \sigma_{zz} &= \sigma_z - 2\nu(\sigma_x - \sigma_y)\cos(2\theta) - 4\nu\tau_{xy}\sin(2\theta) \\ \tau_{\theta z} &= 2(-\tau_{xz}\sin\theta + \tau_{yz}\cos\theta) \\ \tau_{r\theta} &= \tau_{rz} = 0 \end{aligned} \qquad \text{(Eq. 51)}$$

In these equations, θ is the angle around the drift as measured from the x axis towards the y axis, so σ_θ is the hoop stress. Also, σ_r (not in the equations above) is the radial stress, but it is zero at the tunnel wall (until pressurized by magma, which is considered later). All of these stresses are at the drift wall, where the stress concentration is highest.

6.4.11.1.5 Drift Pressurization

The pressurization of the drift, to a value P_W, induces a radial and a tangential component. These are given by:

$$\begin{aligned} \sigma_{pr} &= P_w \\ \sigma_{p\theta} &= -P_w \\ \sigma_{pz} &= \nu\left(\sigma_{pr} + \sigma_{p\theta}\right) = 0 \end{aligned} \qquad \text{(Eq. 52)}$$

because it is assumed that there is no leak-off of magma into the pore space to induce poroelastic stress variations. Thermoelastic stresses are not considered here, but the heating of the drift by magma would cause the drift to expand and increase the hoop stress, further reducing the potential for initiation of a fracture.

6.4.11.1.6 Principal Stresses

To examine if fracture initiation could occur, the principal stresses around the borehole must be determined. The radial stress is always a principal stress because there are no shear components in the radial plane at the drift surface. In the z-θ plane, the principal stresses are given by:

$$\sigma_p, \sigma_q = \frac{1}{2}(\sigma_\theta + \sigma_z) \pm \frac{1}{2}\left[(\sigma_\theta - \sigma_z)^2 + 4\tau_{\theta z}^2\right]^{\frac{1}{2}} \qquad \text{(Eq. 53)}$$

and the angle of failure is given by:

$$\alpha = \tfrac{1}{2}\tan^{-1}\left(\frac{2\tau_{xy}}{\sigma_x - \sigma_y}\right) \qquad \text{(Eq. 54)}$$

6.4.11.2 Fracture Criteria

6.4.11.2.1 Assessment of Fracture Re-initiation

A new fracture can initiate from the drift only if the magma pressure is sufficient to increase either the hoop stress or the axial stress to overcome the smallest compressive stress that exists on the tunnel wall. Thus, the determination of the smallest principal stress at the tunnel wall solves this aspect of the problem. This determination can be done rigorously by superposing the pressurization stresses with the stress concentration around the tunnel. However, for the particular geometry of the repository (e.g., the drifts nearly aligned with the stress field), the effects of the shear stresses are minimal, and the stress field is almost aligned with the drift.

Thus, the principal stresses are essentially in the hoop, radial, and axial directions, and direct comparisons with the pressure can be made by examining the tunnel stress concentrations.

6.4.11.2.2 Assessment of Fracture Propagation

An assessment of fracture propagation is direct. The pressure in the drift must be greater than the minimum principal stress at that location. If it is less, the pressure cannot open the fracture and propagate.

6.4.11.3 Results of "Dog-Leg" Stress Calculations

An evaluation of the stress field (due to the presence of the pressurized dike) around the repository drifts was performed for a number of the cases run for the dike propagation analysis. This evaluation includes the stress perturbation (due to the dike) as well as the stress concentration around the drift. These calculations allow for assessment of the conditions under which a potential secondary dike could initiate from the drift and/or propagate in the far field.

Calculations using the NPHF2D code [DIRS 163665] require some manipulation of the dimensionless parameters in order to choose the location of the repository, the distance away from the dike, the location of the dike tip and magma front, the pressure, and other parameters. An example using one of the base-case calculations (Case 8) is given below to demonstrate the process.

The scaled parameters derived from the input described in Section 4 for this case are given by:

Length	$l^* = (\mu' E'^3 q_\infty / \delta^4)^{1/6} = 945.01$ m
Pressure	$p^* = (\mu' E'^3 \delta^2 q_\infty)^{1/6} = 8488596$ Pa
Time	$t^* = (\mu' E' / \delta^2 q_\infty)^{1/2} = 43.309$ s

and the resultant dike far-field width and velocity are given by:

Width	$w_\infty^* = (\mu' q_\infty / \delta')^{1/3} = 0.5112$ m
Velocity	$v_\infty^* = (\delta'' q_\infty^2 / \mu')^{1/3} = 19.5617$ m/s

Because the problem is formulated in terms of dimensionless parameters and only two of the dimensionless parameters are critical, a wide suite of calculations can be derived from each numerical run. In this particular case with zero cavity pressure and zero confining stress, only one dimensionless quantity needs to be considered, namely:

$$\mathbf{D} = \frac{\kappa\rho_r}{\kappa\rho_r - \rho_f} = \frac{g\kappa\rho_r}{\delta'} \qquad \text{(Eq. 55)}$$

Since the input conditions that will be matched are those of dike propagation rate and width at infinity (v_∞ and w_∞), and using the scaled-width equation to substitute for δ', then the dimensionless group can be reformulated as:

$$\mathbf{D} = \frac{g\kappa\rho_r w_\infty^2}{\mu' v_\infty} \qquad \text{(Eq. 56)}$$

As long as this dimensionless group is kept constant, this case can be used to extract numerous valid solutions.

To continue with this example, suppose that this is a case where:

- A lower horizontal stress is preferred (e.g., as determined by the relative density difference)
- The desired infinite velocity is 1.0 m/s, as expected for locations near the repository.

The dimensionless group is kept constant if the far-field width drops from0.5112 to 0.1634. However, making these changes alters the scaling parameters. These must be recomputed from the new values of the parameters and it is sensible to do so using somewhat more simple relations. For this case, these are:

Length $l_* = (E' w_\infty^3 / \mu' v_\infty)^{1/2} = 755.3$ m
Pressure $p_* = (\mu' E' v_\infty / w_\infty)^{1/2} = 3394736$ Pa
Time $t_* = (w_\infty^3 E' / \mu' v_\infty^3)^{1/2} = 755.3$ s

Note that the scaled length and time are the same for this case only because $v_\infty = 1$.

Given the information above, the output data from each calculation can be rescaled for the appropriate desired case. To determine the position of the dike or the magma front or to find a position in space (e.g., the location of the repository or the position where a stress determination is required), it is necessary to take the output and rescale by:

Length_data_new = Length_data_calc multiplied by (l_*/l^*).

To determine the pressure or the stress at any position, it is necessary to rescale by:

Pressure_data_new = Pressure_data_calc multiplied by (p_*/p*).

To determine the correct time, it is necessary to rescale by:

Time_data_new = Time_data_calc multiplied by (t_*/t^*) .

To determine the opening of the dike at any position, it is necessary to rescale by:

Opening_data_new = Opening_data_calc multiplied by (w_∞/w_∞^*) .

For this same example, the repository location is nominally at a 300 m depth, however, the mathematically correct scaled location is the inverse of the rescaling calculation, or a depth of 375.35 m. Similarly, offset distances normal to the fracture are scaled in the same manner. For desired offset values of 10, 20, 40, 80, 160, 320, and 640 m, the input values must be 12.51, 25.02, 50.05, 100.09, 200.19, 400.37, and 800.75 m, respectively. Note, however, that these values will not be the correct depth positions for different density or far-field velocity rescalings.

Applying this process to Case 8, the additional stress induced by the pressurized dike can be computed (as measured at the repository level and as a function of distance from the dike). Figures 130 through 133 show the induced horizontal, vertical, and shear stress as a function of distance at four different times when the dike tip is below the repository, at the repository, halfway between the repository and the surface, and as close to the surface as the calculations allow (i.e., the time when dike unstably propagates to the surface). Since this calculation is two-dimensional, the other horizontal stress would be calculated by multiplying Poisson's ratio times the sum of the vertical and horizontal calculated stresses.

In these cases, the effect of the dike on the stress field is somewhat different than that commonly observed with hydraulic fractures occurring at depth. Of particular interest is the large size of the tensile zone and the extension of the tensile region along the dike. In most hydraulic fractures, the tensile zone is narrow and the stress becomes compressive just behind the fracture tip. In this case however, the large size of the dike, the large cavity region, and the pressure gradient dominated by the weight of the magma, serve to generate a large amount of curvature in a sizable area around the tip resulting in a large extension of the tensile zone. For example, Figures 130 and 131 show the horizontal stress decreasing as the dike tip approaches, but Figures 132 and 133 show that the stress around the dike remains tensile even when the fracture tip is near the surface (nearly 300 m above the repository).

The vertical stress also becomes tensile ahead of the crack tip, but it is slightly compressive a few hundred meters beyond the side of the dike. In addition, there is a stress reversal behind the tip that is probably due to the adjustment required to match the cavity pressure condition existing at the dike wall (or to match the magma pressure if the fluid front passed this location, as illustrated in Figure 133).

Finally, the stress decay length is on the order of several hundred meters. Beyond this point, the effect of the dike is minimal. Clearly, this decay length is a function of the dike tip position and other conditions.

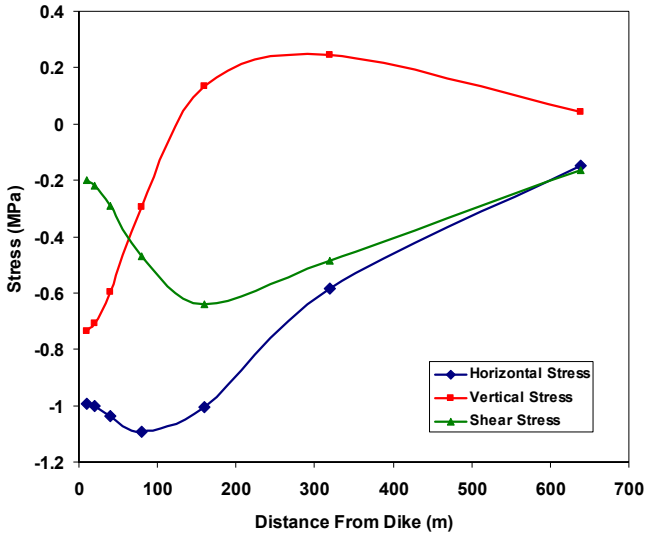

DTN: SN0304T0504203.003

Figure 130. Dike-Induced Stresses as a Function of Horizontal Distance when the Tip is at a 411-m Depth

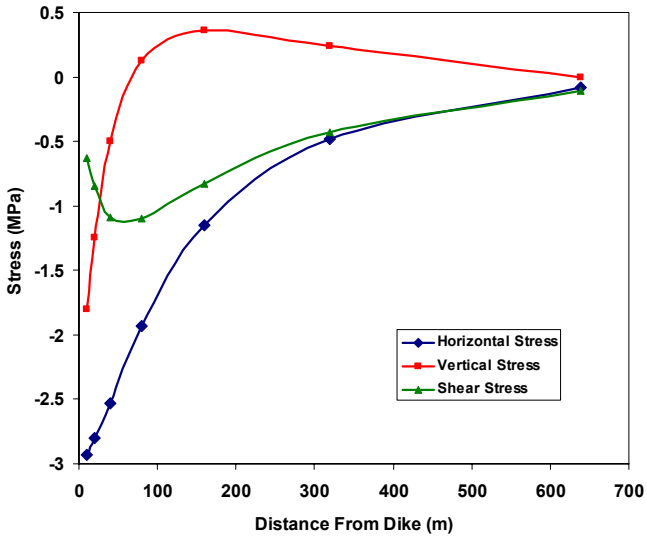

DTN: SN0304T0504203.003

Figure 131. Dike-Induced Stresses as a Function of Horizontal Distance when the Tip is at a 300-m Depth

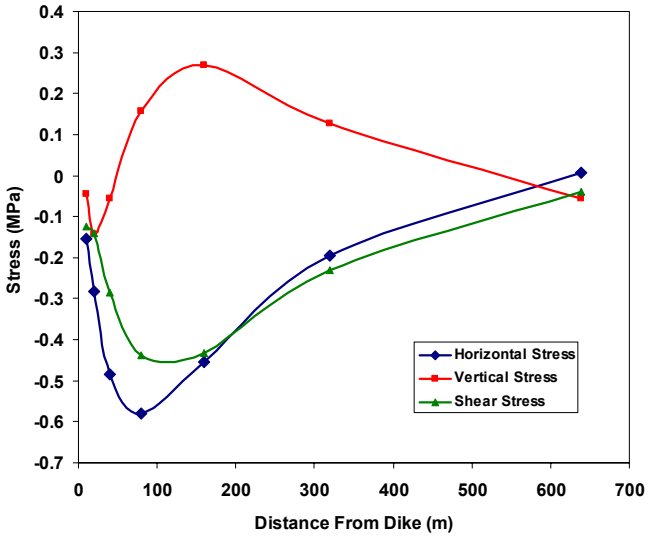

DTN: SN0304T0504203.003

Figure 132. Dike-Induced Stresses as a Function of Horizontal Distance when the Tip is at a 150-m Depth

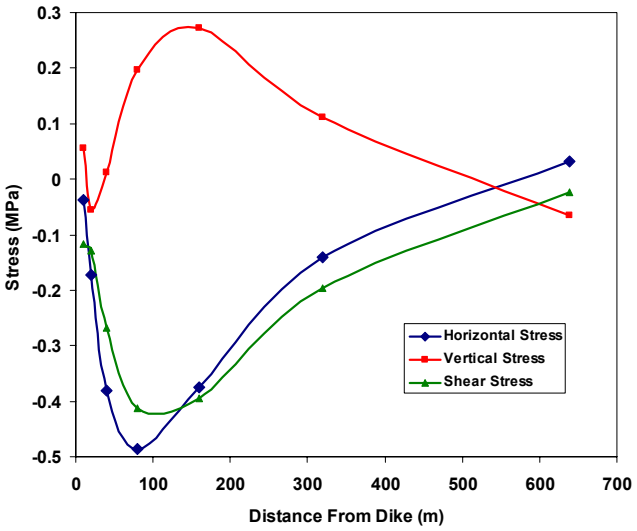

DTN: SN0304T0504203.003

Figure 133. Dike-Induced Stresses as a Function of Horizontal Distance when the Tip is at a 16-m Depth

To assess the importance of these stress perturbations on the repository, it is necessary to superimpose them on the existing stress field, determine the resultant effect on the stress field and the stress concentrations around the repository drifts. Assuming that:

- The minimum horizontal stress is 3.6 MPa (e.g., this analysis was rescaled to a net rock density of 1200 kg/m, which would yield a scaled stress of 3.6 MPa)
- The maximum horizontal stress is somewhat greater (5.5 MPa)
- The overburden stress is about 7 MPa
- The orientation of the maximum horizontal stress is N55°E, and
- The drift orientation is approximately N70°E.

Then, the full stress field in the vicinity of the dike can be calculated.

Figure 134 shows the new stress field acting on the repository when the dike is 411 m below the surface. This plot shows the principal stresses having been tilted slightly from the original, although the overburden stress is still near vertical.

Figures 135 to 137 show the same results for dike tip positions of 300, 150, and 16 m from the surface. As expected from the previous plots, the largest perturbation on the existing in-situ stresses occurs when the dike tip is near the repository and extends for a few hundred meters along it.

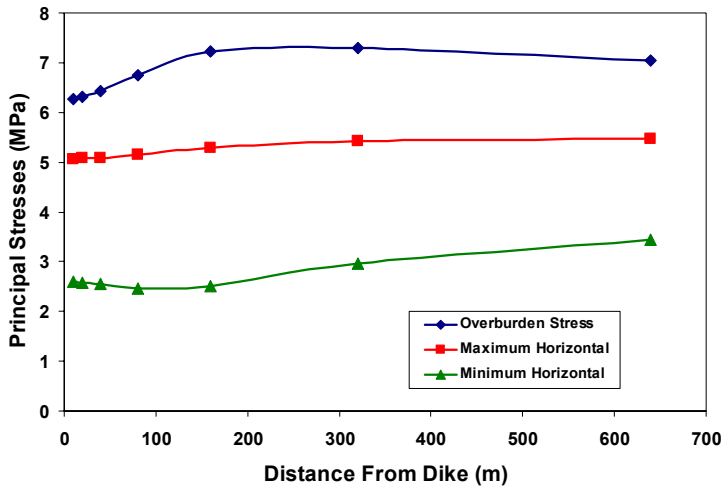

DTN: SN0304T0504203.003

Figure 134. Total Stresses Acting on the Repository when the Crack Tip is at a 411-m Depth

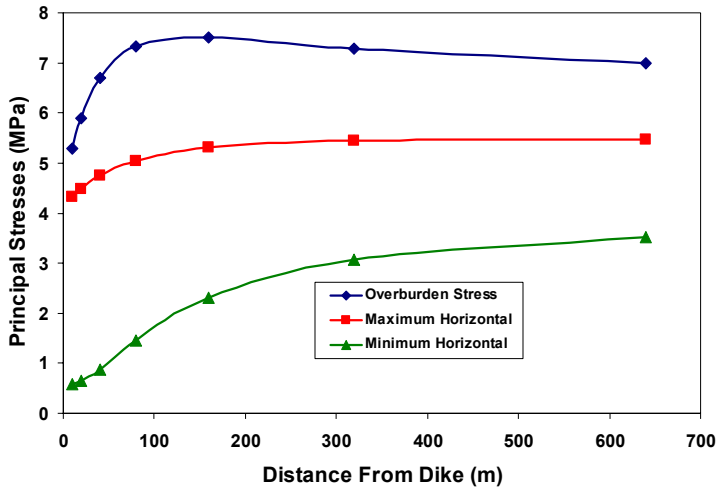

DTN: SN0304T0504203.003

Figure 135. Total Stresses Acting on the Repository when the Crack Tip is at a 300-m Depth

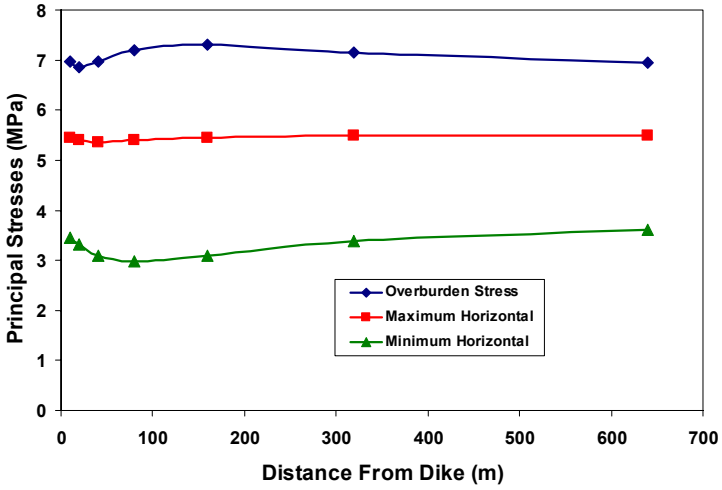

DTN: SN0304T0504203.003

Figure 136. Total Stresses Acting on the Repository when the Crack Tip is at a 150-m Depth

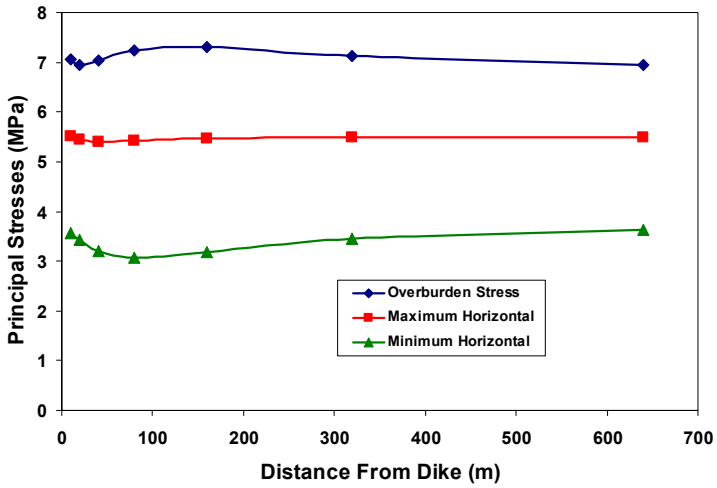

DTN: SN0304T0504203.003

Figure 137. Total Stresses Acting on the Repository when the Crack Tip is at a 16-m Depth

Given the principal stresses acting on the tunnel, the stress concentrations around the tunnel are calculated as a function of angular position. The principal stresses along the tunnel are also calculated for several distances from the dike. Examples are shown in Figures 138 through 140 for a dike tip positioned at distances of 10, 40, and 640 m from the dike at the repository 300 m from the surface. In general, the principal stresses are not very different from hoop and axial stresses because the repository is nearly aligned with the stress field, but near the dike stress re-orientation does become significant. The non-symmetric behavior of the stress field is due to shear stresses generated by the dike and by the misalignment of the repository with the stress field. Near the dike, hoop stresses are reduced and less stress will be required to initiate the fracture than is required to propagate it far from the dike.

Taking the minimum cyclic stress values from Figures 138 through 140, along with data from other positions in the curves, the plot of Figure 141 can be developed. This plot shows the minimum principal stress present on the drift wall at any angular position as a function of distance. This stress is the minimum pressure required to start a secondary dike at that position. In this case, the most likely place for re-initiation of a new dike is close to the original dike. Nevertheless, at this time the magma is still a long distance from reaching the repository, so the consequences are minimal. By the time the magma reaches the repository, the stress perturbation is small (e.g., Figure 133) and the effect on the stress concentrations around the tunnel are minimal. Of course, if the dike is to propagate any significant distance, it must also exceed the minimum stresses shown in Figures 134 through 137.

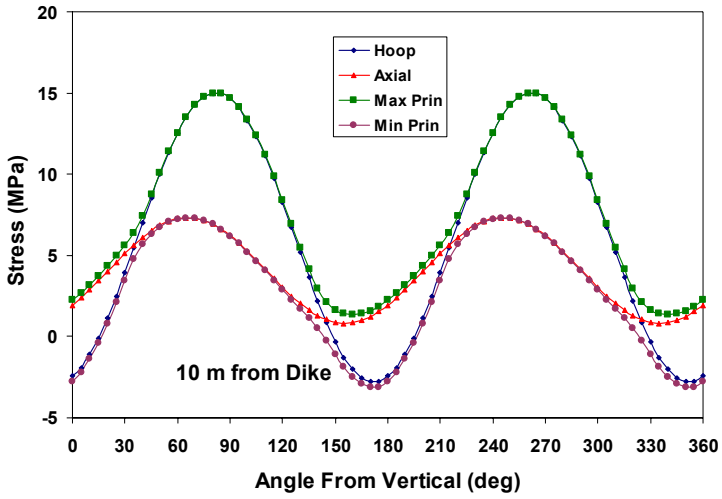

DTN: SN0304T0504203.003

Figure 138. Stresses around the Drift Wall at 10 m from the Dike

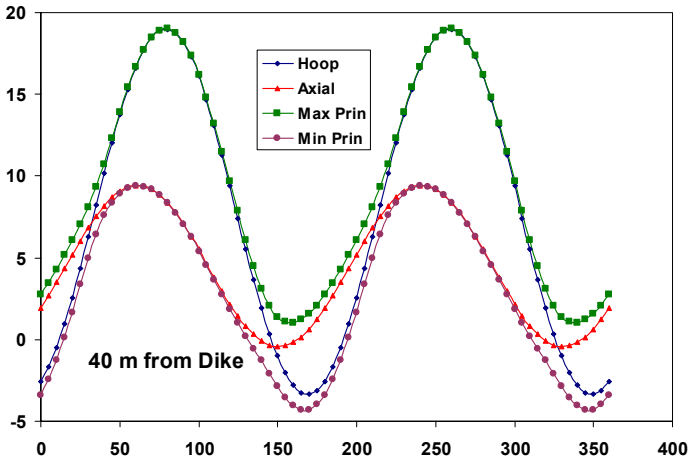

DTN: SN0304T0504203.003

Figure 139. Stresses around the Drift Wall at 40 m from the Dike

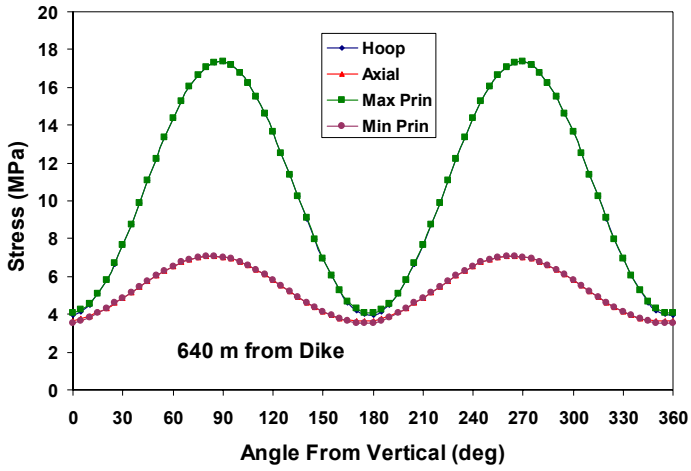

DTN: SN0304T0504203.003

Figure 140. Stresses around the Drift Wall at 640 m from the Dike

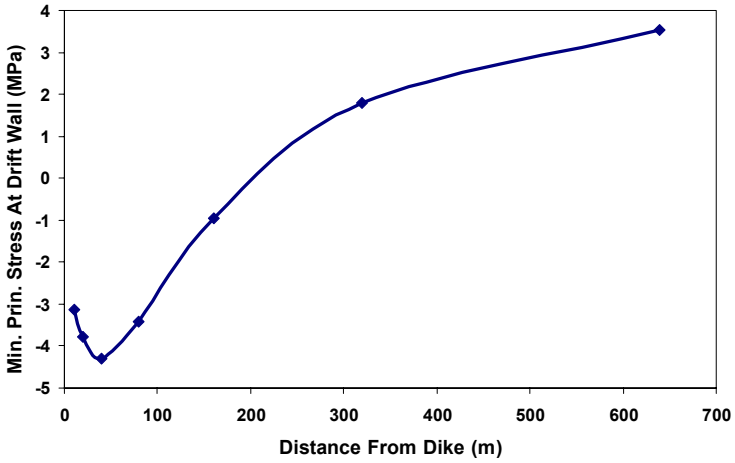

DTN: SN0304T0504203.003

Figure 141. Minimum Principal Stress at the Drift Wall versus Distance from the Dike

Similar plots can be developed for various cases so that an assessment can be made for stress conditions where a dog-leg scenario could be developed. Other cases may have the magma front extending higher, and may show significant differences in behavior as the dike propagates closer to the surface.

6.4.11.4 Magma Cooling Rates

In Section 6.4.10.2.1, the rate at which a potential new dike (or sill in Case 104) would open under a variety of conditions was discussed. This section presents an analysis of how fast such an opening dike would be chilled by the surrounding cold rock to the extent that magma could no longer feed the crack-tip region and force the crack to continue growing. Our analysis follows that of *Final Report of the Igneous Consequences Peer Review Panel* (Detournay et al.

[DIRS 162914], Appendix 3.4, p. 53). Following Carslaw and Jaeger (1959 [DIRS 100968], Chapter 11, Section 11.2) the thickness of the chilled margin δ of a sheet of magma in cold rock is:

$$\delta = 2\lambda_d \sqrt{\kappa t} \quad \text{(Eq. 57)}$$

where:

t = time
κ = the thermal diffusivity

and where:

parameter λ_d is the solution to:

$$\frac{\sqrt{\pi}\Lambda}{k(T_m - T_r)} = \frac{e^{-\lambda_d^2}}{\lambda_d}\left[\frac{1}{1+erf(\lambda_d)} - \frac{T_m - T_s}{(T_m - T_r)erfc(\lambda_d)}\right] \quad \text{(Eq. 58)}$$

where:

Λ = is the latent heat of fusion for the magma
k = is the thermal conductivity
T_m = is the initial magma temperature
T_s = is the temperature at which the magma viscosity becomes high enough to stop dike growth
T_r = the temperature of the surrounding rock
erf and *erfc* = the error function and the complimentary error function, respectively

The simplifying assumption is made that all properties of the magma and the host rock are identical. The parameter λ_d is solved for by trial and error given values of the other parameters in the equations.

6.4.11.4.1 Inputs to Analysis

Calculations were done for the six different magma compositions (differing in water content) used in the analysis report *Characterize Eruptive Processes at Yucca Mountain, Nevada* (BSC 2001 [DIRS 160130]). Input for these calculations is given in Table 14 and discussed in Section 6.4.5.3. The determination of "solidification" temperatures, T_s, is described next.

6.4.11.4.1.1 "Solidification" Temperatures

To stop a newly forming dike by "thermal death," it is not necessary that the magma freeze, completely. As the fraction of crystals increases in the magma, the apparent viscosity of the mixture increases very dramatically. A rigorous treatment of this phenomenon is beyond the scope of this report. The apparent viscosity, $\eta_A(T)$, of a partially crystallized magma at temperature T below its liquidus temperature T_L is given by:

$$\eta_A(T) = \eta_o(T)\left(1 - \frac{(T_L - T)}{(T_L - T_{\phi_{mx}})}\right)^{-2.5} e^{0.04(T_L - T)} \quad \text{(Eq. 59)}$$

where:

$\eta_0(T)$ = the viscosity of the pure liquid at T calculated with the method of Shaw used in *Characterize Eruptive Processes at Yucca Mountain, Nevada* (BSC 2001 [DIRS 160130])

ϕ_{mx} = the maximum crystal volume fraction that will allow flow

$T_{\phi_{mx}}$ = the temperature at which the volume fraction of solids is ϕ_{mx}

This equation is derived from Griffiths (2000 [DIRS 163625], Equation 2 by way of Equation 3) with these postulates:

- The initial temperature is the liquidus temperature, so the initial volume fraction of solids is 0.
- The volume fraction of crystals varies linearly with temperature.
- ϕ_f is equal to ϕ_{mx} with $T_f = T_{\phi_{mx}}$.

Estimates of ϕ_{mx} in the literature, summarized by Griffiths (2000 [DIRS 163625]), range from 0.4 to 0.6; the central value 0.5 has been used in this analysis.

Using this relation, the apparent viscosity of partially crystallized alkali basalt magmas of several water contents as functions of temperature both above and below their liquidus temperatures are shown in Figure 142. The effect of only 10 to 20 percent of crystals on the rheology of the partially crystallized magma is dramatic—an increase in viscosity of 1.5 to 2 orders of magnitude.

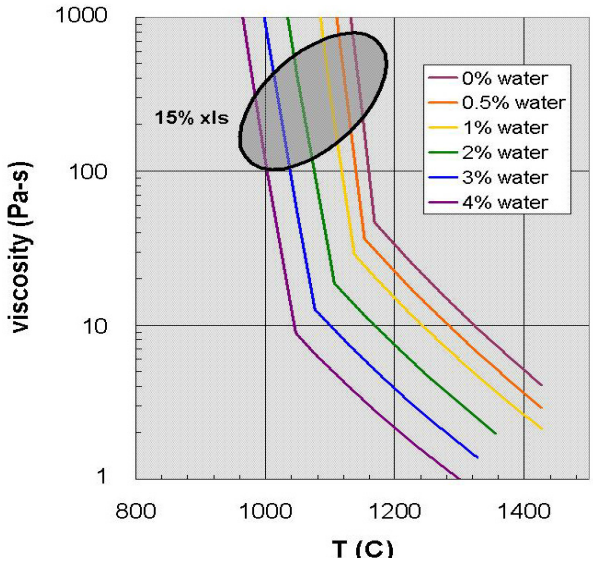

DTN: LA0307EG831811.002

NOTE: Liquidus = a line drawn through the break in slope of each plotted curve.

Figure 142. Apparent Viscosity of Alkali Basalt Magmas During Crystallization

In light of the vary rapid increase of apparent viscosity as temperatures drop, the temperature at which the apparent viscosity reaches 1000 Pa-s has been chosen as T_s in Table 14.

6.4.11.4.2 Thermal Stoppage of New Dike

From the input values shown in Table 14, the time needed for new dikes to solidify in cold country rock can be calculated. These times vary as the square of the thickness of the dike. The results are illustrated in Figure 143. The "new dike" values plotted are:

- For the triangles bottom to top, respectively: the time for a new crack to reach the widths plotted for the most extreme conservative Case 103 of the previous section (see Figure 60) when the crack has initiated parallel to the drift and propagated 3.67 m, 7.79 m and 16.04 m. By the time a new dike has reached 16 m from the drift, the most favorable direction for it to continue opening will be normal to the drift axis. Propagation in that orientation is less favorable.

- For the squares bottom to top, respectively: the time for a new crack to reach the widths plotted for (Case 105, Figure 71) where the crack has initiated perpendicular to the drift axis and propagated to a range of 3.08 m, 5.08 m and 43.8 m.

- For the circle: the highly unfavorable case of sill formation where the crack has reached a range of 3.67 m (Case 104, Figure 65).

Clearly such cracks will not be able to grow to any appreciable width before they are halted by solidification.

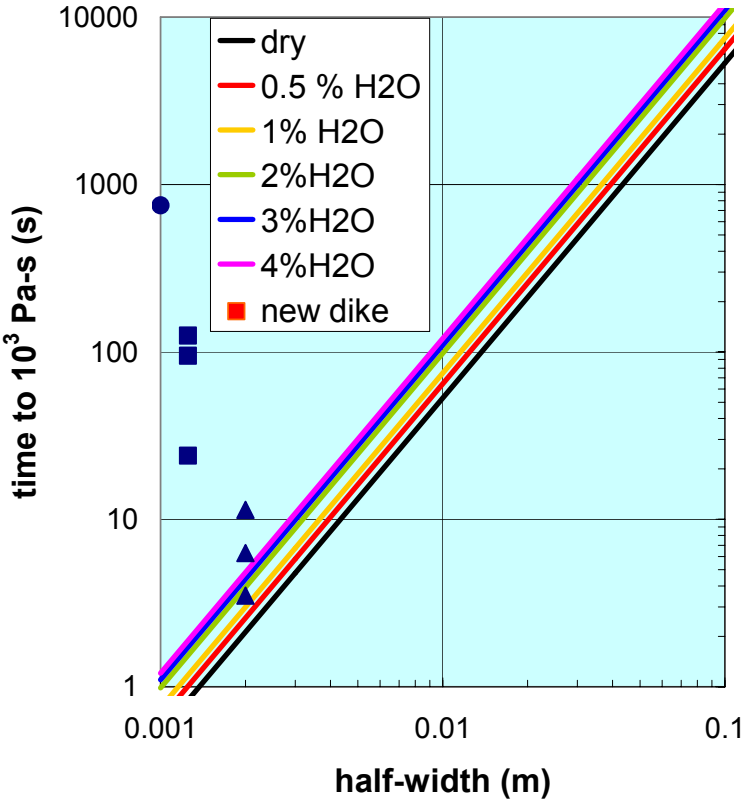

DTN: LA0307EG831811.002

Figure 143. Time to Chill a Dike from Liquidus Temperature to the Temperature at Which the Apparent Viscosity is 1000 Pa-s, the Assumed Effective "Solidus" Temperature

6.4.11.5 Synthesis for "Dog-Leg"

Figure 143 shows time and width points from calculations from Section 6.4.10.2 of the growth history for a new dike under the most favorable assumptions for growth of Case 103. The new dike, in that case, started out at 1-mm half-width and took 4 s to grow to a width of only 4 mm at a range of 3.67 m from the edge of the drift. At greater ranges the time to reach the same width is greater (11 s at 16 m from the drift). Comparing this growth history for a constant viscosity magma with the results of the chill-zone growth rate, it is seen that the dike will never be able to propagate more than a few meters from the drift because the magma will chill rapidly, blocking off the flow of fluid to drive the crack growth.

6.4.11.6 Dike Continues to Surface

In Section 6.38.2, it was shown that during an encounter with a drift, the crack will intersect the drift before the magma to wit:

- For a relatively slow magma rise velocity of 1 m/s, the crack tip will lead the magma by 45 to 55 s (Cases 8 and 9, Figures 4b and 4c). So before any magma can be diverted into the drifts, the crack will already be more than 50 m above the drift.

- For a magma velocity of 5 m/s, the tip has already broken out at the surface before the magma reaches the drift level except for the case of large overburden stresses (Figure 7). Even with diversion of 40 percent of the flow into the drift (Figure 6), the time required for the crack tip to reach the surface is increased by only about 55 percent.

Another portrayal of the same calculations (Figure 22) reveals that the crack tip for these cases with 40 percent leak-off reaches the surface about 35 to 125 s after the magma reaches the drift level.

These numerical results are supported by the analysis of magma flow into drifts presented above in Section 6.3.9.2.3.1. This support is seen in Figure 19 depicting the height above the drift to which magma will rise in the dike while the dike is filling. For dikes with magma rising at 5 m/s, a single drift, even an empty one, cannot take the entire flow of magma within the centerlines between drifts. By the time the drift is filled, the magma has already reached 15 to 200 m above the drift, depending on the case considered.

Results of Section 6.3.9.2.3.3 indicate that, as magma continues up the original dike path while also being diverted into the drifts, the vertical velocity will be lower directly above a drift than at the midpoint between two drifts. This result can be seen most clearly in Figure 26, which is a snapshot shortly after magma first encounters a drift. But the effect persists at least as long as the simulation ran (Figure 28). It is also seen that pressures in the dike above the drift are almost an order of magnitude lower than between drifts (Figure 29).

Based on the results discussed in the preceding paragraphs, it is concluded that the most likely scenario for magma to erupt to the surface after intruding the drift complex is for it to continue along the trajectory of the original dike. The analysis report *Characterize Eruptive Processes at Yucca Mountain, Nevada* (BSC 2001 [DIRS 160130]) describes the basic processes by which the sheet flow of a dike is transformed into the more concentrated flow of a conduit, and that is considered the most likely outcome of a dike intersecting the repository.

6.5 POST-EMPLACEMENT EFFECTS

This section discusses the effects of dike intrusion into drifts after the flow of magma has stopped. Such “post-emplacement” events take place over the months and years after drifts have been filled. Specifically, this section addresses cooling and solidification of the magma and transport of heat and magmatic gases from a magma-filled drift to an adjacent unintruded drift. The objective of these analyses is to determine the environmental effects seen by waste packages in adjacent drifts.

6.5.1 Gas Flow Between Drifts

In the event of the intrusion of an igneous dike into the repository block, the volcanic gas that is exsolved from the magma as it depressurizes and crystallizes and the latent and sensible heat of the magma have the potential for affecting waste packages in drifts not directly intersected by the dike. The migration of volcanic gas associated with a dike emplaced in a waste-emplacement drift into a neighboring drift is discussed in this section based on reaction-transport modeling that couples thermal, hydrological, and chemical processes for a multiphase, multicomponent, multimineralic system. Results are presented for the migration of volcanic gas out of a waste-emplacement drift through the fractured tuff repository rock and, alternatively, through a backfilled access drift. Note that a gas flow analysis is also addressed in *Igneous Intrusion Impacts on Waste Package and Waste Form* (BSC 2003 [DIRS 161810]), and those results are consistent with the results presented in this report.

6.5.1.1 Description

The intersection of a basaltic dike with one or more drifts would potentially result in a region directly affected by the magma (Zone 1) and a region (including nearby drifts) that could be impacted (Zone 2) as depicted in Figure 144).

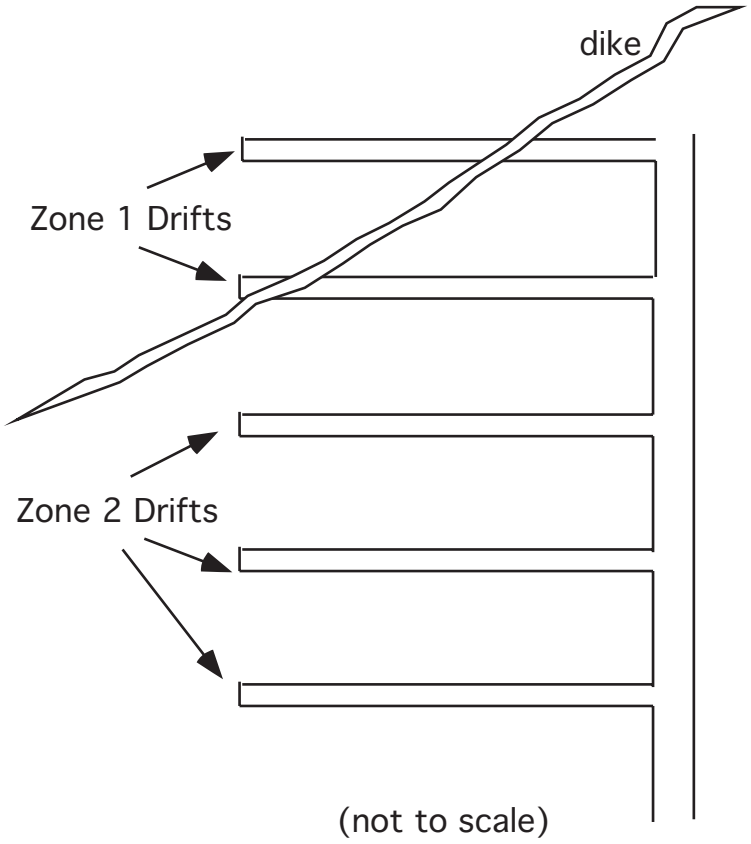

NOTE: For illustration purposes only.

Figure 144. Plan View Schematic of Dike-Drift Intersection and Zones 1 and 2

The pressure, volume, composition, and temperature history of volcanic gas potentially entering a repository drift depends on several factors, including the volume of magma emplaced in a drift, its rate of ascent, and its composition. Given these uncertainties, a simple conceptual model was employed to consider the effects of gas migration out of a drift into the surrounding fractured host tuff, as follows:

- The models consider a volcanic gas source inside the drift that allows gas species to migrate via advection and diffusion either through the fractured tuff around the drift, or alternatively, through a backfilled connecting drift.

- The rate of advance of the volcanic gas in the fracture network is examined to assess the potential effect on a neighboring drift. The actual emplacement of magma in a drift is not simulated, nor are the actual pressure-temperature conditions over time realistically evaluated.

Several simulations are performed to bound the potential rate of advance of the gas and to examine the controls on the migration of soluble gas species.

Diffusive and advective gas-phase transport of air, H_2O, CO_2, and SO_2 were modeled along with the appropriate equilibrium gas-water solubility relations. Calculations of gas density and pressure considered only water vapor and air. The molecular diameter of SO_2 (used for the calculation of the diffusion coefficient) was calculated from its molar volume of 0.05636 liters/mole. All other transport properties are given in Drift-Scale Coupled Processes (DST and THC Seepage) Models (BSC 2003 [DIRS 163506], Section 4.1.6).

The model of the geochemical system includes the major aqueous species, minerals, and gaseous components in the unsaturated zone. Additionally, minor species, such as F^-, are included for their relevance to waste package corrosion. The geochemical model consists of the following primary aqueous species: H^+, Na^+, K^+, Ca^{2+}, Mg^{2+}, AlO_2^-, NO_3^{2-}, SO_4^{2-}, SO_2(aq), F^-, Cl^-, HCO_3^-, SiO_2(aq), and $HFeO_2$(aq). Gaseous components include air, H_2O, CO_2, and SO_2. Oxidation-reduction reactions were not treated; however, reactions involving sulfur oxidation would result in stronger retardation of SO_2.

The initial mineralogy of the tuff matrix and fracture coatings is represented by the following assemblage (some as end members of an ideal solid-solution phase): α-cristobalite, opal, tridymite, quartz, K-feldspar, albite, anorthite, Ca-smectite, Na-smectite, Mg-smectite, illite, calcite, fluorite, rhyolitic glass, hematite, stellerite, clinoptilolite, mordenite, and heulandite. Several other potential secondary phases are considered (e.g., amorphous silica, kaolinite, sepiolite, gypsum) as well as various salt phases, such as halite and sylvite, which precipitate only under conditions of complete evaporation. A complete description of the rationale for these phases/components, thermodynamic and kinetic data, derivation of various properties, and sources for all data can be found in BSC 2003 [DIRS 163506].

6.5.1.2 Documentation

The numerical model for this analysis was originally developed for the chemical evaluation of water and gas potentially seeping into repository drifts and concomitant changes to permeability

and unsaturated flow under thermal conditions associated with radionuclide decay. The numerical model, sources of input data, and approximations are described in the model report *Drift-Scale Coupled Processes (DST and THC Seepage) Models* (BSC 2003 [DIRS 163506]). Specific aspects of model input and development related to the volcanic gas thermodynamic and transport properties, boundary conditions, and simulation parameters are given in this section and documented in Wang (2003 [DIRS 164068], SN: YMP-LBNL-ELS-LH-1, pp. 1–32). Changes to the model described in BSC 2003 [DIRS 163506] are as follows:

- Addition of SO_2 (aq) and gas thermodynamic properties to input database. Addition of SO_2 (gas) molecular diameter to database for calculation of diffusion coefficient. All other species and minerals are the same.
- Waste package volume increased to be instead a volcanic gas source (T, P, composition).
- For the backfilled access drift simulations, a drift-wide zone is set to the properties of the crushed tuff invert to approximate a backfilled access drift.
- Volcanic gas composition added to input file.

6.5.1.3 Description of Inputs

The numerical mesh and all other geochemical parameters defining the initial conditions prior to emplacement of the gas are described in *Drift-Scale Couple Processes (DST and THC Seepage) Models* BSC 2003 [DIRS 163506]. Modifications to the model as part of this report are presented here. In short, the model represents a cross-section of a proposed repository drift, which by symmetry has been cut in half. The mesh extends vertically from the ground surface to the water table and horizontally from the drift center to the midpoint between drifts (40.5 m). An enlargement of the numerical mesh showing the in-drift configuration is shown in Figure 145.

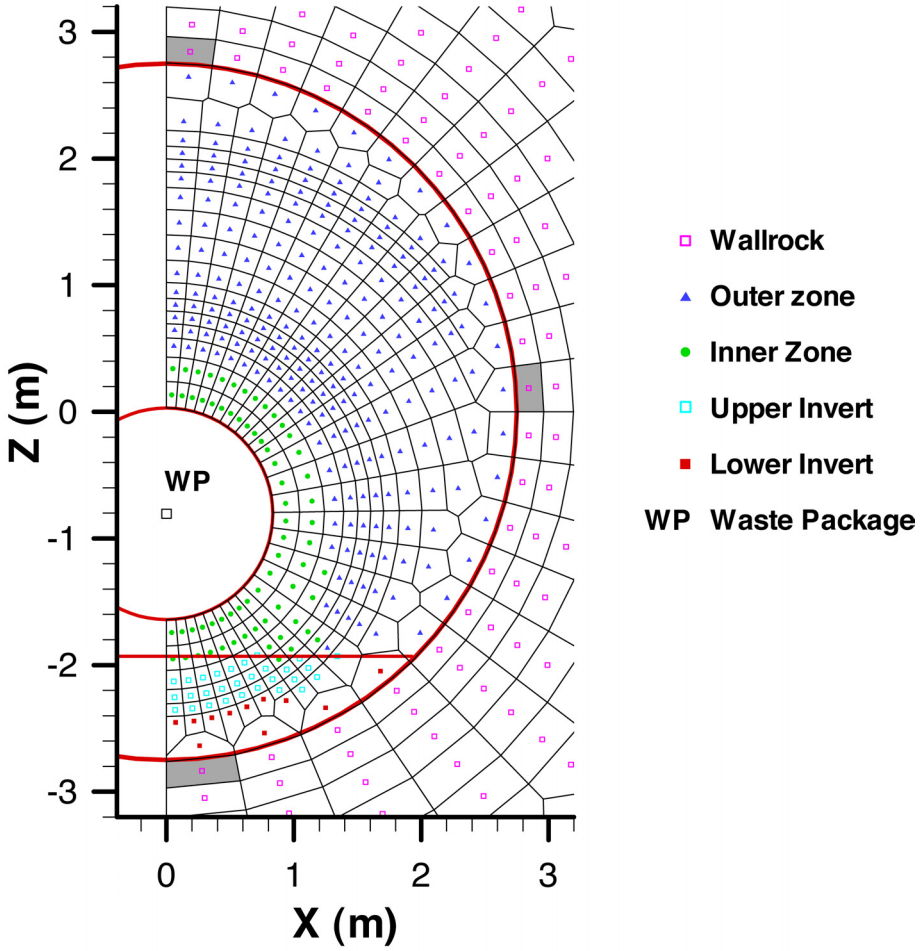

Source: BSC 2003 [DIRS 163506], Figure 6.7-2

Figure 145. Enlargement of THC Seepage Model Numerical Mesh Showing In-Drift Discretization

With this geometry, the effects up to the mid-pillar region can be evaluated, from which the potential effects to an adjacent drift may be assessed. The half-drift model is useful for assessing the initial rate of advance of the volcanic gas; however, once the concentration front reaches the mid-pillar boundary the results are no longer representative of the case in which the gas is migrating toward the adjacent drift.

A dual-permeability approach was adopted whereby coexisting fracture and rock-matrix continua are used to model the separate yet interacting effects of flow and transport in and between fractures and the rock matrix. Each continuum is assigned its own hydrological, geochemical, and mineralogical properties.

To evaluate the potential effect of gas escaping from the end of one drift and migrating through a zone of backfill in a connecting drift, a zone of approximately 5.5 m in diameter and extending from the drift to the mid-pillar region (with a locally open boundary condition) was given the hydrological (e.g., porosity is 0.545) and thermal properties of the crushed-tuff invert as a proxy for backfill material.

6.5.1.4 Boundary and Initial Conditions

The model was set up such that at the usual location of a waste package, a constant gas composition and temperature were prescribed. Two temperature regimes were considered: (1) fixed 300°C gas temperature and (2) the ambient temperature of approximately 23°C. Three cases for the pressure of the volcanic-gas-phase source were investigated: (1) fixed ambient pressure of ~0.88 bars, (2) fixed total pressure of 2 bars, and (3) fixed total pressure of 2 bars for 1 day followed by the ambient pressure. The ambient pressure was fixed to approximately 0.88 bars.

Although the 300°C used for the drift temperature is much lower than the temperature of the magma emplaced in the drift (greater than 1000°C), the wall-rock temperature would be considerably lower. As will be shown in the simulation results below, the effect of increasing temperature is to boil more water, resulting in significant amounts of vapor condensation in fractures. The increased liquid saturation in the fractures then allows for a greater mass of soluble gas species to dissolve and also to retard further gas-phase diffusion. Therefore, temperatures above 300°C are likely to retard gas transport to a greater degree. Furthermore, the effect of rock thermal expansion, which is not treated in this analysis, would reduce the fracture permeability even more at elevated temperatures, additionally reducing the migration of gas through the fracture network.

The volcanic gas composition (in mole percent) was set to 14.3 CO_2 and 9.3 percent SO_2, with the water content fixed to that given by the pressure-temperature conditions for a vapor plus air mixture calculated by TOUGHREACT V3.0 [DIRS 161256]. The CO_2 and SO_2 percentages were derived from Table 3 in Characterize Eruptive Processes at Yucca Mountain, Nevada (BSC 2001 [DIRS 160130]), which is a mean value of several measured compositions from volcanoes having different magmatic compositions (tholeiitic and alkali basalts, hawaiite, and nephelinite). The approach taken for the set-up of the volcanic gas concentration boundary conditions is considered to be conservative because the concentration is fixed to the magmatic gas composition for several years, whereas the actual volcanic gas amount would be limited by the volume of magma emplaced and its volatile content.

The initial pore-water chemistry (Table 18) was based on a sample that was ultracentrifuged from the repository host rock (Tptpmn).

Table 18. Initial Pore-Water and Gas Compositions[1]

Component or Variable	Units	Water Input Type	
		Fracture and Matrix	Boundary
Temperature	°C	25	17
pH (measured)	pH	8.31	—
pH (calc)[2]	pH	—	7.750
Na^+	mg/L	61.5	61.3
K^+	mg/L	8	8
Ca^{2+}	mg/L	101	101
Mg^{2+}	mg/L	17	17
SiO_2(aq)	mg/L	70.5	70.5
Cl^-	mg/L	117	117
SO_4^{2-}	mg/L	116	116
HCO_3^- (measured)	mg/L	—	—
HCO_3^- (calc)[2]	mg/L	200	216
NO_3^-	mg/L	6.5	6.5
F^-	mg/L	0.86	0.86
Al^{3+} (calc)[2]	molal	6.173×10^{-10}	9.775×10^{-11}
Fe^{3+} (calc)[2]	molal	1.155×10^{-12}	5.162×10^{-13}
$\log(P_{CO_2})$[2]	bars	-3.1	-2.5
CO_2 (approx)[3]	ppmv	900	3100

Sources: [1] BSC 2003 [DIRS 163506], Table 6.2-1
[2] Calculated (BSC 2003 [DIRS 163506, Table 6.2-1])
[3] Converted to ppmv using total pressure equal to one bar

NOTE: Sample ID: HD-PERM (Alcove 5) Lithostratigraphic unit: Tptpmn

6.5.1.5 Numerical Formulation

Simulations were performed using TOUGHREACT V3.0 [DIRS 161256] that couples multiphase fluid flow (water and air), heat flow, aqueous and gaseous species transport, and kinetic and equilibrium mineral-water-gas reactions. Gas species are transported via advection and diffusion. Gaseous species diffusion coefficients are calculated as a function of molecular weight, molecular diameter, temperature, and pressure, with effective diffusivities related to porosity, tortuosity, and water saturation.

6.5.1.6 Results

The following discussion describes briefly some of the relevant results pertaining to gas transport over time from the five model simulations. Included in the data submittal (Output DTN: LB0306AMRT0020.001) are results for all aqueous and gaseous species concentrations over time, changes to mineral abundances, as well as pressure, temperature, and changes to hydrological properties. The model scenarios discussed in this section are:

- Model I: Elevated-Temperature Gas Transport—Effect of a constant-300°C-temperature, ambient-pressure gas source in the drift
- Model II: Low-Temperature Gas Transport—Effect of a constant-ambient-temperature, ambient-pressure gas source in the drift
- Model III: Gas Transport Through a Backfilled Connecting Drift (at 300°C)—Effect of a constant-300°C-temperature, constant-ambient-pressure gas source in the drift, connected to a backfilled drift
- Model IV: Elevated-Temperature-and-Pressure Gas Transport—Effect of a constant-300°C-temperature and constant-2 bar-total-pressure gas source in the drift
- Model V: Elevated-Temperature-and-Pressure (1-Day) Gas Transport—Effect of a constant-300°C-temperature and a 2-bar-total-pressure gas source for 1 day in the drift, followed by ambient pressure conditions

Several other simulations were also performed to assess the effect of time-step size on the results, as well as different conceptualizations of the boundary conditions. Documentation of these sensitivity studies can be found in Wang (2003 [DIRS 164068], pp. 1–32).

6.5.1.6.1 Model I: Elevated-Temperature Gas Transport

Volcanic gas temperature is fixed at 300°C and the pressure at ~0.88 bar in the drift.

Modeled distributions of CO_2 concentrations (log-volume fractions) and temperature are shown at 1 year, 5 years, 10 years, and 20 years in Figure 146. The higher temperature near the drift (between approximately the 100°C and 200°C isotherms) results in CO_2 increasing in the vapor phase through degassing of the pore water as well as diffusion from the volcanic gas source in the drift. After 5 years, higher-CO_2-concentration regions are restricted to the area above the drift (between approximately the 40°C and 80°C isotherms).

Figure 147 shows modeled SO_2 concentrations (log-volume fractions) and temperature after 1, 5, 10, and 20 years. The white color in Figures 147 through 159, except for Figure 154, indicates values lower than indicated by dark red. The distribution of SO_2 concentrations is similar to the distribution of CO_2 concentrations except that the SO_2 concentrations are lower. The advance of SO_2 is slower as a result of its greater solubility and smaller diffusivity.

Figure 148 shows the changes in pH and temperature after 1, 5, 10, and 20 years. In general, pH decreases as CO_2 concentrations increase. In the region where CO_2 declines due to boiling, the pH increases. This high-pH region enlarges and moves away from the center of the drift with time.

The development of a boiling zone appears to be an important factor in retarding the transport of gas out of the drift for a at least two reasons. First, the boiling zone creates a region of higher pressure in the rock that forces vapor back to the drift. Second, boiling of water out of the matrix creates a zone of condensation in the fractures. This phenomenon promotes a greater quantity of gas to be dissolved, which is followed by strong drainage of the condensate water because of the high fracture permeability. Comparison to the simulation described below performed at ambient temperature confirms this interpretation.

6.5.1.6.2 Model II: Low-Temperature Gas Transport

Model II considers the same volcanic gas components (H_2O, CO_2, and SO_2) and pressure as Model I but with lower temperature (22.8°C). Compare Model II with Model I.

Modeled distributions of CO_2 concentrations (log-volume fractions) are shown after 1, 5, 10, and 20 years in Figure 149. In this model, the high-CO_2-concentration region increases in a radial pattern with time (before 20 years). Gas-phase CO_2 decreases as the distance from drift increases. Because of the low initial gas temperature (at 22.8°C), CO_2 does not increase in the gas phase due to degassing of pore water. After 20 years, the volcanic gas CO_2 has already reached the 40-m mid-pillar region.

Figure 150 shows modeled SO_2 concentrations (log-volume fractions) after 1, 5, 10, and 20 years. The distribution of SO_2 concentrations is similar to that of CO_2 except the SO_2 migrates more slowly than CO_2 as a result of its smaller diffusivity and greater solubility. The higher SO_2 concentration front only reaches 20 m after 20 years.

Figure 151 shows changes in pH after 1, 5, 10, and 20 years from Model II. Because of the high CO_2 concentration, pH decreases with time. The region close to the drift has the lowest pH as a result of the increased partial pressure of CO_2.

Even though the solubilities of CO_2 and SO_2 are higher and the diffusivity smaller at lower temperatures, the migration of these gas species away from the drift is greater under ambient temperatures. This effect can be attributed to the absence of a boiling zone that retards the migration of these soluble species.

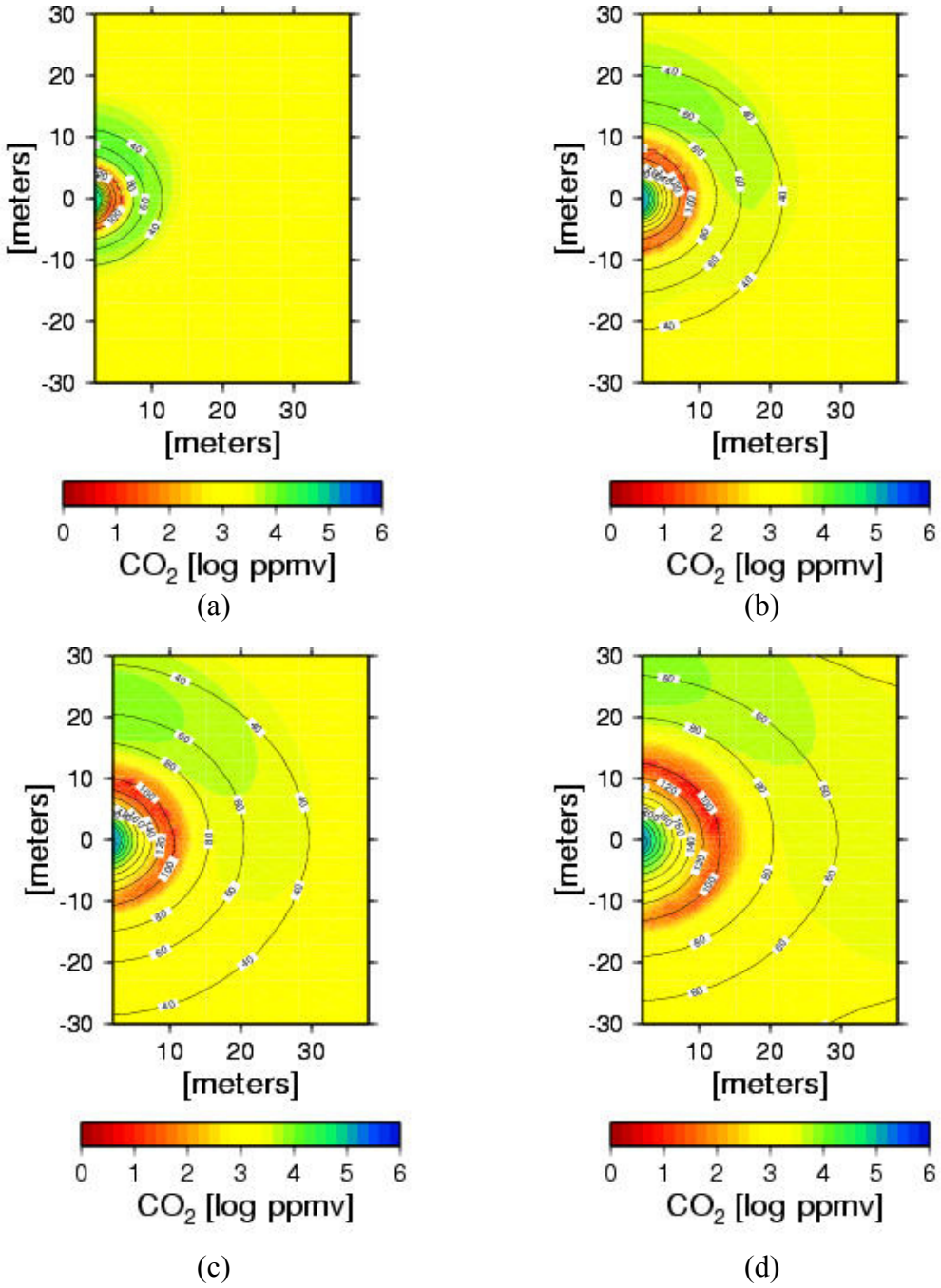

Output DTN: LB0306AMRT0020.001

Figure 146. Gas-Phase CO_2 Concentration (colors) and Temperature (contour lines) Around the Drift in Model I After (a) 1 Year, (b) 5 Years, (c) 10 Years, and (d) 20 Years

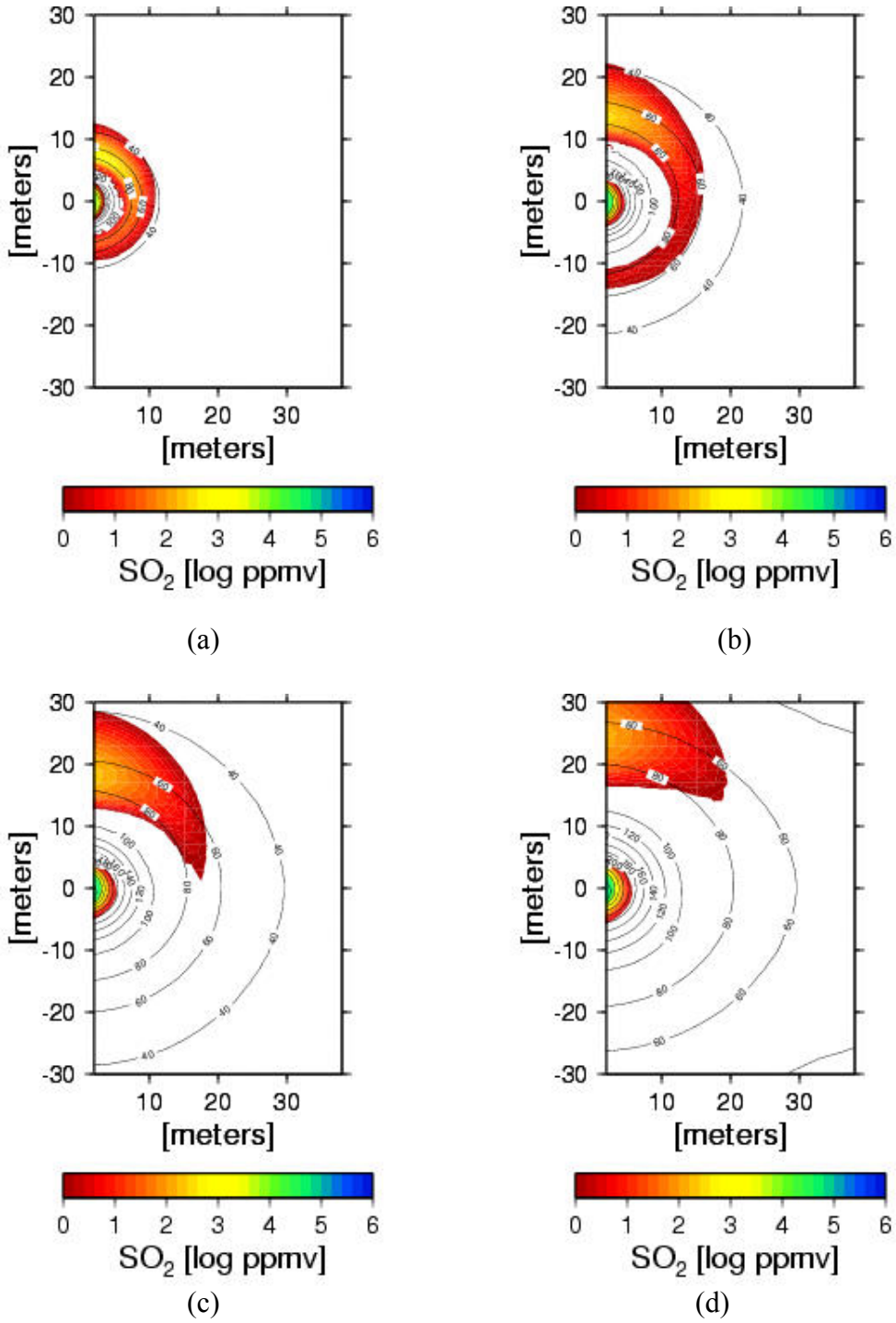

Output DTN: LB0306AMRT0020.001

Figure 147. Gas-Phase SO_2 Concentration (colors) and Temperature (contour lines) Around the Drift in Model I After (a) 1 Year, (b) 5 Years, (c) 10 Years, and (d) 20 Years

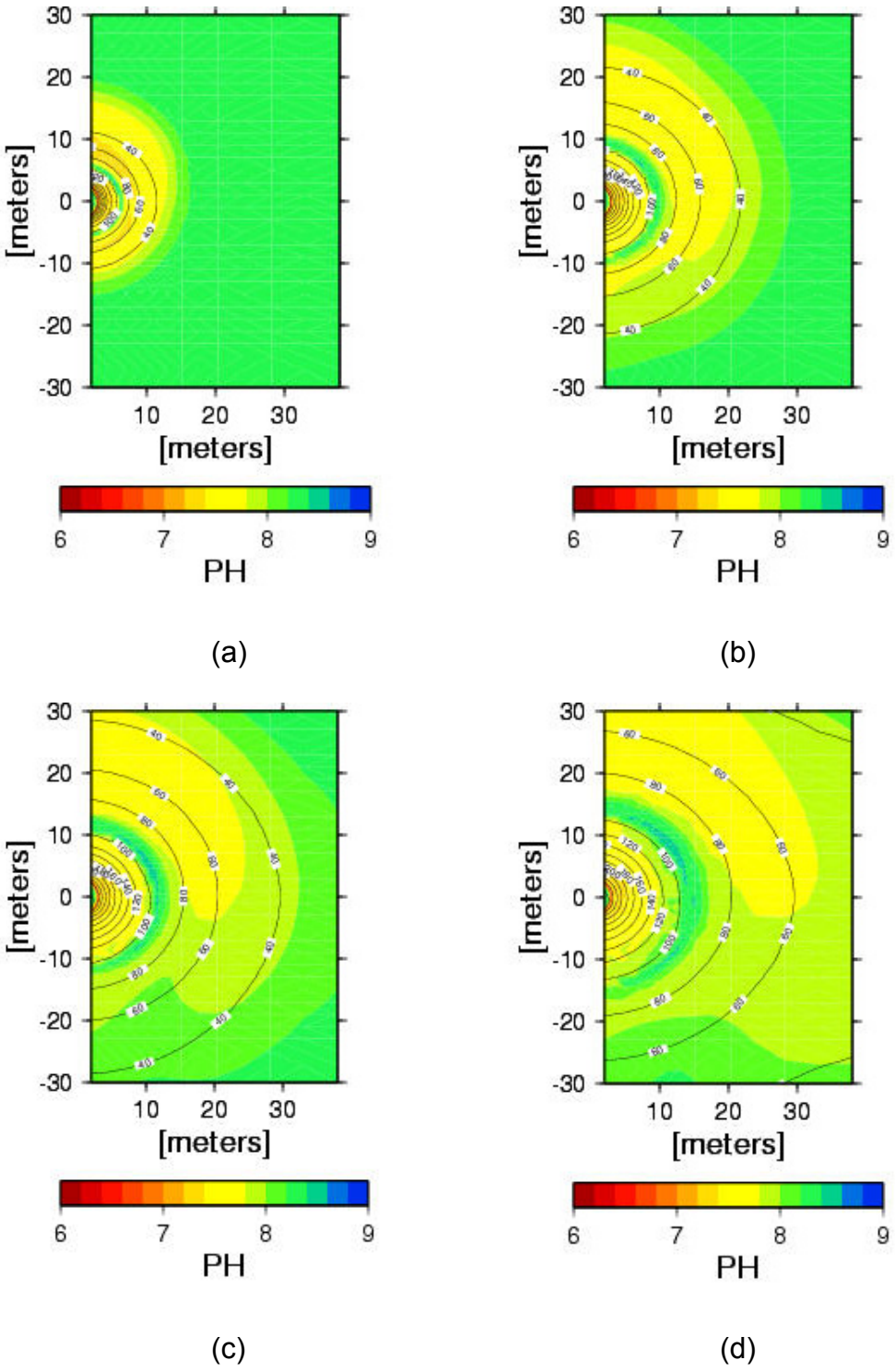

OUTPUT DTN: LB0306AMRT0020.001

Figure 148. Distribution of pH (colors) and Temperature (contour lines) Around the Drift in Model I After (a) 1 Year, (b) 5 Years, (c) 10 Years, and (d) 20 Years

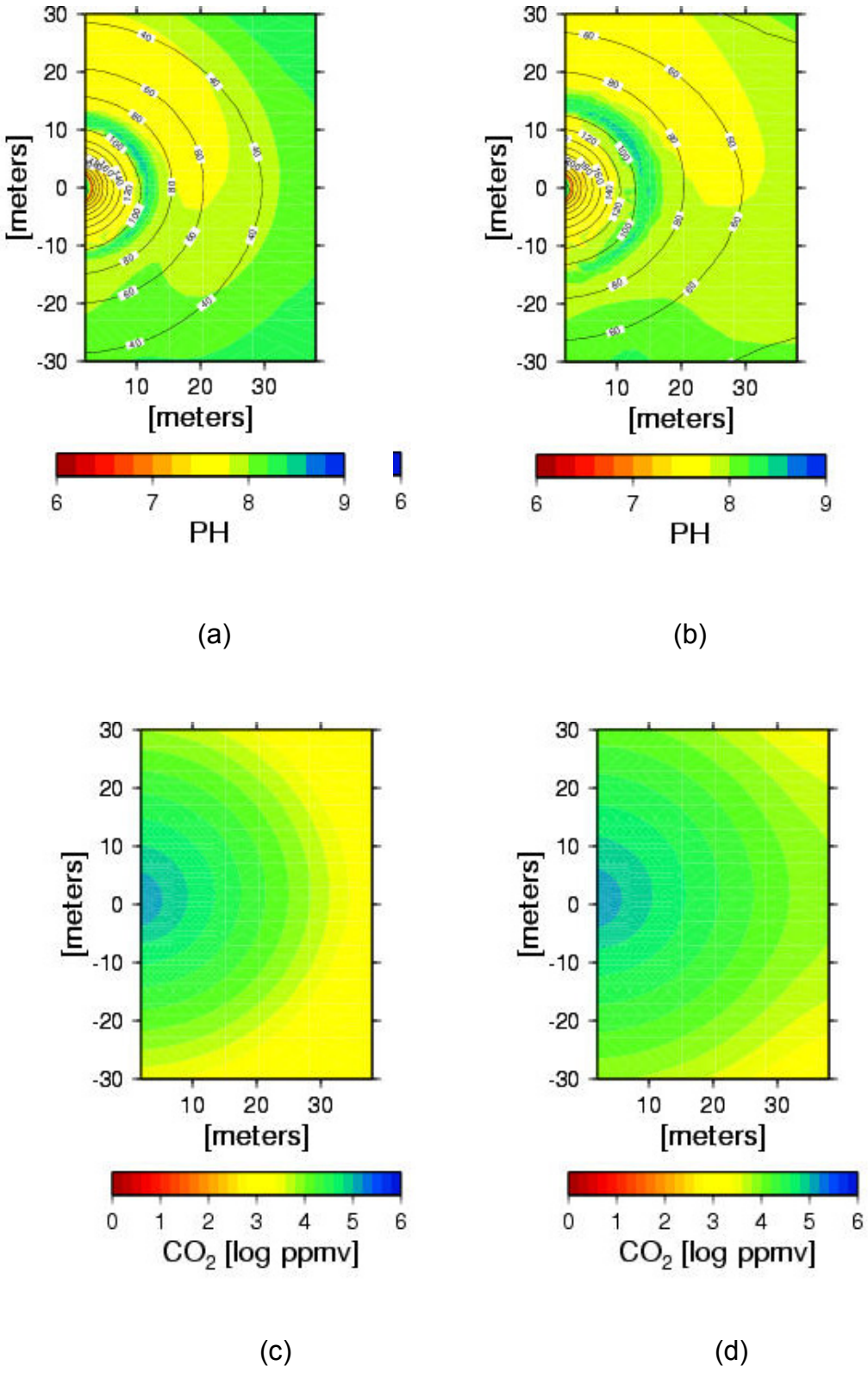

Output DTN: LB0306AMRT0020.001

Figure 149. Gas-Phase CO_2 Concentration (colors) Around the Drift in Model II After (a) 1 Year, (b) 5 Years, (c) 10 Years, and (d) 20 Years

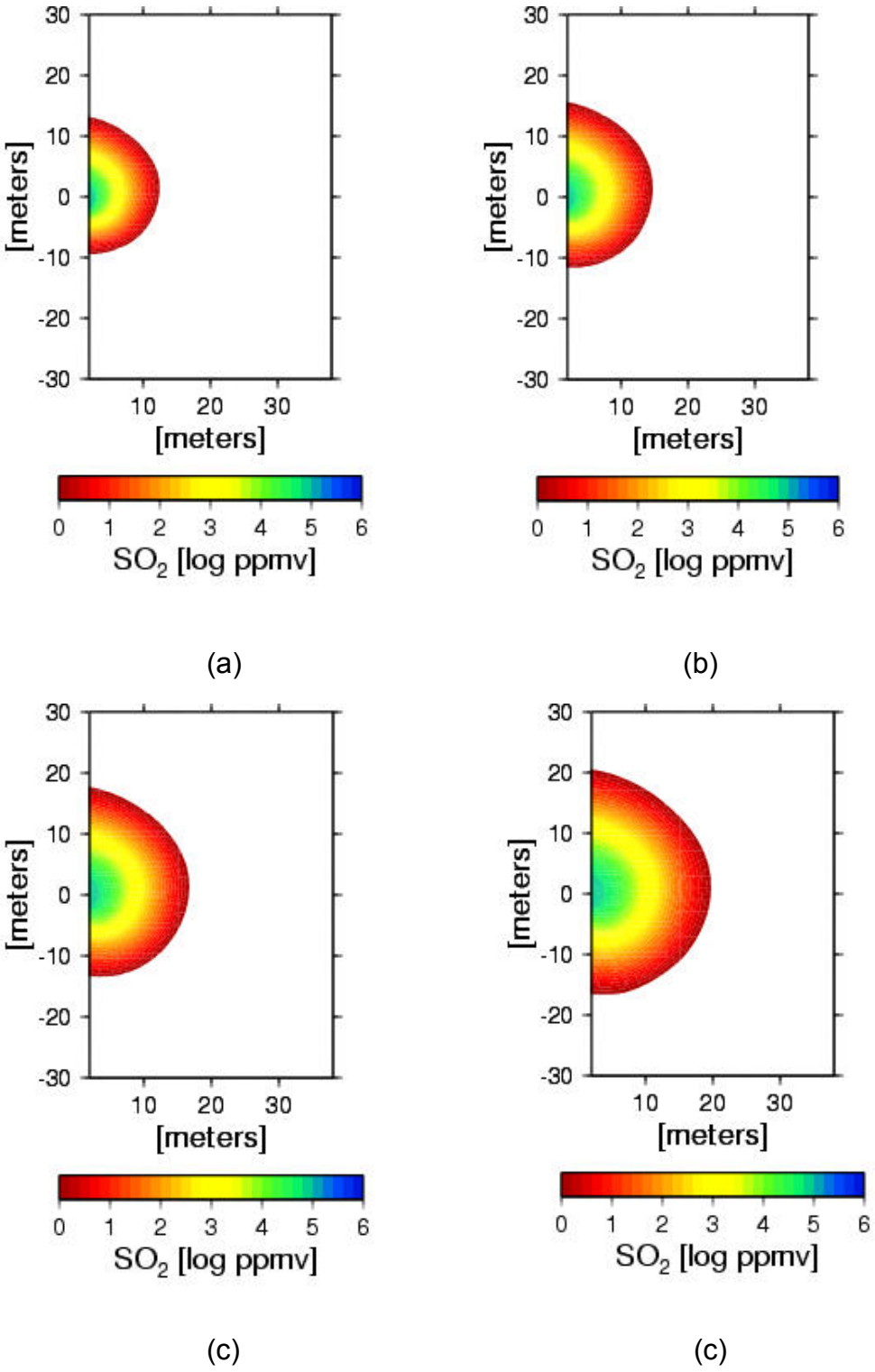

Output DTN: LB0306AMRT0020.001

Figure 150. Gas-Phase SO_2 Concentrations Around the Drift in Model II After (a) 1 Year, (b) 5 Years, (c) 10 Years, and (d) 20 Years

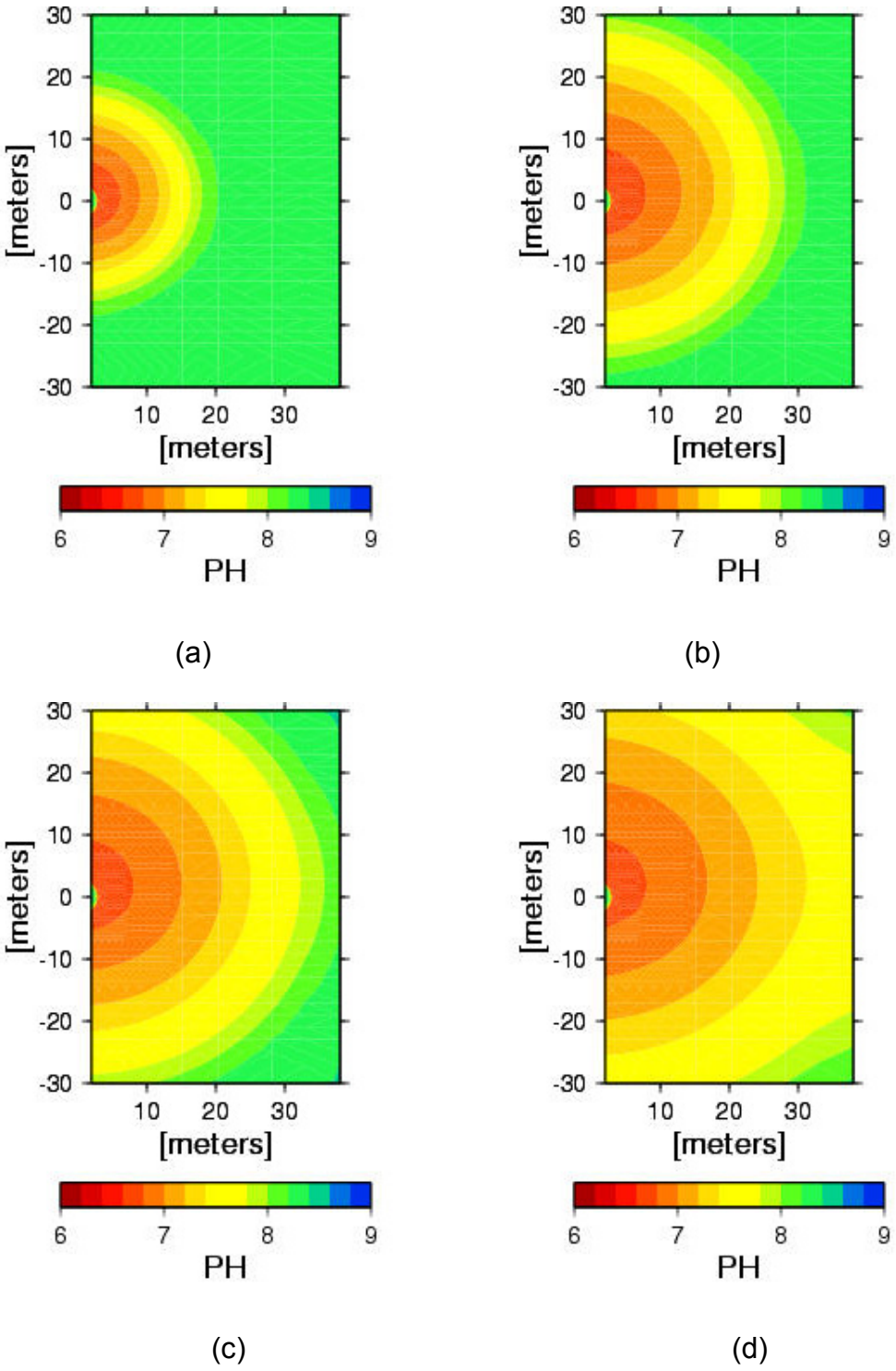

Output DTN: LB0306AMRT0020.001

Figure 151. Distribution of pH Around the Drift in Model II After (a) 1 Year, (b) 5 Years, (c) 10 Years, and (d) 20 Years

6.5.1.6.3 Model III: Gas Transport through a Backfilled Connecting Drift (at 300°C)

Model III considers the same volcanic gas components, temperature (300°C), and pressure (~0.88 bar) as Model I. This model considers a horizontal region (about 5.5 m in width) filled with crushed tuff extending from the drift wall to the right boundary of the model. The backfill material is given the same porosity as the invert (0.545; BSC 2003 [DIRS 163506] Table 4.1-5). The saturation of the crushed tuff is considered to be zero initially (BSC 2003 [DIRS 163506]). The purpose of this model is to study the migration of volcanic gas through a backfilled connecting drift.

Modeled distributions of CO_2 concentrations (log-volume fractions) are shown after 10 days, 20 days, 30 days, and 40 days in Figure 152. A high-CO_2-concentration region migrates rapidly along the horizontal region that is filled with crushed tuff. At 45 days, volcanic CO_2 reaches the distance of 30 m along the backfilled connecting drift.

Figure 153 shows modeled SO_2 concentrations (log-volume fractions) after 10 days, 20 days, 30 days, and 40 days.

Figure 154 shows the distribution of pH at 10 days, 20 days, 30 days, and 40 days from Model III. The black color in Figure 154 indicates pH below 6. Two low-pH regions extend horizontally along the edges of the backfilled tunnel from the drift toward to the right. These regions formed through diffusion of CO_2 into the rock, followed by dissolution in the ambient pore water and a lowering of the pH. Disturbances seen at about 2-8 m and 14-18 m are numerical artifacts caused by mesh irregularities.

Simulation results are shown only for 40 days because gas transport is much more rapid through this material, reaching the boundary 40.5 m away in less than 1.5 months. Temperatures are slightly depressed in this zone relative to that in the rock because of the low thermal conductivity of this mostly gas-filled porous material and the lack of a significant advective component out of the drift, which would result in higher temperatures and faster gas migration. Although in the actual system, vapor condensation and redox reactions would likely cause some retardation of the gas migration front, these reactions would likely not be a major factor because of the high porosity and low water saturation of the crushed tuff.

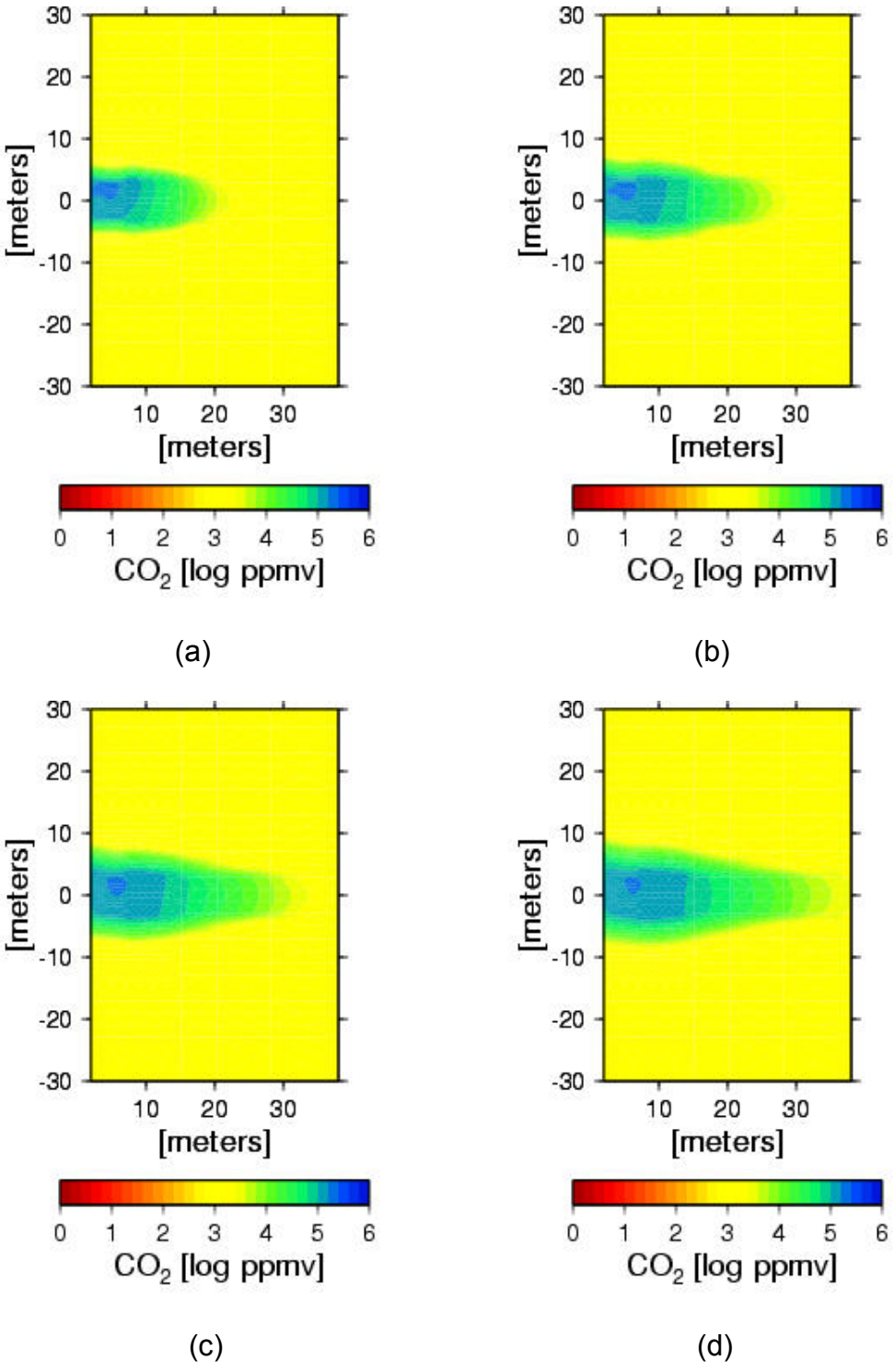

Output DTN: LB0306AMRT0020.001

Figure 152. Gas-Phase CO_2 Concentration (colors) in Model III After (a) 10 Days, (b) 20 Days, (c) 30 Days, and (d) 40 Days

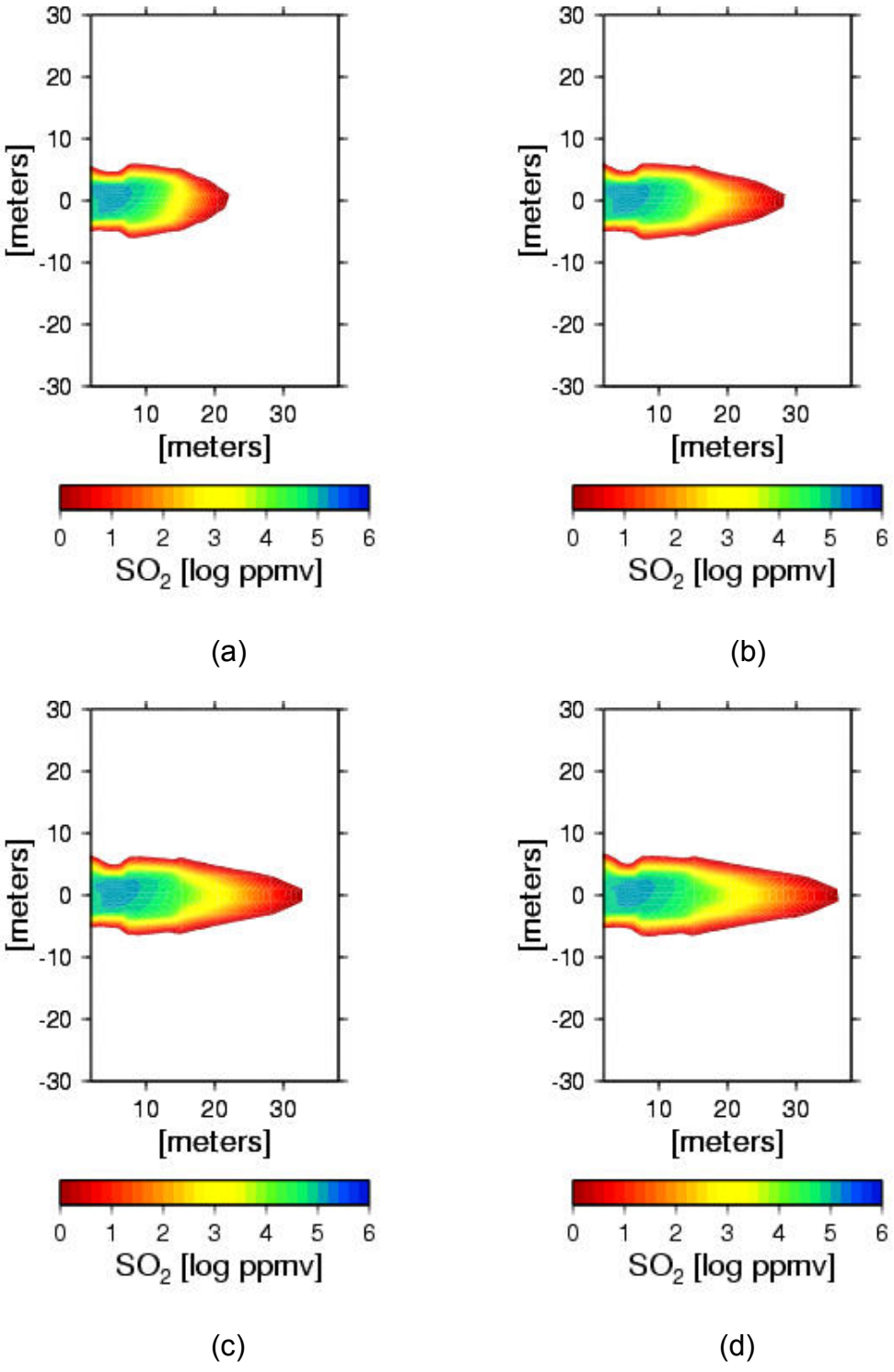

Output DTN: LB0306AMRT0020.001

Figure 153. Gas-Phase SO_2 Concentrations in Model III After (a) 10 Days, (b) 20 Days, (c) 30 Days, and (d) 40 Days

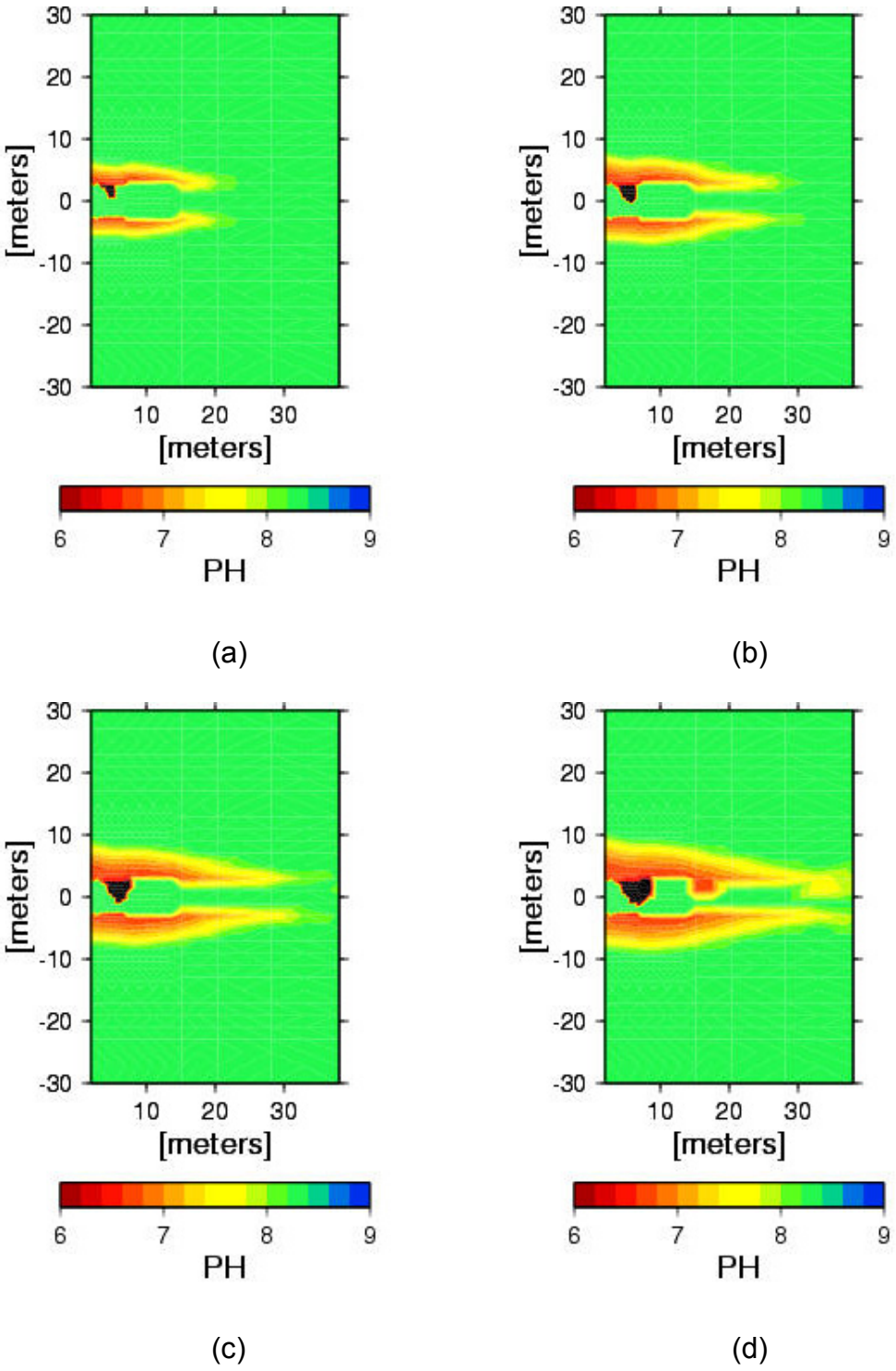

Output DTN: LB0306AMRT0020.001

Figure 154. Distribution of pH in Model III After (a) 10 Days, (b) 20 Days, (c) 30 Days, and (d) 40 Days

6.5.1.6.4 Model IV: High-Temperature-and-Pressure (300°C and 2 bars) Gas Transport

Model IV considers the same volcanic gas components and temperature (300°C) as Model I but with fixed pressure at 2 bars. The purpose of this model is to study how volcanic gas is transported through the fractured tuff at higher pressure.

Modeled distributions of CO_2 concentrations (log-volume fractions) are shown after 1 day, 15 days, and 0.1 year in Figure 155. The higher gas pressure results in rapid CO_2 transport through fractures. In less than 0.1 year, elevated CO_2 concentrations in fractures reach approximately 30 m from the drift.

Figure 156 shows modeled SO_2 concentrations (log-volume fractions) after 1 day, 15 days, and 0.1 year. The advance of SO_2 is slower as a result of its greater solubility and smaller diffusivity.

Figure 157 shows changes in pH at 1 day, 15 days, and 0.1 year from Model IV. The whole region near the drift (< 30 m) has a low pH value of approximately 6.

6.5.1.6.5 Model V: High-Temperature-and-Pressure (300°C and 2 bars for 1 day then 0.88 bar) Gas Transport

Model V was run in two phases: Phase I fixed the volcanic gas temperature at 300°C and the pressure at 2 bars for 1 day. Phase II fixed the volcanic gas temperature at 300°C and the ambient gas pressure at approximately 0.88 bar for 10 years. The purpose of this model was to study how volcanic gas is transported when the pressure is elevated for a relatively short period.

Modeled distributions of CO_2 concentrations (log-volume fractions) are shown after 1 day, 0.1 year, 1 year, and 10 years in Figure 158. By comparing with the results of Model I at 1 year and 10 years, it is evident that after the first day under higher pressure (2 bars) there is a much greater advance of the volcanic gas through the fracture network.

Figure 159 shows modeled SO_2 concentrations (log-volume fractions) after 1 day, 0.1 year, 1 year, and 10 years.

Figure 160 shows changes in pH after 1 day, 0.1 year, 1 year, and 10 years from Model V. Volcanic gas (with high pressure) causes a significant region with low pH after the first day. The pH value increases with time as CO_2 is evolved from the aqueous phase.

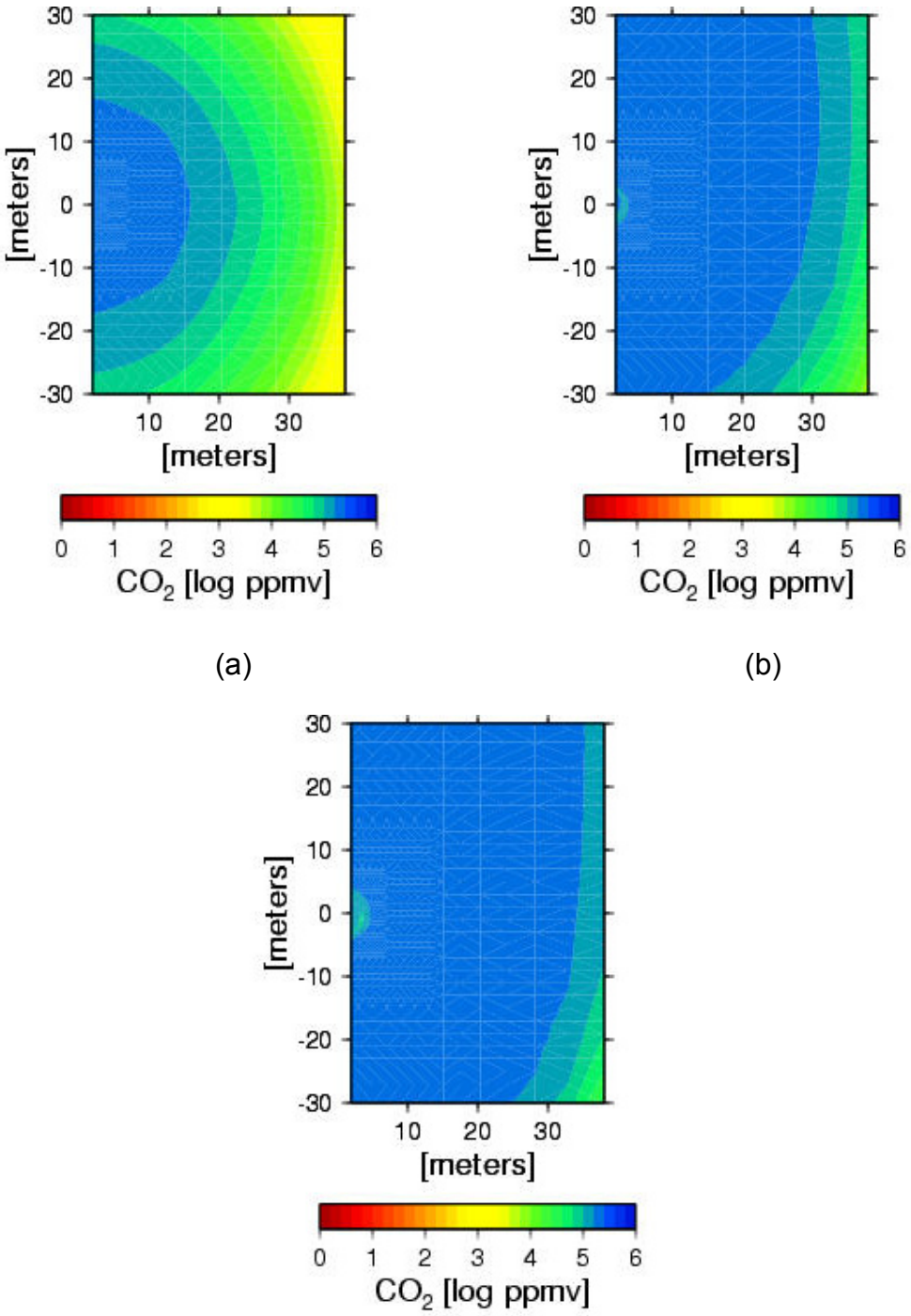

Output DTN: LB0306AMRT0020.001

Figure 155. Gas-Phase CO_2 Concentrations Around the Drift in Model IV After (a) 1 Day, (b) 15 Days, and (c) 0.1 Year

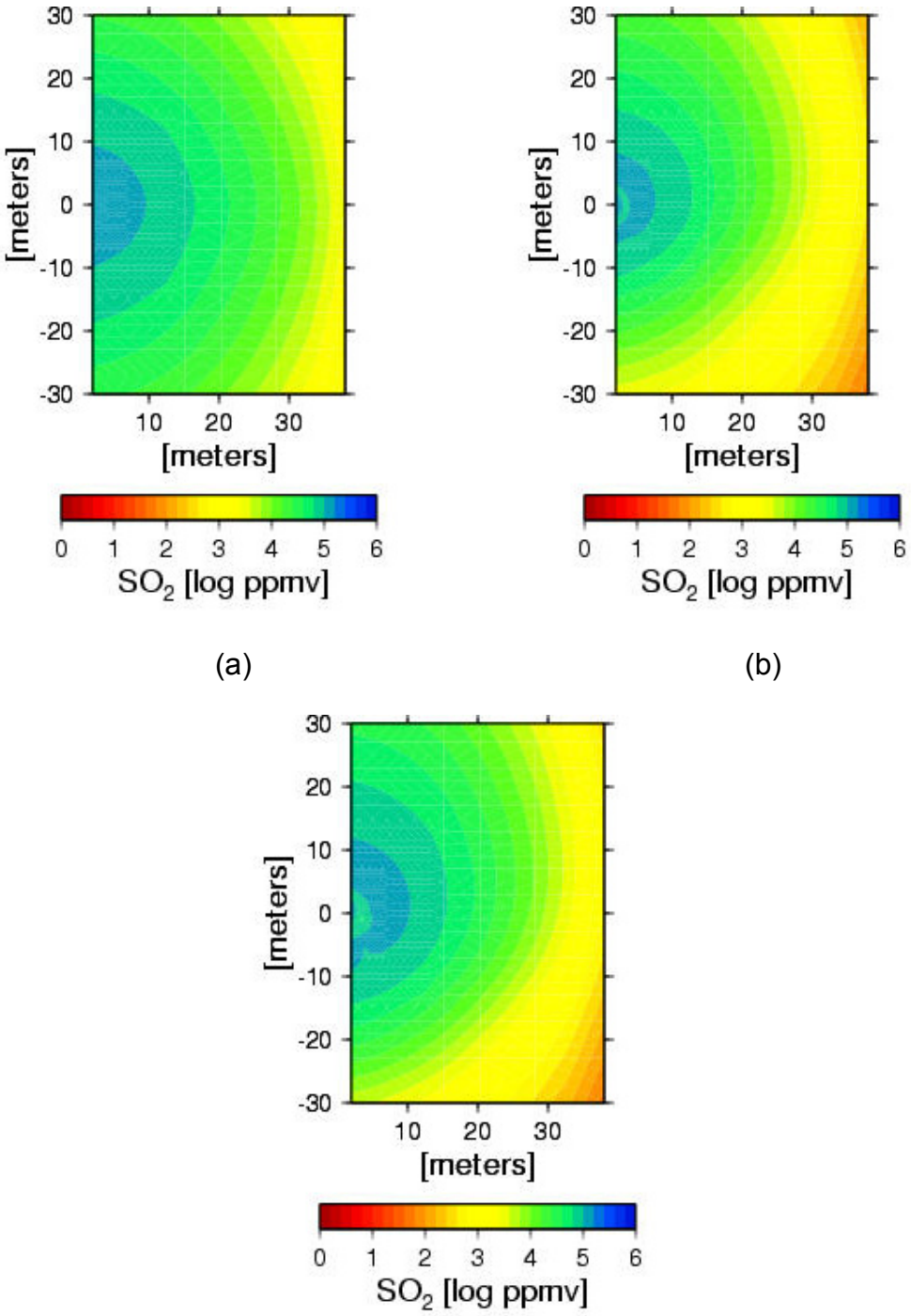

Output DTN: LB0306AMRT0020.001

Figure 156. Gas-Phase SO_2 Concentrations Around the Drift in Model IV After (a) 1 Day, (b) 15 Days, and (c) 0.1 Year

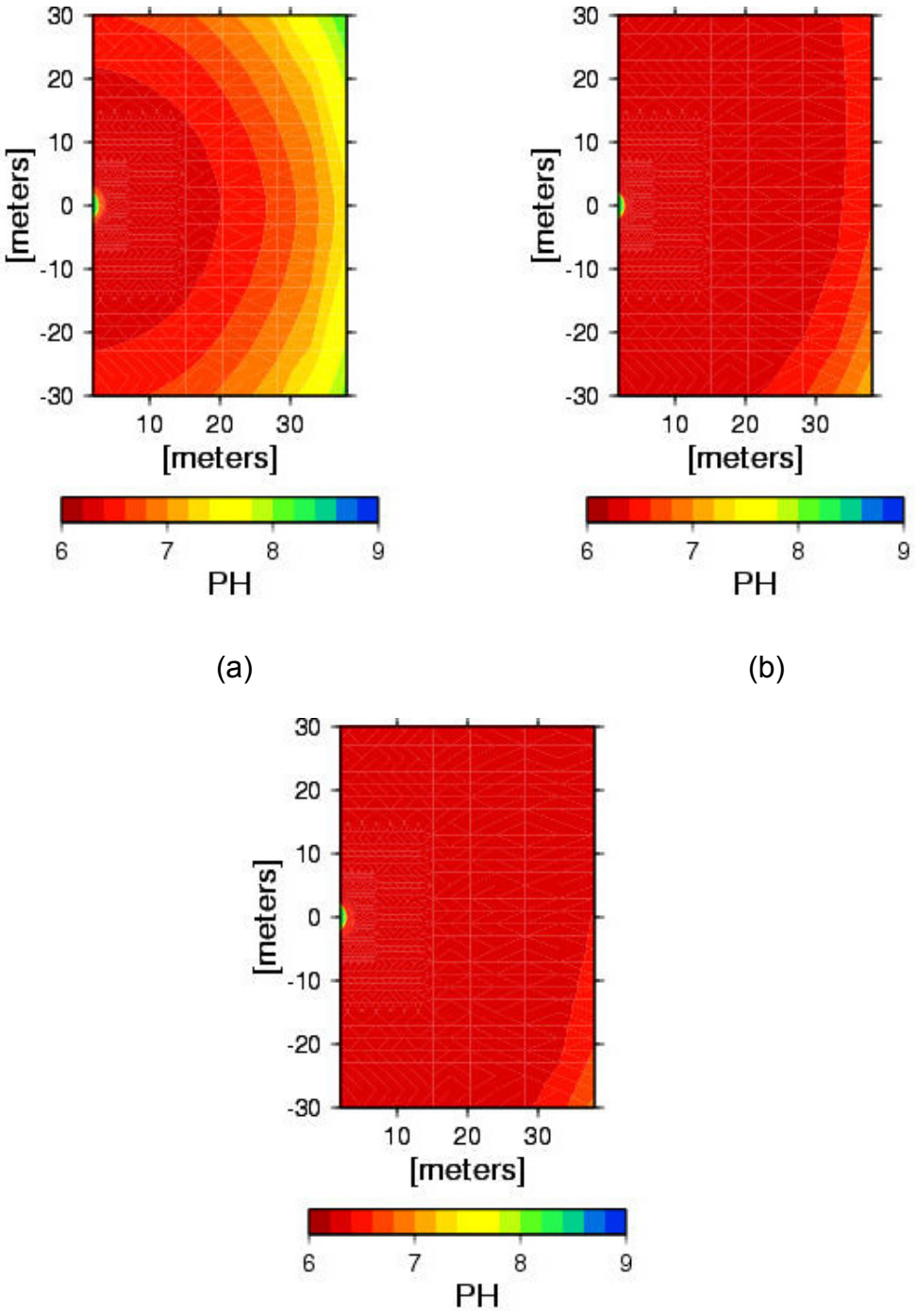

Output DTN: LB0306AMRT0020.001

Figure 157. Distribution of pH Around the Drift in Model IV After (a) 1 Day, (b) 15 Days, and (c) 0.1 Year

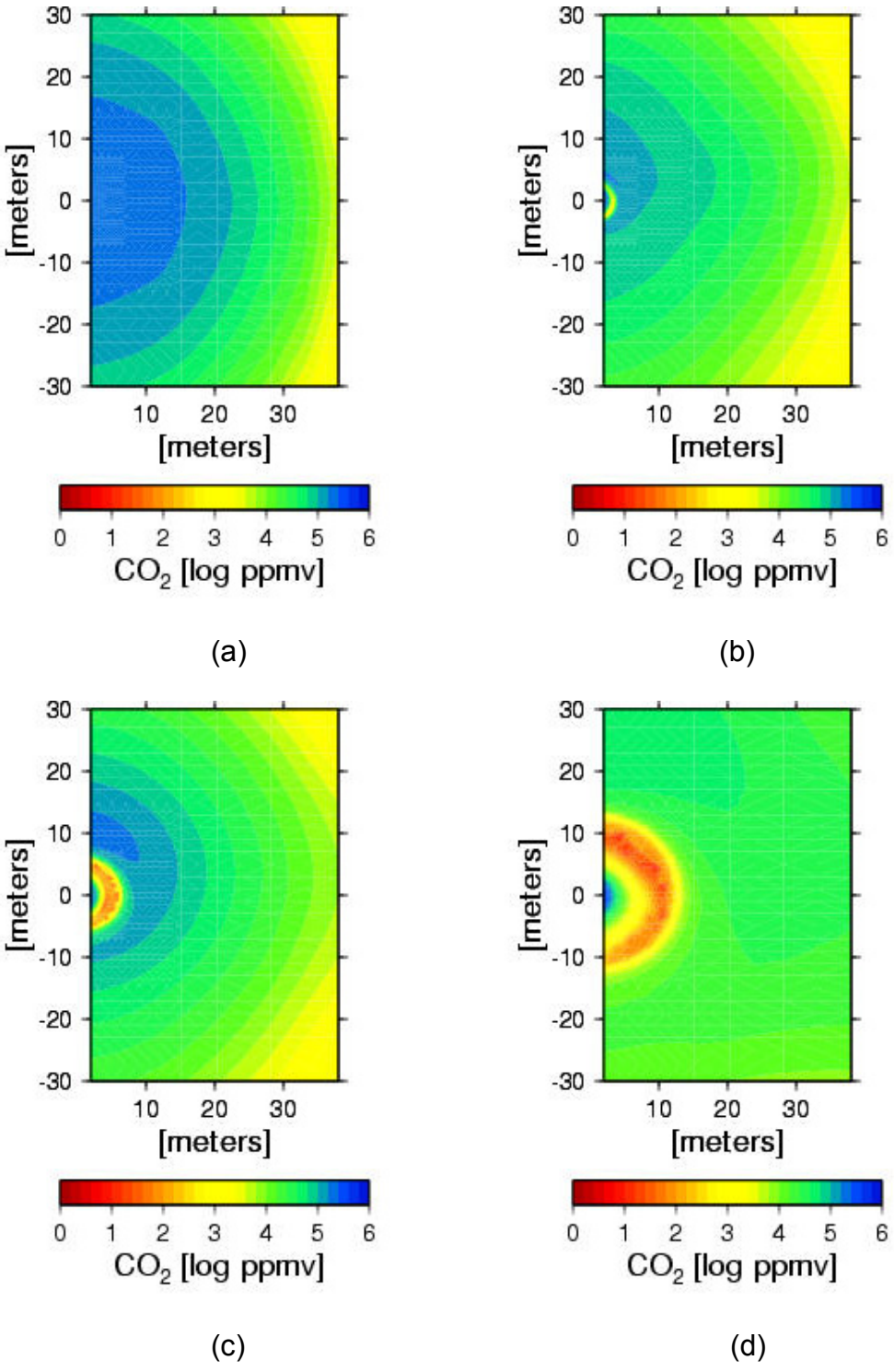

Output DTN: LB0306AMRT0020.001

Figure 158. Gas-Phase CO_2 Concentrations Around the Drift in Model V After (a) 1 Day, (b) 0.1 Year, (c) 1 Year, and (d) 10 Years

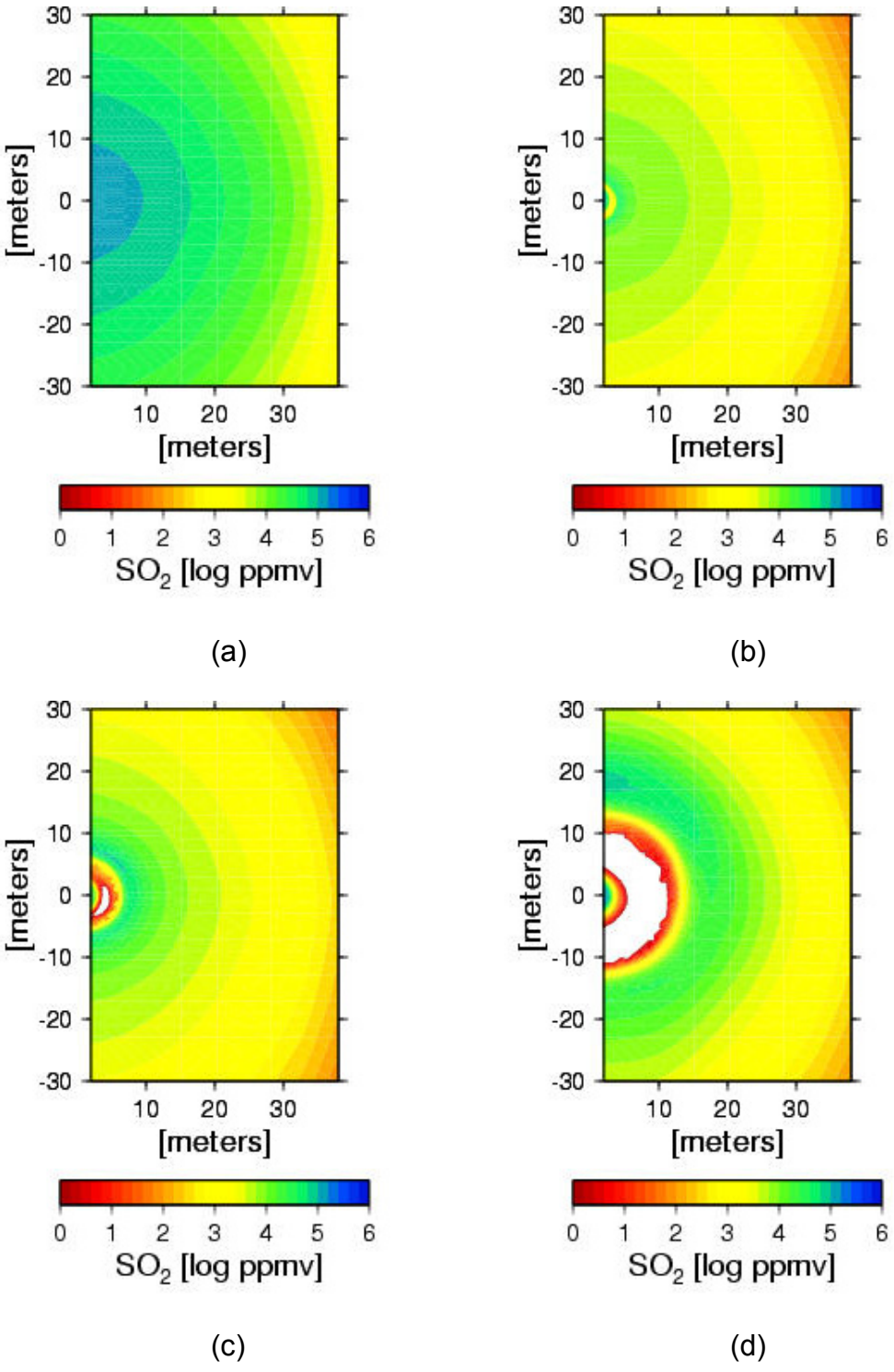

Output DTN: LB0306AMRT0020.001

Figure 159. Gas-Phase SO_2 Concentrations Around the Drift in Model V After (a) 1 Day, (b) 0.1 Year, (c) 1 Year, and (d) 10 Years

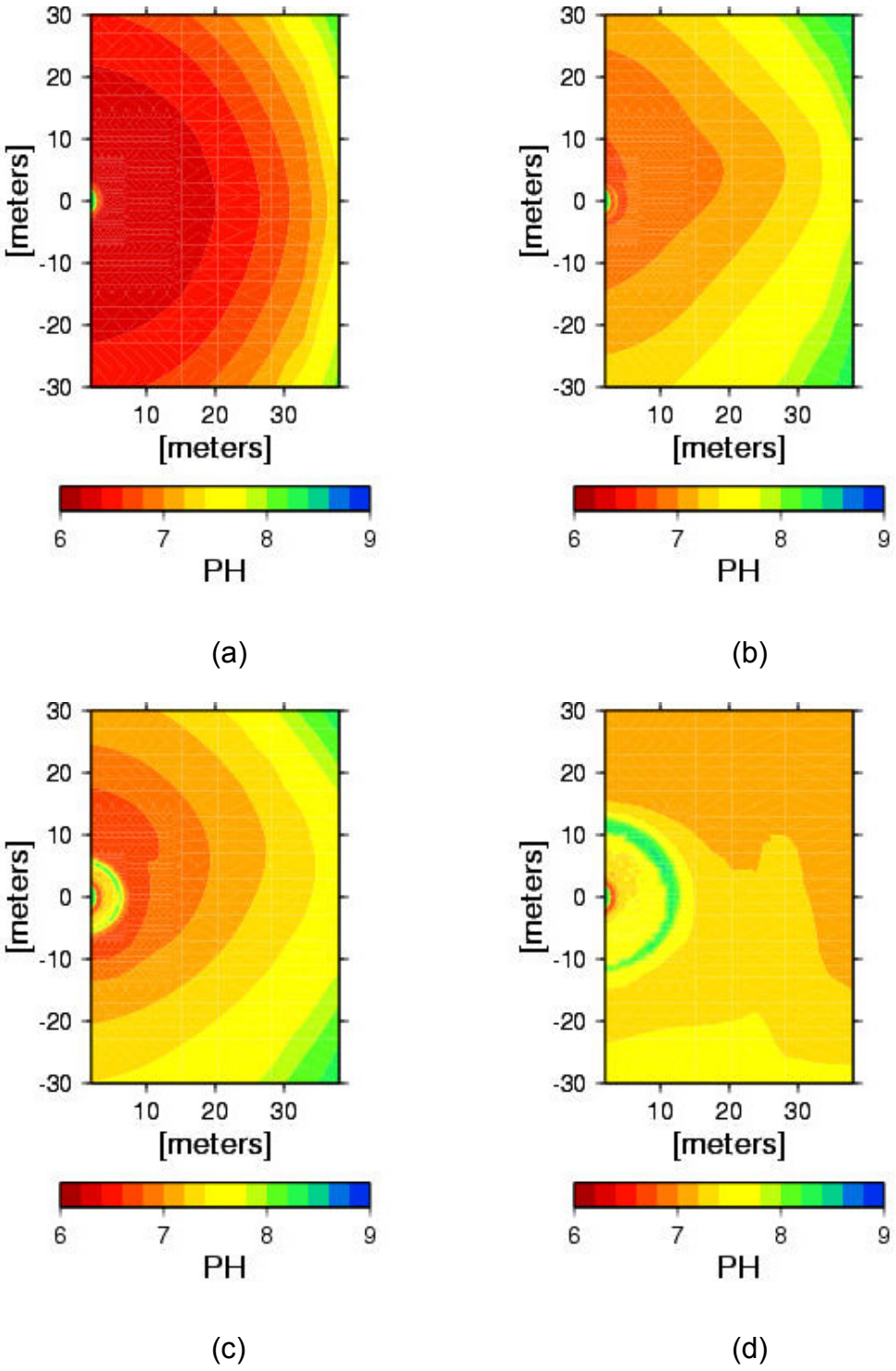

Output DTN: LB0306AMRT0020.001

Figure 160. Distribution of pH Around the Drift in Model V After (a) 1 Day, (b) 0.1 Year, (c) 1 Year, and (d) 10 Years

6.5.1.6.6 Summary

The high solubility in water of SO_2 (and to a lesser extent CO_2), along with the development of a boiling zone around a drift where magma has been emplaced, limits the migration of these gases through the repository host rock. The model results under ambient pressure conditions indicate that these gases would not migrate to an adjacent drift through the rock in less than ten years. This period of time is significantly longer than the period over which any significant amount of volcanic gas would be present from the single intrusion of magma into a 5.5-m diameter drift. In addition to the dissolution of SO_2 into the aqueous phase, oxidation-reduction reactions involving sulfur species that were not considered in the model would further retard gas migration in two ways. First, the mineral-water reactions would generate sulfide or sulfate phases. Second, sulfur reduction would likely result in acidic fluids, thus enhancing mineral alteration in fractures. The resulting formation of clay minerals in fractures would reduce the permeability, thereby retarding further migration of gas through the rock.

The transport of gas through the fracture network is more extensive under ambient temperatures than an elevated temperature regime in which boiling takes place. The development of a boiling zone results in increased liquid saturation in the fractures (owing to vapor condensation) and therefore a smaller effective permeability for gas and also increased dissolution of the gas phase into the water in the fractures. Therefore, although the model did not consider the temperature history of a cooling and crystallizing magma in a drift, it can be shown to be conservative with respect to the processes involved in gas migration in the rock.

Under prolonged elevated pressure conditions (2 bars for 1 day or more), gas transport through the relatively dry high-permeability fractured tuff is rapid. However, the volume of the gas would be relatively small because it is moving through fractures that make up less than 1 percent of the total rock volume (BSC 2003 [DIRS 163506] Table 6.4-1). After the pressure subsides back to ambient values, the CO_2 and SO_2 in the fractures diffuse into the rock matrix where they dissolve readily and are immobilized. Reductions in pH in the pore fluid reflect the diffusion of gas into the rock and subsequent CO_2 dissociation.

Volcanic gas migration may also be relatively rapid through a connecting drift filled with coarse crushed tuff. In this case, an adjacent emplacement drift could be affected by migrating volcanic gas within a year or less without any strong advective flow due to large pressure differences, if the gas production is constant for some time (a month or longer). As the gas migrates through the connecting drifts and into a neighboring emplacement drift, the volcanic gas will be diluted by air, and as the gas source from the magma declines over time the extent of dilution by air will increase. The crushed tuff filling the connecting drifts would likely have some initial water content, and therefore retardation of the gas would likely be somewhat greater than the case modeled.

In addition to the dissolution of SO_2 into the aqueous phase, oxidation-reduction reactions involving sulfur species that were not considered in the model would further retard gas migration in two ways. First, the mineral-water reactions would generate sulfide or sulfate phases. Second, sulfur reduction would likely result in acidic fluids, thus enhancing mineral alteration in fractures. The resulting formation of clay minerals in fractures would reduce the permeability, thereby retarding further migration of gas through the rock.

Note that a gas flow analysis is also addressed in *Igneous Intrusion Impacts on Waste Package and Waste Form* (BSC 2003 [DIRS 161810]), and those results are consistent with the results presented above.

6.5.2 Magma Cooling and Solidification

The thermal history of a magma-filled drift after filling will impact the evolution of the integrity of the waste packages and the waste form and also will affect the movement of volatile phases through the pore volume of the surrounding rock. Therefore, this section discusses the dispersal of the heat associated with the magma over the years following intrusion.

6.5.2.1 Problem Definition

Consider a drift 5.5 m in diameter and 637 m long created in tuff at a depth of 300 m below the surface and where the ambient tuff temperature is 30°C. If that drift were to be instantaneously filled with basaltic magma at a temperature of 1150°C, the tuff surrounding the drift would begin to heat up as the magma cooled. The temperature profile through the drift and surrounding rock evolves with time.

Analysis of energy conservation can only provide exact solutions for thermal evolution when simplifying assumptions are made about the effects of dimensionality, latent heat, and contrasting thermal properties. These simplifying assumptions are necessary to make analytical solutions bear any resemblance to the problem, but the results must be regarded as approximate.

The analytical theory described below derives a solution first in Cartesian coordinates, treating the drift as a slab, and then in cylindrical coordinates, treating the drift as an infinitely long cylinder. Because solutions for the effects of latent heat are only valid for cooling times up to the point of complete solidification of the magma, late-time solutions must employ an approximate solution mated to the early time solution. To these results are added the effects of contrasting thermal properties between the magma and tuff.

Calculations based on these solutions were performed in the Microsoft Excel™ 2000 (SP 3) spreadsheet file: *Analytical Solutions of Heat Flow.xls*, which is documented in Scientific Notebook SN-LANL-SCI-279-V1, pp. 17 to 30 (Gaffney 2002 [DIRS 163631]). These results are shown for radial distances from the drift to 40.5 m (half of the nominal spacing between parallel drifts) and are discussed and shown in Figure 161 through Figure 166.

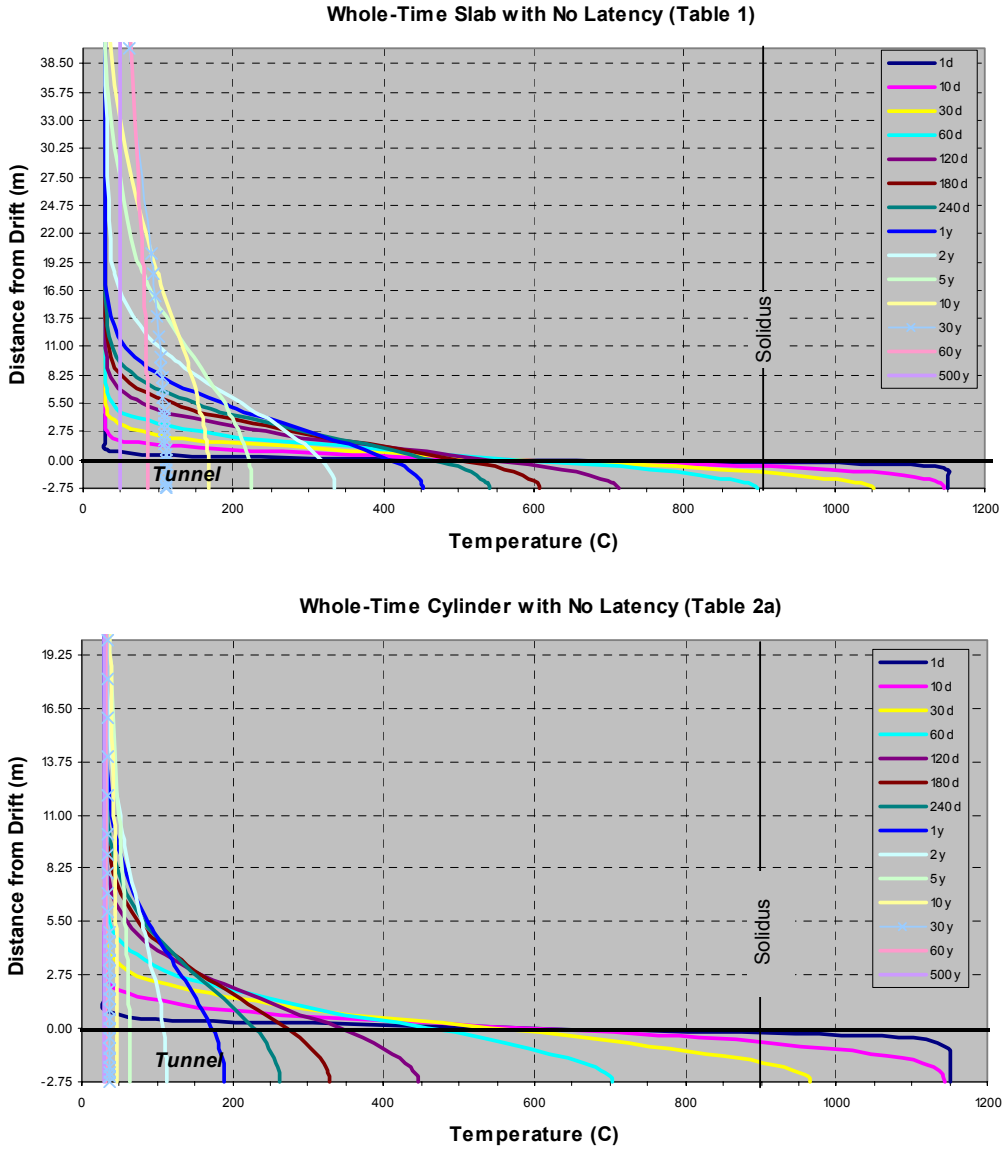

Output DTN: LA0307EG831811.001

NOTES: Tables 1 and 2a are found in the spreadsheet of Gaffney (2002 [DIRS 163631]).

Calculations are for a drift in tuff at an initial temperature of 30°C and filled with basaltic magma at an initial temperature of 1150°C. This whole-time solution does not account for thermal property contrasts and the effects of latent heat.

Figure 161. Plot of Calculated Temperature Profiles for Various Cooling Times Comparing Results for a 1D Slab-Like Geometry (upper plot) With Results for a 2D Cylindrical Drift Geometry (lower plot)

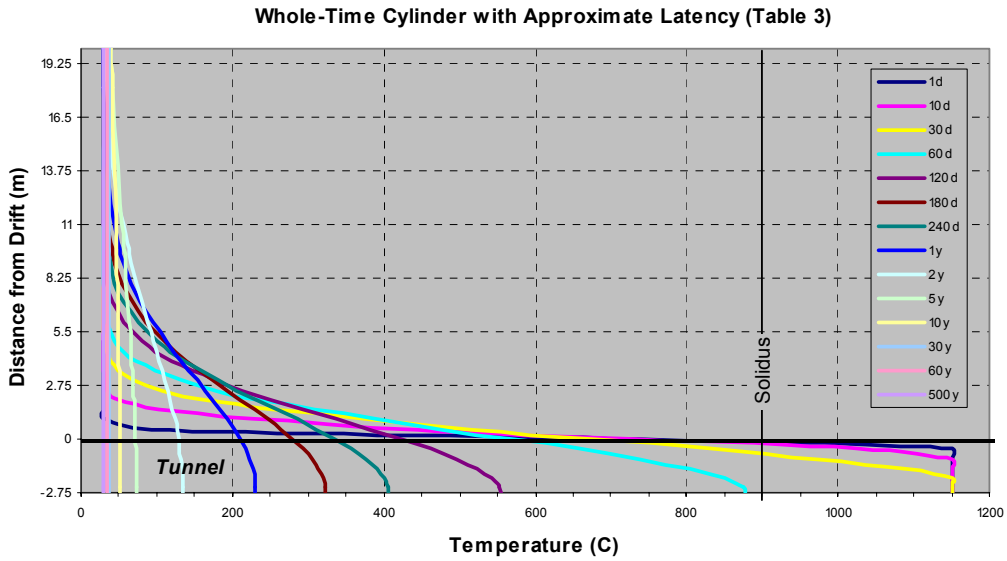

Output DTN: LA0307EG831811.001

NOTE: Table 3 is found in the spreadsheet of Gaffney (2002 [DIRS 163631]).

Figure 162. Plot of Calculated Whole-Time Temperature Profiles for Various Cooling Times Assuming a Cylindrical Drift Geometry and Showing the Approximate Effect of Latent Heat

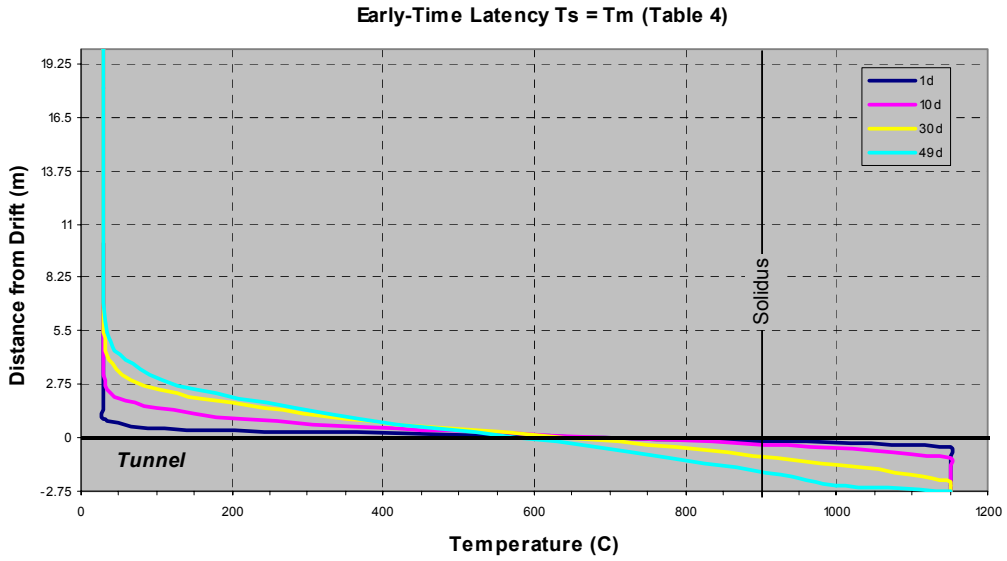

Output DTN: LA0307EG831811.001

NOTES: Table 4 is found in the spreadsheet of Gaffney (2002 [DIRS 163631]).
These calculations are valid only for early times when the temperature of the magma at the drift center are above the assumed solidus at 900°C.

Figure 163. Plot of Calculated Temperature Profiles for Various Cooling Times With Latency Modeled as Occurring at a Specific Temperature (Ts = Tm)

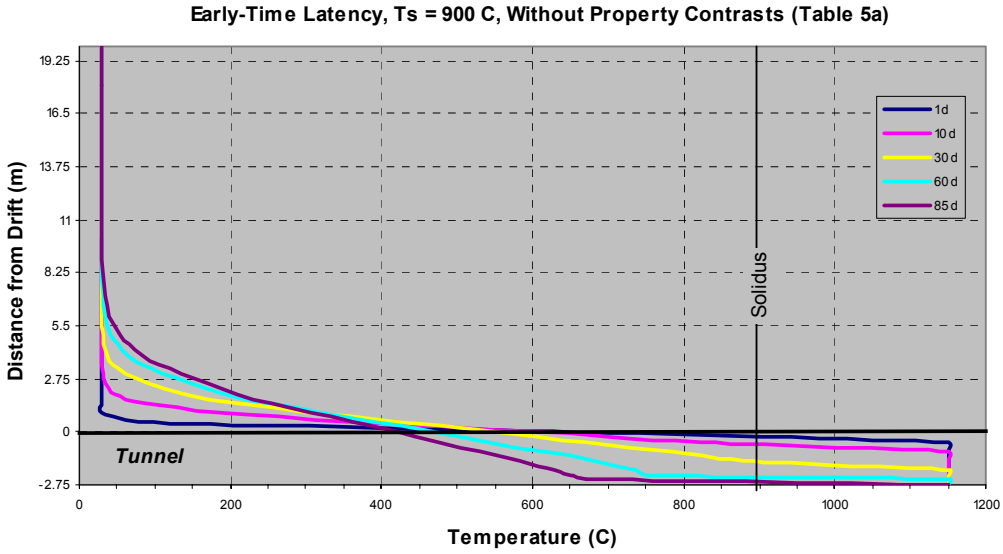

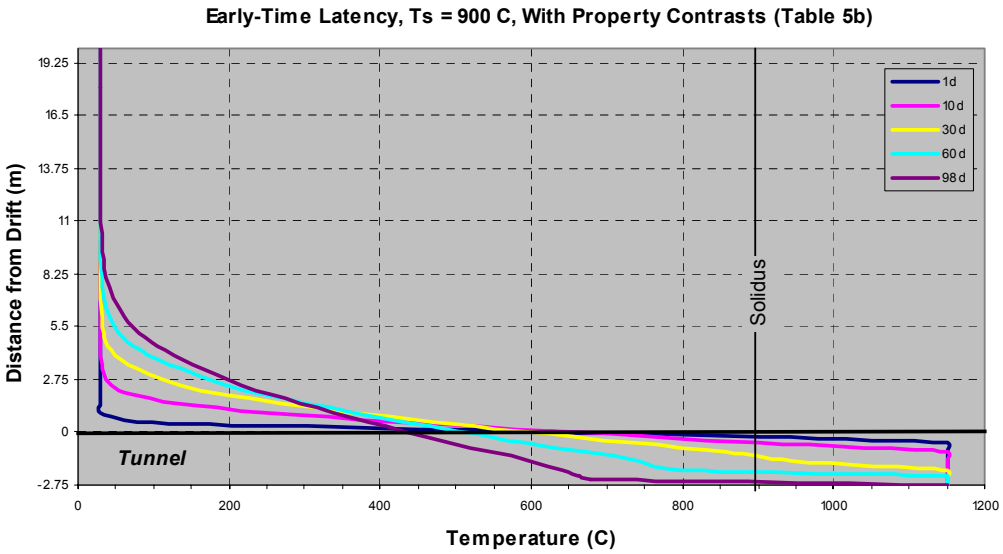

Output DTN: LA0307EG831811.001

NOTES: Tables 5a and 5b are found in the spreadsheet of Gaffney (2002 [DIRS 163631]).

These calculations are valid only for early times when the temperature of the magma at the drift center is above the assumed solidus at 900°C.

Figure 164. Plot of Calculated Temperature Profiles for Various Cooling Times With Latent Heat, Calculated for T_s = 900°C and for the Cases With (lower panel) and Without (upper panel) Property Contrasts Between Magma and Tuff

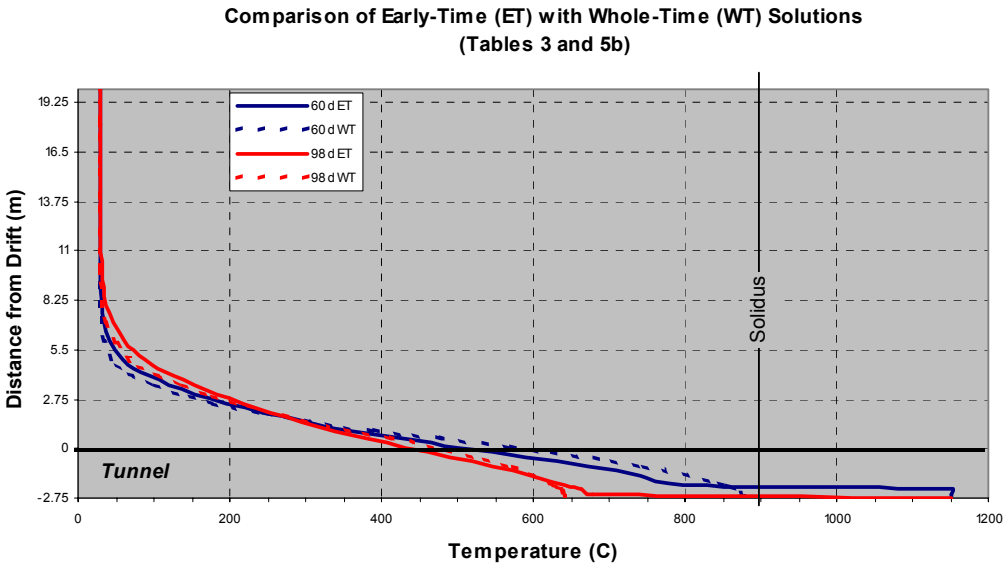

Output DTN: LA0307EG831811.001

NOTE: Dashed curves are the whole-time solutions from Figure 162; solid curves are early-time solutions from Figure 164.

Figure 165. Plot of Calculated Temperature Profiles at 60 and 99 Days Comparing the Whole-Time Solutions With Early-Time Solutions

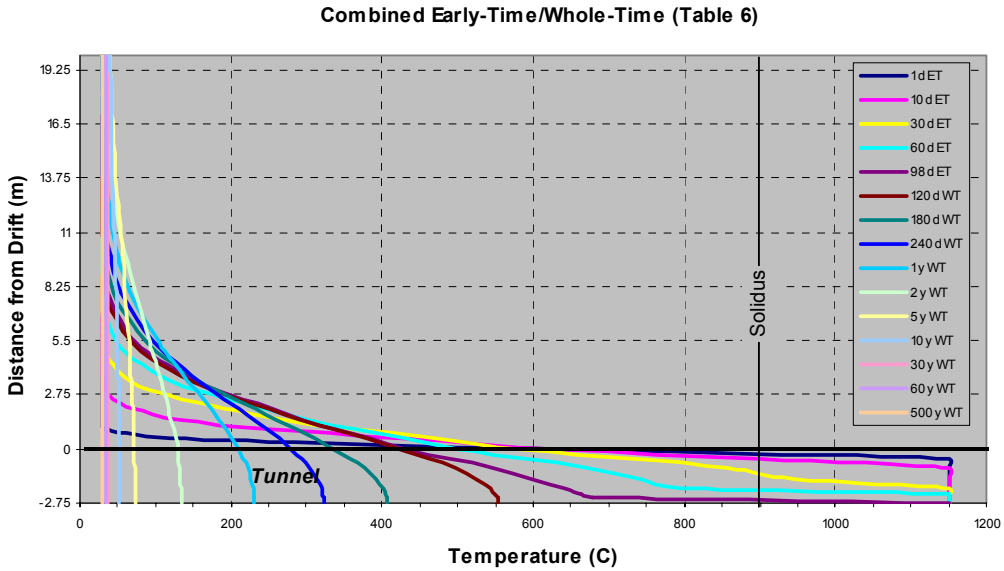

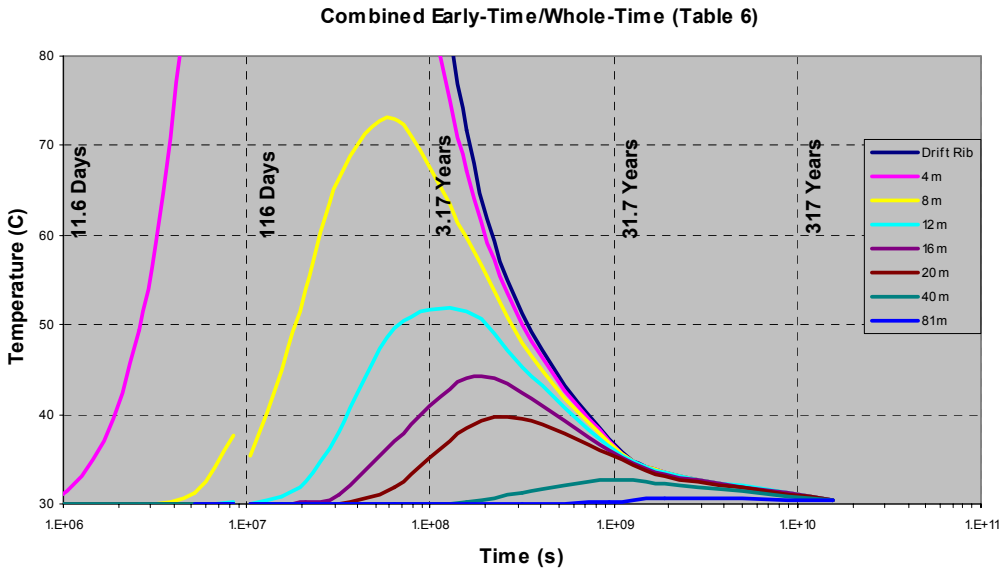

Output DTN: LA0307EG831811.001

NOTES: Table 6 is found in the spreadsheet of Gaffney (2002 [DIRS 163631]).

Figure 166. Whole-Time Solution Combining the Results for Early-Time Latency (Turcotte and Schubert (1982 [DIRS 139651, pp. 168–170]) With Those Late-Time Results Calculated by the Modified Method of Delaney (1987 [DIRS 102776])

6.5.2.1.1 Material Property Inputs

For the YMP problem, the thermal properties shown in Table 19 are applied, and an initial tuff temperature of 30°C without any thermal gradient is assumed. Although values are given for density (ρ), specific heat (c), and thermal conductivity (k), those properties always appear in the solutions a in combination in the form of the thermal diffusivity ($\kappa = k/\rho c$). Further, for the simplest solutions presented, it is assumed that the diffusivities of the magma and the host rock are equal with a value of the mean diffusivity of the two rocks used by the Igneous Consequences Peer Review Panel in their Final Report (Detournay et al. 2003 [DIRS 162914]). The Panel's sources for these numbers are given in Table 2. For more detailed solutions presented, thermal property contrasts between the magma and the tuff are included, and these set the diffusivities of the magma and tuff to 0.3×10^{-6} m^2 s^{-1} and 0.7×10^{-6} m^2 s^{-1}, respectively.

The other property inputs affecting the results of this section are the temperatures of the magma and the host rock and the latent heat of solidification of the magma. The magma temperature used is a round number that is about 0.3 percent above the value listed for a magma with 0.5 percent water in *Characterize Eruptive Processes at Yucca Mountain, Nevada* (BSC 2001 [DIRS 160130]. The host rock temperature is a round number close to room temperature. The net result of these two round-number approximations will be less than 2 percent at early times, and the percentage error will decrease with time. The latent heat of solidification is the value used by the ICPRP, and their source is listed in Table 2.

Table 19. Thermal Properties of Magma and Tuff

Property	Value
Magma	
Temperature, T_m	1150°C
Latent heat, Λ	350 kJ/kg
Tuff	
Temperature, T	30°C
Average	
Thermal diffusivity, κ	0.5×10^{-6} m^2 s^{-1}

The solutions given below are sensitive to magma temperature; an approximately 10 percent variation in T_m produces a 10 percent variation in T near the magma-tuff contact for cooling times up to 1 year but falling to ~3 percent after 30 years. The solutions are less sensitive to diffusivity, with a 10 percent variation in κ producing only ~1 to ~6 percent change in T near the magma-tuff contact during the first year or so of cooling.

6.5.2.2 One-Dimensional Cartesian Equations

Assuming that the magma is emplaced in the drift instantaneously and that it experiences no further movement nor loss or gain of mass, the cooling and heat transfer is governed by the conservation of energy:

$$\frac{\partial T}{\partial t} = \nabla \cdot (\kappa \nabla T) - \mathbf{u} \cdot \nabla T + q \qquad \text{(Eq. 60)}$$

where:

T = temperature
t = time
κ = thermal diffusivity
$\mathbf{u}$ = the magma convective velocity vector
q = represents heat sources and sinks.

This equation describes the change of temperature with time (left-hand side), with the right-hand side summing the effects of thermal conductivity (first term) and thermal convection (second term) with heat sources and sinks (third term). Given the height of the drift as 5.5 m, one may show by consideration of the magnitude of the thermal Rayleigh number that magma convection will not occur within the drift. No heat sinks or sources other than the latent heat of magma crystallization are considered.

To start the analysis, any latent heat released during magma crystallization is ignored and there are no thermal property contrasts between the magma and tuff. First, consider the case for 1D Cartesian coordinates, such that the drift is represented by a slab of a finite thickness but of infinite length and width. These simplifications allow a 1D expression of Equation 60 as:

$$\frac{\partial T}{\partial t} = \kappa \frac{\partial^2 T}{\partial x^2} \qquad \text{(Eq. 61)}$$

for which x represents distance measured perpendicular to the surface of the slab. An analytical solution of Equation 61 for geological systems has most commonly been achieved by using self-similarity solutions (Carslaw and Jaeger 1959 [DIRS 100968]) in which temperature is expressed nondimensionally as θ:

$$\theta = \frac{T - T_0}{T_m - T_0} \qquad \text{(Eq. 62)}$$

for which subscripts m and 0 refer to the initial temperature of the magma and tuff, respectively. A single similarity variable, η, that combines both temporal and spatial effects can be defined as the ratio of distance to twice the characteristic thermal diffusion distance:

$$\eta = \frac{x}{2\sqrt{\kappa t}} \qquad \text{(Eq. 63)}$$

Rewriting Equation 61 using nondimensional temperature, θ, and the similarity variable, η, requires the derivation of θ with respect to t and x in terms of η and reduces Equation 61 from a partial differential equation to an ordinary differential equation:

$$-\eta\left[\frac{d\theta}{d\eta}\right]=\frac{1}{2}\frac{d^2\theta}{d\eta^2} \qquad \text{(Eq. 64)}$$

To solve Equation 64, one may define a variable $\varphi = d\theta/d\eta$ so that the equation becomes:

$$-\eta d\eta=\frac{1}{2}\frac{d\varphi}{\varphi} \qquad \text{(Eq. 65)}$$

With integration and exponentiation of Equation 65, one can show:

$$\frac{d\theta}{d\eta}=ce^{-\eta^2} \qquad \text{(Eq. 66)}$$

in which c is a constant of integration. Considering the boundary between a magma and rock where $\eta = 0$ and $\theta(0) \equiv 1/2$, integration of Equation 66 yields:

$$\theta=c\int_0^{\eta}e^{-n^2}dn+1/2 \quad \text{and} \quad \theta=c\int_{-\eta}^{0}e^{-n^2}dn-1/2\ , \qquad \text{(Eq. 67)}$$

for which n is an arbitrary integration variable. For the boundary condition $\theta(\infty) = 0$:

$$0=c\int_0^{\infty}e^{-n^2}dn+1/2 \qquad \text{(Eq. 68a)}$$

and for $\theta(-\infty) = 0$:

$$0=c\int_{-\infty}^{0}e^{-n^2}dn-1/2\ . \qquad \text{(Eq. 68b)}$$

For $n \geq 0$, the definite integral in Equation 68a is equal to $\pi^{1/2}/2$, and the constant $c = -(2/\pi^{1/2})/2$, so that:

$$\theta=1/2-\left(\frac{1}{2}\right)\frac{2}{\sqrt{\pi}}\int_0^{\eta}e^{-z^2}dz=1/2-\left(\frac{1}{2}\right)\mathrm{erf}(\eta)=\left(\frac{1}{2}\right)\left[1-\mathrm{erf}\left(\frac{x}{2\sqrt{\kappa t}}\right)\right] \qquad \text{(Eq. 69a)}$$

For $n \leq 0$, $c = (2/\pi^{1/2})/2$ and recalling that $\mathrm{erf}(-\eta) = -\mathrm{erf}(\eta)$, the solution is:

$$\theta=-1/2+\left(\frac{1}{2}\right)\frac{2}{\sqrt{\pi}}\int_{-\eta}^{0}e^{-n^2}dz=-1/2-\left(\frac{1}{2}\right)\mathrm{erf}(-\eta)=\left(\frac{1}{2}\right)\left[\mathrm{erf}\left(\frac{x}{2\sqrt{\kappa t}}\right)-1\right] \qquad \text{(Eq. 69b)}$$

Jaeger (1968 [DIRS 163630], p. 54) defines a problem for cooling of a sheet-like magma body of thickness 2*a*, intruded beneath deep cover, for which the *x*-axis origin is defined at the center of the sheet. For this problem, θ must be evaluated away from both surfaces of the sheet (*x*-*a* and *x*+*a*), and because the solution of Equations 69a and 69b are linear, they can be summed:

$$\theta = \frac{1}{2}\left[1 - \operatorname{erf}\left(\frac{x-a}{2\sqrt{\kappa t}}\right)\right] + \frac{1}{2}\left[\operatorname{erf}\left(\frac{x+a}{2\sqrt{\kappa t}}\right) - 1\right] = \frac{1}{2}\left[\operatorname{erf}\left(\frac{x+a}{2\sqrt{\kappa t}}\right) - \operatorname{erf}\left(\frac{x-a}{2\sqrt{\kappa t}}\right)\right] \quad \text{(Eq. 70)}$$

The above equations are valid only in a one-dimensional Cartesian system, which will provide a good temperature solution for the case of a sill, but which is not adequate for the roughly cylindrical geometry of a magma-filled drift.

6.5.2.3 One-Dimensional Cylindrical Equations

This section derives the model a drift of circular cross-section and finite length. Consider the 3D form of Equation 61, expressed in Cartesian coordinates:

$$\frac{\partial T}{\partial t} = \kappa\left(\frac{\partial^2 T}{\partial x^2} + \frac{\partial^2 T}{\partial y^2} + \frac{\partial^2 T}{\partial z^2}\right). \quad \text{(Eq. 71)}$$

Carslaw and Jaeger (1959 [DIRS 100968], p. 56, Section 2.2(10)) show that the solution to Equation 71 is similar to Equation 70, but with added terms for the extra dimensions:

$$\theta = \left[\frac{1}{2}\left(\operatorname{erf}\frac{x+a}{2\sqrt{\kappa t}} - \operatorname{erf}\frac{x-a}{2\sqrt{\kappa t}}\right)\right]\left[\frac{1}{2}\left(\operatorname{erf}\frac{y+b}{2\sqrt{\kappa t}} - \operatorname{erf}\frac{y-b}{2\sqrt{\kappa t}}\right)\right]\left[\frac{1}{2}\left(\operatorname{erf}\frac{z+c}{2\sqrt{\kappa t}} - \operatorname{erf}\frac{z-c}{2\sqrt{\kappa t}}\right)\right] \quad \text{(Eq. 72)}$$

for which

a = the half-height
b = the half-width
c = the half-length of the drift.

The drift cross-section is best represented as a circle. Because in 3D the drift is a cylinder, Equation 71 can be simplified by using cylindrical coordinates with radial distance, *r*, azimuth ϕ, and length, *z*:

$$\frac{\partial T}{\partial t} = \kappa\left(\frac{\partial^2 T}{\partial r^2} + \frac{1}{r}\frac{\partial T}{\partial r} + \frac{1}{r^2}\frac{\partial^2 T}{\partial \phi^2} + \frac{\partial^2 T}{\partial z^2}\right) \quad \text{(Eq. 73)}$$

Assuming that magma temperature within the drift is homogeneous with azimuth then $\partial^2 T/\partial \phi^2 = 0$. Because the drift half-length *c* is more than 100 times greater than its radius *a*, $\partial^2 T/\partial z^2$ vanishes for radial solutions midway through the drift, where *z* = 0 at all times earlier than the *z*-coordinate diffusive time. This time can be easily determined for the value of the last term of Equation 72, which is within 0.001 percent of unity for erf(*n*), where $n \geq \pi$. Letting $n \geq c/(2(\kappa t)^{1/2}) \geq \pi$, then $t \leq c^2/4\pi^2\kappa$ or ~200 years for *c* = 318.5 m and κ = 0.0000004 m^2/s. In fact,

even after 500 years of cooling, the *z*-component accounts for less than a half of percent. With this consideration, Equation 73 is suitably expressed as:

$$\frac{\partial T}{\partial t} = \kappa\left(\frac{\partial^2 T}{\partial r^2} + \frac{\partial T}{r\partial r}\right). \qquad \text{(Eq. 74)}$$

From Carslaw and Jaeger (1959 [DIRS 100968], §2.2(9), the solution of Equation 74 is that of an infinite cylinder where ω = the cylinder radius and Carslaw and Jaeger's *x*-coordinate is replaced by *r* and their *y*-coordinate is set to zero ($z = 0$):

$$\theta = \frac{1}{2}\left(\operatorname{erf}\frac{r+\omega}{2\sqrt{\kappa t}} - \operatorname{erf}\frac{r-\omega}{2\sqrt{\kappa t}}\right)\left(\operatorname{erf}\frac{\omega}{2\sqrt{\kappa t}}\right) \qquad \text{(Eq. 75)}$$

The above solutions assume that no latent heat is released during magma cooling and that the magma and tuff do not display thermal property contrasts (i.e., $\kappa_m/\kappa_r = k_m/k_r = 1$), where *k* is thermal conductivity ($k = \rho c \kappa$), ρ is density, *c* is heat capacity, and subscript *m* and *r* refer to magma and tuff, respectively.

The average diffusivity, κ, is applied to the following calculations based on Equations 70 and 75. Results using values from Tables 1 and 2a of the spreadsheet *Analytical Solutions of Heat Flow.xls* are shown in plots of *T* versus *x* at various times (Figure 161) for both slab-like and cylindrical geometries. The former is appropriate for dike or sill geometries; the latter is appropriate for application to drift geometry.

6.5.2.4 Thermal Property Contrasts and Latent Heat

Addressing the issue of contrasting thermal properties between the magma and host rock, Delaney (1987 [DIRS 102776]) shows the initial contact temperature θ_{ci} as:

$$\theta_{ci} = \frac{k_m / k_t}{k_m / k_t + \sqrt{\kappa_m / \kappa_t}} \qquad \text{(Eq. 76)}$$

where the subscripts *m* and *t* refer to the magma and tuff, respectively. Using the values listed under the heading "Assumed Thermal Properties" in Gaffney (2002 [DIRS 163631], p. 17), then $\theta_{ci} \approx 0.54$ and the initial contact temperature is ~630°C, which is ~10°C (~7 percent) higher than that predicted by no thermal-property contrasts. One must recognize that conductivities generally rise with falling temperature; for example, at 30°C, k_m may reach 2 W m^{-1} K^{-1} or more. However, Delaney (1987 [DIRS 102776]) finds that, although thermal-property contrasts affect the maximum temperature achieved in the host rock (tuff in this case), they do not have large influence over solutions at late times. In fact Delaney (1987 [DIRS 102776]) points out that most workers do not consider thermal-property contrasts.

The effect of latent heat (Λ) production is not negligible, but, as Delaney (1987 [DIRS 102776]) points out, there is no analytically exact method to include its effects. Assuming $\Lambda = 350$ kJ/kg, a first approximation of its effect is to find an effective initial magma temperature T^*_m by adding

to the temperature of the magma the amount Λ/c_m (Λ/c_m = 350 kJ kg^{-1}/1.2 kJ kg^{-1} K^{-1} = 292°C). Delaney (1987 [DIRS 102776]) finds that setting $T^*_m = T_m + \Lambda/c_m$ provides for adequate solutions for temperatures in host rocks at a distance of more than a quarter of a dike thickness away from the contact. Results for this consideration from Table 3 in the spreadsheet of Gaffney (2002 [DIRS 163631]) are shown in Figure 162, for which T_c is 736°C.

In Figure 166 the upper plot shows temperatures at specific times as a function of distance from the drift, whereas the lower plot shows temperatures at specific locations as a function of time. The discontinuity at ~120 days in the curve at 8 m from the drift (yellow) is a result of combining calculation methods.

The main problem with this approximate approach for including the effect of latent heat is that temperature profiles within and near the magma-filled drift are not realistic and are too high. A more physically accurate method to account for latent heat is discussed by Turcotte and Schubert (1982 [DIRS 139651, pp. 168–170]). They follow the classical Stefan problem in which the cooling of a body of magma has a definite solidification temperature $T_s = T_m$. Considering a 1D case (slab-like geometry) with magma intruded at $x < 0$, the solidification surface occurs at X_s:

$$X_s = -2\lambda\sqrt{\kappa t} \qquad \text{(Eq. 77)}$$

for which λ is a constant to be determined. With this approach, one needs a solution that fits the conditions that $\theta = 1$ ($T = T_m = T_s$), where $x = X_s$. The solution implies that the temperature at any point, defined by η (from Equation 71), is proportional to the position of the solidification surface defined by λ:

$$\theta = \frac{\operatorname{erfc}(\eta)}{\operatorname{erfc}(-\lambda)} \qquad \text{(Eq. 78)}$$

For $x \le X_s$, $T = T_m$, and for $X_s < x < 0$, $T_m > T > T_t$. This solution is valid only for times at which latent heat is being released in the magma (i.e., the temperature at the hottest part of the magma, the center of the drift, is above the magma's solidus temperature).

Because $T_s = T_m$, solidification occurs immediately during cooling from T_m, releasing latent heat at a rate $\rho\,\Lambda(dx_m/dt)\delta_t$. Equating this rate with the rate of heat conduction by Fourier's law gives:

$$\rho\Lambda\left(\frac{dX_s}{dt}\right) = k\left(\frac{\partial T}{\partial x}\right)_{X=X_s} \qquad \text{(Eq. 79)}$$

The derivative on the left-hand side of Equation 87 can be found by differentiating Equation 77:

$$\frac{dX_s}{dt} = \frac{-\lambda\sqrt{\kappa}}{\sqrt{t}} \ . \qquad \text{(Eq. 80)}$$

The derivative on the right-hand side of Equation 79 can be found by differentiating Equation 78:

$$\left(\frac{\partial T}{\partial x}\right)_{x=X_s} = \left(\frac{d\theta}{d\eta}\right)_{\eta=-\lambda}\left(\frac{\partial \eta}{\partial x}\right)(T_m - T_0) = \frac{-(T_m - T_0)}{2\sqrt{\kappa t}}\frac{2}{\sqrt{\pi}}\frac{e^{-\lambda^2}}{[1+erf(\lambda)]} \quad \text{(Eq. 81)}$$

A transcendental equation of λ is derived by substituting Equations 80 and 81 into Equation 79 and recalling that $k = \rho c \kappa$:

$$\frac{\Lambda\sqrt{\pi}}{c(T_m - T_0)} = \frac{e^{-\lambda^2}}{\lambda[1+erf(\lambda)]} \quad \text{(Eq. 82)}$$

With Equations 78 and 82, temperatures in time and space can be calculated for 1D problems that involve release of latent heat. Furthermore, Equation 77 can be used to calculate the time for all the magma to solidify (i.e., when the solidification surface reaches the center of the slab and $X_s^2 = a^2$, where a is the slab half-thickness). The solidification time is a function of one-quarter of the area a^2:

$$t_s = \frac{a^2}{4\kappa\lambda^2} \quad \text{(Eq. 83)}$$

Considering cylindrical geometry, the area expressed by the term a^2 in Equation 83 becomes $\pi a^2/4$. Replacing the Cartesian position of the solidification surface by its cylindrical equivalent, R_s, Equation 77 becomes:

$$R_s = -4\lambda\sqrt{\kappa t/\pi} \quad \text{(Eq. 84)}$$

and the transcendental equation for λ is:

$$\frac{2\Lambda}{c(T_m - T_0)} = \frac{e^{-\lambda^2}}{\lambda[1+erf(\lambda)]} \quad \text{(Eq. 85)}$$

For given values of Λ, c, T_m, and T_0, λ can be found by iteratively calculating the right-hand side of Equation 85 until it equals the left-hand side. For a system for which r is 0 at the contact between magma and host rock and increases towards the center of the magma body, the following solutions depend upon the value of R_s, which is a function of λ:

$$T = T_m \quad (r \geq R_s) \quad \text{(Eq. 86)}$$

$$T = T_c\left(1 + erf\frac{r}{2\sqrt{\kappa t}}\right)\left(erf\frac{\omega}{2\sqrt{\kappa t}}\right) \quad (R_s > r) \quad \text{(Eq. 87)}$$

where:

$$T_c = T_0 + \frac{(T_s - T_0)}{1 + erf(\lambda)} \quad \text{(Eq. 88)}$$

As Carslaw and Jaeger (1959 [DIRS 100968]) point out, there is no exact solution for a cylinder beyond its radius. Equation 87 takes into account the cylindrical geometry in the same fashion as Equation 75. As such, this solution is approximate, but comparisons of its calculated results (Gaffney 2002 [DIRS 163631], Table 4; Figure 163) with those shown in Figure 162 show remarkable similarity, as will be shown later. The solutions are valid for early times when liquid magma (above its solidus) exists: T_c = 664°C and λ = 0.84. The full solidification time occurs when the solidification surface, R_s, reaches the center of the drift ($R_s(\lambda, \kappa, t)$ = 2.75 m, t_s = 49 days). This time is shorter than the ~81 days that would be predicted for a 1D slab, using Eq. 85, which is not unexpected because of the smaller cooling surface involved with cylindrical geometry. It is interesting to note that calculated drift-center magma temperatures at this point in time are at 900°C, which is the assumed solidus temperature to be considered in the following discussions.

Because magma solidifies over a range of temperatures ($T_s < T_m$) and displays a small but finite contrast in thermal properties with tuff, one can follow the more complicated analysis of Carslaw and Jaeger (1959 [DIRS 100968]). For conditions for which the conductivity of liquid and solid magma are equal ($k_m = k_s$), the transcendental equation in λ from Carslaw and Jaeger (1959 [DIRS 100968]) can be modified for cylindrical geometry and property contrasts cf. Carslaw and Jaeger (1959 [DIRS 100968], Section 2.16 and Section 11.2[42]):

$$p\frac{\sqrt{\pi}(T_m - T_s)}{4T_s} = \frac{[1 - erf(p\lambda)]\exp[(p^2 - 1)\lambda^2]}{\zeta + erf(\lambda)} \quad \text{(Eq. 89)}$$

Equation 89 accounts for the effects of latent heat by the variable p, which is the square-root of the ratio of diffusivities (κ) of the solid (subscript s) and liquid (subscript m). The magma diffusivity reflects the effect of a higher effective heat capacity from the addition of latent heat:

$$p = \left[\frac{\kappa_s}{k_m / \rho_m[c_m + \Lambda/(T_m - T_s)]}\right]^{1/2} \quad \text{(Eq. 90)}$$

The effect of property contrasts between the magma and tuff in Equation 89 are accounted for by the variable ζ,

$$\zeta = \frac{k_m\sqrt{\kappa_r}}{k_r\sqrt{\kappa_m}} \quad \text{(Eq. 91)}$$

The solution temperatures are like those in Equations 86 to 88 and depend upon the temporal radial position of the cooling surface R_s.

$$T_c = T_0 + \frac{\zeta(T_s - T_0)}{[\zeta + erf(\lambda)]} \quad \text{(Eq. 92)}$$

$$T = T_m \quad (r \geq R_s) \quad \text{(Eq. 93)}$$

$$T = T_c\left(1 + \frac{1}{\zeta} erf\left(\frac{r}{2\sqrt{\kappa_m t}}\right)\right) \bullet \left(erf\left(\frac{\omega}{2\sqrt{\kappa t}}\right)\right) \quad (0 < r < R_s) \quad \text{(Eq. 94)}$$

$$T = T_c\left(1 + erf\left(\frac{r}{2\sqrt{\kappa_t t}}\right)\right) \bullet \left(erf\left(\frac{\omega}{2\sqrt{\kappa t}}\right)\right) \quad (r < 0) \quad \text{(Eq. 95)}$$

Again the effect of cylindrical divergence is accounted for, as in Equation 87. Equations 89 to 95 take into account latent heat being released between T_m and T_s (solidus temperature) as well as property contrasts between the magma (subscript *m*) and tuff (subscript *t*).

Assuming a solidus temperature of 900°C, the effect of $T_s < T_m$ (without property contrasts) results in a lower predicted contact temperature, T_c = 563°C, as well as a lower value of λ (0.64). If the effect of property contrasts is also calculated, then T_c rises to 600°C and λ falls to a value of 0.60. In both cases, a 50°C change in solidus temperature results in a ~16°C change in T_c.

Compared to the calculation for latent heat in which $T_s = T_m$, the effect of $T_s < T_m$ increases the length of time for complete solidification from 49 days to 85 days (without property contrasts) to 98 days (with property contrasts). Figure 164 shows results from Table 5 in Gaffney (2002 [DIRS 163631]) for the cases in which ζ = 1 (no property contrast) and ζ = 1.19.

6.5.2.5 Whole-Time Solutions

Because the analytical results for latency are only valid at early times, a plot of whole-time solutions requires a combination. The whole-time calculations for approximated latency (Figure 166; Gaffney 2002 [DIRS 163631], Table 3) are valid for all times, with the caveat that they are inaccurate for temperatures in or near the magma while it is still molten. On the other hand, the early-time results shown in Figure 164 (Gaffney 2002 [DIRS 163631], Table 5b) are believed to be analytically more accurate. Figure 165 shows a comparison of results for 60 and 99 days for these whole-time and early-time solutions. The comparison demonstrates that temperatures are within ~10°C for the two methods at the time when solidification is complete (99 days).

Accordingly, results from Gaffney (2002 [DIRS 163631], Table 5b) until 99 days of calculated time are combined with those of Gaffney (2002 [DIRS 163631], Table 3) (120 days to 500 years) in the upper panel of Figure 166. The lower panel of Figure 166 shows the evolution of temperature at specific points in space as a function of time.

6.5.2.6 Conclusions

Analytical solutions for heat flow within and around a drift filled with magma and that use cylindrical symmetry, the effects of latent heat, and property contrasts, can only be approximate and, thus, must be viewed as model results only (Figure 166).

Several variations of analytical solutions show slight variations in predicted thermal profiles at different cooling times for a drift filled with magma. The approximate effects of thermal properties contrasts between the magma and tuff host rock are shown to be small. In contrast, latent heat of crystallization, which cannot be exactly accounted for by analytical means, does have a significant effect; it prolongs the cooling times within the magma and causes early-time temperatures within the magma and tuff near the contact to be ~100°C hotter.

The values for the thermal properties of the magma and tuff may vary from those of newer measurements, which might differ by up to 10 percent. Calculations based on varying these properties by 10 percent (with the exception of the initial magma temperature) shows that each property varied accounts for only ~3 percent of the change in calculated temperatures.

With respect to the thermal effects on neighbor drifts (~81 m distant), a slight thermal pulse (~1°C) might be felt after 60 years of cooling. After 500 years of cooling, the magma-filled drift and surrounding tuff has cooled to within 0.5°C of the initial temperature (30°C).

These results are consistent with the findings of BSC 2003 [DIRS 161810], which indicate an increase in temperature of less than 10°C a few years after intrusion.

INTENTIONALLY LEFT BLANK

7. VALIDATION

AP-SIII.10Q, *Models*, requires that models supporting TSPA model components be validated to the level of confidence required by the component's relative importance to the potential performance of the repository system. The outputs of this report do not directly input into TSPA-LA. However, the outputs directly support assumptions used in the *Number of Waste Packages Hit by Igneous Intrusion* analysis report, (BSC 2003 [DIRS 161851]), whose outputs directly input into TSPA-LA.

The *Scientific Processes Guidelines Manual* (BSC 2002 [DIRS 160313], Appendix B) prescribes guidelines for minimum levels of model importance and validation for each TSPA model component. This report analyses scenarios that directly impact the *Number of Waste Packages Intersected by a Conduit* and the *Number of Waste Packages Disrupted by Magma* subcomponents of the TSPA model component, *Damage to Engineered Barriers by Igneous Activity* (BSC 2002 [DIRS 160313], Appendix B). Consequently, this report is assigned a Level-III model validation level because variations in the model could lead to a potentially significant effect on the estimate of mean annual dose.

As described in *Technical Work Plan* for *Igneous Activity Analysis for Disruptive Events,* (BSC 2003 [DIRS 164143]), two methods were employed for confidence building (post-development model validation). These two methods, peer review and corroboration of results with data from analogs (AP-SIII.10Q, 5.4.1c), are documented in the sections below.

7.1 IGNEOUS CONSEQUENCES PEER REVIEW

The models and supporting analyses presented in this model report are consistent with, and have been modified in response to, the recommendations and technical information presented in *Final Report of the Igneous Consequences Peer Review Panel* (Detournay et al. 2003 [DIRS 162914]). The confidence garnered through interactions with the peer review represent an important part of the technical basis for considering this model valid for its intended use. It is important to note that the development of a mathematical model to represent a dike intersecting a repository and the interaction of the magma with the surrounding rock are at the limits of scientific understanding and computational capabilities. In referring to the state of the dike/drift interactions model, Detournay et al. (2003 [DIRS 162914]) state that "the overall conceptual model (namely that of a rising dike intersecting several drifts into which magma flow, followed by localization into a pyroclastic Strombolian eruption along a conduit) is both adequate and reasonable. It would be unreasonable to expect major advances in understanding of the localization process within the next three years, and we do not recommend any alteration to the present overall model."

Detournay et al. (2003 [DIRS 162914]) document two analyses related to the "dog-leg" scenario that support the conclusions of this report. The first analysis relates to the length of the dike tip cavity and position of the tip relative to the ground surface when the magma front reaches repository depths. The second relates to the thermal fate of magma that injects small pre-existing fractures that intersect the drift away from the initial dike/drift intersection point.

For the dike-tip analysis, Detournay et al. (2003 [DIRS 162914]), who also used the NPHF2D V 1.0 [DIRS 163665] code for some of their analyses but with independent input, conclude the following:

> "Perhaps most importantly, as is shown below, there exist plausible conditions at Yucca Mountain for which the dike daylights at the ground surface before the magma front reaches the repository depth, thus greatly reducing the possibility of a dog-leg scenario. Solutions of propagating dike models show that the lag length increases as the under-pressure, $\sigma_o - p_\lambda$, within the lag zone decreases in order to satisfy the fracture propagation criterion at the dike tip. With p_λ constant and σ_o increasing with depth, these solutions indicate that the lag length increases with ascent of the dike. For example, under the simplifying assumptions that λ is small compared to other relevant length scales (in particular, so that $\sigma_o - p_\lambda$ does not vary significantly over the cavity height), the rock toughness is negligible, and the effect of the free surface small, λ is given by (Garagash and Detournay, 2000 [DIRS 164112]):
>
> $$\lambda \approx \frac{4\eta V E^2}{(\sigma_O - p_\lambda)^3}$$
>
> This expression yields a cavity length of $\lambda \sim 200$ m for $\eta = 10$ Pa s, $E^2 = 10^4$ MPa, $\sigma_o = 3$ MPa, $p_\lambda = 0$, and a tip ascent velocity V = 1 m/s, which are within the range of plausible estimates of the relevant parameters for the proposed YMR site. The dike aperture at the magma front is about 0.15 m for the same parameters. However, for this model, the lag would be reduced to less than 20 m if $\sigma_o = 10$ MPa, a value which reflects the peak horizontal thermal stress in the current design scenario. It is worthwhile to emphasize that the inference that the cavity pressure is essentially atmospheric results in a conservative (i.e., minimum) tip cavity length.
>
> Improved estimates of the cavity length λ can be computed with analytical or numerical models including additional physics. For example, Figure 3-3 shows the evolution with time of the magma front, dike tip and lag, computed with a two-dimensional model that takes into account a linear increase of the horizontal stress with depth and the presence of the free surface. This plot clearly shows that the tip becomes unstable when the tip depth is at about 90 m and the magma depth at about 210 m (corresponding to a cavity length of 120 m) for a length scale $l_* \approx 575$ m. (The length scale l_* is a function of several parameters, among them the magma viscosity and density; see Appendix 3.3). Physically, this length scale corresponds to the vertical distance over which the dike excess pressure is substantially larger than that in the dike "tail" at great depth, or, equivalently, the distance over which the pressure gradient for vertical flow deviates significantly from $\Delta\rho g$. This instability is preceded by a gradual increase of the tip velocity compared to the magma front velocity, the latter of which remains virtually constant.

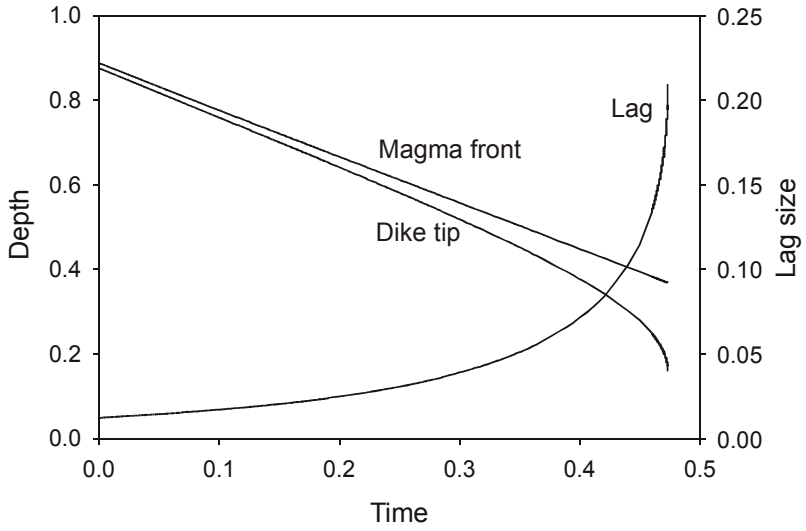

Source: Figure 3-3 of Detournay et al. (2003 [DIRS 162914])

NOTE: "This figure shows the evolution of the lag size, the depth of the magma front and the depth of the dike tip as a function of time. The calculations are based on the assumption of plane strain and take into account the influence of the free surface. The results are expressed in dimensionless form, with the lag size and depth scaled by the length scale l; see Appendix 3.3. (As in Figure 3.2, $l_* \approx 575$ m is a plausible value.) The results show that the velocity of the magma front remains virtually constant and equal to the magma velocity at the source."

This instability of the crack tip may be rationalized by an approximate analytical solution discussed in Appendix 3.2. This model suggests that the dike tip will become unstable when the under-pressure at the tip is 1/2 that at the magma front. In the context of Yucca Mountain, this implies that the dike tip might become unstable when its depth is ~ 1/2 that of the magma front if the instability takes place when the tip cavity is mainly in the unsaturated rock horizon, as the lag pressure, p_λ, is then likely to be near atmospheric. Thus, in the absence of large-scale inelastic deformation, it seems entirely plausible that the dike tip could reach the surface before magma reached drifts at a depth of 200 m to 300 m. (Length scales l_* larger than 575 m, as seem appropriate for analog dikes, yield instability at correspondingly greater depths than shown in Figure 3-3.) If, on the other hand, thermal stresses increased the dike-normal stress at repository depths to 10 MPa, reasonable lag lengths might be only a few meters, according to models where the dike normal stress increases linearly with depth."

Detournay et al. (2003 [DIRS 162914], Section 3.2.2.2).

Confidence has been gained regarding the approach taken for dike tip analysis because the above conclusions are consistent with the conclusions discussed in Section 8.1 of this report and are also consistent with observations of a natural analogue (Paricutin volcano) discussed in Detournay et al. (2003 [DIRS 162914], Appendix 3.4, p. 55) and Sections 7.4 of this report.

For the magma cooling analysis, Detournay et al. (2003 [DIRS 162914], Section 3.4.5) state:

> "As a concrete example, a typical dike thickness:length aspect ratio is ~ 1:1000, and a typical propagation velocity for a km-scale dike is 1 m/s. A reasonable estimate is that a 1-m long dike is ~ 1-mm wide, propagates at ~ 1 mm/s, and widens at ~10^{-3} mm/s. The chilled margin in the same dike would reach 1 mm (the dike thickness) in ~ 1 s. Such a dike could not grow. This is not an argument that dikes cannot form — clearly, they do. However, those that survive thermally must satisfy conditions (discussed in Appendix 3.4) that cannot easily be met by dikes initiating from a drift."

Again, the conclusions regarding magma cooling that are presented in Section 8.3 of this report are supported by the peer review findings, adding substantial confidence to the results of this analysis.

Additional confidence-building information is presented in the following sections.

7.2 SELECTION OF INPUTS

All input parameters are well within applicability of the formulation of the numerical model but also conservative regarding the expected conditions in the repository.

7.2.1 Dike Propagation Model

The dike propagation model is, in the most general case, a function of three dimensionless numbers, which reflect toughness, rock density (defined in Equation 13), and reference stress (defined in Equation 14). The dimensionless toughness is a small number compared to unity under very general conditions of dike propagation. This implies that rock toughness can be neglected completely when considering dike propagation; thus, it is not considered in this section.

The simulations of dike ascent were carried out for variation of relative density between 2.67 and 20.28, which is a range of almost one order of magnitude. Such variation of the relative rock density corresponds to the variation in the difference between normal far-field stress and magma density (buoyancy) between 600 Pa/m and 9000 Pa/m (assuming rock mass densities of 1,200 kg/m^3 and 2400 kg/m^3). For example, Rubin (1995 [DIRS 164118]) assumed this difference to be 3,000 Pa/m. Dimensional results are generated for a number of far-field magma velocities and dike openings, which satisfy the scaling laws and are within the expected ranges for the opening, $0.1\ \text{m} \le w_\infty \le 10\ \text{m}$; for the velocity, $0.1\ \text{m/s} \le v_\infty \le 15\ \text{m/s}$.

The dimensionless reference stress accounts for the effects of gas pressure inside the tip cavity and the increase in horizontal stress normal to the dike. Most of the simulations were carried out assuming that the reference stress is zero — i.e., in-situ stress conditions and atmospheric gas pressure inside the tip cavity. The effect of the cavity gas pressure (although unlikely to be much larger than the atmospheric pressure) is investigated by assuming it to be as large as 2.1 MPa, which is very close to the pressure that would trigger dike-tip instability at the repository depth. The maximum far-field horizontal stress of 8 MPa, which is less than the predicted thermally

induced stress of 10 MPa (Section 6.3.9.2.2), was considered. The maximum horizontal stress of 10 MPa is localized spatially and occurs for a short time (between 1500 and 2000 years). Use of the smaller far-field stress (8 MPa) does not affect the results of the Dike Propagation Model or the conclusions regarding the dike/drift interaction.

The leak-off of 40 percent of the total magma flow rate inside the dike is a maximum for which a 2D model is a reasonable approximation of the processes of rock/mass deformation and magma flow inside the dike. A 3D model was used for larger leak-off rates (Section 6.3.9.2.3.4).

The model assumes homogeneous rock mass properties. All dimensionless results presented in the report were generated assuming a Young's modulus of 15 GPa. This value is representative of the stiffness of the rock mass at Yucca Mountain on the scale of a potential dike. However, results for any other value of Young's modulus could be obtained readily by rescaling the existing results. Section 6.3.9.2.3.1 provides an example of such rescaling.

The 3D analysis of dike propagation simulated two representative cases. Because these simulations indicated that the drifts would be filled with magma before the magma front reaches the surface, no simulations were conducted of different combinations of input parameters. From the perspective of the potential for the "dog-leg" scenario, it was only important to determine whether it is possible to fill the drifts with magma before magma in the main dike reaches the surface.

The analysis of magma injection into the pre-existing cracks inside the emplacement drift was conducted for a wide range of input parameters. The considered range in Young's modulus of rock mass is between 5 and 15 GPa, which covers the most likely variability of rock mass deformability on the repository horizon. In-situ stresses corresponding to overburdens of 250 and 300 m and a lateral stress coefficient between 0.35 and 0.5 were investigated. Most of the analysis was carried out for a minimum overburden of 250 m, which is the most critical condition from the perspective of crack initiation. The analysis demonstrated that magma bulk modulus is not a critical parameter regarding the conditions of secondary crack propagation for the range of parameters considered. Magma viscosity in the range between 10 and 100 Pa s was used. Most of the analysis was done using a viscosity of 10 Pa s, which is conservative, because it results in a shorter time scale for evolution of the analyzed processes. Also, an initial crack opening between 1 mm and 3 mm is conservatively assumed, whereas the initial crack opening is likely to be much smaller.

7.3 CORROBORATION WITH BOUNDARY CONDITONS

Determination that model boundary conditions have been met was accomplished by comparing analytic solutions with the results of model calculations. The outcomes of each comparison were evaluated against acceptance criteria that enhance confidence in model output.

7.3.1 Dike Propagation Boundary Conditions

The example in Section 7.3.1.1 demonstrates, by comparison with the analytical solution, the ability of the model to simulate the process of fracturing of rock mass according to LEFM. Although LEFM is based on significant idealizations of the mechanical behavior of rock mass, it

has been successfully applied to the simulation of large-scale hydraulic fractures in the petroleum industry.

The example in Section 7.3.1.2 compares model predictions with the Lister (1990 [DIRS 126865]) solution, which is an analytical solution for the case of a deep dike, of the same differential equations used in the formulation of the dike propagation model. This comparison illustrates the ability of the model to correctly simulate the propagation of a vertical crack and the effect of buoyancy. To the extent that LEFM and lubrication theories are applicable and magma behaves as an incompressible fluid and is injected at a deep source, the Lister (1990 [DIRS 126865]) solution is a good representation of the condition of dike ascent.

The example in Section 7.3.1.3 illustrates that the logic used in the mathematical representation of leak-off can appropriately be used to represent magma diversion into the drifts.

7.3.1.1 Uniformly Pressurized Fracture

Pressure applied to the walls of a crack makes the crack grow by widening the crack. Therefore, the opening of a crack in response to uniform internal pressure is a necessary validation. Numerical results were compared with the analytical solution for a uniformly pressurized crack of length l in an infinite domain having Young's modulus E and Poisson's ratio v. For a pressure p in the crack, the stress-intensity factor is:

$$K_f = p\sqrt{\pi l} \qquad \text{(Eq. 96)}$$

and the opening at the middle of the crack is:

$$w(0) = \frac{4pl(1-v^2)}{E} \qquad \text{(Eq. 97)}$$

7.3.1.1.1 Acceptance Criterion

Given a stress-intensity factor as input, calculated values for the pressure and the crack opening at its center should agree with the analytical solution within 5 percent or better.

7.3.1.1.2 Results

The pressure (almost uniform) at the end of the simulation for crack length of 0.25 m is 0.895 MPa. The corresponding stress intensity factor, according to Equation 32, is 0.726 MPa $m^{1/2}$, which has a 3.2 percent error compared to the specified toughness of 0.75 MPa $m^{1/2}$. The fracture opening in the middle of the crack is computed to be $4.68 \cdot 10^{-5}$ m, for $E = 15$ GPa and $\nu = 0.28$. The error (compared to the analytical solution of $4.62 \cdot 10^{-5}$ m) is 1.3 percent.

7.3.1.2 Self-Similar Problem of Deep Dike

The problem of self-similar propagation of the vertical dike is solved using NPHF2D V 1.0 [DIRS 163665]. For the case in which the lag does not exist, the solution depends on dimensionless fracture toughness only. That case, for zero toughness (actually, $K \sim 0$), was

considered here. The self-similar solution is achieved when both the dimensionless dike length and the dimensionless distance from the ground surface are larger than 2. (Dimensionless lengths are obtained by scaling lengths with characteristic length defined in Equation 15.) For that reason, the initial position of the fracture tip was selected to be at 4000-m depth (dimensionless depth equal to 5.208). The dike was propagated for 2000 m, or half-way to the ground surface. At that point, the model results were compared with the Lister (1990 [DIRS 126865]) solution. The dimensional model parameters used in the particular simulations were:

- Young's modulus: 15 GPa
- Poisson's ratio: 0.21
- Horizontal stress gradient: 6645 Pa/m
- Magma viscosity: 1Pa s
- Magma density: 400 kg/m^3
- Magma injection rate: 0.2 m^2/s.

7.3.1.2.1 Acceptance Criterion

The maximum dike opening and opening at infinity should agree with the analytical solution within 5 percent or better.

7.3.1.2.2 Results

The comparison between the numerical and the analytical solutions of the dimensionless dike opening (obtained by rescaling dike opening with far-field opening defined in Equation 16) and pressure (obtained by rescaling magma pressure with characteristic pressure defined in Equation 20) versus distance from the fracture tip is shown in Figures 167 and 168.

The agreement between the results is good. The solutions far below the tip are almost coincident. (The dimensionless dike opening far from the tip should be 1; the dimensionless pressure far from the tip should be 0.) According to the Lister (1990 [DIRS 126865]) solution, the dimensionless fracture opening has a maximum equal to 1.27407 at a dimensionless distance from the tip equal to 0.72945. The NPHF2D V 1.0 [DIRS 163665] code yields a maximum opening of 1.21806, which is an error of 4.4 percent. The discrepancy is due to the finite fracture length and an effect of the free surface in the model, compared to the idealized conditions of a semi-infinite fracture in an infinite elastic medium assumed in the Lister (1990 [DIRS 126865]) solution.

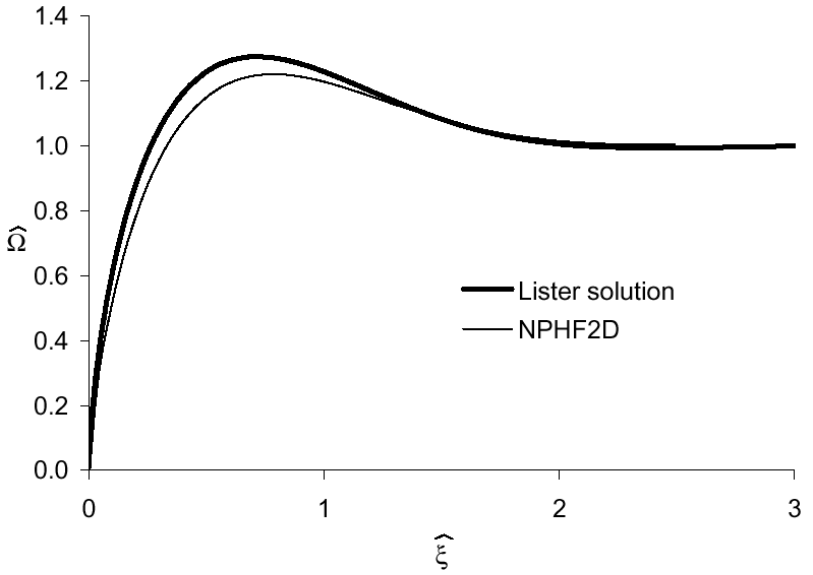

Figure 167. Self-Similar Dike Problem for K = 0: Dimensionless Opening versus Dimensionless Distance From the Crack Tip

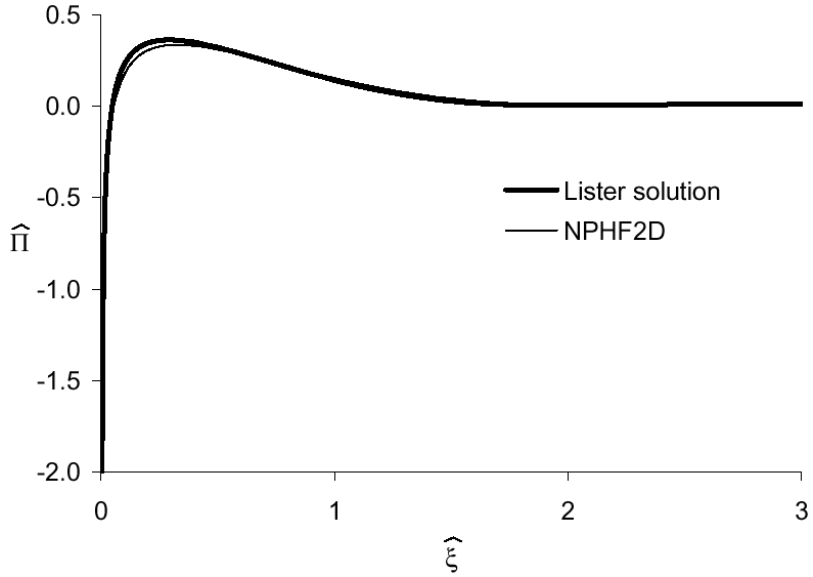

Figure 168. Self-Similar Dike Problem for K = 0: Dimensionless Pressure versus Dimensionless Distance From the Crack Tip

7.3.1.3 Self-Similar Problem of Deep Dike With Leak-Off

The problem of the deep dike (using the same inputs as in the previous test) was also solved for an initial fracture tip at 5000-m depth and a 0.1-m^2/s localized leak-off at 4600-m depth. This analysis was conducted to enhance confidence that the leak-off logic implemented in NPHF2D V1.0 [DIRS 163665] provides an appropriate representation of magma diversion into drifts. The far-field dike opening, w_∞, defined in Equation 22, is, for a given magma viscosity and

buoyancy, a function of magma flow rate. (This asymptotic behavior is confirmed by the numerical solution shown in Figure 171. The dimensionless dike opening converged to 1 at large distance below the dike tip.)

7.3.1.3.1 Acceptance Criterion

The dimensionless dike opening should converge to 1 at some distance above the leak-off point, but far below the dike tip.

7.3.1.3.2 Results

The dimensionless fracture opening shown in Figure 169 is scaled with $w_\infty = 0.077$ m, which is calculated using $q_\infty = 0.1\,\mathrm{m}^2/\mathrm{s}$, a resultant fluid flux above the leak-off point once the steady-state condition is reached at the leak-off point. The result in Figure 169 shows that the dimensionless fracture opening is 1.02 at the location above the leak-off point. The 2-percent error is, to a large extent, a consequence of the finite distance from the fracture tip to the leak-off point.

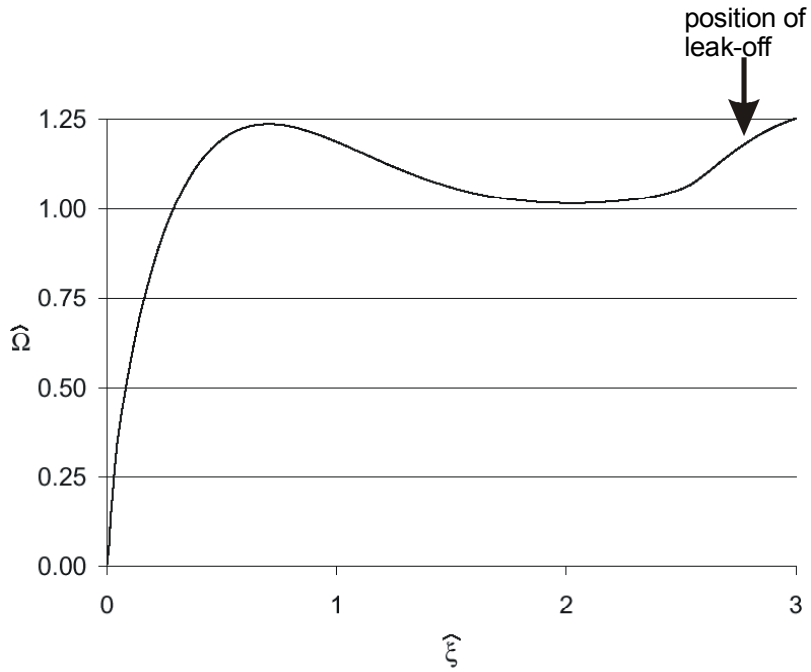

Figure 169. Self-similar Dike Problem With Leak-Off for K = 0: Dimensionless Opening Versus Dimensionless Distance From the Crack Tip

7.3.2 Coupled Hydromechanical Boundary Conditions

This example demonstrates the ability of the model to simulate coupled hydromechanical processes. In the 3D model of dike/drift interaction, the magma flow inside the dike is represented as a flow in the porous medium with conductivity adjusted to account for a change in dike opening. A change in pressure inside the dike causes deformation of surrounding

formations, which results in a change in dike opening. The model results are compared with the analytical Theis (1935 [DIRS 150327]) solution, which involves the coupling of flow in a porous medium with mechanical deformation (similar to the processes expected to take place during dike propagation).

7.3.2.1 Transient Fluid Flow to a Well in a Shallow Confined Aquifer

A shallow confined aquifer of large horizontal extent is characterized by a uniform initial pore pressure, p_0, and initial isotropic stress, σ_{zz}^0. A well that fully penetrates the aquifer is producing water at a constant rate, q, per unit depth from time, $t = t_0$. The elastic porous medium is homogeneous and isotropic, and Darcy's law governs the flow of groundwater. Transient effects are linked to the compressibility of water and the soil matrix.

In this problem the vertical stress in the aquifer may be assumed to remain constant with time. Also, horizontal strains are neglected compared to the vertical ones. The conditions of fluid flow to the well are illustrated schematically in Figure 170.

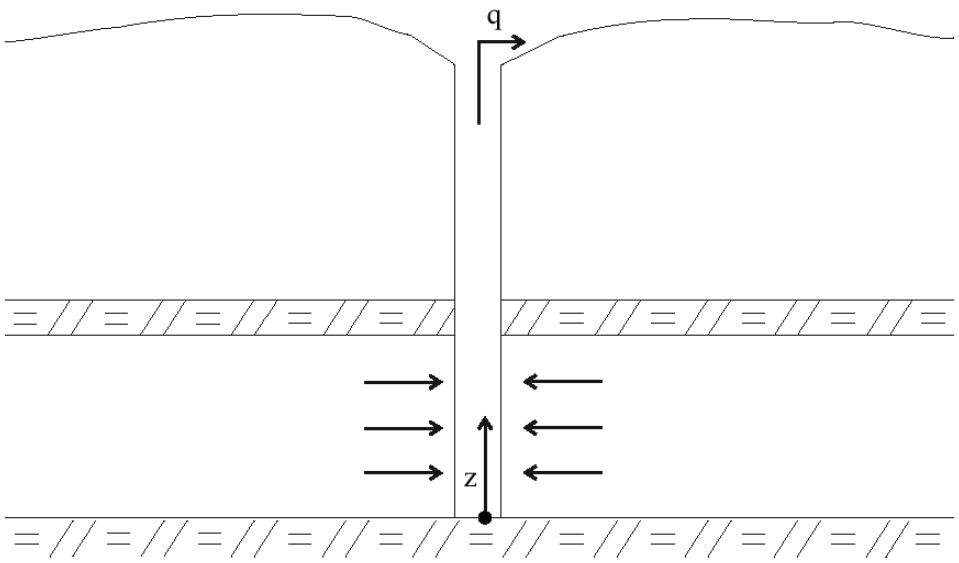

Figure 170. Flow to a Well in a Shallow Confined Aquifer

A cylindrical system of coordinates is chosen with the z-axis pointing upward in the direction of the well axis. Taking into consideration that $\varepsilon_{rr} = \varepsilon_{\theta\theta} = 0$, substitution of the transport law in the fluid mass-balance equation gives the following:

$$\frac{\partial p}{\partial t} = M\left(k\nabla^2 p - \alpha\frac{\partial \varepsilon_{zz}}{\partial t}\right) \qquad \text{(Eq. 98)}$$

where k is the permeability coefficient, M is the Biot modulus, and α is the Biot coefficient. Knowing that the vertical strain is due to change in pore pressure only, and after some manipulation, Equation 1 can be written in the following form:

$$\frac{\partial p}{\partial t} = c\nabla^2 p \qquad \text{(Eq. 99)}$$

where $c = k/S$ is the diffusion coefficient, $S = 1/M + \alpha^2/\alpha_1$ is the storage coefficient, $\alpha_1 = K + 4G/3$, and K and G bulk and shear moduli of soil, respectively.

The solution to this differential equation (in the cylindrical coordinate system) with boundary conditions:

$$\lim_{r\to\infty} p = p_0$$
$$\lim_{r\to 0} 2\pi r \frac{\partial p}{\partial r} = \frac{q}{k} \qquad \text{(Eq. 100)}$$

is due to Theis (1935 [DIRS 150327]). It has the form:

$$\hat{p} = -\frac{1}{4\pi} E_1(u) + \hat{p}_0 \qquad \text{(Eq. 101)}$$

where $\hat{p} = pk/q$. The dimensionless variable u is given by:

$$u = \frac{r^2}{4c(t - t_0)} \qquad \text{(Eq. 102)}$$

and E_1 is the exponential integral, defined as:

$$E_1(u) = \int_u^\infty \frac{e^{-\xi}}{\xi} d\xi \qquad \text{(Eq. 103)}$$

The vertical displacement may be obtained by integration of the equilibrium equation $\partial\sigma_{zz}/\partial z = 0$. This yields, after substitution of the boundary condition, and using Equation 101:

$$\hat{u}_z = -\frac{\hat{z}}{4\pi} E_1(u) \qquad \text{(Eq. 104)}$$

where $\hat{u}_z = uk\alpha_1/(\alpha q H)$ and $\hat{z} = z/H$.

7.3.2.2 Acceptance Criterion

The numerical result for pore pressure should agree with the analytical solution to within 2 percent. The numerical result for draw-down outside of 10-m range from the well should agree with the analytical solution to within 2 percent.

7.3.2.3 Results

The analysis was done using a grid with 31 zones graded in the radial direction. The properties for this example are defined as follows:

- Dry bulk modulus (K): 118 MPa
- Dry shear modulus (G): 71 MPa
- Water bulk modulus (K_f): 2 GPa
- Biot coefficient (α): 1.0
- Porosity (n): 0.4
- Permeability (k): $2.98 \cdot 10^{-8}$ m^2/Pa s.

The initial pore pressure is 147 kPa, and the initial isotropic stress is –147 kPa. The well pumping rate per unit aquifer thickness is 2.21 10^{-3} m^2/s, and the well radius is selected as 1 m.

Pore pressure distributions at different times for calculated and analytical solution are shown in Figure 171. Vertical displacement profiles after 32 seconds are obtained using the numerical and analytical approaches and compared in Figure 172. The agreement is very good, adding confidence that coupled hydromechanical processes that occur during magma flow inside the dike are adequately represented by the numerical approach.

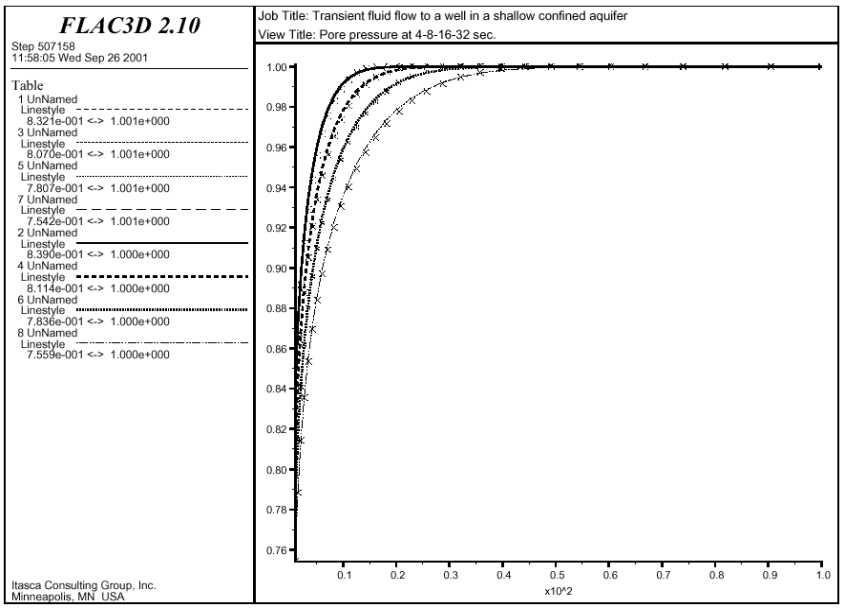

NOTE: Analytical values = dashed line; numerical values = crosses.

Figure 171. Pore-pressure (scaled with initial pore pressure) Versus Distance From the Well (m) at 4, 8, 16 and 32 Seconds

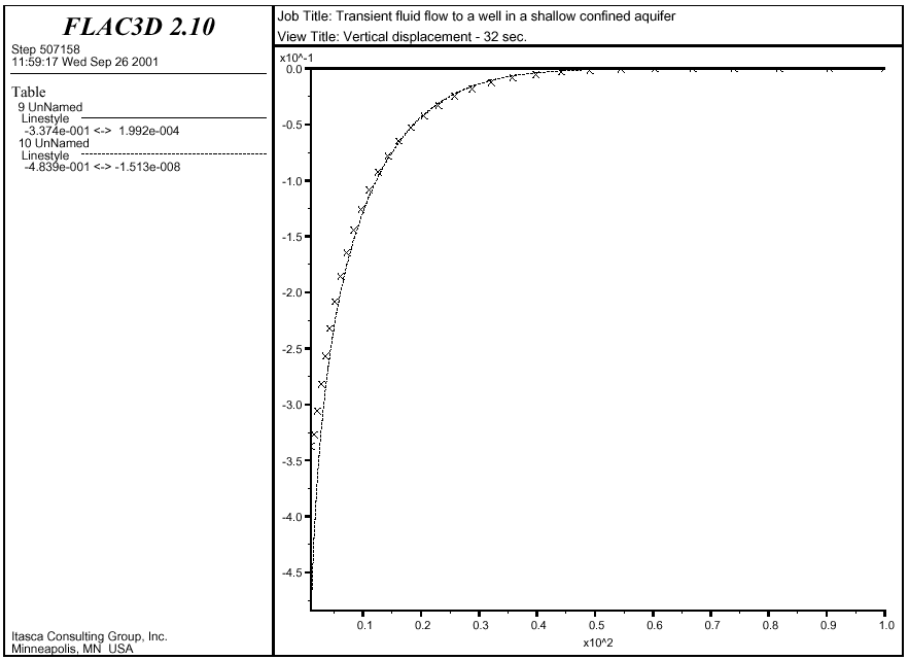

NOTE: Analytical values = dashed line; numerical values = crosses.

Figure 172. Vertical Displacement (scaled according to relation in Equation 7) Versus Distance From the Well (m) at 32 s

7.3.3 One-Dimensional Filling of a Porous Region

An objective of the 3D model of dike/drift interaction is to track the position of the magma front as a function of time. This example demonstrates on a simple problem, by comparison with the analytical solution, that the model is appropriately predicting fluid front advance. The analytical solution is derived assuming a sharp fluid front, which is certainly an idealization of conditions at the magma front, but this approach should give a good estimate of front movement.

In this problem, flow is driven through an initially dry porous layer of large lateral extent under a constant pressure, p_0, applied at the base. The transient location of the filling front is compared to an exact sharp-front solution for the cases with and without gravity.

Voller et al. (1996 [DIRS 163880]) give an analytic solution for this problem under the assumptions of a sharp front, rigid porous matrix and incompressible Newtonian fluid. In their solution, Darcy's law governs the flow, and there is a constant atmospheric pressure in the air ahead of the free surface.

Let the x-axis of reference be oriented in the direction of flow, with the origin at the base of the layer. The solution for the front location, x_f, may be expressed in terms of two dimensionless variables, $\hat{t} = t/T^*$ and $\hat{x} = x_f/L^*$, and a dimensionless parameter, γ. Characteristic time, length and dimensionless parameter are defined as follows: $T^* = n\mu/p_0$, $L^* = \sqrt{\kappa}$ and

$\gamma = \sqrt{\kappa}\rho g / p_0$. In these equations, n is porosity, κ is intrinsic permeability (product of mobility coefficient k and dynamic viscosity μ), ρ is fluid density and g is gravity.

When gravity is ignored, the solution has the form:

$$\hat{t} = \frac{1}{2}\hat{x}^2 \qquad \text{(Eq. 105)}$$

otherwise:

$$\hat{t} = -\frac{\hat{x}}{\gamma} - \frac{\ln(1-\gamma\hat{x})}{\gamma^2} \qquad \text{(Eq. 106)}$$

The solution presented in Equation 106 converges to the solution in Equation 105 when γ goes to zero.

7.3.3.1 Acceptance Criterion

The numerical position of the front should agree with the analytical solution to within a single grid-element length.

7.3.3.2 Results

This problem is solved numerically using FLAC3D V 2.1 [DIRS 161947]. Scaled properties are used in the simulation: $p_0 = 1$, $k = 0.25$, $n = 0.5$, and for gravity flow $\rho_w = 1$ and $g = 1$. Using $\mu = 4$ in the definitions, the characteristic parameters for the simulation are: $T^* = 2, L^* = 1, \gamma = 1$. The grid is a column of 25 zones, 0.625 unit high and 0.025 units wide. Initial pore pressure and saturation are zero. The numerical and analytical solutions for a problem with and without gravity are presented in Figures 173 and 174, respectively.

As may be seen in these figures, the sharp-front solution is bounded above and below by the 99% and 1% saturation fronts. In fact, the vertical distance between these fronts corresponds directly to the grid size in the direction of propagation of the filling front. (The saturation at a node can only start to increase when the pore pressure at the node below it becomes positive, and, thus, full saturation is reached there.) Increase in the number of zones in the column height can reduce this distance. The evolution of nodal pore pressure with time follows a stepwise pattern, more pronounced as the fluid is less compressible. This behavior occurs because a node must be fully saturated before its pore pressure can increase. The results of this example provide confidence that the 3D model of dike/drift interactions correctly simulates the process of magma front advance, under the assumption that the magma is a single-phase fluid.

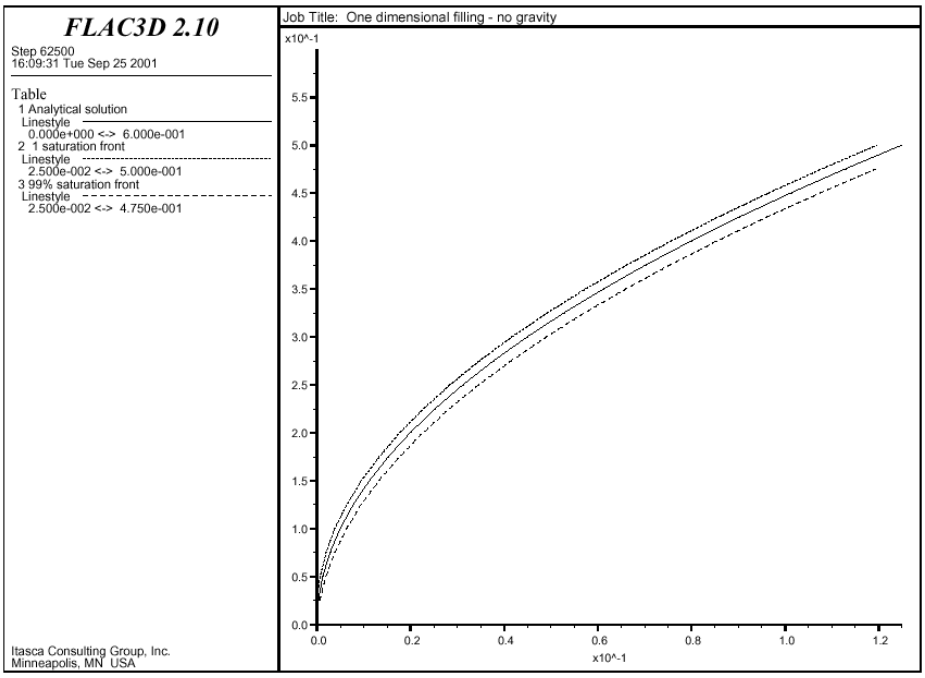

NOTE: Analytical solution = solid line; numerical values = dashed line.

Figure 173. Location of Filling Front ($\hat{x}$ vs $\hat{t}$) — No Gravity

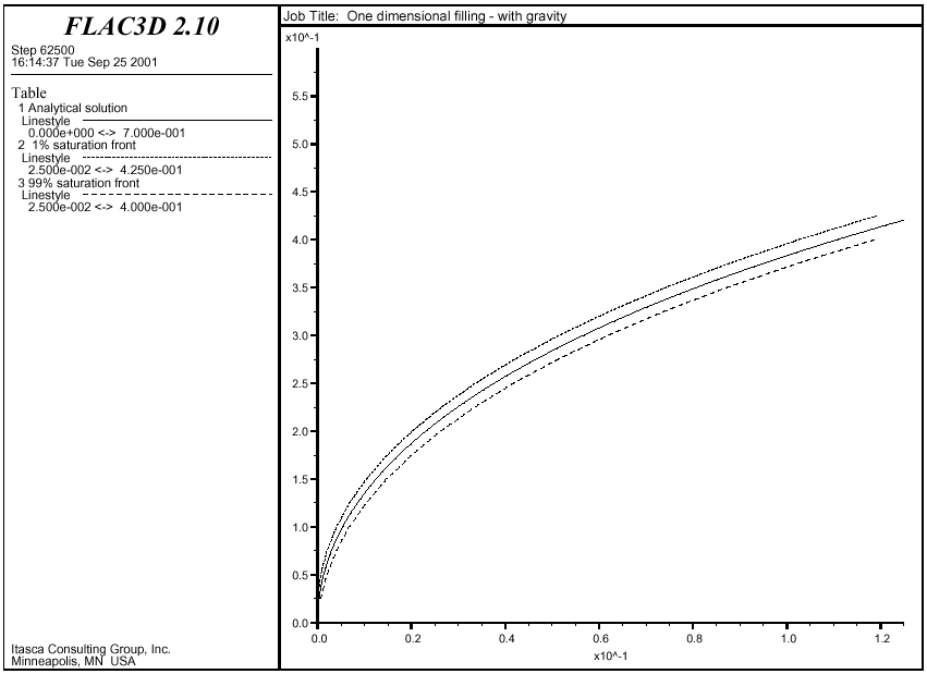

NOTE: Analytical solution = solid line; numerical values = dashed line.

Figure 174. Location of Filling Front ($\hat{x}$ vs $\hat{t}$) — With Gravity

7.3.4 Pressure Distribution in a Fracture With Uniform Permeability

Magma injection into pre-existing joints around a drift is a coupled hydromechanical problem. Magma flow inside the joints can be represented by the Poiseuille's law; deformation of the rock surrounding the drift due to magma pressure inside the drift and the joint can be represented using a linear theory of elasticity. The three examples in Sections 7.3.4 through 7.3.6 demonstrate, by comparison with analytical solutions, the ability of the model to simulate those processes and, consequently, the process of magma injection into the joints.

To build confidence in understanding the process of magma injection into pre-existing joints in the rock mass, an example analysis was undertaken. In this analysis, a transient variation of pressure distribution in a joint due to fluid pressure (P_o) was suddenly applied to one end of the fracture (see Figure 175).

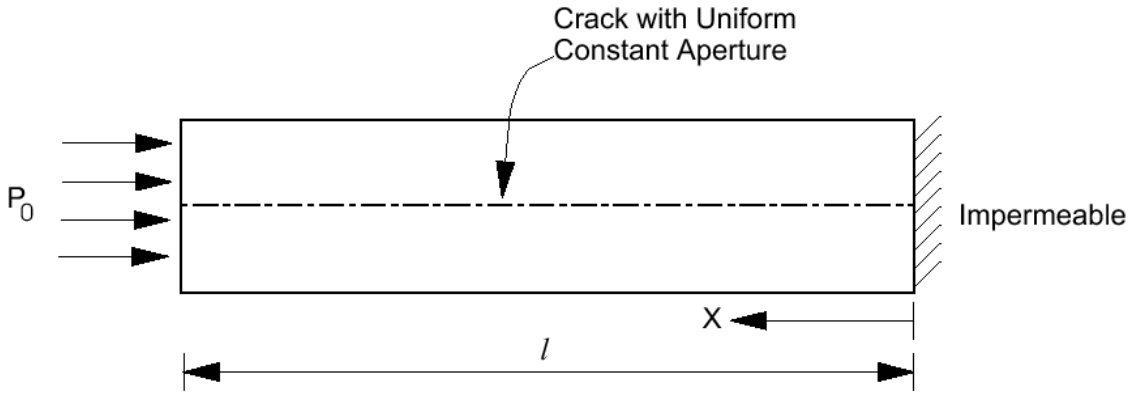

Figure 175. The Geometry of the Problem

This problem is equivalent mathematically to a 1D heat-conduction problem, for which the analytical solution (Carslaw and Jaeger 1959 [DIRS 100968]) can be written in the following form:

$$\frac{P}{P_o} = 1 + \frac{4}{\pi}\sum_{n=0}^{\infty}\left[e^{-(2n+1)^2 (T/4)\pi^2} \cdot \cos\left(\frac{(2n+1)\pi}{2}\zeta\right) \cdot \left(\frac{(-1)^{n+1}}{2n+1}\right)\right] \qquad \text{(Eq. 107)}$$

where the dimensionless time is: $T = \dfrac{(a^2/12\mu)t}{\beta \ell^2}$

and where:

a = the hydraulic aperture
β = the fluid compressibility
μ = the fluid dynamic viscosity
$\zeta = \dfrac{x}{\ell}$
P = the pore pressure at a distance x from the impermeable side

7.3.4.1 Acceptance Criterion

The numerical result should agree with the analytical solution to within 2 percent.

7.3.4.2 Results

The input values selected for this problem are:

- length (ℓ) : 1m
- *fluid pressure (P) :* 9.5 *MPa*
- hydraulic aperture (α) : 3×10^{-5} m
- fluid compressibility (β) : 5×10^{-8} $1/\mathrm{Pa}$
- fluid dymanic (μ) : 10^{-3} Pa • S

A comparison of analytical and UDEC solutions [DIRS 161949] (1-m long model using mesh with 0.2-m zone size) for dimensionless times T = 0.1, 0.3 and 0.5 is shown in Figure 176. The figure illustrates excellent agreement. These results build confidence that single-phase fluid flow in a joint is simulated correctly and provides an appropriate representation of fluid flow into joints.

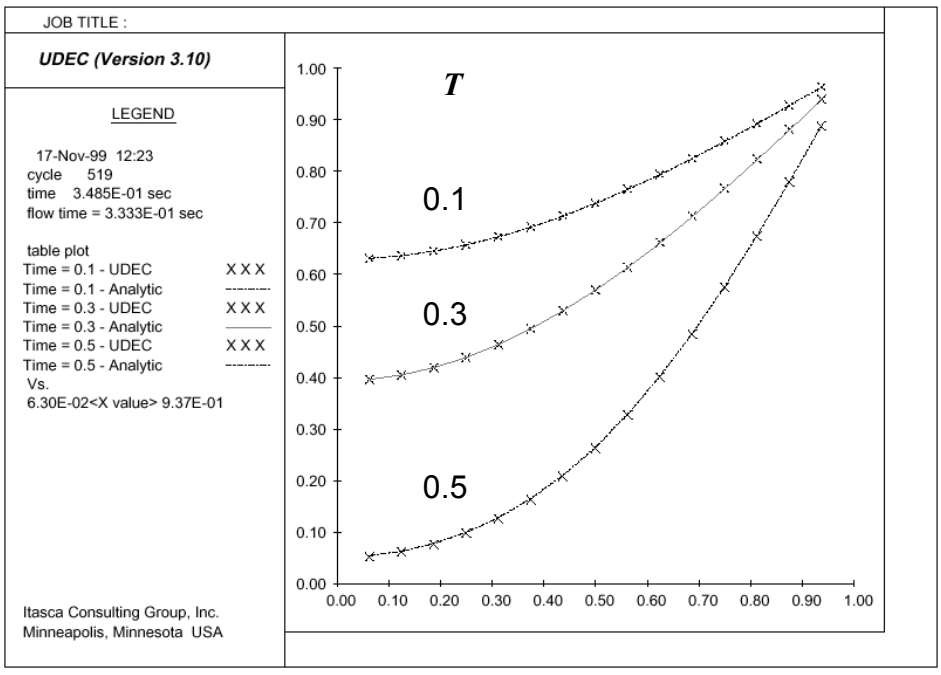

Figure 176. Comparison of Analytical and UDEC Solutions for Joint Fluid Pressure (P/P_o) as a Function of Location (x/ℓ)

7.3.5 Equivalent Permeability Tensor

The capability of UDEC V 3.1 [DIRS 161969] to correctly simulate fluid flow through joints in a rock mass was validated by analyzing fluid flow through a block with two mutually orthogonal joint sets (shown in Figure 177).

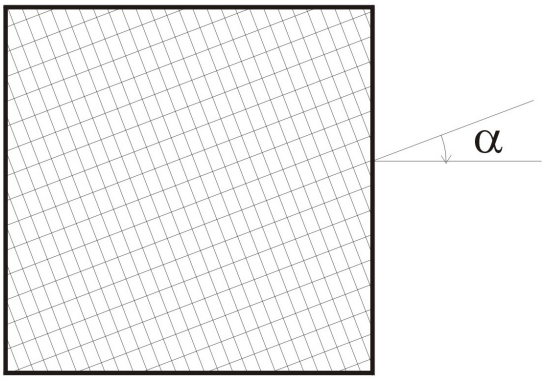

Figure 177. The Geometry of the Block

The relation between the head gradient, ΔH, and the permeability tensor, $\tilde{K}$, can be written in the following form:

$$\begin{bmatrix} K_{xx} & K_{xy} \\ K_{yx} & K_{yy} \end{bmatrix} = \begin{bmatrix} q_{xx} & q_{xy} \\ q_{yx} & q_{y} \end{bmatrix} \begin{bmatrix} 1/\Delta H_x & 0 \\ 0 & 1/\Delta H_y \end{bmatrix} \quad \text{(Eq. 108)}$$

where:

q_{xx} is the flow rate in the x-direction through a rock mass under the gradient in the x-direction

q_{xy} is the flow rate in the x-direction through a rock mass under the gradient in the y-direction

q_{yx} is the flow rate in the y-direction through a rock mass under the gradient in the x-direction

q_{yy} is the flow rate in the y-direction through a rock mass under the gradient in the y-direction.

Principal permeabilities and their directions can be calculated as follows:

$$K_{\max} = \frac{K_{xx} + K_{yy}}{2} + \frac{\left| K_{xy} / \sin 2\alpha \right|}{2} \quad \text{(Eq. 109)}$$

$$K_{\min} = \frac{K_{xx} + K_{yy}}{2} - \frac{\left| K_{xy} / \sin 2\alpha \right|}{2} \quad \text{(Eq. 110)}$$

$$2\alpha = \arctan \frac{-2K_{xy}}{K_{xx} - K_{yy}} \quad \text{(Eq. 111)}$$

7.3.5.1 Acceptance Criterion

The numerical results should agree to within 5 percent with those calculated analytically based on the permeability of a single joint and the joint spacing.

7.3.5.2 Results

Details of this problem can be found in Zhang and Sanderson (2002 [DIRS 163874]). In one case, the head gradient is imposed in the *x* direction; in another case, the head gradient is imposed in the *y* direction. The flow rates were measured in directions of the coordinate axes, and the permeabilities calculated from that document's Equations (11) through (14). The analyses were carried out for four different values of angle α: 0°, 15°, 30° and 45°.

Orientations of the principal permeabilities were compared with orientations of the joints. The values of the principal permeabilities as calculated from UDEC V 3.1 [DIRS 161969] were compared with those calculated analytically, based on the permeability of a single joint and the joint spacing.

The results meet the acceptance criteria. The maximum error of less than 5 percent is due to a slight variation in the number of fractures intersecting the boundaries of the pattern when rotated. This example provides additional confirmation of the model's ability to simulate flow in both a single fracture and multiple fractures that intersect each other.

7.3.6 Thick-Walled Cylinder Subject to Internal Pressure

Change in stress and deformation of the rock mass around the drift due to pressurization by magma (when the drifts are filled with magma) affect conditions of magma injection into the pre-existing joints. The ability of the model to predict correctly deformation around the pressurized circular opening is demonstrated by simulation of deformation and yielding of a thick-walled cylinder. The geometry of the problem is shown in Figure 178. The material is assumed to be elastic and isotropic, with yielding of the material according to the Tresca yield criterion (yielding shear stress k_T).

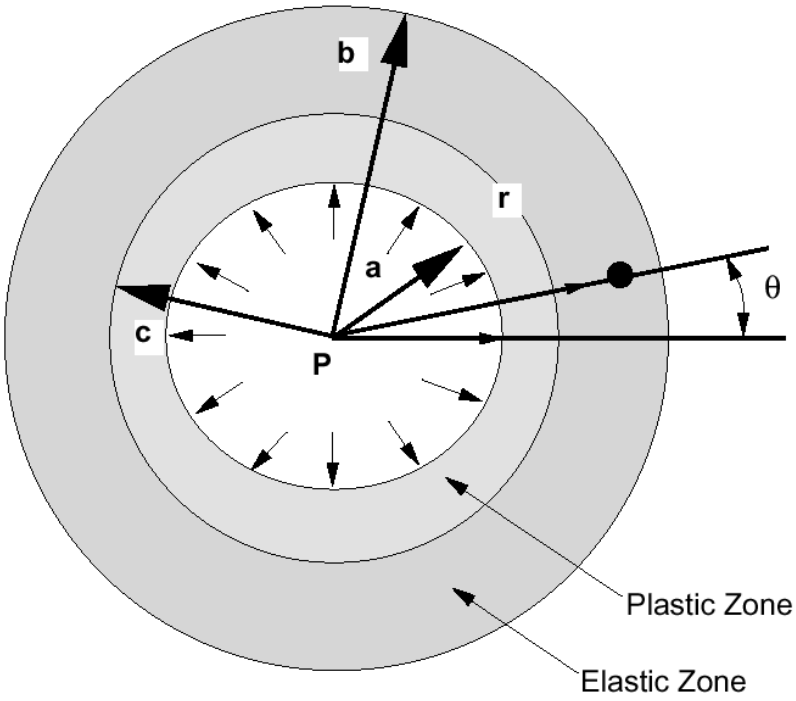

Figure 178. The Geometry of the Problem

The location of the elastic-plastic interface, (c/b), is a solution of the following non-linear equation:

$$\frac{P}{k_T} = 2\left(\ln\frac{c}{b} - \ln\frac{a}{b}\right) + \left(1 - \frac{c^2}{b^2}\right) \qquad \text{(Eq.112)}$$

The analytic solution (Ford and Alexander 1967 [DIRS 163868]) also provides elastic displacements:

$$\frac{u}{b}\frac{E}{k_T} = \frac{P}{k_T}\frac{1+\nu}{\left[(b/a)^2 - 1\right]}\left[(1-2\nu) + \left(\frac{b}{r}\right)^2\right] \qquad \text{(Eq. 113)}$$

and displacements within the plastic zone:

$$\frac{u}{b}\frac{E}{k_T} = (1+\nu)\left(\frac{c}{b}\right)^2\left[(1-2\nu) + \left(\frac{b}{r}\right)^2\right] \qquad \text{(Eq. 114)}$$

The problem is solved numerically using different discretizations of the UDEC model domain (i.e., a number of zones over the thickness of the cylinder equal to 4, 6, and 8).

7.3.6.1 Acceptance Criterion

The numerical results should be within 3 percent of the analytical solution.

7.3.6.2 Results

The problem was solved for the following input parameters:

a: 3.9 m
b: 6.0 m
k_T: 170 MPa
E: 42500 MPa
v: 0.2

The results are compared with the analytical solution in Table 20. Clearly, the agreement between UDEC and the analytical results is excellent. For the eight zones used to discretize the wall thickness, the maximum error is less than 2 percent. Thus, the UDEC V 3.1 software [DIRS 161969] can accurately predict deformation and stresses of an elastic, plastic material in response to applied pressure, thus adding substantial confidence to the results of the backfill deformation analysis (see Section 6.4.10.1).

Table 20. Comparison of UDEC and Analytical Results

	Analytic solution		*UDEC* results $n = 4$		*UDEC* results $n = 6$		*UDEC* results $n = 8$	
P/k_T	c^*	U^*	c^*	U^*	c^*	U^*	c^*	U^*
0.65	0.694	0.926	0.696	0.932	0.700	0.939	0.696	0.941
0.70	0.731	1.025	0.737	1.037	0.727	1.038	0.724	1.042
0.75	0.774	1.150	0.759	1.161	0.771	1.169	0.775	1.169

NOTE: $c^* = c/b$
$U^* = (u/b)(E/k_T)$

7.4 CORROBORATION WITH OBSERVATIONS AT THE PARÍCUTIN ANALOGUE

Although the model and underlying software have been validated for deep hydrofracture applications, as described in the two previous sections, there is a need to validate the description of phenomena associated with interaction of a dike with a free surface.

One of the best-documented new volcanic eruptions occurred near the west Mexican village of Parícutin on 20 February 1943. The eruption was preceded by felt earthquakes and regionally recorded earthquakes. The dike-tip cavity was observed almost immediately at the surface by farm workers in the field where the fissure appeared. The rate of magma production is also well documented from the very beginning of the eruption. The first lava erupted was a basaltic andesite with about 55 percent silica (Wilcox 1954 [DIRS 163659]). Although this is considerably richer in silica than the alkali basalt of the Lathrop Wells volcano, it nonetheless provides an opportunity to corroborate the model output with analog volcanic activity.

7.4.1 Acceptance Criteria

The observed phenomena and features of the eruption at Parícutin include the times of seismicity, of first opening of the fissure at the surface, and of the beginning of magma eruption at the surface; the nature of the first emanations from the fissure and the chemical and physical properties of the magma; estimates of ground displacements; and the rate of magma eruption over the first several weeks or months.

The model output will be considered corroborated if the output is consistent with the timing within a factor of two, given the observed or inferred properties of the magma. The sequence of emanations should agree with observations. The rate of magma volume rising in the dike should be within a factor of two of the observed rate of eruption, given reasonable assumptions about the length of the dike feeding Parícutin. The ground displacements from the model should be within a factor of two of those observed.

7.4.2 Observations and Inferences at Parícutin

This account of the eruption of Parícutin is taken from the compilation prepared for the Smithsonian Institution by Luhr and Simkin (1993 [DIRS 144310]). Page references in that volume are shown as {*page* #}.

The eruption was preceded by felt earthquakes beginning about noon on 5 February. (Times are reported in local time, which is GMT-0600.) The first seismic activity recorded in Mexico City 320 km to the east was at 0325 on 8 February. There was seismic activity, some accompanied by ground noises, from these first indications until the eruption. 12 February was apparently a particularly active day seismically according to records from Mexico City {51}.

Luhr and Simkin (1993 [DIRS 144310]) provide a wealth of detail on events immediately following the first surface manifestations at Parícutin, but it is presented here in a very abbreviated outline.

February 20, 1943 {54–65}
- 1600: Half-meter deep fissure noticed (~5 cm wide and 30 m long).
- A few minutes later, the ground swelled up to 2–2.5 m and “smoke” began rising from the fissure.
- A few minutes more, hissing sounds and smoke and smell of sulfur.
- The spring near the fissure had dried up (time not observed).
- 1800: km-long fissure with activity concentrated in a central depression about 12 m wide and 20 m long, “smoke” and sulfurous vapors issued from pit, small rocks thrown 5 m high.
- ~2300–0000 (21 Feb): volcano began to roar, incandescent stone hurled up with great force, column of “smoke” arose.

February 21, 1943 {66–68}
- 8 AM: a 10-m high hill had formed and rocks were hurled out with great violence.
- 11 A.M. lava flow {66}
- By 1 PM: a 30-m high cone.
- By evening, explosions and bombs hurled to 500 m.

February 22, 1943
3 AM: heavy seismic activity, lava flows, cone about 50–60 m high. {68–69}
That night: "lava was flowing from three vents aligned from east to west and located precisely in the center of the crater." {65}
February 25, 1943 {68–69}
First lava flow ceases to be fed from vent.
February 26, 1943 {69–70}
Volume of cone 0.0195 km^3, growing at 0.00333 km^3/day.
Volume of lava flow 0.007 km^3.

The composition of material erupted on 22 February was reported to be a basaltic-andesite with the following major oxide weight percentages: SiO_2 55.04, Al_2O_3 18.82, Fe_2O_3 1.92, FeO 5.69, CaO 7.17, MgO 5.68, K_2O 0.85, Na_2O 3.88, TiO_2 0.94, H_2O 0.16 {328}. Eggler estimates, on the basis of the phenocryst compositions, that the actual water content of the source lava was higher, on the order of 2.2 weight percent {362}. However, others {350–351} have estimated that about half of the original water exsolved during ascent leading to an effective water content of about 1 percent.

There were no measurements of lava temperature at this early stage. The earliest reliable measurements were from May 1945, when optical pyrometer measurements of lava yielded a temperature of 1200–1250°C (1475–1525 K) {318}. Wilcox (1954 [DIRS 163659]) reports compositions for material from 6 months earlier and 6 months later than that. Silica by that time had increased to 55.6 to 56.4 percent and alumina had decreased to 17.7 percent {328}. The liquidus of such a magma would be slightly lower than for the original magma, but the 1946 material had slightly fewer phenocrysts than the earliest material, so we may assume that the temperature of the material being erupted in February 1943 was similar. The liquidus temperature for a magma with the composition given in the previous paragraph and calculated by the method used in BSC (2001 [DIRS 160130]) is 1104°C (1377 K), much lower than the measurements. Given the primitive nature of the instrumentation available at the time, the latter seems likely to be better. In addition, the early Parícutin magma had about 3.3 percent phenocrysts {326}, therefore 1325 K (1052°C) represents the most appropriate estimate of magma temperature. This value is slightly lower than the estimate of Eggler (Luhr and Simkin 1993 [DIRS 144310]), but the oldest rock he worked with was not erupted until 1947, four years after the first eruption began {360-363}.

Krauskopf (Luhr and Simkin 1993 [DIRS 144310]) calculated the viscosity of lava at Parícutin based on flow speeds, flow depths, and slope values and found viscosities of 10^4 to 10^5 Pa-s. This range is considered to be on the high side because drag at the edges of the channel and cooled blocks on the surface would result in a higher value than for the nearly pure liquid in the dike {320}. Using the composition above, a temperature of 1325 K, and the method of Shaw used in BSC (2001 [DIRS 160130]), the viscosity is calculated to be about 420 Pa-s. The incorporation of a few percent of phenocrysts would raise this slightly, so the value of 500 Pa-s will be used.

The estimate given above of magma supply to Parícutin in the early days (0.00333 km^3/day, 38 m^3/s) agrees well with the total supply rate for all of the year 1943 estimated at 17 m^3/s {314}.

There is little information on the depth of the magma chamber that fed Parícutin. Eggler's experimental petrology studies (Luhr and Simkin 1993 [DIRS 144310]) indicated some pressure and water were needed to prevent pyroxene phenocrysts from forming but did not establish any strong limits. His experiments that most closely replicated the real Parícutin phases were at pressures of about 550 MPa, equivalent to a depth of about 20 km. Experiments at the same water content but at 750 MPa (about 28 km) contained pyroxene, so we assume the depth was less than about 25 km {361}. Wilcox 1954 [DIRS 163659] {Figure 198, p. 345}, presents a figure, which is apparently roughly to scale without vertical exaggeration, that depicts the dike as arising from a magma cupola about 5 to 6 km deep. A figure from {Fig. 209, p. 357} does not appear to be to scale. Yokoyama and de la Cruz-Reyna (1990 [DIRS 108740]) estimated source depth of 10 to 20 km based on relative arrival times of direct and refracted P-waves measured at regional distances.

Given that both the beginning of seismic activity related to dike formation and the depth of origin of the dike feeding the new Parícutin volcano are uncertain, we can only develop a rough order-of-magnitude estimate of the velocity of magma moving up the dike. The range of possible values is illustrated in Table 21.

Table 21. Dike Propagation Velocities at Parícutin

Seismic Precursor		Depth (km)				
		5	7.5	10	15	20
Days	Hours	Velocity (m/s)				
15	12	0.0037	0.0056	0.0075	0.011	0.015
12	20	0.0045	0.0068	0.0090	0.014	0.018
8		0.0072	0.011	0.014	0.022	0.029

Source: Luhr and Simkin 1993 [DIRS 144310]

7.4.3 Results

The dike propagation results from the model of Section 6.3 can be scaled to the Parícutin condition, while taking into account the difference in viscosity.

The calculations of dike propagation for Yucca Mountain were applied to the Parícutin test case of about a 7-hour delay between the arrival of the dike at the surface (e.g., parting of the earth) and the eruption of magma from the fissure, as given in the chronology shown in Section 7.4.2. Viscosities of the Parícutin eruption were thought to be 10^3 to 10^4 times that of the expected dike at Yucca Mountain.

Based upon these observations, the model output, which was calculated using dimensionless parameters, were rescaled for the higher-viscosity magma and slower dike-tip velocities to determine if they would be reasonably in agreement with the Parícutin example. Flow rates at Parícutin are well established, as is the delay between first cracking at the surface and arrival of the magma. At the other extreme, viscosities are only roughly estimated for the first few weeks of the eruption.

The three base cases of Section 6 (see Table 7) have each been scaled to viscosities and elastic properties appropriate to Parícutin with the scaling approach described in Section 6 and using an Excel spreadsheet as follows. A viscosity was selected, and values on q_∞ and w_∞ were computed for several values of v_∞. The value of v_∞ giving q_∞ = 0.17 m^2/s was found by trial and error. This result was used to calculate the scaling parameters l^*, p^* and t^*, which were then used to rescale the base case. The result is a table of crack-tip position and magma-front position as functions of time. Because the calculation ends when the crack tip reaches the surface, the lag between first crack opening at the surface and magma arrival is obtained by extrapolating the magma front position linearly until magma arrival at the surface elevation. If the calculated lag time was not consistent with the observed lag time, a new viscosity was selected and the process repeated until an acceptable lag time was obtained.

Because Young's modulus appears only in the dimensionless group **S**, which is zero, the scaling parameters can be adjusted directly for changes in the elastic properties of the country rock. Reference to Section 6.3.10.1 shows that all of the scaling parameters vary as the square root of E'. To account for the stiffer midcrustal rocks of the Trans Mexican Volcanic Field, the process of the preceding paragraph was repeated using larger scaling parameters calculated from E= 30 GPa and ν = 0.3, as estimated by Yokoyama and de la Cruz-Reyna (1990 [DIRS 108740]).

The results for both stiffnesses and all three base cases are given in Table 22 along with a summary of the observations. The results in the outlined box, scaled from Base Case 10, with a viscosity of 5×10^4 Pa-s and Young's modulus of 3×10^{10}, agree very well with the observations.

Figure 179 illustrates the dike propagation over about 7 days as the crack grows from a starting depth of 22.5 km, reaching the surface after 6.6 days with magma following 7.7 hours later. Because most of the history of dike propagation is at midcrustal depths, where pressures are high enough to keep most of the water in solution, the 2280 kg/m^3 magma density for Base Case 10 is clearly a better match to the natural case than either of the smaller densities of Base Cases 8 and 9.

Table 22. Rescaling Results of Section 6 to Parícutin

Base Case	8	9	10	8	9	10	Observed
Flux (m^2/s)	0.172	0.172	0.174	0.172	0.170	0.173	0.17
Viscosity (Pa-s)	3.00×10^5	2.50×10^5	1.00×10^5	3.00×10^5	1.40×10^5	5.00×10^4	10^4–10^5
Magma Velocity (m/s)	0.042	0.034	0.031	0.042	0.041	0.039	—
Dike Width (m)	4.1	5.1	5.6	4.1	4.2	4.4	—
Magma Depth (m)	949	865	822	1370	1130	1060	—
Lag Time (hours)	6.2	7.1	7.5	8.9	7.5	7.7	7.5
Seismic Time (days)	1.3	2.9	6.4	1.9	3.2	6.6	8–15
Magma Density (kg/m^3)	1500	2000	2280	1500	2000	2280	
Source Depth (km)	5.5	8.9	17.4	7.9	11.7	22.5	6–20
Young's Modulus (Pa)	1.50×10^{10}	1.50×10^{10}	1.50×10^{10}	3.00×10^{10}	3.00×10^{10}	3.00×10^{10}	3.00×10^{10}
Poisson's Ratio	0.21	0.21	0.21	0.30	0.30	0.30	0.30
Rock Density (kg/m^3)	2400	2400	2400	2400	2400	2400	

Source: Luhr and Simpkin [DIRS 144310] (N/A – reference only)

These results meet the acceptance criteria, and the model output has been corroborated with the analog volcanic activity. Furthermore, the model is considered to be valid for applications that include a free surface and an appreciable lag time between the first cracking at the surface and the arrival of the magma front.

Regarding the natural case, the uncertainty in the source depth and time has a direct impact on the magma rise velocities. The horizontal extent of the dike carrying magma to the surface, in particular whether flow at depth is as restricted in that direction as it was at the surface, has a direct relation to the calculated flux.

Model output has been scaled using the calculations intended to simulate an alkali basalt comparable to that found at the Lathrop Wells volcano. It is likely that an attempt to simulate the Parícutin eruption directly using the best available field evidence would produce even better results. Furthermore, the model assumed a single density and viscosity for all magma in the dike, whereas there will be vertical gradients in both properties in reality. A final model-based source of divergence may be that the real magma at Parícutin was compressible, with about 1-percent water by weight and several percent by volume.

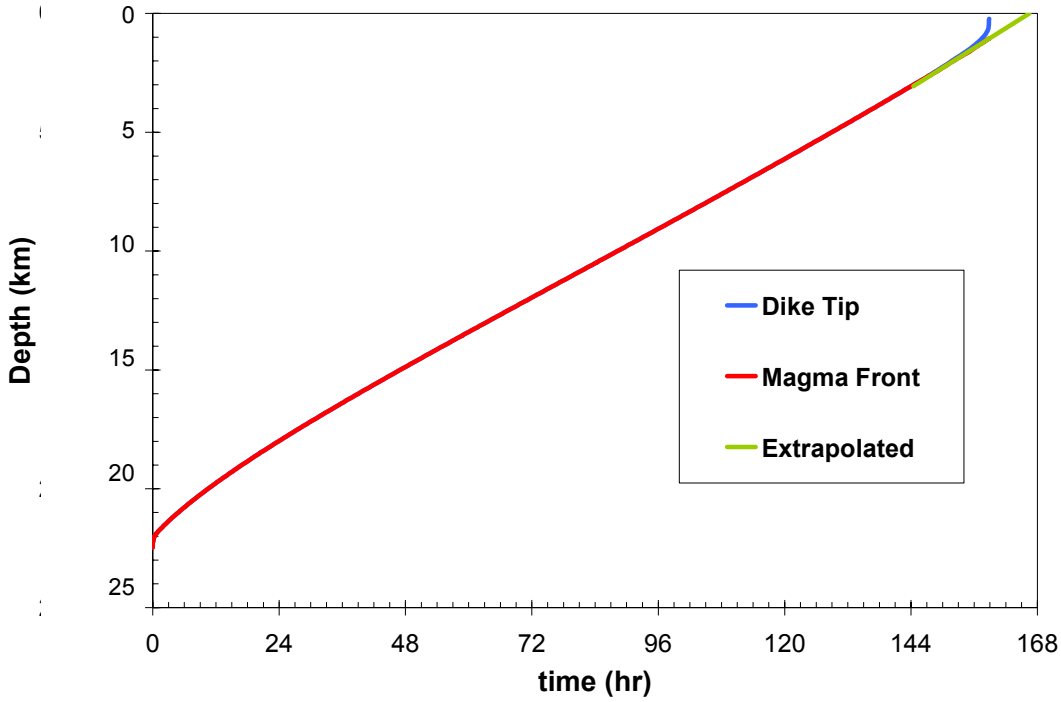

DTN: SN0304T0504203.001

Figure 179. Dike Propagation Results of Rescaling to Parícutin

7.4.4 Conclusions

Based on comparison with both analytical solutions of hydrofracture problems, the model output can be expected to provide valid solutions for the propagation of a dike from depth through the repository to the surface. Comparisons with field observations at Parícutin are not quite as good but still support most of the phenomenology described in the model. The deviations from the field observations can be attributed to: (1) uncertainties associated with lay observers and the primitiveness of the instrumentation available at the time, and (2) the fact that the model was scaled from one of the existing simulations rather than being developed specifically for the volcanic activity at Parícutin.

7.5 CORROBORATION OF THE MECHANICAL BEHAVIOR OF THE BACKFILL WITH ANALOGUE BEHAVIOR FROM SOUTH AFRICAN GOLD MINES

Backfill is used in deep South African gold mines to alleviate problems due to rockbursts and rockfalls. Clark et al. (1988 [DIRS 164121]) investigated the behavior of the backfill and its effect on the stability of the rock mass. Laboratory testing was carried out as part of the study to approximate the stress-strain response of the backfill under conditions similar to those occurring under ground. Laboratory results provided input parameters for the Double-Yield constitutive model in FLAC3D V 2.1 [DIRS 161947], which was used to simulate the mining conditions and validate the model by comparison with in-situ stress measurement.

The laboratory uniaxial strain test was modeled with FLAC using the Double-Yield model. The model parameters were adjusted in order to match the measured stress-strain response (Figure 180). Based on this match, the Double-Yield model could be applied to the prediction and interpretation of underground backfill behavior.

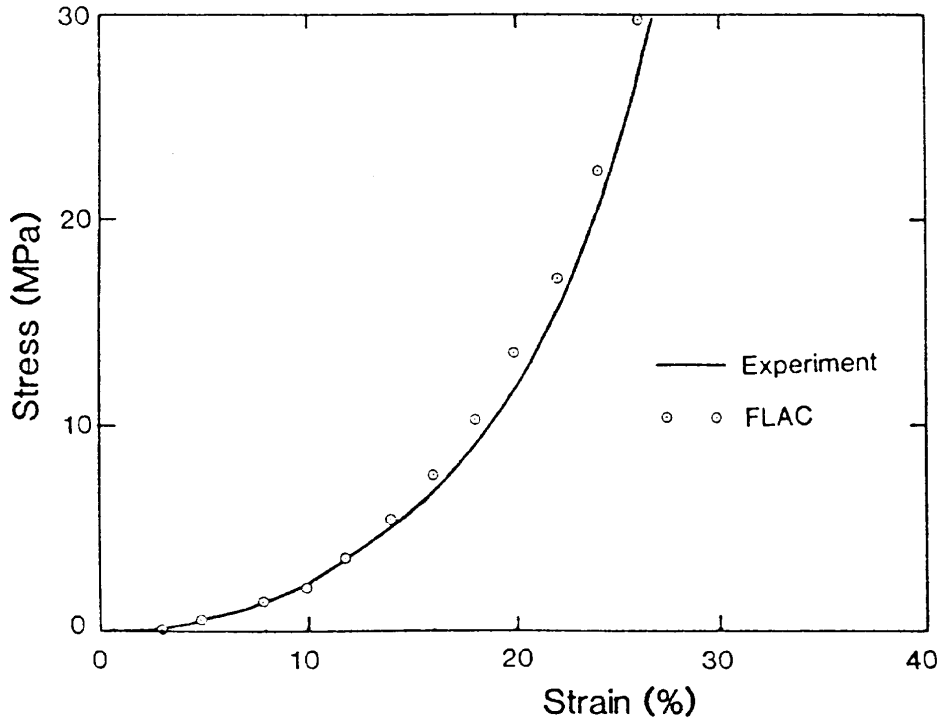

Source: Clark et al. (1988 [DIRS 164121])

Figure 180. Comparison of the Experimental and FLAC Results for Uniaxial Strain Test

7.5.1 Acceptance Criterion

Calculated stresses should be within the scatter of the experimental data up to at least 7 MPa.

7.5.2 Results

In-situ response of the backfilled panel was analyzed using a rectangular grid. The loading was simulated by applying a constant velocity across the upper and lower model boundaries. The numerical stress-strain response in the center of the panel (point B) and closer to the edge of the panel (point A) are compared with in-situ stress measurements (shown in Figure 181). Results at both points agree well with measurements up to 15 percent of strain or 7 MPa of stress. However, results at point A match in-situ measurements for even larger ranges of stress and strain. Better agreement could have been obtained if a more realistic geometry of the stope had been used and if the mining sequence had been accounted for properly in the model. This increases confidence that the backfill deformations in Section 6.4.10.1 are appropriate.

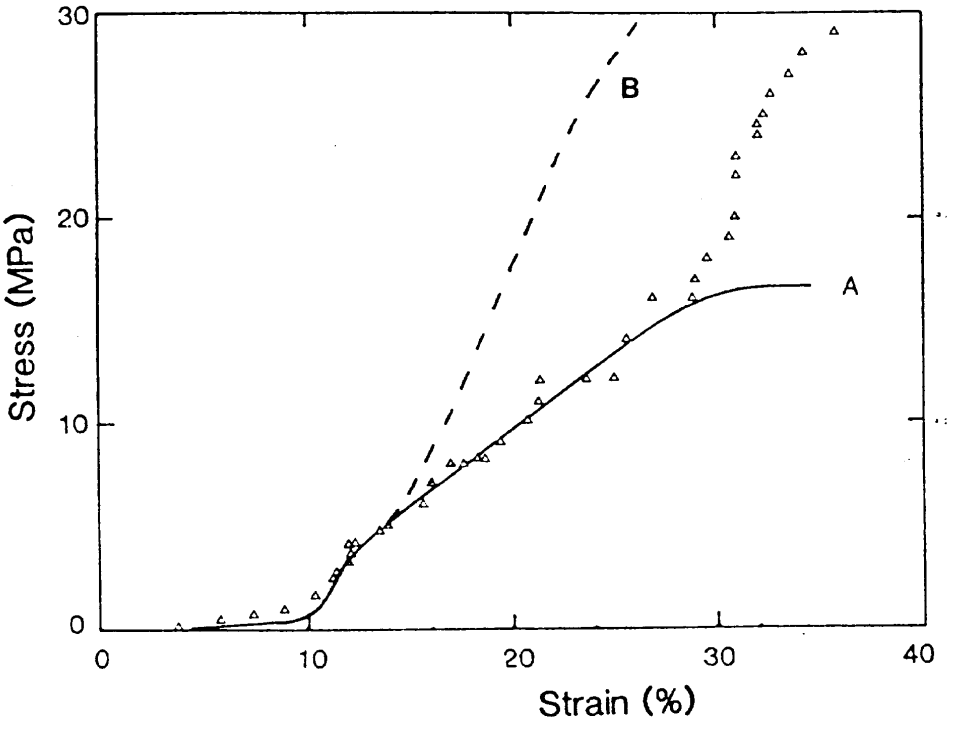

Source: Clark et al. (1988 [DIRS 164121)

NOTE: FLAC3D V 2.1 [DIRS 161947] results are shown as solid and dashed lines; point B is in the middle of the backfill panel; point A is near the edge of the panel; discrete points represent in-situ stress measurements.

Figure 181. Comparison of Model Predictions to In-Situ Measured Stress-Strain Response

INTENTIONALLY LEFT BLANK

8. CONCLUSIONS

8.1 SUMMARY OF MODELING ACTIVITIES

Information concerning dike propagation, the fluid dynamics and thermal evolution of magma, and the migration of magmatic gases through rock was assessed to form a model describing the interactions of a rising basaltic dike with a cylindrical drift mined in silicic tuff. The model is summarized in Sections 8.1.1 through 8.1.3 below. A series of validation activities were completed to build confidence in the model. Limitations of the use of this model are discussed in Section 1.3. YMRP acceptance criteria have been met as described in Attachment III of this report. Finally, results of this model are provided as outputs in Section 8.2, and the associated uncertainties discussed in Section 8.3.

8.1.1 Dike Propagation

The topographic relief of Yucca Mountain causes vertical stresses directly under the mountain to be about 3.5 MPa higher than under the adjacent valleys. This characteristic will result in higher horizontal stresses as well, although the exact amount of the increase cannot be reliably calculated. Based on earlier field measurements (DTN: SNF37100195002.001 [DIRS 131356]), the increase in horizontal stresses under the topographic high is expected to be 1 to 2 MPa. The effect of the vertical relief is expected to broaden laterally downward, and at depths below a few kilometers, no topographic effect on horizontal stress is expected. Because of the uncertainty in the depth to which the topographic effect on horizontal stress extends, it is uncertain to what extent the stress might result in a tendency for a dike, coming from great depth, to avoid the higher stress region under the mountain, to veer away, and to break out in an adjacent valley region. (See Section 6.3.9.1 for a discussion of this point.)

Heating from radioactive decay of waste in canisters will induce compressive stresses in the rock surrounding the drifts. The maximum increase, about 8 MPa for a “hot repository” design, will occur 500 to 1000 years after waste emplacement. This excess compression will attenuate away from the drifts and will not extend to a range of more than about 200 m. Only for about 50 to 60 m above and below the repository will the minimum compressive stress become vertical rather than horizontal. This change is not expected to be sufficient to cause the deviation of a dike from great depth or sill formation. (See Section 6.3.9.2 for a discussion.)

When the magma front reaches the drifts of the repository, magma will be diverted into the drifts from the dike. Analysis of fragmentation and pyroclastic flow of magma into the drift is beyond the scope of this document. For intrusive conditions, pyroclastic flow will not result in the very large 3D expansions that would be expected for an extrusive pyroclastic event. The alternative of effusive flow of partially degassed magma is possible and is much more readily analyzed. Under that assumption, magma rising from depth at 1 m/s would flood the drifts in about 5 minutes; viscosity variations between 10 Pa-s and 100 Pa-s would have little effect on that length of time. The magma front will not rise much above the drift level until the drifts are essentially filled. Magma rising at 5 m/s would fill the drifts in about 1 minute, the difference being that this magma would continue rising in the dike, although not as fast as in the absence of drifts. Drainage of magma into drifts would reduce magma front velocities from 5 m/s to only

0.1 to 0.3 m/s for lower-viscosity (10 Pa-s) magma and to about 2 m/s for the higher-viscosity (100 Pa-s) magma. (See Section 6.3.9.2.3.2 for a discussion.)

As the dike approaches the free surface, the crack tip accelerates, although the speed of the magma front is little changed. As a result, the vapor-filled cavity between the tip and the magma will lengthen. For a dike with the properties postulated, this process will already be underway when the tip reaches repository level. In the absence of any drifts, the crack would take about 100 s to grow from repository depth to breakout at the surface. This conclusion is based on treating the magma as an incompressible fluid. (See Section 6.3.9.2.3.2 for a discussion.)

Although leak-off of magma into drifts may slow the progress of the magma front to the surface, it will have little effect on the dike tip of the dike cavity, which will already have begun accelerating in response to the presence of the free surface and will reach it only seconds after passing the drift horizon. (See Section 6.3.9.2.3.2.2 for a discussion.)

3D simulation of the diversion of magma from a dike to a drift has demonstrated that the diversion will cause both the height of magma in the dike and the pressure in the magma to be depressed directly above the dike relative to the centerline between successive drifts. (See Section 6.3.9.2.3.4 for a discussion.)

The shock wave calculated by Woods et al. (2002 [DIRS 163662]) is an artifact of their initial conditions. The presence of a tip cavity preceding magma in the dike will result in a gradual exposure of magma to the drift. Intrusion of magma into a drift could result in shock-wave formation if there is standing water in the invert. In such a situation, magma could entrap the standing water, causing a hydrovolcanic explosion. Such explosions, which are not uncommon in nature, are analogous to fuel-coolant interaction (FCI) explosions encountered in industry. A hydrovolcanic outburst in a drift could produce a strong shock in the air filling the drift. Because of the lateral confinement of the drift walls, such a shock would not dissipate due to geometric spreading. However, there are many features of the drift environment that would act to attenuate a shock. Magma filling the drifts will be near its liquidus temperature of 1379 ± 60 K. The nominal magma will flood the drifts at velocities of 8 to 22 m/s and take about 5 minutes to fill 600 m of drift. Peak and "final" values of other environmental variables are listed in Table 12. (See Section 6.3.9.4.3 for a discussion.)

8.1.2 Magma Flow in Drifts

The efficacy of backfill used in main drifts and turnouts of the repository to restrict magma to emplacement drifts intersected by a dike was found to be poor. Under influence of the pressure applied by the magma, the fill will heave in a hump away from the fill slope. For backfill that does not originally extend to the back of the drift, the amount of heave will be inadequate to block the remaining open space. The sealing efficiency of a segment of tight backfill is not much better. Numerical experiments show progression of a gap forming at the roof as the magma advances. The effect is caused by the existence of a pressure component acting on the fill in the direction normal to the back and occurs because of the sloping geometry of the fill near the contact with the back. Magma freezing is one mechanism that could control advancement of the magma. However, this effect alone is probably inadequate to stop magma in even the tight

backfill situation. An alternative approach is suggested to address the uncertainties in the problem. (See Section 6.4.10.1 for a discussion.)

The "dog-leg" scenario of Woods et al. (2002 [DIRS 163662]) was evaluated extensively and was not found to be credible. Based on an extensive simulation of crack-opening rates, the distance of the magma front from the drift periphery 300 s after magma has repressurized in the drift will be between 5 m and 60 m. However, in the same time, 300 s after the drifts are completely filled, magma flowing up the main dike would reach ground surface (assuming a magma front velocity of 1m/s). Under extreme conditions of 10-MPa magma pressure inside the drift, the velocity of a magma front inside a joint is approximately 0.5 m/s (with a tendency to decrease as the pressure gradient decreases in response to the increasing length of the magma-filled portion of the joint), which is less than the expected velocity of the magma front inside the main dike. Analysis of the loss of heat from newly forming magma-filled cracks in cold rock show clearly that such cracks will not be able to grow to any appreciable width before they are halted by solidification. (See Section 6.4.11.6 for a discussion.)

The tip of the crack leading the dike will accelerate as it nears the free surface, so the crack will reach the surface only seconds after passing the drift horizon. This already open path for flow will be the most likely path that magma will take to the surface after encountering the drift complex. Once magma reaches the surface in a fissure, there will be a tendency for flow to concentrate forming a conduit. Although it is impossible to predict where along the length of the dike a conduit will develop, the drainage of magma into drifts may lead to a higher probability of conduit formation between drifts than directly over drifts. If a 50-m-diameter conduit forms between drifts, it would be difficult to move any waste packages to the surface. (See Section 6.4.11.6 for a discussion.)

8.1.3 Post-Emplacement Effects

The high solubility in water of SO_2 and to a lesser extent CO_2, along with the development of a boiling zone around a drift where magma has been emplaced, limits the migration of these gases through the repository host rock. Model results, under ambient pressure conditions, indicate that these gases would not migrate to an adjacent drift through the rock in less than 10 years. This period of time is significantly longer than the period over which any significant amount of volcanic gas would be present from the single intrusion of magma into a 5.5-m-diameter drift. Prolonged elevated pressure will move gas through fractures rapidly, but the volume of the gas would be small. After the pressure returns to ambient, the gases in the fractures diffuse into the rock matrix and dissolve readily. Volcanic gas migration may be relatively rapid through a connecting drift filled with coarse crushed tuff. In this case, an adjacent emplacement drift could be affected by migrating volcanic gas within a year or less without any strong advective flow due to large pressure differences, if the gas production is constant for some time (a month or longer). As the gas migrates through the connecting drifts and into a neighboring emplacement drift, the volcanic gas will be diluted by air, and as the gas source from the magma declines over time the extent of dilution by air will increase. The crushed tuff filling the connecting drifts would likely have some initial water content, and therefore retardation of the gas would likely be somewhat greater than the case modeled. In addition, the assumption of a constant gas source term is conservative compared to a limited volume of gas emplaced instantaneously in an intersected drift. (See Section 6.5.1 for a discussion.)

The long-term heat transfer caused by magma intrusion into a drift will take about 3 months for full solidification of the magma (ignoring radioactive heat generation from the waste). A heat pulse will move out into the surrounding rock slowly. At 8 m from the edge of a filled drift, the maximum temperature of about 73°C will be reached in about two years. The maximum temperature rise at the range of the next drift (81 m) will not occur until about 60 years and will be less than 1°C. (See Section 6.5.2 for a discussion.)

8.2 OUTPUTS

YMRP acceptance criteria have been met as described in Attachment III of this report.

8.2.1 Technical Output

The technical output of this report is comprised of a model for dike interactions with a drift and associated input and output files. The output supports conceptual models of waste package damage from interactions with magma and magmatic gases as well as the number of waste packages damaged during a volcanic eruption through the proposed repository.

8.2.2 Recommendation

Even tight backfilling of the drifts does not seem to provide a sufficient barrier to prevent magma spreading from the intersected drifts into the rest of the repository and eventually to the ground surface. Magma spreading over the top of the backfill may occur whenever there is a sharp angle between the backfill slope (at an angle of repose) and the drift roof. There are numerous engineering solutions such as backfill "keyways" developed into the roof or plugs made from cementitious materials that could be used to prevent magma flow into adjoining emplacement drifts. These will be investigated during the detailed design phase of the repository.

8.2.3 Developed Output Listed by Data Tracking Number

The outputs associated with the Dike/Drift Interaction model are listed in Table 23 by data tracking number.

Table 23. Outputs for the Dike/Drift Interaction Model Report

Sub-Model Component	Data Tracking Number
Dike Propagation Model	MO0307MWDDDINT.000 SN0304T0504203.001
Magma Flow Model	LA0303EG831811.001
Post-Emplacement Effects	
Gas Transport	LB0306AMRT0020.001
Thermal Evolution	LA0307EG831811.001

8.3 OUTPUT UNCERTAINTY

8.3.1 Uncertainties for the Dike Propagation Model

Dike ascent is a complex process involving non-linear behavior of both magma and the surrounding rock mass. The model assumes the rock mass to be a linearly elastic material and a process of dike-tip propagation according to LEFM. Magma is assumed to be an incompressible, single-phase, Newtonian fluid.

The dike propagation is a large-scale phenomena involving a number of geological units with varying material characteristics. The model represents the rock mass as a homogeneous, isotropic medium. The dike propagation is a 3D problem (particularly in certain stages of dike propagation), whereas it is modeled as 2D.

The in-situ stress conditions at Yucca Mountain and magma density indicate negative buoyancy for a wide range of possible magma densities. Positive buoyancy is required to keep magma moving upwards in this model.

However, the dike-propagation model considered a wide range of different model inputs to reduce uncertainties resulting from the simplifying assumptions used. Using a dimensional analysis, the model parameter space was reduced to a minimum.

There are only two dimensionless parameters (in a problem without leak-off) of the model because dimensionless toughness is for all practical purposes negligible in the case of dike propagation. A wide range (almost one order of magnitude) of relative density was investigated. The second dimensionless parameter, the dimensionless far-field stress, is a function of cavity gas pressure and thermally induced stress. Although the cavity gas pressure is not likely to be much larger than atmospheric pressure, it was considered in the model to be as large as 2.1 MPa. Thermally induced far-field stresses as predicted by the large-scale thermomechanical model were used as input.

8.3.2 Uncertainties for the Magma/Backfill Interaction Model

All uncertainties involved in the model of magma/backfill interaction are offset by conservative simplifications in the modeling approach. The most significant simplification is that magma flow was not considered. Instead, magma pressure was always applied on all exposed surfaces of the backfill. Magma is viscous material, and viscosity of magma interacting with backfill will increase both due to heat loss by conduction and to mixing with the crushed rock in the backfill.

8.3.3 Uncertainties for the Magma Flow Model

Given that the dike propagation problem and interactions with the repository structure are very complex, any attempt at numerical modeling will have numerous embedded uncertainties. The approach taken in most of the present modeling employs 1D or 2D models of a 3D process. Although the large scale of a dike is very favorable for creating 2D processes in the center of the dike, the effect of 3D features will dominate the interactions between the propagating dike and the magma. Therefore, it must be understood that there is considerable uncertainty associated with the outputs of this report. Where possible, this report attempts to show results for ranges of

input parameters that span the range likely to occur, so that the effect of variations of input parameters on outputs can be discerned.

8.3.4 Uncertainties for the Drift Scale Gas Flow Model

The rate of transport of soluble gas species derived from an intruding magma in a drift is dependent primarily on the fracture permeability and porosity, gas temperature and pressure, gas species diffusivity, water saturation, gas species solubility, and mineral-water reactions involving dissolved gas species. Uncertainties specific to the transport of volcanic gas are the gas composition and the gas flux and duration.

Uncertainties associated with the transport of gas in the unsaturated zone over a range of temperatures (up to approximately 250°C) have been treated through validation by extensive measurements and modeling of CO_2 exsolution and transport in the Drift Scale Heater Test over more than four years of heating (Section 7.4, BSC 2003 [DIRS 163506] Section 7.1). This validation study gives confidence in the processes and parameters used to model gas transport in the unsaturated fractured tuff at Yucca Mountain. Because the model is not calibrated to data from the Drift Scale Test and is a fully predictive forward numerical model, it can be used with confidence for the prediction of gas transport resulting from other processes such as volcanic gas migration associated with dike-drift interaction.

The uncertainties specific to the transport of volcanic gas are treated through conservatism in the model initial and boundary conditions discussed in Section 6.5.1. These conservative model conditions are: (1) a constant composition gas source used in the drift over a duration much longer than the time over which gas would be produced in significant quantities by the magma, (2) the extended time of elevated pressure in the drift, longer than the probable time of pressures above atmospheric pressure, and (3) limited gas-phase dilution in the backfilled access drift by mixing with air because of the 2D domain used and the limited volume for migration and mixing with air.

It was also shown in Section 6.5.1 that the transport of gas through the fracture network is more extensive under ambient temperatures compared to an elevated temperature regime in which boiling takes place. The development of a boiling zone results in increased liquid saturation in the fractures (owing to vapor condensation) and, therefore, a smaller effective permeability for gas and also increased dissolution of the gas phase into the water in the fractures. Therefore, although the model did not consider the temperature history of a cooling and crystallizing magma in a drift, it can be shown to be conservative with respect to the processes involved in gas migration in the rock.

8.3.5 Uncertainties for the Magma Cooling and Solidification Model

As stated in Section 6.5.2, 2D analytical solutions can only be approximate for magma cooling and solidification, where the effects of latent heat of crystallization and the contrasts in thermal properties of the magma and rocks are included. Added to the approximate nature of the solutions are uncertainties in initial conditions, namely the thermal properties of the magma and tuff.

The magma's initial temperature is assumed and realistically might vary by up to 10 percent (1035–1265°C), which reflects uncertainty in its composition and phase state at time of intrusion. By the same reasoning the magma's thermal conductivity and its variation with temperature are also uncertain: the analytical model assumed a constant value of conductivity at 1.0 W $m^{-1}K^{-1}$ (a diffusivity of ~0.3×10^{-6} m^2 s^{-1}) and typical basalt conductivities range from 2 to 4 W $m^{-1}K^{-1}$ and vary with temperature. Latent heat of crystallization was shown to have important effects on cooling and solidification of magma; it contributes up to 25 percent more heat to the magma as it cools. Added to the approximate method of including its effects in solutions is the fact that there is ~15 percent uncertainty in its magnitude and ~5 percent uncertainty in the temperature range over which it is released.

The thermal properties of the tuff are better constrained than those of the magma, but the main uncertainty regarding them are the macroscopic variations of the tuff with location. These variations include its porosity, permeability, and saturation. While such variations can cause thermal conductivity variations of 10 percent or more, their main influence is on convective heat transport. The analytical model does not consider convection but, if it were to occur, the solutions provided above are simply invalid.

Assessment of the overall uncertainty caused by the approximate nature of the solutions and the uncertainties in thermal properties is not simple. Ignoring the obvious effect of magma temperature uncertainty, latent heat uncertainty is demonstrated to be the most important, while those of other thermal properties less important. Some examples of how uncertainties combine to affect results are discussed in the text above. Overall, these uncertainties mainly affect the magma cooling times and tuff temperatures within several drift radii; at further distances from the drift the tuff temperatures are affected by uncertainties by <10 percent.

INTENTIONALLY LEFT BLANK

9. INPUTS AND REFERENCES

9.1 CITED DOCUMENTS

NOTE: In this report, the six-digit numerical identifier in brackets next to each reference callout is the YMP Document Input Reference System ([DIRS]) number, the purpose of which is to assist the reader in locating a specific reference in the DIRS database. That DIRS number is included below as the first item in the list of references.

164113 Abé, H.; Mura, T.; and Keer, L.M. 1976. "Growth Rate of a Penny-Shaped Crack in Hydraulic Fracturing of Rocks." *Journal of Geophysical Research, 81,* (29), 5335-5340. [Washington, D.C.]: American Geophysical Union. TIC: 254483.

164114 Advani, S.H.; Lee, T.S.; Dean, R.H.; Pak, C.K.; and Avasthi, J.M. 1997. "Consequences of Fluid Lag in Three-Dimensional Hydraulic Fractures." *International Journal for Numerical and Analytical Methods in Geomechanics, 21,* 229-240. New York, New York: John Wiley & Sons. TIC: 254560.

103750 Altman, W.D.; Donnelly, J.P.; and Kennedy, J.E. 1988. *Qualification of Existing Data for High-Level Nuclear Waste Repositories: Generic Technical Position.* NUREG-1298. Washington, D.C.: U.S. Nuclear Regulatory Commission. TIC: 200652.

103597 Altman, W.D.; Donnelly, J.P.; and Kennedy, J.E. 1988. *Peer Review for High-Level Nuclear Waste Repositories: Generic Technical Position.* NUREG-1297. Washington, D.C.: U.S. Nuclear Regulatory Commission. TIC: 200651.

103289 Batchelor, G.K. 1967. *An Introduction to Fluid Dynamics.* Page 594. New York, New York: Cambridge University Press. TIC: 241827.

160130 BSC (Bechtel SAIC Company, LLC) 2001. *Characterize Eruptive Processes at Yucca Mountain, Nevada*. ANL-MGR-GS-000002 REV 00 ICN 01. Las Vegas, Nevada: Bechtel SAIC Company. ACC: MOL.20020327.0498.

159124 BSC (Bechtel SAIC Company) 2002. Geologic Framework Model (GFM2000). MDL-NBS-GS-000002 REV 01. Las Vegas, Nevada: Bechtel SAIC Company. ACC: MOL.20020530.0078.

160313 BSC 2002. *Scientific Processes Guidelines Manual*. MIS-WIS-MD-000001 REV 01. Las Vegas, Nevada: Bechtel SAIC Company. ACC: MOL.20020923.0176.

158966 BSC 2002. *The Enhanced Plan for Features, Events, and Processes (FEPs) at Yucca Mountain*. TDR-WIS-PA-000005 REV 00. Las Vegas, Nevada: Bechtel SAIC Company. ACC: MOL.20020417.0385.

161838 BSC (Bechtel SAIC Company) 2003. Characterize Eruptive Processes at Yucca Mountain, Nevada. ANL-MGR-GS-000002 REV 01C. Las Vegas, Nevada: Bechtel SAIC Company. ACC: MOL.20030711.0107.

162711 BSC 2003. *Drift Degradation Analysis.* ANL-EBS-MD-000027 REV 02. Las Vegas, Nevada: Bechtel SAIC Company. ACC: DOC.20030709.0003.

163506 BSC 2003. *Drift-Scale Coupled Processes (DST and THC Seepage) Models*. MDL-NBS-HS-000001 REV 02C. Las Vegas, Nevada: Bechtel SAIC Company. ACC: MOL.20030507.0274. TBV-5120

163573 BSC 2003. *Features, Events, and Processes: Disruptive Events*. ANL-WIS-MD-000005 REV 01A. Las Vegas, Nevada: Bechtel SAIC Company. ACC: MOL.20030711.0100.

161810 BSC 2003. *Igneous Intrusion Impacts on Waste Package and Waste Form*. MDL-EBS-GS-000002 REV 00A. Las Vegas, Nevada: Bechtel SAIC Company. ACC: MOL.20030711.0096.

161851 BSC 2003. *Number of Waste Packages Hit by Igneous Intrusion*. ANL-MGR-GS-000003 REV 00C. Las Vegas, Nevada: Bechtel SAIC Company. ACC: MOL.20030711.0098.

162289 BSC 2003. *Repository Design, Repository/PA IED Subsurface Facilities*. 800-IED-EBS0-00401-000-00C. Las Vegas, Nevada: Bechtel SAIC Company. ACC: ENG.20030303.0002.

164493 BSC 2003. *Repository Design Project, Repository/PA IED Subsurface Facilities*. 800-IED-WIS0-00101-000-000Ad. Las Vegas, Nevada: Bechtel SAIC Company. ACC: MOL.20030730.0337. TBV-5310

164143 BSC 2003. *Technical Work Plan -- Igneous Activity Analysis for Disruptive Events. Work Packages Numbers: P4A1224DF1 / ADEM03, P4D1224DFR / ADET03, ATMT11*. TWP-WIS-MD-000007 REV 03. Las Vegas, Nevada: Bechtel SAIC Company. ACC: DOC.20030721.0003.

161770 Canori, G.F. and Leitner, M.M. 2003. *Project Requirements Document*. TER-MGR-MD-000001 REV 01. Las Vegas, Nevada: Bechtel SAIC Company. ACC: DOC.20030404.0003.

100968 Carslaw, H.S. and Jaeger, J.C. 1959. *Conduction of Heat in Solids*. 2nd Edition. Oxford, Great Britain: Oxford University Press. TIC: 206085.

164336 Clark, I.H. 1991. "The Cap Model for Stress Path Analysis of Mine Backfill Compaction Processes." *Computer Methods and Advances in Geomechanics, [Proceedings of the Seventh International Conference on Computer Methods and Advances in Geomechanics, Cairns, 6-10 May 1991]*. Beer, G.; Booker, J.R.; and Carter, J.P., eds. Pages 1293-1298. [Brookfield, Vermont]: A.A. Balkema. TIC: 254553. TIC: 254553.

164121 Clark, I.H.; Gurtunca, R.G.; and Piper, P.S. 1988. "Predicting and Monitoring Stress and Deformation Behaviour on Backfill in Deep-Level Mining Excavations." *[Prediction Versus Performance], Fifth Australian-New Zealand Conference on Geomechanics, Sydney, 22-23 August 1988, [Preprints of Papers]*. National Conference Publication No. 88/11. Pages 214-218. Barton, A.C.T., Australia: Institution of Engineers. TIC: 254570..

139600 Crouch, S.L. and Starfield, A.M. 1983. *Boundary Element Methods in Solid Mechanics, with Applications in Rock Mechanics and Geological Engineering*. Boston, Massachusetts: Allen & Unwin. TIC: 4370.

151552 CRWMS M&O 2000. *Dike Propagation Near Drifts*. ANL-WIS-MD-000015 REV 00 ICN 1. Las Vegas, Nevada: CRWMS M&O. ACC: MOL.20001213.0061.

151553 CRWMS M&O 2000. *Features, Events, and Processes: Disruptive Events*. ANL-WIS-MD-000005 REV 00 ICN 1. Las Vegas, Nevada: CRWMS M&O. ACC: MOL.20001218.0007.

153246 CRWMS M&O 2000. *Total System Performance Assessment for the Site Recommendation*. TDR-WIS-PA-000001 REV 00 ICN 01. Las Vegas, Nevada: CRWMS M&O. ACC: MOL.20001220.0045.

102776 Delaney, P.T. 1987. "Heat Transfer During Emplacement and Cooling of Mafic Dykes." *Mafic Dyke Swarms, A Collection of Papers Based on the Proceedings of an International Conference held at Erindale College, University of Toronto, Ontario, Canada, June 4 to 7, 1985*. Halls, H.C. and Fahrig, W.F., eds. Special Paper 34. Pages 31-46. St. John's, Newfoundland, Canada: Geological Association of Canada. TIC: 225006.

164115 Desroches, J.; Detournay, E.; Lenoach, B.; Papanastasiou, P.; Pearson, J.R.A.; Thiercelin, M.; and Cheng, A. 1994. "The Crack Tip Region in Hydraulic Fracturing." *Proceedings of the Royal Society of London, Series A, Mathematical and Physical Sciences, 447,* 39-48. London, England: The Royal Society. TIC: 254561.

162914 Detournay, E.; Mastin, L.G.; Pearson, J.R.A.; Rubin, A.M.; and Spera, F.J. 2003. *Final Report of the Igneous Consequences Peer Review Panel*. Las Vegas, Nevada: Bechtel SAIC Company. ACC: MOL.20030325.0227.

161776 Duncan, J.M.; Byrne, P.; Wong, K.S.; and Mabry, P. 1980. *Strength, Stress-Strain and Bulk Modulus Parameters for Finite Element Analyses of Stresses and Movements in Soil Masses*. UCB/GT/80-01. Berkeley, California: University of California, College of Engineering, Office of Research Services. TIC: 253873.

163868 Ford, H. and Alexander, J.M. 1963. *Advanced Mechanics of Materials.* New York, New York: Halsted Press. On Order

154365 Freeze, G.A.; Brodsky, N.S.; and Swift, P.N. 2001. *The Development of Information Catalogued in REV00 of the YMP FEP Database*. TDR-WIS-MD-000003 REV 00 ICN 01. Las Vegas, Nevada: Bechtel SAIC Company. ACC: MOL.20010301.0237.

161774 Fruchtbaum, J. 1988. "Handling Special Materials." *Bulk Materials Handling Handbook*. Pages 327-375. New York, New York: Van Nostrand Reinhold. TIC: 253872.

163631 Gaffney, E.S. 2002. Magma and Gas Flow Analysis. Scientific Notebook SN-LANL-SCI-279-V1. ACC: MOL.20030313.0072.

164112 Garagash, D. and Detournay, E. 2000. "The Tip Region of a Fluid-Driven Fracture in an Elastic Medium." *Journal of Applied Mechanics, 67,* (1), 183-192. New York, New York: American Society of Mechanical Engineers. TIC: 254482.

163624 Geertsma, J. and de Klerk, F. 1969. "A Rapid Method of Predicting Width and Extent of Hydraulically Induced Fractures." *Journal of Petroleum Technology, [21], ([12])*, 1571–1581. [Dallas, Texas: American Institute of Mining and Metallurgical Engineers]. TIC: 254512.

163625 Griffiths, R.W. 2000. "The Dynamics of Lava Flows." *Annual Review of Fluid Mechanics, 32*, 477–518. [Palo Alto, California]: Annual Reviews. TIC: 254466.

164124 Henderson, F.M. 1966. *Open Channel Flow*. 175. New York, New York: MacMillan. On Order

161507 Hess, K.G. 2002. "Contract No. DE-AC28-01RW12101-Revision to Peer Review Plan for the Igneous Consequences Peer Review." Letter from K.G. Hess (BSC) to J.R. Dyer (DOE/YMSCO), September 17, 2002, TER:jar-0912024183 with enclosure. ACC: MOL.20021017.0028.

163626 Hills, D.; Kelly, P.; Dai, D.; and Korsunsky, A. 1996. *Solution of Crack Problems: The Disturbed Dislocation Technique*. Solid Mechanics and its Applications Volume 44. Boston, Massachusetts: Kluwer Academic. TIC: 254533..

163628 Howard, G.C. and Fast, C.R. 1957. "Optimum Fluid Characteristics for Fracture Extension." *Drilling and Production Practices*. 261–270. Washington, D.C.: American Petroleum Institute. On Order

163630 Jaeger, J.C. 1968. "Cooling and Solidification of Igneous Rocks." *Basalts, The Poldervaart Treatise on Rocks of Basaltic Composition*. Volume 2. Hess, H.H. and Poldervart, A., eds. Pages 503–536. New York, New York: Interscience Publishers. TIC: 254505.

164111 Jeffrey, R.G. and Mills, K.W. 2000. "Hydraulic Fracturing Applied to Inducing Longwall Coal Mine Goaf Falls." *Pacific Rocks 2000, 'Rock Around the Rim', Proceedings of the Fourth North American Rock Mechanics Symposium, NARMS 2000, Seattle, Washington, USA, 31 July-3 August 2000.* Girard, J.; Liebman, M.; Breeds, C.; and Doe, T., eds. Pages 423-430. Brookfield, Vermont: A.A. Balkema. TIC: 249510.

164120 Jeffrey, R.G. 1989. "The Combined Effect of Fluid Lag and Fracture Toughness on Hydraulic Fracture Propagation." *Proceedings, SPE Joint Rocky Mountain Regional/Low Permeability Reservoirs Symposium and Exhibition, March 6-8, 1989, Denver, Colorado.* 269-276. [Richardson, Texas]: Society of Petroleum Engineers. TIC: 254562.

164511 Khristianovic, S.A. and Zheltov, Y.P. 1955. "Formation of Vertical Fractures by Means of Highly Viscous Liquid." *Proceedings, Fourth World Petroleum Congress, Rome, Italy, June 1955*. Section II: Drilling Production. Pages 579-586. Rome, Italy: Carlo Colombo Publishers. Copyright Requested

100909 Kotra, J.P.; Lee, M.P.; Eisenberg, N.A.; and DeWispelare, A.R. 1996. *Branch Technical Position on the Use of Expert Elicitation in the High-Level Radioactive Waste Program.* NUREG-1563. Washington, D.C.: U.S. Nuclear Regulatory Commission. TIC: 226832

126865 Lister, J.R. 1990. "Buoyancy-Driven Fluid Fracture: Similarity Solutions for the Horizontal and Vertical Propagation of Fluid-Filled Cracks." *Journal of Fluid Mechanics, 217*, 213-239. Cambridge, United Kingdom: Cambridge University Press. TIC: 225065.

126877 Lister, J.R. 1990. "Buoyancy-Driven Fluid Fracture: The Effects of Material Toughness and of Low-Viscosity Precursors." *Journal of Fluid Mechanics, 210,* 263-280. Cambridge, United Kingdom: Cambridge University Press. TIC: 246674.

163635 Lister, J.R. 1995. "Fluid-Mechanical Models of the Interaction Between Solidification and Flow in Dykes." *Physics and Chemistry of Dykes*. Baer and Heimann, eds. Pages 115–124. Rotterdam, The Netherlands: Balkema. On Order

126889 Lister, J.R. and Kerr, R.C. 1991. "Fluid-Mechanical Models of Crack Propagation and Their Application to Magma Transport in Dykes." *Journal of Geophysical Research, 96*, (B6), 10,049-10,077. Washington, D.C.: American Geophysical Union. TIC: 225066.

144310 Luhr, J.F. and Simkin, T., eds. 1993. *Paricutin, The Volcano Born in a Mexican Cornfield*. Phoenix, Arizona: Geoscience Press. TIC: 247017.

157883 Marachi, N.D.; Chan, C.K.; and Seed, H.B. 1972. "Evaluation of Properties of Rockfill Materials." *Journal of the Soil Mechanics and Foundations Division, Proceedings of the American Society of Civil Engineers, 98*, (SM1), 95-114. New York, New York: American Society of Civil Engineers. TIC: 252235.

164110 Nilson, R.H. 1986. "An Integral Method for Predicting Hydraulic Fracture Propagation Driven by Gases or Liquids." *International Journal for Numerical and Analytical Methods in Geomechanics, 10*, 191-211. [New York, New York]: John Wiley & Sons. TIC: 254484.

163641 Nordgren, R.P. 1972. "Propagation of a Vertical Hydraulic Fracture." *Society of Petroleum Engineers Journal, 12*, (4), 306–314. Dallas, Texas: Society of Petroleum Engineers. TIC: 254486.

163274 NRC (U.S. Nuclear Regulatory Commission) 2003. *Yucca Mountain Review Plan, Final Report.* NUREG-1804, Rev. 2. Washington, D.C.: U.S. Nuclear Regulatory Commission, Office of Nuclear Material Safety and Safeguards. TIC: 254568.

106453 Olsson, W.A. and Brown, S.R. 1997. *Mechanical Properties of Fractures from Drillholes UE25-NRG-4, USW-NRG-6, USW-NRG-7, USW-SD-9 at Yucca Mountain, Nevada*. SAND95-1736. Albuquerque, New Mexico: Sandia National Laboratories. ACC: MOL.19970224.0064.

163644 Perkins, T.K. and Kern, L.R. 1961. "Widths of Hydraulic Fractures." *Journal of Petroleum Technology, [13*], ([9]), 937–949. [Dallas, Texas: American Institute of Mining and Metallurgical Engineers]. TIC: 254487.

164405 Rice, J.R. 1968. "Mathematical Analysis in the Mechanics of Fracture." *Fracture, An Advanced Treatise*. Liebowitz, H., ed. Volume II: Mathematical Fundamentals. Pages 191-311. New York, New York: Academic Press. TIC: 254573.

164118 Rubin, A.M. 1995. "Propagation of Magma-Filled Cracks." *Annual Review of Earth and Planetary Science, 23*, 287-336. [Palo Alto, California]: Annual Reviews. TIC: 254554.

163648 Sneddon, I.N. [1946[."The Distribution of Stress in the Neighbourhood of a Crack in an Elastic Solid." *[Proceedings of the Royal Society of London, Series A: Mathematical and Physical Sciences, 187*], 229–260. [London, England: Harrison and Son]. TIC: 254550.

127086 Spence, D.A. and Turcotte, D.L. 1990. "Buoyancy-Driven Magma Fracture: A Mechanism for Ascent Through the Lithosphere and the Emplacement of Diamonds." *Journal of Geophysical Research, 95*, (B4), 5133-5139. Washington, D.C.: American Geophysical Union. TIC: 246860.

127068 Spence, D.A. and Turcotte, D.L. 1985. "Magma-Driven Propagation of Cracks." *Journal of Geophysical Research, 90*, (B1), 575-580. Washington, D.C.: American Geophysical Union. TIC: 225148.

164109 Spera, F.J. 2000. "Physical Properties of Magma." *Encyclopedia of Volcanoes*. Sigurdsson, H.; ed. Pages 171-190. San Diego, California: Academic Press. TIC: 254454.

164459 Stasiuk, M.V.; Barclay, J.; Carroll, M.R.; Jaupart, C.; Ratté, J.C.; Sparks, R.S.J.; and Tait, S.R. 1996. "Degassing During Magma Ascent in the Mule Creek Vent (USA)." *Bulletin of Volcanology, 58*, ([2-3]), 117-130. [New York, New York]: Springer-Verlag. TIC: 254576.

101027 Stock, J.M.; Healy, J.H.; Hickman, S.H.; and Zoback, M.D. 1985. "Hydraulic Fracturing Stress Measurements at Yucca Mountain, Nevada, and Relationship to the Regional Stress Field." *Journal of Geophysical Research, 90*, (B10), 8691-8706. Washington, D.C.: American Geophysical Union. TIC: 219009.

150327 Theis, C.V. 1935. "The Relation Between the Lowering of the Piezometric Surface and the Rate and Duration of Discharge of a Well Using Ground-Water Storage." *Transactions of the American Geophysical Union Sixteenth Annual Meeting, April 25 and 26, 1935, Washington, D.C.* Pages 519-524. Washington, D.C.: National Academy of Science, National Research Council. TIC: 223158.

134364 Turcotte, D.L.; Emerman, S.H.; and Spence, D.A. 1987. "Mechanics of Dyke Injection." *Mafic Dyke Swarms, A Collection of Papers Based on the Proceedings of an International Conference held at Erindale College, University of Toronto, Ontario, Canada, June 4-7, 1985*. Halls, H.C. and Fahrig, W.F., eds. Pages 25-29. St. John's, Newfoundland, Canada: Geological Association of Canada. TIC: 246897.

139651 Turcotte, D.L. and Schubert, G. 1982. *Geodynamics, Applications of Continuum Physics to Geological Problems*. New York, New York: John Wiley & Sons. TIC: 235924.

164389 Voller, V.R. and Peng, S. 1995. "An Algorithm for Analysis of Polymer Filling of Molds." *Polymer Engineering and Science, 35*, (22), 1758-1765. [Brookfield, Connecticut: Society of Plastics Engineers]. TIC: 254571..

163880 Voller, V.; Peng, S.; and Chen, Y.F. 1996. "Numerical Solution of Transient, Free Surface Problems in Porous Media." *International Journal for Numerical Methods in Engineering, 39*, (17), 2889–2906. Sussex, England: John Wiley & Sons. TIC: 254521.

164068 Wang, J.S. 2003. "Scientific Notebook Referenced in Model Report, MDL-MGR-GS-000005 REV 00, Dike/Drift Interaction." Memorandum from J.S. Wang (BSC) to File, July 2, 2003, with attachment. ACC: MOL.20030707.0261.

163649 Warpinski, N.R.; Abou-Sayed, I.S.; Moschovidis, Z.; and Parker, C. 1993. *Hydraulic Fracture Model Comparison Study: Complete Results*. GRI-93/0109. Chicago, Illinois: Gas Research Institute. TIC: 254276.

163657 Warpinski, N.R.; Moschovidis, Z.A.; Parker, C.D.; and Abou-Sayed, I.S. 1994. "Comparison Study of Hydraulic Fracturing Models—Test Case: GRI Staged Field Experiment No. 3." *SPE Production & Facilities, 9*, (1), 7–16. Richardson, Texas: SPE Production & Facilities. TIC: 254277.

163659 Wilcox, R.E, 1954. "Petrology of the Paricutin Volcano." *Petrology of the Parícutin Volcano Mexico, Geologic Investigations in the Parícutin Area, Mexico*. Geological Survey Bulletin 965-C. Pages 281-353. Washington, D.C: U.S. Government Printing Office. TIC: 254485.

162731 Williams, N.H. 2003. "Thermal Inputs for Evaluations Supporting TSPA-LA, Supplement." Interoffice memorandum from N.H. Williams (BSC) to Distribution, April 4, 2003, 0205035938, with enclosures. ACC: MOL.20030501.0081.

163662 Woods, A.W.; Sparks, S.; Bokhove, O.; LeJeune, A-M.; Conner, C.B.; and Hill, B.E. 2002. "Modeling Magma-Drift Interaction at the Proposed High-Level Radioactive Waste Repository at Yucca Mountain, Nevada, USA." *Geophysical Research Letters, 29*, (13), 19-1 through 19-4. [Washington, D.C.]: American Geophysical Union. TIC: 254467.

108740 Yokoyama, I. and de la Cruz-Reyna, S. 1990. "Precursory Earthquakes of the 1943 Eruption of Paricutin Volcano, Michoacan, Mexico." *Journal of Volcanology and Geothermal Research, 44,* 265-281. Amsterdam, The Netherlands: Elsevier. TIC: 234990.

164368 Zhang, X.; Jeffrey, R.; and Detournay, E. 2002. *NPHF2D, Non-Planar Hydraulic Fracture 2D User's Manual*. Minneapolis, Minnesota: University of Minnesota, Department of Civil Engineering. TIC: 253445.

164402 Zhang, X.; Jeffrey, R.; and Detournay, E. 2001. *Propagation of a Plane-Strain Hydraulic Fracture Parallel to the Free Surface of an* Report. CSIRO Petroleum Restricted Report No. 01-007. Glen Waverley, Victoria, Australia: CSIRO Petroleum. TIC: 254569.

163874 Zhang, X. and Sanderson, D.J. 2002. *Numerical Modelling and Analysis of Fluid Flow and Deformation of Fractured Rock Masses*. Boston, Massachusetts: Pergamon. TIC: 254577.

9.2 CODES, STANDARDS, REGULATIONS, AND PROCEDURES

156605 10 CFR 63. Energy: Disposal of High-Level Radioactive Wastes in a Geologic Repository at Yucca Mountain, Nevada. Readily available.

AP-2.22Q, Rev. 0, ICN 1. *Classification Criteria and Maintenance of the Monitored Geologic Repository Q-List.* Washington, D.C.: U.S. Department of Energy, Office of Civilian Radioactive Waste Management. ACC: DOC.20030422.0009.

AP-SIII.10Q, Rev. 1, ICN 2. *Models.* Washington, D.C.: U.S. Department of Energy, Office of Civilian Radioactive Waste Management. ACC: DOC.20030627.0003.

9.3 SOFTWARE

161947 BSC 2002. *Software Code: FLAC3D.* V2.1. PC WINDOWS 2000/NT 4.0. 10502-2.1-00.

163665 BSC 2002. *Software Code: NPHF2D.* V 1.0. PC, Windows 2000. 10904-1.0-00.

161949 BSC 2002. *Software Code: UDEC.* V3.1. PC WINDOWS 2000/NT 4.0. 10173-3.1-00.

161256 LBNL (Lawrence Berkeley National Laboratory) 2002. *Software Code: TOUGHREACT.* V3.0. DEC-Alpha with Unix OSF1 V5.1 and OSF1 V5.0, Sun Solaris 5.5.1, Linux Redhat 7.2. 10396-3.0-00.

9.4 SOURCE DATA, LISTED BY DATA TRACKING NUMBER

150930 MO0005PORWATER.000. Perm-Sample Pore Water Data. Submittal date: 05/04/2000.

160708 LA0107GV831811.001. Parameters for Igneous Consequences Analysis. Submittal date: 07/11/2001.

164744 LB0302DSCPTHCS.001. Drift-Scale Coupled Processes (THC Seepage) Model: Simulations. Submittal date: 02/11/2003.

164462 MO0304DQRIRPPR.002. Intact Rock Properties Data On Poisson's Ratio And Youngs's Modulus.. Submittal date: 04/03/2003.

131356 SNF37100195002.001. Hydraulic Fracturing Stress Measurements in Test Hole: ESF-AOD-HDFR1, Thermal Test Facility, Exploratory Studies Facility at Yucca Mountain. Submittal date: 12/18/1996.

108410 SNL02030193001.027. Summary of Bulk Property Measurements Including Saturated Bulk Density for NRG-2, NRG-2A, NRG-2B, NRG-3, NRG-4, NRG-5, NRG-6, NRG-7/7A, SD-9, and SD12. Submittal date: 08/14/1996.

9.5 OUTPUT DATA, LISTED BY DATA TRACKING NUMBER

LA0303EG831811.001. Magma Flow into Drifts. Submittal date: 03/26/2003.

LA0307EG831811.001. Analytical Calculations of Heat Flow for YMP Drift Filled with Basaltic Magma. Submittal date: 07/24/2003.

LB0306AMRT0020.001. Volcanic Gas Transport Simulations. Submittal date: 06/12/2003.

MO0307MWDDDINT.000. Dike/Drift Interactions Model Output. Submittal date: 07/18/2003.

SN0304T0504203.001. Dike Propagation Model Results Using NPHF2D. Submittal date: 04/02/2003. DIRS 163762

INTENTIONALLY LEFT BLANK

ATTACHMENT I

HYDRAULIC FRACTURE NEAR THE FREE SURFACE — MATHEMATICAL FORMULATION OF THE NPHF2D CODE

ATTACHMENT I

HYDRAULIC FRACTURE NEAR THE FREE SURFACE — MATHEMATICAL FORMULATION OF THE NPHF2D CODE

I.1 INTRODUCTION

Modeling fluid-driven fracture propagation has progressed since the 1950s due to its importance in the oil and gas industries. Early studies concentrated on analytical solutions for hydraulic fracture and assumed simple geometries for the fracture, such as 2D plane strain and axisymmetric penny-shaped geometries. This early work did not consider in detail the mechanics associated with the fluid lag (Perkins and Kern 1961; Geertsma and de Klerk 1969; Abé et al. 1976). The issue of the lag was addressed recently by some researchers. For example, the analytical solutions for deeply buried fractures have been given by the weight function approach in Jeffrey (1989), with assumed pressure profiles (Pressure was not calculated from a coupled solution.), and by the integral approach in Nilson (1986), with assumed wedge shapes. With the recent improvement of computational power, many complex problems became tractable. The three-dimensional rectangular fracture was investigated numerically by Advani et al. (1997), who assumed lag sizes and pressure profiles. The research focus of hydraulic fracturing has also shifted to the exploitation of numerical algorithms that are able to address more of the mechanisms involved in the process. More complete and realistic fracture growth models have been, and are being, developed as a result. In addition, recent application of hydraulic fracturing to induce caving in mining have raised the issue of fluid lag development in fractures growing near a free surface where the confining stress is low or even tensile (Jeffrey and Mills 2000).

The near-tip solutions for a semi-infinite plane-strain fracture in elastic media with arbitrary toughness were constructed by Garagash and Detournay (2000). A fluid lag was assumed to exist in the region near the fracture tip in order to account for the effects of finite rock toughness. This effort on finite-toughness solutions was extended to the case of finite fracture size and non-zero confining stress using numerical schemes implemented in the Non-Planar Hydraulic Fracture 2D (NPHF2D) code.

The application of the NPHF2D code is to simulate the evolution of the subsurface fracture length, ℓ, and the fluid front, ℓ_f, with time, t, as well as the dependence of the fracture opening, w, and net pressure, $p = p_f - \sigma_o$, upon position in fracture x and time t. The fracture is located at depth H from the free surface and propagates in the (predominantly) horizontal or vertical direction (i.e., parallel or perpendicular to the free surface). Fracture can turn (change its direction) as a function of stress field.

This attachment contains parts of the *N*PHF2D User's Manual (Zhang, Jeffrey, and Detourany 2002) in which the mathematical formulation of the code is described. In Sections I.2 and I.3, the governing equations for elasticity and fluid flow, as well as the corresponding boundary conditions, are formulated. The equations are then written in dimensionless and scaled forms. Section I.4 provides details of the numerical algorithm used.

I.2 MATHEMATICAL FORMULATION OF FLUID-DRIVEN HORIZONTAL FRACTURE

The schematic illustration of the horizontal fracture (parallel to free surface) is given in Fig. I-1. The confining stress, σ_o, may arise from the in-situ stress or from the gravity, αH. The parameter α takes the values 0 or $\pm\rho_r g$ — with $\rho_r g$ denoting the unit weight of the rock mass — depending on the orientation of the half-plane and whether gravity needs to be accounted for in the analysis. In particular, we are interested in mapping the dependence of the solution on the injection rate, Q_o, and on the three material parameters, μ', E', K', which are defined as

$$\mu' = 12\mu, \qquad E' = \frac{E}{1-\nu^2}, \qquad K' = 4\left(\frac{2}{\pi}\right)^{1/2} K_{Ic} \qquad \text{(Eq. I-1)}$$

where μ is the fluid viscosity, E and ν are the rock Young's modulus and Poisson's ratio, respectively, and K_{Ic} is the rock fracture toughness. (While E' is the so-called plane strain modulus, μ' and K' are introduced simply to keep equations uncluttered by numerical factors.) For convenience, μ', E', and K' will be referred to as viscosity, elastic modulus, and toughness, respectively.

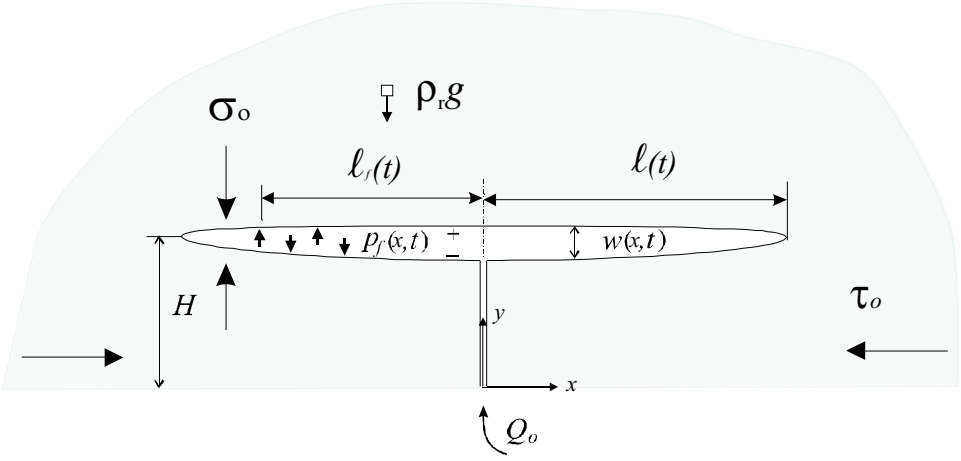

Figure I-1 Plane-strain, fluid-driven horizontal fracture with a lag zone at the tip

In general, the problem of real-time tracking of the fluid fronts in the simulation of hydraulic fractures has not been solved. Moving-grid and adaptive-grid methods can be usefully employed for such problems. However, in the formulation of NPHF2D, a fixed-grid method is used due to its relatively simple description and greater ease of programing. The volume-of-fluid (VOF) method, which is widely used for modeling free surface flow in mould filling (Voller and Peng 1995), is implemented to track the fluid front in the hydraulic fracture.

There are three parameters that have a dimension of length in the above stated fracture problem: the fracture length; the fracture depth; and the lag size. These parameters are coupled and interact with each other to produce a fluid pressure distribution that is consistent with rock fracture toughness and width distribution. The multiple length scale aspect of the problem gives rise to some complicated responses because the fracture behavior depends on all of these lengths. It is a challenging task to account for the influence and interaction of the important physical factors that are associated with these multiple length scales.

I.2.1 Governing Equations

Elasticity. A non-local elasticity relation exists between the normal and shear displacement discontinuities (DDs) of the fracture walls, w and v, and the net pressure, p. Such a relation can be accounted for through superposition of singular displacement discontinuity solutions. Although the fracture is symmetrically loaded by an internal pressure, the geometric asymmetry caused by the presence of a free surface is responsible for the existence of a shear displacement discontinuity, v.

Following Hills et al. (1996), the governing equations are written based on the influence functions for displacement discontinuity singularities:

$$\frac{4\pi}{E'} p(\mathbf{x}^m) = -\int_{-\ell}^{\ell} \{L_{xx}^{xx}(\mathbf{x}^m, \mathbf{x}^n) w(\mathbf{x}^n) + L_{xx}^{xy}(\mathbf{x}^m, \mathbf{x}^n) v(\mathbf{x}^n)\} \mathrm{d}s(\mathbf{x}^n) \qquad \text{(Eq. I-2)}$$

$$0 = \int_{-\ell}^{\ell} \{L_{xy}^{xx}(\mathbf{x}^m, \mathbf{x}^n) w(\mathbf{x}^n) + L_{xy}^{xy}(\mathbf{x}^m, \mathbf{x}^n) v(\mathbf{x}^n)\} \mathrm{d}s(\mathbf{x}^n) \qquad \text{(Eq. I-3)}$$

where the general expressions for the dipole influence functions, which can be inclined to the coordinate axes, are $L_{ij}^{kl}(\mathbf{x}^m, \mathbf{x}^n) = (-1)^{k+1} \frac{\partial [G_{lij}(\mathbf{x}^m, \mathbf{x}^n)]}{\partial x_k^n}$, in which i, j, k, l represent $\{x, y\}$; and x_k^n denotes the coordinate at node n in the k-direction.

In principle, Eq. I-3 can be inverted to yield

$$v = \mathcal{N}\{w; \mathcal{L}\} \qquad \text{(Eq. I-4)}$$

where the length ratio, $\mathcal{L} = \ell / H$, and $\mathcal{N}$ is a linear operator. Thus, with regard to Eq. I-3, the first integral equation (Eq. I-2) can be rewritten as

$$\mathcal{H}\left\{\frac{1}{\ell}\frac{\partial w}{\partial \xi}; \mathcal{L}\right\} = \frac{p}{E'} \qquad \text{(Eq. I-5)}$$

where $\mathcal{H}$ is a linear functional, and ξ is the coordinate along the fracture.

Lubrication. The equation governing the flow of viscous fluid in the fluid-filled zone ($0 < x < \ell_f$) is the non-linear Reynolds differential equation from the lubrication theory

$$\frac{\partial w}{\partial t} = \frac{1}{\mu'}\frac{\partial}{\partial x}\left(w^3 \frac{\partial p}{\partial x}\right) \qquad \text{(Eq. I-6)}$$

This equation is obtained by combining Poiseuille law (Batchelor 1967):

$$q = -\frac{w^3}{\mu'}\frac{\partial p}{\partial x} \qquad \text{(Eq. I-7)}$$

in which q is the fluid flux, with the local continuity equation:

$$\frac{\partial w}{\partial t} + \frac{\partial q}{\partial x} = 0 \qquad \text{(Eq. I-8)}$$

Boundary and Initial Conditions. The problem formulation is completed by specifying a propagation criterion and the boundary conditions at the fracture inlet $x = 0$ and at the tip $x = \ell(t)$, as well as at the fluid front $x = \ell_f(t)$. The condition that the fracture is in mobile equilibrium, $K_I = K_{Ic}$, can be expressed as

$$w(x,t) \simeq \frac{K'}{E'}(\ell - x)^{1/2} \qquad \ell - x \ll \ell \tag{Eq. I-9}$$

The condition $w(\ell, t) = 0$ at the tip is obviously implied by the opening asymptote (Eq. I-9). In addition, the net pressure in the lag zone is assumed to take the form

$$p(x,t) = -\sigma_o \qquad \ell - \ell_f < x < \ell \tag{Eq. I-10}$$

in which σ_o is the initial stress across the fracture path. (The gas pressure in the lag zone is assumed to be zero in the case of horizontal fracture.) The boundary conditions on fluid flow consist of

$$p(\ell_f, t) = -\sigma_o \quad \text{and} \quad \dot{\ell}_f = -\frac{w^2}{\mu'}\frac{\partial p}{\partial x} \tag{Eq. I-11}$$

$$q(0,t) = Q_o/2 \tag{Eq. I-12}$$

Alternatively, the fluid source can be taken into account by the global continuity equation:

$$2\int_0^{\ell_f} w \mathrm{d}x = Q_o t \tag{Eq. I-13}$$

I.2.2 Scaling and Dimensionless Formulation

The set of equations (Eq. I-5 - Eq. I-13) fully defines the fracture length, $\ell(t)$, the fluid front, $\ell_f(t)$, the fracture displacement, $w(x,t)$ and $v(x,t)$, and the net pressure, $p(x,t)$. In the following, particular forms of the governing equations are derived by using the scaling initially introduced for the infinite domain case, ($\mathcal{L} = \ell(t)/H \equiv 0$).

First, the small dimensionless parameter $\varepsilon(t)$ and a length scale $L(t)$, which is of the same order as the fracture length $\ell(t)$, are introduced. The fracture opening, $w(x,t)$, the shear displacement, $v(x,t)$, the net pressure, $p(x,t)$, the fracture length, $\ell(t)$ and the fluid front position, $\ell_f(t)$, can be expressed as

$$w = \varepsilon(t)L(t)\Omega(\xi; \mathcal{P}_1, \mathcal{P}_2, \mathcal{L}) \tag{Eq. I-14}$$

$$v = \varepsilon(t)L(t)\Xi(\xi; \mathcal{P}_1, \mathcal{P}_2, \mathcal{L}) \tag{Eq. I-15}$$

$$p = \varepsilon(t)E'\Pi(\xi; \mathcal{P}_1, \mathcal{P}_2, \mathcal{L}) \tag{Eq. I-16}$$

$$\ell(t) = \gamma(\mathcal{P}_1, \mathcal{P}_2, \mathcal{L})L(t) \tag{Eq. I-17}$$

$$\ell_f(t) = \varphi(\mathcal{P}_1, \mathcal{P}_2, \mathcal{L})L(t) \tag{Eq. I-18}$$

The scaled opening, Ω, shear displacement, Ξ, and pressure, Π, are functions of the spatial coordinate, $\xi = x/\ell(t)$, and the dimensionless parameters, $\mathcal{P}_1$, $\mathcal{P}_2$, and $\mathcal{L}$, all of which are expected to

be functions of time t. The two length factors γ and φ are also functions of $\mathcal{P}_1$, $\mathcal{P}_2$, and $\mathcal{L}$; γ and φ are related through the relation $\varphi = \gamma\xi_f$, with $\xi_f = \ell_f(t)/\ell(t)$ identifying the position of the fluid front, and $1-\xi_f$ corresponding to the scaled length of the lag zone.

The governing equations can be rewritten in terms of the new variables, after noting the following expressions for the spatial and time derivatives

$$\left.\frac{\partial}{\partial x}\right|_t = \frac{1}{\ell}\frac{\partial}{\partial \xi} \qquad \text{(Eq. I-19)}$$

$$\left.\frac{\partial}{\partial t}\right|_x = \sum_{i=1}^{2}\left(\dot{\mathcal{P}}_i\frac{\partial}{\partial \mathcal{P}_i} - \xi\frac{\dot{\mathcal{P}}_i}{\mathcal{P}_i}\frac{\partial}{\partial \xi}\right) + \left(\dot{\mathcal{L}}\frac{\partial}{\partial \mathcal{L}} - \xi\frac{\dot{\mathcal{L}}}{\mathcal{L}}\frac{\partial}{\partial \xi}\right) \qquad \text{(Eq. I-20)}$$

Hence, the governing equations can be summarized as follows.

- *Elasticity*

$$\Pi(\xi) = \mathcal{H}\{\Omega/\gamma\} \qquad 0 < \xi < \xi_f \qquad \text{(Eq. I-21)}$$

$$-\mathcal{G}_s = \mathcal{H}\{\Omega/\gamma\} \qquad \xi_f < \xi < 1 \qquad \text{(Eq. I-22)}$$

- *Lubrication*

$$\left(\frac{\dot{\varepsilon}t}{\varepsilon} + \frac{\dot{L}t}{L}\right)\Omega + \dot{\mathcal{P}}_1 t\frac{\partial\Omega}{\partial\mathcal{P}_1} + \dot{\mathcal{P}}_2 t\frac{\partial\Omega}{\partial\mathcal{P}_2} + \dot{\mathcal{L}}t\frac{\partial\Omega}{\partial\mathcal{L}} - \xi t\left(\frac{\dot{\mathcal{P}}_1}{\mathcal{P}_1} + \frac{\dot{\mathcal{P}}_2}{\mathcal{P}_2} + \frac{\dot{\mathcal{L}}}{\mathcal{L}}\right)\frac{\partial\Omega}{\partial\xi}$$
$$= \frac{1}{\mathcal{G}_m\gamma^2}\frac{\partial}{\partial\xi}\left(\Omega^3\frac{\partial\Pi}{\partial\xi}\right) \qquad 0 < \xi < \xi_f \qquad \text{(Eq. I-23)}$$

- *Fluid front*

$$\dot{\mathcal{P}}_1 t\frac{\partial\varphi}{\partial\mathcal{P}_1} + \dot{\mathcal{P}}_2 t\frac{\partial\varphi}{\partial\mathcal{P}_2} + \dot{\mathcal{L}}t\frac{\partial\varphi}{\partial\mathcal{L}} + \varphi\frac{\dot{L}t}{L} = -\frac{1}{\mathcal{G}_m\gamma}\frac{\partial\Pi}{\partial\xi} \qquad \xi = \xi_f \qquad \text{(Eq. I-24)}$$

- *Global fluid volume balance*

$$2\gamma\int_0^{\xi_f}\Omega\,\mathrm{d}\xi = \mathcal{G}_v \qquad \text{(Eq. I-25)}$$

- *Propagation criterion*

$$\Omega = \mathcal{G}_k\gamma^{1/2}(1-\xi)^{1/2}, \quad 1-\xi \ll 1 \qquad \text{(Eq. I-26)}$$

Four dimensionless groups appear in these equations

$$\mathcal{G}_v = \frac{Q_o t}{\varepsilon L^2}, \qquad \mathcal{G}_m = \frac{\mu'}{\varepsilon^3 E' t}, \qquad \mathcal{G}_k = \frac{K'}{\varepsilon E' L^{1/2}}, \qquad \mathcal{G}_s = \frac{\sigma_o}{\varepsilon E'} \qquad \text{(Eq. I-27)}$$

Here, we consider the viscosity scaling that corresponds to setting

$$\mathcal{G}_v = 1 \qquad \text{and} \qquad \mathcal{G}_m = 1 \qquad \text{(Eq. I-28)}$$

in order to identify the small parameter, ε_m, and the length scale, L_m (with the subscript m denoting the viscosity scaling), as

$$\varepsilon_m = \left(\frac{\mu'}{E't}\right)^{1/3}, \quad L_m = \left(\frac{E' Q_o^3 t^4}{\mu'}\right)^{1/6} \qquad \text{(Eq. I-29)}$$

The first condition, $\mathcal{G}_v = 1$, implies that the length scale, L_m, will be of the same order as the fracture length, as long as the fluid lag is small. Note, also, that by imposing $\mathcal{G}_m = 1$, the viscosity "disappears" from lubrication equation (Eq. I-23).

The two other groups, $\mathcal{G}_k$ and $\mathcal{G}_s$, can be identified respectively to a dimensionless toughness $\mathcal{K}$ and a dimensionless far-field stress $\mathcal{S}$ — i.e.,

$$\mathcal{K} = \frac{K'}{\left(E'^3 \mu'\, Q_o\right)^{1/4}} \qquad \text{and} \qquad \mathcal{S} = \sigma_o \left(\frac{t}{E'^2 \mu'}\right)^{1/3} \qquad \text{(Eq. I-30)}$$

We note that the dimensionless toughness is time-independent (a property of plane strain hydraulic fracture).

Therefore, the lubrication equation simplifies to

$$\frac{1}{3}\Omega_m + \dot{\mathcal{L}} t \frac{\partial \Omega_m}{\partial \mathcal{L}} + \frac{\mathcal{S}}{3}\frac{\partial \Omega_m}{\partial \mathcal{S}} - \xi\left(\frac{\dot{\mathcal{L}} t}{\mathcal{L}} + \frac{1}{3}\right)\frac{\partial \Omega_m}{\partial \xi} = \frac{1}{\gamma_m^2}\frac{\partial}{\partial \xi}\left(\Omega_m^3 \frac{\partial \Pi_m}{\partial \xi}\right) \qquad \text{(Eq. I-31)}$$

The equation governing the motion of the fluid front is reduced to

$$\dot{\mathcal{L}} t \frac{\partial \varphi_m}{\partial \mathcal{L}} + \frac{\mathcal{S}}{3}\frac{\partial \varphi_m}{\partial \mathcal{S}} + \frac{2}{3}\varphi_m = -\frac{1}{\gamma_m}\frac{\partial \Pi_m}{\partial \xi} \qquad \text{at } \xi = \xi_f \qquad \text{(Eq. I-32)}$$

The global mass balance reduces to

$$2\gamma_m \int_0^{\xi_f} \Omega_m \mathrm{d}\xi = 1 \qquad \text{(Eq. I-33)}$$

and the propagation criterion in terms of the opening tip asymptote (Eq. I-26) becomes

$$\Omega_m = \mathcal{K}\gamma_m^{1/2}(1-\xi)^{1/2}, \quad 1-\xi \ll 1 \qquad \text{(Eq. I-34)}$$

Finally, we need to solve the coupled fracture problems with Eq. I-32 and Eq. I-33 for fluid flow and Eq. I-21, Eq. I-22 and Eq. I-34 for fracture propagation.

The location of the fracture tip at any time t can be obtained through solving the implicit equation

$$\mathcal{L} = \frac{\gamma_m(\mathcal{K}, \mathcal{L}, \mathcal{S}) L(t)}{H} \qquad \text{(Eq. I-35)}$$

once the form of the functions $\gamma_m(\mathcal{K}, \mathcal{L}, \mathcal{S})$ is obtained. In the same way, the fluid front location can be determined once $\varphi_m(\mathcal{K}, \mathcal{L}, \mathcal{S})$ is known.

I.3 MATHEMATICAL FORMULATION OF FLUID-DRIVEN VERTICAL FRACTURE (DIKE PROBLEM)

Consider a vertical fracture propagating in a semi-infinite impermeable elastic medium (see Fig. I-2). The fracture is driven by an incompressible Newtonian fluid, which is injected at the base of the fracture at a constant volumetric rate.*

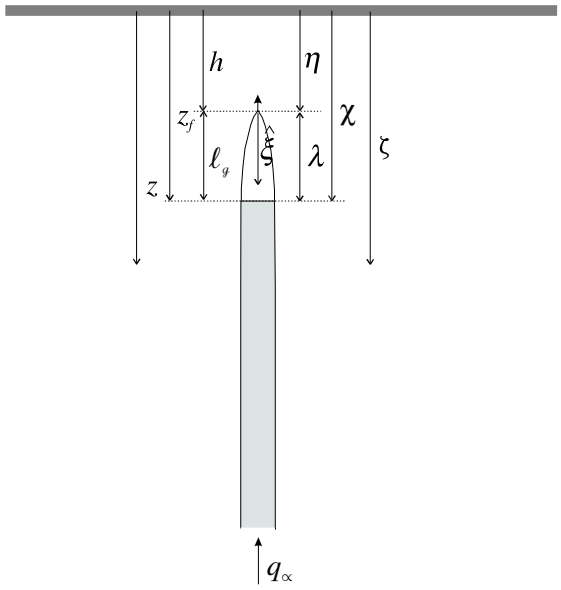

Figure I-2 Plane-strain, fluid-driven vertical fracture with a lag zone at the tip

The material constants needed to represent deformation of the rock are Young's modulus, E, Poisson's ratio, ν, toughness K_{Ic}, and density ρ_r, while the relevant constants for the fluid are the dynamic viscosity, μ, and the density, ρ_f. For convenience, we introduce the same reduced constants as in Eq. I-1 of Section I.2.

The horizontal stress field, σ_o, is assumed to vary with depth z according to

$$\sigma_o = \sigma_c + \kappa \rho_r g\, z \qquad \text{(Eq. I-36)}$$

where σ_c is a constant stress, g is the acceleration of gravity, and κ is a number that is typically in the range $0.3 \leq \kappa \leq 1$. Finally, the boundary conditions at infinity correspond to a constant injection flow rate q_∞.

We seek to determine the fracture aperture, $w(z,t)$, the fluid pressure, $p_f(z,t)$ and the flow rate, $q(z,t)$, as functions of depth z and time t, as well as determine the dependence of the solution

*The ascent of a two-dimensional dike in Earth's crust can be represented by vertical hydraulic fracture model implemented in NPHF2D if several assumptions are introduced to simplify the dike problem:

(1) plane strain conditions apply;

(2) the magma is injected at infinity;

(3) the dike propagates continuously in mobile equilibrium; and

(4) lubrication theory and linear elastic fracture mechanics are applicable.

on the problem parameters. (Note that q is taken positive when directed upward, in the opposite direction to the z-axis.) The system of equations governing w, p_f, and q are summarized in the next section.

I.3.1 Governing Equations

Elasticity Equation. The elastic relation between the fluid pressure, $p_f(z,t)$, and the fracture aperture, $w(z,t)$, is expressed by a singular integral equation (Hills et al. 1996)

$$p_f(z,t) - \sigma_o(z) = E' \int_{h(t)}^{\infty} M(z,s) \frac{\partial w(s,t)}{\partial s} \mathrm{d}s \qquad \text{(Eq. I-37)}$$

where $M(z,s)$ is an elastic kernel that accounts for the presence of a free surface

$$M(z,s) = M_\infty(z,s) - \frac{1}{4\pi\,(z+s)} - \frac{2s}{4\pi\,(z+s)^2} + \frac{4s^2}{4\pi\,(z+s)^3} \qquad \text{(Eq. I-38)}$$

with $M_\infty(z,s)$ denoting the Cauchy singular kernel for the infinite plane

$$M_\infty(z,s) = \frac{1}{4\pi\,(z-s)} \qquad \text{(Eq. I-39)}$$

We will refer to $p_f - \sigma_o$ as the net pressure p.

Lubrication. According to lubrication theory, the equation governing the flow of a Newtonian fluid within the fracture is given by (Batchelor 1967):

$$q = -\frac{w^3}{\mu'} \left(\frac{\partial p_f}{\partial z} - \rho_f g \right) \qquad \text{(Eq. I-40)}$$

where ρ_f is the fluid density, and g the acceleration of gravity.

By assuming incompressibility of the fracturing fluid, the local mass balance can be expressed as

$$\frac{\partial w}{\partial t} - \frac{\partial q}{\partial z} = 0 \qquad \text{(Eq. I-41)}$$

Boundary and Initial Conditions. The propagation criterion imposes the asymptotic form of w at the tip (Rice 1968)

$$w \simeq \frac{K'}{E'} (z-h)^{1/2}, \quad z \to h \qquad \text{(Eq. I-42)}$$

This criterion obviously implies that $w = 0$ at $z = h$.

$$p_f = p_{fo},\ h(t) \le z < z_f(t) \qquad \text{(Eq. I-43)}$$

At the fluid front, $z = z_f(t)$, the fluid pressure is the pressure p_{fo} in the lag zone and the velocity of the front corresponds to the average fluid velocity at the front. Hence,

$$p_f = p_{fo}, \quad \frac{\mathrm{d}z_f}{\mathrm{d}t} = \frac{w^2}{\mu'}\left(\frac{\partial p_f}{\partial z} - \rho_f g\right) \quad \text{at } z = z_f(t) \qquad \text{(Eq. I-44)}$$

where the position of the fluid front, z_f, is given by

$$z_f = h + \ell_g \qquad \text{(Eq. I-45)}$$

with ℓ_g being the length of the tip cavity.

The condition at infinity corresponds to a constant injection rate, q_∞:

$$q = q_\infty \quad \text{at } z = \infty \qquad \text{(Eq. I-46)}$$

It can actually be shown that this condition corresponds to a constant mean velocity v_∞.

The set consisting of the elasticity equation (Eq. I-37), Poiseuille law (Eq. I-40), fluid continuity (Eq. I-41), the propagation criterion (Eq. I-42), the conditions at the fluid front (Eq. I-44) and the conditions at infinity (Eq. I-46) forms a complete system for determining $w(z, t)$, $p_f(z, t)$, $h(t)$ and $\ell_g(t)$, starting from known values of these quantities at an initial time t_o. The issue of the initial conditions will be discussed below.

I.3.2 Scaling and Dimensionless Formulation

Scaling of this problem hinges on introducing the following characteristic quantities: length, ℓ_*; time, t_*; width, w_*; pressure, p_*; and flow rate, q_*. Then, we naturally define the dimensionless depth, ζ, and time, τ, as

$$\zeta = z/\ell_* \quad \text{and} \quad \tau = t/t_* \qquad \text{(Eq. I-47)}$$

the dimensionless fracture opening, $\Omega(\zeta, \tau)$, net pressure, $\Pi(\zeta, \tau)$, and flow rate, $\Psi(\zeta, \tau)$, as

$$\Omega = w/w_*, \ \Pi = p/p_*, \ \Psi = q/q_* \qquad \text{(Eq. I-48)}$$

as well as the depth of the fracture tip, $\eta(\tau)$, the length of the tip cavity, $\lambda(\tau)$, and the position of the fluid front, $\chi(\tau)$:

$$\eta = h/\ell_*, \ \lambda = \ell_g/\ell_*, \ \chi = z_f/\ell_* \qquad \text{(Eq. I-49)}$$

Recall that $\chi = \eta + \lambda$. The characteristic quantities ℓ_*, t_*, w_*, p_*, and q_* will be identified below.

Using Eq. I-47 - Eq. I-49, the system of equations governing $\Omega(\zeta, \tau)$, $\Pi(\zeta, \tau)$, $\Psi(\zeta, \tau)$, $\eta(\tau)$, and $\chi(\tau)$ become

- *Elasticity equation*

$$\Pi = \mathcal{G}_e \int_\eta^\infty M(\zeta, s)\, \frac{\partial \Omega}{\partial s}\mathrm{d}s \qquad \text{(Eq. I-50)}$$

- *Poiseuille law*

$$\mathcal{G}_m \Psi = \Omega^3 \left(\frac{\partial \Pi}{\partial \zeta} + \mathcal{G}_\gamma\right) \qquad \text{(Eq. I-51)}$$

- *Fluid continuity*

$$\mathcal{G}_w \frac{\partial \Omega}{\partial \tau} - \frac{\partial \Psi}{\partial \zeta} = 0 \qquad \text{(Eq. I-52)}$$

- *Fracture propagation criterion*

$$\Omega = \mathcal{G}_k \, (\zeta - \eta)^{1/2} \text{ as } \zeta \to \eta \qquad \text{(Eq. I-53)}$$

- *Boundary condition in the tip cavity*

$$\Pi = -\left(\mathcal{G}_s + \mathcal{G}_d \zeta\right), \; \eta < \zeta \leq \chi \qquad \text{(Eq. I-54)}$$

- *Boundary condition at the fluid front*

$$\mathcal{G}_m \mathcal{G}_w \dot{\chi} = -\Omega^3 \left(\frac{\partial \Pi}{\partial \zeta} + \mathcal{G}_\gamma \right) \qquad \text{(Eq. I-55)}$$

- *Boundary condition at infinity*

$$\Psi = \mathcal{G}_q \text{ as } \zeta \to \infty \qquad \text{(Eq. I-56)}$$

The eight dimensionless groups $\mathcal{G}_e$, $\mathcal{G}_m$, $\mathcal{G}_\gamma$, $\mathcal{G}_w$, $\mathcal{G}_q$, $\mathcal{G}_k$, $\mathcal{G}_s$, $\mathcal{G}_d$ are defined as follows:

$$\mathcal{G}_e = \frac{E' w_*}{p_* \ell_*}, \; \mathcal{G}_m = \frac{\mu' q_* \ell_*}{w_*^3 p_*}, \; \mathcal{G}_\gamma = \frac{\delta' \ell_*}{p_*}, \; \mathcal{G}_w = \frac{w_* \ell_*}{t_* q_*}, \; \mathcal{G}_q = \frac{q}{q_*} \qquad \text{(Eq. I-57)}$$

$$\mathcal{G}_k = \frac{K' \ell_*^{1/2}}{E' w_*}, \; \mathcal{G}_s = \frac{\sigma_c - p_{fo}}{p_*}, \; \mathcal{G}_d = \frac{\kappa \rho_r g \ell_*}{p_*} \qquad \text{(Eq. I-58)}$$

where $\delta' = \left(\kappa \rho_r - \rho_f\right) g$. The particular scaling used in this problem is selected by imposing that the five dimensionless groups in (Eq. I-57) are all equal to one,

$$\mathcal{G}_e = \mathcal{G}_m = \mathcal{G}_\gamma = \mathcal{G}_w = \mathcal{G}_q = 1 \qquad \text{(Eq. I-59)}$$

in order to define the five characteristic quantities, ℓ_*, t_*, w_*, p_*, and q_*, which are then given by

$$\ell_* = \left(\frac{\mu' E'^3 q_\infty}{\delta'^4} \right)^{1/6}, \; w_* = \left(\frac{\mu' q_\infty}{\delta'} \right)^{1/3}, \; p_* = \left(\mu' E'^3 \delta'^2 q_\infty \right)^{1/6} \qquad \text{(Eq. I-60)}$$

$$t_* = \left(\frac{\mu' E'}{\delta'^2 q_\infty} \right)^{1/2}, \; q_* = q_\infty \qquad \text{(Eq. I-61)}$$

Also, the three remaining groups are renamed as

$$\mathcal{G}_k \equiv \mathcal{K}, \; \mathcal{G}_s \equiv \mathcal{S}, \; \mathcal{G}_d \equiv \mathcal{D} \qquad \text{(Eq. I-62)}$$

where $\mathcal{K}$ has the meaning of a toughness, $\mathcal{S}$ of a reference stress, and $\mathcal{D}$ of a relative host rock density:

$$\mathcal{K} = K' \left(\frac{1}{\mu' E'^3 q_\infty} \right)^{1/4}, \; \mathcal{S} = \frac{\sigma_c - p_{fo}}{\left(\mu' E'^3 \delta'^2 q_\infty \right)^{1/6}}, \; \mathcal{D} = \frac{\kappa \rho_r}{\kappa \rho_r - \rho_f} \qquad \text{(Eq. I-63)}$$

This scaling is an extension of that used by Lister (1990), to solve the self-similar propagation of a dike, to the time-dependent case. Note that this scaling collapses if $\delta' = 0$. (For example, $\delta' = 0$ if $\kappa = 1$ and $\rho_r = \rho_f$.) In that case, an appropriate scaling would correspond to

$$\mathcal{G}_e = \mathcal{G}_m = \mathcal{G}_d = \mathcal{G}_w = \mathcal{G}_q = 1, \text{ when } \mathcal{G}_\gamma = 0 \qquad \text{(Eq. I-64)}$$

from which new expressions for ℓ_*, t_*, w_*, p_*, and q_* can easily be derived.

In summary, the set of governing equations can be written as

$$\Pi = \int_\eta^\infty M(\zeta, s)\, \frac{\partial \Omega}{\partial s} \mathrm{d}s, \quad \Psi = \Omega^3 \left(\frac{\partial \Pi}{\partial \zeta} + 1 \right), \quad \frac{\partial \Omega}{\partial \tau} - \frac{\partial \Psi}{\partial \zeta} = 0 \qquad \text{(Eq. I-65)}$$

with the propagation criterion and the conditions in the lag zone, at the fluid front and at infinity given by

$$\Omega = \mathcal{K}\, (\zeta - \eta)^{1/2}, \ \zeta \to \eta \qquad \text{(Eq. I-66)}$$

$$\Pi = -\left(\mathcal{S} + \mathcal{D}\zeta\right), \ \eta < \zeta \leq \chi \qquad \text{(Eq. I-67)}$$

$$\dot{\chi} = -\Omega^2 \left(\frac{\partial \Pi}{\partial \zeta} + 1 \right), \ \zeta = \chi \qquad \text{(Eq. I-68)}$$

$$\Psi = 1, \ \zeta \to \infty \qquad \text{(Eq. I-69)}$$

The system of equations (Eq. I-65 - Eq. I-69) is closed in the sense that it can be used to determine the solution $\mathcal{F}(\zeta, \tau; \mathcal{K}, \mathcal{S}, \mathcal{D})$ where $\mathcal{F} = \{\Omega, \Pi, \Psi, \eta, \chi\}$ given a suitable set of initial conditions.

The dependence of the solution on time arises through the boundary conditions in the tip cavity (which is changing with the depth η) and through the elastic kernel which accounts for the distance to the free surface. It is important to realize, however, that time is immaterial in this solution, if indeed the initial conditions are made to correspond to the self-similar solution of Lister (1990) for a deep dike (see discussion below). The dependence on time can then be replaced by a dependence on the depth η, once the solution has been determined (i.e., once $\eta(\tau)$ is known). Thus, the solution can be expressed as $\bar{\mathcal{F}}(\hat{\xi}, \eta; \mathcal{K}, \mathcal{S}, \mathcal{D})$, with $\bar{\mathcal{F}} = \{\bar{\Omega}, \bar{\Pi}, \bar{\Psi}, \bar{\lambda}\}$, where we have chosen to use the moving coordinate $\hat{\xi} = \zeta - \eta$ rather than ζ, and the lag instead of the fluid front position. (The overbar denotes that the field quantities depend on $\hat{\xi}$ and η; also, $\bar{\lambda} = \bar{\lambda}(\eta)$.)

I.3.3 Simplifications in the Case of the Dike Problem

It has been noted by various authors that rock toughness in the case of dike propagation through the Earth crust often is not relevant, as $\mathcal{K} \ll 1$ (Spence and Turcotte 1985; Lister and Kerr 1991; Rubin 1995). Also, the case $\mathcal{S} = 0$ is an appropriate case. In other words, the particular solution $\mathcal{K} = \mathcal{S} = 0$ is very relevant. We denote this solution by $\mathcal{F}_o(\zeta, \tau; \mathcal{D})$ or by $\bar{\mathcal{F}}_o(\hat{\xi}, \eta; \mathcal{D})$; it only depends on parameter $\mathcal{D}$. Because $\mathcal{K} = 0$, aperture Ω behaves at the dike tip according to (Rice 1968)

$$\Omega \sim (\zeta - \eta)^{3/2}, \quad \zeta \to \eta \qquad \text{(Eq. I-70)}$$

where the coefficient of proportionality is unknown *a priori*, as it is part of the solution. For this case, the condition of zero toughness is best imposed by

$$\int_{\eta}^{\infty} \frac{\Pi(s)}{s^{1/2}}\,\mathrm{d}s = 0 \qquad \text{(Eq. I-71)}$$

which uses the integral representation of the stress intensity factor. Note that the particular asymptotic behavior (Eq. I-70) predicates on the assumption that λ is not very small. (The term in $(\zeta-\eta)^{3/2}$ actually corresponds to the next term of the fracture opening expansion when $\mathcal{K} > 0$, according to linear elastic fracture mechanics.) When $\lambda \ll 1$, the behavior (Eq. I-70) takes place over a region so small that it is not visible in this scaling. Under these conditions, an intermediate asymptote develops

$$\Omega \sim (\zeta-\eta)^{2/3}, \quad \zeta \to \eta \qquad \text{(Eq. I-72)}$$

(See Section I.3.5 for a discussion of cases characterized by small tip cavities.)

It can be shown readily (as recognized by Lister (1990) for the self-similar case) that the solution behaves at infinity as

$$\Omega = 1,\ \Pi = \frac{1}{4\pi\zeta},\ \zeta \to \infty \qquad \text{(Eq. I-73)}$$

Hence the average fluid velocity, $\Upsilon \equiv \Psi/\Omega = 1$ at $\zeta = \infty$. In dimensional terms, the average fluid velocity at infinity, v_∞, is given as

$$v_\infty = \left(\frac{\delta' q_\infty^2}{\mu'}\right)^{1/3} \qquad \text{(Eq. I-74)}$$

Actually, it is convenient to formulate the boundary conditions at infinity in terms of v_∞ rather than q_∞; hence, the characteristic quantities can be formulated as follows

$$\begin{aligned} \ell_* &= \left(\frac{\mu' E'^2 v_\infty}{\delta'^3}\right)^{1/4},\ w_* = \left(\frac{\mu' v_\infty}{\delta'}\right)^{1/2},\ p_* = \left(\mu' E'^2 \delta' v_\infty\right)^{1/4} \\ t_* &= \frac{\ell_*}{v_\infty},\ q_* = v_\infty w_* \end{aligned} \qquad \text{(Eq. I-75)}$$

and

$$\mathcal{K} = K'\left(\frac{\delta'}{\mu'^3 E'^6 v_\infty^6}\right)^{1/8}, \quad \mathcal{S} = \frac{\sigma_c - p_{fo}}{\left(\mu' E'^2 \delta' v_\infty\right)^{1/4}} \qquad \text{(Eq. I-76)}$$

Far from the free surface, the speed of the dike ascent is expected to be approximately equal to the far-field magma mean velocity — $\dot{\eta} = O(1)$ for $\eta \gg 1$.

I.3.4 Self-Similar Problem of a Deep Dike

Formulation of the deep dike problem solved by Lister (1990) can be deduced from the more general equations derived in the previous subsections of this section (Section I.3). First, the equations are

reformulated in terms of the moving coordinates $\hat{\xi} = \zeta - \eta$. The solution is now of the form $\hat{\mathcal{F}}(\hat{\xi}, \tau; \mathcal{K}, \mathcal{S}, \mathcal{D})$, where $\hat{\mathcal{F}} = \{\hat{\Omega}, \hat{\Pi}, \hat{\Psi}, \eta, \lambda\}$. The spatial and time derivative transform as

$$\frac{\partial}{\partial \zeta} = \frac{\partial}{\partial \hat{\xi}}, \quad \left.\frac{\partial}{\partial \tau}\right|_{\zeta} = \left.\frac{D}{D\tau}\right|_{\hat{\xi}} - \dot{\eta}\frac{\partial}{\partial \hat{\xi}} \tag{Eq. I-77}$$

In summary, the set of governing equations can be written as

$$\hat{\Pi} = \int_0^{\infty} \hat{M}(\hat{\xi}, \hat{s}; \eta)\, \frac{\partial \hat{\Omega}}{\partial \hat{s}} \mathrm{d}\hat{s}, \quad \hat{\Psi} = \hat{\Omega}^3 \left(\frac{\partial \hat{\Pi}}{\partial \hat{\xi}} + 1\right), \quad \frac{D\hat{\Omega}}{D\tau} - \dot{\eta}\frac{\partial \hat{\Omega}}{\partial \hat{\xi}} - \frac{\partial \hat{\Psi}}{\partial \hat{\xi}} = 0 \tag{Eq. I-78}$$

where the elastic kernel $\hat{M}(\hat{\xi}, s; \eta)$ is now given by

$$\hat{M}(\hat{\xi}, \hat{s}; \eta) = \hat{M}_{\infty}(\hat{\xi}, \hat{s}) - \frac{1}{4\pi\left(\hat{\xi} + \hat{s} + 2\eta\right)} - \frac{2(\hat{s} + \eta)}{4\pi\left(\hat{\xi} + \hat{s} + 2\eta\right)^2} + \frac{(4\hat{s} + \eta)^2}{4\pi\left(\hat{\xi} + \hat{s} + 2\eta\right)^3} \tag{Eq. I-79}$$

with $M_{\infty}(z, s)$ denoting the Cauchy singular kernel for the infinite plane

$$M_{\infty}(z, s) = \frac{1}{4\pi\left(\hat{\xi} - \hat{s}\right)} \tag{Eq. I-80}$$

The propagation criterion and the conditions in the lag zone, at the fluid front and at infinity are given by

$$\hat{\Omega} = \mathcal{K}\hat{\xi}^{1/2}, \ \hat{\xi} \to 0 \tag{Eq. I-81}$$

$$\hat{\Pi} = -\left[\mathcal{S} + \mathcal{D}\left(\hat{\xi} + \eta\right)\right], \ 0 < \hat{\xi} \leq \lambda \tag{Eq. I-82}$$

$$\dot{\eta} + \dot{\lambda} = -\Omega^2\left(\frac{\partial \Pi}{\partial \zeta} + 1\right), \ \zeta = \chi \tag{Eq. I-83}$$

$$\hat{\Psi} = 1, \ \zeta \to \infty \tag{Eq. I-84}$$

The equations of the problem solved by Lister (1990) can be deduced from the general system (Eq. I-78 - Eq. I-84) by assuming (1) that the dike is deep enough that the effect of the free surface is negligible and (2) the solution is self-similar. It can be shown easily that the second assumption implies that the average magma velocity is constant along the dike and equal to the velocity of ascent of the dike. These assumptions imply, therefore, that

$$\hat{M} = \hat{M}_{\infty}, \quad \frac{D\hat{\Omega}}{D\tau} = 0, \quad \dot{\lambda} = 0, \quad \dot{\eta} = -1 \tag{Eq. I-85}$$

The solution is now of the form $\hat{\mathcal{F}}_{ss}(\hat{\xi}; \mathcal{K}, \mathcal{S}, \mathcal{D}, \eta)$, where $\hat{\mathcal{F}}_{ss} = \{\hat{\Omega}, \hat{\Pi}, \hat{\Psi}, \lambda\}$ and is governed by

$$\hat{\Pi} = \int_0^{\infty} \hat{M}_{\infty}(\hat{\xi}, \hat{s})\, \frac{\mathrm{d}\hat{\Omega}}{\mathrm{d}\hat{s}} \mathrm{d}\hat{s}, \quad \hat{\Omega}^2\left(\frac{\mathrm{d}\hat{\Pi}}{\mathrm{d}\hat{\xi}} + 1\right) = 1 \tag{Eq. I-86}$$

and

$$\hat{\Omega} = \mathcal{K}\hat{\xi}^{1/2},\ \hat{\xi} \to 0;\ \hat{\Pi} = -\left[\mathcal{S} + \mathcal{D}\left(\hat{\xi} + \eta\right)\right],\ 0 < \hat{\xi} \le \lambda;\ \hat{\Omega} = 1,\ \zeta \to \infty \qquad \text{(Eq. I-87)}$$

Note, however, that a strictly self-similar solution does not exist, as depth η enters into the problem formulation via the boundary condition in the lag zone. Thus, within the assumption of self-similarity, the evolution problem is actually seen as a sequence of self-similar solutions.

Numerical solution of the system of equations (Eq. I-86 - Eq. I-87) is given by Lister (1990)[†]. This solution actually could be used as a suitable initial condition for the general problem — i.e.,

$$\mathcal{F}(\zeta - \eta_o, 0; \mathcal{K}, \mathcal{S}, \mathcal{D}, \eta) = \mathcal{F}_{ss}(\hat{\xi}; \mathcal{K}, \mathcal{S}, \mathcal{D}, \eta_o) \qquad \text{(Eq. I-88)}$$

where $\eta_o \gg 1$. (However, in practical terms, $\eta_o \simeq 2$, as the free-surface effect is negligible at those depths).

I.3.5 Tip Considerations for Small Tip Cavity Size

Calculations for the particular case $\mathcal{S} = 0$ and $\mathcal{K} \ll 1$ indicate that there are regions in the parametric space $(\mathcal{D}, \eta)$ where λ is very small; for example, when both $\mathcal{D}$ and η are $O(1)$ or larger. This suggests that the lag and the region of rapid change of the fluid pressure scale by a lengthscale other than ℓ_* when $\lambda \ll 1$. (In other words, $\lambda \simeq 0$ does not imply that $\ell_g = 0$.) The need to rescale the lag when the far-field stress is "large" and the toughness is "small" is also a feature of the solutions for hydraulic fractures where gravity effects are neglected.

When a small lag exists, another strategy for computing the solution is needed, in view of the near impossibility of numerically discretizing the lag region and, at the same time, capturing the global solution.

Asymptotically, when $\lambda \ll 1$ for $\mathcal{K} \ll 1$, the solution is characterized by the presence of a boundary layer. The solution at length scale ℓ_* (the "outer" solution) has a tip asymptote for opening and pressure given by

$$\Omega = \beta_{mo}\Upsilon_o^{1/3}(\zeta - \eta)^{2/3}, \quad \Pi = \delta_{mo}\Upsilon_o^{1/3}(\zeta - \eta)^{-1/3}, \qquad \text{(Eq. I-89)}$$

where $\beta_{mo} = 2^{1/3}\,3^{5/6}$, $\delta_{mo} = -6^{-2/3}$, and Υ_o is the dimensionless tip velocity $\Upsilon_o = v_o/v_\infty$ (also $\Upsilon_o = -\dot{\eta}$). The asymptotes (Eq. I-89) are determined by rescaling the autonomous solution for zero toughness given by Desroches et al. (1994)

$$\hat{\Omega}_{mo} = \beta_{mo}\,\hat{\xi}_m^{2/3},\ \hat{\Pi}_{mo} = \delta_{mo}\,\hat{\xi}_m^{-1/3} \qquad \text{(Eq. I-90)}$$

where $\hat{\Omega}_{mo} = w/\ell_m$, $\hat{\xi}_m = (z-h)/\ell_m$ and $\hat{\Pi}_{mo} = p/E'$, with the viscosity length scale ℓ_m defined as

$$\ell_m = \frac{\mu' v_o}{E'} \qquad \text{(Eq. I-91)}$$

[†]Lister use $\hat{x}$, $\hat{h}$, $\hat{p}$ to denote the characteristic quantities used to scale distance, half-aperture, and net pressure, respectively. These quantities are related to the those defined here according to $\hat{x} = \ell_*/2$, $\hat{h} = w_*/2$, $\hat{p} = p_*/2$.

Note that Eq. I-89 applies in the tip region where $|\partial\Pi/\partial\zeta| \gg 1$; hence, the asymptotic region is expected to be small [about $O(10^{-2})$ or less], according to Eq. I-89.

The tip asympotic behavior (Eq. I-89) is characteristic of a situation in which the viscous dissipation in the tip region is much larger than the energy rate spent in creating new surface in the rock. Unlike the toughness-dominated case, the strength of the tip singularity in the viscosity-dominated case depends on the tip velocity, Υ_o, which is itself part of the solution. Note, however, that Υ_o is a function of η only (under conditions of "small" tip cavity) — i.e., $\Upsilon_o = \Upsilon_o(\eta)$ — and that $\Upsilon_o = 1$ for η large.

The lag and the region of rapid change of the fluid pressure scale by ℓ_{ms} when $\lambda \ll 1$

$$\ell_{ms} = \left(\frac{E'}{\sigma_o}\right)^3 \frac{\mu' v_o}{E'} \qquad \text{(Eq. I-92)}$$

where v_o is the tip velocity and σ_o is the effective confining stress in the lag zone [$\sigma_o \simeq (\mathcal{S} + \mathcal{D}\eta)\, p_*$, for zero gas pressure in the tip cavity]. The solution at length scale ℓ_{ms} (the "inner" solution) corresponds to the solution of a semi-infinite fracture moving steadily at velocity $v_o(\eta)$, without gravity effect. In fact, this solution is similar to the solution obtained by Garagash and Detournay (2000), except for the elastic kernel, which accounts for the presence of the free-surface. This inner solution is characterized by $\hat{\Omega} \sim \hat{\xi}^{2/3}$ and $\hat{\Pi} \sim \hat{\xi}^{-1/3}$ at infinity. This viscosity singularity, which provides the matching between the inner and outer solution, is actually an intermediate asymptote.

I.4 NUMERICAL SCHEME

A fixed-grid implicit scheme for solving the boundary-value problem consisting of Eq. I-5 through Eq. I-13 is provided below. The same numerical scheme is used for solution of the problem of the vertical fracture as formulated in Eq. I-37 through Eq. I-46. Let T be an arbitrary time scale and $\bar{L}_m = L_m(T)$ be a fixed reference length, which is defined to have a form similar to the one in Eq. I-29

$$\bar{L}_m = \left(\frac{E' Q_o^3 T^4}{\mu'}\right)^{1/6} \qquad \text{(Eq. I-93)}$$

and let the small number $\bar{\varepsilon}_m$

$$\bar{\varepsilon}_m = \left(\frac{\mu'}{E' T}\right)^{1/3} \qquad \text{(Eq. I-94)}$$

If $\sigma_o \neq 0$, the characteristic time t_{ms} can be defined as

$$t_{ms} = \frac{E'^2 \mu'}{\sigma_o^3} \qquad \text{(Eq. I-95)}$$

to scale the time (i.e., $T = t_{ms}$). This characteristic time is introduced

$$\mathcal{S} = \left(\frac{t}{t_{ms}}\right)^{1/3} \qquad \text{(Eq. I-96)}$$

We can also define a far-field stress,

$$\bar{\mathcal{S}} = \mathcal{S}(T). \qquad \text{(Eq. I-97)}$$

In addition, we introduce dimensionless time τ and dimensionless coordinate ζ:

$$\tau = \frac{t}{T} \qquad \zeta = \frac{x}{\bar{L}_m} \qquad \text{(Eq. I-98)}$$

Similarly, we can define the scaled opening and pressure, as well as the fracture length and the fluid front, as follows:

$$\begin{aligned} w &= \bar{\varepsilon}_m \bar{L}_m \bar{\Omega}(\zeta,\tau) \qquad p = \bar{\varepsilon}_m E' \bar{\Pi}(\zeta,\tau) \\ \ell &= \bar{L}_m \bar{\gamma}(\tau) \qquad\qquad \ell_f = \bar{L}_m \bar{\varphi}(\tau) \end{aligned} \qquad \text{(Eq. I-99)}$$

If $\sigma_o \neq 0$, the scaled far-field can be written as $\bar{\mathcal{S}} = 1$.

A comparison of Eq. I-99 with the viscosity scaling in Eq. I-14 through Eq. I-18 leads to

$$\gamma_m = \tau^{-2/3}\bar{\gamma} \qquad \text{(Eq. I-100)}$$

$$\varphi_m = \tau^{-2/3}\bar{\varphi} \qquad \text{(Eq. I-101)}$$

$$\Omega_m = \tau^{-1/3}\bar{\Omega}/\gamma_m \qquad \text{(Eq. I-102)}$$

$$\Pi_m = \tau^{1/3}\bar{\Pi} \qquad \text{(Eq. I-103)}$$

In summary, the following equations form a closed system that completely defines the evolution of the hydraulically driven fracture.

- *Governing equations*

$$\bar{\Pi} = \mathcal{H}\left\{\bar{\Omega}/\bar{\gamma};\mathcal{L}\right\} \qquad 0 < \zeta < \bar{\varphi} \qquad \text{(Eq. I-104)}$$

$$-\bar{\mathcal{S}} = \mathcal{H}\left\{\bar{\Omega}/\bar{\gamma};\mathcal{L}\right\} \qquad \bar{\varphi} < \zeta < \bar{\gamma} \qquad \text{(Eq. I-105)}$$

$$\frac{\partial \bar{\Omega}}{\partial \tau} = \frac{\partial}{\partial \zeta}\left(\bar{\Omega}^3 \frac{\partial \bar{\Pi}}{\partial \zeta}\right) \qquad 0 < \zeta < \bar{\varphi} \qquad \text{(Eq. I-106)}$$

in which $\bar{\mathcal{S}} = \begin{cases} 0 & \text{If } \sigma_o = 0 \\ 1 & \text{If } \sigma_o \neq 0 \end{cases}$

- *Propagation condition*

$$\bar{\Omega} = \mathcal{K}\,(\bar{\gamma} - \zeta)^{1/2} \qquad \text{at } \zeta = \bar{\gamma} \qquad \text{(Eq. I-107)}$$

- *Boundary conditions at inlet and at the fluid front*

$$\bar{\Omega}^3 \frac{\partial \bar{\Pi}}{\partial \zeta} = -\frac{1}{2} \qquad \text{at } \zeta = 0 \qquad \text{(Eq. I-108)}$$

$$\bar{\Pi} = \bar{\mathcal{S}} \qquad \text{at } \zeta = \bar{\varphi} \qquad \text{(Eq. I-109)}$$

$$\frac{\partial \varphi}{\partial \tau} = \bar{\Omega}^2 \frac{\partial \bar{\Pi}}{\partial \zeta} \qquad \text{at } \zeta = \bar{\varphi} \qquad \text{(Eq. I-110)}$$

I.4.1 Discretized Equations

A discretized form of equations (Eq. I-104 - Eq. I-110) with boundary conditions (Eq. I-108 - Eq. I-109) is presented now as the basis of the algorithm. We establish our numerical solutions based on a fixed element size, $\Delta\zeta$, and a small fixed time step, $\Delta\tau$. The current element number for the fracture at time step m is denoted by N; and the corresponding element number for fluid flow is $M \leq N$. The volume of fluid (VOF) for the partially filled element $M+1$ is ϕ. Then, the fracture length is $\bar{\gamma} = N\Delta\zeta$, and the fluid front is at $\bar{\varphi} = (M+\phi)\Delta\zeta$. Also, the notations involve three indices: the subscript i for the nodes at the center of the spatial element, the superscript m for the time step, and another superscript r for the iteration step. The governing equation for the fluid filled part of the fracture is

$$\frac{\bar{\Omega}_i^{m,r+1} - \bar{\Omega}_i^{m,r}}{\Delta\tau} = \frac{1}{\Delta\zeta^2}[\alpha_{out}(\bar{\Pi}_{i+1}^{m,r+1} - \bar{\Pi}_i^{m,r+1}) - \alpha_{in}(\bar{\Pi}_i^{m,r+1} - \bar{\Pi}_{i-1}^{m,r+1})],\ i = 2,\ M-1 \quad \text{(Eq. I-111)}$$

in which

$$\alpha_{out} = \left(\frac{\bar{\Omega}_i^{m,r} + \bar{\Omega}_{i+1}^{m,r}}{2}\right)^3 \quad \text{(Eq. I-112)}$$

$$\alpha_{in} = \left(\frac{\bar{\Omega}_i^{m,r} + \bar{\Omega}_{i-1}^{m,r}}{2}\right)^3 \quad \text{(Eq. I-113)}$$

for the first element $\alpha_{in} = 0$ and for the fluid front element $\alpha_{out} = (\bar{\Omega}_M^{mr})^3$. Considering the boundary conditions at the inlet and at the fluid front, we have

$$\frac{\bar{\Omega}_1^{m,r+1} - \bar{\Omega}_1^{m,r}}{\Delta\tau} = \frac{1}{\Delta\zeta^2}\left[\alpha_{out}\left(\bar{\Pi}_2^{m,r+1} - \bar{\Pi}_1^{m,r+1}\right)\right] + \frac{1}{2\Delta\zeta} \quad \text{(Eq. I-114)}$$

$$\frac{\bar{\Omega}_M^{m,r+1} - \bar{\Omega}_M^{m,r}}{\Delta\tau} = \frac{1}{\Delta\zeta^2}\left[-(\bar{\Omega}_M^{m,r})^3\left(\bar{\Pi}_M^{m,r+1} + \bar{s}\right) - \alpha_{in}\left(\bar{\Pi}_M^{m,r+1} - \bar{\Pi}_{M-1}^{m,r+1}\right)\right] \quad \text{(Eq. I-115)}$$

The linear equations (Eq. I-104) can be expressed as

$$\bar{\Pi}_i^{m(r+1)} = (1-\omega)\bar{\Pi}_i^{mr} + \omega(-\sum_{j=1}^{N} D_{ij}^{m(r+1)}\bar{\Omega}_j^{m(r+1)}) \quad \text{(Eq. I-116)}$$

in which ω is the relaxation factor, equal to 0.3-0.5; and D_{ij} is the matrix of coefficients derived from Eq. I-104. (See Zhang et al. (2001) for the details concerning the generation of the coefficient matrix.)

For the elasticity equations in the lag zone, we use the DD method with constant strength along each element, with a singular element (square root shape function) used at the fracture tip (Crouch and Starfield 1983). Also, $\bar{\Pi}_i^{m(r+1)} = -\bar{s}$ is applied to $N - M$ elements in the lag zone. Based

on Eq. I-111 through Eq. I-116, we solve using an implicit scheme for the fracture opening, shear displacement DD and pressure at time $t + \Delta t$. Zero shear stress is assumed to exist along the fracture surface. The accumulated time from time steps and the time calculated from the balance of volume of fluid should be equal; this fact can be used as one check on the accuracy of the numerical results.

The VOF for the partially filled elements is determined in the following way. We begin with the dimensionless form of the continuity equation:

$$\frac{\partial \bar{\Omega}_M^m}{\partial \tau} + \frac{\partial \bar{\Psi}_M}{\partial \zeta} = 0 \qquad \text{(Eq. I-117)}$$

in which $\bar{\Psi}_M$ is the scaled fluid flux for the filling element. Integrate Eq. I-117 in the filling element. Thus,

$$\bar{\Psi}_M = \bar{\Psi}_{M-1/2} - \phi \Delta\zeta \frac{\Delta \bar{\Omega}_M^m}{\Delta \tau} \qquad \text{(Eq. I-118)}$$

where $\bar{\Psi}_{M-1/2}$ is the scaled flux at the starting points of the filling element and

$$\bar{\Psi}_{M-1/2} = \frac{\bar{\Omega}_{M-1/2}^{m3}}{\mu'} \frac{\bar{\Pi}_M^m - \bar{\Pi}_{M+1}^m}{\Delta\zeta}, \quad \bar{\Pi}_{M+1}^m = -\bar{s} \qquad \text{(Eq. I-119)}$$

Hence, the fluid front velocity, $v_f = \bar{\Psi}_M / \bar{\Omega}_M^m$, is

$$v_f = \frac{\bar{\Psi}_{M-1/2}}{\bar{\Omega}_M^m} - \frac{\phi \Delta x}{\bar{\Omega}_M^m} \frac{\Delta \bar{\Omega}_M^m}{\Delta \tau} \qquad \text{(Eq. I-120)}$$

or

$$\Delta\phi = \frac{\Delta\tau}{\Delta\zeta} \frac{\Psi_{M-1/2}}{\bar{\Omega}_M^m} - \frac{\phi \Delta \bar{\Omega}_M^m}{\bar{\Omega}_M^m} \qquad \text{(Eq. I-121)}$$

Finally, if we know the value of $\bar{\Omega}_i^{mr}$ at the center of the tip element, we can calculate the stress intensity factors according toEq. I-107

$$\mathcal{K}_I = \bar{\Omega}_i^{m,r} \sqrt{\frac{2}{\Delta\zeta}} \qquad \text{(Eq. I-122)}$$

Then, if $\mathcal{K}_I = \mathcal{K}$, the fracture propagates.

I.4.2 Numerical Method

Assume that at time τ^{m-1}, the element numbers N and M, the opening $\bar{\Omega}_i^{m-1,r}$ and the pressure $\bar{\Pi}_i^{m-1,r}$ at the nodes are known, as well as VOF ϕ^{m-1} for the partially filled element $M+1$. At time τ^m, all the quantities from the previous step are passed on as initial conditions — that is, $\bar{\Omega}_i^{m,0} = \bar{\Omega}_i^{m-1,r}$, $\bar{\Pi}_i^{m,0} = \bar{\Pi}_i^{m-1,r}$ and $\phi^m = \phi^{m-1}$ for the inner loops described below. When the fracture criterion is met at the tip, a finite fracture increment (i.e., a new element) is added to the fracture. The computation is carried out based on the following algorithm until a given fracture length or total number of elements is reached. The computation process is organized as follows.

(1) Initial conditions for opening and pressure are taken from the previous step. The stiffness is recomputed if the fracture has advanced one element.

(2) There are two nested computational loops organized as follows:

Outer iteration on the time step

Inner iteration on the fracture opening and the net pressure. Calculate the opening, $\bar{\Omega}_i^{m(r+1)}$, and the net pressure, $\bar{\Pi}_i^{mr}$, in the fracture based on Eq. I-111 and Eq. I-116 for M elements in the fluid zone and Eq. I-116 for $N - M$ elements in the lag zone. Check convergence of the solution based on the comparison of the openings at the two last iterations

$$\frac{1}{N}\sum_{j=1}^{M}\left|\frac{\bar{\Omega}_i^{m(r+1)} - \bar{\Omega}_i^{mr}}{\bar{\Omega}_i^{mr}}\right| \leq \varepsilon_{op} \qquad \text{(Eq. I-123)}$$

in which $\varepsilon_{op} = 10^{-7}$. If the above condition is met, exit the inner loop; otherwise, set $\bar{\Omega}_i^{m(r+1)} \rightarrow \bar{\Omega}_i^{mr}$ and repeat the inner loop.

(3) Calculate VOF $\phi^m = \phi^{m-1} + \Delta\phi$ for the filling element based on Eq. I-121. If $\phi^m > 1$, set $\phi^m = 0$ for the new filling element $M + 2$.

(4) Update the opening for the next time step and calculate the stress by Eq. I-122. Check the fracture propagation criterion. If satisfied, print the results and extend the fracture; otherwise go back to 1.

(5) Stop the calculation if the number of elements is larger than the specified value.

I.4.3 Initial Conditions

Whenever the fracture is extended, a starting fluid lag solution is required to begin the iterations for the new fracture length. Once a fluid lag solution has been obtained, the solution for the next propagation step can be started by using the solution obtained for the previous growth step. A simple start-up solution, which can be used for the initial fracture geometry, has been obtained by Jeffrey (1989) based on the weight function approach. This approach requires that the pressure at the well and the pressure distribution are assumed. The weight function approach described here simply enforces that the assumed pressure and fluid lag are compatible with the rock fracture toughness. Using this approach, the stress intensity factor caused by the pressure along the fracture is

$$K_I = \int_0^{\ell} p(x)m(x, \ell)\mathrm{d}x \qquad \text{(Eq. I-124)}$$

in which $m(x, \ell)$ is the weight function. The explicit form of $m(x, \ell)$ for a plane strain fracture of length 2ℓ, along the x-axis, subject to loading that is symmetrical about the fracture center, is

$$m(x, \ell) = \frac{\left(\frac{\ell}{\pi}\right)^{1/2}}{\sqrt{\ell^2 - x^2}} \qquad \text{(Eq. I-125)}$$

Based on the above scalings in Eq. I-99, Eq. I-124 and Eq. I-125 can be rewritten as

$$\frac{\mathcal{K}}{4\left(\frac{2}{\pi}\right)^{1/2}} = \int_0^{\bar{\gamma}} \bar{\Pi}(\zeta, 0)\bar{m}(\zeta, \bar{\gamma})\mathrm{d}\zeta \qquad \text{(Eq. I-126)}$$

$$\bar{m}(\zeta, \bar{\gamma}) = \frac{\left(\frac{\bar{\gamma}}{\pi}\right)^{1/2}}{\sqrt{\bar{\gamma}^2 - \zeta^2}} \qquad \text{(Eq. I-127)}$$

At the beginning, fracture length $\bar{\gamma}$ and fluid front $\bar{\varphi}$ are given, as well as far-field stress $\bar{s}$. Then, the negative value of $\bar{s}$ is the net pressure in the lag zone. It should be mentioned that fracture length $\ell(0)$ should be very small compared with the fracture depth. According to the formulae given by Jeffrey (1989), we define an angle by

$$\bar{\varphi} = \bar{\gamma}\sin(\alpha) \qquad \text{(Eq. I-128)}$$

(1) If the pressure is constant $\bar{\Pi}_0$ in the fluid pressurized part of the fracture, the lag can be obtained by the following formula (Jeffrey 1989):

$$\bar{\Pi}_0 = \frac{\frac{\pi\mathcal{K}}{4\sqrt{2}} + \bar{s}\pi\sqrt{\bar{\gamma}}}{2\alpha\sqrt{\bar{\gamma}}} - \bar{s} \qquad \text{(Eq. I-129)}$$

(2) Assume that the pressure is linearly distributed along the fluid-filled zone according to

$$\bar{\Pi}(\zeta, 0) = \bar{\Pi}_0\left(1 - \frac{\zeta}{\bar{\varphi}}\right) \qquad \text{(Eq. I-130)}$$

As the distribution of pressure is known, we can calculate the stress intensity factor based on the weight function. Substituting Eq. I-130 in Eq. I-126, we can get the formula for the pressure at the inlet:

$$\bar{\Pi}_0 = \frac{\frac{\pi\mathcal{K}}{8\sqrt{2\bar{\gamma}}} + \bar{s}\left(\frac{\pi}{2} - \alpha\right)}{\alpha - \tan\left(\frac{\alpha}{2}\right)} \qquad \text{(Eq. I-131)}$$

When the pressure is determined, we can obtain the fracture opening by the elasticity equation.

For shallow fractures, the initial conditions on fracture openings and net pressures can make use of the deep-fracture solutions with the same confining stress. In addition, as relatively large time steps and element sizes are used for long fractures, the problem can also be started using initial conditions based on the small fracture length solutions. The results obtained here used both of the above two initial condition sets to start the solution process, and good results were obtained consistently. Therefore, the problem solution is not sensitive to choice of the initial conditions.

INTENTIONALLY LEFT BLANK

ATTACHMENT II

ANALYSIS OF DIKE PROPAGATION USING NPHF2D

ATTACHMENT II

ANALYSIS OF DIKE PROPAGATION USING NPHF2D

II.1 INTRODUCTION

This attachment examines the effects of different initial and boundary conditions (within reasonable ranges) on the ascent of a dike in the region of the proposed repository at Yucca Mountain. The analysis was done using the NPHF2D code (Zhang, Jeffrey, and Detourany 2002), which simulates propagation of a fluid-driven, vertical, or horizontal fracture in an infinite half-space. The code fully couples the equations of LEFM (Linearly Elastic Fracture Mechanics) for deformation of a solid medium and fracture propagation with the non-linear Reynolds differential equation representing fluid flow inside the fracture. In this formulation, the viscosity and density of the fluid are considered constant — i.e., independent of pressure or temperature.

II.2 SCALING LAWS

The problem of dike propagation was formulated in dimensionless form by Zhang et al. (2002). Five characteristic quantities are used in the scaling. Characteristic length, ℓ_*, time, t_*, opening, w_*, pressure, p_*, and injection rate, q_*, are defined as follows:

$$\ell_* = \left(\frac{\mu' E'^3 q_\infty}{\delta'^4}\right)^{1/6}, \; w_* = \left(\frac{\mu' q_\infty}{\delta'}\right)^{1/3}, \; p_* = \left(\mu' E'^3 \delta'^2 q_\infty\right)^{1/6} \qquad \text{(Eq. II-1)}$$

$$t_* = \left(\frac{\mu' E'}{\delta'^2 q_\infty}\right)^{1/2}, \; q_* = q_\infty \qquad \text{(Eq. II-2)}$$

where

$$\mu' = 12\mu, \; E' = \frac{E}{1-\nu^2}, \; \delta' = (\kappa\rho_r - \rho_f)g \qquad \text{(Eq. II-3)}$$

and

$g =$ 9.81 m/s^2, gravity acceleration,

κ coefficient of horizontal pressure,

ρ_r rock mass density,

E rock mass Young's Modulus,

ν rock mass Poisson's ration,

ρ_f magma density,

μ magma viscosity, and

q_∞ injection flow rate at infinity.

The solution is a function of the three following dimensionless groups:

$$\mathcal{K} = K' \left(\frac{1}{\mu' E'^3 q_\infty} \right)^{1/4}, \quad \mathcal{S} = \frac{\sigma_c - p_{fo}}{\left(\mu' E'^3 \delta'^2 q_\infty\right)^{1/6}}, \quad \mathcal{D} = \frac{\kappa \rho_r}{\kappa \rho_r - \rho_f} \qquad \text{(Eq. II-4)}$$

where

$$K' = 4 \left(\frac{2}{\pi} \right)^{1/2} K_{Ic} \qquad \text{(Eq. II-5)}$$

and K_{Ic} is the rock fracture toughness. $\mathcal{K}$ is essentially a toughness, $\mathcal{S}$ a reference stress, and $\mathcal{D}$ a relative host rock density.

II.3 BOUNDARY AND INITIAL CONDITIONS

The initial and boundary conditions required for analysis of fluid-driven fractures, in addition to the in-situ stress state, are the initial depth of the fracture tip and the fluid pressure or flow rate at the starting point of the fracture. The exact depth of the magma chamber and the type of boundary condition at the dike entrance are not known. However, on average, according to field observations (Rubin 1995), the dike openings are in the range between 0.1 m and 10 m. Also, the average speed of dike ascent is of the order of 1 m/s. It can be shown (Lister 1990) that for the case of semi-infinite dike, the dike opening and magma velocity at large distances from the dike tip are:

$$w_\infty = \left(\frac{\mu' q_\infty}{\delta'} \right)^{1/3} \qquad \text{(Eq. II-6)}$$

$$v_\infty = \left(\frac{\delta' q_\infty^2}{\mu'} \right)^{1/3} \qquad \text{(Eq. II-7)}$$

Combining relations Eq. II-6 and Eq. II-7, the following expression is obtained:

$$v_\infty = \frac{\delta'}{\mu'} w_\infty^2 \qquad \text{(Eq. II-8)}$$

Relation Eq. II-8 is plotted in Figure II-1 for different values of ratio $\delta'/\mu' = (\kappa\rho_r - \rho_f)g/12\mu$. Using the chart in Figure II-1, it is possible, as a function of controlling parameters, $\kappa\rho_r - \rho_f$, and μ, to select dike opening and dike ascent velocity* at large depth. "Large" in this context is defined by comparison with the characteristic length defined in Eq. II-2.

It appears, from the dike propagation simulations conducted so far, that depth $h > 2\ell_*$ is sufficiently deep as a starting point for an "infinitely" deep dike.

*At sufficient depth, the dike propagates as self-similar (Lister 1990). One of consequences of self-similarity is that the dike tip velocity, magma front velocity and magma velocity are the same.

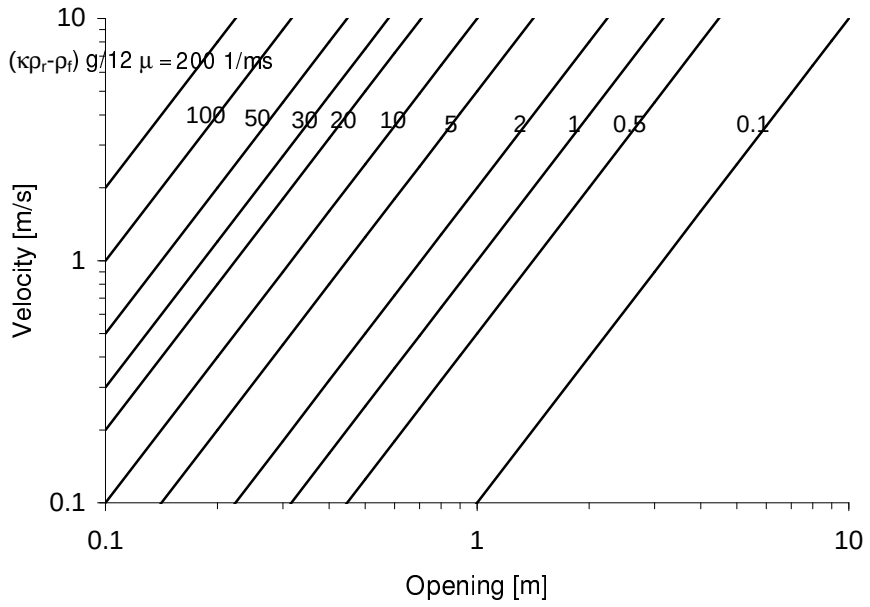

Figure II-1 Relation between fluid velocity and dike opening at a distance from the ground surface

II.4 REFORMULATION OF SCALING

As discussed in the previous section, boundary conditions for dike propagation are not given as a rate of magma influx at infinity, q_∞, but in terms of a dike opening at infinity, w_∞, and the dike velocity at infinity, v_∞. Therefore, it is more convenient to express scaling quantities and dimensionless groups in terms of the dike opening and the dike velocity at infinity (i.e., at large distance from the dike tip). Using the following relations:

$$q_\infty = v_\infty w_\infty \qquad \text{(Eq. II-9)}$$

$$\delta' = \frac{\mu' v_\infty}{w_\infty^2} \qquad \text{(Eq. II-10)}$$

the scaling quantities can be written:

$$\ell_* = \left(\frac{E' w_\infty^3}{\mu' v_\infty}\right)^{1/2}, \; p_* = \left(\frac{\mu' E' v_\infty}{w_\infty}\right)^{1/2} \qquad \text{(Eq. II-11)}$$

$$t_* = \left(\frac{w_\infty^3 E'}{\mu'^2 v_\infty^3}\right)^{1/2}, \; q_* = w_\infty v_\infty \qquad \text{(Eq. II-12)}$$

and the dimensionless groups become:

$$\mathcal{K} = K' \left(\frac{1}{\mu' E'^3 v_\infty w_\infty}\right)^{1/4}, \; \mathcal{S} = \frac{\sigma_c - p_{fo}}{\left(\frac{\mu' E' v_\infty}{w_\infty}\right)^{1/2}}, \; \mathcal{D} = \frac{\kappa \rho_r g w_\infty^2}{\mu' v_\infty} \qquad \text{(Eq. II-13)}$$

II.5 PROBLEM SOLUTION

The dimensionless fracture toughness for the range of mechanical parameters representative of the Yucca Mountain site is much smaller than 1 — $\mathcal{K} \ll 1$. Consequently, if there is no leak-off, the

problem solution is a function of two parameters only: $\mathcal{S}$, and $\mathcal{D}$. Leak-off introduces two new parameters: location of the leak-off point, and magnitude of the leak-off. The analysis presented in this attachment was conducted assuming the leak-off to occur at the depth of the repository, and different magnitudes of leak-off were considered as percentages of the magma injection rate at infinity.

The problem is solved first for the base case, with conditions of atmospheric pressure inside the tip cavity, $p_{fo} = 0$, and constant, far-field horizontal stress equal to zero, $\sigma_c = 0$. Under these conditions $\mathcal{S} = 0$. The base case corresponds to the in-situ conditions, unaffected by the repository (i.e., there is no increase in the horizontal stresses due to heating or leak-off into the repository drifts). Also, considering the diffusivity of the gas in the rock formations, the assumption of atmospheric gas pressure inside the tip cavity appears to be realistic. However, the problem was also analyzed for $\mathcal{S} \neq 0$, to investigate the effects of gas pressure inside the tip cavity and increased horizontal stresses due to repository heating. The effect of leak-off was also investigated.

II.5.1 Base Case

The solutions for the three values of $\mathcal{D}$: 2.67, 6.02 and 20.28, are shown in Figure II-2. Different combinations of effective rock mass density (i.e., rock density multiplied by the horizontal stress coefficient), $\kappa\rho_r$, and magma buoyant density, $\kappa\rho_r - \rho_f$, for selected values of $\mathcal{D}$ are shown in Table II-1. The selected range of $\mathcal{D}$ covers the expected range of variation of $\kappa\rho_r - \rho_f$. The curves shown in Figure II-2 confirm that the solution is independent of $\mathcal{D}$ until the tip cavity develops (Zhang et al. 2002). As can be expected intuitively, the tip cavity forms earlier for smaller values of $\mathcal{D}$. For large values of $\mathcal{D}$, i.e. $\mathcal{D} \sim O(10)$, the tip cavity forms "close" to the ground surface.

Table II-1 Relative rock mass density

$\mathcal{D}$	$\kappa\rho_r$ kg/m^3	$\kappa\rho_r - \rho_f$ kg/m^3
2.67	1200	449.44
6.02	1200	199.34
20.28	1200	59.17
2.67	2400	898.88
6.02	2400	398.67
20.28	2400	118.34

The dimensionless results from Figure II-2 are rescaled using the relations from Section II.4 to provide the results in dimensional form, assuming different values of v_∞ and w_∞. The positions of the dike tip and the fluid front as functions of time are shown in Figures II-3 through II-10. The results have been obtained for four velocities, v_∞: 1 m/s, 5 m/s, 10 m/s and 15 m/s. Corresponding dike openings, w_∞ were calculated from the condition that $\mathcal{D}$ remains invariant (see Eq. II-13). The solution is presented for each value of $\mathcal{D}$ assuming two values for $\kappa\rho_r$: 2400 kg/m^3 and 1200 kg/m^3. The value of $\kappa\rho_r$ equal to 2400 kg/m^3 represents the case of a hydrostatic in-situ stress state, in which the horizontal stress at the repository level (i.e., 300 m below the ground surface) would be 7.2 MPa. Existing measurements (DTN: SNF37100195002.001 [131356]) at the site

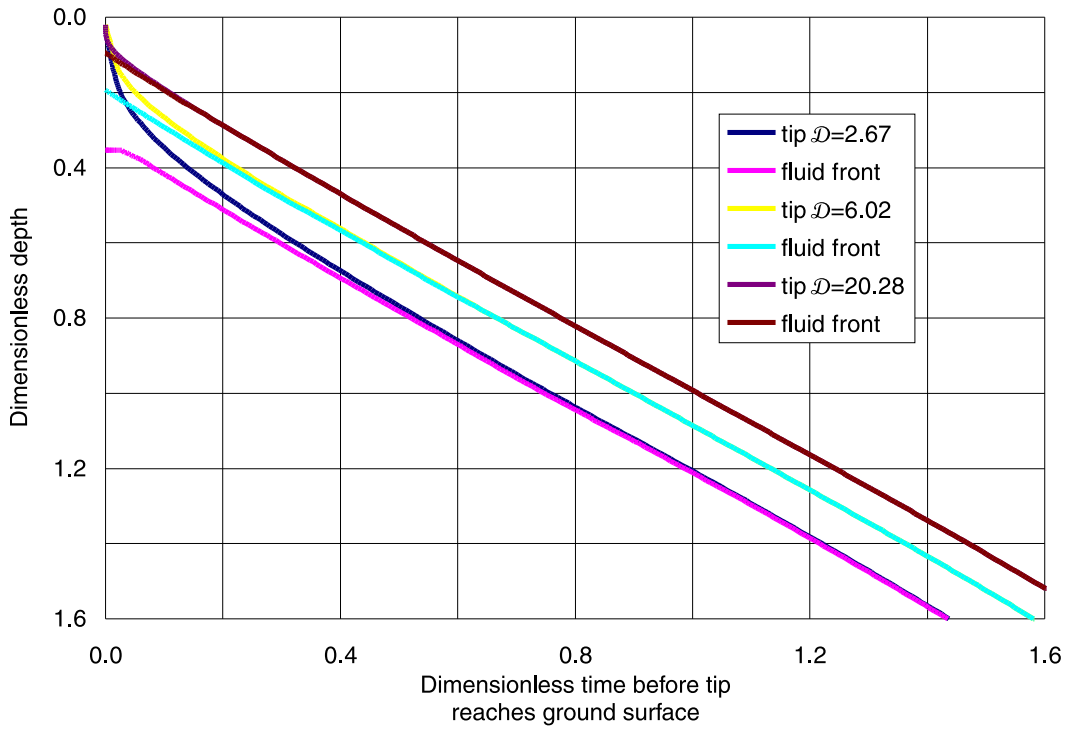

Figure II-2 Dimensionless solution for dike tip and fluid front as functions of time

and knowledge of the regional stress state indicate that horizontal stress at the repository level is in the range of 3.5 MPa (i.e., κ is close to 0.5). Therefore, $\kappa\rho_r$ equal to 1200 kg/m^3 seems to be a better representation of the in-situ stress state at Yucca Mountain than $\kappa\rho_r$ equal to 2400 kg/m^3. Most of the results were generated for magma viscosity equal to 10 Pa s (Figs. II-3 through II-8). However, in the case of $\mathcal{D} = 20.28$, the results for $\mu = 40$ Pa s are also presented (Figs. II-9 and II-10).

In all the cases considered, the tip cavity forms before the dike tip reaches the repository level. The cavity size at the repository level varies from case to case. As expected, the solutions for $\kappa = 1$ yield shorter cavity lengths than solutions for the more relevant, $\kappa = 0.5$. (Similarly, the dike opening, w_∞, for the same velocities, v_∞, is smaller for $\kappa = 1$ than for $\kappa = 0.5$.) In fact, results for $\kappa = 0.5$ indicate (see Figs. II-4, II-6 and II-8) that the magma does not reach the repository level (i.e., a 300 m depth) before the dike tip hits the ground surface except for the cases of the lowest velocity considered, i.e., $v_\infty = 1$ m/s and for $\mathcal{D}$ equal to 2.67 and 6.02 (Figs. II-4 and II-6). In these two cases the length of the tip cavity is between 100 m and 200 m when the magma is at the repository horizon. In the case of $\mathcal{D} = 20.28$ shown in Figure II-8, the tip cavity is longer than 300 m when the dike tip reaches the ground surface. An increase in magma viscosity, μ, results in an increase in the tip cavity length, as shown in Figures II-9 and II-10 (for $\mu = 40$ Pa s), compared to results in Figures II-7 and II-8 (for $\mu = 10$ Pa s).

One objective of the analysis of dike ascent is to estimate the magma pressure history at the repository level as the dike passes through the repository. However, the NPHF2D simulation stops when the dike tip reaches the ground surface. Consequently, the model does not provide the pressure history at all in those cases where the magma does not reach the repository level by the time the tip reaches

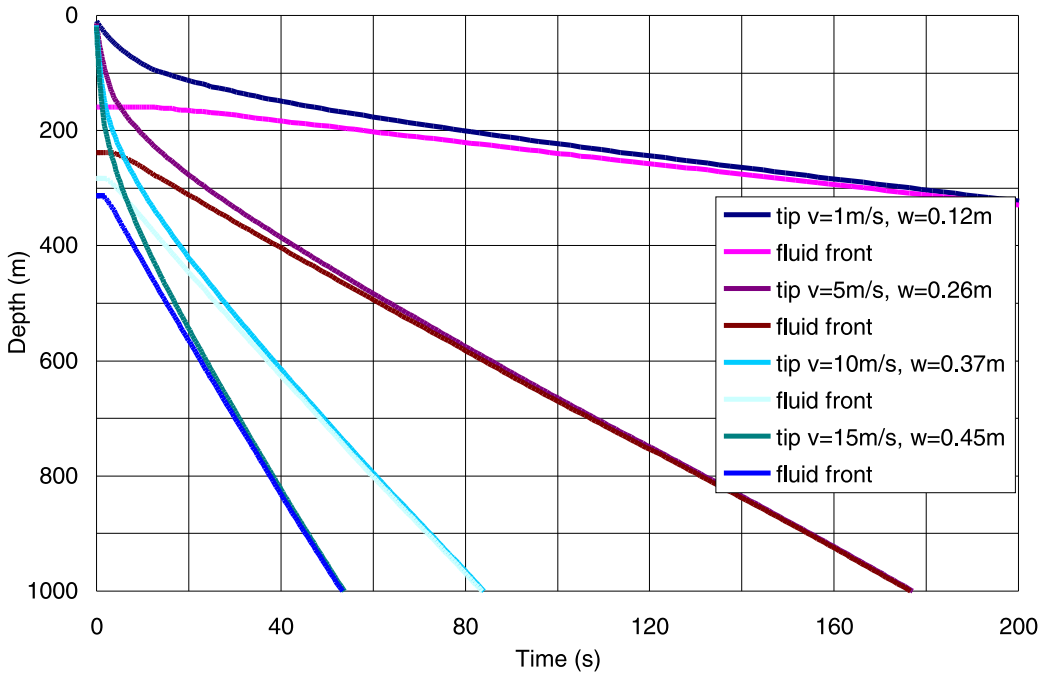

Figure II-3 Dike tip and fluid front as functions of time: $\mathcal{D} = 2.67$, $\kappa\rho_r = 2400$ kg/m^3, $\mu = 10$ Pa s

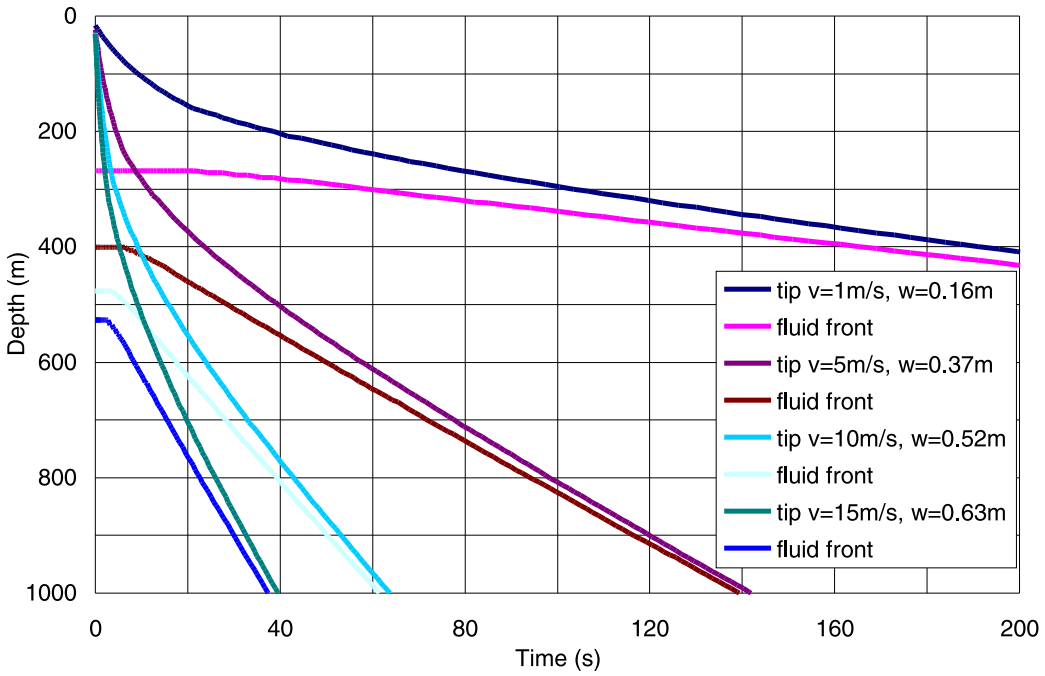

Figure II-4 Dike tip and fluid front as functions of time: $\mathcal{D} = 2.67$, $\kappa\rho_r = 1200$ kg/m^3, $\mu = 10$ Pa s

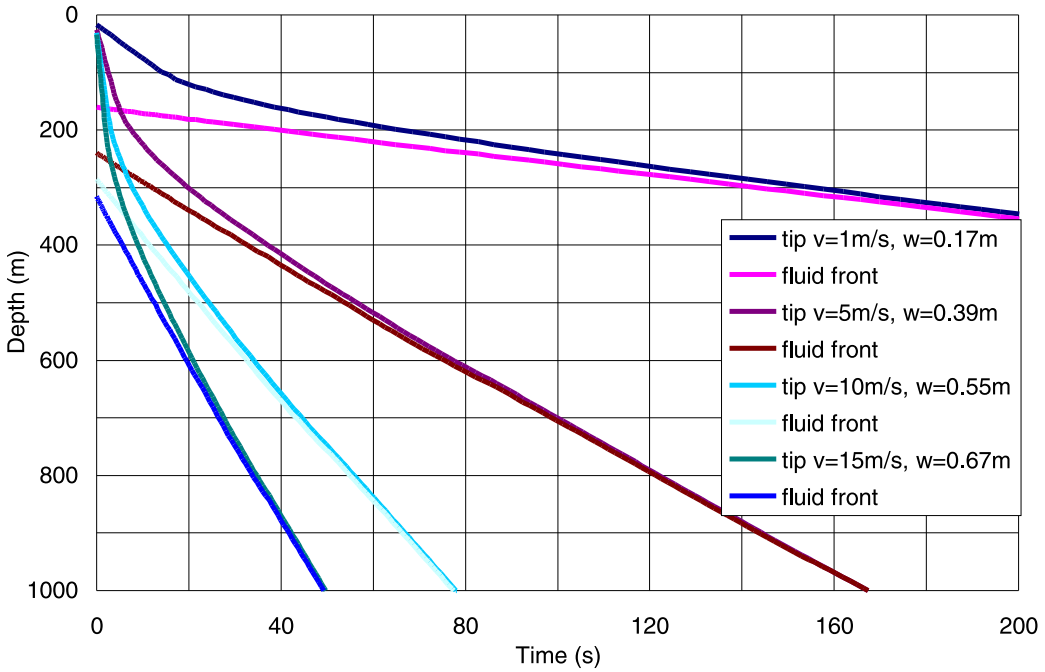

Figure II-5 Dike tip and fluid front as functions of time: $\mathcal{D} = 6.02$, $\kappa\rho_r = 2400$ kg/m^3, $\mu = 10$ Pa s

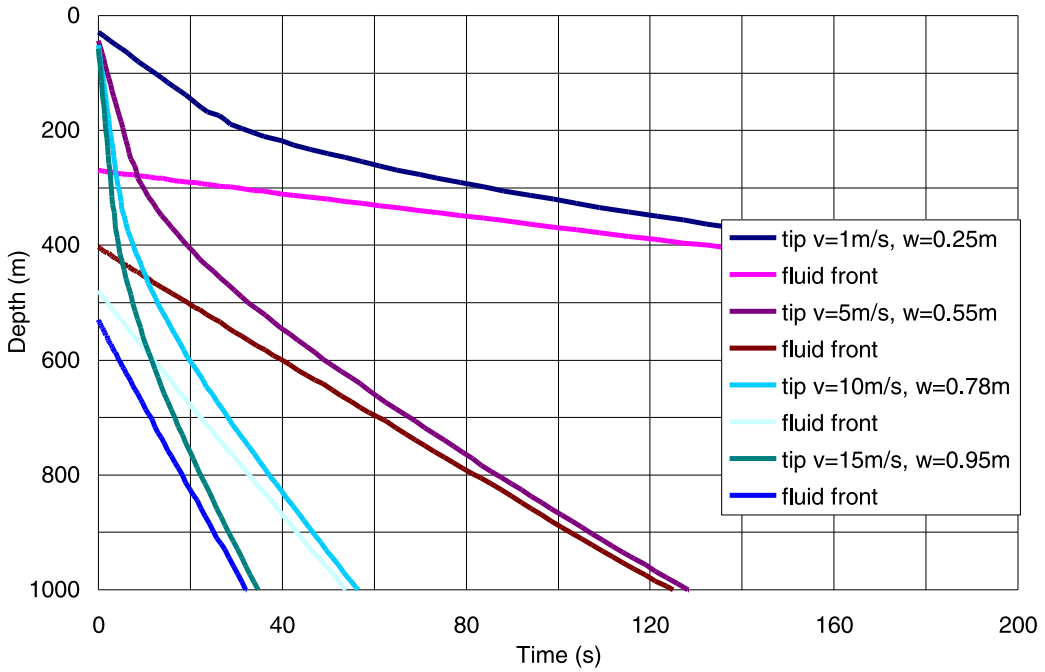

Figure II-6 Dike tip and fluid front as functions of time: $\mathcal{D} = 6.02$, $\kappa\rho_r = 1200$ kg/m^3, $\mu = 10$ Pa s

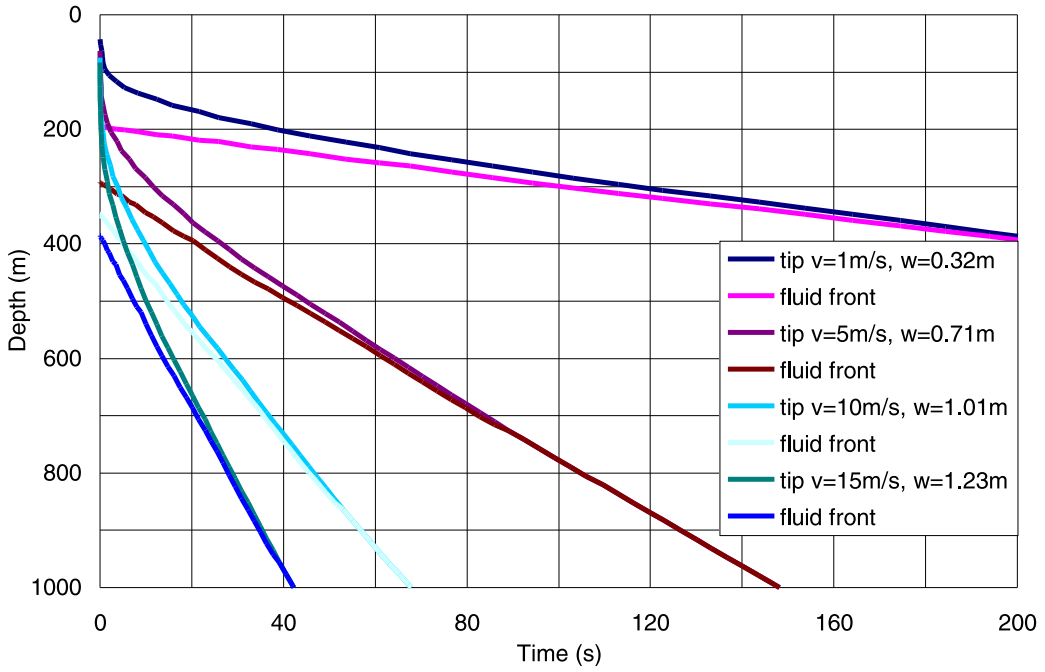

Figure II-7 Dike tip and fluid front as functions of time: $\mathcal{D} = 20.28$, $\kappa\rho_r = 2400$ kg/m^3, $\mu = 10$ Pa s

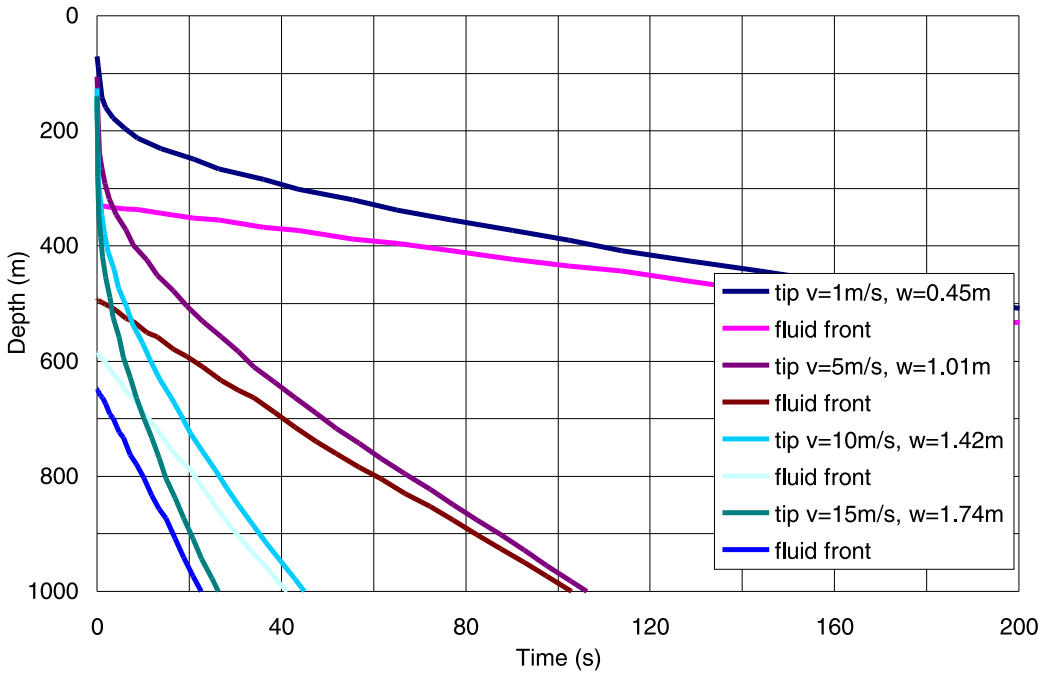

Figure II-8 Dike tip and fluid front as functions of time: $\mathcal{D} = 20.28$, $\kappa\rho_r = 1200$ kg/m^3, $\mu = 10$ Pa s

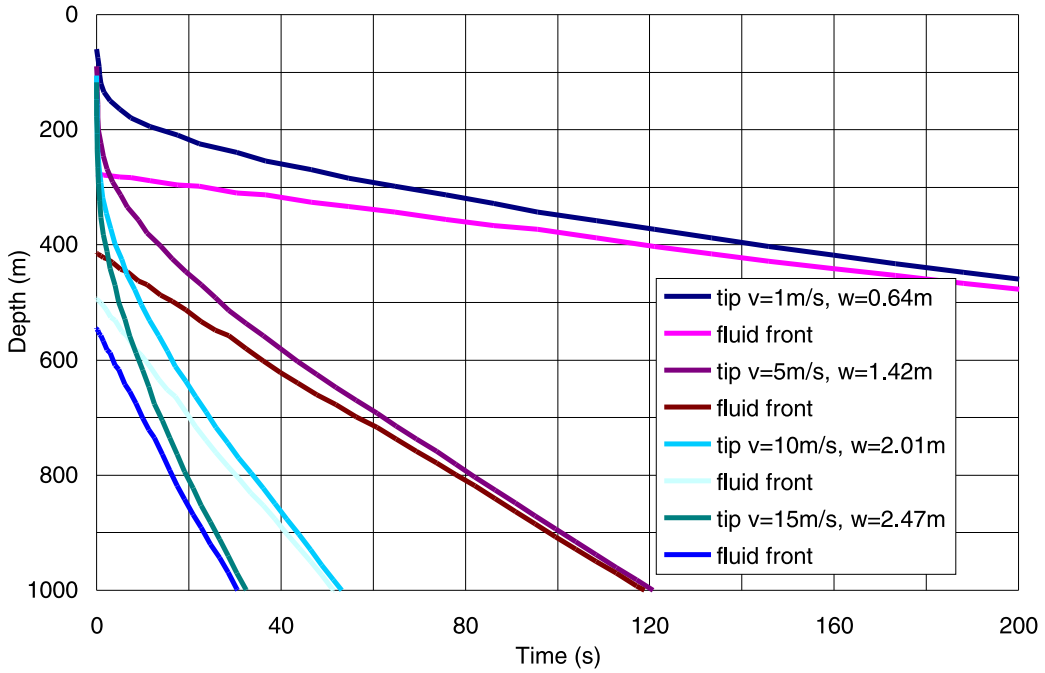

Figure II-9 Dike tip and fluid front as functions of time: $\mathcal{D} = 20.28$, $\kappa\rho_r = 2400$ kg/m^3, $\mu = 40$ Pa s

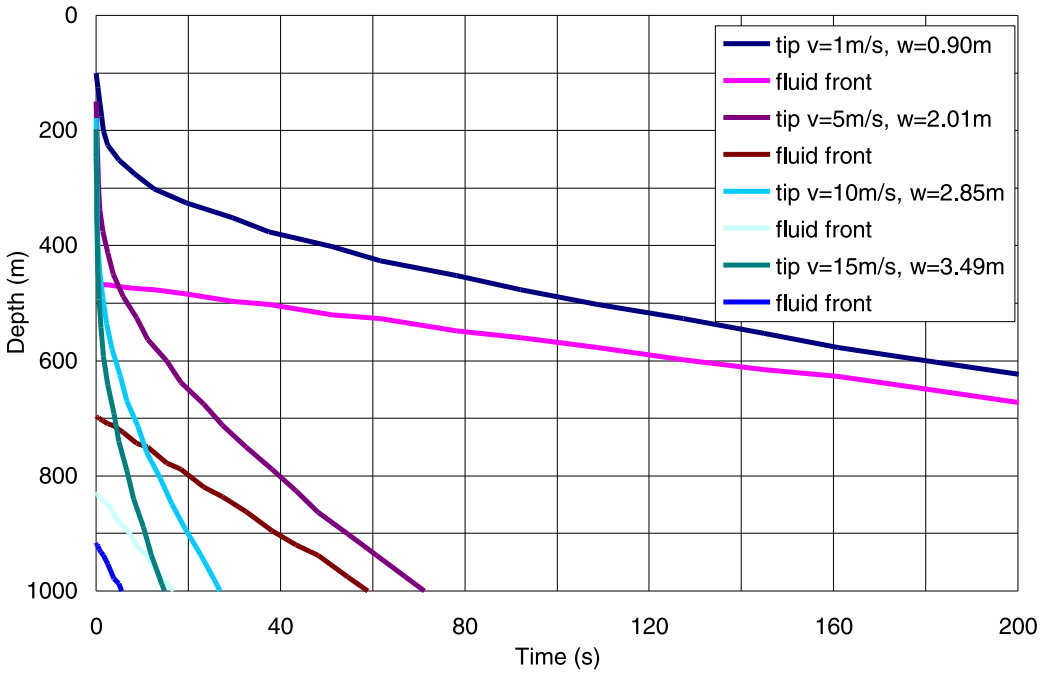

Figure II-10 Dike tip and fluid front as functions of time: $\mathcal{D} = 20.28$, $\kappa\rho_r = 1200$ kg/m^3, $\mu = 40$ Pa s

the ground surface. In other cases, when the magma is at the repository level before the dike ruptures the ground surface, the history is usually provided for a short period of time. The proper solution of this problem requires a three-dimensional model (to account for the strike dimension of the dike) of fluid flow in a pre-existing fracture (there being then no need for simulation of fracture propagation). At this stage, a pragmatic approach was adopted. The pressure profile in the magma behind the front remains invariant until magma is close to the ground surface. The only change in the net pressure profile is a variation of the minimum, which is controlled by the net pressure inside the cavity, and is equal to the horizontal far-field stress. The net pressure profiles for $\mathcal{D}$ equal to 2.67 and 20.28, at different times (the earliest being when the magma reaches a repository depth of 300 m), are shown in Figures II-11 and II-13. Clearly, in the case of $\mathcal{D} = 20.28$ shown in Figure II-13, all four pressure profiles (at different times) have the same shape. All curves could have been obtained by horizontally translating the curve for $t = 4086$ s and truncating those portions below the line corresponding to the horizontal far-field stress. The same argument can be applied to pressure profiles at $t = 1339$ s and $t = 1367$ s for $\mathcal{D} = 2.67$ shown in Figure II-11. However, the pressure profile at $t = 1392$ s does not follow the same trend. The reason for this is that, in the case of $\mathcal{D} = 2.67$, there is an effect on the magma front velocity when the dike tip approaches the ground surface (shown in Figure II-2): the magma front becomes almost stationary. (The low lateral confinement and a large increase in model compliance as the dike tip approaches the ground surface accommodate the influx of additional magma without forward movement of the magma front.) The pressure – time histories at the repository level are constructed by convecting the pressure profile at the repository horizon using the known fluid front velocity. Pressure histories constructed using such an approach for $\mathcal{D}$ equal to 2.67 and 20.28, for different velocities (1 m/s, 5 m/s, 10 m/s and 15 m/s), are shown as solid lines in Figures II-12 and II-14. (The only curve for 1 m/s velocity is a pressure history at the depth of 300 m. Other curves are at different depths, which correspond to the same dimensionless depth as a 300 m depth for a 1 m/s curve.) The actual pressure histories (sink data) at the repository depth for the case in which $v_\infty = 1$ m/s are shown in Figures II-12 and II-14. The agreement between pressure histories derived from pressure profiles and fluid velocities, and the actual pressure – time history at the sink is very good.

It appears from the pressure history plots in Figures II-12 and II-14 that the two major factors controlling the evolution of magma pressure at a given depth are: far-field horizontal stress and magma front velocity. The maximum magma pressure is at most 1 MPa larger than the horizontal far-field stress at the given depth. Therefore, the maximum magma pressure at a 300 m depth is: (a) approximately 4.5 MPa in the case of $\kappa\rho_r = 1200$ kg/m^3 (horizontal far-field stress 3.6 MPa); and (b) approximately 8.0 MPa in the case of $\kappa\rho_r = 2400$ kg/m^3 (horizontal far-field stress is 7.6 MPa). Clearly, a larger magma front velocity results in a larger rate of pressure change at a given depth. The length of the tip cavity provides a measure of the distance over which the magma pressure behind the front changes from zero to the maximum value. Consequently, as the tip cavity becomes shorter, the pressure gradient becomes larger, and the rate of pressure change at a given depth increases.

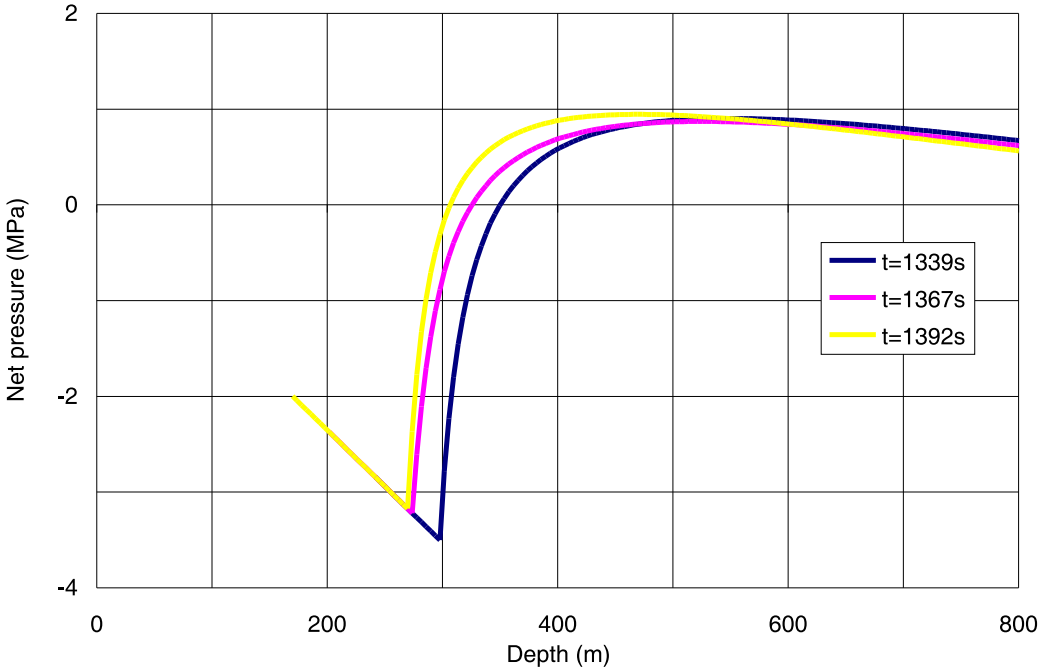

Figure II-11 Net pressure profile as a function of depth: $\mathcal{D} = 2.67$, $\kappa\rho_r = 1200$ kg/m^3, $\mu = 10$ Pa s, $v_\infty = 1$ m/s, $w_\infty = 0.16$ m

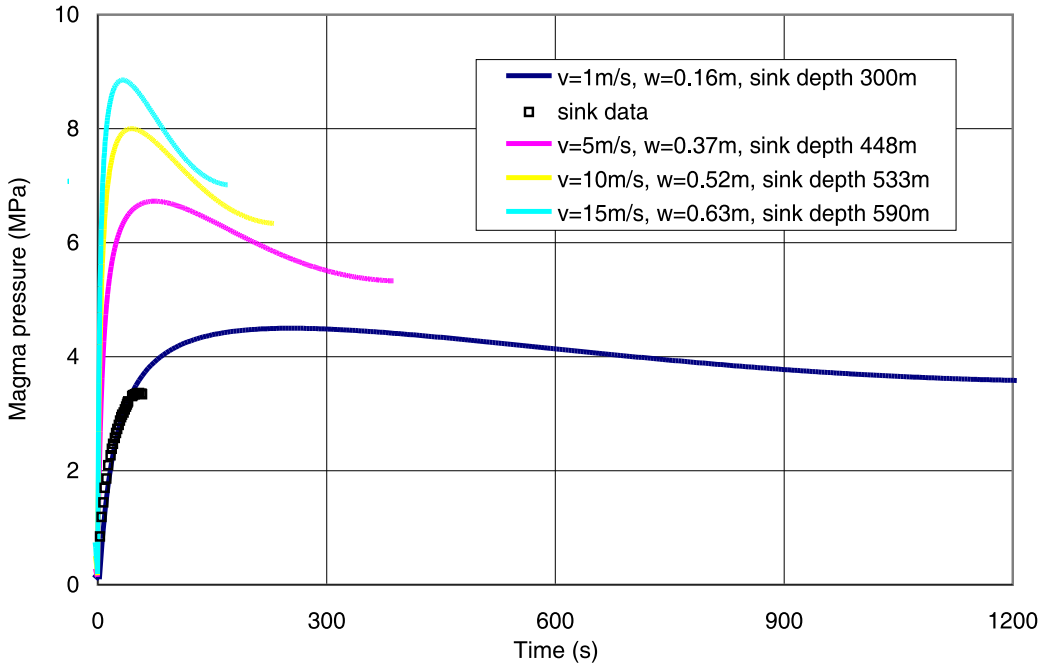

Figure II-12 Pressure history at leak-off point: $\mathcal{D} = 2.67$, $\kappa\rho_r = 1200$ kg/m^3, $\mu = 10$ Pa s

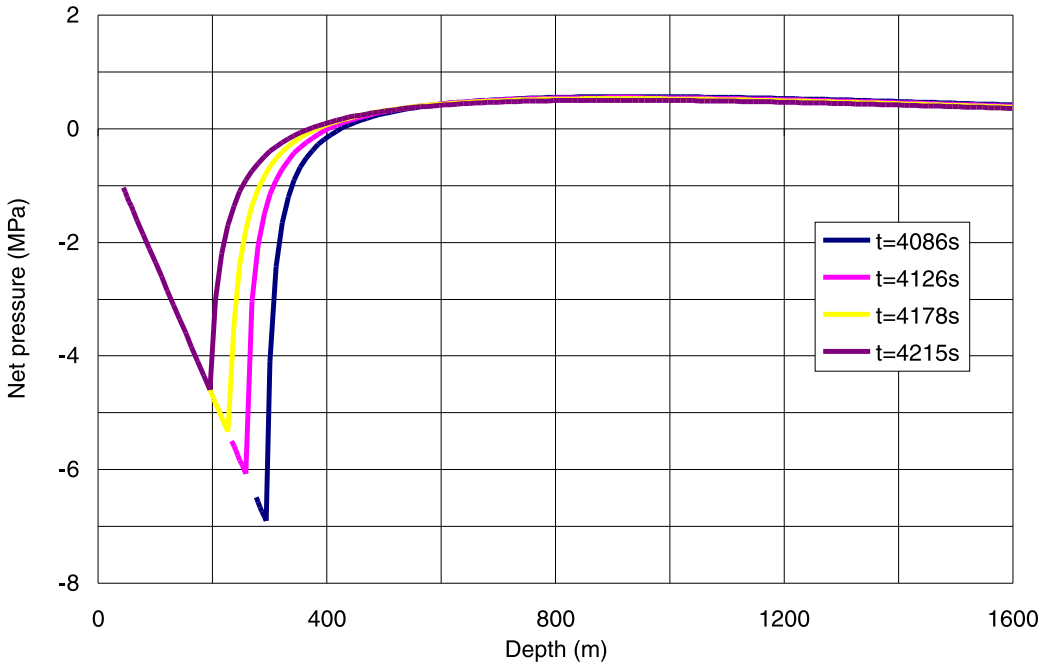

Figure II-13 Net pressure profile as a function of depth: $\mathcal{D} = 20.28$, $\kappa\rho_r = 2400$ kg/m^3, $\mu = 10$ Pa s, $v_\infty = 1$ m/s, $w_\infty = 0.32$ m

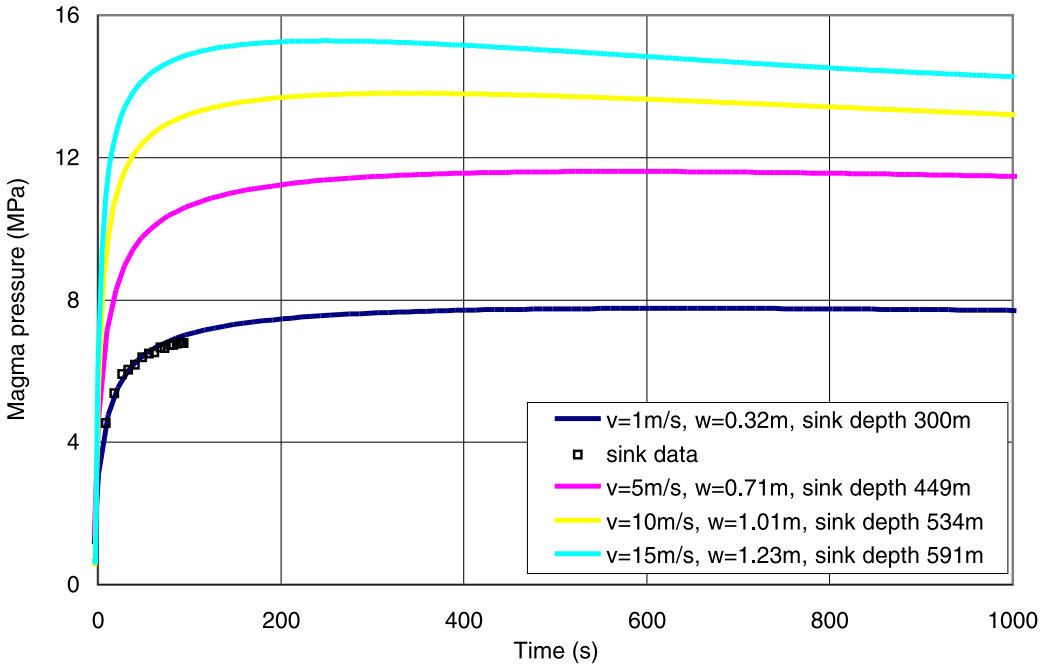

Figure II-14 Pressure history at leak-off point: $\mathcal{D} = 20.28$, $\kappa\rho_r = 2400$ kg/m^3, $\mu = 10$ Pa s

II.5.2 Effect of Pressure Inside the Tip Cavity

Magmas have a certain amount of volatiles (gases and steam). At high pressures, the gases are completely dissolved in the magma. As the magma pressure falls below a certain threshold pressure (i.e., as the magma approaches the ground surface), exsolution takes place, and gases form bubbles inside the melt. The volumetric percentage of the bubbles increases as the magma pressure decreases. In the magma near the tip cavity, the gases move (due to the pressure gradient) and are released into the cavity. At the same time, as pressure builds inside the cavity, the gases will leak-off from the cavity, by diffusion, into the surrounding rock formations. The model discussed in this report does not simulate any of these processes. However, a simplified analysis (Detournay et al. 2003), based on consideration of the gas diffusivity in tuff at Yucca Mountain, shows that the cavity gas pressure will be insignificantly larger than the gas pressure in the surrounding formation (i.e., atmospheric pressure). Because this simplified analysis is still preliminary, the effect of gas pressure inside the tip cavity on the conditions of dike propagation was investigated.

The results of the numerical model are shown in Figures II-15 through II-18. (The dimensionless results are in Figs. II-15 and II-17; the dimensional results are in Figs. II-16 and II-18.) Two cases were considered: a) $\mathcal{D} = 2.67$, $\mathcal{S} = -0.25$; and b) $\mathcal{D} = 20.28$, $\mathcal{S} = -0.20$. (The former corresponds to 1 MPa, and the latter to 0.49 MPa cavity gas pressure in the case of $\kappa\rho_r = 2400\,\text{kg/m}^3$, $\mu = 10$ Pa s and $v_\infty = 1$ m/s.) The cavity gas pressure does not significantly affect the velocity of the magma front. The velocity of the dike tip is affected, particularly when the tip gets close to the ground surface (i.e., when the cavity pressure becomes a significant proportion of the horizontal far-field stress). Thus, the cavity pressure increases the cavity length. Also, the cavity pressure reduces the maximum magma pressure at a given depth.

Neglecting the cavity gas pressure is a conservative assumption with respect to analysis of the magma flow inside the repository drifts, because it will overpredict both the rate of change of magma pressure and the maximum magma pressure.

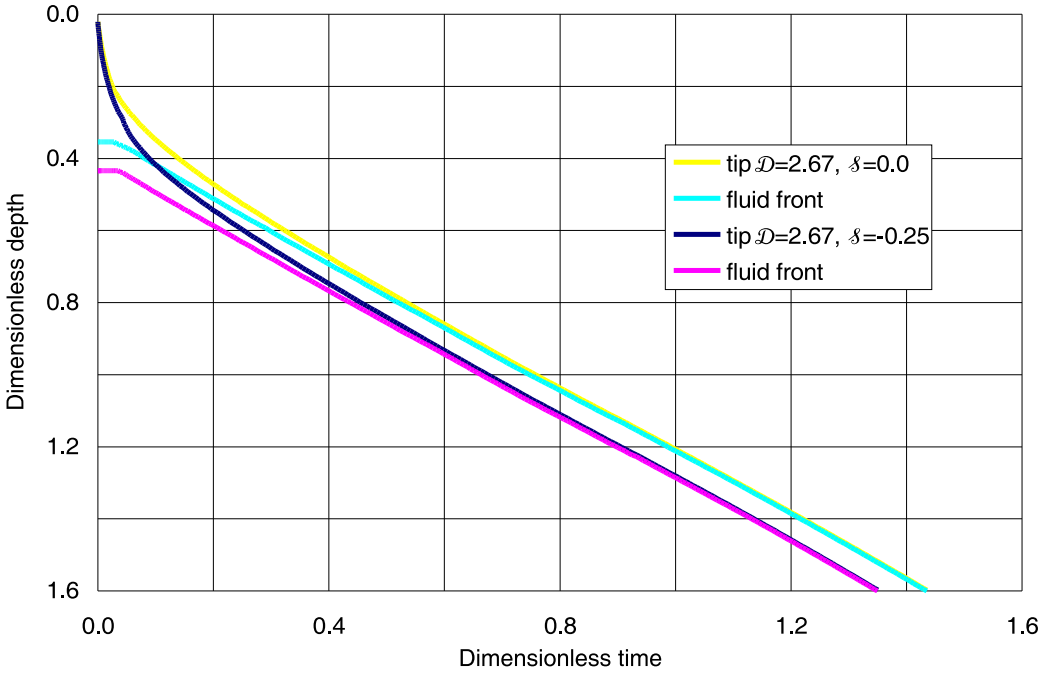

Figure II-15 Dimensionless solution for dike tip and fluid front as functions of time: effect of $\mathcal{S}$ for $\mathcal{D} = 2.67$

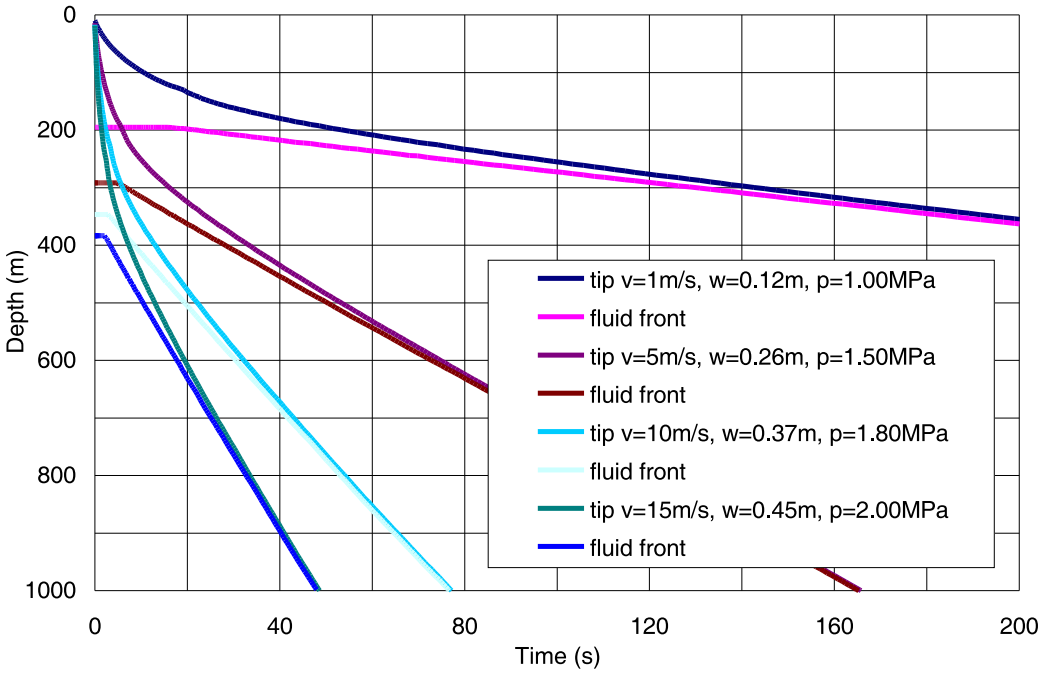

Figure II-16 Dike tip and fluid front as functions of time: $\mathcal{D} = 2.67$, $\mathcal{S} = -0.25$, $\kappa\rho_r = 2400$ kg/m^3, $\mu = 10$ Pa s

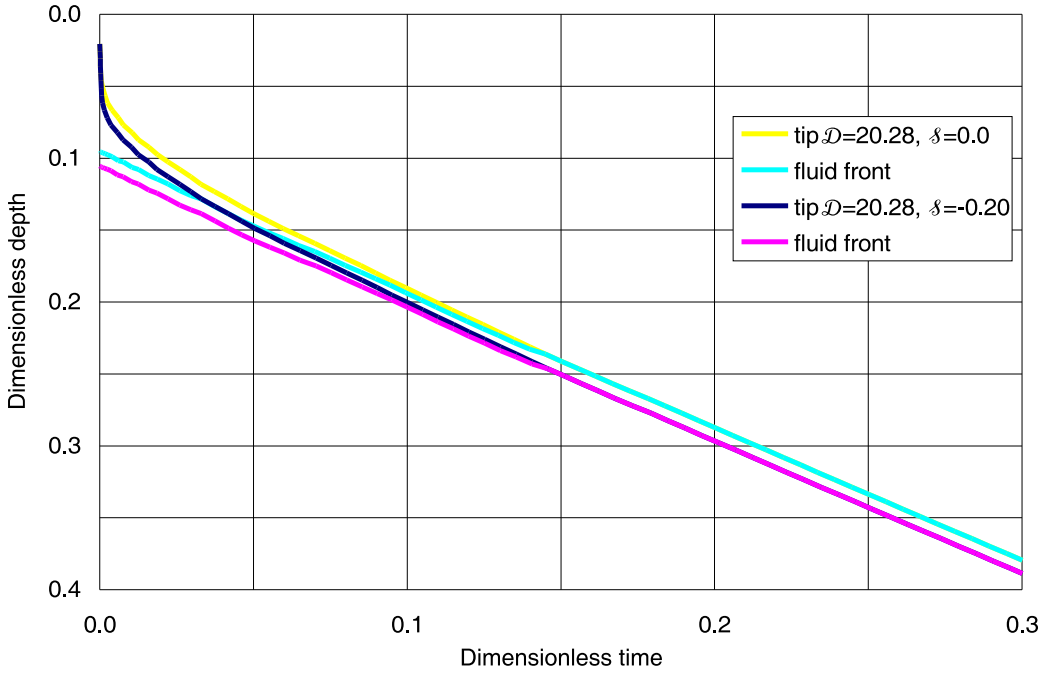

Figure II-17 Dimensionless solution for dike tip and fluid front as functions of time: effect of $\mathcal{S}$ for $\mathcal{D} = 20.28$

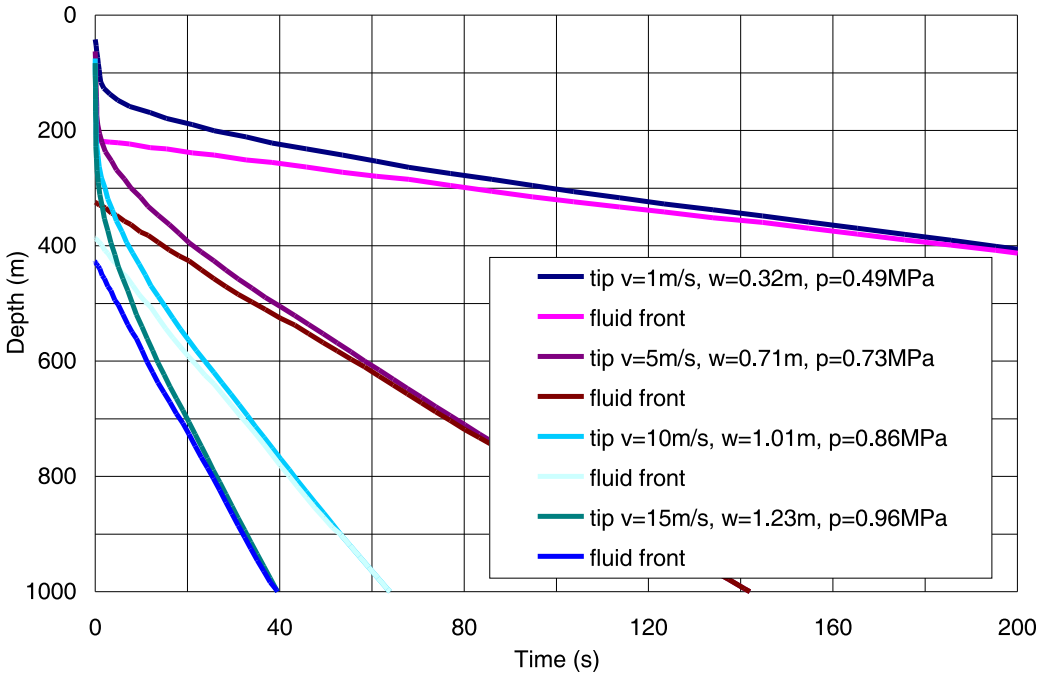

Figure II-18 Dike tip and fluid front as functions of time: $\mathcal{D} = 20.28$, $\mathcal{S} = -0.2$, $\kappa\rho_r = 2400$ kg/m^3, $\mu = 10$ Pa s

II.5.3 Leak-Off Effect

At the moment the magma reaches the repository level, some of it will start to flow into the emplacement drifts (5.5 m diameter drifts at 81 m center-to-center spacing). The rate of magma flow into the drifts, propagation of the dike tip and movement of the magma front inside the dike are functions of the interaction between the processes taking place inside the dike and the drifts. The adopted approach to solve the problem was to simulate the processes of magma flow inside the drifts and dike ascent separately, and to couple the two models at the point of intersection between the dike and the repository by exchange of the magma pressure (calculated in the "dike" model and passed to the "drift" model as a boundary condition) and magma flow rate (calculated in the "drift" model and passed to the "dike" model as a localized leak-off). However, the calculation of the magma flow rates inside the drifts (Section 6.3.9.2.3.1.6) shows that, in most of the cases considered, 100 percent of the magma flow inside the dike will be diverted into the drifts. The magma flow into the drifts up to a maximum of 40 percent of flow rate inside the dike was investigated using the NPHF2D code. In the case of a larger leak-off, this model is inappropriate approximation of the simulated processes (particularly magma flow inside the dike).

The cases for which the leak-off effect was simulated are shown in Table II-2. The dimensionless leak-off depths were selected such that the actual leak-off depth is 300 m for: a) case 1, assuming $\kappa\rho_r = 1200$ kg/m^3, $\mu = 10$ Pa s, $v_\infty = 1$ m/s; b) case 2, assuming $\kappa\rho_r = 1200$ kg/m^3, $\mu = 10$ Pa s, $v_\infty = 1$ m/s; and c) case 3, assuming $\kappa\rho_r = 2400$ kg/m^3, $\mu = 10$ Pa s, $v_\infty = 1$ m/s.

Table II-2 Simulated cases of leak-off effect

Case	$\mathcal{D}$	Dimensionless leak-off depth	Leak-off* percent
1	2.67	0.397	40
2	6.02	0.216	40
3	20.28	0.146	20

* Leak-off rate is given as a percentage of the magma injection rate at infinity.

The results are shown for: case 1 in Figures II-19 through II-23; case 2 in Figures II-24 through II-28; and case 3 in Figures II-29 through II-33. Positions of the dike tip and the magma front as functions of time are shown in dimensionless form in Figures II-19, II-24 and II-29. The dimensional velocities (for $v_\infty = 1$ m/s) are shown in Figures II-23, II-28 and II-33. The main effect of the leak-off on dike ascent is a slow-down of the dike tip and magma front velocities. As expected, the effect of leak-off on the magma velocity is larger than it is on the tip velocity. In case 2, when leak-off occurs at the moment the dike tip is close to the ground surface and has already begun to accelerate, it does not even affect the tip velocity (shown in Figs. II-24 and II-28). The leak-off does not arrest the dike tip, nor does it completely stop upward movement of the magma front in any of the cases (even for leak-offs as large as 20 percent and 40 percent).

The pressure histories at the repository level are shown in Figures II-22, II-27 and II-32. The solid lines represent pressure histories constructed from the magma pressure gradients behind the magma front. The pressure histories for cases for $v_\infty = 1$ m/s are constructed assuming reduced

magma front velocities based on the velocity curves shown in Figures II-23, II-28 and II-32. The magma front velocity was selected to be: a) 0.5 m/s for case 1; b) 3.3 m/s for case 2; and c) 6.7 m/s for case 3. The agreement between the constructed pressure histories (solid lines) and the actual pressure histories at the leak-off point is good. The effect of leak-off is a reduction of the rate of pressure change. Leak-off does not affect the maximum magma pressure.

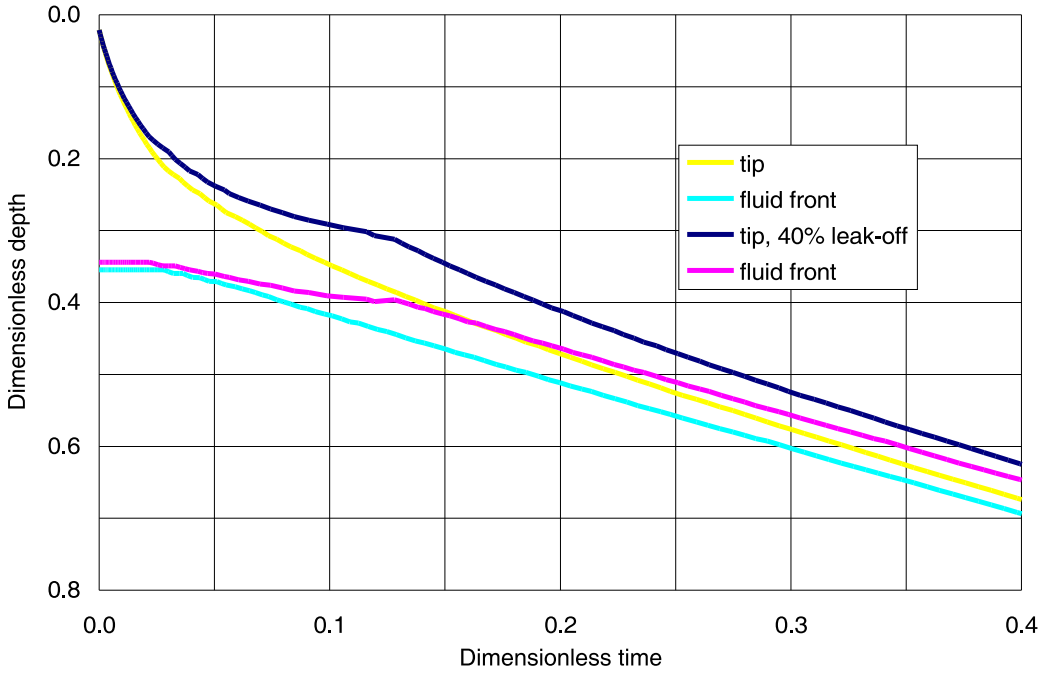

Figure II-19 Dimensionless solution for dike tip and fluid front as functions of time: effect of leak-off at dimensionless depth of 0.397 for $\mathcal{D} = 2.67$

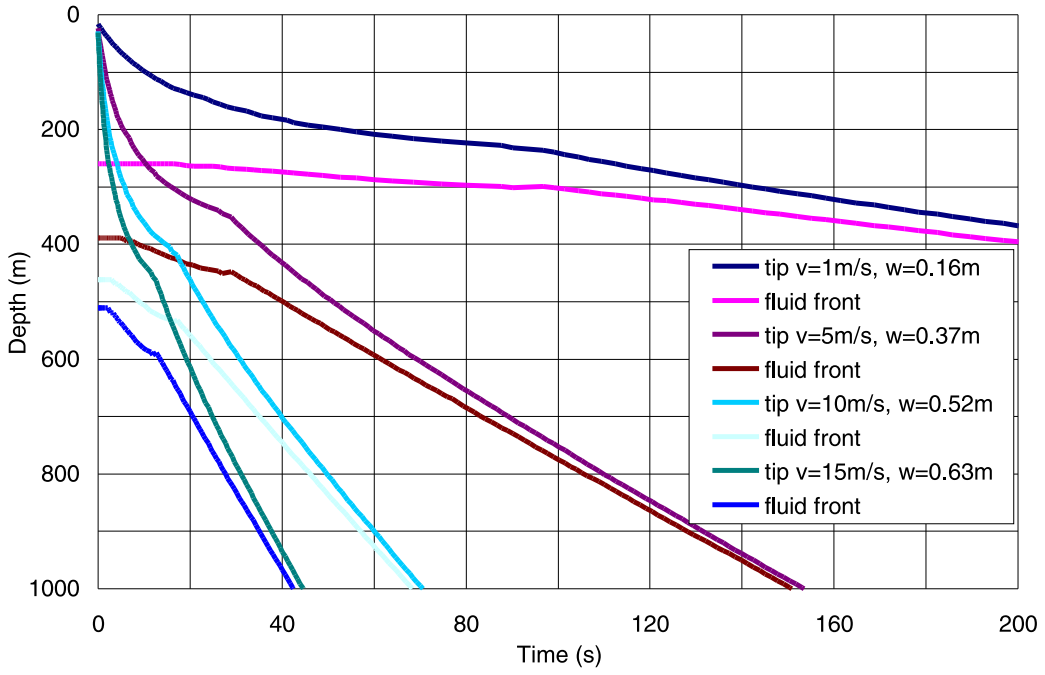

Figure II-20 Dike tip and fluid front as functions of time: $\mathcal{D} = 2.67$, $\kappa\rho_r = 1200$ kg/m^3, $\mu = 10$ Pa s, 40 percent leak-off

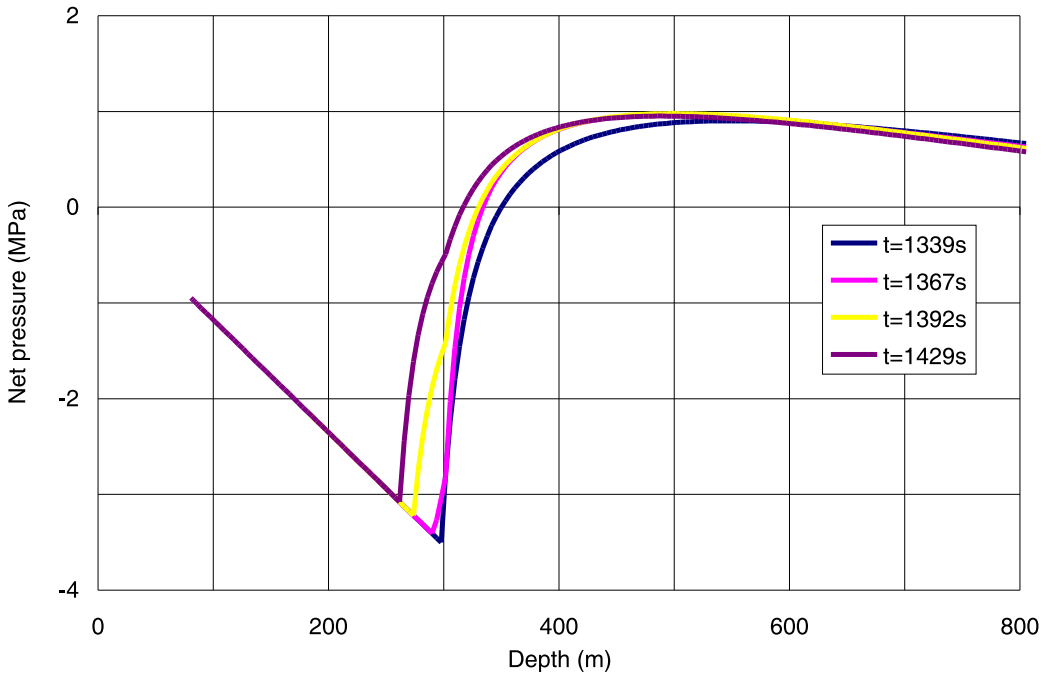

Figure II-21 Net pressure profile as a function of depth: $\mathcal{D} = 2.67$, $\kappa\rho_r = 1200$ kg/m^3, $\mu = 10$ Pa s, $v_\infty = 1$ m/s, $w_\infty = 0.16$ m, 40 percent leak-off at 300 m depth

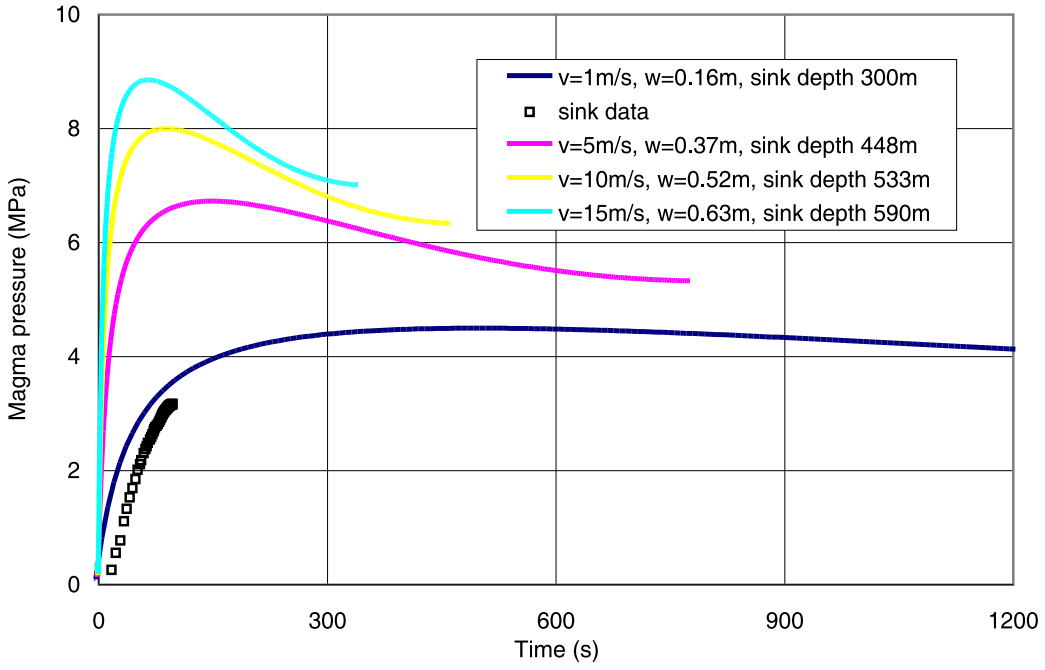

Figure II-22 Pressure history at leak-off point: $\mathcal{D} = 2.67$, $\kappa\rho_r = 1200$ kg/m^3, $\mu = 10$ Pa s, 40 percent leak-off

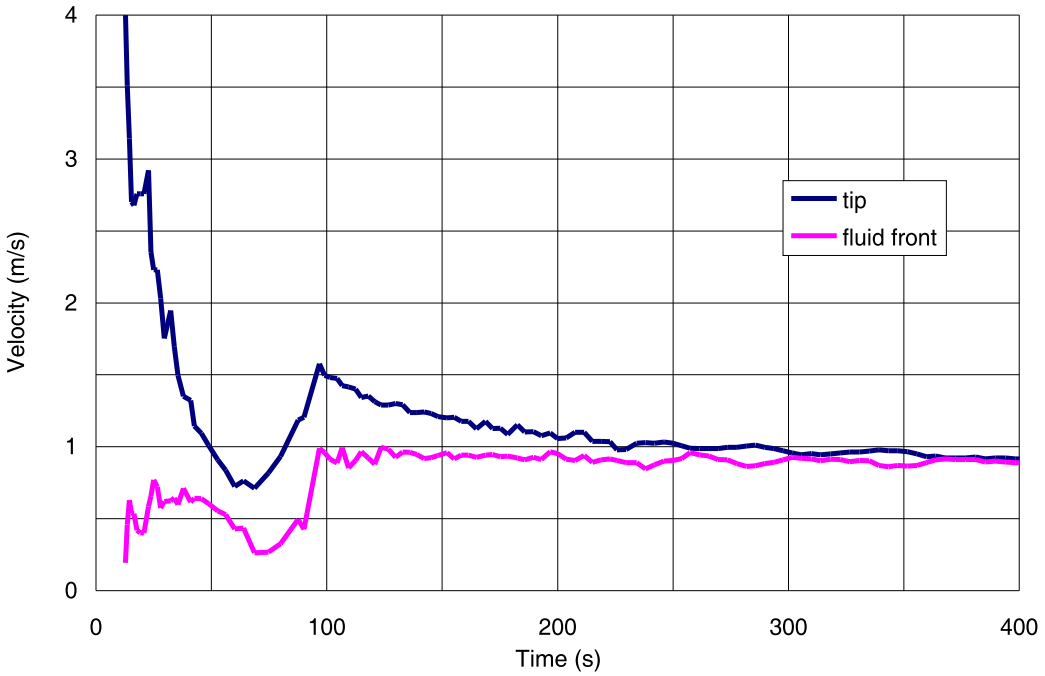

Figure II-23 Velocity of the dike tip and fluid front: $\mathcal{D} = 2.67$, $\kappa\rho_r = 1200$ kg/m^3, $\mu = 10$ Pa s, $v_\infty = 1$ m/s, $w_\infty = 0.16$ m, 40 percent leak-off at 300 m depth

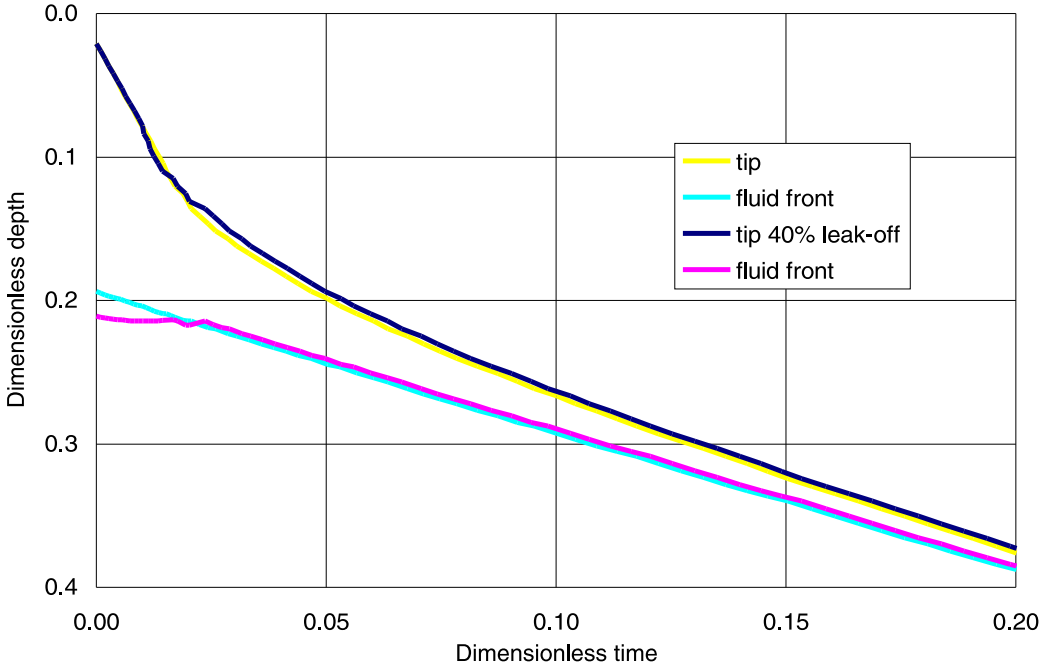

Figure II-24 Dimensionless solution for dike tip and fluid front as functions of time: effect of leak-off at dimensionless depth of 0.216 for $\mathcal{D} = 6.02$

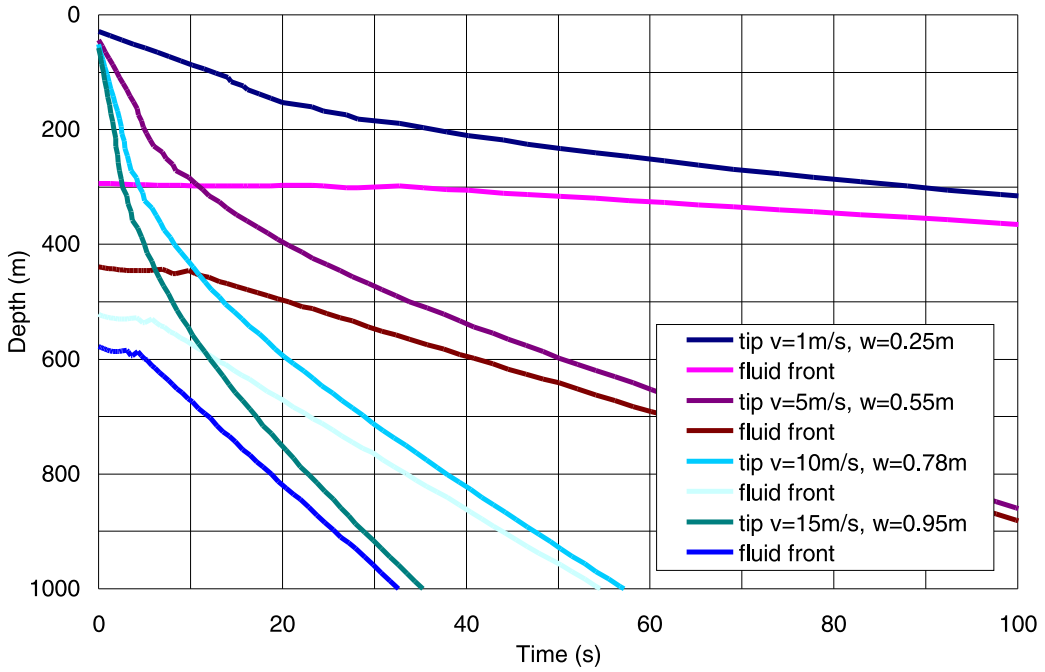

Figure II-25 Dike tip and fluid front as functions of time: $\mathcal{D} = 6.02$, $\kappa\rho_r = 1200$ kg/m^3, $\mu = 10$ Pa s, 40 percent leak-off

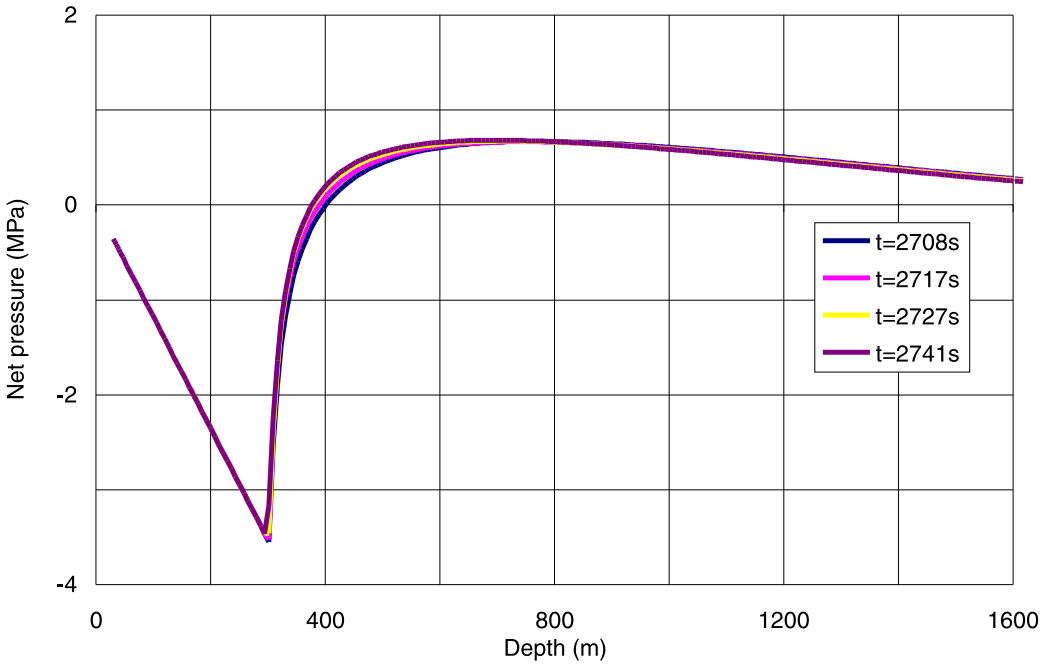

Figure II-26 Net pressure profile as a function of depth: $\mathcal{D} = 6.02$, $\kappa\rho_r = 1200$ kg/m^3, $\mu = 10$ Pa s, $v_\infty = 1$ m/s, $w_\infty = 0.25$ m, 40 percent leak-off at 300 m depth

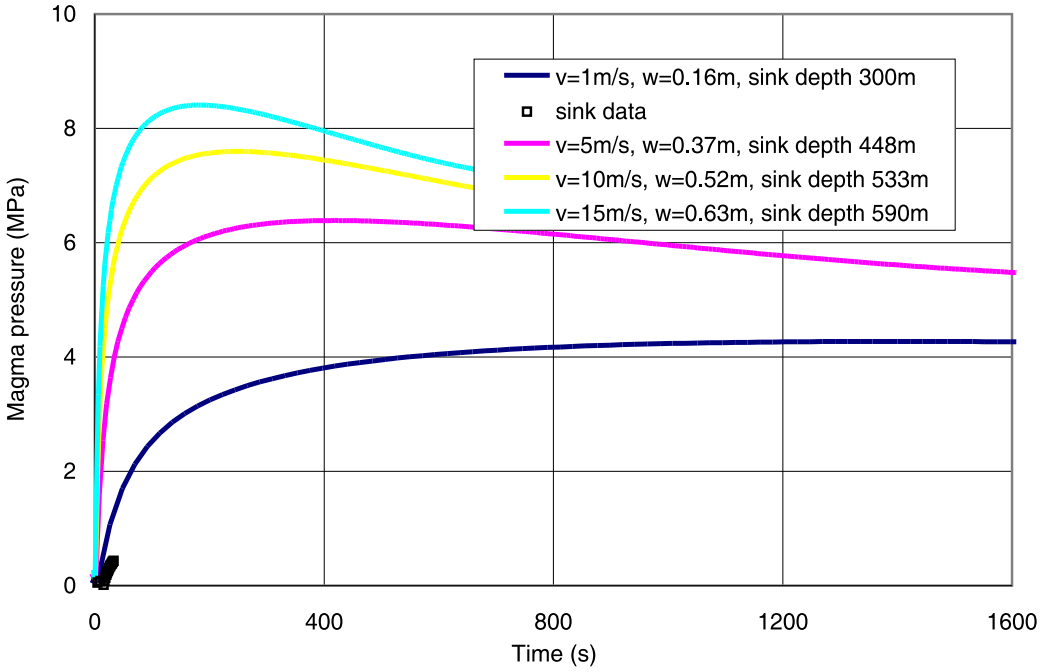

Figure II-27 Pressure history at leak-off point: $\mathcal{D} = 6.02$, $\kappa\rho_r = 1200$ kg/m^3, $\mu = 10$ Pa s, 40 percent leak-off

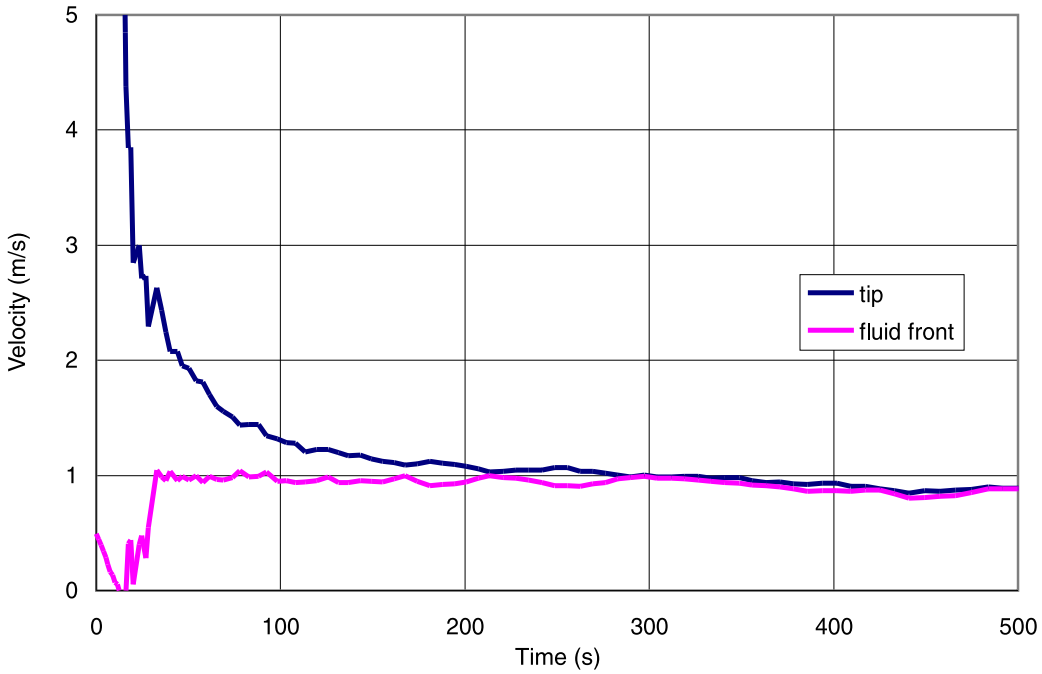

Figure II-28 Velocity of the dike tip and fluid front: $\mathcal{D} = 6.02$, $\kappa\rho_r = 1200$ kg/m^3, $\mu = 10$ Pa s, $v_\infty = 1$ m/s, $w_\infty = 0.25$ m, 40 percent leak-off at 300 m depth

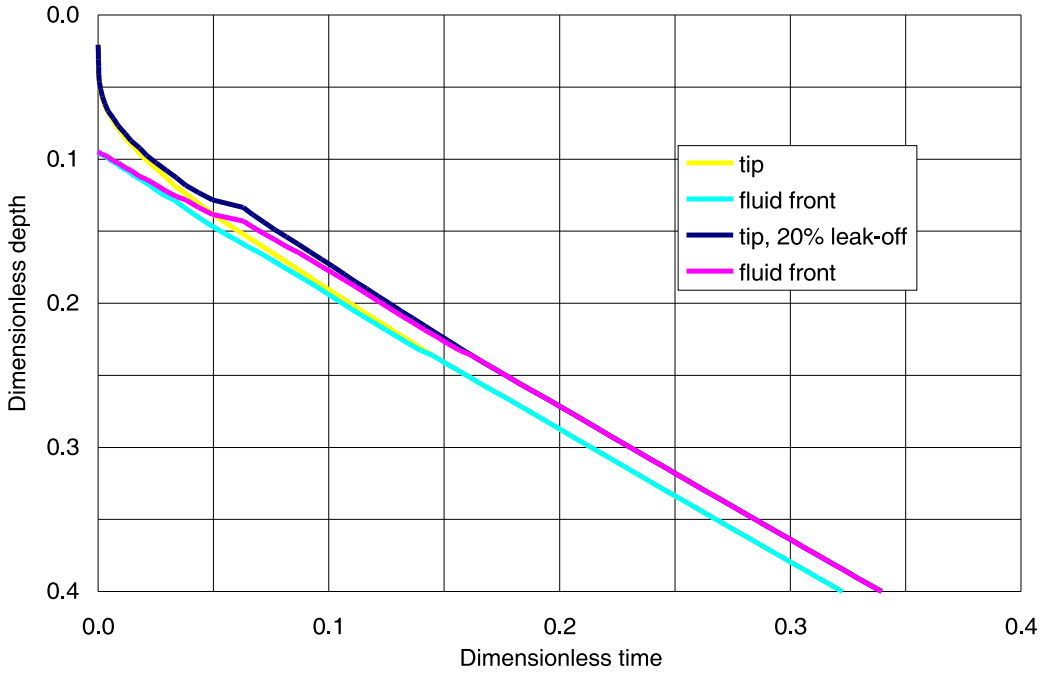

Figure II-29 Dimensionless solution for dike tip and fluid front as functions of time: effect of leak-off at dimensionless depth of 0.146 for $\mathcal{D} = 20.28$

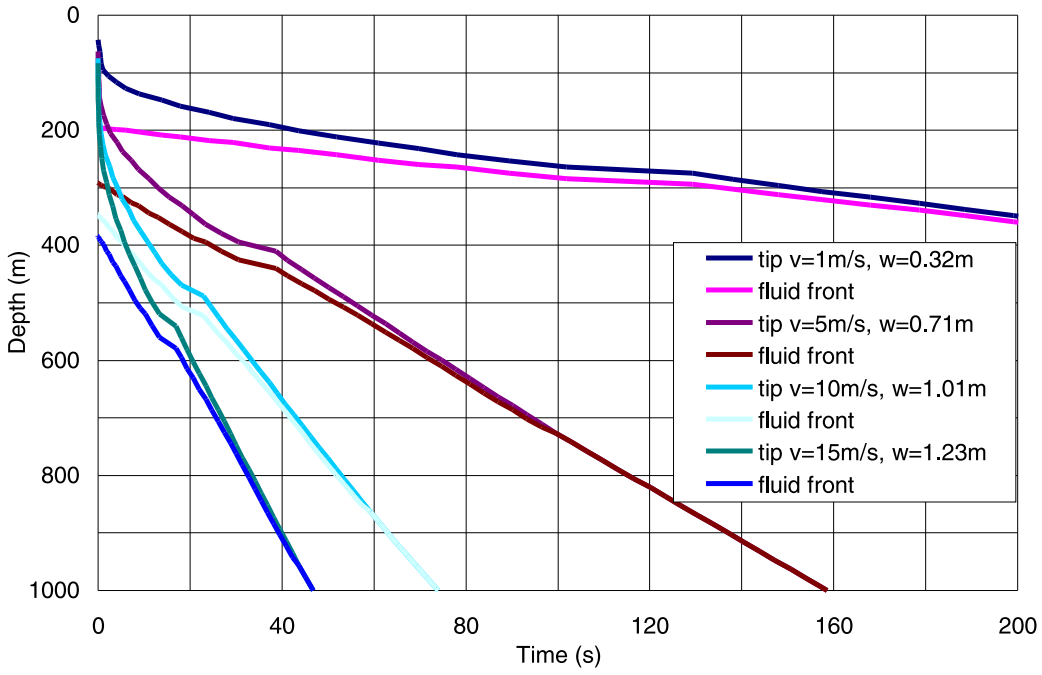

Figure II-30 Dike tip and fluid front as functions of time: $\mathcal{D} = 20.28$, $\kappa\rho_r = 2400$ kg/m^3, $\mu = 10$ Pa s, 20 percent leak-off

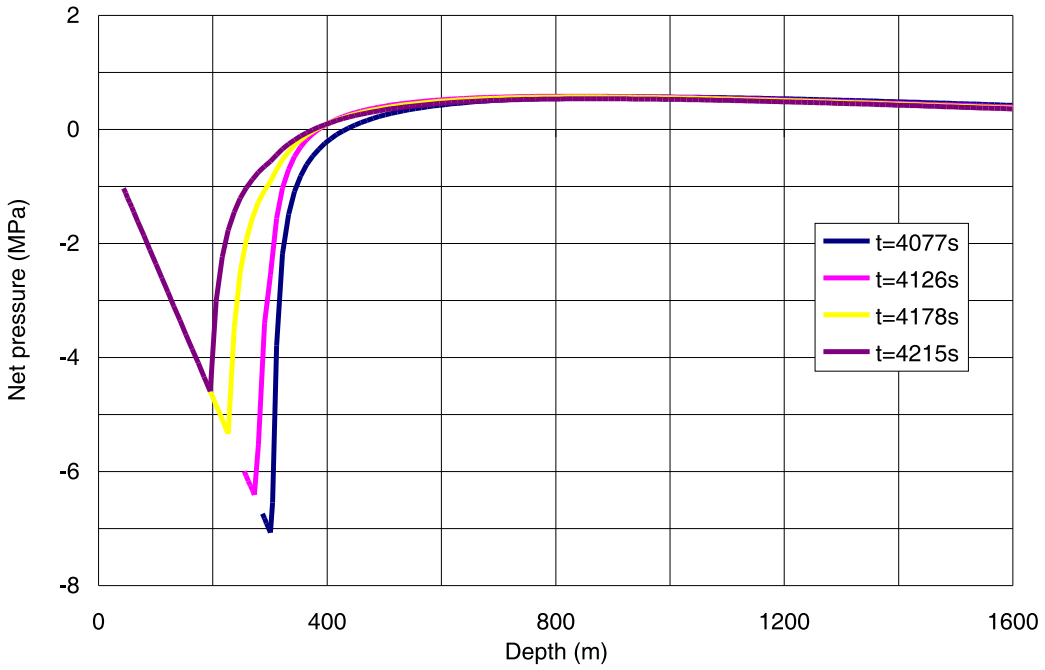

Figure II-31 Net pressure profile as a function of depth: $\mathcal{D} = 20.28$, $\kappa\rho_r = 2400$ kg/m^3, $\mu = 10$ Pa s, $v_\infty = 1$ m/s, $w_\infty = 0.32$ m, 20 percent leak-off at 300 m depth

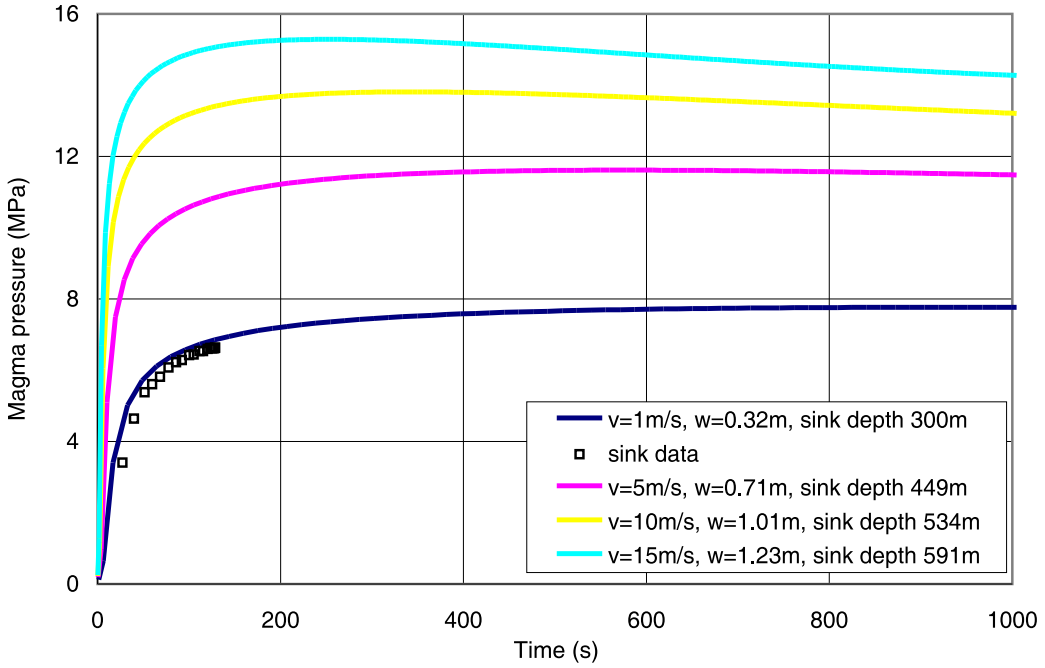

Figure II-32 Pressure history at leak-off point: $\mathcal{D} = 20.28$, $\kappa\rho_r = 2400$ kg/m^3, $\mu = 10$ Pa s, 20 percent leak-off

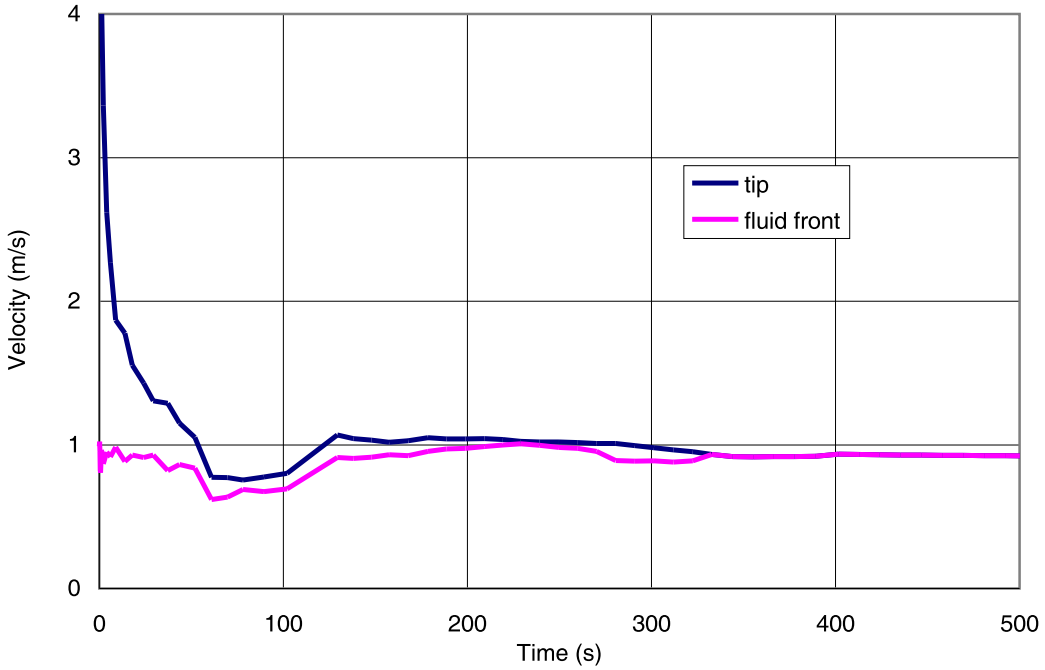

Figure II-33 Velocity of the dike tip and fluid front: $\mathcal{D} = 6.02$, $\kappa\rho_r = 1200$ kg/m^3, $\mu = 10$ Pa s, $v_\infty = 1$ m/s, $w_\infty = 0.25$ m, 40 percent leak-off at 300 m depth

II.5.4 Effect of Increased Horizontal Stress

The analysis of thermally induced stresses in a large scale model (Section 6.3.9.2.2) shows that the least compressive horizontal stress increases to a maximum of approximately 10 MPa at the repository level. This maximum stress occurs in the limited volume of the rock mass and during relatively short period of time. Dike propagation was simulated assuming the maximum confining stress of 8 MPa. The conditions of dike ascent under increased confinement are analyzed, assuming that increased horizontal stress does not cause the dike to turn towards the region of smaller confinement (conservative assumption), i.e., the dike is assumed to intersect the emplacement drifts. Two cases were considered: $\mathcal{D}$ equal to 2.67 and 6.02. Dimensional results are constructed in both cases for $\kappa\rho_r = 1200$ kg/m^3 and $\mu = 10$ Pa s. The additional confining stress was applied to achieve the total stress of 8 MPa at a 300 m depth (i.e., 3.6 MPa stress due to $\kappa\rho_r$ plus 4.4 MPa thermally induced stress) for the case in which $v_\infty = 1$ m/s. The horizontal, thermally induced stress is applied to the model uniformly over its entire height. Such a simplification is justified because it provides bounding condition due to stress increase.

The results of the analysis are shown in Figures II-34 through II-41. The increase in confinement does not significantly affect the velocity of the magma front. However, the velocity of the dike tip is considerably slowed by the confinement. The dike tip progresses to the ground surface steadily, without acceleration near the ground surface, as was observed in the cases with no additional horizontal confinement. Consequently, the tip cavity length is significantly reduced, in both cases analyzed, to the order of 10 m at a 300 m depth (for $v_\infty = 1$ m/s) increasing to a maximum of 30 m at the ground surface. (The tip cavity length in the unconfined cases was up to 300 m.) The pressure histories (shown in Figs. II-37 and II-41) have a larger maximum of 9 MPa (due to a horizontal stress of 8 MPa) and a larger rate of increase (due to the reduced cavity length) than the pressure histories for the unconfined cases.

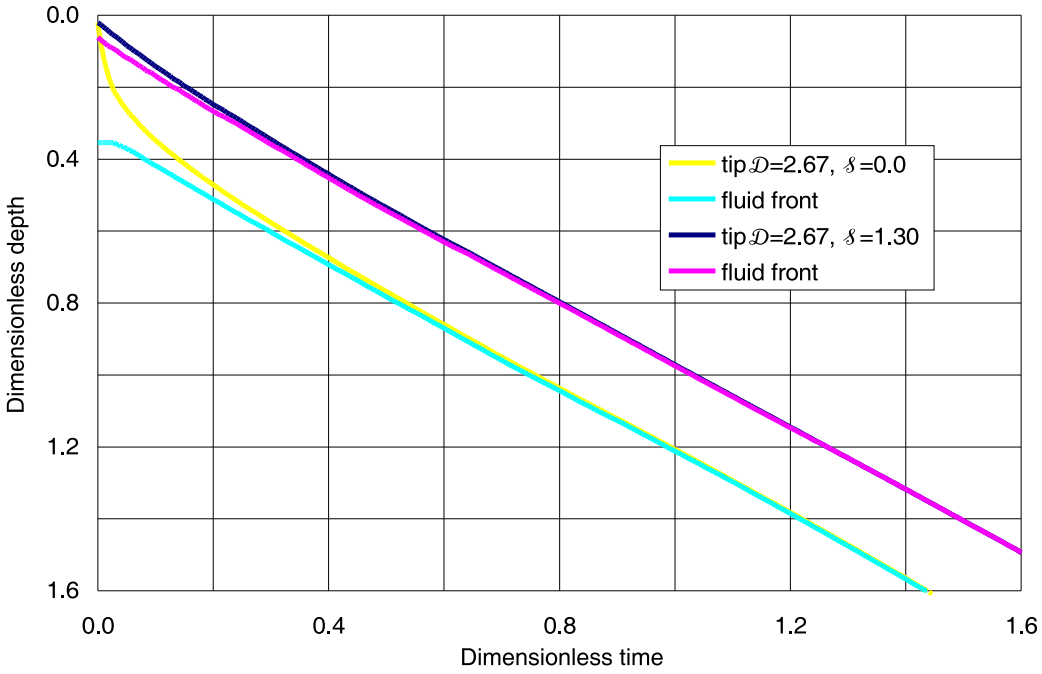

Figure II-34 Dimensionless solution for dike tip and fluid front as functions of time: effect of σ_c for $\mathcal{D} = 2.67$

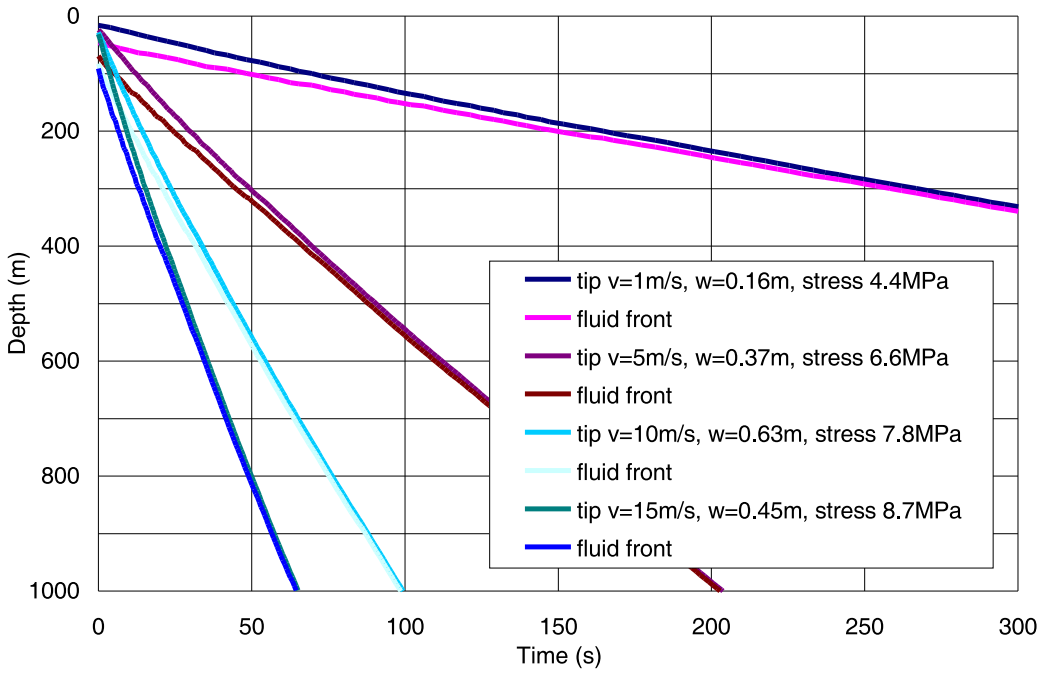

Figure II-35 Dike tip and fluid front as functions of time and leak-off: $\mathcal{D} = 2.67$, $\kappa\rho_r = 1200$ kg/m^3, $\mu = 10$ Pa s

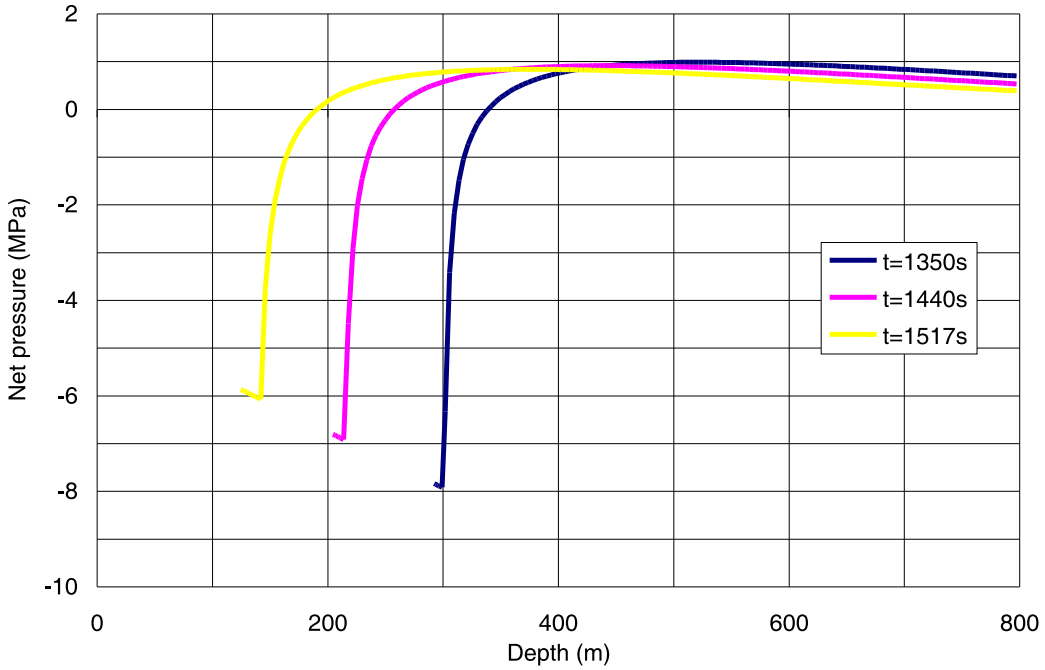

Figure II-36 Net pressure profile as a function of depth: $\mathcal{D} = 2.67$, $\kappa\rho_r = 1200$ kg/m^3, $\mu = 10$ Pa s, $v_\infty = 1$ m/s, $w_\infty = 0.16$ m, $\mathcal{S} = 1.3$

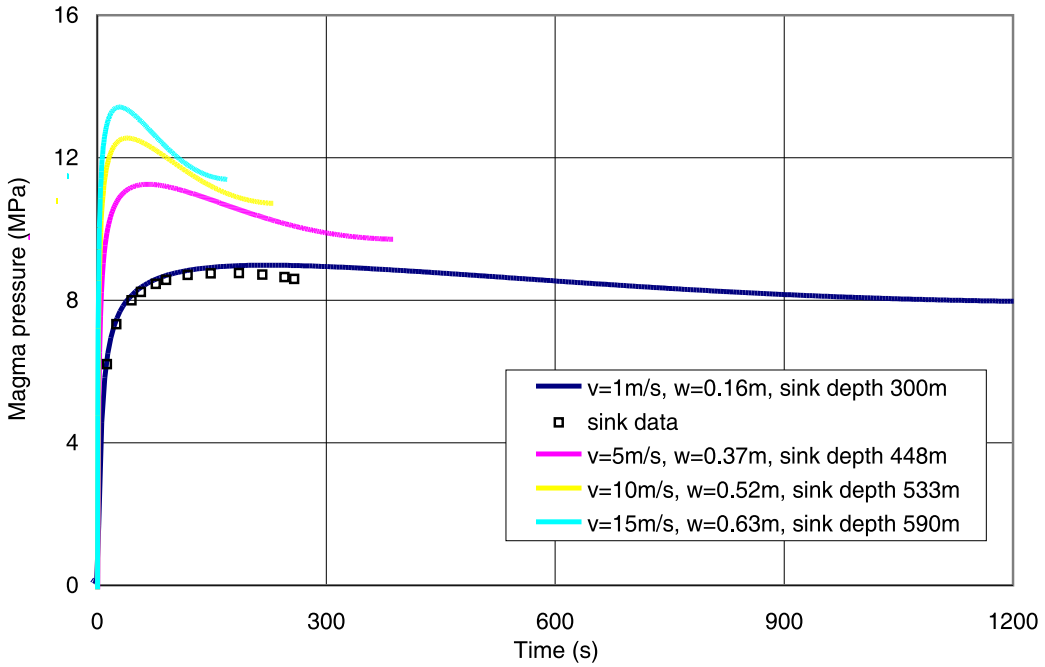

Figure II-37 Pressure history at leak-off point: $\mathcal{D} = 2.67$, $\kappa\rho_r = 1200$ kg/m^3, $\mu = 10$ Pa s, $\mathcal{S} = 1.3$

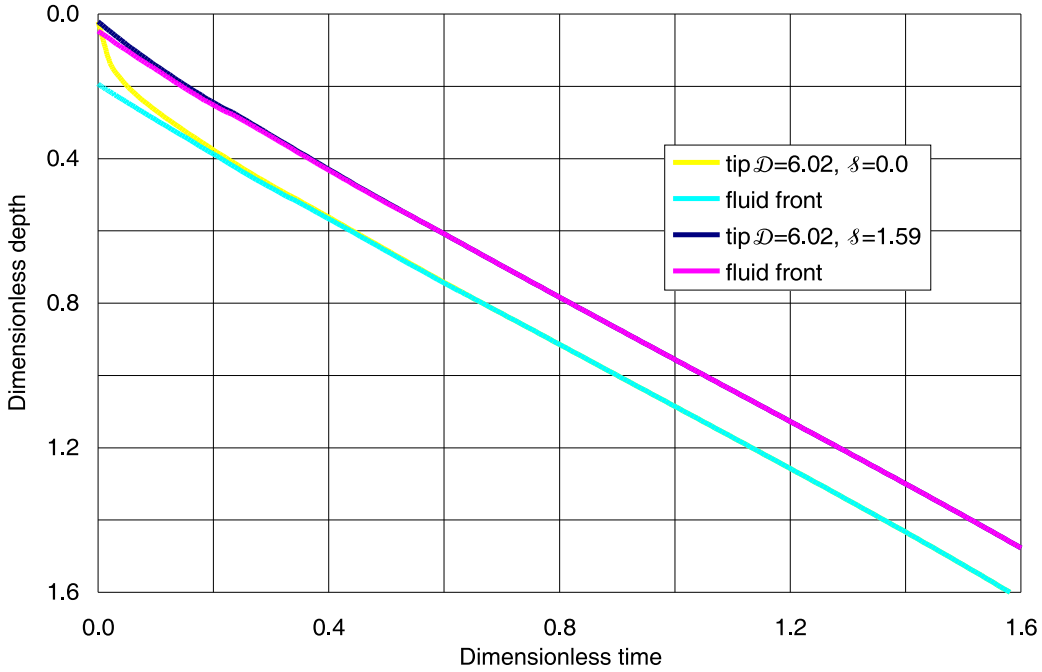

Figure II-38 Dimensionless solution for dike tip and fluid front as functions of time: effect of σ_c for $\mathcal{D} = 6.02$

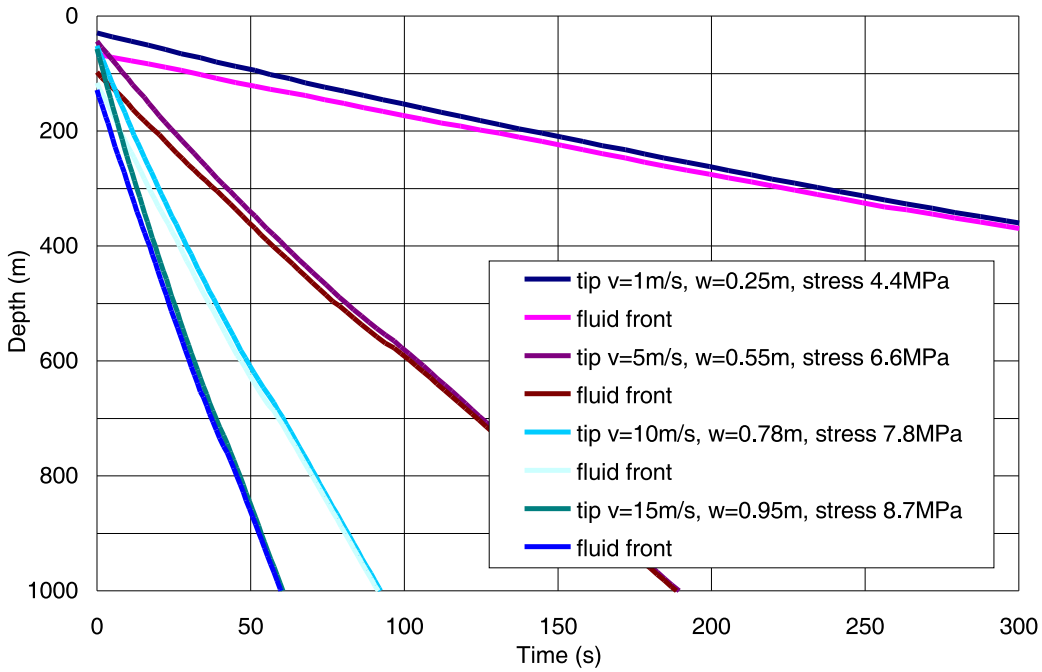

Figure II-39 Dike tip and fluid front as functions of time and leak-off: $\mathcal{D} = 6.02$, $\kappa\rho_r = 1200$ kg/m^3, $\mu = 10$ Pa s

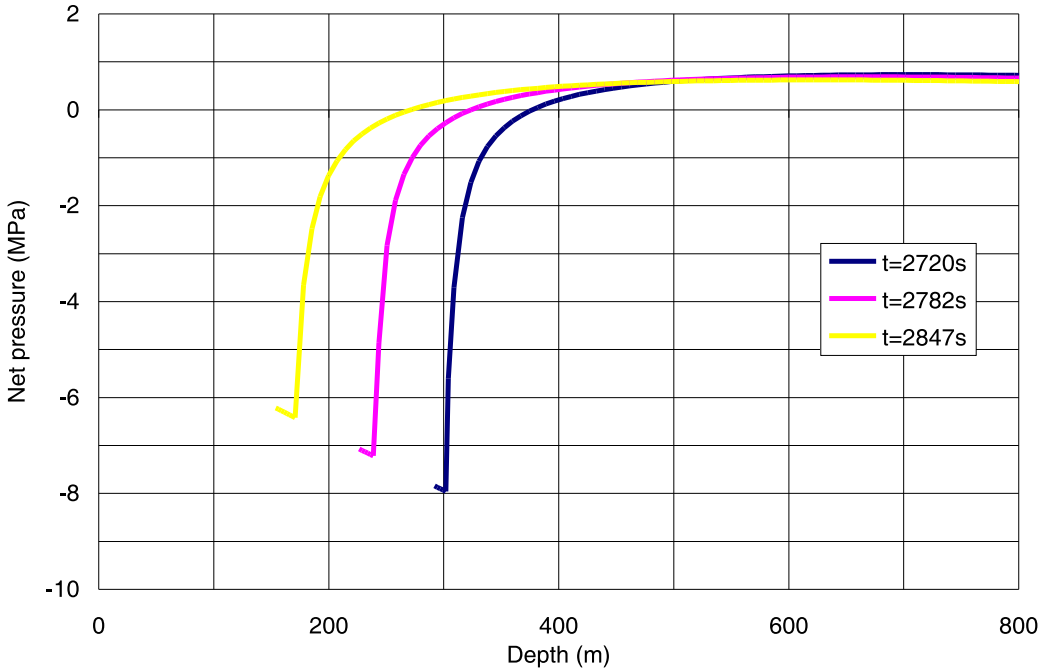

Figure II-40 Net pressure profile as a function of depth: $\mathcal{D} = 6.02$, $\kappa\rho_r = 1200$ kg/m^3, $\mu = 10$ Pa s, $v_\infty = 1$ m/s, $w_\infty = 0.25$ m, $\mathcal{S} = 1.59$

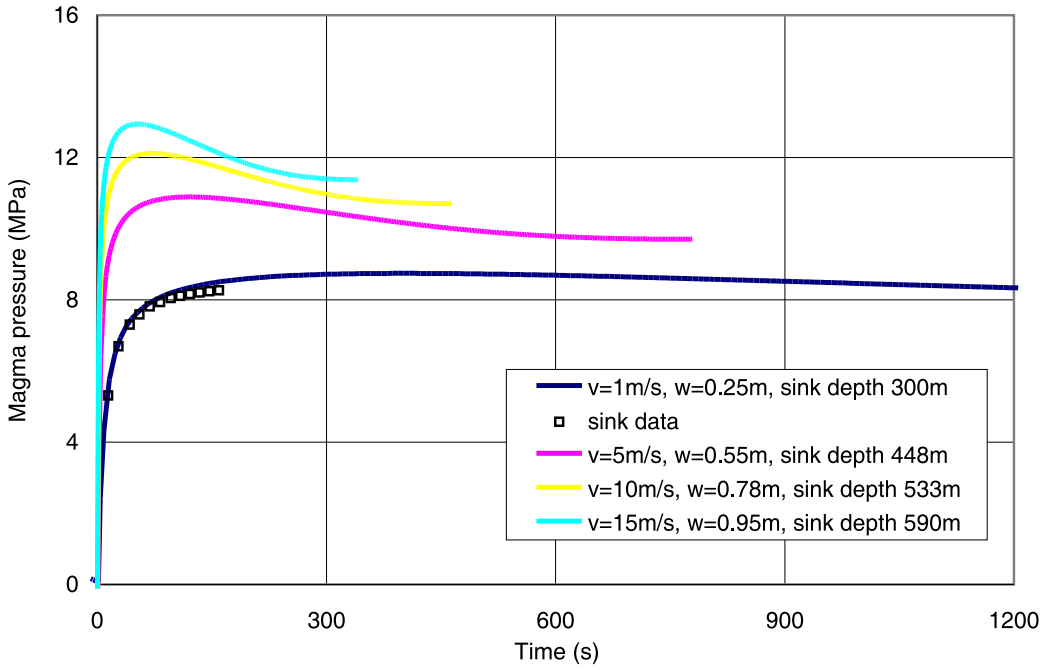

Figure II-41 Pressure history at leak-off point: $\mathcal{D} = 6.02$, $\kappa\rho_r = 1200$ kg/m^3, $\mu = 10$ Pa s, $\mathcal{S} = 1.59$

II.5.5 Effect of Increased Horizontal Stress with Leak-Off

The results of simulations of dike ascent in the region of increased confinement with the effect of localized leak-off are shown in Figures II-42 through II-49. Two cases were analyzed.

Case 1 is for $\mathcal{D} = 2.67$, 15 percent leak-off at 0.397 dimensionless depth.

Case 2 is for $\mathcal{D} = 6.02$, 25 percent leak-off at 0.216 dimensionless depth.

The dimensionless depth of the leak-off point was selected, in both cases, to correspond to a 300 m depth for $\kappa\rho_r = 1200$ kg/m^3, $\mu = 10$ Pa s and $v_\infty = 1$ m/s. Additional confinement of 4.4 MPa (resulting in 8-MPa total stress) was used for the same conditions.

The leak-off considered in these cases has relatively small effect on the velocities of the dike tip and the magma front. The pressure histories are constructed assuming magma front velocities equal to v_∞ (shown as solid lines in Figs. II-45 and II-49). The lines for $v_\infty = 1$ m/s agree rather well with measured pressure histories at the leak-off depth, even without accounting for any velocity change due to leak-off. Also, these pressure histories are almost the same as the pressure histories without leak-off shown in Figures II-37 and II-41.

II.6 SUMMARY

Dike ascent was analyzed for a variety of conditions. The effects of horizontal stress gradient, far-field dike velocity and opening, pressure inside the tip cavity, leak-off and additional horizontal confinement were considered. The dike ascent was analyzed in this model assuming maximum leak-off of 40 percent. Although the dimensional results were provided for different values of v_∞ (up to 15 m/s), the main focus was on $v_\infty = 1$ m/s (the "expected" dike velocity).

The existing horizontal stress controls the maximum magma pressure, which is approximately 1 MPa larger than the horizontal stress at the repository depth. Therefore, the maximum magma pressure would be about 4.5 MPa under in-situ stress conditions, but would increase to 9 MPa in the case of far-field stress in rock perpendicular to the dike equal to 8 MPa. Horizontal stress also has a significant effect on the tip cavity length. A gradient of magma pressure is linked to the cavity length (i.e., a short cavity will result in a large gradient).

The main effect of leak-off is to slow the advance of the dike tip, and particularly of the magma front. However, even in cases of 40 percent leak-off, the magma front is not fully arrested. Leak-off also reduces the rate of pressure change at the leak-off location.

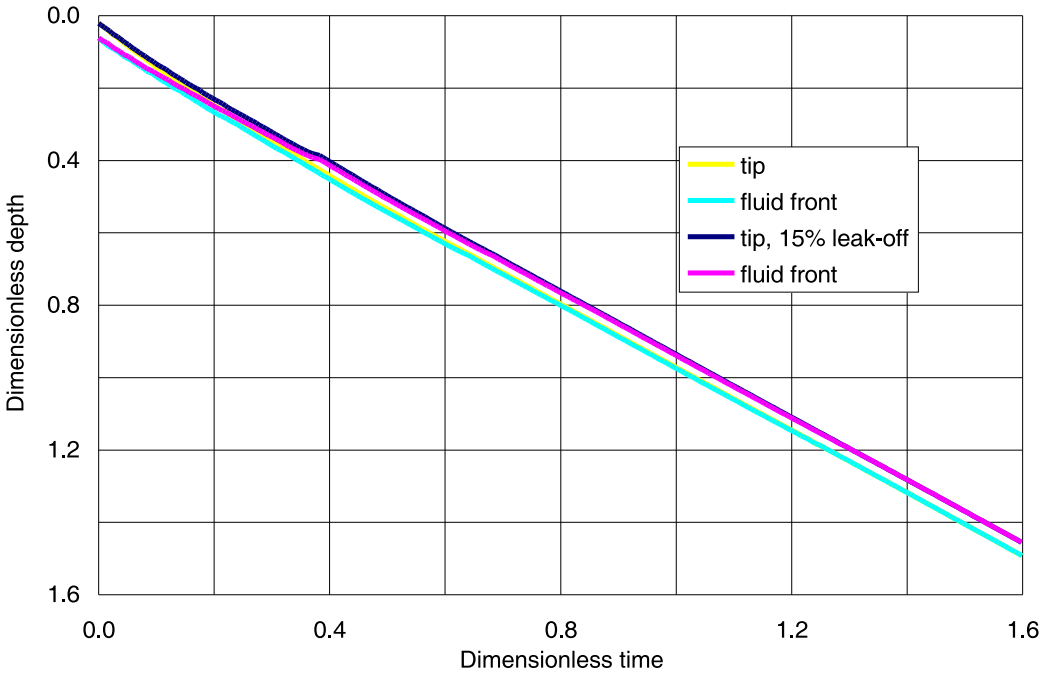

Figure II-42 Dimensionless solution for dike tip and fluid front as functions of time: effect of leak-off at dimensionless depth 0.397 for $\mathcal{D} = 2.67$

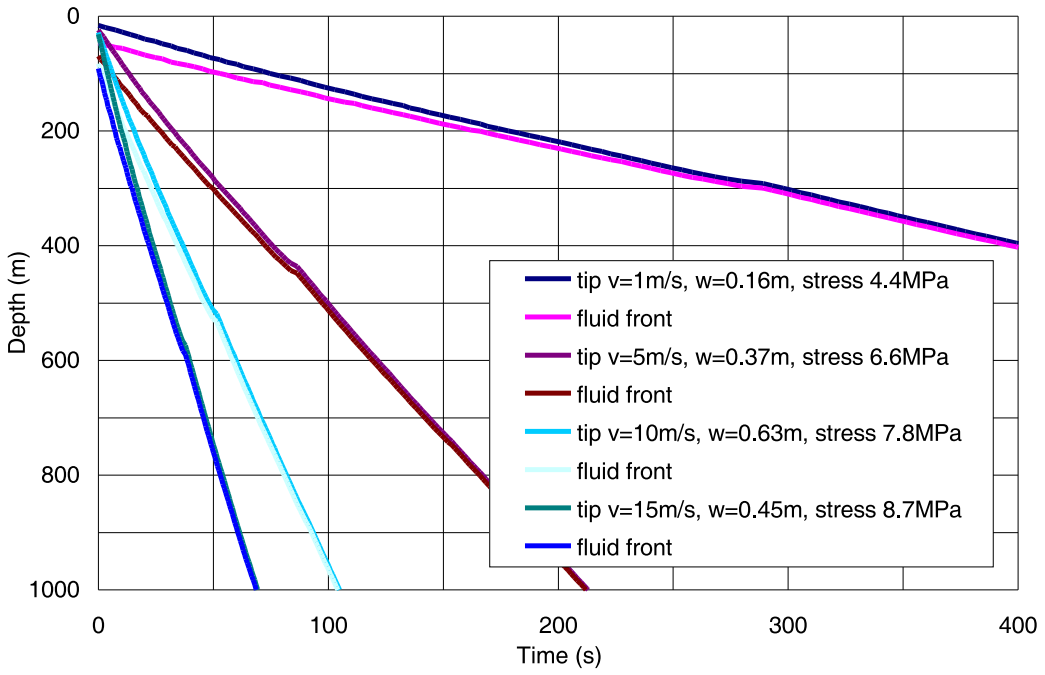

Figure II-43 Dike tip and fluid front as functions of time: $\mathcal{D} = 2.67$, $\kappa\rho_r = 1200$ kg/m^3, $\mu = 10$ Pa s, 15 percent leak-off

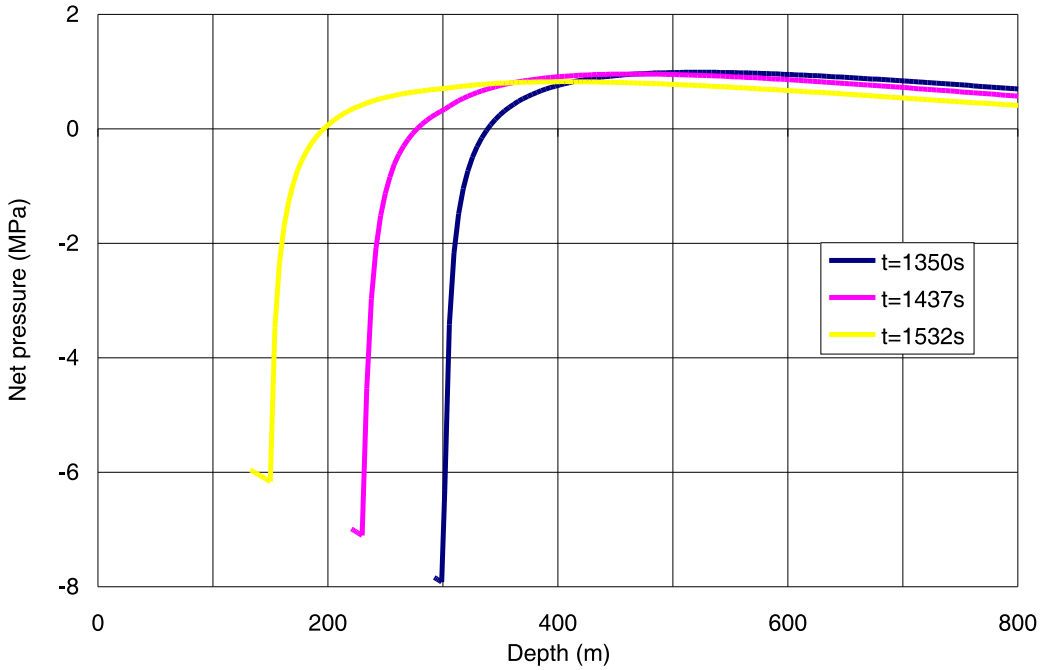

Figure II-44 Net pressure profile as a function of depth: $\mathcal{D} = 2.67$, $\kappa\rho_r = 1200$ kg/m^3, $\mu = 10$ Pa s, $v_\infty = 1$ m/s, $w_\infty = 0.16$ m, $\mathcal{S} = 1.3$, 15 percent leak-off at 300 m depth

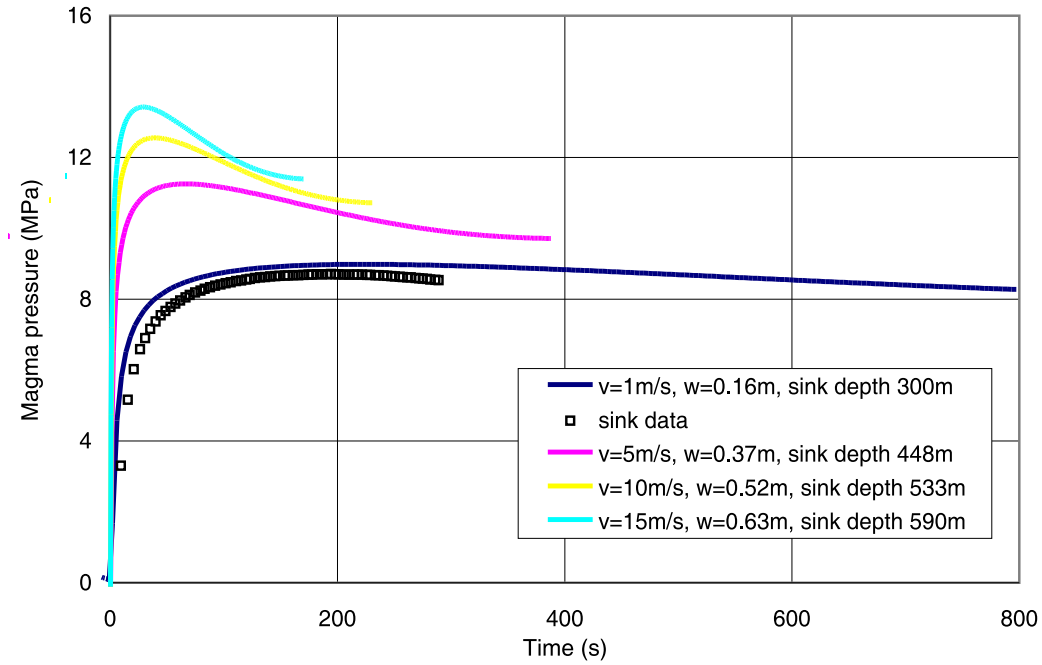

Figure II-45 Pressure history at leak-off point: $\mathcal{D} = 2.67$, $\kappa\rho_r = 1200$ kg/m^3, $\mu = 10$ Pa s, $\mathcal{S} = 1.3$, 15 percent leak-off

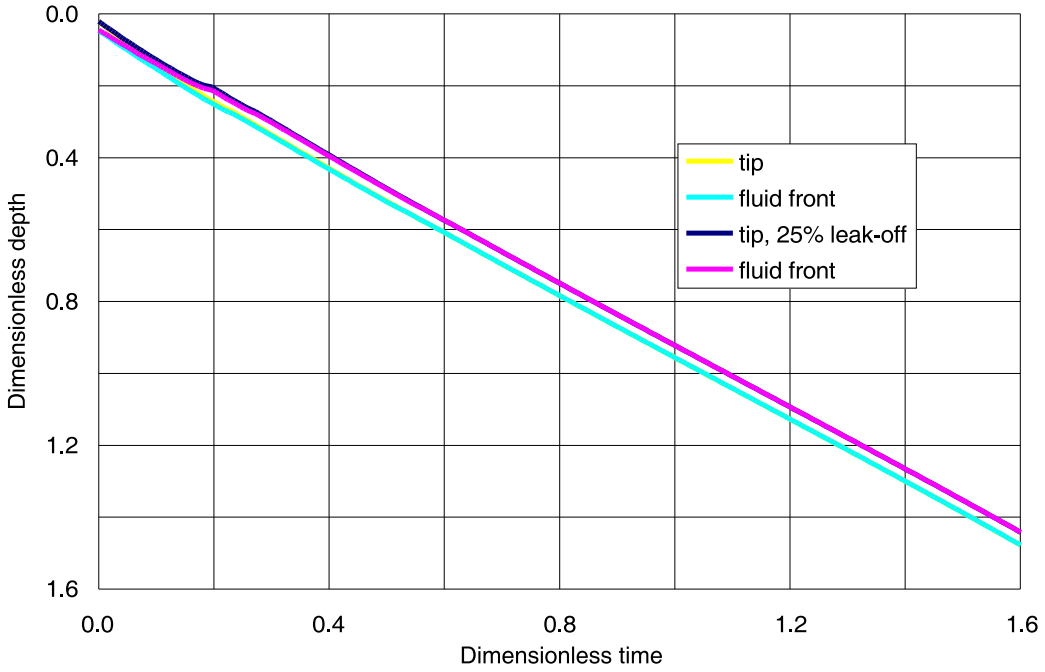

Figure II-46 Dimensionless solution for dike tip and fluid front as functions of time: effect of leak-off at dimensionless depth 0.216 for $\mathcal{D} = 6.02$

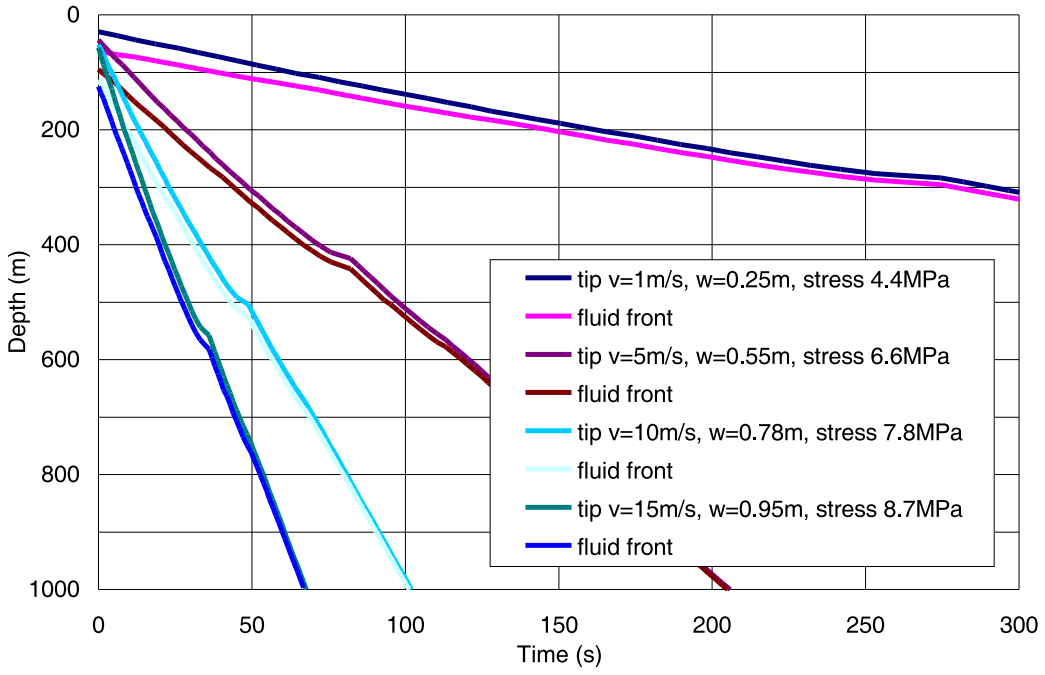

Figure II-47 Dike tip and fluid front as functions of time: $\mathcal{D} = 6.02$, $\kappa\rho_r = 1200$ kg/m^3, $\mu = 10$ Pa s, 25 percent leak-off

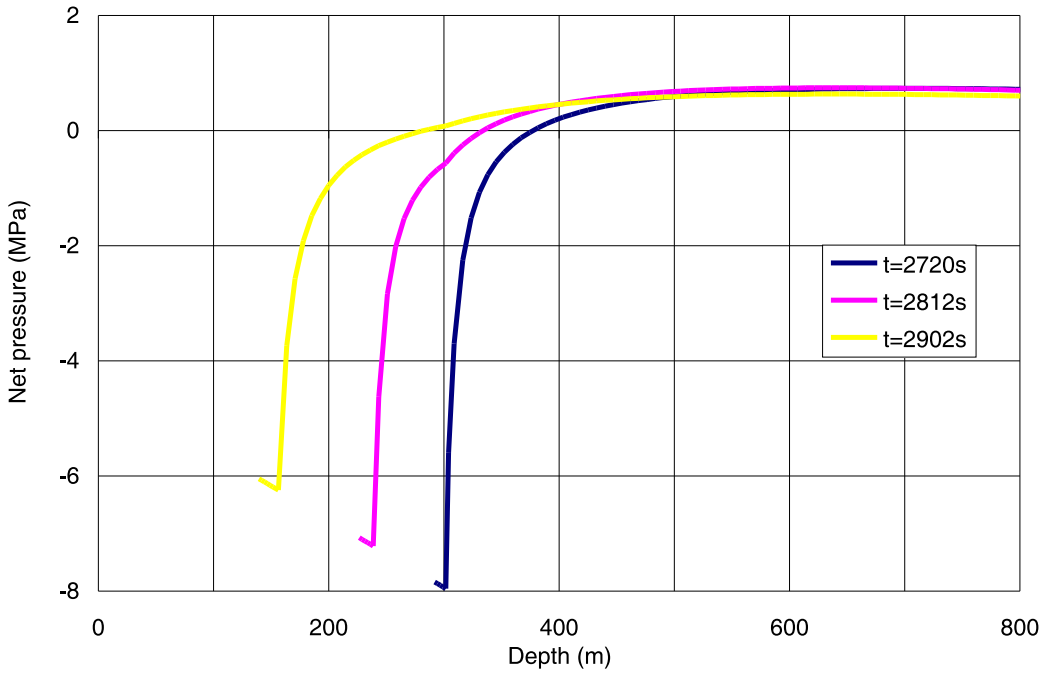

Figure II-48 Net pressure profile as a function of depth: $\mathcal{D} = 6.02$, $\kappa\rho_r = 1200$ kg/m^3, $\mu = 10$ Pa s, $v_\infty = 1$ m/s, $w_\infty = 0.25$ m, $\mathcal{S} = 1.59$, 25 percent leak-off at 300 m depth

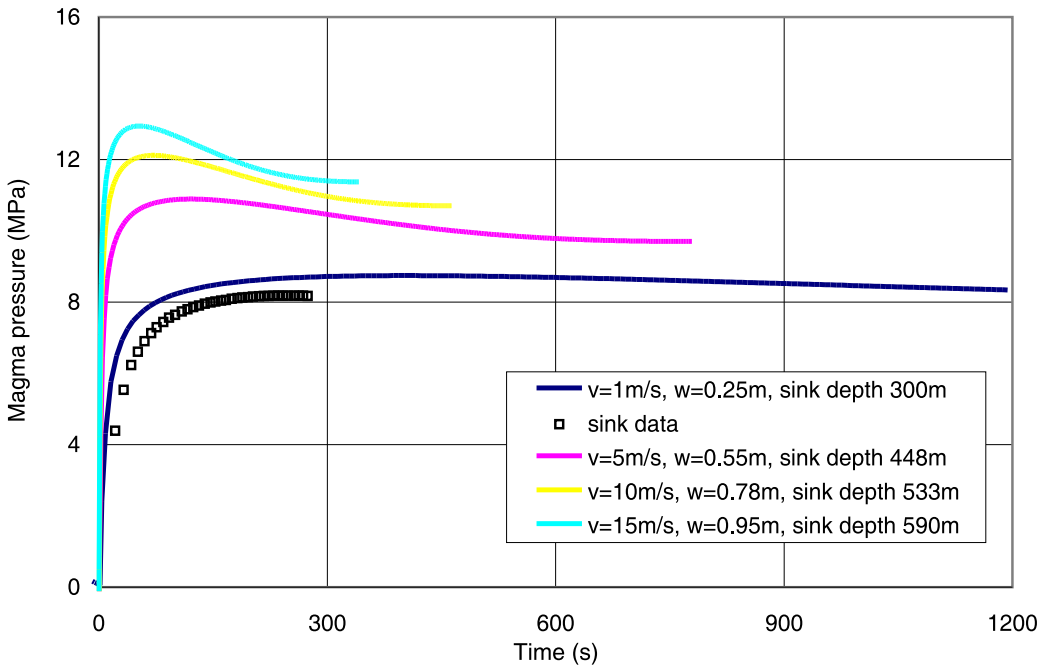

Figure II-49 Pressure history at leak-off point: $\mathcal{D} = 6.02$, $\kappa\rho_r = 1200$ kg/m^3, $\mu = 10$ Pa s, $\mathcal{S} = 1.59$, 25 percent leak-off

ATTACHMENT III

ACCEPTANCE CRITERIA AND KTIS

ATTACHMENT III
ACCEPTANCE CRITERIA AND KTIS

Information in this attachment identifies information in the Dike/Drift Interactions model report that addresses the YMRP acceptance criteria (NRC 2003 [DIRS 163274], Section 2.2.1.3.2.3.) associated with:

- Integrated subissues mechanical disruption of engineered barriers
- Volcanic disruption of waste packages
- Airborne transport of radionuclides.

This information is required by 10 CFR 63.21(c)(1), (3), (9), (10), (15), and (19) and 10 CFR 63.114 ((a) – (c) and (e) – (g).

The following discussion identifies the relevant acceptance criteria associated with each of the integrated subissues and briefly summarizes how the information in this report addresses the acceptance criteria.

III.1 INTEGRATED SUBISSUES MECHANICAL DISRUPTION OF ENGINEERED BARRIERS

III.1.1 Acceptance Criterion 1: System Description and Model Integration Are Adequate

The objective for modeling dike/drift interactions is described in Section 6.1 of the model report and includes describing the mechanical, thermal, and chemical environment that would be applied to waste packages should a future volcanic event disrupt the proposed repository.

1. Total System Performance Assessment (TSPA) adequately incorporates important design features, physical phenomena, and couplings, and uses consistent and appropriate assumptions throughout the mechanical disruption of engineered barrier abstraction process.

   This report documents the base-case model for dike propagation (Section 6.3.1) and alternative conceptual models (Section 6.3.3). Assumptions related to the model are described in Section 6.3.5, and uncertainties associated with the model are described in Section 6.3.2. Alternative models of dike propagation are described in Section 6.3.3. Results from exercise of the base-case model are described in Section 6.3.8. The magma flow model is described in Section 6.4.1. Assumptions related to the model are described in Section 6.4.6, and uncertainties are described in Section 6.4.3. Alternative models of magma flow are described in Section 6.4.4.

   Results from the exercise of the model are described in Section 6.4.10. Post-emplacement effects are described in terms of gas flow between drifts and magma cooling and solidification. A description of the model of gas flow between drifts is provided in Section 6.5.1.1. Principal uncertainties associated with the model are described in Section 6.5.1.1, and modifications to accommodate modeling of gas flow between drifts are described in Section 6.5.1.2.

Assumptions related to the model and boundary and initial conditions are described in Sections 6.5.1.3 and 6.5.1.4. Results of gas flow modeling for five (5) scenarios (that is, elevated-temperature gas transport, low-temperature gas transport, gas transport through a backfilled connecting drift, high-temperature-and-pressure gas transport, and high-temperature-and-pressure for a shorter period) are described in Section 6.5.1.6.

The analysis of magma cooling and solidification is described in Section 6.5.2. These analyses provide a basis to limit the flows of heat and gas to drifts adjacent to those directly intersected by a dike.

Partially coupled liquid and vapor phases associated with dike propagation modeling are described in Section 6.3.3.5. Process couplings in the analysis of gas flow between drifts are described in Section 6.5.1.

Coupled hydromechanical boundary conditions associated with dike propagation are described in Section 7.3.2.

Section 8.1.1 describes the conclusions with regard to dike propagation and provides the basis to discount the potential for development of the shock wave scenario proposed by Woods et al. 2002 [DIRS 163662]. Similarly, Section 8.1.2 provides a basis to discount the likelihood that a "dog-leg" scenario (Woods et al. 2002 [DIRS 163662]) would develop. Section 8.1.3 provides the basis to discount the likelihood that waste packages in Zone 2 would be damaged by thermal and/or gas flow effects. This last result is consistent with results documented in the model report *Igneous Intrusion Impacts on Waste Package and Waste Form* (BSC 2003 [DIRS 161810]).

2. The description of geological and engineering aspects of design features, physical phenomena, and couplings that may affect mechanical disruption of engineered barriers, is adequate. For example, the description may include materials used in the construction of engineered barrier components, environmental effects (e.g., temperature, water chemistry, humidity, radiation, etc.) on these materials, and mechanical failure processes and concomitant failure criteria used to assess the performance capabilities of these materials. Conditions and assumptions in the abstraction of mechanical disruption of engineered barriers are readily identified and consistent with the body of data presented in the description.

   Parameters used in the analysis of dike/drift interactions are summarized in Table 5. Assumptions related to modeling of dike propagation are described in Sections 5.1 and 6.3.5. Assumptions related to modeling of magma flow are described in Sections 5.2 and 6.4.6. Assumptions related to drift scale gals flow modeling are described in Section 5.3, and assumptions related to modeling of magma cooling and solidification are described in Section 5.4.

   Results of the modeling of dike propagation through the repository horizon are described in Sections 6.3.8 and 8.1.1. Results of modeling of magma flow, including flow in drifts and the effects on dike propagation to the surface, are described in Sections 6.4.10 and 8.1.2. Results of the analysis of post-emplacement effects,

including gas flow between drifts and magma cooling and solidification, are described in Sections 6.5.1.6, 6.5.2.6, and 8.1.3.

3. The abstraction of mechanical disruption of engineered barriers uses assumptions, technical bases, data, and models that are appropriate and consistent with other related U.S. Department of Energy abstractions. For example, assumptions used for mechanical disruption of engineered barriers are consistent with the abstraction of degradation of engineered barriers (NRC 2003 [DIRS 163274], Section 2.2.1.3.1). The descriptions and technical bases provide transparent and traceable support for the abstraction of mechanical disruption of engineered barriers.

   Parameters used in the analysis of dike/drift interactions are summarized in Table 5. Assumptions related to modeling of dike propagation are described in Sections 5.1 and 6.3.5. Assumptions related to modeling of magma flow are described in Sections 5.2 and 6.4.6. Assumptions related to drift scale gals flow modeling are described in Section 5.3, and assumptions related to modeling of magma cooling and solidification are described in Section 5.4. Results of the modeling of dike propagation through the repository horizon are described in Sections 6.3.8 and 8.1.1. Results of modeling of magma flow, including flow in drifts and the effects on dike propagation to the surface, are described in Sections 6.4.10 and 8.1.2. Results of the analysis of post-emplacement effects, including gas flow between drifts and magma cooling and solidification, are described in Sections 6.5.1.6, 6.5.2.6, and 8.1.3. Technical outputs of the modeling are described in Section 8.2.1, and output uncertainties are documented in Section 8.3. Use of the output of the dike propagation model are described in Section 6.3.10.

4. Boundary and initial conditions used in the TSPA abstraction of mechanical disruption of engineered barriers are propagated throughout the abstraction approaches.

   Boundary and initial conditions used in the modeling of dike propagation are described in Section 6.3.6. Boundary and initial conditions used in modeling magma flow are described in Section 6.4.7, and boundary and initial conditions used in modeling of gas flow between drifts are described in Section 6.5.1.4. Propagation of those boundary and initial conditions are described in the formulation of the models in Sections 6.3.7, 6.4.8, and 6.5.1.5, respectively.

5. Sufficient data and technical bases to assess the degree to which features, events, and processes have been included in this abstraction are provided.

   Features, events, and processes (FEPs) that are specifically addressed by information in this model report are identified in Section 6.2 and described in more detail in Table 4. The table identifies sections of the report in which disposition of the FEP is described and includes a summary of the Total System Performance Assessment – License Application (TSPA-LA) disposition. Basically, the output of the model provides descriptions of physical and chemical conditions for application in the TSPA-LA in-drift submodels.

6. The conclusion, with respect to the impact of transient criticality on the integrity of the engineered barriers, is defensible.

   This model report does not address the impact of transient criticality on the integrity of the engineered barriers.

7. Guidance in NUREG-1297 (Altman et al. 1988 [DIRS 103597]) and NUREG-1298 (Altman et al. 1988 [DIRS 103750]). or other acceptable approaches, is followed.

   NUREG-1297 describes the generic technical position with respect to the use of peer reviews on high-level waste repository programs. The use of information from the *Final Report of the Igneous Consequences Peer Review Panel* (Detournay et al. 2003 [DIRS 162914]) is summarized in Section 7.1. NUREG-1298 describes the generic technical position with respect to qualification of existing data. This report does not document the results of qualification of existing data.

III.1.2 Acceptance Criterion 2: Data Are Sufficient for Model Justification

1. Geological and engineering values used in the license application to evaluate mechanical disruption of engineered barriers, are adequately justified. Adequate descriptions of how the data were used, and appropriately synthesized into the parameters, are provided.

   Inputs for the modeling of dike propagation are described in Section 6.3.4. Inputs for the modeling of magma flow are described in Section 6.4.5, and inputs for the modeling of gas flow between drifts are described in Section 6.5.1.3. Use of the inputs are described in detail in Sections 6.3.7, 6.4.8, and 6.5.1.5, which describe the formulations of the dike propagation model, the magma flow model, and the model of gas flow between drifts, respectively.

2. Sufficient data have been collected on the geology of the natural system, engineering materials, and initial manufacturing defects, to establish initial and boundary conditions for the TSPA abstraction of mechanical disruption of engineered barriers.

   This acceptance criterion is not directly addressed by information in this model report. This report describes models for dike propagation, magma flow, gas flow between drifts, and evaluates the effects of magma cooling and solidification on the migration of heat and volatiles from drifts that are intersected by an ascending dike. Initial and boundary conditions used to develop models for dike propagation are described in Section 6.3.6. Initial and boundary conditions for the magma flow model are described in Section 6.4.7, and initial and boundary conditions for the model of gas flow between drifts are described in Section 6.5.1.4. Propagations of those boundary and initial conditions through the analysis are described in the formulation of the models in Sections 6.3.7, 6.4.8, and 6.5.1.5, respectively.

3. Data on geology of the natural system, engineering materials, and initial manufacturing defects used in the TSPA abstraction, are based on appropriate techniques. These techniques may include laboratory experiments, site-specific field measurements, natural analogue research, and process-level modeling studies. As appropriate, sensitivity or uncertainty analyses used to support the U.S. Department of Energy TSPA abstraction are adequate to determine the possible need for additional data.

   Parameters used in the analysis of dike/drift interactions are summarized in Table 5. Assumptions related to modeling of dike propagation are described in Sections 5.1 and 6.3.5. Assumptions related to modeling of magma flow are described in Sections 5.2 and 6.4.6. Assumptions related to drift scale gals flow modeling are described in Section 5.3, and assumptions related to modeling of magma cooling and solidification are described in Section 5.4. Results of the modeling of dike propagation through the repository horizon are described in Sections 6.3.8 and 8.1.1. Results of modeling of magma flow, including flow in drifts and the effects on dike propagation to the surface are described in Sections 6.4.10 and 8.1.2. Results of the analysis of post-emplacement effects, including gas flow between drifts and magma cooling and solidification, are described in Sections 6.5.1.6, 6.5.2.6, and 8.1.3.

4. Engineered barrier mechanical failure models for disruption events are adequate. For example, these models may consider effects of prolonged exposure to the expected emplacement drift environment, material test results not specifically designed or performed for the Yucca Mountain site, and engineered barrier component fabrication flaws.

   This acceptance criterion is not directly addressed by information in this model report. This report describes models for dike propagation, magma flow, gas flow between drifts, and evaluates the effects of magma cooling and solidification on the migration of heat and volatiles from drifts that are intersected by an ascending dike. Thus, this report provides the environmental parameters that could be used by downstream models or analyses of damage to waste packages and waste forms that result from exposure to magma or magmatic products. Results from the dike propagation model are described in Section 6.3.8, and use of the outputs is described in Section 6.3.10. Results from the magma flow model are described in Section 6.4.10, and results from the model of gas flow between drifts are described in Section 6.5.1.5. Technical outputs from these models are summarized in Section 8.2.1.

III.1.3 Acceptance Criterion 3: Data Uncertainty Is Characterized and Propagated Through the Model Abstraction

1. Models use parameter values, assumed ranges, probability distributions, and bounding assumptions that are technically defensible, reasonably account for uncertainties, and variabilities, and do not result in an under-representation of risk.

   Parameters used in the analysis of dike/drift interactions are summarized in Table 5. Assumptions related to modeling of dike propagation are described in Sections 5.1 and 6.3.5. Assumptions related to modeling of magma flow are described in Sections 5.2 and 6.4.6. Assumptions related to drift scale gals flow modeling are described in Section 5.3, and assumptions related to modeling of magma cooling and solidification are described in Section 5.4. Results of the modeling of dike propagation through the repository horizon are described in Sections 6.3.8 and 8.1.1. Results of modeling of magma flow, including flow in drifts and the effects on dike propagation to the surface, are described in Sections 6.4.10 and 8.1.2. Results of the analysis of post-emplacement effects, including gas flow between drifts and magma cooling and solidification, are described in Sections 6.5.1.6, 6.5.2.6, and 8.1.3.

   The representation of risk is a TSPA-LA responsibility. This report describes no results that could be used to evaluate the representation of risk from magma-drift and magma-waste package interactions. It is important to note that no parameters are passed from these models directly to the TSPA-LA. Rather, parameter time histories developed in this report could be used by the waste form and waste package groups to determine possible damage states, which then are passed to TSPA-LA.

2. Process-level models used to represent mechanically disruptive events, within the emplacement drifts at the proposed Yucca Mountain repository, are adequate. Parameter values are adequately constrained by Yucca Mountain site data, such that the estimates of mechanically disruptive events on engineered barrier integrity are not underestimated. Parameters within conceptual models for mechanically disruptive events are consistent with the range of characteristics observed at Yucca Mountain.

   The base-case conceptual models are described in Sections 6.3.1, 6.4.1, and 6.5.1.1, respectively. Alternative conceptual models of dike propagation and magma flow are described in Sections 6.3.3 and 6.4.4, respectively. Alternative models used in the analysis of gas flow between drifts are described in Section 6.5.1.6. Selection and use of parameter values was described in item 1 of this section.

   Assumptions needed to support the modeling of dike propagation and magma flow interactions are described in Section 5. Additional descriptions of the assumptions supporting the dike propagation model are provided in Sections 6.3.5. Similar descriptions of the assumptions supporting the magma flow model are provided in Section 6.4.6. Boundary and initial conditions for the modeling of gas flow between drifts are described in Section 6.5.1.4, and information needed for the analysis of magma cooling and solidification are described in Section 6.5.2.1.

Inputs for modeling dike propagation are described in Section 6.3.4, and inputs for modeling magma flow are described in Section 6.4.5. Inputs for modeling gas flow between drifts are described in Section 6.5.1.4, and inputs to analyze magma cooling and solidification are described in Section 6.5.2.4.

Modeling results for the dike propagation model are described in Section 6.3.8, and results for the magma flow model are described in Section 6.4.10. Results from the modeling of gas flow between drifts are described in Section 6.5.1.6, and conclusions from the analysis of magma cooling and solidification are presented in Section 6.5.2.6. For waste packages in Zone 2, results described in Sections 6.5.1.6 and 6.5.2.6 indicate that exposure to magmatic products would produce only limited damage because the repository host rock is expected to limit heat conduction and migration of volatile components to Zone 2.

It is important to note the no parameters are passed from these models directly to the TSPA-LA. Rather, parameter time histories developed here could used by the waste form and waste package groups to determine possible damage states, which then are passed to TSPA-LA.

3. Uncertainty is adequately represented in parameter development for conceptual models, process-level models, and alternative conceptual models considered in developing the TSPA abstraction of mechanical disruption of engineered barriers. This may be done either through sensitivity analyses or use of conservative limits.

   Uncertainties associated with the dike propagation model are described in Section 6.3.2, and alternative models are described in Section 6.3.3. Uncertainties associated with the magma flow model are described in Section 6.4.3, and alternative models are described in Section 6.4.4. Uncertainties associated with the model of gas flow between drifts are described in Section 6.5.1.1. Uncertainties associated with the analysis of magma cooling and consolidation are described in Section 6.5.2.1. Supporting analyses and model applications related to the use of the dike propagation model are described in Section 6.3.9. Supporting analyses and model applications related to the use of the magma flow model are described in Section 6.4.11, and testing, sensitivity, and calibration activities for the magma flow model are described in Section 6.4.9. Boundary and initial conditions for the dike propagation model are described in Section 6.3.6. Boundary and initial conditions for the magma flow model are described in Section 6.4.7. Boundary and initial conditions for the model of gas flow between drifts are described in Section 6.5.1.4, and thermal property contrasts and latent heat information used in the analysis of magma cooling and solidification are described in Section 6.5.2.4.

   It is important to note the no parameters are passed from these models directly to the TSPA-LA. Rather, parameter time histories developed here could used by the waste form and waste package groups to determine possible damage states, which then are passed to TSPA-LA.

4. Where sufficient data do not exist, the definitions of parameter values and conceptual models are based on appropriate use of expert elicitation, conducted in accordance with NUREG-1563 (Kotra et al. 1996 [DIRS 100909]). If other approaches are used, the U.S. Department of Energy adequately justifies their use.

   Expert elicitation was not used in the development of the models of dike propagation, magma flow, gas flow between drift or magma cooling and solidification. However, results of the *Final Report of the Igneous Consequences Peer Review Panel* (Detournay et al. 2003 [DIRS 162914]) were used in the development of the dike propagation and magma flow models.

III.1.4 Acceptance Criterion 4: Model Uncertainty Is Characterized and Propagated Through the Model Abstraction

1. Alternative modeling approaches of features, events, and processes are considered and are consistent with available data and current scientific understanding, and the results and limitations are appropriately considered in the abstraction.

   Alternative conceptual models that were considered in the development of the models of dike propagation, magma flow, gas flow between drifts, and magma cooling and solidification were documented in Sections 6.3.3, 6.4.4, 6.5.1.1, and 6.5.2.1, respectively. Features, events and processes that were considered in developing these models were identified in Section 6.2 and described in Table 4. Consistency of the modeling approaches is described in terms of corroboration with boundary conditions in Section 7.3, corroboration with observations at the Parícutin analogue (Section 7.4), and corroboration of the mechanical behavior of the backfill with analogue behavior from South African gold mines (Section 7.5). Uncertainties associated with the outputs from these models are described in Section 8.3, and limitations associated with the models are documented in Section 1.3.1.

2. Consideration of conceptual model uncertainty is consistent with available site characterization data, laboratory experiments, field measurements, natural analog information and process-level modeling studies; and the treatment of conceptual model uncertainty does not result in an under-representation of the risk estimate.

   Model uncertainties associated with the dike propagation model are described in Section 6.3.2. Uncertainties associated with the magma flow model are described in Section 6.4.3. Uncertainties associated with the model of gas flow between drifts are described in Section 6.5.1.1. Uncertainties associated with the analysis of magma cooling and consolidation are described in Section 6.5.2.1.

   Inputs for the dike propagation model are described in Section 6.3.4. Inputs for the magma flow model are described in Section 6.4.5. Inputs for the model of gas flow between drifts are described in Section 6.5.1.3, and inputs needed for the analysis of magma cooling and solidification are described in Section 6.5.2.1.1.

   Consistency of the modeling approaches are described in terms of corroboration with boundary conditions in Section 7.3, corroboration with observations at the Parícutin

analogue (Section 7.4), and corroboration of the mechanical behavior of the backfill with analogue behavior from South African gold mines (Section 7.5). Uncertainties associated with the outputs from these models are described in Section 8.3, and limitations associated with the models are documented in Section 1.3.1.

The representation of risk is a TSPA-LA responsibility. This report describes no results that could be used to evaluate the representation of risk from magma-drift and magma-waste package interactions.

3. Appropriate alternative modeling approaches are investigated that are consistent with available data and current scientific knowledge and that appropriately consider their results and limitations using tests and analyses that are sensitive to the processes modeled.

   Alternative conceptual models that were considered in the development of the models of dike propagation, magma flow, gas flow between drifts, and magma cooling and solidification were documented in Sections 6.3.3, 6.4.4, 6.5.1.1, and 6.5.2.1, respectively. Results from the models are described in Sections 6.3.8, 6.4.10, 6.5.1.6, and 6.5.2.6, respectively. Uncertainties associated with model outputs are described in Sections 8.3.1, 8.3.2, 8.3.3, and 8.3.4, respectively. Limitations associated with the models are documented in Section 1.3.1.

III.1.5 Acceptance Criterion 5: Model Abstraction Output Is Supported by Objective Comparisons

1. Models implemented in this TSPA abstraction provide results consistent with output from detailed process-level models and/or empirical observations (laboratory and field testings and/or natural analogues).

   Results from the models are described in Sections 6.3.8, 6.4.10, 6.5.1.6, and 6.5.2.6, respectively. Uncertainties associated with model outputs are described in Sections 8.3.1, 8.3.2, 8.3.3, and 8.3.4, respectively. Limitations associated with the models are documented in Section 1.3.1.

   Zone 1 environmental conditions documented in Section 6.4.10 support the TSPA-LA assumption that all waste packages contacted by magma are damaged to the extent that they provide no further protection for the waste. However, results documented in Sections 6.5.1.6 and 6.5.2.6 indicate that temperatures and volatile concentrations in Zone 2 drifts are not likely to reach levels that the integrity of waste packages in Zone 2 are adversely affected.

2. Outputs of mechanical disruption of engineered barrier abstractions reasonably produce or bound the results of corresponding process-level models, empirical observations, or both.

   This model report provides environmental conditions related to dike propagation, magma flow, gas flow between drifts, and magma cooling and solidification that could be used to develop models of waste package and waste form damage from exposure to

magma or magmatic products. However, this report does not develop models or analyses of waste package or waste form damage. Those models are developed in the model report *Igneous Intrusion Impacts on Waste Package and Waste Form* (BSC 2003 [DIRS 161810]). It is important to note the no parameters are passed from these models directly to the TSPA-LA. Rather, parameter time histories developed here could used by the waste form and waste package groups to determine possible damage states, which then are passed to TSPA-LA.

3. Well-documented procedures that have been accepted by the scientific community to construct and test the mathematical and numerical models, are used to simulate mechanical disruption of engineered barriers.

   The computer codes used in the modeling activities documented in this report are described in Table 1. Validation of the models documented in this report is described in Section 7. Acceptance criteria used to evaluate the models in terms of corroboration with boundary conditions are described in Sections 7.3.2.2, 7.3.3.1, 7.3.4.1, 7.3.5.1, and 7.3.6.1, respectively. Acceptance criteria used in the corroboration with observations at the Parícutin analogue are described in Section 7.4.1, and acceptance criteria for corroboration of the mechanical behavior of the backfill with analogue behavior from South African gold mines are described in Section 7.5.1.

4. Sensitivity analyses or bounding analyses are provided to support the TSPA abstraction of mechanical disruption of engineered barriers that cover ranges consistent with site data, field or laboratory experiments and tests, and natural analogue research.

   Supporting analyses and model applications related to the use of the dike propagation model are described in Section 6.3.9. Supporting analyses and model applications related to the use of the magma flow model are described in Section 6.4.11, and testing, sensitivity, and calibration activities for the magma flow model are described in Section 6.4.9. Boundary and initial conditions for the dike propagation model are described in Section 6.3.6. Boundary and initial conditions for the magma flow model are described in Section 6.4.7. Boundary and initial conditions for the model of gas flow between drifts are described in Section 6.5.1.4, and thermal property contrasts and latent heat information used in the analysis of magma cooling and solidification are described in Section 6.5.2.4.

   It is important to note that no parameters are passed from these models directly to the TSPA-LA. Rather, parameter time histories developed here could used by the waste form and waste package groups to determine possible damage states, which then are passed to TSPA-LA.

III.2 VOLCANIC DISRUPTION OF WASTE PACKAGES

III.2.1 Acceptance Criterion 1: System Description and Model Integration Are Adequate

1. TSPA adequately incorporates important design features, physical phenomena, and couplings, and uses consistent and appropriate assumptions throughout the volcanic disruption of the waste package abstraction process.

   The information in this report describes the basic model for dike propagation (Section 6.3.1). The model for magma flow in drifts is described in Section 6.4.1, and the model for gas flow between drifts is described in Section 6.5.1). Assumptions for the dike propagation model are documented in Sections 5.1 and 6.3.5. Assumptions for the magma flow model are described in Sections 5.2 and 6.4.6.

   Assumptions for the drift scale gas flow model are described in Section 5.3. Assumptions for magma cooling and solidification are documented in Section 5.4. Descriptions of process couplings are also provided—e.g., effects of natural stresses on dike propagation (in Section 6.3.9.1), effects of repository structures on dike propagation (in Section 6.2.9.2), effects of material losses from a dike (in Section 6.3.9.3), and phenomena associated with first intrusion (in Section 6.3.9.4).

   Effects of natural stresses, including topographic effects, on fracture and dike propagation are discussed in Section 6.3.9.1. Effects of stresses caused by repository structures are described in Section 6.3.9.2, and thermal stresses are described in Section 6.3.9.2.2, but effects of volatile exsolution on fracture and dike propagation are generally not included as described in Section 6.3.9.2.3.1.7. Effects of loss of hydrofracture driving fluid due to flow of magma into drifts are described in Section 6.3.9.2.3.2.2. Effects of vesiculation and fragmentation of a magma in a drift are also generally not included, as described in Section 6.3.9.2.3.1.7, but the restrictions on the development of the "dog-leg" scenario are described in Section 6.4.10.2.

2. Models used to assess volcanic disruption of waste packages are consistent with physical processes generally interpreted from igneous features in the Yucca Mountain region and/or observed at active igneous systems.

   Consistency of fracture and dike propagation models used in this report with physical processes is documented in Section 7.3. Dike propagation boundary conditions are described in Section 7.3.1. Coupled hydromechanical boundary conditions are described in Section 7.3.2. One-dimensional filling of a porous region is described in Section 7.3.3, and pressure distribution in a fracture with uniform permeability is described in Section 7.3.4. Corroboration of the model with observations at Parícutin are described in Section 7.4. Limitations of the dike propagation model are described in Section 1.3.1.1. Limitations of the magma flow model and post-emplacement analyses are described in Sections 1.3.1.2 and 1.3.1.3, respectively.

3. Models account for changes in igneous processes that may occur from interactions with engineered repository systems.

Effects of stresses from excavation of the repository are described in Section 6.3.9.2.1, and thermal stresses are described in Section 6.3.9.2.2. Effects of gas seepage on fracture and dike propagation are generally not included, as described in Section 6.3.9.2.3.1.7, but effects of loss of hydrofracture driving fluid due to flow of magma into drifts are described in Section 6.3.9.2.3.2.2. Effects of vesiculation and fragmentation of a magma in a drift are also generally not included, as described in Section 6.3.9.2.3.1.7, but the restrictions on the development of the "dog-leg" scenario are described in Sections 6.4.10.2 and 6.4.11.3.

A summary of the effects of drifts on dike propagation is presented in Section 8.1.1. A summary of magma-induced environments in drifts is presented in Section 8.1.2 and 8.1.3, and magma breakout to the surface in summarized in Section 8.1.2.

4. Guidance in NUREG-1297 (Altman et al. 1988 [DIRS 103597]) and NUREG-1298 (Altman et al. 1988 [DIRS 103750], or other acceptable approaches is followed.

   The *Final Report of the Igneous Consequences Peer Review Panel* (Detournay et al. 2003 [DIRS 162914], p. 44–45) addressed the limitations of modeling dike propagation, when assuming that the magma is an incompressible fluid (whereas real magma would be compressible). The peer review conclusions with respect to effects of compressibility are addressed in Section 1.3.1.1 in this model report. Use of the results of the Peer Review for model validation purposes is described in Section 7.1. Documentation of the peer review process consistency with NUREG-1297 (Altman et al. 1988 [DIRS 103597]) was provided in the *Peer Review Plan for the Igneous Consequences Peer Review*, *Revision 1* (Hess, K.G. 2002 [DIRS 161507]).

III.2.2 Acceptance Criterion 2: Data Are Sufficient for Model Justification

1. Parameter values used in the safety case to evaluate volcanic disruption of waste packages are sufficient and adequately justified. Adequate descriptions of how the data were used, interpreted, and appropriately synthesized into the parameters are provided.

   This report provides an alternative model for the analysis of volcanic disruption of waste packages that is documented in *Igneous Intrusion Impacts on Waste Package and Waste Form* (BSC 2003 [DIRS 161810]). Results of base-case modeling documented in this report are described in Section 6.3.8, and supporting analyses and model applications are described in Section 6.3.9. Parameter values and associated uncertainties for environmental variables associated with effusive flow into drifts are summarized in Table 11. Use of outputs from the model of dike propagation is described in Section 6.3.10.

   Results from the model for magma flow through mined openings are described in Section 6.4.10.1, and results addressing the "dog-leg" scenario are described in Section 6.4.10.2. Results of the analysis of post-emplacement effects are described in Section 6.5.1.6.

2. Data used to model processes affecting volcanic disruption of waste packages are derived from appropriate techniques. These techniques may include site-specific field measurements, natural analogue investigations, and laboratory experiments.

   The models described in this report provide basic parameters associated with the in-drift environmental conditions that would attend intersection of the repository by an ascending basalt dike. Inputs to the dike propagation model are described in Section 6.3.4. Inputs to the magma flow model are described in Section 6.4.5. Inputs for the analysis of post-emplacement effects are described in Section 6.5.1.3.

3. Sufficient data are available to integrate features, events, and processes, relevant to volcanic disruption of waste packages into process-level models, including determination of appropriate interrelationships and parameter correlations.

   Features, events, and processes included in the dike/drift interaction model are identified in Section 6.2. Table 4 describes the features, events, and processes considered for TSPA-LA, provides a linkage to the TSPA-SR, and summarizes the TSPA-LA disposition.

4. Where sufficient data do not exist, the definition of parameter values and associated conceptual models is based on appropriate use of expert elicitation, conducted in accordance with NUREG-1563 (Kotra et al. 1996 [DIRS 100909]). If other approaches are used, the U.S. Department of Energy adequately justifies their use.

   Inputs to the dike propagation model are described in Section 6.3.4. Inputs to the magma flow model are described in Section 6.4.5. Inputs for the analysis of post-emplacement effects are described in Section 6.5.1.3. Expert elicitation was not used in the development of these models.

III.2.3 Acceptance Criterion 3: Data Uncertainty Is Characterized and Propagated Through the Model Abstraction

This report documents the development of process models for dike propagation, magma flow in drifts, gas-flow between drifts, and magma breakout to the surface. Uncertainties associated with each process model and the treatment of those uncertainties are documented in this report. Sources for all inputs and references to sections of this report that provide further discussion of the use of the inputs are provided in Table 2.

1. Models use parameter values, assumed ranges, probability distributions, and bounding assumptions that are technically defensible, and reasonably account for uncertainties and variabilities, and do not result in an under-representation of the risk estimate.

   Detailed discussions of the enumeration of the process models describe how parameter uncertainties are propagated. Attachment I in this model report describes the mathematical formulation of the NPHF2D code for modeling hydraulic fractures near the free surface. Attachment II in this model report documents the formulation of the analysis of dike propagation using NPHF2D.

The information in this report describes the basic model for dike/drift interactions in terms of process models for dike propagation (Section 6.3.1), magma flow in drifts (Section 6.4.1), gas flow between drifts (Section 6.5.1). Magma breakout to the surface is treated as a supporting analysis (Section 6.4.11.6). Assumptions for the dike propagation model are described in Sections 5.1 and 6.3.5. Assumptions for the magma flow model are described in Sections 5.2 and 6.4.6. Assumptions for the drift-scale gas flow model are described in Section 5.3.

Descriptions of process couplings are also provided—e.g., effects of natural stresses, including topographic effects, on dike propagation (in Section 6.3.9.1), effects of repository structures on dike propagation (in Section 6.2.9.2), effects of material losses from a dike (in Section 6.3.9.3), and phenomena associated with first intrusion (in Section 6.3.9.4)).

Effects of stresses from excavation of the repository are described in Section 6.3.9.2.1. Effects of thermal stresses are described in Section 6.3.9.2.2, but effects of gas seepage on fracture and dike propagation are generally not included, as described in Section 6.3.9.2.3.1.7. Effects of loss of hydrofracture driving fluid due to flow of magma into drifts are described in Section 6.3.9.2.3.2.2. Effects of vesiculation and fragmentation of a magma in a drift are also generally not included, as described in Section 6.3.9.2.3.1.7.

Inputs for the dike propagation model are described in Section 6.3.4, and uncertainties associated with the dike propagation model are described in Section 6.3.2. Inputs for the magma flow model are described in Section 6.4.5, and uncertainties associated with the model are described in Section 6.4.3. Inputs for the drift-scale gas flow model are described in Section 6.5.1.3, and uncertainties associated with the model are described in Section 6.5.1.1.

Discussion of the effects of parameters developed in this report on the TSPA-LA estimation of risk is beyond the scope of this report.

2. Parameter uncertainty accounts quantitatively for the uncertainty in parameter values observed in site data and the available literature (i.e., data precision), and for the uncertainty in abstracting parameter values to process-level models (i.e., data accuracy).

   Data, parameters, and other model inputs are described in Section 4.1.1 and Table 2. Tables 2 also includes identification of the specific sources for the parameters. Additional discussion of the inputs for the dike propagation model is provided in Section 6.3.4, and similar discussions for the magma flow model and the gas flow model are provided in Sections 6.4.5 and 6.5.1.3, respectively. A summary of the cases run and the input parameters for the dike/drift model are presented in Table 7. Table 9 presents similar information for the magma flow model. Results of gas flow modeling for five (5) model scenarios are presented in Section 6.5.1.6.

3. Where sufficient data do not exist, the definition of parameter values and associated conceptual models is based on appropriate use of expert elicitation, conducted in accordance with NUREG-1563 (Kotra et al. 1996 [DIRS 100909]). If other approaches are used, the U.S. Department of Energy adequately justifies their use.

   Inputs to the dike propagation model are described in Section 6.3.4. Inputs to the magma flow model are described in Section 6.4.5. Inputs for the analysis of gas flow between drifts are described in Section 6.5.1.3. Expert elicitation was not used in the development of these models.

III.2.4 Acceptance Criterion 4: Model Uncertainty Is Characterized and Propagated Through the Model Abstraction

1. Alternative modeling approaches to volcanic disruption of waste packages are considered and are consistent with available data and current scientific understandings, and the results and limitations are appropriately considered in the abstraction.

   Uncertainties associated with the dike propagation model are described in Section 6.3.2, and uncertainties associated with the magma flow model are described in Section 6.4.3. Alternative modeling approaches considered in the development of the dike propagation model, the magma and gas flow model, and the drift-scale gas flow model are described, respectively, in Sections 6.3.3, 6.4.4, and 6.5.1.6.

   Consistency of the models with available data and current scientific understanding is described in Sections 6.3.1, 6.4.1, and 6.5.1.1. Limitations of the models are described in Sections 1.3.1.1, 1.3.1.2, and 1.3.1.3, respectively.

   Modeling results and use of outputs from the models are described in Sections 6.3.10, 6.4.10, and 6.5.1.6. Base case model results for the dike propagation model are described in Section 6.3.8.

   Effects of material loss on dike propagation are described in Section 6.3.9.3. Phenomena associated with first intrusion into a drift (magma-induced environments in drifts) are described in Section 6.3.9.4, and magma breakout to the surface is described in Section 6.4.11.6.

   This report does not address how outputs and results documented in this report are considered by downstream users.

2. Uncertainties in abstracted models are adequately defined and documented, and effects of these uncertainties are assessed in the TSPA.

   Effects of uncertainties in data and models have been addressed in descriptions of supporting analyses and model applications. For the dike propagation model, the analyses are described in Section 6.3.9, and for the magma flow model the analyses are described in Section 6.4.11. Similar analyses for the gas flow model, based on five model cases, are documented in Section 6.5.1.6. However, this report does not discuss the how the parameters are used in the downstream models; nor does this report

discuss methods used to abstract parameter values into the downstream, process-level models. This report also does not address the propagation of the effects of uncertainties into the TSPA.

3. Consideration of conceptual model uncertainty is consistent with available site characterization data, laboratory experiments, field measurements, natural analogue information and process-level modeling studies; and the treatment of conceptual model uncertainty does not result in an under-representation of the risk estimate.

   Limitations associated with the dike propagation model, the magma flow model, and the post-emplacement analysis (gas flow model) are described in Sections 1.3.1.1, 1.3.1.2, and 1.3.1.3, respectively. Specific uncertainties associated with the dike propagation model are described in Section 6.3.2, and alternative models for dike propagation are described in Section 6.3.3. Uncertainties associated with the magma flow model are described in Section 6.4.3, and alternative models considered are described in Section 6.4.4.

   Corroboration of boundary conditions for the dike propagation model are described in Section 7.3.1. Use of the results of the Peer Review for model validation purposes is described in Section 7.1.

   Consistency of the conceptual models with site data and other information is described in the model descriptions in Sections 6.3.1, 6.4.1, and 6.5.1.1. Discussion of uncertainties in outputs from the dike propagation model is provided in Section 8.3.1. Similar discussions for the magma-backfill interaction model, the magma flow model, and the drift-scale gas flow model are provided in Sections 8.3.2, 8.3.3, and 8.3.2, respectively.

   Discussion of the effects of conceptual model uncertainty on the TSPA-LA representation of the risk estimate is beyond the scope of this report.

III.2.5 Acceptance Criterion 5: Model Abstraction Output Is Supported by Objective Comparisons

The models described in this report describe dike propagation near drifts, magma and gas flow in drifts, and drift-scale gas flow. The report provides conclusions about effects of drifts on dike propagation, magma-induced environments in drifts, and magma breakout to the surface. Consistency of model abstractions with observations is described in Section 7.3.

The report does not describe the effects on waste packages of exposure to magma or magmatic environmental conditions; nor does the report document abstractions of the volcanic disruption of waste packages.

III.3 AIRBORNE TRANSPORT OF RADIONUCLIDES

The models of dike propagation near drifts, magma and gas flow in drifts, and drift-scale gas flow constrain the conceptual models that support generation of the source term for the analysis of airborne transport of radionuclides.

The outputs from this report provide no direct parameter inputs to the analysis and modeling of airborne transport of radionuclides.

III.3.1 Acceptance Criterion 1: System Description and Model Integration Are Adequate

Models account for changes in igneous processes that may occur from interactions with engineered repository systems.

This report documents three (3) models related to interactions between repository emplacement drifts and an ascending basaltic dike that intersects the repository. The dike propagation model describes the processes of fracture development and propagation of the dike (Section 6.3.1). The effects of repository structure on dike propagation, including stresses produced by excavation of the repository and the effects of thermal stresses produced by loading of the repository, are described in Sections 6.3.9.2 and 8.1. The effects on dike propagation of loss of magmatic material through leakage into the repository are described in Section 6.3.9.3. The changes that occur in the ascending dike when it intersects the repository are described in Section 6.3.9.4, including effects of decompression, separation, and release of volatile components. Magma flow through mined openings, magma-backfill interactions, and backfill-drift interactions are described in Section 6.4.10.1.

The models provide constraints on the in-drift environment that could develop after a dike has intersected the repository. Some model results, such as the likelihood of the "dog-leg" scenario (Sections 6.4.10.2, 6.4.11.3, and 6.4.11.5), constrain the conceptual models of extent and severity of damage to waste packages. Other results describe the environmental conditions that could develop in an intersected drift (Sections 6.3.9.4, 6.4.10.1, and 6.4.10.2), the durations of those conditions (Sections 6.4.11.4, 6.5.1, and 6.5.2), and constrain analyses of damage to waste packages exposed to magmatic conditions but not directly contacted by magma. These same results could be used to constrain analyses of high-level waste incorporation in magma because some of the incorporation mechanisms are related to the chemical environment that would exist at the time of exposure of the waste.

III.3.2 Acceptance Criterion 2: Data Are Sufficient for Model Justification

Data developed in this report do not provide direct inputs for the modeling of airborne transport of radionuclides. Thus, data developed in this report do not support justification of the use of the ASHPLUME model. Data used to model airborne transport of radionuclides will be documented in a model report entitled *Atmospheric Dispersal and Deposition of Tephra from a Potential Volcanic Eruption at Yucca Mountain, Nevada*.

III.3.3 Acceptance Criterion 3: Data Uncertainty Is Characterized and Propagated Through the Model Abstraction

Data developed in this report do not provide direct inputs for the modeling of airborne transport of radionuclides. Thus, data developed in this report do not support characterization of the uncertainties associated with the use of the ASHPLUME model. Data uncertainties associated with modeling airborne transport of radionuclides will be documented in a model report entitled *Atmospheric Dispersal and Deposition of Tephra from a Potential Volcanic Eruption at Yucca Mountain, Nevada*.

III.3.4 Acceptance Criterion 4: Model Uncertainty Is Characterized and Propagated Through the Model Abstraction

This report documents models of dike propagation near drifts, magma and gas flow in drifts, and drift-scale gas flow. None of these models is used directly in the representation of airborne transport of radionuclides. Descriptions of the ASHPLUME model and model uncertainty will be documented in a model report entitled *Atmospheric Dispersal and Deposition of Tephra from a Potential Volcanic Eruption at Yucca Mountain, Nevada*.

III.3.5 Acceptance Criterion 5: Model Abstraction Output Is Supported by Objective Comparisons

This report documents models of dike propagation near drifts, magma and gas flow in drifts, and drift-scale gas flow. None of these models is used directly in the representation of airborne transport of radionuclides. ASHPLUME model outputs will be documented in a model report entitled *Atmospheric Dispersal and Deposition of Tephra from a Potential Volcanic Eruption at Yucca Mountain, Nevada*.

INTENTIONALLY LEFT BLANK